Medical Radiology
Diagnostic Imaging

M.F. Reiser
H. Hricak
M. Knauth

Christoph Johannes Zech
Carlo Bartolozzi
Richard Baron
Maximilian F. Reiser
Editors

Multislice-CT of the Abdomen

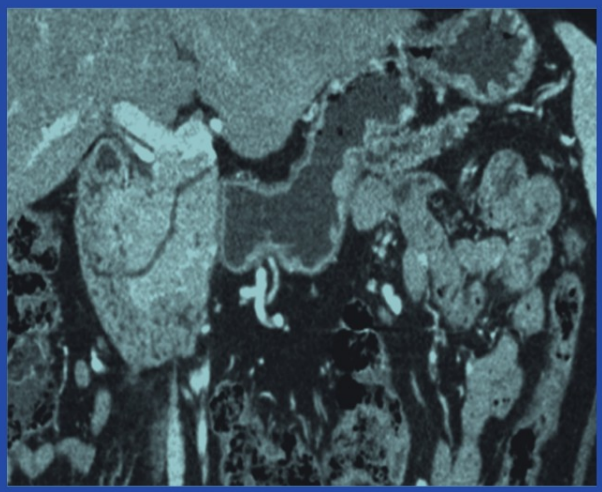

Springer

Medical Radiology

Diagnostic Imaging

For further volumes:
http://www.springer.com/series/4354

Christoph Johannes Zech
Carlo Bartolozzi • Richard Baron
Maximilian F. Reiser
Editors

Multislice-CT of the Abdomen

Foreword by
Maximilian F. Reiser

Springer

Christoph Johannes Zech
Department of Clinical Radiology
University Hospitals Munich, Großhadern
Marchioninistraße 15
81377 Munich
Germany

Richard Baron
Department of Radiology
The University of Chicago
5841 S. Maryland Ave MC, 2026
Chicago, IL 60611
USA

Carlo Bartolozzi
Department of Oncology
Department of Transplants
and Advanced Technology
University of Pisa,Via Paradisa 2
56127 Pisa
Italy

Maximilian F. Reiser
Department of Clinical Radiology
University Hospitals Munich, Großhadern
Marchioninistraße 15
81377 Munich
Germany

ISSN 0942-5373
ISBN 978-3-642-17862-7 ISBN 978-3-642-17863-4 (eBook)
DOI 10.1007/978-3-642-17863-4
Springer Heidelberg New York Dordrecht London

Library of Congress Control Number: 2012936367

Printed on acid-free paper

Springer is part of Springer Science+Business Media (www.springer.com)

Foreword

Computed Tomography, in contrast to other imaging modalities, has long been regarded as a not very attractive working horse in diagnostic imaging. This notion greatly changed when Spiral-CT and Multislice-CT (MSCT) came up. A large number of acquisition parameters, reconstruction modes and contrast media protocols are available and have to be scientifically explored. Since MSCT proved so effective and versatile, there was a steep increase in the utilization of this modality. The consequence was a considerable increase of radiation exposure of the population which in turn provoked criticism that resulted in reconsidering the use of MSCT by the radiological community.

In this edition of Medical Radiology/Diagnostic Imaging recognized experts in the field will elucidate the technique and physical background, future technological developments, radiation dose as well as contrast media application in protocols in MSCT of the abdomen.

I would like to express my sincere gratitude to the editors of this volume for gathering such a unique group of authors covering the fields of technique, liver and biliary system, pancreas and spleen, kidney and urogenital system as well as bowel and peritoneal cavity. The different sections are organized according to pathologic mechanisms, such as inflammatory lesions, tumors, traumatic and post-surgical findings. In this way, an excellent overview on aspects important for the daily clinical practice could be achieved.

I am confident, that this monograph will become indispensable for all those who are involved in abdominal imaging and will provide an excellent guideline for performing state-of-the-art MSCT examinations of the abdomen with adequate technique following diligent selection of the patients and for interpretation of MSCT scans.

This volume of Medical Radiology/Diagnostic Imaging also is in line with the mission and vision of the series—to bring together well known experts in the field, in order to offer our readers an up-to-date and scientifically based overview. I would also like to thank Springer Publishers for their great support and continuous enthusiasm in promoting this important endeavour.

Prof. Dr. med. Dr. h.c. Maximilian F. Reiser FACR, FRCR
Professor and Chairman
Institute of Clinical Radiology
Ludwig-Maximilians-University Hospital Munich

Preface

Diagnostic imaging of abdominal pathologies represents a large amount of the daily workload in radiology facilities worldwide. The impact of Radiology in the management of such patients is clearly evidenced by the fact that most clinical decisions in abdominal disease depend on the outcome of imaging procedures in ambulatory and hospital settings. Computed tomography (CT) has evolved over the past 40 years and become the widely acknowledged key component in the diagnostic work-up of patients with abdominal diseases. The development of multislice CT (MSCT) has been a major contributing factor adding to the breadth and depth of abdominal evaluation possible with imaging. It is therefore natural and timely to develop a book solely dedicated to current techniques and applications of *MSCT in the abdomen*.

While other modalities such as ultrasound or magnetic resonance imaging have proved to be superior in certain specific situations, MSCT remains the most used and relied upon technique as a general abdominal imaging tool, offering robust versatility with detailed anatomic and physiologic information , equally applicable in unstable patients. Due to developments in scanner technology and reconstruction algorithms, the radiation dose is continuing to decrease. All these unique properties make MSCT the backbone of abdominal evaluation for most institutions.

The concept for this book is to provide a broad overview of relevant abdominal pathologies and associated CT findings. In order to keep the length of the book within reasonable limits we focused on frequent and relevant findings to provide a practical educational and clinical tool. Our aim is to help radiologists in daily practice meet their practical clinical needs in determining the examination strategy, optimizing the examination protocol and interpretation of the images rather than being another encyclopaedia of abdominal pathologies.

We want to thank all contributing authors, internationally known experts in their field, for their outstanding contributions. Our publisher Springer-Verlag has supported us from the draft of this book to the final editing process with their invaluable professional and kind assistance. Finally we want to thank our readers for the trust in our book and we hope that in using it we have helped you to advance your practices and aid in the care of patients.

Munich — Christoph J. Zech
Chicago — Richard Baron
Pisa — Carlo Bartolozzi
Munich — Maximilan F. Reiser

Contents

Contributors

S. Ahmed Johns Hopkins School of Medicine, Baltimore, MD 21205, USA

M. C. Ambrosetti Department of Radiology, Policlinico G.B. Rossi, University of Verona, P.le Scuro 10, 37134 Verona, Italy

P. Baldassari Department of Radiological Sciences, Oncology and Pathology, Sapienza-University of Rome, Viale Regina Elena 324, 00161 Rome, Italy

M. Barillari Department of Radiology, Policlinico G.B. Rossi, University of Verona, P.le Scuro 10, 37134 Verona, Italy

C. Bartolozzi Diagnostic and Interventional Radiology, University of Pisa, Via Roma 67, 56100 Pisa, Italy

P. Bemi Diagnostic and Interventional Radiology, University of Pisa, Via Roma 67, 56100 Pisa, Italy

G. Brancatelli Department of Radiology, University of Palermo, 90127 Palermo, Italy; Radiology Unit, La Maddalena Hospital, 90146 Palermo, Italy

G. Brix Department of Medical and Occupational Radiation Protection, Federal Office for Radiation Protection, Ingolstädter Landstrasse 1, 85764 Neuherberg, Germany, e-mail: gbrix@bfs.de

W. C. Chan Department of Radiology and Biomedical Imaging, University of California San Francisco, San Francisco, CA 94143-0628, USA

R. Cianci Department of Neurosciences and Imaging, Section of Imaging, G. d'Annunzio University, Chieti-Pescara.SS. Annunziata Hospital, via dei Vestini, 66100 Chieti, Italy

M. Ciolina Department of Radiological Sciences, Oncology and Pathology, Sapienza-University of Rome, Viale Regina Elena 324, 00161 Rome, Italy

Eva M. Coppenrath Departments of Radiology, University of Munich Hospitals, Marchioninistrasse 15, 81377 Munich, Germany

A. R. Cotroneo Department of Neurosciences and Imaging, Section of Imaging, G. d'Annunzio University, Chieti-Pescara.SS. Annunziata Hospital, via dei Vestini, 66100 Chieti, Italy

C. Cugini Radiological Department, General Hospital Ca' Foncello, Piazza Ospedale 1, 31100 Treviso, Italy

L. Faggioni Diagnostic and Interventional Radiology, University of Pisa, Via Roma 67, 56100 Pisa, Italy

A. Filippone Department of Neurosciences and Imaging, Section of Imaging, G. d'Annunzio University, Chieti-Pescara.SS. Annunziata Hospital, via dei Vestini, 66100 Chieti, Italy, e-mail: a.filippone@rad.unich.it

S. Fishback Department of Radiology, University of Wisconsin School of Medicine and Public Health, E3/311 Clinical Science Center, 600 Highland Avenue, Madison, WI 53792-3252, USA

E. K. Fishman The Russell H. Morgan Department of Radiology and Radiological Science, Johns Hopkins Hospital, 601 N. Caroline Street, Room 3125, Baltimore, MD 21287, USA, e-mail: efishman@jhmi.edu

T. Flohr Computed Tomography and Radiation Oncology, Siemens Healthcare, Ingolstädter Landstrasse 1, 91301 Forchheim, Germany, e-mail: thomas.flohr@siemens.com

A. Graser Department of Clinical Radiology, University of Munich, Marchioninistrasse 15, 81377 Munich, Germany; Departments of Radiology, University of Munich Hospitals, Marchioninistrasse 15, 81377 Munich, Germany, e-mail: Anno.Graser@med.uni-muenchen.de

R. Graziani Department of Radiology, Policlinico G.B. Rossi, University of Verona, P.le Scuro 10, 37134 Verona, Italy

K. M. Horton The Russell H. Morgan Department of Radiology and Radiological Science, Johns Hopkins Hospital, 601 N. Caroline Street, Room 3125, Baltimore, MD 21287, USA

F. Iafrate Department of Radiological Sciences, Oncology and Pathology, Sapienza-University of Rome, Viale Regina Elena 324, 00161 Rome, Italy

H.-J. Jang Department of Medical Imaging, Toronto General Hospital, 585 University Avenue, Toronto, ON M5G 2N2, Canada

P. T. Johnson Department of Radiology and Radiological Science, The Russell H. Morgan Johns Hopkins Hospital, 601 N. Caroline Street, Room 3140D, Baltimore, MD 21287, USA

M. S. Juchems Diagnostic and Interventional Radiology, University Hospitals Ulm, Steinhoevelstrasse 9, 89075 Ulm, Germany, e-mail: markus.juchems@uniulm.de

K. Khalili Department of Medical Imaging, Toronto General Hospital, 585 University Avenue, Toronto, ON M5G 2N2, Canada

D. H. Kim Department of Radiology, University of Wisconsin School of Medicine and Public Health, E3/311 Clinical Science Center, 600 Highland Avenue, Madison, WI 53792-3252, USA

T. K. Kim Department of Medical Imaging, Toronto General Hospital, 585 University Avenue, Toronto, ON M5G 2N2, Canada, e-mail: TaeKyoung.Kim@uhn.on.ca

A. Laghi Department of Radiological Sciences, Oncology and Pathology, Sapienza-University of Rome, Via Franco Faggiana 34, 04100 Latina, Italy, e-mail: andrea.laghi@uniroma1.it

D. H. Lee Department of Radiology, Seoul National University, College of Medicine, Yeon gon dong 28, Jongno gu, Seoul, South Korea

J. M. Lee Department of Radiology, Seoul National University, College of Medicine, Yeon gon dong 28, Jongno gu, Seoul, South Korea, e-mail: jmsh@snu.ac.kr

D. K. Lenhart Division of Abdominal Imaging and Intervention, Radiology, Harvard Medical School, Massachusetts General Hospital, 55 Fruit Street, White 270, Boston, MA 02114, USA

P. Lucchesi Department of Radiological Sciences, Oncology and Pathology, Sapienza-University of Rome, Viale Regina Elena 324, 00161 Rome, Italy

R. Manfredi Department of Radiology, Policlinico G.B. Rossi, University of Verona, P.le Scuro 10, 37134 Verona, Italy, e-mail: rmanfredi@univr.it

A. Mantarro Diagnostic and Interventional Radiology, University of Pisa, Via Roma 67, 56100 Pisa, Italy

D. Marin Department of Radiology, Duke University Medical Center, Durham, NC 27710, USA, e-mail: danielemarin2@gmail.com

B. Marincek, University of Zurich, 8802 Kilchberg, Switzerland; Emergency Radiology, Case Western Reserve University, University Hospitals Case Medical Center, Cleveland, OH 44106, USA

S. Mautone Department of Radiology, Policlinico G.B. Rossi, University of Verona, P.le Scuro 10, 37134 Verona, Italy

W. W. Mayo-Smith Department of Diagnostic Imaging, Rhode Island Hospital-Warren Alpert Medical School of Brown University, 593 Eddy Street, Providence, RI 02903, USA

A. J. Megibow, NYU-Langone Medical Center, 560 First Avenue, New York, NY 10016, USA, e-mail: Alec.megibow@nyumc.org

G. Morana Radiological Department, General Hospital Ca' Foncello, Piazza Ospedale 1, 31100 Treviso, Italy, e-mail: gmorana@ulss.tv.it

U. G. Mueller-Lisse Departments of Radiology, University of Munich Hospitals, Marchioninistrasse 15, 81377 Munich, Germany

E. A. Nekolla Department of Medical and Occupational Radiation Protection, Federal Office for Radiation Protection, Ingolstädter Landstrasse 1, 85764 Neuherberg, Germany

E. Neri Diagnostic and Interventional Radiology, University of Pisa, Via Roma 67, 56100 Pisa, Italy, e-mail: emanuele.neri@med.unipi.it

A. Oto Chief of Abdominal Imaging and Body MRI Department of Radiology, University of Chicago, 5841 S Maryland Ave, MC 2026, Chicago, IL 60637, USA, e-mail: aoto@radiology.bsd.uchicago.edu

R. Perez-Johnston Division of Abdominal Imaging and Intervention, Radiology, Harvard Medical School, Massachusetts General Hospital, 55 Fruit Street, White 270, Boston, MA 02114, USA

P. J. Pickhardt Department of Radiology, University of Wisconsin School of Medicine and Public Health, E3/311 Clinical Science Center, 600 Highland Avenue, Madison, WI 53792-3252, USA, e-mail: ppickhardt2@uwhealth.org

D. F. Pinho Division of Abdominal Imaging and Intervention, Radiology, Harvard Medical School, Massachusetts General Hospital, 55 Fruit Street, White 270, Boston, MA 02114, USA

R. Pozzi Mucelli Department of Radiology, Policlinico G.B. Rossi, University of Verona, P.le Scuro 10, 37134 Verona, Italy

M. Rengo Department of Radiological Sciences, Oncology and Pathology, Sapienza-University of Rome, Via Franco Faggiana 34, 04100 Latina, Italy

P. Rogalla Department of Medical Imaging, University of Toronto, Toronto, ON M5G 2N2, Canada, e-mail: patrik.rogalla@uhn.ca

D. V. Sahani Division of Abdominal Imaging and Intervention, Radiology, Harvard Medical School, Massachusetts General Hospital, 55 Fruit Street, White 270, Boston, MA 02114, USA, e-mail: dsahani@partners.org

R. Scandiffio Diagnostic and Interventional Radiology, University of Pisa, Via Roma 67, 56100 Pisa, Italy

A. Sibert Department of Radiology, Hôpital Beaujon, 92118 Clichy, France

J. H. Song Department of Diagnostic Imaging, Rhode Island Hospital-Warren Alpert Medical School of Brown University, 593 Eddy Street, Providence, RI 02903, USA, e-mail: jsong2@lifespan.org

V. Vilgrain Department of Radiology, Hôpital Beaujon, 92118 Clichy, France, e-mail: valerie.vilgrain@bjn.aphp.fr

B. M. Yeh Department of Radiology and Biomedical Imaging, University of California San Francisco, San Francisco, CA 94143-0628, USA, e-mail: ben.yeh@ucsf.edu

J.-H. Yoon Department of Radiology, Seoul National University, College of Medicine, Yeon gon dong 28, Jongno gu, Seoul, South Korea

M. Zappa Department of Radiology, Hôpital Beaujon, 92118 Clichy, France

Physical Background of Multi Detector Row Computed Tomography

Thomas Flohr

Contents

Abstract

We explain the physical background of multi detector row CT (MDCT) technology. We demonstrate the clinical benefits of MDCT, which are faster scan time, increased volume coverage and improved through-plane resolution. We discuss the design of X-ray tubes and MDCT detectors as well as scan and image reconstruction techniques and their specific properties. Finally, we give an outlook to modern high-pitch acquisition techniques.

1 History of MDCT

The introduction of spiral (helical) CT in the early nineties was a major step in the ongoing development of CT-imaging techniques (Kalender et al. 1990, Crawford and King 1990). Entire organs, such as lung or liver, could now be examined within one breath-hold and without the danger of mis- or double-registration of anatomical details. Images could be reconstructed with an increment smaller than the slice width to improve through-plane resolution. The through-plane direction, also called z-direction, is the cranio-caudal or caudo-cranial direction of the patient. Spiral CT was a pre-requisite for the development of three-dimensional image processing techniques such as multi-planar reformations (MPR), maximum intensity projections (MIP), surface shaded displays or volume rendering techniques (VRT) (Napel et al. 1993).

Nevertheless, single-slice spiral CT suffered from insufficient through-plane resolution as a consequence of wide slice collimation if larger anatomical volumes

T. Flohr (✉)
Computed Tomography and Radiation Oncology,
Siemens Healthcare,
Ingolstädter Landstrasse 1, 91301
Forchheim, Germany
e-mail: thomas.flohr@siemens.com

C. J. Zech et al. (eds.), *Multislice-CT of the Abdomen*, Medical Radiology. Diagnostic Imaging,
DOI: 10.1007/174_2011_404, © Springer-Verlag Berlin Heidelberg 2012

had to be examined within one breath-hold. Isotropic resolution, i.e. equal resolution in all three spatial axes, was only possible for very limited scan ranges (Kalender 1995).

In 1998, all major vendors introduced multi detector row CT (MDCT) systems into the market. These systems offered simultaneous acquisition of 4 slices with 1 or 1.25 mm collimated slice width at a rotation time of down to 0.5 s, which resulted in faster scan speed, improved through-plane resolution and better utilization of the available X-ray power (Klingenbeck-Regn et al. 1999; McCollough and Zink 1999; Hu et al. 2000). MDCT also expanded into new clinical areas, such as CT angiography of the coronary arteries with the addition of ECG gating capability (Kachelriess et al. 2000; Ohnesorge et al. 2000). Despite all promising advances, clinical challenges and limitations remained for 4-slice CT systems. True isotropic resolution could not be achieved in many routine applications, and often scan times were still too long. An examination of the entire thorax with 1 mm collimated slice width at 0.5 s gantry rotation time, for example, required a 25–30 s breath-hold of the patient. Reliable CT angiography of the coronary arteries was not possible in patients with higher heart rates because of limited temporal resolution.

An 8-slice CT system, introduced in 2000, enabled shorter examination times, but no improved spatial resolution (thinnest collimation 8 × 1.25 mm). Since 2001, 16-slice CT systems (Flohr et al. 2002a, b) have been commercially available, with a thinnest collimation of 16 × 0.5, 16 × 0.625 or 16 × 0.75 mm and faster gantry rotation (down to 0.42 s and later 0.375 s). With the use of these systems routine examinations of larger anatomical volumes at isotropic sub-millimeter spatial resolution became possible, such as CT-angiographic studies of the entire thorax and abdomen. ECG-gated cardiac scanning was enhanced by both, improved temporal resolution and improved spatial resolution (Nieman et al. 2002; Ropers et al. 2003). Figure 1 illustrates the improvements in clinical performance from single-slice CT to 16-slice CT.

In 2004, all major CT manufacturers introduced MDCT-systems with simultaneous acquisition of 64-slices at 0.5, 0.6 or 0.625 mm collimated slice width, and further reduced rotation times (down to 0.33 s). GE, Philips and Toshiba aimed at an increase in volume coverage speed by using detectors with 64 rows instead of 16, thus providing 32–40 mm z-coverage. Siemens used 32 physical detector rows in combination with double z-sampling, a refined z-sampling technique enabled by a z-flying focal spot (see "MDCT Scan and Image Reconstruction Techniques"), to simultaneously acquire 64 overlapping 0.6 mm slices with the goal of pitch-independent increase of through-plane resolution and reduction of spiral artifacts (Flohr et al. 2004, 2005). With 64-slice CT systems, CT scans with sub-mm resolution became feasible even for extended anatomical ranges. The improved temporal resolution due to faster gantry rotation increased clinical robustness of ECG-gated scanning, thereby facilitating the successful integration of CT coronary angiography into routine clinical algorithms (Leber et al. 2005; Raff et al. 2005), although higher and irregular heart rates were still problematic.

In 2007, one vendor introduced a MDCT-system with 128 simultaneously acquired slices, based on a 64-row detector with 0.6 mm collimated slice width and double z-sampling by means of a z-flying focal spot. Recently, simultaneous acquisition of 256 slices has become available, with a CT system equipped with a 128-row detector (0.625 mm collimated slice width) and double z-sampling.

Clinical experience with 64-, 128- or 256-slice CT indicates that adding even more detector rows will not by itself translate into increased clinical benefit. Instead, developments are ongoing to solve remaining limitations of MDCT.

A remaining challenge for MDCT is the visualization of dynamic processes in extended anatomical ranges, e. g. volume perfusion studies. In 2007, a CT system with 320 × 0.5 mm detector collimation and 0.35 s gantry rotation time was introduced, after a long evaluation phase using prototype systems with 256 × 0.5 mm collimation and 0.5 s gantry rotation time (Mori et al. 2004, 2006; Kondo et al. 2005). This system has the potential to cover the heart, the kidneys or the brain in one single sequential acquisition (Rybicki et al. 2008; Dewey et al. 2009; Shankar et al. 2010). Another way to acquire dynamic volume data is the introduction of "shuttle modes" with periodic table movement between two z-positions (e. g. Goetti et al. 2010).

Motion artifacts due to insufficient temporal resolution remain the most important challenge for coronary CTA even with the latest generation of MDCT. In 2006, a Dual Source CT (DSCT) system, i. e. a CT with two X-ray tubes and two corresponding detectors offset by 90°, was introduced by one vendor (Flohr

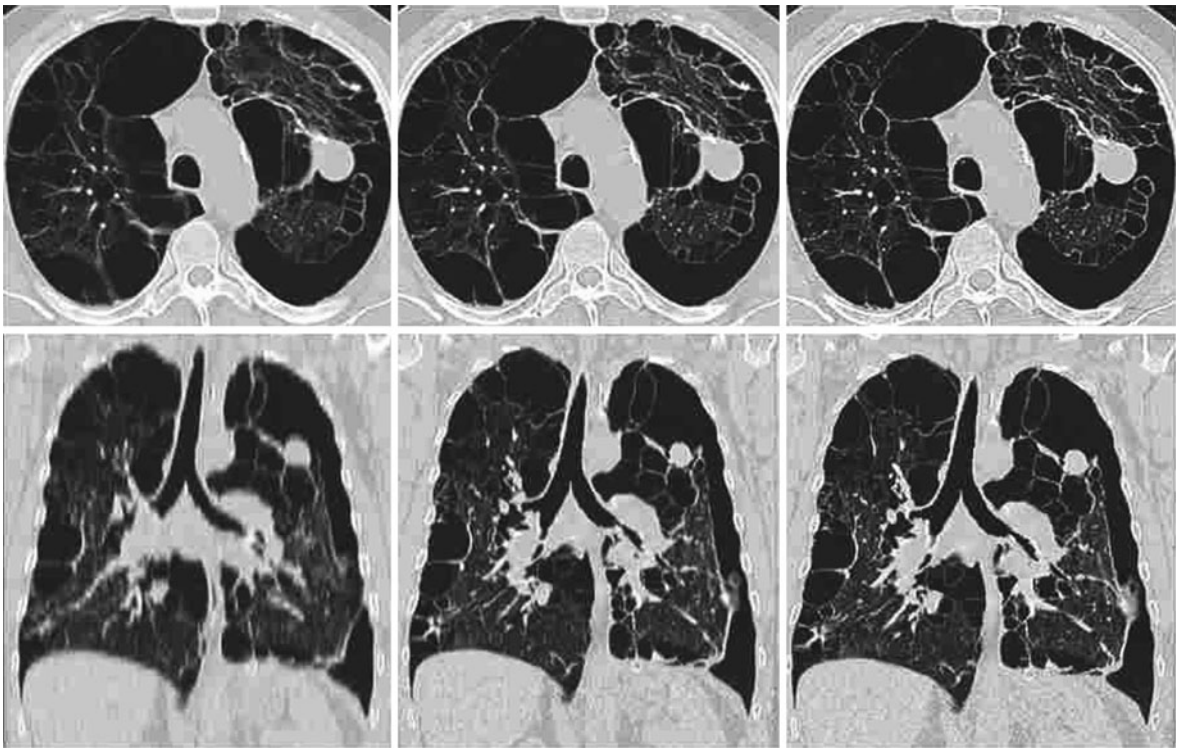

Fig. 1 Axial slices and coronal reformats of a thorax scan to illustrate the image quality improvement with different generations of CT systems. Single-slice CT with 8 mm slice width, scan time for the entire thorax about 25–30 s (*left*), 4-slice CT with 1.25 mm slice width, scan time with 0.5 s rotation about 25–30 s (*center*), and 16-slice CT with 0.75 mm slice width, scan time with 0.5 s rotation about 8–10 s (*right*). The differences are most obvious in the reformats. 16-slice CT approaches the ideal of isotropic resolution. The single-slice and 4-slice images were synthesised from a 16-slice scan (courtesy of Dr. U. J. Schöpf, Medical University of South Carolina, USA)

et al. 2006), followed by a second generation DSCT in 2009 (Flohr et al. 2009). The key benefit of DSCT for cardio-thoracic examinations and coronary CT angiography is improved temporal resolution. A scanner of this type provides temporal resolution of a quarter of the gantry rotation time, independent of the patient's heart rate (83 ms with the first generation DSCT, 75 ms with the second generation DSCT). DSCT scanners also show promising properties for general radiology applications, such as the potential of dual energy acquisitions.

2 Clinical Benefits of MDCT

The introduction of MDCT has been the clinically most important innovation in CT since the development of spiral CT. Clinical applications benefit from MDCT technology in several ways:

- *Shorter scan time*. Examination times for standard protocols can be significantly reduced. This is of immediate clinical benefit for the examination of non-cooperative patients, such as trauma victims or pediatric cases, or in CT angiography.
- *Extended scan range*. Larger scan ranges can be examined within one breath-hold time of the patient. This is relevant for CT angiography with extended coverage and for oncological staging. Chest and abdomen, as an example, can be examined in one scan with one contrast bolus.
- *Improved through-plane resolution*. The most important clinical benefit is the ability to examine a scan range of interest within a breath-hold time of the patient with substantially thinner slices than in single-slice CT. The significantly improved through-plane resolution is beneficial for all reconstructions, in particular when 3D post-processing is part of the clinical protocol.

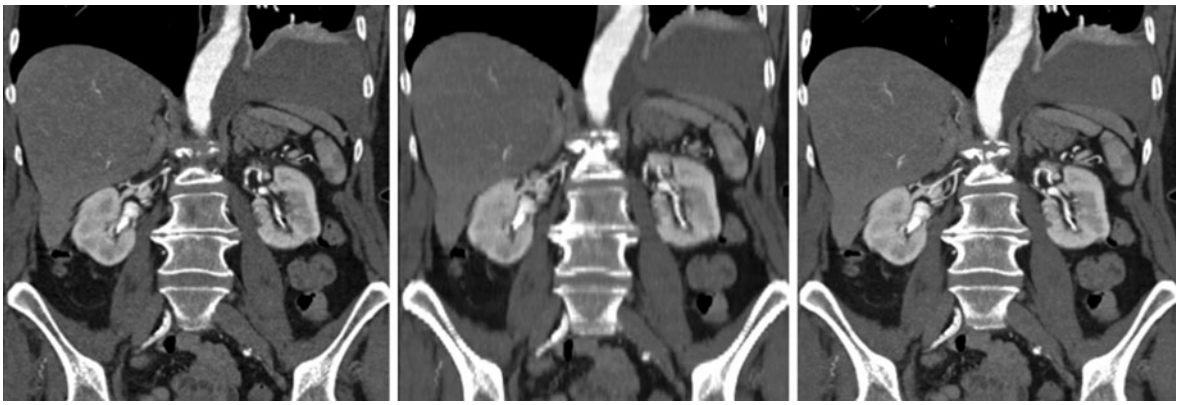

Fig. 2 Coronal MPR based on a 16-slice data set with 1 mm axial slices (*left*) and 3 mm axial slices (*center*). Using thicker primary slices reduces the image noise in the reformats, but degrades spatial resolution (*center*). This can be avoided by using thin primary slices (1 mm) in combination with slab MPRs or slab MIPs (a 3 mm slab MIP in the example on the *right*)

In clinical practice, most scan protocols benefit from a combination of these advantages. The close-to or true isotropic spatial resolution in routine examinations—depending on the scanner generation—enables 3D renderings of diagnostic quality and oblique MPRs and MIPs with a resolution comparable to the axial images. The wide availability of MDCT-systems has transformed CT from a modality acquiring cross-sectional slices of the patient to a volume imaging modality. In many scan protocols, the use of narrow collimation is recommended independently of what slice width is desired for primary viewing. In practice, different slice widths are commonly reconstructed by default: thick slices for PACS archiving and primary viewing and thin slices for 3D post-processing and evaluation. The image noise in close-to-isotropic high-resolution volumes can be limited by making use of slab MPRs or slab MIPs (Fig. 2).

As a consequence, the traditional viewing of axial slices is being replaced by interactive manipulation of volume images, with only the key slices or views in arbitrary directions stored for a demonstration of the diagnosis.

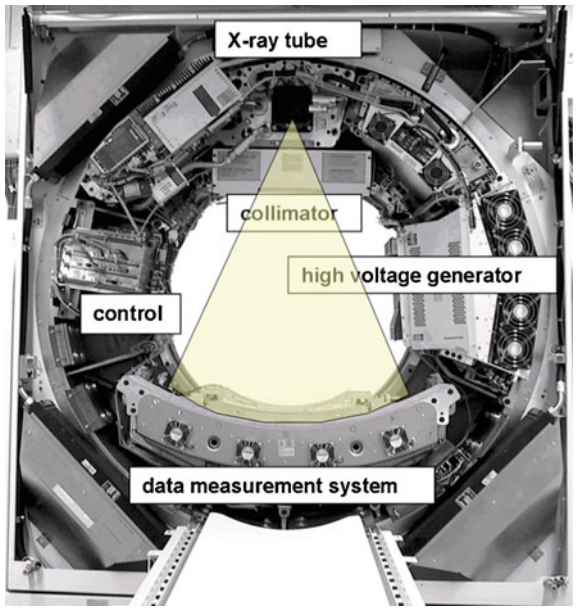

Fig. 3 Basic system components of a modern MDCT-system. The X-ray fan beam is indicated in *yellow*, it covers a SFOV of typically 50 cm in diameter. The data measurement system consists of detector and detector electronics

3 MDCT-System Design

The basic system components of a modern MDCT-system are shown in Fig. 3. Both the X-ray tube and the detector rotate about the patient. The detector comprises several rows of 700 and more detector elements which cover a scan field of view (SFOV) of usually 50 cm in diameter. The X-ray attenuation of the object is measured by the individual detector elements. All measurement values acquired at the same angular position of the measurement system are

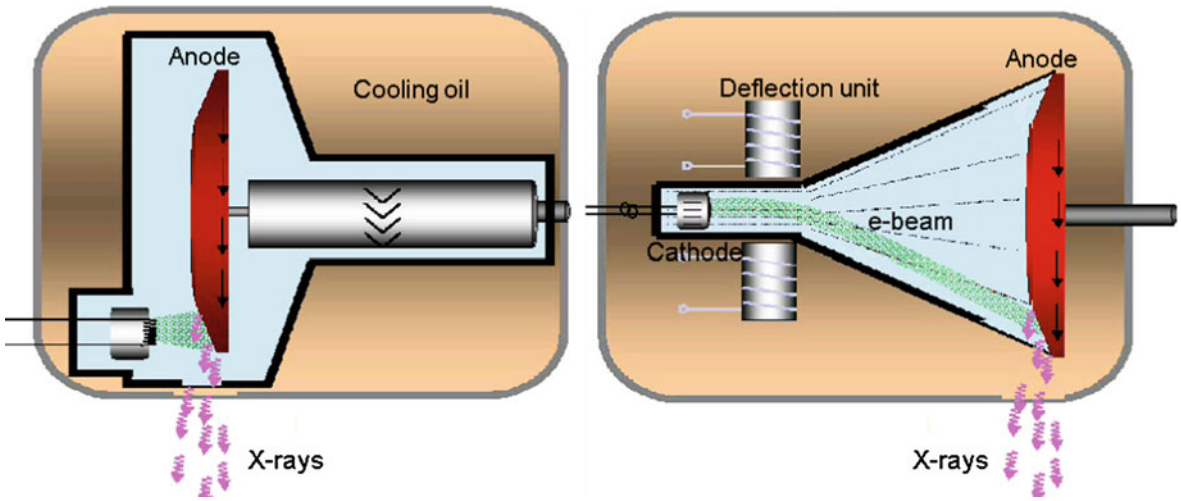

Fig. 4 Schematic drawings of a conventional X-ray tube (*left*) and a rotating envelope tube (*right*). A high voltage is applied between cathode and anode. The electrons emitted by the cathode are shown as *green lines*, the X-rays generated in the anode as *purple arrows*. In a conventional X-ray tube the anode plate rotates in a vacuum housing. In a rotating envelope tube, the anode plate forms an outer wall of the tube housing and is in direct contact with the cooling oil. Heat is dissipated by thermal conduction, and the cooling rate is significantly increased. Rotating envelope tubes have no moving parts and no bearings in the vacuum

a "projection" or "reading". During each 360° rotation about 1,000 projections are acquired.

State-of-the-art X-ray tube/generator combinations provide a peak power of 60–120 kW at various, user-selectable voltages, e. g. 80, 100, 120 and 140 kV. Different clinical applications require different X-ray spectra and hence different kV-settings. Low tube voltage (80 or 100 kV) is favorable for contrast enhanced examinations because the CT number of iodine significantly increases at lower kV. Vessels filled with iodine appear brighter in the images, and higher image noise can be tolerated to maintain the contrast-to-noise ratio. This opens the potential to reduce the radiation dose to the patient (Schaller et al. 2001a; Wintersperger et al. 2005; McCollough et al. 2009). On the other hand, CT images suffer from more pronounced beam hardening artifacts at lower kV. At high tube voltage (120 or 140 kV) more power reserves are available, which is beneficial for the examination of obese patients.

In a conventional tube design, an anode plate of typically 160–220 mm diameter rotates in a vacuum housing (Fig. 4). The heat storage capacity of anode plate and tube housing—measured in mega heat units (MHU)—as well as the heat dissipation rate determine the performance level: they limit the rate at which scans can be repeated and the maximum available power for each scan. An alternative design (Schardt et al. 2004) is the rotating envelope tube (STRATON, Siemens, Forchheim, Germany). The anode plate forms an outer wall of the rotating tube housing, it is in direct contact with the cooling oil and can be efficiently cooled by thermal conduction (Fig. 4). This way, a very high heat dissipation rate of 5 MHU/min is achieved, eliminating the need for heat storage in the anode which consequently has a heat storage capacity close to zero. Due to the central rotating cathode permanent electro-magnetic deflection of the electron beam is needed to position the focal spot on the anode.

MDCT-systems are equipped with solid state detectors. Each detector element consists of a radiation-sensitive solid state material (such as Cadmium Tungstate, Gadolinium-oxide or Gadolinium oxisulfide) with suitable dopings, which converts the absorbed X-rays into visible light. The light is then detected by an attached Si photodiode. The resulting electrical current is amplified and converted into a digital signal. Key requirements for a suitable detector material are good detection efficiency, i. e. high atomic number, and very short afterglow time to enable the fast gantry rotation speeds that are essential for ECG-gated cardiac imaging.

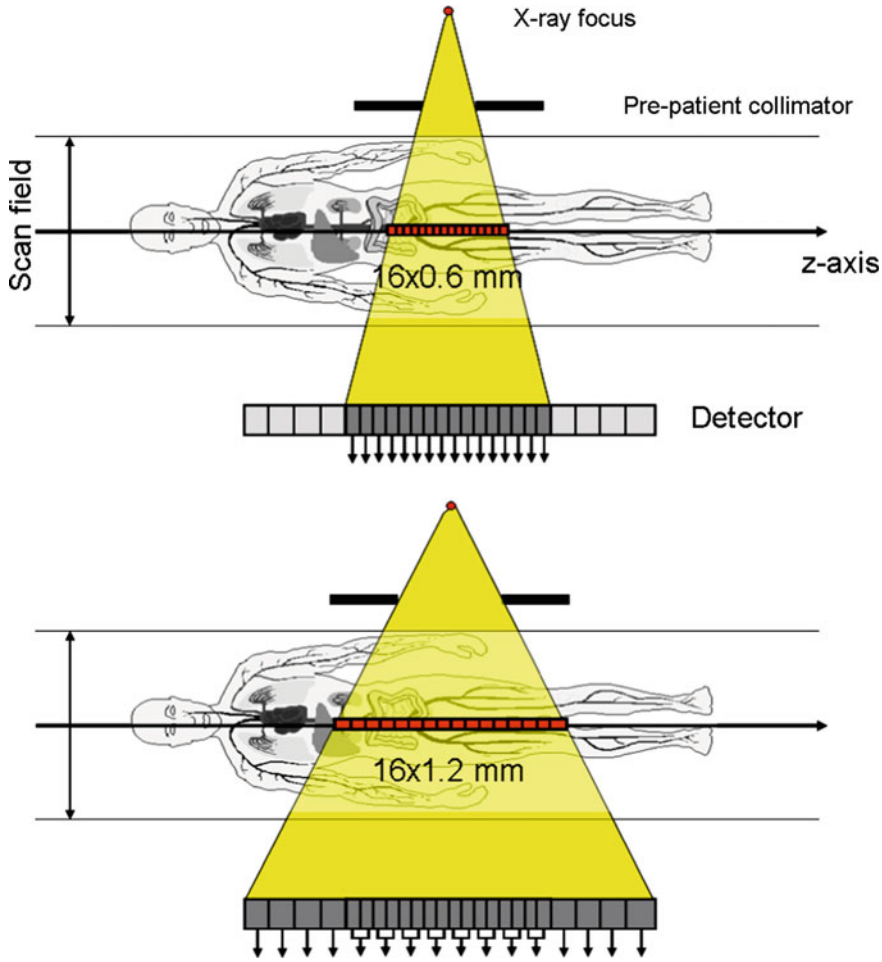

Fig. 5 MDCT slice collimation. Example of a 16-slice detector, which consists of 24 detector rows and provides either 16 collimated 0.6 mm slices (*top*) or—by combination of the signals of every 2 central rows—16 collimated 1.2 mm slices (*bottom*)

A CT detector must provide different slice widths to adapt scan speed and through-plane resolution to the clinical requirements of different scan protocols. In single-slice CT the collimated slice width is adjusted by pre-patient collimation of the X-ray beam.[1] This principle can be extended to 2-slice CT if the detector is separated midway along the z-extent of the X-ray beam. To simultaneously acquire more than 2 slices at different slice widths, however, detectors with a larger number of detector rows than finally read-out slices have to be used. The required total beam width in the z-direction is adjusted by pre-patient collimation, and the signals of every two (or more) detectors along the z-axis are electronically combined to thicker slices. The detector of a 16-slice CT (Siemens SOMATOM Emotion 16) as an example consists of 16 central rows, each with 0.6 mm collimated slice width, and 4 outer rows on either side, each with 1.2 mm collimated slice width—in total, 24 rows with a z-width of 19.2 mm at iso-center (Fig. 5). If only the central 16 rows are irradiated, they are read-out individually, and the detector provides 16 collimated 0.6 mm slices (Fig. 5, top). To obtain 16 collimated 1.2 mm slices, the pre-patient collimator is opened. The full z-width of the detector is irradiated, and the signals of every 2 central rows are electronically combined. This results in 8 central 1.2 mm slices plus 4 outer 1.2 mm slices on either side of the detector, in total 16 collimated 1.2 mm slices (Fig 5, bottom). The 16-slice detectors of other vendors are similarly designed, providing e. g. 16 collimated 0.625 mm slices or 16 collimated 1.25 mm slices.

[1] Note that the slice width is always measured at the iso-center of the CT system.

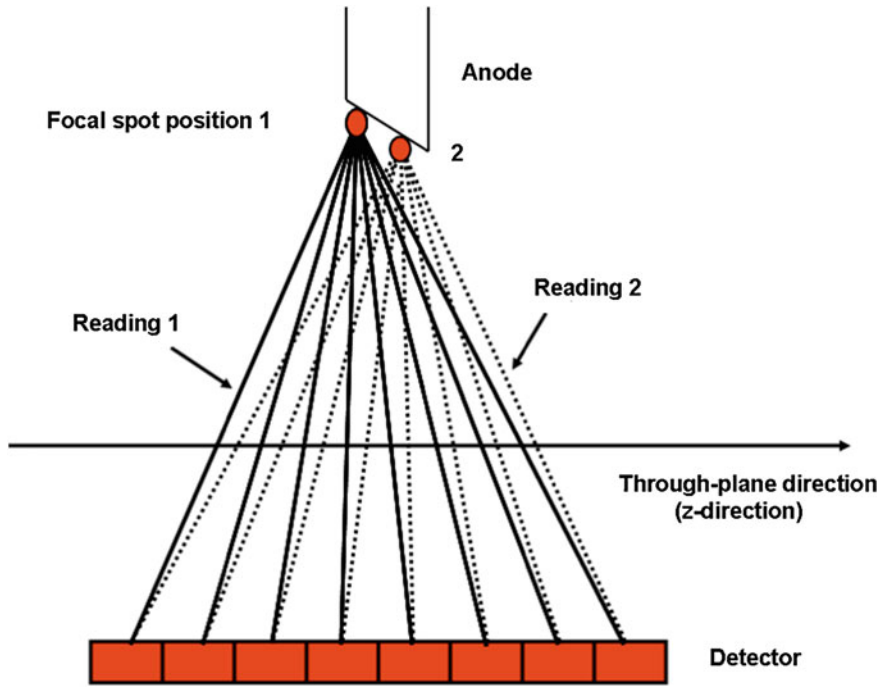

Fig. 6 Principle of a z-flying focal spot. Consecutive readings are shifted by half a collimated slice width (at *iso-center*) by means of a periodic motion of the focal spot on the anode plate. Every two readings are interleaved to one projection with double the number of slices and half the z-sampling distance

MDCT detectors with 64 detector rows provide 0.5, 0.6 or 0.625 mm collimated slice width, depending on the manufacturer. They allow acquisition of thicker slices by electronic combination of every 2 detector rows. This results in 32 collimated 1.0, 1.2 or 1.25 mm slices. One CT system has a detector with 128 collimated 0.625 mm slices (total z-width 8 cm at iso-center). The widest commercially available CT detector covers 16 cm at iso-center, it acquires 320 collimated 0.5 mm slices.

Some CT systems double the number of simultaneously acquired slices by means of a z-flying focal spot. Fast electromagnetic deflection of the electron beam in the X-ray tube is used to periodically shift the focal spot between two z-positions on the anode plate (Flohr et al. 2004, 2005). At iso-center, two consecutive readings are shifted by half a collimated slice width in the patient's through-plane direction, e. g. by 0.3 mm for 0.6 mm collimated slice width (Fig. 6). The measurement rays of every two consecutive readings are interleaved to one projection with double the number of slices, but half the z-sampling distance. Two 64-slice readings with 0.6 mm slice width and 0.6 mm z-sampling distance, as an example, are combined to one projection with 128 overlapping 0.6 mm slices at 0.3 mm z-sampling distance.

The z-flying focal spot provides better data sampling in the z-direction, this improves through-plane resolution and reduces spiral windmill-artifacts which typically are more pronounced at higher table-feed (Fig. 7).

The collimated slice width is the slice width at which the measurement data are acquired. Practically all MDCT-systems allow reconstruction of images with different reconstructed slice widths from the same CT raw data, e. g. by means of modern spiral interpolation methods such as z-filtering (see Chapter 4). This way, several image volumes with different reconstructed slice widths can be obtained from the same raw data set. The reconstructed slice width, however, cannot be smaller than the collimated slice width.

4 MDCT Scan and Image Reconstruction Techniques

With the advent of MDCT, axial "step-and-shoot" scanning has remained in use for only few clinical applications, such as examinations of the brain, high-resolution examinations of the lung, perfusion CT and interventional applications. A recent renaissance of

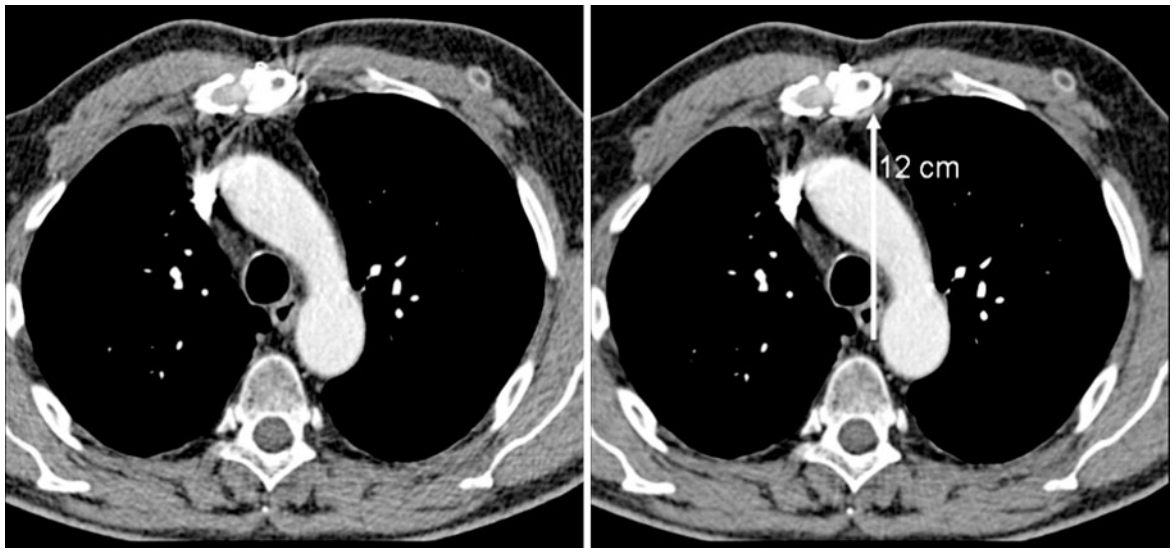

Fig. 7 Reduction of spiral artifacts by means of a z-flying focal spot. *Right* Thorax scan with 32 × 0.6 mm collimation in a 64-slice acquisition mode with z-flying focal spot at pitch 1.5. *Left* same scan, using only one focus position of the z-flying focal spot for image reconstruction. This corresponds to 32-slice acquisition without z-flying focal spot. Due to the improved sampling in the z-direction with z-flying focal spot spiral interpolation artifacts (windmill structures at high-contrast objects) are suppressed without degradation of through-plane resolution

step-and-shoot scanning in ECG-controlled cardiac examinations has mainly been caused by the low radiation dose associated with ECG-triggered sequential CT (Earls et al. 2008; Scheffel et al. 2008). For the vast majority of all MDCT examinations, however, spiral scanning is the method of choice.

An important parameter to characterize a spiral scan is the pitch. According to IEC specifications (International Electrotechnical Commission 2002) the pitch p is given by $p =$ tablefeed per rotation/total z-width of the collimated beam.

This definition applies to single-slice CT as well as to MDCT. It indicates whether data acquisition occurs with gaps ($p > 1$) or with overlap ($p < 1$) in the through-plane direction. With e. g. 16 × 0.75 mm collimation and a table-feed of 15 mm/rotation, the pitch is $p = 15/(16 \times 0.75) = 15/12 = 1.25$.

During the past 10 years image reconstruction techniques have been developed that cope with the technical challenges of MDCT scanning, such as the complicated z-sampling patterns or the cone-angle problem. Two-dimensional image reconstruction approaches used in single-slice CT systems require all measurement rays that contribute to an image to be perpendicular to the z-axis. In MDCT-systems this requirement is obviously violated: the measurement rays are tilted by the so-called cone-angle with respect to a plane perpendicular to the z-axis. The cone-angle is largest for the detector rows at the outer edges of the detector and it increases with increasing number of rows if their width is kept constant (Fig. 8).

It has to be carefully analyzed if and to which extent single-slice reconstruction approaches can be extended to MDCT. MDCT spiral algorithms have to provide images without severe cone-beam artifacts, they should allow for a certain variation of the pitch to adjust the table-feed of the scanner to clinical requirements, and they should make full use of the available data, i. e. they should not waste radiation dose.

For CT systems with up to 8 simultaneously acquired slices, cone-beam artifacts stay at a clinically acceptable level if the cone-angle of the measurement rays is neglected in the image reconstruction algorithms. The rays are then treated as if they were perpendicular to the z-axis, and 2D filtered back-projection is used to reconstruct the images after spiral interpolation. For CT systems with more than 8 slices the cone-angle has to be taken into account at least approximately.

Pertinent algorithms neglecting the cone-angle of the measurement rays are the 180 and 360°MLI multi-slice linear spiral interpolation approaches

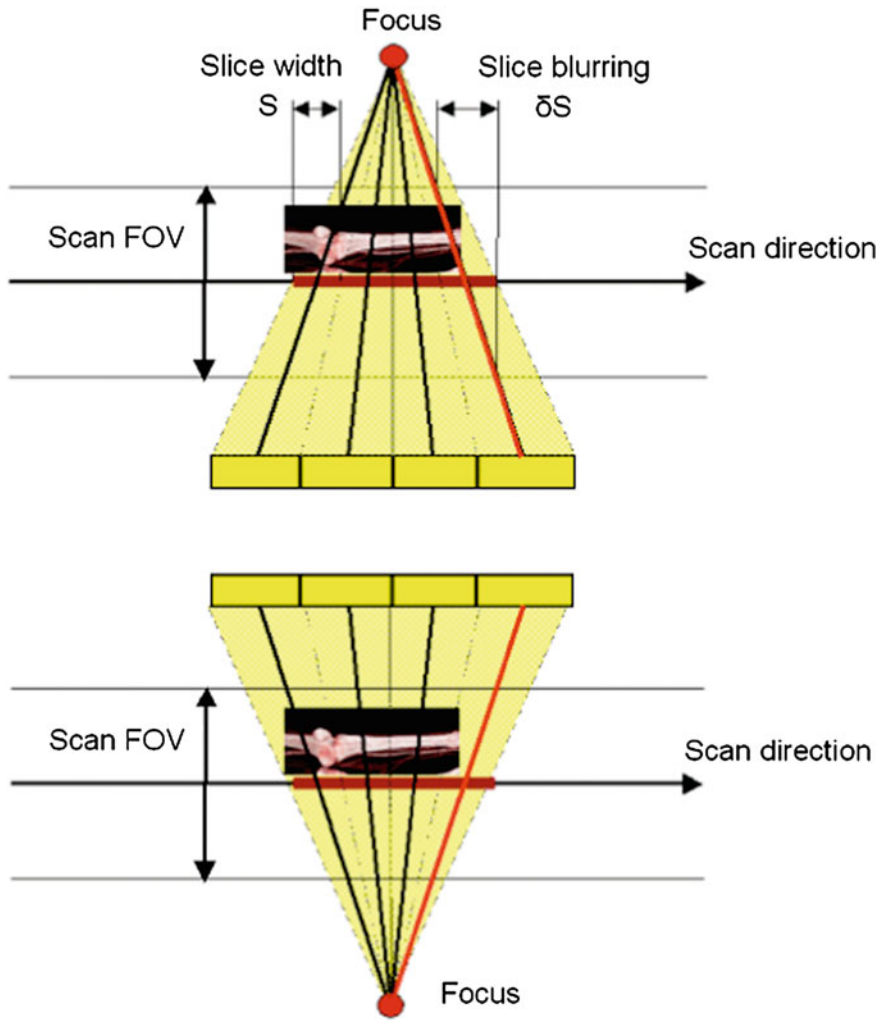

Fig. 8 Geometry of a 4-slice CT-scanner demonstrating the cone-angle problem: the measurement rays are tilted by the so-called cone-angle with respect to the center plane. *Top and bottom* Illustration of two projections of an axial scan which are half a rotation (180°) apart so that the positions of X-ray tube and detector are interchanged. With a single-slice CT system identical measurement values would be acquired. With a MDCT-system, different measurement values are acquired, and the data are inconsistent (see the *red ray*, which hits the bone in the *top* position but not in the *bottom* position)

(Hu 1999; Hsieh 2003) and z-filter techniques (Taguchi and Aradate 1998; Schaller et al. 2000).

Multi-slice linear interpolation (180 and 360°MLI) is characterized by a projection-wise linear interpolation between two rays on either side of the image plane. MDCT-systems using this technique offer selected discrete pitch values to the operator, such as 0.75 and 1.5 for 4-slice scanning (Hu 1999) or 0.5625, 0.9375, 1.375 and 1.75 for 16-slice scanning (Hsieh 2003). At low pitch ($p = 0.5625$ or 0.9375 for 16 slices), the effective slice width, i. e. the reconstructed slice width after spiral interpolation, equals the collimated slice width. A collimated 1.25 mm slice, e. g., results in an effective 1.25 mm slice. The narrow slice sensitivity profile is achieved by 180°MLI reconstruction using conjugate interpolation at the price of increased image noise (Hu 1999; Hsieh 2003). At high pitch (at $p = 1.375$ or 1.75 for 16 slices), spiral interpolation results in wider effective slices. A collimated 1.25 mm slice, e. g., turns out to be an effective 1.6 mm slice. Image noise at identical tube current (identical mA), however, is reduced compared with the situation at low pitch. Scanners offering discrete optimized pitch values based on 180 and 360°MLI techniques are comparable to single-slice CT systems in some core aspects: at high pitch the slice widens and through-plane resolution degrades. At low pitch narrow effective slices are obtained, but higher dose is necessary to maintain low image noise. Scanning at low pitch optimizes image quality and through-plane resolution at a given collimation, yet at the expense of increased radiation dose to the patient. To reduce patient dose, high-pitch values should be chosen.

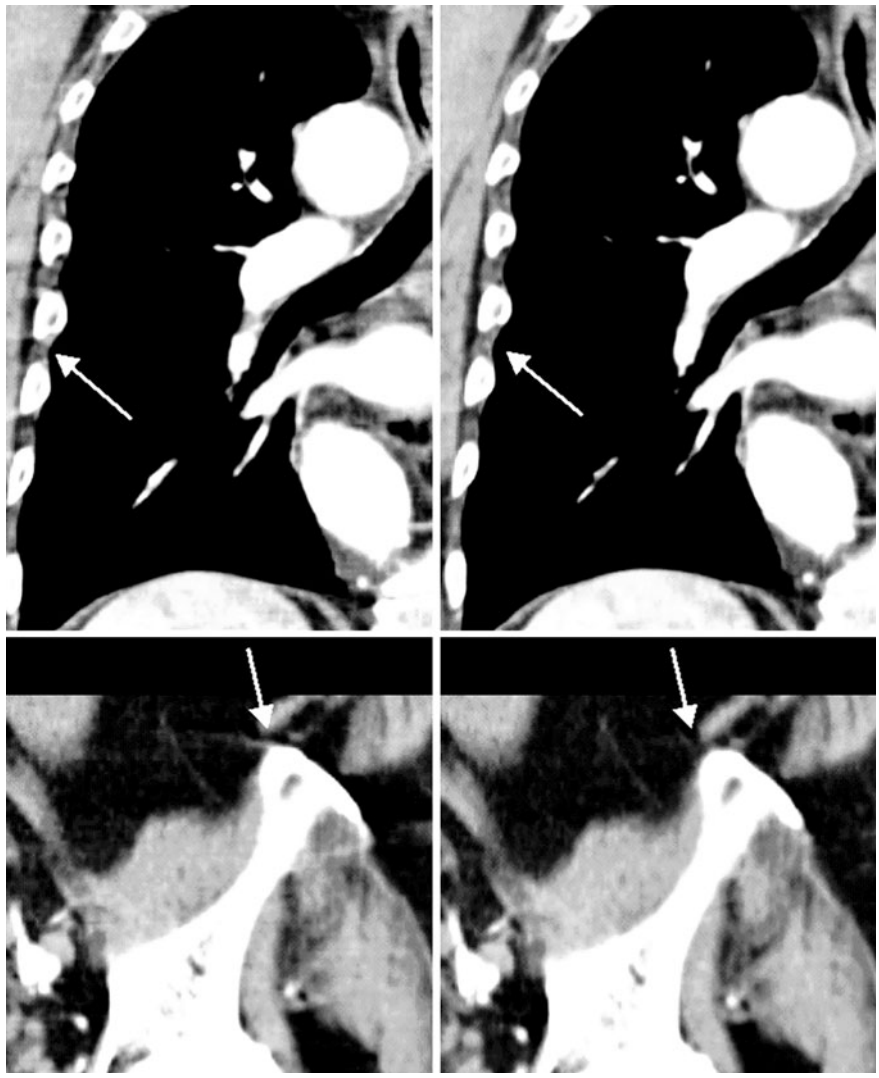

Fig. 9 Coronal reformats of a thorax-abdomen scan (16 × 1.5 mm collimation, 2 mm reconstructed slice width, pitch 1.25). *Left* 2D filtered back-projection neglecting the cone-angle of the measurement rays. cone-beam artifacts are indicated by *arrows*. *Right* Nutating slice reconstruction AMPR. Cone-beam artifacts are reduced

In a z-filter multi-slice spiral reconstruction, the spiral interpolation for each projection is no longer restricted to the two rays in closest proximity to the image plane. Instead, all direct and complementary rays within a selectable distance from the image plane contribute to the image. Images with different slice widths can be retrospectively reconstructed from the same CT raw data. Hence, z-filtering allows the system to trade-off z-axis resolution with image noise (which directly correlates with required dose). The reconstructed slice width cannot be smaller than the collimated slice width. Some z-filter approaches, e. g. the Adaptive Axial Interpolation used by Siemens (Schaller et al. 2000), provide a continuous range of user-selectable pitch values (e.g. from 0.4 to 1.5), and the effective slice width is kept constant at any pitch. Therefore, through-plane resolution is independent of the pitch. CT-scanners with Adaptive Axial Interpolation rely on an "effective mAs" concept. The user selects an effective mAs-value, and the tube current (mA) is automatically adapted to the spiral pitch according to

$$\mathrm{mA} = \mathrm{eff.\ mAs} \cdot p / t_{rot}$$

p is the pitch, t_{rot} is the rotation time. As a consequence, radiation dose is independent of the spiral pitch and equals the dose of an axial scan with the same mA and the same rotation time. Using higher pitch does not result in a reduction of radiation dose, but through-plane resolution is maintained. This is a

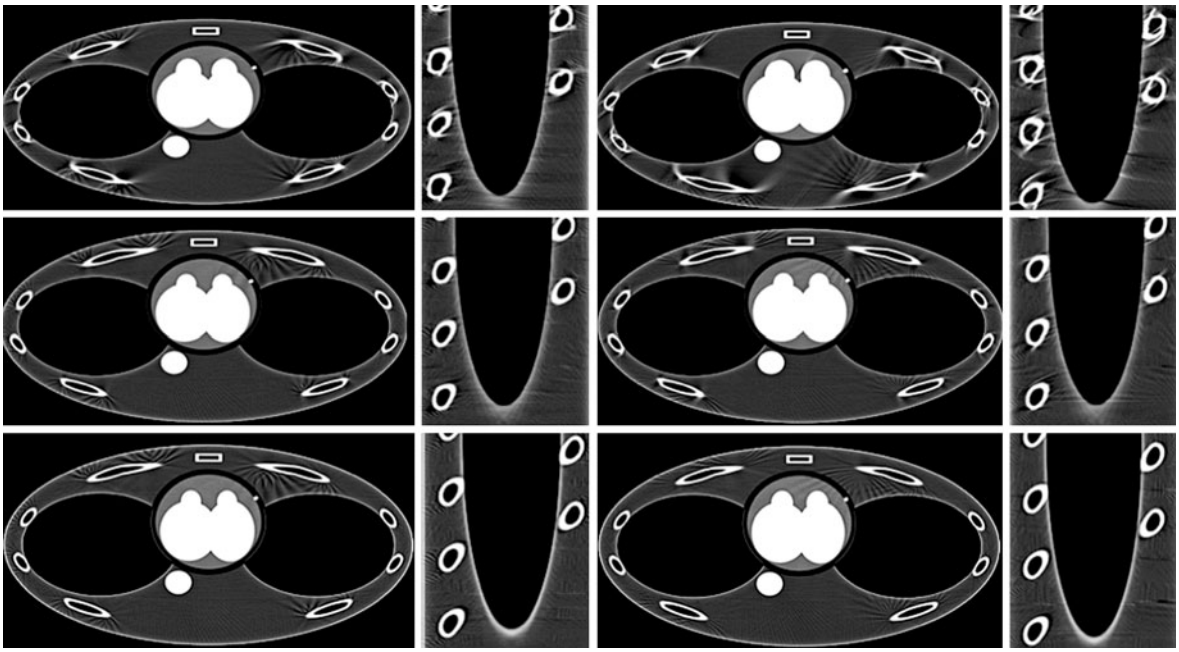

Fig. 10 Axial slices and MPRs of an anthropomorphic thorax phantom. Scan data for 16 × 0.75 mm collimation (*left*) and 32 × 0.75 mm collimation (*right*) at pitch 1 were reconstructed at 1 mm slice width, with 2D back-projection neglecting the cone-angle of the measurement rays (*top*), with the nutating slice algorithm AMPR (*center*) and with 3D back-projection (*bottom*). Neglecting the cone-angle leads to *cone-beam* artifacts at high-contrast objects (*top*) that increase with increasing number of detector rows. Both AMPR and 3D back-projection reduce *cone-beam* artifacts and are practically equivalent for CT systems with up to 32 detector rows. At higher number of detector rows, 3D back-projection is superior

major difference to single-slice CT or MDCT with 180/360°MLI reconstruction.

Some other manufacturers who use z-filter approaches, such as the MUSCOT algorithm developed by Toshiba, do not provide completely free selection of the spiral pitch, but recommend a selection of fixed pitch values which are aimed at optimizing the z-sampling scheme and reducing spiral artifacts, such as 0.625, 0.75, 0.875, 1.125, 1.25, 1.375 and 1.5 for 4-slice scanning (Taguchi and Aradate 1998).

Commonly used reconstruction methods considering the cone-beam geometry in an approximate way are nutating slice algorithms and 3D filtered back-projection. In the early days of 16-slice CT, nutating slice algorithms were used that split the 3D reconstruction task into a series of conventional 2D reconstructions on tilted intermediate image planes optimally adapted to the spiral path, e.g. the AMPR used by Siemens (Schaller et al. 2001b; Flohr et al. 2003), see Fig. 9. This allowed the use of efficient and simple 2D back-projectors, however, image quality was not sufficient for CT systems with 64 slices and more.

Nowadays, 3D filtered back-projection is the reconstruction method of choice for most MDCT-systems (Grass et al. 2000; Hein et al. 2003; Stierstorfer et al. 2004). With this approach, the measurement rays are back-projected into a 3D volume along the lines of measurement, this way accounting for their cone-beam geometry. 3D filtered back-projection, even though it is an approximate algorithm, can significantly reduce cone-beam artifacts (Fig. 10). Techniques used in z-filtering to reconstruct different slice widths from the same CT raw data can be extended to 3D filtered back-projection. The characteristics of Adaptive Axial Interpolation, as an example, originally developed for 4-slice CT, also apply to newer generations of 64-slice and 128-slice CT systems.

Regardless of the specific reconstruction algorithm used in a particular CT-scanner, narrow collimation scanning is recommended because it leads to better suppression of partial volume artifacts, even if the pitch has to be increased for equivalent volume coverage. Similar to single-slice spiral CT, narrow collimation scanning is the key to reduce artifacts and

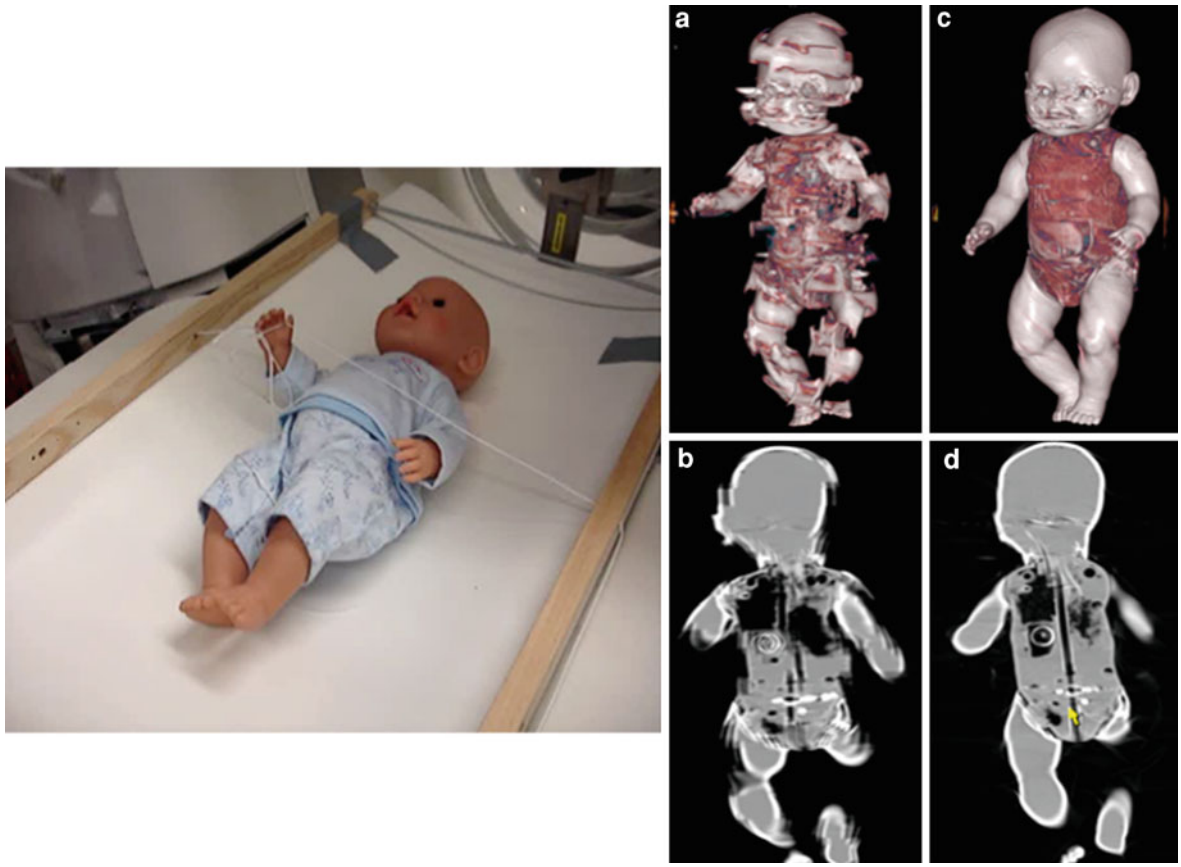

Fig. 11 CT scans of a moving doll phantom simulating motion of a child without sedation. **a** and **b** VRTs and MPRs of the phantom scanned with a standard spiral (pitch 1, 0.33 s rotation time) show significant motion artifacts. **c** and **d** Using the DSCT high-pitch spiral (pitch 3.4, 0.33 s rotation time) motion artifacts are significantly reduced

improve image quality. Best suppression of spiral artifacts is achieved by using both narrow collimation relative to the desired slice width and reducing the spiral pitch.

5 Volume Coverage in Spiral MDCT

In MDCT spiral scans, the volume coverage speed can be increased by selecting wider collimated slice widths S, by reducing the gantry rotation time t_{rot}, by increasing the pitch p and by increasing the number M of simultaneously acquired slices. A simple equation relates the volume coverage speed v to these parameters:

$$v = \frac{MSp}{t_{\text{rot}}}$$

A scanner with $M = 64$ collimated detector rows, $S = 0.625$ mm, $p = 1.375$ and $t_{\text{rot}} = 0.5$ s can be as fast as 110 mm/s.

Dual source CT (DSCT) systems offer a way to significantly increase the volume coverage speed without using wider detectors. With a single-source CT, the spiral pitch p is limited to $p \leq 1.5$ to ensure gapless volume coverage along the z-axis. If the pitch is increased to $p > 1.5$, sampling gaps occur that hamper the reconstruction of images without excessive image artifacts. With DSCT systems, however, data acquired with the second measurement system can be used to fill these gaps. In this way, the pitch can be increased up to $p = 3.4$ in a limited SFOV that is covered by both detectors (Petersilka et al. 2008; Flohr et al. 2009). At a pitch of 3.4 and 0.28 s gantry rotation, the table-feed with 38.4 mm detector z-coverage (2nd generation DSCT) is 450 mm/s.

Meanwhile, several clinical studies have demonstrated the successful use of the high-pitch scan technique for coronary CT angiography in patients with sufficiently low and stable heart rate, with the potential to scan the entire heart in one beat at very low radiation dose (Achenbach et al. 2009; Lell et al. 2009; Leschka et al. 2009). In a non-ECG-gated version the high-pitch mode has been used for the examination of larger anatomical volumes in very short scan times, e.g. when the patient has limited ability to cooperate, such as in pediatric radiology (Fig. 11)

References

Achenbach S, Marwan M, Schepis T, Pflederer T, Bruder H, Allmendinger T, Petersilka M, Anders K, Lell M, Kuettner A, Ropers D, Daniel WG, Flohr T (2009) High-pitch spiral acquisition: a new scan mode for coronary CT angiography. J Cardiovasc Comput Tomogr 3:117–121

Crawford CR, King KF (1990) Computed tomography scanning with simultaneous patient translation. Med Phys 17: 967–982

Dewey M, Zimmermann E, Deissenrieder F, Laule M, Dübel HP, Schlattmann P, Knebel F, Rutsch W, Hamm B (2009) Noninvasive coronary angiography by 320-row computed tomography with lower radiation exposure and maintained diagnostic accuracy: comparison of results with cardiac catheterization in a head-to-head pilot investigation. Circulation 120(10):867–875

Earls JP, Berman EL, Urban BA, Curry CA, Lane JL, Jennings RS, McCulloch CC, Hsieh J, Londt JH (2008) Prospectively gated transverse coronary CT angiography versus retrospectively gated helical technique: improved image quality and reduced radiation dose. Radiology 246(3):742–753

Flohr T, Stierstorfer K, Bruder H, Simon J, Schaller S (2002a) New technical developments CT in multislice: part 1: approaching isotropic resolution with sub-mm 16-slice scanning. Röfo Fortschr Geb Rontgenstr Neuen Bildgeb Verfahr 174:839–845

Flohr T, Bruder H, Stierstorfer K, Simon J, Schaller S, Ohnesorge B (2002b) new technical developments CT in multislice: part 2: sub-millimeter 16-slice scanning and increased gantry rotation speed for cardiac imaging. Röfo Fortschr Geb Rontgenstr Neuen Bildgeb Verfahr 174:1022–1027

Flohr T, Stierstorfer K, Bruder H, Simon J, Polacin A, Schaller S (2003) Image reconstruction and image quality evaluation for a 16-slice CT scanner. Med Phys 30(5):832–845

Flohr T, Stierstorfer K, Raupach R, Ulzheimer S, Bruder H (2004) Performance evaluation of a 64-slice CT-system with z-flying focal spot. Röfo Fortschr Geb Rontgenstr Neuen Bildgeb Verfahr 176:1803–1810

Flohr TG, Stierstorfer K, Ulzheimer S, Bruder H, Primak AN, McCollough CH (2005) Image reconstruction and image quality evaluation for a 64-slice CT scanner with z-flying focal spot. Med Phys 32(8):2536–2547

Flohr TG, McCollough CH, Bruder H, Petersilka M, Gruber K, Süß C, Grasruck M, Stierstorfer K, Krauss B, Raupach R, Primak AN, Küttner A, Achenbach S, Becker C, Kopp A, Ohnesorge BM (2006) First performance evaluation of a dual-source CT (DSCT) system. Eur Radiol 16(2): 256–268

Flohr TG, Leng S, Yu L, Aiimendinger T, Bruder H, Petersilka M, Eusemann CD, Stierstorfer K, Schmidt B, McCollough CH (2009) Dual-source spiral CT with pitch up to 3.2 and 75 ms temporal resolution: image reconstruction and assessment of image quality. Med Phys 36(12):5641–5653

Goetti R, Leschka S, Desbiolles L, Klotz E, Samaras P, von Boehmer L, Stenner F, Reiner C, Stolzmann P, Scheffel H, Knuth A, Marincek B, Alkadhi H (2010) Quantitative computed tomography liver perfusion imaging using dynamic spiral scanning with variable pitch: feasibility and initial results in patients with cancer metastases. Invest Radiol 45(7):419–426

Grass M, Köhler T, Proksa R (2000) 3D cone-beam CT reconstruction for circular trajectories. Phys Med Biol 45(2):329–347

Hein I, Taguchi K, Silver MD, Kazarna M, Mori I (2003) Feldkamp-based cone-beam reconstruction for gantry-tilted helical multislice CT. Med Phys 30(12):3233–3242

Hsieh J (2003) Analytical models for multi-slice helical CT performance parameters. Med Phys 30(2):169–178

Hu H (1999) Multi-slice helical CT: scan and reconstruction. Med Phys 26(1):5–18

Hu H, He HD, Foley WD, Fox SH (2000) Four multidetector-row helical CT: image quality and volume coverage speed. Radiology 215:55–62

International Electrotechnical Commission 60601-2-44 (2002) Amendment 1: medical electrical equipment: part 2–44: particular requirements for the safety of X-ray equipment for computed tomography. International Electrotechnical Commission, Geneva

Kachelriess M, Ulzheimer S, Kalender W (2000) ECG-correlated image reconstruction from subsecond multi-slice spiral CT scans of the heart. Med Phys 27:1881–1902

Kalender W, Seissler W, Klotz E, Vock P (1990) Spiral volumetric CT with single-breath-hold technique, continuous transport and continuous scanner rotation. Radiology 176:181–183

Kalender W (1995) Thin-section three-dimensional spiral CT: is isotropic imaging possible? Radiology 197:578–580

Klingenbeck-Regn K, Schaller S, Flohr T, Ohnesorge B, Kopp AF, Baum U (1999) Subsecond multi-slice computed tomography: basics and applications. EJR 31:110–124

Kondo C, Mori S, Endo M, Kusakabe K, Suzuki N, Hattori A, Kusakabe M (2005) Real-time volumetric imaging of human heart without electrocardiographic gating by 256-detector row computed tomography: initial experience. J Comput Assist Tomogr 29(5):694–698

Leber AW, Knez A, von Ziegler F, Becker A, Nikolaou K, Paul S, Wintersperger B, Reiser M, Becker CR, Steinbeck G, Boekstegers P (2005) Quantification of obstructive, nonobstructive coronary lesions by 64-slice computed tomography. JACC 46(1):147–154

Lell M, Marwan M, Schepis T, Pflederer T, Anders K, Flohr T, Allmendinger T, Kalender W, Ertel D, Thierfelder C, Kuettner A, Ropers D, Daniel WG, Achenbach S (2009) Prospectively ECG-triggered high-pitch spiral acquisition for coronary CT angiography using dual source CT: technique and initial experience. Eur Radiol 19(11): 2576–2583

Leschka S, Stolzmann P, Desbiolles L, Baumueller S, Goetti R, Schertler T, Scheffel H, Plass A, Falk V, Feuchtner G, Marincek B, Alkadhi H (2009) Diagnostic accuracy of high-pitch dual-source CT for the assessment of coronary stenoses: first experience. Eur Radiol 19:2896–2903

McCollough CH, Zink FE (1999) Performance evaluation of a multi-slice CT system. Med Phys 26:2223–2230

McCollough CH, Primak AN, Braun N, Kofler J, Yu L, Christner J (2009) Strategies for reducing radiation dose in CT. Radiol Clin North Am 47(1):27–40

Mori S, Endo M, Tsunoo T, Kandatsu S, Tanada S, Aradate H et al (2004) Physical performance evaluation of a 256-slice CT-scanner for four-dimensional imaging. Med Phys 31(6):1348–1356

Mori S, Kondo C, Suzuki N, Hattori A, Kusakabe M, Endo M (2006) Volumetric coronary angiography using the 256-detector row computed tomography scanner: comparison in vivo and in vitro with porcine models. Acta Radiol 47(2):186–191

Napel S, Rubin GD, Jeffrey RB (1993) STS-MIP: a new reconstruction technique for CT of the chest. JCAT 17(5):832–838

Nieman K, Cademartiri F, Lemos PA, Raaijmakers R, Pattynama PMT, de Feyter PJ (2002) Reliable noninvasive coronary angiography with fast submillimeter multislice spiral computed tomography. Circulation 106:2051–2054

Ohnesorge B, Flohr T, Becker C, Kopp A, Schoepf U, Baum U, Knez A, Klingenbeck-Regn K, Reiser M (2000) Cardiac imaging by means of electrocardiographically gated multisection spiral CT—initial experience. Radiology 217:564–571

Petersilka M, Bruder H, Krauss B, Stierstorfer K, Flohr TG (2008) Technical principles of dual source CT. Eur J Radiol 68(3):362–368

Raff GL, Gallagher MJ, O'Neill WW, Goldstein JA (2005) Diagnostic accuracy of non-invasive coronary angiography using 64-slice spiral computed tomography. JACC 46(3):552–557

Ropers D, Baum U, Pohle K et al (2003) Detection of coronary artery stenoses with thin-slice multi-detector row spiral computed tomography and multiplanar reconstruction. Circulation 107:664–666

Rybicki FJ, Otero HJ, Steigner ML, Vorobiof G, Nallamshetty L, Mitsouras D, Ersoy H, Mather RT, Judy PF, Cai T, Coyner K, Schultz K, Whitmore AG, Di Carli MF (2008) Initial evaluation of coronary images from 320-detector row computed tomography. Int J Cardiovasc Imaging 24(5): 535–546

Schaller S, Flohr T, Klingenbeck K, Krause J, Fuchs T, Kalender WA (2000) Spiral interpolation algorithm for multi-slice spiral CT—part I: theory. IEEE Trans Med Imaging 19(9):822–834

Schaller S, Stierstorfer K, Bruder H, Kachelrieß M, Flohr T (2001a) Novel approximate approach for high-quality image reconstruction in helical cone beam CT at arbitrary pitch. Proc SPIE Int Symp Med Imaging 4322:113–127

Schaller S, Niethammer MU, Chen X, Klotz E, Wildberger JE, Flohr T (2001) Comparison of signal-to-noise and dose values at different tube voltages for protocol optimization in pediatric CT. In: Abstract book of the 87th Scientific assembly and annual meeting of the RSNA, p 366

Schardt P, Deuringer J, Freudenberger J, Hell E, Knuepfer W, Mattern D, Schild M (2004) New X-ray tube performance in computed tomography by introducing the rotating envelope tube technology. Med Phys 31(9):2699–2706

Scheffel H, Alkadhi H, Leschka S, Plass A, Desbiolles L, Guber I, Krauss T, Gruenenfelder J, Genoni M, Luescher TF, Marincek B, Stolzmann P (2008) Low-dose CT coronary angiography in the step-and-shoot mode: diagnostic performance. Heart 94(9):1132–1137

Shankar JJS, Lum C, Sharma M (2010) Whole-brain perfusion imaging with 320-MDCT scanner: reducing radiation dose by increasing sampling interval. AJR 195:1183–1186

Stierstorfer K, Rauscher A, Boese J, Bruder H, Schaller S, Flohr T (2004) Weighted FBP—a simple approximative 3D FBP algorithm for multislice spiral CT with good dose usage for arbitrary pitch. Phys Med Biol 49:2209–2218

Taguchi T, Aradate H (1998) Algorithm for image reconstruction in multi-slice helical CT. Med Phys 25(4):550–561

Wintersperger B, Jakobs T, Herzog P, Schaller S, Nikolaou K, Suess C, Weber C, Reiser M, Becker C (2005) Aorto-iliac multidetector-row CT angiography with low kV settings: improved vessel enhancement and simultaneous reduction of radiation dose. Eur Radiol 15:334–341

Future Developments for MSCT

Patrik Rogalla

Contents

Abstract

Development and engineering are continually progressing and it would not be the first time in the evolution of computed tomography that some believe we have reached the zenith. Radiologists see technical improvements year after year Chen et al. (Med Phys 38(2):584–588, 2011), sometimes even quantum leaps and breakthroughs in all fields including data acquisition, image processing and post-processing Liu et al. (Radiology 253(1):98–105, 2009). Hounsfield's CT prototype featured a rotation time of about 300 s with a maximum image matrix of 80 × 80 pixels Hounsfield (Br J Radiol 68(815): H166–H172, 1995). In comparison, today's 320-slice scanner delivers rotation times of 350 ms and an image matrix of 512 × 512 pixels Rogalla et al. (Radiol Clin North Am 47(1):1–11, 2009). The pace is breathtaking and technological advances appear limitless if there was not radiation exposure that sets clear boundaries to uncontrolled expansion or unrestrained utilisation of CT in humans. However, priorities regarding the direction of development are laid out clearly: more diagnostic information with less radiation in a shorter scanning time and higher resolution. We may look into a crystal ball in an attempt to predict the future, but let us rather take a step-wise approach to illustrate where technological improvements are clinically desired and where short- and long-term advances can be expected.

P. Rogalla (✉)
Department of Medical Imaging, University of Toronto,
Toronto, ON M5G 2N2, Canada
e-mail: patrik.rogalla@uhn.ca

C. J. Zech et al. (eds.), *Multislice-CT of the Abdomen*, Medical Radiology. Diagnostic Imaging,
DOI: 10.1007/174_2012_569, © Springer-Verlag Berlin Heidelberg 2012

1 Speed of Scanning

1.1 Clinical Demand

Speed of scanning reflects several aspects during the examination procedure. It might refer to the overall duration of diagnostic procedure in its entirety; it might simply reflect body coverage per time, or even refer to temporal resolution both in-plane (i.e., within a given axial slice) and through-plane (i.e., larger body coverage per time).

- *Overall duration*
  Most abdominal imaging protocols in CT are driven by the need to capture specific perfusion phases, thus the overall duration of a CT examination is primarily determined by physiology. Faster scanning would not necessarily result in shorter procedure times.
- *Body coverage per rotation time*
  Clinical necessity to increase body coverage per unit time predominantly arises from the fact that most CT images are acquired during breath-hold in order to reduce motion artefacts. Faster CT scanners achieve greater anatomical coverage during a single breath-hold period. Modern 64-slice scanners need only a few seconds to complete an abdominopelvic CT, however, combined chest, abdomen and pelvis protocols may still exceed the possible breath-hold length for some patients. In addition, new CT applications in perfusion imaging greatly benefit from faster and wider coverage no matter whether helical or axial scanning modes are used.
- *In-plane and through-plane (Z-axis) temporal resolution*
  Dramatic improvements in through-plane resolution have been achieved with the advent of helical scanning technique, but the hunger for further increases in in-plane resolution is mainly driven by cardiac imaging in need of short exposure times to allow motion free images. For abdominal applications, in-plane temporal resolution plays a less important role with the exception of motion artefact reduction in patients who cannot hold their breath or physically move during data acquisition.

1.2 Technological Development

Most modern CT scanners revolve the gantry at least twice per second. It seems appealing to have faster gantry revolving times, however centrifugal forces

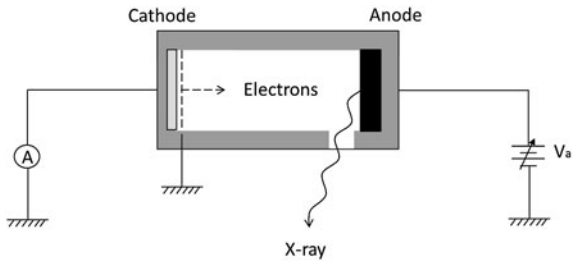

Fig. 1 Simplified principle of carbon nanotubes (CNT). CNTs offer unique advantages for a new generation of X-ray tubes including low power consumption, long lifetime and pulse capability

physically set mechanical limits given current gantry and more importantly, X-ray tube designs. G-forces already exceed 30 g in some current CT scanners. Smaller and lighter X-ray generating tubes are a prerequisite for faster gantry revolving times. It is hard to predict, but minimal gantry revolving times of 150–200 ms may well be a physical limit given today's system components. Such revolving times combined with dual-source technology will lower the exposure window for an axial slice (often inaccurately referred to as in-plane temporal resolution) to less than 40 ms, likely sufficient for virtually all potential cardiac applications.

Another problem becomes more evident with faster scan speeds: the shorter the exposure, the higher the necessary tube output in order to ensure sufficient photon flux on the detector side. Maximum tube power ranges around 100 kW in most CT current scanners. Distributing the energy to two focal spots is current practice and predominantly designed to increase spatial resolution; at the same time, the heat is distributed to a larger area on the anode that helps prevent heat damage to the tube.

Will more tubes, maybe a triple-source CT, solve the problem of limited temporal resolution? Likely not. Unless alternative sources of X-rays such as carbon nanotubes (Fig. 1) will emit enough power sufficient for clinical use, it appears unlikely that more than two conventional tubes (based on a heated tungsten filament) will find space within a given gantry geometry, not to mention subsequent issues with detector position and respective configuration, anti-scatter grids and many more. Inverse geometry CT technology composed of a large distributed X-ray source with an array of discrete electron emitters and focal spots is believed to carry the potential

breakthrough in volumetric coverage, dose efficiency, temporal and spatial resolution (Mazin et al. 2007).

Faster helical scanning—including dual source helical scanning—has been a quantum leap towards rapid longitudinal coverage, albeit a small "overall" enhancement. Apart from the fact that patient acceleration and deceleration may set boundaries to further increase in table speed, faster coverage is beneficial in recently developed scanning techniques for perfusion imaging of the abdomen. The so-called "shuttle mode" enables coverage of larger body areas for perfusion imaging not limited to the effective detector width (Okada et al. 2011).

Sixteen centimetre effective detector coverage represents the current pinnacle in area detector CT and allows for complete organ imaging without table motion in less than 350 ms. Further increases in volumetric coverage inevitably result in increased scattered radiation, cone-beam artefacts, heel effect and over beaming. It remains to be determined where the acceptable boundaries are, however, 20–25 cm coverage appear reasonable and would relevantly reduce scanning time. The entire abdomen, for instance, could be examined using a single gantry rotation.

2 Spatial Resolution

2.1 Clinical Demand

Higher spatial resolution appears to be key to success in CT imaging. In abdominal imaging, both low- and high-contrast resolution are of equal and critical importance. As a classical example: detecting contrast material washout in hepatocellular carcinoma on delayed imaging requires low-contrast resolution, detecting small arterial branches within the liver on arterial perfusion phase images requires high-contrast resolution.

2.2 Technological Development

Many factors influence the maximum achievable spatial resolution. In XY-direction (axial plane), high-contrast spatial resolution is predominantly determined by the number of projections (sampling frequency) and the number and size of detector elements. High-resolution scans should not be acquired with the fastest gantry rotation on any of the currently available CT scanners, because the sampling rate usually stays constant thereby limiting spatial resolution; conversely, longer gantry rotation times facilitate an increased number of projections. The spatial resolution currently achieved on scanners from all manufacturers varies from 0.33 to 0.47 mm (with a high-frequency reconstruction kernel). The higher the sampling frequency, the more data are to be collected, stored and eventually transmitted to the reconstruction unit. Managing the sheer amount of raw-data signifies a technological challenge, and further advancements in data transmission will facilitate faster sampling rates, provided the detector material allows for respective limiting afterglow effects.

Minimising detector element apertures continues to marshal engineering efforts given extremely high physical demands. As anti-scatter grids and optical barriers (to prevent detector cross-talk) remain necessary, the overall geometrical efficiency of detector arrays may suffer even further using smaller elements. On the other hand, higher resolution aperture should dramatically improve mid- to high- frequency performance allowing for image reconstruction with higher spatial resolution, especially in unification with iterative reconstruction methods to overcome associated increases in image noise (see below). Reconstructible axial slice widths of less than 0.3 mm will become clinical reality in the future.

Image noise represents the limiting factor for low-contrast resolution. Radiation dose concerns in the public and amongst professionals have shifted research and development in CT towards dose reduction techniques. Fewer photons inevitably lead to a lower signal above baseline noise, subsequently resulting in noisier images. A myriad of techniques to confine image noise have been developed, amongst which the recently introduced iterative image reconstruction method attracts the most attention. Currently, model-based iterative reconstruction techniques in both the image and data domain (Fig. 2) are being evaluated (Mieville et al. 2012) and partially implemented into clinical practice. It is foreseeable that further advances in purely raw-data-based iterative reconstruction methods and improved modelling of scanner properties into the algorithm will dramatically improve image quality thus allowing for very low-dose CT imaging in most abdominal indications. Both low- and high-contrast resolution will likely be improved using these new methods.

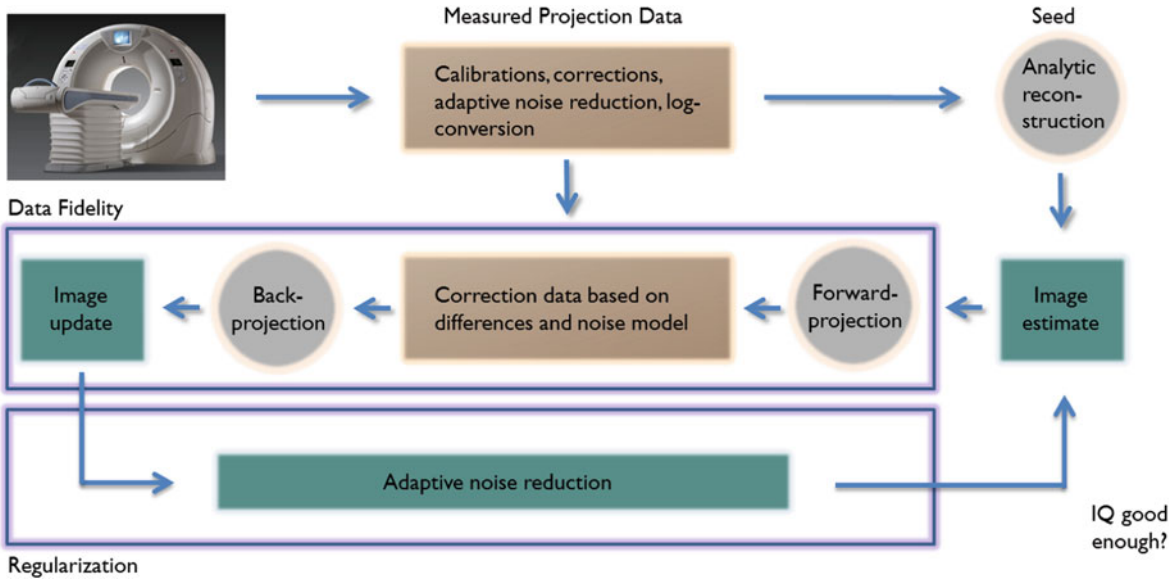

Fig. 2 Schematic drawing of the data flow in raw-data-based iterative reconstruction

3 Temporal Resolution

3.1 Clinical Demand

Improvements in temporal resolution may not lie in the forefront of priorities in abdominal imaging, the demand is mainly driven by cardiac CT. On the other hand, shorter in-plane exposure times will reduce in-plane motion artefacts from breathing, bowel movements, vessel pulsation or patient unrest during scanning.

3.2 Technological Development

Accelerating the gantry is an appealing proposal, however, as described above, basic physical constrains limit faster gantry revolving times. Nevertheless, with the advent of lighter tubes and further miniaturization of all electronic components, revolving times of 150–200 ms are feasible and likely to become reality soon.

Mounting more than one tube within the gantry represents another solution; dual-source CT units have been on the market since 2007 and have significantly contributed to the success story of cardiac CT. Mounting more than two conventional tubes within a gantry might not only be challenging from the engineering point of view as the gantry becomes even heavier, the diagnostic value might be rather limited in light of subsequent problems including scattered radiation and geometrical constraints (limited fields-of view for each tube-detector system).

Why not remove mechanical constraints as the limiting factor entirely for enhanced temporal resolution? Electron-beam CT with its unrivalled exposure time of 50 ms per sweep has been extensively evaluated for cardiac imaging (Enzweiler et al. 2004). Image quality never reached the standard of conventional gantry designs and output restrictions of the X-ray gun limited its ubiquitous use in abdominal imaging. The scenario might change again as soon as alternative small X-ray sources in fixed position within the gantry (such as CNTs) will produce sufficient power for clinical imaging needs. Prototype scanners, albeit for non-clinical applications, are currently being developed and tested. Preliminary results are promising (inverse geometry CT) (Mazin et al. 2007; Schmidt 2011).

4 Image Quality

4.1 Clinical Demand

Generating artefact-free high-quality images is the essence of research and development in CT technology. Apart from high-contrast, low-contrast, temporal

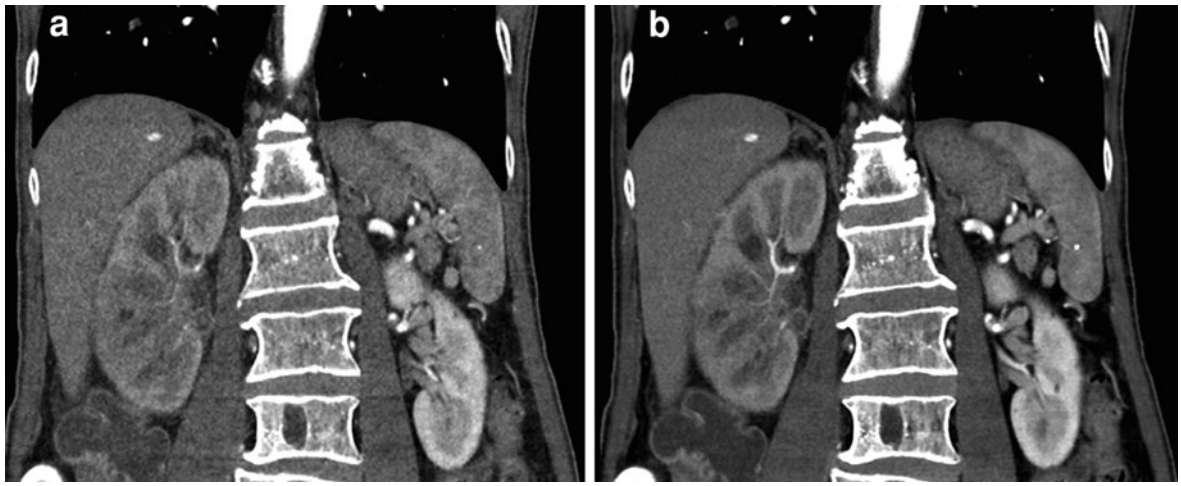

Fig. 3 Example of image quality improvement by means of model-based iterative reconstruction. *Note*: Not only contains image (**b**) less image noise (translating into ~50% radiation dose reduction), the vascular contrast (best seen within the kidney) is perceptibly increased at the same time. **a** Conventional filtered back-projection (FBP). **b** Model-based iterative econstruction (AIDR 3)

resolution and artefact reduction: pixel noise—often referred to as "image noise"—is perceived as the leading parameter that determines overall image quality. With the current focus on radiation dose amongst the public and professionals, dose reduction has attracted a lot of attention and evolved as a determining factor for modality decision making. Unfortunately, radiation dose reduction, unless compensated for by other methods, inevitably leads to noisier images which is why a significant volume of research is devoted towards noise reduction methods. High image noise and severe artefacts may render CT images non-diagnostic (Barrett and Keat 2004).

4.2 Technological Development

Currently, the key to success in noise reduction is iterative image reconstruction techniques (Yu et al. 2011). Be they based on image data, raw-data domain or a combination of both, iterative methods have already demonstrated their effectiveness in noise suppression while maintaining diagnostic image quality. Although available clinical data are still preliminary, it seems that radiation dose reduction of more than 50% is clinically achievable without jeopardising overall diagnostic image quality (Fig. 3). Since image noise predominantly degrades low-contrast resolution, one might expect relevant improvements in low-contrast resolution using the new reconstruction methods. It is expected that in the near future, raw-data-based iterative reconstruction algorithms with improved modelling will become the standard method in CT imaging.

Reduction of artefacts mainly from radio-dense implants such as metallic prostheses has been a focus of research for decades. Many mathematical approaches for metal artefact reduction (MAR) have been developed and explored of which the most simple, linear interpolation to gap the metal shadow, performed not dissimilar as more complex approaches (Kalender et al. 1987). However, all previously assessed MAR algorithms, besides removing the metal artefacts, introduced new artefacts and cannot completely recover the information from the metal trace. More advanced methods such as empirical beam-hardening correction (EBHC) and normalised MAR (NMAR) are currently under investigation; both have proven to be quite effective in phantom studies and initial clinical applications (Kyriakou et al. 2010; Meyer et al. 2010) (Fig. 4). Without doubt, these or similar mathematical methods will be integrated into future CT reconstruction algorithms and thus will contribute to further image quality improvements in abdominal imaging.

Motion plays a minor role in abdominal CT, although pulsation artefacts may occur in the aorta or

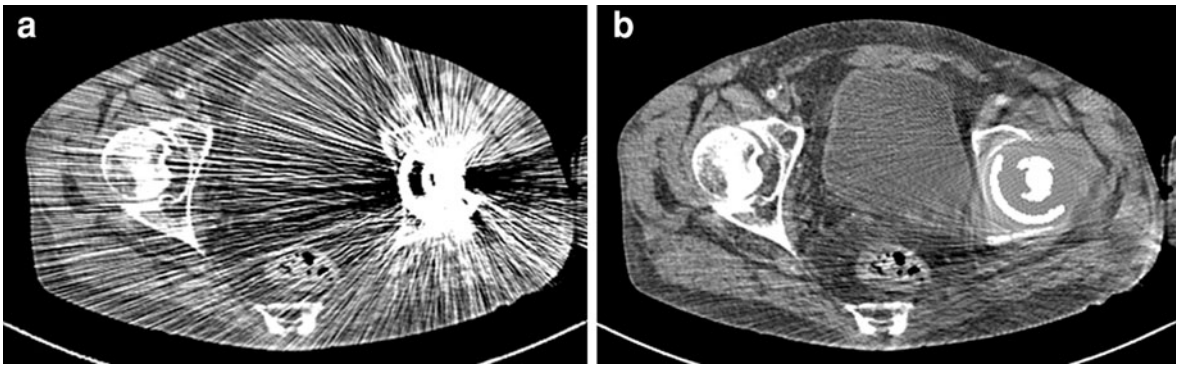

Fig. 4 Axial scan though the hip. The original uncorrected image (**a**) exhibits severe amounts of streak artefacts caused by the metallic hip implant. Diagnostic image quality may be restored image (**b**) using normalised metallic artefact reduction (NMAR) (*courtesy* Marc Kachelriess)

renal arteries and thus reduce conspicuity of small vascular details. In cardiac imaging, repeated (and to the major part predictable) motion occurs. In principle, feeding preexisting anatomical knowledge into the reconstruction process may be utilised in many ways, contributing to improved temporal resolution and motion correction (Tang et al. 2010). Prior image constrained compressed sensing (PICCS) has been shown to improve temporal resolution especially in cardiac CT. One might expect improvements of temporal resolution by a factor of 2 without modification of scanner hardware, however, evaluation of these methods are necessary in order to assess their applicability and usefulness in general body CT.

5 Radiation Dose

5.1 Clinical Demand

Exposure to radiation has become a major public concern (see following chapter) in particular as hypothetical risks have been falsely perceived as evidenced-based knowledge. In any event, radiation dose concerns have driven research endeavours in CT for the past decade and we are about to see major technological steps towards low-dose and ultra-low-dose imaging strategies. Radiation dose reduction today is all about increased dose efficiency along the chain of detectors, amplifiers (data acquisition system, DAS), data transmission and reconstruction algorithms. The goal however is to utilise the least amount of radiation in order to obtain an image quality that is believed to be diagnostically sufficient. For that reason, dose reduction may be achieved in many ways including image noise reduction alone or improving low-contrast resolution. Improved temporal resolution may translate into lower radiation doses if shorter exposure times can be applied for motion capture.

5.2 Technological Development

Image noise reduction is the most obvious method for dose reduction as one can afford less radiation dose to achieve similar noise levels in the final image. Quantum noise dominates at higher doses, whereas electronic noise (i.e., noise originating from all electronic components within the detector and amplifier chain) typically dominates at low-dose levels. Increased integration and further miniaturisation of electronic components will contribute to a lower electronic noise floor allowing for improved signal-to-noise ratio in ultra-low-dose applications.

Another development for further noise reduction at the detector side is to reduce the number of steps required for conversion of X-ray photons into an electrical signal. In current solid-state detectors, X-ray photons are converted to light and light is converted to an electrical signal. Photon-counting detectors convert X-ray photons directly into an electrical charge (Fig. 5). The pulses created in the detector by the incident photons are easily detected, since the pulse height is typically an order of magnitude higher than the electronic noise in the detector. Thus the detector counts the number of peak pulses

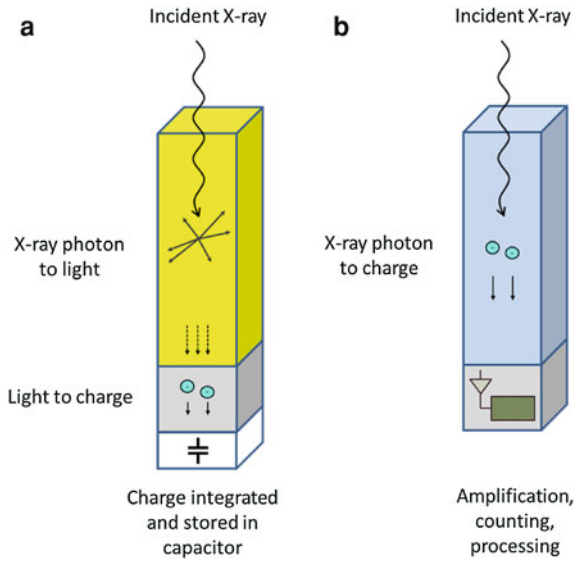

Fig. 5 Conventional detector design. **a** Incident photons are converted to light within the solid-state detector material, and in a second process, light is converted to an electrical charge. The charge is then integrated and stored in a capacitor. Photon-counting detectors (**b**) directly convert X-ray photons to charge that is amplified, counted and processed

and virtually no other signal. Following processing steps including pulse shaping and height analysis, the electric signal may be assigned to more than one energy bin, allowing for spectral analysis of the original X-ray signal(s) (Mieville et al. 2012; Wang et al. 2011). The lack of electronic noise and the ability to perform spectral analysis are paired with other advantages of photon-counting detectors, such as nearly 100% geometric efficiency (in comparison: current CT detector arrays range between 60 and 80% geometric efficiency), potentially higher spatial resolution and contrast-to-noise optimisation. Although the advantages of photon-counting detectors are appealing and obvious, their utilisation in clinical scanners remains far down the road as many challenges are to be overcome, including count-rate capability and count-rate-dependent energy response, not to mention the increased cost of this technology.

The current and near future perspective is that iterative reconstruction techniques, as described above, will continue to be the frontrunner of all dose reduction efforts. The impact of iterative methods is highest when data quality is poor such as with low-dose protocols or in large patients. Dose reduction without loss of diagnostic image quality has already been proven to be possible by means of statistical reconstruction and simple iterations in the image domain. Further sophistication predominantly in the field of modelling scanner characteristics into the reconstruction process invigorate the assumption that dose reduction of more than 75% will be clinically manageable.

6 And Even More …

Many current and future developments aim at improving image quality, reducing artefacts and radiation dose at the same time. kV adaptation serves as a good example. Based on the fact that X-ray penetration depends on its energy, kV adaptation to body size, similar to tube current modulation, will reduce artefacts and thereby improve image quality (Pinho et al. 2011). This will likely translate into some radiation dose savings.

Refinements in dual-energy CT regardless of its technical implementation (kV switching, dual-source, back-to-back or dual-energy helical scanning) are imminent and will make this interesting application even more suitable for general clinical use. New scintillator material that features a negligible afterglow in conjunction with a 100-fold faster reaction time allows for recording of 7,000 views per second and may be one of the prerequisites for single-source ultra-fast dual-energy switching, promising almost simultaneous spatial and temporal registration and material decomposition without limiting the scan field-of-view. Fewer beam-hardening artefacts, metal artefact reduction and further improvements in contrast-to-noise ratio are some of the benefits resulting from new scintillator material.

As photon-counting detectors are far from being introduced into clinical scanners, a simple but effective solution for post-patient energy separation lies in a double-layer detector design (Rogalla et al. 2009). The upper layer predominantly receives photons with lower energy and the lower layer receives photons with higher energy. Summing the signal from both detector layers returns the full signal as in a single-layer detector, but separate readouts from both layers allow for simple spectral analysis of the X-ray beam. This technology remains currently under clinical evaluation.

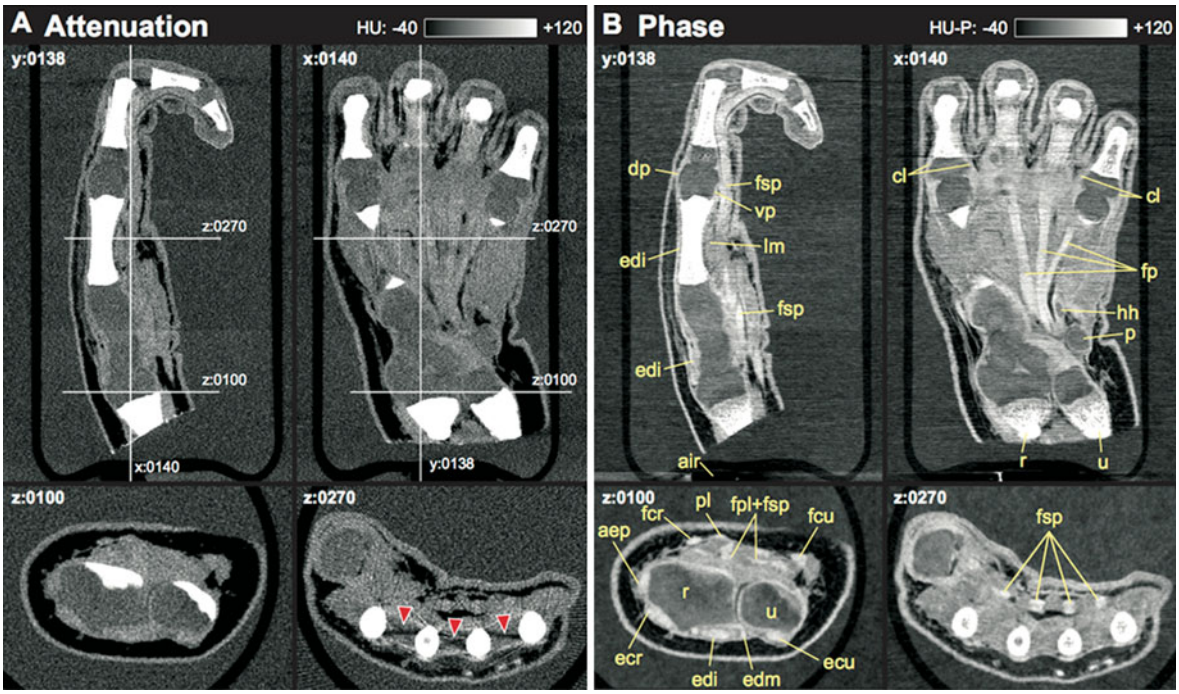

Fig. 6 Initial imaging experience in human tissue using phase-contrast CT (from: Donath et al. 2010)

Although in its earliest stage of development from the clinical perspective, phase-contrast CT carries a lot of clinical potential (Donath et al. 2010). Promising experimental results have recently been obtained in material science, biological applications (Bronnikov 2002) and in smaller body parts (Fig. 6). Moving away from absorption CT might sound revolutionary: various human tissues demonstrate very weak absorption contrast, however, produce significant phase shifts in the X-ray beam. The use of phase information for imaging purposes therefore appears to be a suitable alternative for imaging, likely contributing to further radiation dose reduction in the future.

7 Summary

MSCT has—without doubt—reached a very high degree of maturity, mastering almost all clinical demands. Nevertheless, it would be foolish to believe that technology has reached its true pinnacle. Whilst acknowledging the risks of drifting into speculation, the following technological advances are likely to become clinical reality in the near future:

- faster gantry revolving times, likely around 200 ms,
- improved temporal resolution, probably around 40–50 ms,
- larger area-detectors for extended anatomical coverage without table motion,
- smaller detector elements leading to higher spatial resolution,
- improved image quality by metal and motion artefact reduction,
- drastic radiation dose reduction, predominantly by improved iterative reconstruction methods.

Technological advances currently on the horizon are:

- new detector materials and designs, photon-counting detectors,
- alternative X-ray sources such as carbon nanotubes,
- inverse geometry CT,
- phase-contrast CT.

In light of most recent quantum leaps in CT technology and all of the above, computed tomography remains one of the most fascinating fields of technological evolution and will undoubtedly

continue to play a pace-maker role for advances in medical imaging on the whole.

References

Barrett JF, Keat N (2004) Artifacts in CT: recognition and avoidance. Radiographics 24(6):1679–1691. doi:10.1148/rg.246045065 , 24/6/1679[pii]

Bronnikov AV (2002) Theory of quantitative phase-contrast computed tomography. J Opt Soc Am A Opt Image Sci Vis 19(3):472–480

Chen GH, Zambelli J, Li K, Bevins N, Qi Z (2011) Scaling law for noise variance and spatial resolution in differential phase contrast computed tomography. Med Phys 38(2):584–588

Donath T, Pfeiffer F, Bunk O et al (2010) Toward clinical X-ray phase-contrast CT: demonstration of enhanced soft-tissue contrast in human specimen. Invest Radiol 45(7): 445–452. doi:10.1097/RLI.0b013e3181e21866

Enzweiler CN, Becker CR, Bruning R et al (2004) Value of electron beam tomography (EBT). Rofo 176(11):1566–1575. doi:10.1055/s-2004-813666

Hounsfield GN (1995) Computerized transverse axial scanning (tomography): part I description of system. 1973. Br J Radiol 68(815):H166–H172

Kalender WA, Hebel R, Ebersberger J (1987) Reduction of CT artifacts caused by metallic implants. Radiology 164(2): 576–577

Kyriakou Y, Meyer E, Prell D, Kachelriess M (2010) Empirical beam hardening correction (EBHC) for CT. Med Phys 37(10): 5179–5187

Liu X, Primak AN, Krier JD, Yu L, Lerman LO, McCollough CH (2009) Renal perfusion and hemodynamics: accurate in vivo determination at CT with a 10-fold decrease in radiation dose and HYPR noise reduction. Radiology 253(1):98–105. doi:10.1148/radiol.2531081677, 253/1/98[pii]

Mazin SR, Star-Lack J, Bennett NR, Pelc NJ (2007) Inverse-geometry volumetric CT system with multiple detector arrays for wide field-of-view imaging. Med Phys 34(6): 2133–2142

Meyer E, Raupach R, Lell M, Schmidt B, Kachelriess M (2010) Normalized metal artifact reduction (NMAR) in computed tomography. Med Phys 37(10):5482–5493

Mieville FA, Gudinchet F, Brunelle F, Bochud FO, Verdun FR (2012) Iterative reconstruction methods in two different MDCT scanners: physical metrics and 4-alternative forced-choice detectability experiments—a phantom approach. Phys Med. doi:10.1016/j.ejmp.2011.12.004, S1120-1797(11)00160-8[pii]

Okada M, Kim T, Murakami T (2011) Hepatocellular nodules in liver cirrhosis: state of the art CT evaluation (perfusion CT/volume helical shuttle scan/dual-energy CT, etc.). Abdom Imaging 36(3):273–281. doi:10.1007/s00261-011-9684-2

Pinho D, Kulkarni N, Savage C, Sahani D (2011) Initial experience with automated kVp selection for abdomen CT scanning. Annual meeting RSNA Chicago

Rogalla P, Kloeters C, Hein PA (2009) CT technology overview: 64-slice and beyond. Radiol Clin North Am 47(1):1–11. doi:10.1016/j.rcl.2008.10.004, S0033-8389(08)00188-7[pii]

Schmidt TG (2011) What is inverse-geometry CT? J Cardiovasc Comput Tomogr 5(3):145–148. doi:10.1016/j.jcct.2011.04.003, S1934-5925(11)00174-2[pii]

Tang J, Hsieh J, Chen GH (2010) Temporal resolution improvement in cardiac CT using PICCS (TRI-PICCS): performance studies. Med Phys 37(8):4377–4388

Wang AS, Harrison D, Lobastov V, Tkaczyk JE (2011) Pulse pileup statistics for energy discriminating photon counting X-ray detectors. Med Phys 38(7):4265–4275

Yu Z, Thibault JB, Bouman CA, Sauer KD, Hsieh J (2011) Fast model-based X-ray CT reconstruction using spatially non-homogeneous ICD optimization. IEEE Trans Image Process 20(1):161–175. doi:10.1109/TIP.2010.2058811

Radiation Exposure and Risk Associated with CT Examinations

Gunnar Brix and Elke A. Nekolla

Contents

Abstract

Medical imaging procedures using ionizing radiation always pose some risk of adverse health effects to the persons examined–in particular radiation-induced cancer. It is thus necessary to carefully balance the benefits and risks of these examinations. This particularly applies to CT examinations being a major source of patient and man-made population exposure. This chapter briefly reviews the evidence on health effects induced by ionizing radiation, presents the essential concepts to estimate radiation doses and risks related to CT examinations, identifies technology-specific factors influencing patient exposure and, finally, outlines application-specific measures to reduce radiation risks to patients undergoing CT procedures.

Medical imaging procedures using ionizing radiation always pose some risk of adverse health effects to the persons examined–in particular radiation-induced cancer. It is thus necessary to carefully balance the benefits and risks of these examinations. This particularly applies to CT examinations because international reviews and recent results from various countries reveal the steadily increasing impact of CT as a major source of patient and man-made population exposure to ionizing radiation (Amis et al. 2007; Brenner and Hall 2007; UNSCEAR 2010). In Germany, for example, CT procedures accounted for 7% of all X-ray examinations conducted in 2008, but for nearly 60% of the resultant collective effective dose which corresponds to a per capita effective dose of 1 mSv (Nekolla et al. 2010). Even higher numbers of per

G. Brix (✉) · E. A. Nekolla
Department of Medical and Occupational Radiation Protection, Federal Office for Radiation Protection, Ingolstädter Landstrasse 1,
85764 Neuherberg, Germany
e-mail: gbrix@bfs.de

C. J. Zech et al. (eds.), *Multislice-CT of the Abdomen*, Medical Radiology. Diagnostic Imaging,
DOI: 10.1007/174_2011_405, © Springer-Verlag Berlin Heidelberg 2012

capita effective doses due to CT are reported for Japan (Nishizawa et al. 2004) and the USA (Mettler et al. 2009). This chapter briefly reviews the evidence on health effects induced by ionizing radiation, presents the essential concepts to estimate radiation doses and risks related to CT examinations, identifies technology-specific factors influencing patient exposure and, finally, outlines application-specific measures to reduce radiation risks to patients undergoing CT procedures.

1 Health Effects Induced by Ionizing Radiation and Principles of Radiation Protection

Exposure to ionizing radiation may lead to early or late health effects which may be either non-stochastic or stochastic. A *non-stochastic (or deterministic) effect* is an effect where the severity increases with increasing dose (e.g., damage of the skin: erythema at low doses, severe tissue damage at high doses). A *stochastic effect*, on the other hand, is an effect where the severity is independent of dose, but the probability of inducing the effect does increase with increasing dose. Examples for stochastic effects are cancer or hereditary disorders.

Cancers caused by ionizing radiation occur several years to decades after the exposure has taken place (latency time). They do not differ in their clinical appearance from cancers that are caused by other factors. A radiation-induced cancer cannot be recognized as such, and it is only by means of epidemiological studies that increases in the spontaneous cancer incidence rates of irradiated groups can be detected. Ionizing radiation is the carcinogen that has been studied most intensely.

Increased cancer rates have been demonstrated in humans through various radio-epidemiological studies at moderate or high doses, i.e. organ or whole-body doses exceeding 50–100 mSv, delivered acutely or over a prolonged period. The so-called *Life Span Study* (LSS) of the survivors of the atomic bombings in Hiroshima and Nagasaki is the most important of these studies (Preston et al. 2007). The follow-up of the atomic bomb survivors has provided detailed knowledge of the relationships between radiation risk and a variety of factors, such as the absorbed dose, the age at exposure, the age at diagnosis and other parameters. The LSS provides data with good radio-epidemiologic evidence due to the large size of the study population (about 86,600 individuals with individual dose estimates), the broad age- and dose-distribution, the long follow-up period (about half a century) and an internal control group (individuals exposed only at a minute level or not at all) (BEIR-VII 2006). The LSS is, therefore, the major source for predicting radiation-induced risks for the general population.

However, radiation risk estimates are not merely based on the follow-up of the atomic bomb survivors. They are also largely supported by a multitude of smaller studies, mostly on groups of persons exposed for medical reasons, both in diagnostics and therapy (BEIR-VII 2006).

There is considerable controversy regarding the risk of low levels of radiation, typical for diagnostic radiation exposures, since radiation risks evaluated at low dose levels are not based on experimental and epidemiological evidence. Given this lack of evidence, estimates on risk, derived from high doses, have been extrapolated down to low dose levels by various scientific bodies, including the 'International Commission on Radiological Protection' (ICRP-103 2007), the 'United Nations Scientific Committee on the Effects of Atomic Radiation' (UNSCEAR 2000), and the 'Biological Effects on Ionizing Radiation' committee (BEIR-VII 2006). Estimates on risk per unit of dose have been derived using the so-called *linear, non-threshold (LNT) hypothesis*, which is based on the assumptions that (a) any radiation dose–no matter how small–may cause an increase in risk and (b) the probability of this increase is proportional to the dose absorbed in the tissue. Although the risk evaluated at low dose levels is thus hypothetical, it is prudent to assume that it exists and that the LNT model represents an upper bound for it. It is for this reason that current radiation protection standards as well as risk assessments are based on the LNT hypothesis (ICRP-103 2007).

In line with this philosophy, the ICRP emphasizes that proper justification and optimization of medical procedures are indispensable principles of radiation protection in medicine (ICRP-105 2007):

(66) *Justification* of a procedure for an individual patient should include checking that the required information is not already available. Usually, no

additional justification is needed for the application of a simple diagnostic procedure to an individual patient with the symptoms or indications for which the procedure has already been justified in general. For high-dose examinations, such as complex diagnostic and interventional procedures, individual justification by the practitioner is particularly important and should take account of all the available information. This includes the details of the proposed procedure and of alternative procedures, the characteristics of the individual patient, the expected dose to the patient, and the availability of information on previous or expected examinations or treatment.

(69) *Optimization* of radiological protection means the same as keeping the doses 'as low as reasonably achievable, economic and societal factors being taken into account,' (ALARA) and is best described as management of the radiation dose to the patient to be commensurate with the medical purpose". (70) Although "dose constraints for patients are inappropriate … management of patient dose is important and often can be facilitated for diagnostic and interventional procedures by use of a diagnostic reference level, which is a method for evaluating whether the patient dose is unusually high or low for a particular medical imaging procedure.

2 CT Dosimetry

2.1 Fundamental Dose Quantities

It is generally assumed that the probability of detrimental radiation effects is directly proportional to the energy deposited by ionizing radiation in a specified organ or tissue, T. Therefore, the fundamental dosimetric quantity is the *absorbed dose*, which is defined as the radiation energy absorbed in a small volume element of matter divided by its mass. In the SI system the absorbed dose, D, is given in the unit *Gray* (1 Gy = 1 J/kg). For radiological protection purposes, the absorbed dose is averaged over an organ or tissue and weighted by a dimensionless *radiation weighting factor*, w_R, to reflect the higher biological effectiveness of high-LET as compared to low-LET radiations. The resulting weighted dose is designated as the *organ or equivalent dose*, H_T, and given in the unit *Sievert* (1 Sv = 1 J/kg). For low-LET radiation, such as X-rays, w_R is equal to 1. Whenever an organ is only partially irradiated, as in the case of an organ extending over the whole body (e.g., red bone marrow or skin) or an organ situated at the border of the irradiated body region, the organ dose may differ markedly from the absorbed dose at different positions within that organ.

Tissues and organs are not equally sensitive to the effects of ionizing radiation. Due to this reason, *tissue weighting factors*, w_T, are provided by the ICRP for a reference population of equal numbers of both sexes and a wide range of ages (ICRP-60 1991, ICRP-103 2007). These factors indicate the relative proportion of each organ or tissue to the total health detriment resulting from a uniform irradiation of the whole body. Detriment is a multidimensional concept: its principal components are the stochastic quantities probability of the attributable fatal cancer, the weighted probability of attributable non-fatal cancer, the weighted probability of severe heritable effects, and the length of life lost if the harm occurs (ICRP-103 2007). If the body is exposed in a nonuniform manner, as for example in a patient undergoing a CT examination, the sum of the products of the organ doses and the corresponding tissue weighting factors determined for each of the various organ or tissue exposed has to be computed.

$$E = \sum_T w_T \cdot H_T \quad \text{with} \quad \sum_T w_T = 1. \qquad (1)$$

The resulting quantity is denoted as *effective dose E* (in Sv). Based on this dose quantity, it is possible to assess and to compare the probability of stochastic radiation effects resulting from different radiation exposures–as for example diverse X-ray procedures yielding a different pattern of dose distribution in the body. It should be noted, however, that the concept of the effective dose facilitates only an over-all, not an organ-specific assessment of stochastic radiation risks and is aimed at large, age and gender averaged collectives such as the working population or the whole population in a country. Nevertheless, this generic approach provides a rational framework for the justification and optimization of radiological imaging procedures.

Based on the latest available scientific information, the tissue weighting factors, w_T, have been modified in 2007 by the ICRP (ICRP-103 2007). As Table 1 reveals, the most significant changes from the previous

Table 1 Tissue weighting factors, w_T, given by the ICRP in 1990 and 2007. They characterize the relative susceptibility of various tissues and organs, T, to ionizing radiation

Tissue or organ	w_T
ICRP-60 1991	
Gonads	0.20
Bone marrow, lungs, colon, stomach	0.12
Liver, thyroid, esophagus, breast, bladder	0.05
Bone surface, skin	0.01
Remainder tissues[a]	0.05
ICRP-103 2007	
Bone marrow (red), colon, lung, stomach, breast, remainder tissues[b]	0.12
Gonads	0.08
Bladder, esophagus, liver, thyroid,	0.04
Bone surface, brain, salivary glands, skin	0.01

The 'remainder tissues' consists of the following group of additional organs and tissues with a lower sensitivity for radiation-induced effects for which the mass-weighted average combined with a 'splitting rule' (ICRP-60) or the simple arithmetic average (ICRP-103) of organ doses must be used

[a] adrenals, brain, extrathoracic airways, small intestine, kidneys, muscle, pancreas, spleen, thymus, and uterus

[b] adrenals, extrathoracic region, gall bladder, heart, kidneys, lymphatic nodes, muscle, oral mucosa, pancreas, prostate, small intestine, spleen, thymus, uterus/cervix

Table 2 Representative dose values for CT scans frequently carried-out in Germany in 2008/09

Examination	$CTDI_{vol}$ (mGy)		DLP (mGy cm)		E[a] (mSv)	
	Median	Inter-quartile range	Median	Inter-quartile range	ICRP-60	ICRP-103
Brain	55.1	46.8–62.4	763	611–888	1.9	1.9
Thorax	9.3	6.9–11.1	292	235–378	4.6	6.1
Upper abdomen	11.5	10.5–13.4	408	309–539	7.4	7.9
Abdomen	13.4	10.4–18.3	631	485–905	10.9	10.0
Lumbar spine	31.5	27.1–42.0	290	221–397	4.4–6.3[b]	5.0–6.5[b]
Pelvis	14.4	10.6–18.9	331	250–456	6.1	4.3

[a] Effective dose derived from organ doses estimated with CT-Expo (V.1.5)

[b] The effective dose depends on the position of the scan range within the lumbar spine

held values (ICRP-60 1991) relate to breast (0.05 → 0.12), gonads (0.2 → 0.08), and the remainder tissues (0.05 → 0.12 using a simplified additive system). These modifications lead to a decrease of the effective dose of CT examinations performed in the pelvis region and to an increase in case of examinations performed in the breast/thorax region (Table 2).

2.2 Dose Descriptors

In practice, neither organ nor effective doses can be measured directly. In order to overcome this difficulty, dose descriptors are frequently used, which can easily be measured with an appropriate phantom. These quantities can be used for comparison of different devices and parameter settings within a particular diagnostic modality (e.g., CT). Moreover, they form the basis for the estimation of organ and effective doses.

The basic dose descriptor in CT is the *computed tomography dose index*, *CTDI* (given in mGy). As illustrated in Fig. 1a, the *CTDI* indicates the dose value inside an irradiated slice that would result if the dose profile were entirely concentrated in a rectangular profile of width equal to the nominal slice thickness. Accordingly, all dose contributions from

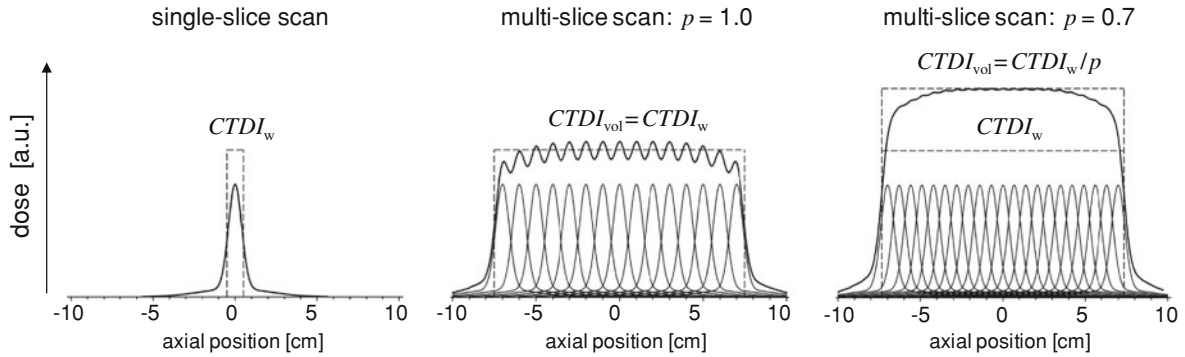

Fig. 1 Axial dose profiles for **(a)** a single-slice CT scan, **(b)** a CT scan series with 15 slices acquired with a pitch of $p = 1.0$ and **(c)** a CT scan series with 21 slices acquired with $p = 0.7$. The nominal slice thickness is 10 mm in each case. Indicated are the weighted CT dose index, $CTDI_w$, as well as the volume CT dose index, $CTDI_{vol}$, in case of the multi-slice scans

Fig. 2 Cylindrical standard CT dosimetry phantoms made from Perspex. The phantoms with a diameter of 16 cm and 32 cm are used for representative *CTDI* measurements of the head and trunk, respectively. For dose measurement the pencil ionization chamber with an active length of 100 mm is inserted into the holes

outside the nominal slice width, i.e. the areas under the tails of the real dose profile, are added to the area inside the slice.

Measurements of the *CTDI* are usually performed with a pencil ionization chamber with an active length of 100 mm, which is positioned at the center ($CTDI_{100,c}$) and at the periphery ($CTDI_{100,p}$) of either a standard body or head CT dosimetry phantom (Fig. 2). On the assumption that the dose decreases linearly with the radial position from the surface to the center of the phantom, the average dose is given by the *weighted CTDI*.

$$CTDI_w = \frac{1}{3} CTDI_{100,c} + \frac{2}{3} CTDI_{100,p} \,. \qquad (2)$$

Because the $CTDI_w$ is directly proportional to the electrical current–time product (Q_{el} in mAs) chosen for the scan, it has to be measured only for a single Q_{el} value but for all combinations of tube potentials (U in kV) and slice collimations (h_{col}) that can be realized at the specific type of scanner.

Whenever several adjacent slices are scanned instead of a single slice—as is usually the case in spiral CT—the dose for a particular slice is increased due to the contributions from slices in its neighborhood (see Figs. 1b, c). Due to this reason, the dose in the central portion of the superimposed dose profile is markedly larger than the peak value for a single slice. In this case, the average dose is given by the *volume CTDI*.

$$CTDI_{vol} = \frac{CTDI_w}{p} \qquad (3)$$

with p being the pitch factor that characterizes the degree of overlap (or packing) of the slice profiles. In multi-slice CT (MSCT) this factor is defined as.

$$p = \frac{TF}{h_{col} \cdot N} \qquad (4)$$

where TF is the table feed, h_{col} the slice (or detector) collimation, and N the number of simultaneously acquired slices. For $p < 1$ the slices overlap, which results in an increase of the local dose. To obtain the average dose for a multiple-slice CT scan performed over a larger body region, it is thus sufficient to measure the $CTDI_w$ from a single rotation by acquiring the dose over the entire dose profile. The situation is illustrated in Figs. 1b, c for the case of two

CT series carried out over the same scan length with $p = 1$ $(CTD_{vol} = CTDI_w)$ and $p < 1 (CTDI_{vol} > CTDI_w)$. respectively. The $CTDI_{vol}$ is the principal dose descriptor in CT, reflecting not only the combined effect of the scan parameters Q_{el}, U, p, and h_{col} on the local dose level, but also of scanner specific factors such as beam filtration, beam shaping filter, geometry, and overbeaming.

Besides the $CTDI_{vol}$, the length of the scan region is the second important parameter that determines radiation exposure of patients undergoing a CT procedure. Therefore, the *dose-length product*

$$DLP = CTDI_{vol} \cdot L \tag{5}$$

(given in mGy·cm) is used as a further dose descriptor that characterizes the integral dose delivered to the patient.

According to the revised IEC-standard 60601-2-44, the $CTDI_{vol}$ and DLP value of a CT scan have to be displayed at the operator's console of the system. Table 2 summarizes median values and inter-quartile ranges of both parameters for CT examinations frequently carried-out in Germany in 2008/09.

2.3 Estimation of Organ and Effective Doses

As already mentioned, the relevant quantity for *generic* risk assessment is the effective dose, which takes not only the organ doses into account but also the relative radiation susceptibility of the various organs and tissues within the scanned body region. According to the generic method presented in the 'European Guidelines for Multislice Computed Tomography' (Bongartz et al. 2004), estimates of the effective dose (defined according to ICRP-60)

$$E = K_E \cdot DLP \tag{6}$$

can be derived from the DLP by using appropriately conversion factors K_E (in mSv/mGy/cm) given in that report for six body regions, namely head (0.0023), neck (0.0054), chest (0.019), abdomen (0.017), pelvis (0.017) and legs (0.0008). The practical applicability of this approach is, however, limited since it does not allow estimating the effective dose for different scan regions.

In order to calculate organ and effective doses for arbitrary scan protocols, complex radiation transport calculations by means of Monte-Carlo techniques were performed for anthropomorphic phantoms simulating the male and female body. The results have been implemented in PC programs that can easily be used to estimate organ dose and effective dose for a given CT scanner and protocol (Kalender et al. 1999; Stamm and Nagel 2002; ImPACT 2010). For one of these software tools (CT-EXPO, Stamm and Nagel 2002), the accuracy of the implemented theoretical formalism has been evaluated by means of dose measurements performed at an anthropomorphic Alderson phantom for a variety of scanners and representative scan protocols (Brix et al. 2004). As Fig. 3 demonstrates, the values of the computed effective dose agree quite well with the values measured by thermoluminescent dosimetry at an Alderson phantom. The currently available dosimetry programs, however, do not account for varying tube currents when using current-modulated automatic exposure control. In these cases, estimates of at least the effective dose can be obtained with an acceptable accuracy when using the average tube current

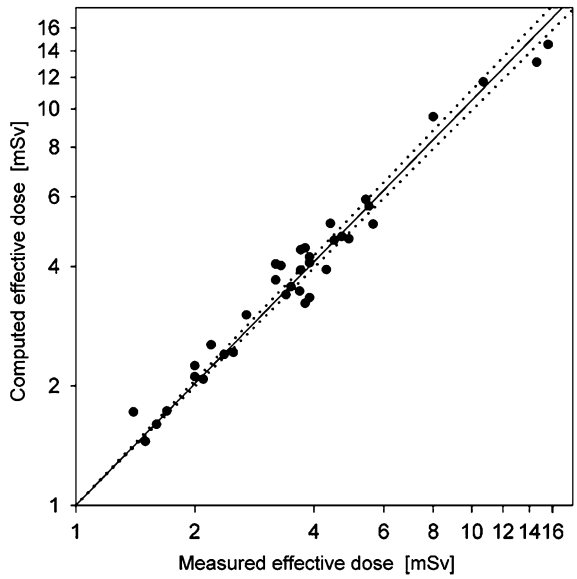

Fig. 3 Correlation between effective doses determined by the program CT-EXPO (V 1.5) and thermoluminescent dosimetry at an anthropomorphic Alderson phantom for 36 CT scans (head, thorax, abdomen, whole-body) performed at 12 different scanners (four 1-slice, four 4-slice, two 16-slice and two 64-slice systems). The solid line give the result of a linear regression analysis (slope, 1.02; correlation coefficient, 0.943) and the dotted curves the 95% confidence interval, which includes the line of identity

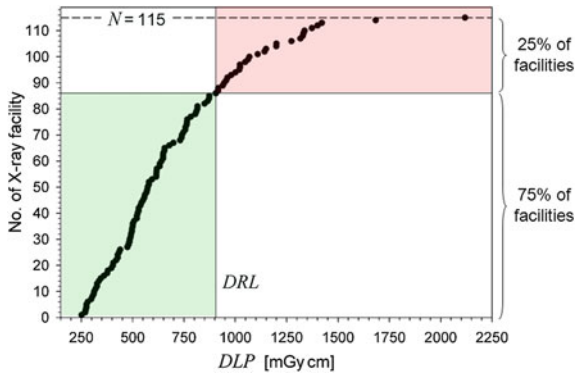

Fig. 4 Distribution of mean *DLP* values for CT examinations of the abdomen determined in 115 German hospitals and private practices (at least 10 patients per facility). Even if the two outliers are neglected, the dose values varied considerably by a factor of more than 5. The vertical line gives the third quartile that was set as *DRL* for this particular examination. The 25% of X-ray facilities with dose levels above the *DRL* (*red area*) have to optimize their procedures or equipment

displayed after the scan on the operator's console (Lechel et al. 2009).

For some frequently performed CT examinations, effective doses computed for both the old and the new ICRP tissue weighting factors are given in Table 2. Depending on the exact position of the scan range, they can vary to some extent in individual patients. CT scans of the brain yield the highest local dose levels ($CTDI_{\mathrm{vol}}$) but only a relatively low effective dose—and, in turn, radiation risk (see below)—because the irradiated tissues have a low tissue weighting factor. Examinations of the abdomen, on the other hand, result in much lower local doses but in a high effective dose due to both an extended scan range and higher tissue weighting factors of the exposed tissues.

2.4 Diagnostic Reference Levels

In its publication on 'Radiological Protection in Medicine' (ICRP-105) the ICRP recommends the use of diagnostic reference levels (*DRL*s) for patient examinations as a measure of optimization of protection. As a form of *investigation level*, they apply to easily measurable dose quantities (in case of CT examinations the $CTDI_{vol}$ and/or *DLP*) and are intended for use as a simple test for evaluating whether the patient dose (with regard to stochastic effects) is unusually high for a particular imaging or interventional procedure. It should be noted, that they do not apply to individual patients but rather to the mean dose value determined in practice for a suitable reference group (comprising at least 10 patients). If patient doses related to a specific procedure are consistently exceeding the corresponding *DRL*, there should be a local review (clinical audit) of the procedures and equipment. Actions aimed at the reduction of dose levels should be taken, if necessary.

Reference levels are defined on the base of dose data from surveys performed in hospitals and private practices in a particular region or state. Generally, the third quartile of the mean dose levels evaluated in these facilities for a particular X-ray procedure becomes the corresponding reference level. They should be set by professional medical bodies in conjunction with national health or radiological protection authorities and reviewed at intervals that represent a compromise between the necessary stability of the protection system and the changes in the observed dose distributions. Figure 4 demonstrates the procedure at the example of CT examinations of the abdomen.

3 Assessment of the Radiation Risk Related to CT Examinations

The effective dose is not recommended for epidemiological evaluations, nor should it be used for detailed specific retrospective investigations of individual exposure and risk (ICRP-103 2007). For the estimation of the potential consequences of a radiation exposure to *individual patients* (or asymptomatic persons in case of screening and preventive diagnosis), it is necessary to use specific data characterizing the exposed individual.

The standard approaches to generate age, gender and organ specific risk estimates are based on the so-called excess absolute risk, ear. It denotes the *additional* risk of a person of gender S, after an exposure to organ dose D at the age e, to be clinically diseased with a specific radiation-induced cancer at the age a or, more specifically, in the interval $[a, a + 1)$. It is commonly calculated from

$$\mathrm{ar}(e, a, D, S) = r_0(a, S) + \mathrm{ear}(e, a, D, S) \qquad (7)$$

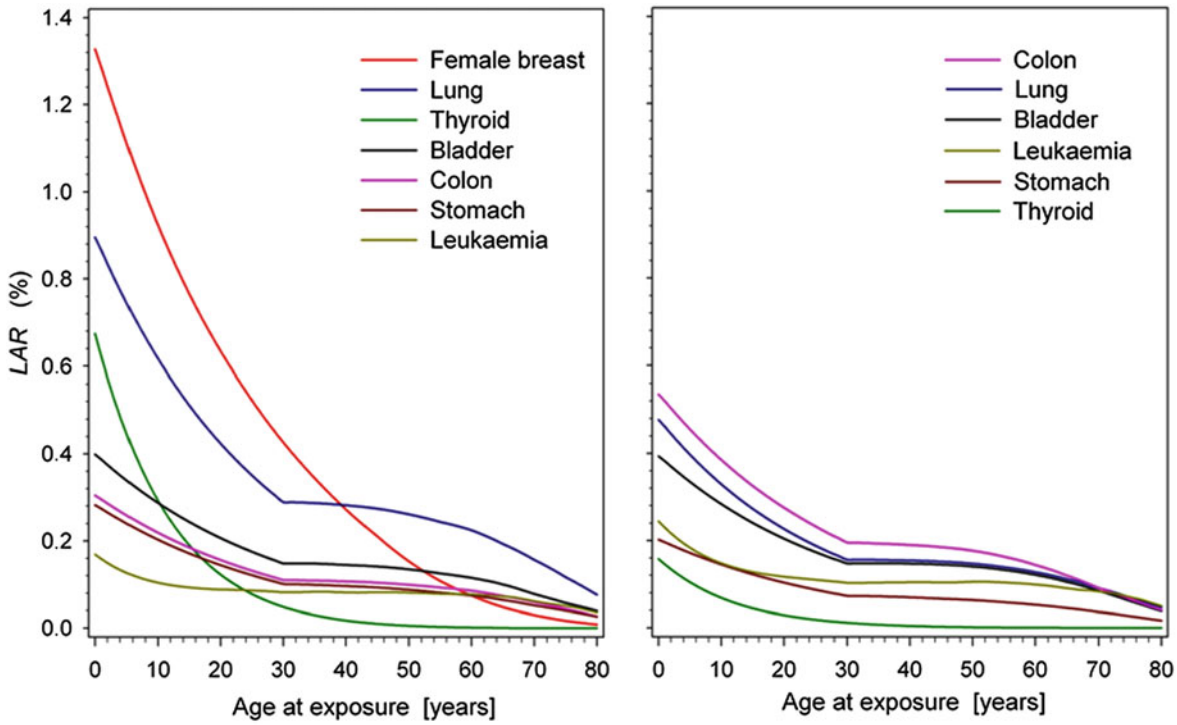

Fig. 5 Lifetime attributable risk (*LAR*) for an organ dose of $H_T = 100$ mSv in dependence on the age at exposure for those cancer sites attributing most to the total lifetime risk for females (*left*) and males (*right*). Risks were estimated according to BEIR-VII models as well as German life tables and cancer incidence rates. For other organ doses, the *LAR* can be derived by assuming a linear dose relationship for solid tumors and a linear-quadratic relationship for leukaemia (multiplication of the given *LAR* values by $9.2H_T + 8H_T^2$, H_T in Sv)

where *ar* denotes the absolute risk and r_0 the normal or baseline risk of a person of gender *S* to be diseased with a specific cancer in the interval $[a, a + 1)$. If a *relative* risk model is used, Eq. (7) can be written as

$$ar(e,a,D,S) = r_0(a,S) \cdot [1 + err(e,a,D,S)] \quad (8)$$

with err (*e,a,D,S*) representing the excess relative risk. For example, an err $(e,a,D,S) = 1$ means that the additional, radiation-induced cancer risk for a person of gender *S* who was exposed at age *e* to an organ dose *D* and attained age *a* is as high as his normal cancer risk. Estimates of the excess (relative) risk for specific organs are usually derived from cancer incidence data of the LSS, where a linear dose dependence is commonly assumed for solid tumors, while a linear-quadratic approach provides better results for leukaemia. The most recent models are summarized in the BEIR-VII report (2006).

The site-specific *excess absolute lifetime risk* or *lifetime attributable risk*, *LAR*, for a person of gender *S* who was exposed at age *e* to an organ dose *D* is calculated by summing up all *ear* (*e,a,D,S*) values between $e + \Delta t$ (with Δt being the minimum latency period) and the age of, e.g., 85 years, commonly used for lifetime risk estimates. The *ear* should be corrected for competing risks by the conditional probability *P* (*e, a*), i.e. the probability that a person of age *e* survives beyond the age *a*

$$LAR(e,D,S) = \int_{a=e+\Delta t}^{85} \mathrm{ear}(e,a,D,S) \cdot P(e,a)da \; . \quad (9)$$

The minimum latency period Δt is the time during which the radiation-induced cancer typically does not show clinical symptoms. A Δt of about 5 years for carcinoma and of about 2 years for leukaemia is widely applied for incidence data. To determine the total *LAR* for a CT examination, all site-specific *LAR*

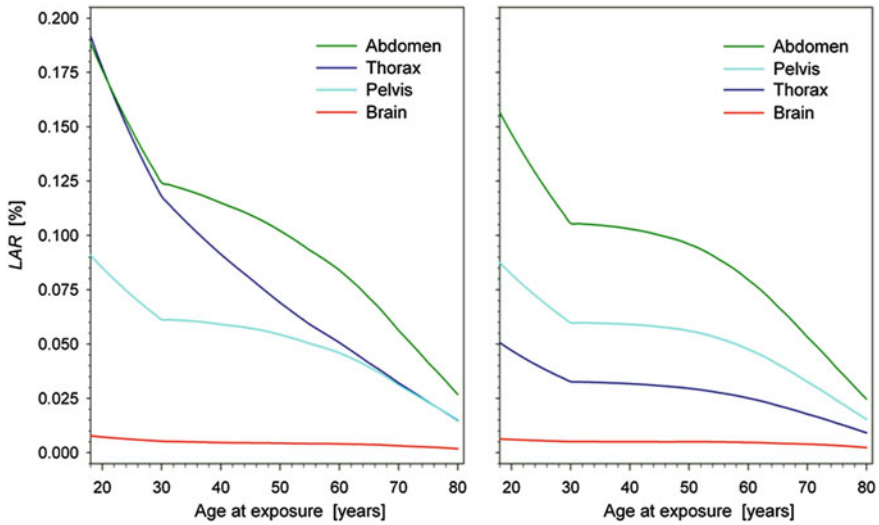

Fig. 6 Lifetime attributable risks (*LAR*) for representative CT examinations of the head, thorax, abdomen, and pelvis performed at different ages in adult female (*left*) and male (*right*) patients. Risks were estimated for the median $CTDI_{vol}$ and *DLP* values given in Table 2 using the BEIR-VII models as well as German life tables and cancer incidence rates

estimates (i.e. for sites with appreciable organ doses) have to be summed up.

Applying the BEIR-VII risk models as well as German disease and life table data (DeStatis 2004, 2010; GEKID 2010), Fig. 5 gives *LAR* estimates for cancer incidence for organ doses of $H_T = 100$ mSv for those cancer sites contributing most to the total *LAR* in dependence on age at exposure. For all organs, the *LAR* decreases with increasing age at exposure. The plots reveal that the female breasts and lungs are particularly susceptible for the induction of cancer at ages below 40 years. For example, a breast dose of $H_T = 100$ mSv at an age of 20 years is associated with a risk of 0.63% to develop a breast cancer in the remaining life. On the other hand, the *LAR* for radiation-induced leukaemia is comparable for both sexes and almost constant when the exposure occurs during adolescence and adulthood.

Figure 6 gives for female and male patients in Germany, estimates of total *LAR* for representative CT examinations of the head, thorax, abdomen, and pelvis in dependence on the age the CT is performed. The *LAR* estimates are based on organ doses calculated from the median $CTDI_{vol}$ and *DLP* values given in Table 2, using the age at exposure and site specific *LAR* estimates plotted in Fig. 5. For both sexes, the highest *LAR* is associated with CT examinations of the abdomen. The *LAR* for an abdomen CT performed at the age of 20 years is about 0.18% for a female patient and about 0.15% for a male patient. The *LAR* for an abdomen CT carried-out at the age of 60 years is about half the value (0.08% for both sexes). For female patients, the *LAR* associated with a thorax CT performed before 30 years of age is virtually the same as the *LAR* due to an abdomen CT. This examination results in a considerably higher *LAR* for females compared to male patients due to the higher radiation risk per dose unit for breast and lung cancer (Fig. 5). The *LAR* for a thorax CT performed at the age of 20/60 years is about 0.18/0.05% for a female patient and about 0.05/0.025% for a male patient. A CT of the pelvis results in about the same radiation risk for both sexes. For a CT at the age of 20/60 years the *LAR* is about 0.085/0.045% for a female patient and about 0.08/0.05% for a male patient. A CT of the brain is associated with a low radiation risk, with *LAR* values of less than 0.01% for both sexes.

These *LAR* values can be compared with estimates of the lifetime baseline cancer risk, i.e. the "normal" risk to incur cancer during the remaining lifetime from, e.g., age 20 years. In Germany, the lifetime baseline cancer risk for all cancers (excluding skin cancer) is about 39% for women, and about 47% for men. The values for lifetime baseline risk for, e.g., lung, colon, and stomach cancer are about 2/7, 4/4, and 2/3% for women/men, and for female breast cancer it is about 10% (GEKID 2010).

It has to be emphasized that a reliable assessment of both beneficial and detrimental effects from medical X-rays, particularly from CT examinations, can

only be performed for well-defined diagnosis-related subgroups of patients. An overall assessment based solely on the average dose per patient (or even inhabitant of a country, Berrington de Gonzalez and Darby 2004) without considering the underlying disease is inadequate, because neither the disease-specific exposure level, age, and life expectancy of the patients nor their diagnostic and therapeutic benefit from the examinations are taken into account. Cancer patients, for example, constitute a small but highly exposed subgroup of the population. According to a study by Brix et al. (2009), 6.8 (1.4) % of the cancer patients in their representative study group received a cumulative 5-year effective dose from medical X-rays of more than 100 (200) mSv, with a dose contribution of about 80% from CT procedures. Nevertheless, the associated radiation risk is low compared to the individual benefit of the patients from the examinations and the much higher detrimental effects associated with an effective tumor treatment. In the majority of cancer patients, radiation exposure is radiobiologically even completely ineffective in the long term due to their reduced life expectancy. More critical are, of course, frequent CT procedures performed in younger cancer patients suffering, for example, from lymphoma (Beyan et al. 2007) or in patients with chronic but not life-threatening conditions and symptoms (Sodickson et al. 2009).

4 Technology-Specific Factors Influencing Patient Exposure in CT

There are various technical factors related either to the hardware design of modern MSCT systems or inherent to the principle of spiral scanning that systematically affect radiation exposure of patients (Nagel et al. 2002):

Detector efficiency. Individual detectors in a multi-row, solid state detector array are separated by narrow strips ('septa') which are not sensitive to radiation and thus do not contribute to the detector signal. Due to the large number of strips, these inactive zones result in geometrical losses, the degree of which depends on the design of the detector array. In addition, further losses occur due to a decrease in sensitivity at the edges of each row that results from cutting the scintillator crystal. In contrast to a single-row detector array whose width can be larger than the maximum slice thickness, the edges of the rows in a multi-row detector array are located inside the beam. Both effects result in a decrease of the net efficiency of a solid-state detector array.

Beam geometry. By using cone beams instead of fan beams, the incidence of scatter is increased and requires the use of either more dose to preserve the contrast-to-noise ratio or technical means associated with a decrease in geometric efficiency. Scatter radiation also plays a crucial role in systems with two sources ('dual-source CT'), where it is not only recorded by the detector opposite to the source, but also by the second detector.

Overbeaming. In MSCT, data from each detector contribute to every reconstructed image. Therefore, the image noise and the slice sensitivity profile for each slice need to be similar to reduce image artifacts. To accommodate this condition for MSCT systems with more than two detector rows, beam collimation is usually adjusted in such a way that the focal spot-collimator blade penumbra falls outside the edge detectors. The resulting overbeaming causes an increase of the radiation dose as compared to single-slice scanners, where the collimator width was in general smaller than the maximum detector width. With the availability of MSCT systems capable of scanning 16 or more slices simultaneously the overbeaming effect becomes less important.

Overranging. In spiral CT, the actual scan range is larger than the range defined at the operator's console, because additional data are required for interpolation at the beginning and the end of the body region to be scanned. The additional exposure of patients resulting from this effect increases with an increasing width of the detector arrays. This constitutes a particular problem when using a limited scan length, as for example in case of CT examinations of a newborn baby or a small child.

Tube output and rotation time. The improved output of modern X-ray tubes in combination with a reduced rotation time allows for significant changes in scan protocol settings. The ability to scan a given volume in a reduced time with a smaller slice thickness, thus enabling the production of 'isotropic voxels', is the most prominent implication that may considerably increase patient exposure if not adequately handled (see below).

5 Application-Specific Measures to Reduce Patient Exposure in CT

The primary measure to reduce radiation risks to patients, notably in the case of CT, is the avoidance of unjustified examinations—whether because the expected diagnostic benefit is low or because the relevant diagnostic information can be obtained by imaging techniques not using ionizing radiation (such as magnetic resonance imaging or sonography). When a particular examination is justified, the emphasis must be on dose optimization. The key factors toward optimization of CT protocols are (Nagel et al. 2002; Brix et al. 2003; Kalra et al. 2005; Catalano et al. 2007; Nievelstein et al. 2010):

- Limiting the region of the body to be scanned to the smallest necessary area, in particular in case of multiphase and follow-up studies.
- Reducing the number of scan series to the bare minimum. For example, multiphase scans of the liver should be avoided unless they are likely to yield useful and relevant information.
- Adaptation of the current–time product and if appropriate of the tube voltage to the size of the patient, particularly in case of children.
- Using a pitch greater than 1 where it is clinically appropriate (at least when the electrical current–time product is not automatically adapted when the pitch is changed).
- Acceptance of a higher noise-level when using a narrow slice collimation. Detail contrast of small lesions is enhanced with narrow slice collimation due to the reduction of partial volume effects in axial direction and thus the contrast-to-noise ratio is considerably improved even in the presence of an increased noise level.
- Shielding of radiation-sensitive organs.

Optimization can further be facilitated by technical means (Kalender et al. 2008). Meanwhile, all CT manufacturers have developed systems for automatic exposure control, which allows reducing the dose to patients of between 20 and 50% (depending on the imaged body region) without sacrificing image quality (Kalra 2004; Gudjónsdóttir et al. 2010). The principal idea of this approach is to adapt the tube current to the changing anatomy of the patient, both, in the transverse plane as well as axial direction. Further solutions are under development or clinical evaluation—such as adaptive collimation (Deak et al. 2009), scatter reduction, adaptive post-processing image filtration (Leander et al. 2010) or iterative image reconstruction (Silva et al. 2010).

However, technical means are only a prerequisite not a guarantee for dose reduction. Of greatest importance is an appropriate training and guidance of both the medical and technical staff operating a CT system with respect to the various factors determining patient exposure at the particular scanner and of its reduction.

References

Amis ES Jr, Butler PF, Applegate KE, Birnbaum SB, Brateman LF, Hevezi JM, Mettler FA, Morin RL, Pentecost MJ, Smith GG, Strauss KJ, Zeman RK (2007) American College of Radiology. American College of Radiology white paper on radiation dose in medicine. J Am Coll Radiol. 4:272–284

Berrington de Gonzalez A, Darby S (2004) Risk of cancer from diagnostic X-rays: Estimates for the UK and 14 other countries. Lancet 363:345–351

BEIR-VII (2006). Committee to assess health risks from exposure to low levels of ionizing radiation. National Research Council. Health risks from exposure to low levels of ionizing radiation: BEIR VII Phase 2. The National Academies Press, Washington

Brenner DJ, Hall EJ (2007) Computed tomography—an increasing source of radiation exposure. N Engl J Med 357:2277–2284

Beyan C, Kaptan K, Ifran A, Ocal R, Ulutin C, Oztürk B (2007) The effect of radiological imaging studies on the risk of secondary malignancy developed in patients with Hodgkin lymphoma. Clin Lymphoma Myeloma 7:467–469

Bongartz G, Golding SJ, Jurik AG, Leonardi M, van Persijn van Meerten E, Rodríguez R, Schneider K, Calzado A, Geleijns J, Jessen KA, Panzer W, Shrimpton PC, Tosi G (2004) European guidelines for multislice computed tomography. http://www.msct.eu/CT_Quality_Criteria.htm. Accessed 12 Dec 2010

Brix G, Nagel HD, Stamm G, Veit R, Lechel U, Griebel J, Galanski M (2003) Radiation exposure in multi-slice versus single-slice spiral CT: Results of a nationwide survey. Eur Radiology 13:1979–1991

Brix G, Lechel U, Veit R, Truckenbrodt R, Stamm G, Coppenrath EM, Griebel J, Nagel HD (2004) Assessment of a theoretical formalism for dose estimation in CT: An anthropomorphic phantom study. Eur Radiol 14:1275–1284

Brix G, Nissen-Meyer S, Lechel U, Nissen-Meyer J, Griebel J, Nekolla EA, Becker C, Reiser M (2009) Radiation exposures of cancer patients from medical X-rays: How relevant are they for individual patients and population Exposure? Eur J Radiol 72:342–347

Catalano C, Francone M, Ascarelli A, Mangia M, Iacucci I, Passariello R (2007) Optimizing radiation dose and image quality. Eur Radiol 17(Suppl 6):F26–F32

Deak PD, Langner O, Lell M, Kalender WA (2009) Effects of adaptive section collimation on patient radiation dose in multisection spiral CT. Radiol 252:140–147

DeStatis (2004) Gesundheitswesen, Todesursachen in Deutschland (Causes of Death in Germany) Fachserie 12/Reihe 4. Ed: Statistisches Bundesamt (Federal Office for Statistics), Wiesbaden

DeStatis (Federal Office for Statistics) (ed) (2010) Statistisches Jahrbuch 2010 für die Bundesrepublik Deutschland (Statistical Yearbook 2010 for the Federal Republic of Germany). Metzler-Poeschel, Stuttgart

GEKID (Association of population-based cancer registries in Germany and Robert-Koch institute) (2010) Cancer in Germany. Incidence and trends. 7th revised, updated edn., Saarbrücken

Gudjónsdóttir J, Ween B, Olsen DR (2010) Optimal use of AEC in CT: a literature review. Radiol Technol 81:309–317

ICRP-60 (1991) Publication 60. The 1990 recommendations of the international commission on radiological protection. Annals of the ICRP 21(1–3)

ICRP-103 (2007) Publication 103. The 2007 recommendations of the international commission on radiological protection. ICRP Publication 103. Annals of the ICRP 37(2–4)

ICRP-105 (2007) Publication 105. Radiological protection in medicine. Annals of the ICRP 37(6)

ImPACT (2010) Imaging performance assessment of CT-scanners group. ImPACT CT patient dosimetry calculator, V. 1.0.3. http://www.impactscan.org. Accessed 12 Dec 2010

Kalender WA, Schmidt B, Zankl M, Schmidt M (1999) A PC program for estimating organ dose and effective dose values in computed tomography. Eur Radiol 9:555–562

Kalender WA, Buchenau S, Deak P et al (2008) Technical approaches to the optimisation of CT. Phys Med 24:71–79

Kalra MK, Maher MM, Toth TL et al (2004) Strategies for CT radiation dose optimization. Radiology 230:619–628

Kalra MK, Naz N, Rizzo SM, Blake MA (2005) Computed tomography radiation dose optimization: scanning protocols and clinical applications of automatic exposure control. Curr Probl Diagn Radiol 34:171–181

Leander P, Söderberg M, Fält T, Gunnarsson M, Albertsson I (2010) Post-processing image filtration enabling dose reduction in standard abdominal CT. Radiat Prot Dosimetry 139:180–185

Lechel U, Becker C, Langenfeld-Jäger G, Brix G (2009) Dose reduction by automatic exposure control in multi-slice computed tomography—Comparison between measurement and calculation. Eur Radiol 19:1027–1034

Mettler FA Jr, Bhargavan M, Faulkner K, Gilley DB, Gray JE, Ibbott GS, Lipoti JA, Mahesh M, McCrohan JL, Stabin MG, Thomadsen BR, Yoshizumi TT (2009) Radiologic and nuclear medicine studies in the United States and worldwide: frequency, radiation dose, and comparison with other radiation sources—1950–2007. Radiology 253:520–531

Nagel HD, Galanski M, Hidajat N, Maier W, Schmidt T (2002) Radiation exposure in computed tomography—fundamentals, influencing parameters, dose assessment, optimisation, scanner data, terminology. 4th edn. CTB Publications (ctb-publications@gmx.de), Hamburg

Nekolla EN, Griebel J, Brix G (2010) Strahlenhygiene in der medizinischen Röntgenbildgebung, Teil 3: Strahlenexposition des Patienten und Risikobewertung. Radiologe 50:1039–1054

Nievelstein RA, van Dam IM, van der Molen AJ (2010) Multidetector CT in children: current concepts and dose reduction strategies. Pediatr Radiol 40:1324–1344

Nishizawa K, Matsumoto M, Iwai K, Maruyama T (2004) Survey of CT practice in apan and collective effective dose estimation. Nippon Acta Radiologica 64:151–158

Preston DL, Ron E, Tokuoka S, Funamoto S, Nishi N, Soda M, Mabuchi K, Kodama K (2007) Solid cancer incidence in atomic bomb survivors: 1958–1998. Radiat Res 168:1–164

Silva AC, Lawder HJ, Hara A, Kujak J, Pavlicek W (2010) Innovations in CT dose reduction strategy: application of the adaptive statistical iterative reconstruction algorithm. Am J Roentgenol 194:191–199

Sodickson A, Baeyens PF, Andriole KP, Prevedello LM, Nawfel RD, Hanson R, Khorasani R (2009) Recurrent CT, cumulative radiation exposure, and associated radiation-induced cancer risks from CT of adults. Radiology 251:175–184

Stamm G, Nagel HD (2002) CT-Expo—ein neuartiges Programm zur Dosisevaluierung in der CT. Fortschr Rontgenstr 174:1570–1576

UNSCEAR (2000) United Nations scientific committee on the effects of atomic radiation. sources and effects of ionizing radiation. UNSCEAR 1994 report, Effects, Annex G, vol 2, United Nations, New York

UNSCEAR (2010) United Nations scientific committee on the effects of atomic radiation. sources and effects of ionizing radiation. UNSCEAR 2008 report, Sources, Annex A: Medical Radiation Exposures, vol 1, United Nations, New York

Contrast Agent Application and Protocols

Markus S. Juchems

Contents

Abstract

Contrast enhanced MDCT is a powerful and continuously evolving technology for non-invasive imaging of the abdomen. As for contrast media application in general, there is a variety of patient-related and injection-related factors that can affect the magnitude and timing of intravenous contrast agent attenuation for abdominal CT scans. MDCT, with its dramatically shorter image acquisition times, permits images with a much better utilization of the peak contrast attenuation. High iodine flux rates—e.g. required by modern angiographic applications—can be achieved with newly developed high concentration iodine contrast agents. In contrast low concentration iodine agents need to be injected at very high flow rates resulting in high volumes administered to meet these requirements. Sporadic failure, though, is unpreventable at the current stage of development. This is due to the fact that the patient's cardiac output is not known prior to scan initiation in most cases. Contrast media administration is an integral part of the ongoing evolution of MDCT and needs to be continuously adopted and optimized to take full advantage of this technology. The purpose of this chapter is to give a basic understanding of physiologic and pharmacokinetic principles, as well as an understanding of the effects of injection parameters on vascular and parenchymal enhancement. This will enable the development of optimized contrast agent delivery protocols for current and future MDCT abdominal scans.

M. S. Juchems (✉)
Diagnostic and Interventional Radiology,
University Hospitals Ulm, Steinhoevelstrasse 9,
89075 Ulm, Germany
e-mail: markus.juchems@uniulm.de

C. J. Zech et al. (eds.), *Multislice-CT of the Abdomen*, Medical Radiology. Diagnostic Imaging,
DOI: 10.1007/174_2011_406, © Springer-Verlag Berlin Heidelberg 2012

1 Basic Principles

MDCT technology continues to evolve rapidly. At the current stage of development, improvements concentrate on gantry rotational speed (up to 270 ms for a single rotation) and detector width (up to 16 cm with a collimation of 320 × 0.5 mm). This allows for a rapid acquisition of large volumes in short time along the patient's z-axis. Subsequently, contrast agent application is an increasingly demanding task that has to synchronize the timely co-incidence of peak enhancement of the tissue at interest and the scan acquisition. For parenchymal imaging such as liver tissue, a wide peak plateau ensues with enough room for securing adequate contrast enhancement. Vascular imaging, on the other hand, has changed tremendously. The peak of contrast attenuation has shortened substantially in order to utilize the contrast agent (CA) efficiently. This is coupled with and enabled by a rapid acquisition of today's scanner generations in <10 s. From the aforementioned it is easily deductible that the timing of a scan in relation to the contrast peak is crucial. It demands both semi-automated scanner protocols and individual protocol adaptation.

2 Factors Affecting Contrast Attenuation

The factors affecting contrast agent attenuation of the tissue of interest can be separated into three general categories: patient related, injection of contrast and CT parameters. The former two factors directly determine and affect the contrast attenuation process itself. CT parameters, only indirectly affecting contrast attenuation, are critical in permitting optimal timing of the acquisition to visualize the peak enhancement of the tissue of interest.

2.1 Patient-Related Factors

The two relevant patient-derived factors that affect contrast enhancement most are body weight and cardiac output (or cardiovascular circulation time).

2.1.1 Body-Weight

Body weight (BW) affects the magnitude of both vascular and parenchyma contrast enhancement (Heiken et al. 1995; Kormano et al. 1983). CA administered to the larger blood volume of a heavy patient is more diluted than that administered to a slim patient. Patient weight and the magnitude of contrast attenuation are inversely related in a linear fashion. However, the timing of enhancement is largely unaffected, due to a concomitant increase of body weight (Kirchner et al. 2000).

Hence, for daily clinical application, overall iodine dose should be increased with increasing body weight of the individual patient. This can be effectively achieved by multiplying the body weight with a constant amount of contrast per kg of BW, keeping the iodine flux rate constant [e.g., 1.2 ml CA (370mgI/ml) × BW, 1.0 ml CA (400mgI/ml) × BW]. The linear increase of CA volume predominantly applies to all parenchymal imaging with a more limited effect on vascular attenuation.

2.1.2 Cardiac Output

Global cardiac function (measured as cardiac output or cardiovascular circulation time) critically affects the timing of contrast attenuation (Bae et al. 1998b). Decreased cardiac function results in a delay of peak vascular and parenchymal attenuation. But this is only one parameter affected by cardiac function. The other one critically affected for all vascular or early enhancing scan applications is magnitude of CA enhancement. CA is typically injected via an antecubital vein and therefore arrives at the right heart via the superior vena cava (SVC). For patients with good to high cardiac output, the densely contrasted blood volume is mixed with 1.5–2 times the volume of non-contrasted blood drained from the inferior vena cava (IVC). For a patient with non-compromised cardiac function at rest, the volume relation of blood drained from IVC and SVC is 1.3:1 or higher (Cheng et al. 2004). For patients with compromised cardiac function this ratio may drop below 1. It is therefore readily apparent that a patient with a low cardiac output situation will mix the densely contrasted blood volume drained from the SVC with a substantially lower amount of unenhanced blood from the IVC.

In patients with reduced cardiac output, once the contrast bolus arrives in the central blood compartment, it is obviously more slowly, resulting in a

Table 1 Effects of cardiac output on contrast material distribution

Cardiac output	Attenuation	Flow rate	Homogeneity	Bolus length
low	↑	↓	↓	↑
high	↓	↑	↑	↓

higher, prolonged enhancement. A consequence of the slower contrast bolus clearance in patients with reduced cardiac output is an increased magnitude and duration of peak aortic and parenchymal enhancement (Coursey et al. 2009). The rate of increase, however, is different in the aorta and liver. Whereas the magnitude of peak aortic enhancement increases substantially in patients with reduced cardiac output, the magnitude of peak hepatic enhancement increases only slightly. For higher cardiac output which can occur for example in patients with anemia, some stages of sepsis, and in patients with cirrhosis and portal hypertension, contrast material distribution behaves contrariwise.

Global cardiac function parameters are usually unknown at CT scan initiation. The test bolus has shown some potential to predict contrast attenuation in situations of variable cardiac output, but the individualization of the scan delay according to automatic bolus tracking is the much more practical approach applied today. The parameters to be adjusted for the individual patient to correct for variable cardiac functions are contrast flow rate and bolus length. Adjustments should be carried out as outlined in Table 1.

2.1.3 Central Venous Return

Central venous blood flow is subject to intrathoracic pressure changes due to respiration (Gosselin et al. 2004). In the setting of CA-enhanced CT, this may be particularly harmful if a patient performs an ambitious Valsalva maneuver during breath holding. During a Valsalva maneuver, the intrathoracic pressure increases, which causes a temporary interruption of venous return from the superior vena cava and a temporary increase of (non-contrasted) venous blood flow from the inferior vena cava. The effect of this flow alteration is a temporary decrease of vascular opacification. In some cases (especially with fast scan times), this may cause non-diagnostic opacification of the entire pulmonary arterial tree.

Avoiding initial deep inspiration before scanning is suggested as a way to limit the transient interruption of the contrast bolus artifact. Although this may result in minor breath holding artifacts, these may be much more tolerable than the loss of diagnostic quality.

2.2 Contrast Injection Parameters

Duration of CA injection and iodine administration rate (iodine flux rate) are the main parameters that determine attenuation within the tissue of interest. The programing of power injectors on the other hand requires volume and rate to be affixed prior to scan initialization. Volume can be easily calculated by multiplying CA flow with duration of injection for that purpose. Another factor that has emerged with the advent of double-barrel injectors is the use of a saline flush for a more efficient utilization of a compact iodine bolus.

2.2.1 Duration and Flow Rate

The duration of iodine injection critically affects both magnitude and timing of contrast attenuation (Awai et al. 2004) (Fig. 1). Increased injection duration at a fixed flow rate leads to a greater deposition of iodine. This is particularly important for parenchyma imaging with the magnitude of enhancement increased by the amount of iodine administered (Megibow et al. 2001). Peak parenchymal enhancement occurs much later than arterial vascular attenuation. Hence, for dedicated parenchymal protocols, the time frame allowed for contrast agent administration is long and ideally suited for a bolus with a long duration at a reasonable flow rate.

In contrast, arterial enhancement depends on iodine administration rate and can be controlled by the injection flow rate (ml/s) (Fig. 2) (Fleischmann et al. 2000). Thus, most of the angiography protocols used on modern MDCT scanners with 64 detector rows or more utilize very high flow rates in order to yield a compact bolus with steep flanks and a high peak.

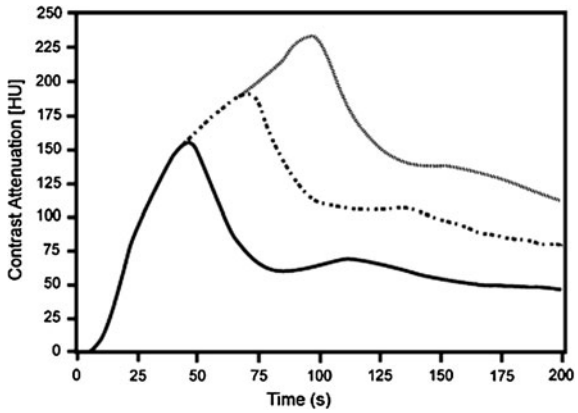

Fig. 1 Simulated contrast enhancement curves of the aorta. The effect of injection duration on contrast accumulation and peak is demonstrated with three different contrast medium volumes (solid line: 75 ml; dashed line: 125 ml; dotted line: 175 ml). Time-to-peak and magnitude of enhancement peak increases with contrast medium volume (Modified after Bae and Heiken 2000)

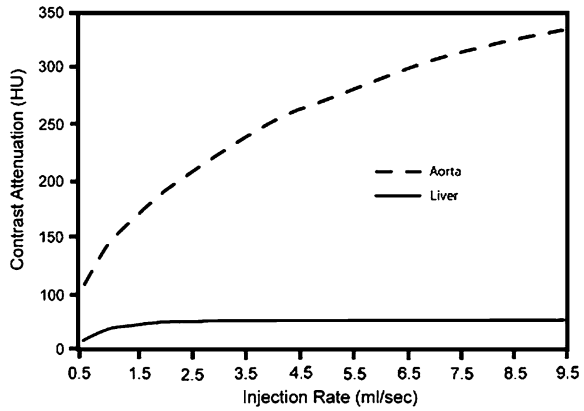

Fig. 2 Simulated contrast enhancement curves of the aorta (dashed line) and liver parenchyma (solid line). Effect of contrast material injection rate on magnitude and peak enhancement. In contrast to parenchymal enhancement, increasing injection rate leads to substantially higher intraluminal enhancement (Modified after Bae and Heiken 2000)

2.2.2 Iodine Concentration

The availability of contrast agents with high iodine concentrations (above 350 mgI/ml) has recently attracted a great deal of interest (Becker et al. 2003; Roos et al. 2004; Suzuki et al. 2004). For injections performed with a fixed duration and flow, a contrast agent with a high iodine concentration will deliver a larger total iodine load more rapidly. The resulting magnitude of peak contrast enhancement is increased (Fig 3). The temporal window at a given level of enhancement is wider. Conversely, time-to-peak enhancement is unaffected because duration and rate of injection remain constant.

On the other hand, contrast agents with a higher concentration deliver a constant total iodine mass at a given flow rate in a shorter duration of time. For daily clinical routine, a contrast agent with high iodine concentrations is an alternative approach to using an increased injection rate in order to increase iodine delivery rate. The rapid improvement of current MDCT generations allows an ever increasing scan speed. This consequently allows utilizing shorter and higher contrast peaks, especially for angiographic applications. In other words, higher iodine concentrations are an ideal match for increasing scan speeds. Many of the rapid angiographic acquisitions amenable on newest scanner generations can only be utilized relying on the highest iodine concentrations (370–400 mgI/ml) available today.

2.2.3 Saline Flush

Current double-barrel power injectors are equipped with two syringes. One is filled with non-diluted contrast agent, the other with normal saline. The saline syringe is activated and injects after the contrast bolus has been administered completely. The arm veins can hold up to 10–15 ml of CA, which is not used for arterial enhancement. Flushing the venous system with saline immediately after the injection pushes the CA column completely into the circulation (Haage et al. 2000). Saline flushing therefore prolongs and slightly increases arterial and parenchymal enhancement (Fig. 4) and allows for the reduced amount of CM (Tatsugami et al. 2007). The favorable effect of saline flushing is relatively greater if high injection rates, small total amounts of CA, and high-concentration CA are used.

2.2.4 Bolus Geometry

During the "first pass" intravenously administered contrast agents will travel to the right heart, lung and left heart before reaching the arterial system. When the contrast medium is distributed in the intravascular and interstitial space and reenters the right heart, recirculation occurs (Fleischmann 2003b). Both the first pass and recirculation account for the shape, or bolus geometry, of the enhancement curve. In ideal bolus geometry, there is an immediate increase in arterial enhancement at the start of the CT acquisition and uniform enhancement during the data acquisition.

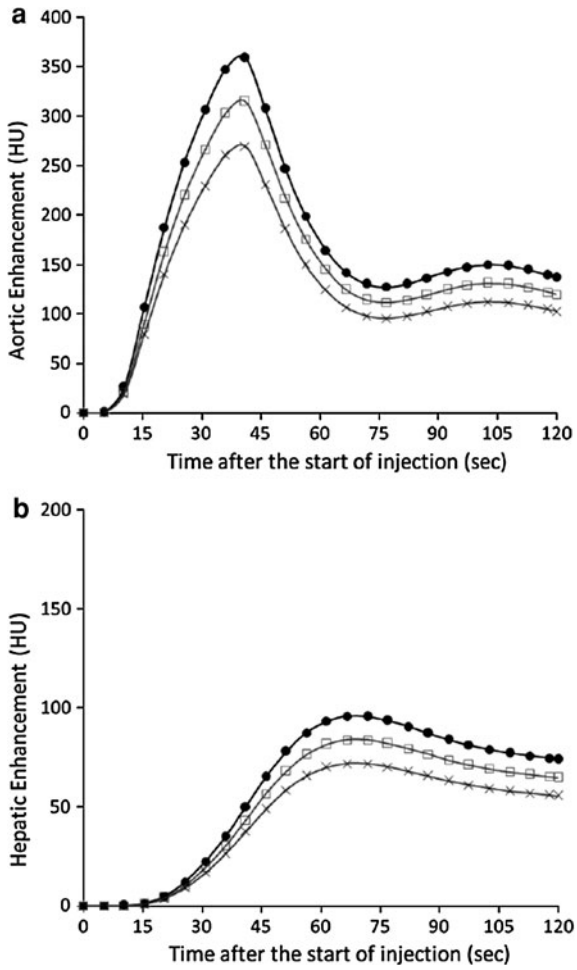

Fig. 3 Contrast enhancement curves of (**a**) the abdominal aorta and (**b**) the liver parenchyma (fixed volume and fixed injection rate). Iodine concentration is 300 (*crosses*), 350 (*squares*) and 400 (*dots*) mg/ml. Contrast medium with a higher concentration delivers a larger dose of iodine faster and with a higher magnitude of peak contrast enhancement (Modified after Bae 2010)

With a uniphasic injection (injection at a constant rate), the enhancement increases to a peak and then declines (Fleischmann 2003b). Because CTA will typically be performed during both the up slope and down slope of the curve, enhancement is not uniform throughout the acquisition. Biphasic injection techniques (fast injection followed by slow injection) and exponentially decelerating injection techniques that can increase uniformity of contrast attenuation have been described (Bae et al. 2000, 2004). However, with short scan times, uniformity of contrast attenuation may be less important for a well-defined application,

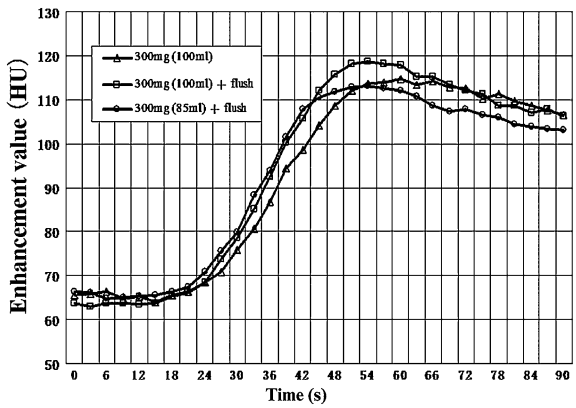

Fig. 4 Graph shows liver parenchyma enhancement. Higher HU values are achieved with saline flush protocols (dots and square curves) than without (*triangles*) (Modified after Tatsugami et al. 2007)

e.g., for coronary angiography (Cademartiri et al. 2004a). Clinical applications that intend to cover a wider range of vascular territories, though, may well ask for more uniformity with a long plateau phase (Vrachliotis et al. 2007).

2.3 CT Parameters

The patient- and injection-related parameters shape the arrival time and distribution of the contrast agent within the organ, tissue or vessel of interest. In order to succeed with an ideally contrasted CT scan that efficiently utilizes the amount of contrast agent administered and that addresses all individualization necessary to account for patient-related factors, the last thing to do correctly is to start the scan at the right time. Inadequately implemented CT parameters will result in a poorly enhanced CT scan, even with perfectly determined patient and injection factors. Scanning parameters such as scan duration, scan delay and, multiphasic acquisitions during different phases of contrast enhancement critically affect contrast enhancement.

Formerly, for scanners with one to four detectors, the determination of scan start times was fairly easy. The scan and subsequently the breath-hold duration was so long that the scan had to be started early. The scan start time was equal to the contrast arrival time determined in a simple test bolus procedure. With the advent of 16 and more detectors in a CT scanner,

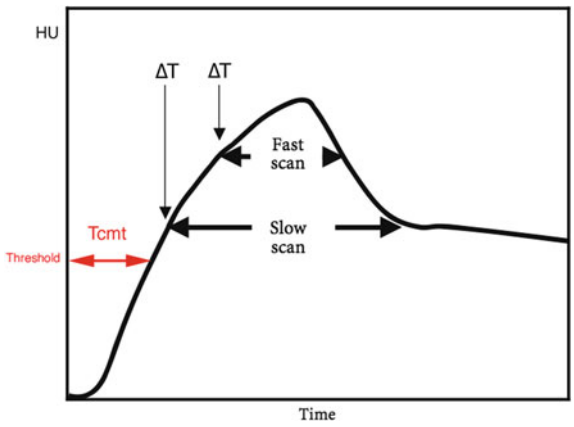

Fig. 5 Aortic contrast enhancement curve with two different scan delays designated for the fast and the slow scans. For given duration of contrast enhancement or injection, the shorter the scan duration, the longer the additional delay. T_{CMT} indicates contrast material arrival time to reach a certain threshold (Modified after Bae)

scans became shorter and shorter, allowing for utilization of the maximum height of the contrast bolus peak. These technical developments rendered scan timing much more complicated and demanding.

2.3.1 Scan Timing

The time interval for an intravenously injected bolus of contrast medium to appear in the arterial territory of interest is generally referred to as the contrast medium arrival time (T_{CMT}). As mentioned above, T_{CMT} can vary substantially between patients, due to patient-related factors, namely if the cardiac output is restricted. The scanning delay therefore needs to be individualized relative to the patient's T_{CMT}. The T_{CMT} can be determined by either using a test bolus injection or using automated bolus-triggering techniques. Both approaches measure contrast arrival time and therefore adapt for varying cardiac output. The bolus tracking method is the most efficient, according to our experience. However, the test bolus has the advantage of testing the venous access line with a small volume of contrast before applying the full volume and flow needed for the scan itself. Both techniques utilize a region of interest (ROI) that is placed in a vessel proximal to the organ of interest.

Traditionally, for slow CTA studies (single-row and four-detector-row scanners), the scan start was chosen to equal a patient's T_{CMT}. The scan time of these scanners was not fast enough to allow capturing the peak of contrast enhancement, but rather to position acquisition around the peak (Fig. 5). Logically, this fact resulted in somewhat inhomogeneous contrast distributions in the acquired axial stack.

Faster helical acquisitions available on newer scanner generations (16-64-row detectors and beyond) allow to better utilize the bolus peak (Fig. 5).

A patient's T_{CMT} may be used as an individual landmark, with an additional time delay ('diagnostic delay', ΔT in Fig 5) before initiation of CT data acquisition. For example,a scanning delay of T_{CMT} +8 s means that scanning will begin 8 s after arrival of the bolus in a patient's aorta (Bae 2003; Fleischmann 2003a).

It has been proven both empirically (Cademartiri et al. 2004b) and theoretically (Bae 2005) that an accurate ΔT may significantly improve CT image quality. Determination of the additional delay, which is related to scan speed and injection duration, is critical for fast MDCT. ΔT can be calculated using complex models either assuming normal cardiac function (so-called "variable" approach) or they can be more or less empirically determined (Bae et al. 1998a). As a rule of thumb ΔT for bolus tracking should be sufficiently long enough to apply breath-hold commands for the patient. The additional delay has to be longer for faster scanners (e.g., for a 64-detector-row scanner, it is in the range of 6–7 s and should be longer for both faster gantry rotation and larger detectors).

3 Sample Protocols

According to the numerous clinical indications for abdominal MDCT, some general considerations have to be made to ensure sufficient arterial and/or parenchymal contrast opacification.

With modern MDCT, it is possible to achieve two arterial contrast phases—the early, which occurs approximately 20 s after injection, and the late arterial phase (30–35 s after injection). In the early arterial phase there is high enhancement in the arterial vessels but relatively little enhancement of the parenchyma or hypervascular lesions.

In the late arterial phase, solid, hypervascular neoplasms, e.g. hepatocellular carcinoma, will enhance maximally, whereas the parenchyma will enhance little due to predominantly portal venous supply.

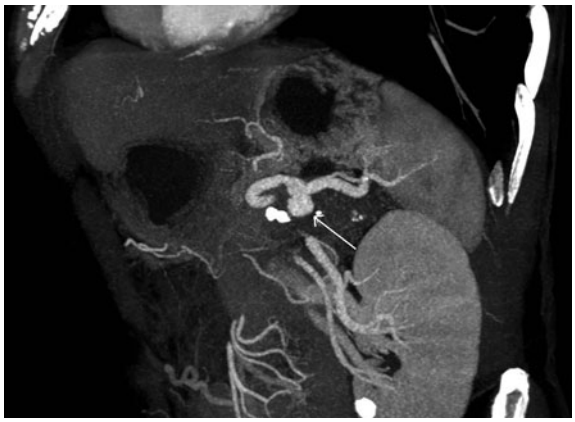

Fig. 6 Arterial scan of the abdominal vessels showing a patient with pseudoaneurysm of the lienal artery after pancreatitis (*arrow*). The scan was performed on a 64-row MDCT. Due to patient related factors, T_{CMT} was long in this case with 28 s to reach 150HU in the abdominal aorta, the additional diagnostic delay was 15 s

The pancreatic parenchymal phase starts 30–70 s (with a peak at 40–45 s) post injection and provides the highest rates of enhancement of the pancreas.

The portal venous phase or hepatic parenchymal phase occurs 60–70 s after the start of CA injection with maximum enhancement of the hepatic parenchyma.

Hypovascular tumors, such as colorectal metastases are seen best in this contrast phase as they appear hypodense to the enhanced parenchyma.

For an elective diagnosis of the bowel wall, the portal venous phase (60 s post injection) with medium flow velocity is suitable for optimal visualization of the layers of the bowel wall.

3.1 CT Angiography

CT angiography has a wide range of applications in the abdomen including vascular pathologies either occlusive or aneurysmal (Fig. 6), detection of gastrointestinal and peritoneal bleeding as well as the illustration of vascular disorders and variants. It enables the radiologist to produce vascular mapping that clearly show tumor invasion of vasculature and the relationship of vessels to mass lesions. It is often helpful in preoperative planning for hepatic resection and preoperative evaluation and planning for liver transplantation.

The scan delay is best achieved with an ROI placed in the descending aorta. The diagnostic delay time (ΔT) should equal peak enhancement for one to four detector rows and is consecutively longer for faster scanners (e.g. 16–64 rows) (Fig. 5).

Arterial enhancement continuously increases over time with longer injection durations due to the cumulative effects of bolus broadening and recirculation. Thus, increasing the injection duration also improves vascular opacification. In order to utilize this mechanism in situations with inappropriate vascular access or other reasons restricting injection flow rates, the scan delay has to be adjusted accordingly. ΔT should be substantially longer to catch the later occurring and higher bolus peak (Fig. 5). Provided that a suitable vascular access allows rapid flow rates the injection duration should be timed according to the equation: 15 s + (scan duration/2). This applies to injections with a saline chaser of 30–40 ml administered at the same flow rate as the preceding contrast agent. For injections without a saline chaster, the above equation should be lengthened by another 5 s.

The strength of an individual's attenuation response to intravenously injected contrast dye is controlled by cardiac output and blood volume, both correlate with body weight. An individual contrast application protocol should therefore be adapted to patient body weight. Lower flux rates apply for slim patients and higher flux rates for heavier ones. Weight-adapted protocols however are less important for vascular attenuation than for parenchymal contrast imaging, but should nevertheless be used in order not to overdose slim patients.

3.2 Hepatic Multi-Phasic Imaging

Hepatic multi-phasic imaging is typically conducted at three discrete phases, namely, early arterial phase, late arterial/portal vein inflow phase and hepatic parenchymal phase. The early arterial phase of enhancement is useful primarily for the acquisition of a pure arterial dataset for CTA and has only limited value for liver evaluations. The late arterial or portal inflow phase is preferred for the detection of hypervascular primary or metastatic liver lesions (Awai et al. 2002). The early phase is acquired with a diagnostic delay (ΔT) equivalent to arterial aortic scanning. The late arterial phase is best centered at

$\Delta T = 20$ s (Laghi 2007). During this phase, the hypervascular hepatic lesions enhance maximally, while the hepatic parenchyma remains relatively unenhanced, correlating to the relatively small contribution of the hepatic artery to the total blood supply of the organ.

The hepatic parenchymal phase, the period of peak hepatic enhancement, is the phase used for routine abdominal CT imaging. Most hepatic lesions, including most metastases, are hypovascular and are therefore best depicted against the maximally enhanced hepatic parenchyma during this phase. The typical delay for this phase is dependent on indication. A fixed delay preceded by a rather slow (typically 2.5–3 ml/s) injection would suffice for single-phase parenchymal imaging. For a bolus tracking approach that interleaves multiple-phase imaging with an early enhancing arterial and a later parenchymal phase, the typical delay post threshold of the bolus tracker would be in the range of 55–65 s. This delay is dependent on the duration of CA injection.

For some dedicated indications it may be useful to acquire an even later phase of parenchymal imaging (>3 min). This phase has shown potential to discern hepatocellular carcinoma (hypoattenuating) and cholangiocarcinoma (delayed contrast enhancement).

Overall, the most important parameter affecting total peak contrast enhancement for liver and parenchymal imaging is the total iodine mass administered. The administration of iodine is governed by the parameters: total CA volume and iodine concentration.

Subsequently the most important patient-related parameter that affects the magnitude of parenchymal attenuation is patient weight. For parenchymal imaging per se, it is much more important to adjust the total amount of deposited iodine to the patient weight than for any vascular application. A multicenter study found that 30 HU was the lowest acceptable diagnostic threshold to allow hepatic enhancement beyond 50 HU. Hence, the recommended iodine dose of 0.5 gl should be injected per kg of patient's body weight to yield the most efficient diagnostic peak enhancement of 50 HU. Hepatic parenchymal enhancement is much less dependent on flow rate than vascular enhancement (Bae et al. 1998c) (Fig. 2), but if combined in multiple-phase imaging, rapid injection rates apply for the early phase. For a single phase application aimed at parenchymal imaging, an injection rate of ≈ 3 ml/s is sufficient (Fig. 2).

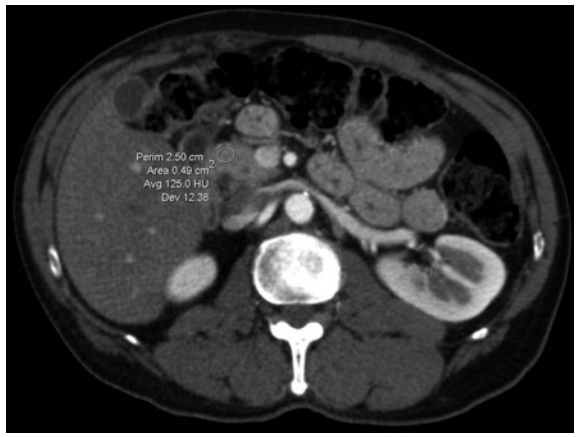

Fig. 7 Optimized pancreatic parenchymal phase. Pancreatic head shows HU values of up to 125. The scan was performed on a 64-row MDCT. T_{CMT} was 22 s, the additional diagnostic delay was 20 s. CM concentration was 1.2 ml CA/kg PW (370mgI/ml) with a flow rate of 3.5 ml/s

3.3 Pancreatic Multi-Phasic Imaging

MDCT of the pancreas is usually conducted in a biphasic (pancreatic parenchymal phase and portalveneous phase) protocol (Fig. 7). However, an arterial phase (scan delay 20 s after start of injection) for the detection of neuroendocrinal tumors and possible vessel infiltrations of tumors as well as an unenhanced phase (for detection of calcifications), resulting in a quadruple-phase scanning protocol, can be helpful.

As the pancreatic parenchyma shows—in contrast to liver parenchyma for example—a higher vascularization, it is necessary to adopt a dedicated pancreatic parenchymal phase.

In helical CT era, a fixed delay for the pancreatic phase of 30–70 s (with a peak at 40–45 s) after contrast agent injection was recommended. This was appropriate for longer scan times (approx. 20 s for a helical scan of the pancreas). MDCT provides much faster acquisition times and needs no longer than 3–5 s for a pancreatic CT. This renders a fixed scan delay suboptimal to catch the peak enhancement of the pancreatic parenchyma. It is well known that an individualized scan delay is superior to a fixed scan

delay (Schueller et al. 2006). Using a 16-row MDCT and a flow rate of 4 ml/s (140 ml, 300 mg/ml), a scan delay of aortic transit time plus a ΔT of 28 s provided optimal parenchymal contrast. In the same study the authors showed superior parenchmyal contrast at a flow rate of 8 ml/s compared to 4 ml/s. Furthermore, it was shown that higher concentrated contrast media (400 mg/ml) provides better opacification of the pancreatic parenchym than lower concentrated (300 mg/ml) (Fenchel et al. 2004).

4 Summary

Many patient-related and injection-related factors can affect the magnitude and timing of intravenous contrast agent attenuation, but these factors may be grossly separated into two categories: (1) factors that predominantly affect the magnitude of contrast attenuation (body size, contrast volume, iodine concentration and saline flush) and (2) factors that predominantly affect the temporal pattern of contrast attenuation (cardiac output, contrast injection duration and contrast injection rate).

MDCT, with its dramatically shorter image acquisition times, permits images with a much better utilization of peak contrast attenuation. High iodine concentrations of contrast media and newer scanner generations are mutually conditional. The very high iodine flux rates required by angiographic applications can be met by low concentration iodine agents only at very high flow rates resulting in high volumes administered, which is not compatible with compromised cardiac output.

Sporadic failure, though, is unpreventable at the current stage of development. This is simply due to the fact that the patient's cardiac output is not known prior to scan initiation in most cases.

MDCT is a powerful and continuously evolving technology for non-invasive imaging. CA administration is an integral part of this evolution and needs to be continuously adopted and optimized to take full advantage of this technology. A basic understanding of physiologic and pharmacokinetic principles, as well as an understanding of the effects of injection parameters on vascular and parenchymal enhancement, allows the development of optimized contrast agent delivery protocols for current and future MDCT.

References

Awai K, Takada K, Onishi H, Hori S (2002) Aortic and hepatic enhancement and tumor-to-liver contrast: analysis of the effect of different concentrations of contrast material at multi-detector row helical CT. Radiology 224:757–763

Awai K, Hiraishi K, Hori S (2004) Effect of contrast material injection duration and rate on aortic peak time and peak enhancement at dynamic CT involving injection protocol with dose tailored to patient weight. Radiology 230:142–150

Bae KT (2003) Peak contrast enhancement in CT and MR angiography: when does it occur and why? Pharmacokinetic study in a porcine model. Radiology 227:809–816

Bae KT (2005) Test-bolus versus bolus-tracking techniques for CT angiographic timing. Radiology 236:369–370, author reply 70.

Bae KT, Heiken JP (2000) Computer modeling approach to contrast medium administration and scan timing for multislice CT. In: Marincek B, Ros PR, Reiser M, Baker ME (eds) Multislice CT: A Practical Guide Springer, Berlin, pp 28–36

Bae KT, Heiken JP, Brink JA (1998a) Aortic and hepatic contrast medium enhancement at CT. Part I. Prediction with a computer model. Radiology 207:647–655

Bae KT, Heiken JP, Brink JA (1998b) Aortic and hepatic contrast medium enhancement at CT. Part II. Effect of reduced cardiac output in a porcine model. Radiology 207:657–662

Bae KT, Heiken JP, Brink JA (1998c) Aortic and hepatic peak enhancement at CT: effect of contrast medium injection rate–pharmacokinetic analysis and experimental porcine model. Radiology 206:455–464

Bae KT, Tran HQ, Heiken JP (2000) Multiphasic injection method for uniform prolonged vascular enhancement at CT angiography: pharmacokinetic analysis and experimental porcine model. Radiology 216:872–880

Bae KT, Tran HQ, Heiken JP (2004) Uniform vascular contrast enhancement and reduced contrast medium volume achieved by using exponentially decelerated contrast material injection method. Radiology 231:732–736

Becker CR, Hong C, Knez A, Leber A, Bruening R, Schoepf UJ, Reiser MF (2003) Optimal contrast application for cardiac 4-detector-row computed tomography. Invest Radiol 38:690–694

Cademartiri F, Luccichenti G, Marano R, Gualerzi M, Brambilla L, Coruzzi P (2004a) Comparison of monophasic versus biphasic administration of contrast material in non-invasive coronary angiography using a 16-row multislice Computed Tomography. Radiol Med 107:489–496

Cademartiri F, Nieman K, van der Lugt A, Raaijmakers RH, Mollet N, Pattynama PM, de Feyter PJ, Krestin GP (2004b) Intravenous contrast material administration at 16-detector row helical CT coronary angiography: test bolus versus bolus-tracking technique. Radiology 233:817–823

Cheng CP, Herfkens RJ, Lightner AL, Taylor CA, Feinstein JA (2004) Blood flow conditions in the proximal pulmonary arteries and vena cavae: healthy children during upright cycling exercise. Am J Physiol Heart Circ Physiol 287:H921–926

Coursey CA, Nelson RC, Weber PW, Howle LE, Nichols EB, Marin D, DeLong D (2009) Contrast material administration protocols for 64-MDCT angiography: altering volume and rate and use of a saline chaser to better match the imaging window–physiologic phantom study. Am J Roentgenol 193:1568–1575

Fenchel S, Fleiter TR, Aschoff AJ, van Gessel R, Brambs HJ, Merkle EM (2004) Effect of iodine concentration of contrast media on contrast enhancement in multislice CT of the pancreas. Br J Radiol 77:821–830

Fleischmann D (2003a) Use of high-concentration contrast media in multiple-detector-row CT: principles and rationale. Eur Radiol 13:M14–20

Fleischmann D (2003b) Use of high concentration contrast media: principles and rationale-vascular district. Eur J Radiol 45:S88–S93

Fleischmann D, Rubin GD, Bankier AA, Hittmair K (2000) Improved uniformity of aortic enhancement with customized contrast medium injection protocols at CT angiography. Radiology 214:363–371

Gosselin MV, Rassner UA, Thieszen SL, Phillips J, Oki A (2004) Contrast dynamics during CT pulmonary angiogram: analysis of an inspiration associated artifact. J Thorac Imaging 19:1–7

Haage P, Schmitz-Rode T, Hubner D, Piroth W, Gunther RW (2000) Reduction of contrast material dose and artifacts by a saline flush using a double power injector in helical CT of the thorax. Am J Roentgenol 174:1049–1053

Heiken JP, Brink JA, McClennan BL, Sagel SS, Crowe TM, Gaines MV (1995) Dynamic incremental CT: effect of volume and concentration of contrast material and patient weight on hepatic enhancement. Radiology 195:353–357

Kirchner J, Kickuth R, Laufer U, Noack M, Liermann D (2000) Optimized enhancement in helical CT: experiences with a real-time bolus tracking system in 628 patients. Clin Radiol 55:368–373

Kormano M, Partanen K, Soimakallio S, Kivimaki T (1983) Dynamic contrast enhancement of the upper abdomen: effect of contrast medium and body weight. Invest Radiol 18:364–367

Laghi A (2007) Multidetector CT (64 Slices) of the liver: examination techniques. Eur Radiol 17:675–683

Megibow AJ, Jacob G, Heiken JP, Paulson EK, Hopper KD, Sica G, Saini S, Birnbaum BA, Redvanley R, Fishman EK (2001) Quantitative and qualitative evaluation of volume of low osmolality contrast medium needed for routine helical abdominal CT. Am J Roentgenol 176: 583–589

Roos JE, Desbiolles LM, Weishaupt D, Wildermuth S, Hilfiker PR, Marincek B, Boehm T (2004) Multi-detector row CT: effect of iodine dose reduction on hepatic and vascular enhancement. Rofo 176:556–563

Schueller G, Schima W, Schueller-Weidekamm C, Weber M, Stift A, Gnant M, Prokesch R (2006) Multidetector CT of pancreas: effects of contrast material flow rate and individualized scan delay on enhancement of pancreas and tumor contrast. Radiology 241:441–448

Suzuki H, Oshima H, Shiraki N, Ikeya C, Shibamoto Y (2004) Comparison of two contrast materials with different iodine concentrations in enhancing the density of the the aorta, portal vein and liver at multi-detector row CT: a randomized study. Eur Radiol 14:2099–2104

Tatsugami F, Matsuki M, Inada Y, Nakai G, Tanikake M, Yoshikawa S, Narabayashi I (2007) Usefulness of saline pushing in reduction of contrast material dose in abdominal CT: evaluation of time-density curve for the aorta, portal vein and liver. Br J Radiol 80:231–234

Vrachliotis TG, Bis KG, Haidary A, Kosuri R, Balasubramaniam M, Gallagher M, Raff G, Ross M, O'Neil B, O'Neill W (2007) Atypical chest pain: coronary, aortic, and pulmonary vasculature enhancement at biphasic single-injection 64-section CT angiography. Radiology 243:368–276

Imaging Findings of Cirrhotic Liver

Jeong Min Lee, Dong Ho Lee, and Jeong-Hee Yoon

Contents

Abstract

The role of imaging in patients with cirrhosis is to characterize the morphologic manifestations of the disease, evaluate the hepatic and extrahepatic vasculature, assess the effects of portal hypertension, and detect and characterize hepatic tumors, especially differentiating hepatocellular caricnoma (HCC) from other tumors. CT plays a major role in the imaging of the liver. The recent development of multidetector row CT (MDCT) technology has helped CT to continue to excel in its currently established indications such as detection and characterization of hepatic lesions. HCC is the fifth most common tumor in the world and the incidence is expected to increase in the future due to hepatitis viral infections and increasing cirrhosis incidence. Approximately 90% of patients with HCC have cirrhosis. The imaging criteria of HCC are usually based on the vascular findings of HCC (e.g. arterial enhancement followed by washout in the portovenous and equilibrium phase). To understand the hemodynamics of HCC is important for the precise imaging diagnosis and treatment since there is a good correlation between their hemodynamics and pathophysiology. In this chapter, the most important and prevalent findings of HCC which can be evaluated by CT scans, and current diagnostic criteria were discussed. In addition, the imaging features of atypical HCC as well as frequent HCC mimickers in cirrhotic liver were also discussed.

J. M. Lee (✉) · D. H. Lee · J.-H. Yoon
Department of Radiology, Seoul National University, College of Medicine, Yeon gon dong 28, Jongno gu, Seoul, South Korea
e-mail: jmsh@snu.ac.kr

C. J. Zech et al. (eds.), *Multislice-CT of the Abdomen*, Medical Radiology. Diagnostic Imaging,
DOI: 10.1007/174_2012_538, © Springer-Verlag Berlin Heidelberg 2012

1 Cirrhosis

1.1 Epidemiology

Cirrhosis is the common end response of the liver to a variety of insults and injuries and defined as the histological development of regenerative nodules surrounded by fibrous bands, which leads to portal hypertension and end-stage liver disease (Schuppan and Afdhal 2008). Histologically, cirrhosis is characterized by vascularized fibrotic septa that link portal tracts with each other and with central veins, resulting in hepatocyte islands surrounded by fibrotic septa and that are devoid of a central vein. The major clinical consequences of cirrhosis are impaired hepatocyte (liver) function, an increased intrahepatic resistance (portal hypertension), and the development of hepatocellular carcinoma (HCC). Cirrhosis is the fourteenth and tenth leading causes of death in the world and in developed countries (Mathers 2006). Although any chronic liver disease may progress to cirrhosis, the most common causes of cirrhosis globally are thought to be hepatitis B virus (HBV), hepatitis C virus (HCV), and alcohol. Hepatitis B is the prevailing cause in most parts of Asia and sub-Saharan Africa, whereas alcoholic liver disease and hepatitis C, and more recently, nonalcoholic steatohepatitis (NASH) are the most significant causes in developed countries (Lim and Kim 2008). Nonalcoholic fatty liver disease (NAFLD) is now recognized as an important clinical entity, affecting approximately 20–30% of the adult population in the Western world (Greenfield et al. 2008).

1.2 Pathophysiology

Cirrhosis is the ultimate result of hepatic injury and hepatic fibrosis causes architectural distortion and results in a diffuse disorganization of hepatic morphology with the development of a spectrum of nodules which are classified into regenerative, dysplastic, and neoplastic (Popper 1986). Cirrhosis has traditionally been divided into three categories: (1) micronodular cirrhosis, in which less than 3 mm in diameter, nodules evenly involve every lobule (Fig. 1); (2) macronodular cirrhosis characterized by variable-sized nodules (3 mm-a few cm) that are focal and do not involve every lobule (Fig. 1); and (3) mixed cirrhosis (Gore 2008). Alcoholism, hepatitis C, and biliary cirrhosis are frequently associated with the micronodular pattern whereas virial hepatitis B is associated with the macronodular pattern. When regenerative nodules contain iron they are called siderotic nodules.

As cirrhosis develops, intrahepatic vascular resistance increases and portal perfusion decreases, which accompanies with increased arterial flow, capillarization of the sinusoid (Schuppan and Afdhal 2008). Consequently, portal hypertension may develop secondary to cirrhosis. In patients with portal hypertension, some of the portal blood may reversely flow and pass through portosystemic collaterals such as left gastric vein, esophageal varices, short gastric vein, umbilical vein, and splenorenal shunt (Fig. 1) (Perez-Johnston et al. 2010; Moubarak et al. 2011).

1.3 CT Features of Liver Cirrhosis

In general, CT is not sensitive enough to detect early changes of cirrhosis, but their specificity is high if the cause obvious (Saygili et al. 2005). Therefore, the primary role of imaging in patients with cirrhosis is to characterize the morphologic manifestations of the disease, evaluate the hepatic and extrahepatic vasculature, assess the effects of portal hypertension, detect and characterize hepatic tumors, especially differentiating hepatocellular caricnoma (HCC) from other tumors (Kamel et al. 2005).

1.3.1 Liver Morphology

At an early stage of cirrhosis, the liver may appear normal on cross-sectional imaging. With disease progression, heterogeneity of liver parenchyma and surface nodularity are observed (Brancatelli et al. 2007). In addition, it gives rise to several intra- and extra-hepatic changes, including regional morphologic changes in the liver, nodularity of the liver surface, splenomegaly, regenerative nodules, iron and fat deposition, and ascites, and the development of varices and collaterals (Fisher and Gore 1985). Although the classically described findings of cirrhosis are common in advanced cirrhosis, they are seen less frequently in the early stage of the disease, at which time the liver may appear nodular on CT (Ito et al. 2000). Enlargement of the hilar periportal space

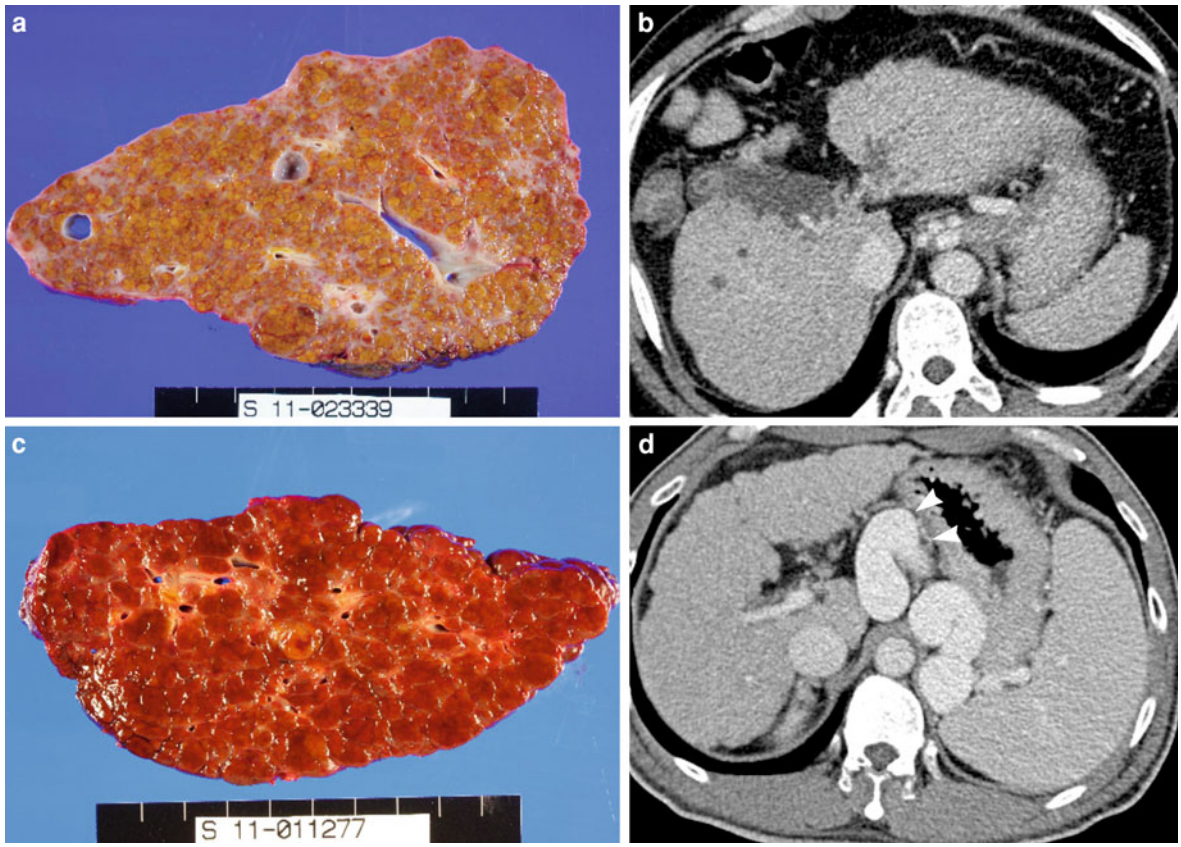

Fig. 1 Cirrhosis: pathologic and CT findings. **a** Micronodular cirrhosis in a patient with alcoholic cirrhosis. **b** Corresponding CT image of micronodular cirrhosis. **c** Macronodular cirrhosis in a patient with hepatitis B cirrhosis. **d** Corresponding CT image of macronodular cirrhosis with nodular contour and the dilated left gastric vein (*arrowheads*)

and expansion of the major interlobar fissure are seen in patients with early cirrhosis (Fig. 2) (Ito and Mitchell 2004). These findings are attributed to atrophy of the medial segment of the left lobe, suggesting that medial segment atrophy may be an initial morphologic change in early cirrhosis (Lafortune et al. 1998).

Although all patients pathologically demonstrate regenerative nodules, those regenerative nodules are infrequently seen at CT. Nodularity of the liver contour caused by regenerative nodules, fibrous scarring, and non-uniform atrophy or hypertrophy could be demonstrated, especially when ascites is present (Fig. 2). Caudate lobe hypertrophy is the most characteristic morphologic feature of liver cirrhosis (Giorgio et al. 1986). The caudate lobe is often spared from atrophic process in cirrhosis because of its dual arterial blood supply and a shorter intrahepatic course of hepatic arteries and portal veins supplying the caudate lobe (Awaya et al. 2002). A ratio of transverse caudate lobe width to right lobe width greater than or equal to 0.65 constitutes a positive indicator for the diagnosis of cirrhosis with high level of accuracy (Fig. 3) (Harbin et al. 1980; Giorgio et al. 1986; Valls et al. 2002). A modified caudate lobe width to right lobe width ratio, using the right portal vein instead of the main portal vein to set the lateral boundary has recently been proposed (Awaya et al. 2002). Other regional changes in hepatic morphology typically seen in advanced cirrhosis are segmental hypertrophy involving the lateral segments (2, 3) of the left lobe (Awaya et al. 2002), and segmental atrophy affecting both the posterior segments (6, 7) of the right lobe and medial segment (4) of the left lobe (Fig. 2) (Lafortune et al. 1998). Enlargement of hilar periportal space, the notch-sign (Ito et al. 2003) an expanded gallbladder fossa (Ito et al. 1999a, b, 2000, 2003), pericaval fat collections (Gibo et al. 2001) and

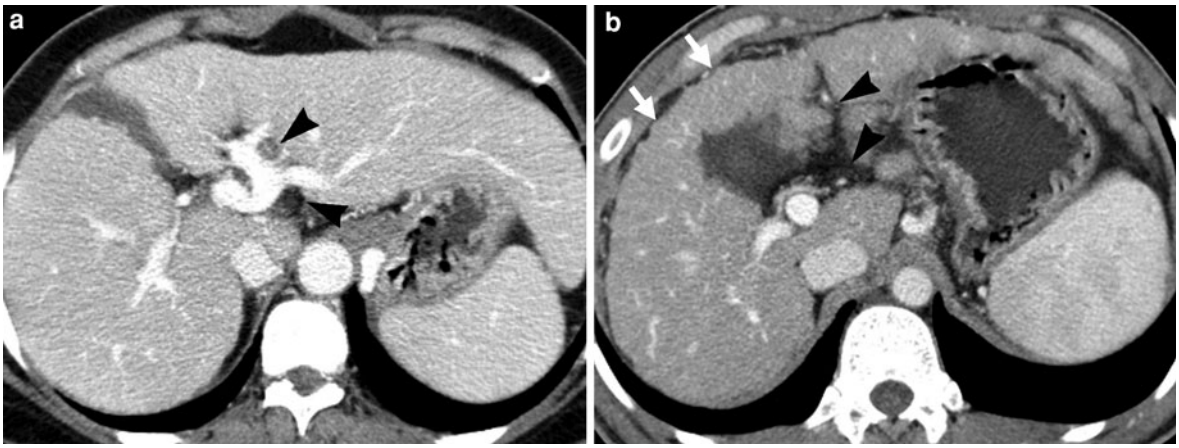

Fig. 2 Cirrhosis: CT findings. **a** Contrast-enhanced CT image shows enlargement of the hilar periportal space (*arrowheads*) and hypertrophy of left hepatic lobe. **b** On portal phase CT image, expansion of the major interlobar fissure (*arrowheads*) and widening of the periportal space are seen. Note enlargement of left hepatic lobe and nodularity of the liver contour (*arrows*)

generalized widening of the interlobar fissures are also considered typical findings of cirrhosis (Figs. 2 and 3) (Gibo et al. 2001; Brancatelli et al. 2007). In advanced liver cirrhosis, colonic interposition between the liver and the anterior-lateral abdominal wall is frequently seen (Fig. 3).

Although the patterns of hepatic morphologic changes overlap among the different causes of cirrhosis, certain imaging features may suggest particular etiologic factors. For example, enlargement of the lateral segment accompanied by shrinkage of both right anterior segment and left medial segment is frequently shown in patients with viral-induced cirrhosis (Khatri et al. 2010; Ozaki et al. 2010). Marked caudate lobe enlargement is typically associated with alcoholic cirrhosis and enlargement of caudate lobe and the presence of the right posterior hepatic notch on MR imaging are more frequent findings of alcoholic cirrhosis than of virus-induced cirrhosis (Okazaki et al. 2000). Primary sclerosing cholangitis (PSC) and primary biliary cirrhosis are frequently associated with hypertrophy of caudate lobe and atrophy of other areas (Ito et al. 1999a, b).

1.3.2 Portal Hypertension and Mesenteric Edema

Advanced cirrhosis is also accompanied by alteration in hepatic blood flow. Periportal fibrosis and regenerative nodules cause extrinsic compression and tapering of the intrahepatic portal and venous branches (Kamel et al. 2005). The decreased portal venous supply that occurs as a result of liver fibrosis is partially compensated by an increase in arterial blood supply. Such an increase in arterial perfusion may be demonstrated by pronounced patchy liver enhancement during the arterial phase (Kim et al. 2009a; Kang et al. 2011). Therefore, cirrhotic liver parenchyma often demonstrates less contrast enhancement than normal liver and appears inhomogeneous due to underlying regeneration, fibrosis, and the altered portal venous flow. Portal hypertension causes complications such as ascites and the development of engorged and tortuous collateral vessels such as left gastric vein, esophageal varices, short gastric vein, paraumbilical vein, and splenorenal shunt (Fig. 4) (Perez-Johnston et al. 2010; Moubarak et al. 2011). The paraumbilical veins and the left gastric vein, both draining into the portal vein, also reopen to form portosystemic shunts. Other shunts between the portal and the systemic circulation include splenorenal collaterals, hemorrhoidal veins, abdominal wall, and retroperitoneal collaterals. In addition, increased venous pressure is also responsible for the prominent mesenteric edema and stranding occurring in 86% of patients with cirrhosis (Chopra et al. 1999). Mesenteric edema can be shown as an increase in the density of the mesenteric fat compared with the retroperitoneal fat.

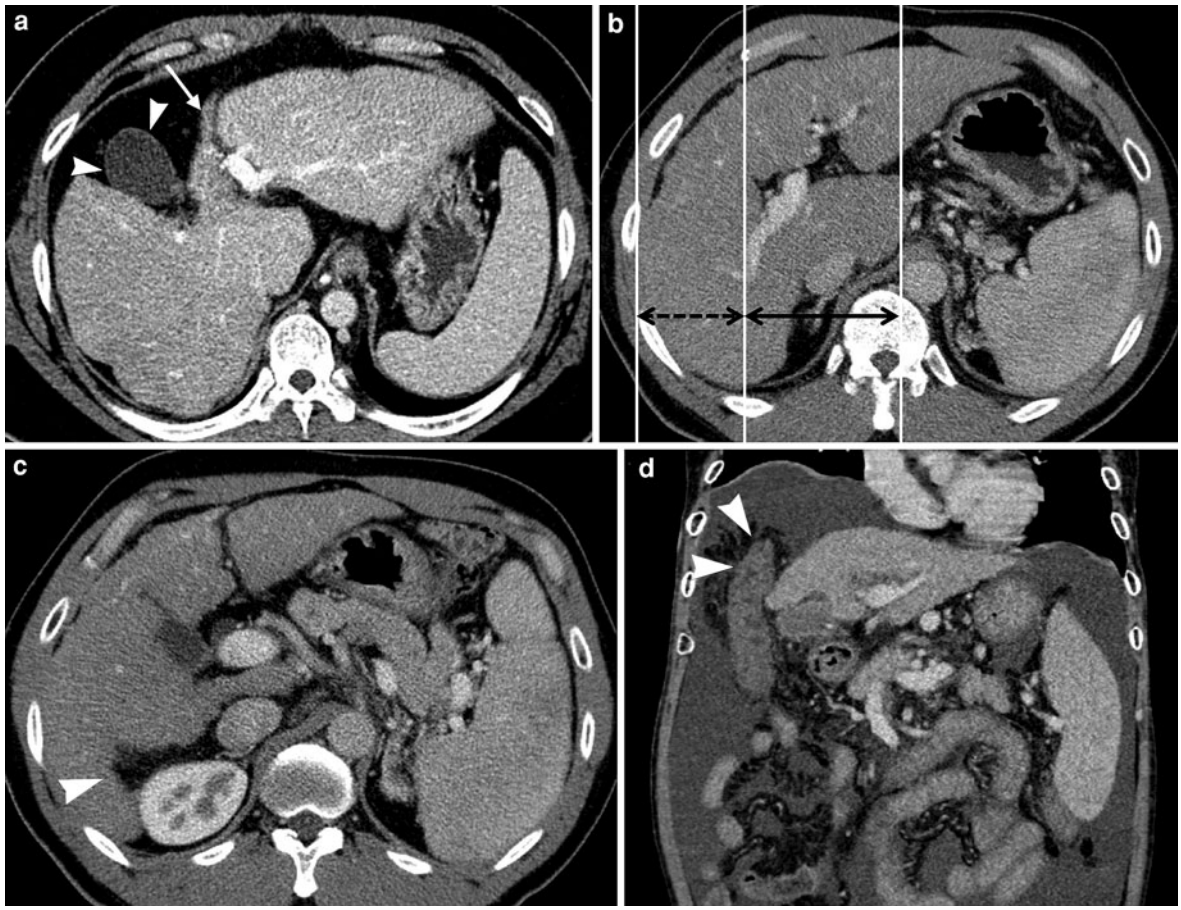

Fig. 3 Advanced Cirrhosis: CT findings. **a** Contrast-enhanced CT image demonstrates enlargement of lateral segment of the left lobe, atrophy of the medial segment of the left lobe (*arrow*), and widening of gallbladder fossa (*arrowheads*). **b** Contrast-enhanced CT image shows caudate lobe hypertrophy and right lobe atrophy. Diagram demonstrates the method of determining caudate lobe/right lobe ratio. A *dashed arrow* indicates transverse diameter of the right lobe whereas *solid arrow* depicts transverse diameter of the caudate lobe. **c** Contrast-enhanced CT image demonstrates widening of the gallbladder fossa (expanded gallbladder fossa sign), enlargement of caudate lobe, and a characteristic notch in the right posterior surface of the liver (*arrowhead*). **d** Coronal reformatted MDCT image shows interposition of colon between the liver and right abdominal wall (*white arrowheads*) due to atrophy of the right lobe and ascites

1.3.3 Fibrosis

Fibrosis is an inherent part of hepatic cirrhosis, and is typically detected as patchy fibrosis, as a lacelike pattern, or as a confluent mass. The lacelike type of fibrosis is best described as thin or thick bands that surround regenerative nodules. This pattern is best visualized on non-enhanced CT, and is usually not well visualized on portal venous phase images (Dodd et al. 1999a, b). Focal confluent fibrosis is observed in end-stage liver disease and is usually a wedge-shaped lesion located in the subcapsular portion of segment 4, 5, or 8, with associated capsular retraction (Ohtomo et al. 1993a, b). Delayed, persistent contrast enhancement, along with the characteristic capsular retraction and typical location and shape help to distinguish confluent fibrosis from HCC (Brancatelli et al. 2009).

2 Hepatocarcinogenesis

2.1 Multi-Step Hepatocarcinogenesis

HCC is the most common primary hepatic malignant tumor and the fifth most common tumor worldwide and is the third most common cause of cancer-related death (Parkin et al. 2001; Schutte et al. 2009; Yang

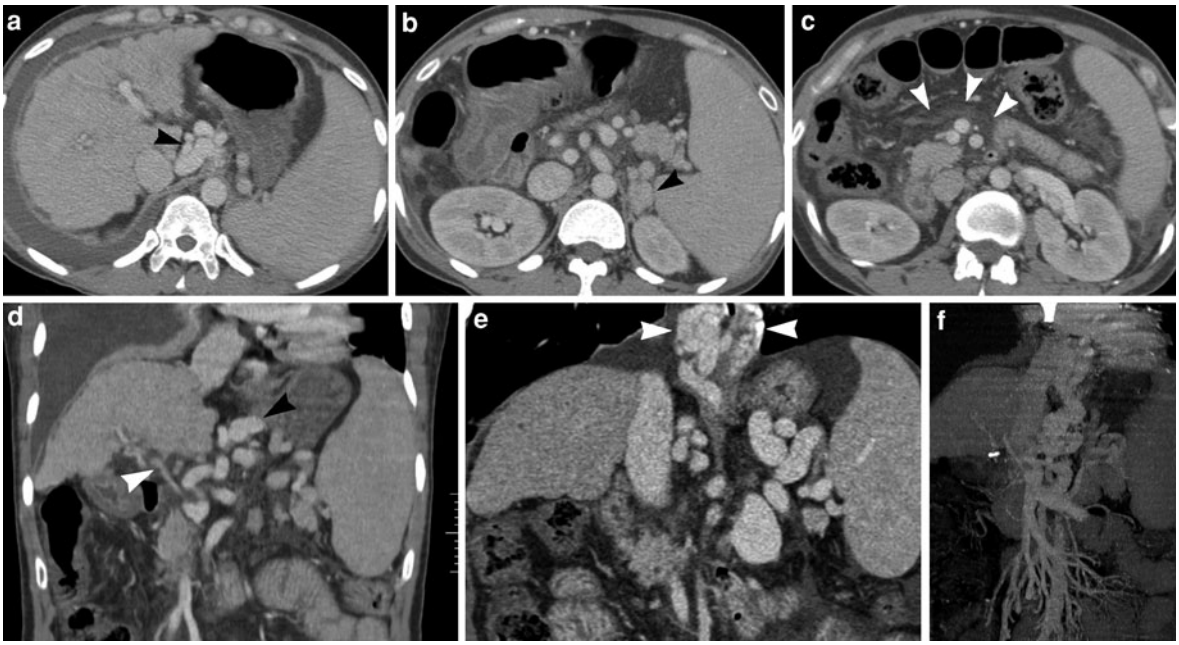

Fig. 4 Portal hypertension and mesenteric edema. **a** and **b** Axial contrast-enhanced CT images demonstrate dilated and tortuous left coronary vein (*arrowhead*) (**a**), and retroperitoneal vein (*arrowhead*) (**b**). **c** Axial contrast-enhanced CT image demonstrates mesenteric edema (*arrowheads*). **d** and **e** Coronal reformatted CT images show decreased caliber of the main portal vein (*white arrowhead*) and dilated left coronary veins (*black arrowhead*) (**d**) and paraesophageal veins (*white arrowheads*) (**e**). **f** Maximum intensity projection image in portal phase after contrast injection shows developments of collateral veins in end-stage cirrhosis

and Roberts 2010). One of major risk factors for developing HCC is chronic hepatitis B and C and alcohol abuse, especially if the liver cirrhosis is already present (Gomaa et al. 2008). In case of underlying cirrhosis, multistep hepatocarcinogenesis from areas of regeneration to overt HCC has been reported (Fig. 5) (Choi et al. 1993; Fan et al. 2011). According to this multistep carcinogenesis, the most common terminology of the International Working Party of the World Congress of Gastroenterology (ICGHN) defined regenerating nodules (RNs), low-grade dysplastic nodules (DNs), high-grade DNs, and HCC as steps from regeneration to HCC (Ferrell et al. 1993, 1995; Hytiroglou et al. 2007, 2009; Desmet 2009; Roncalli et al. 2011). In addition, small HCCs measuring less than 2 cm in diameter are of two types: vaguely nodular, well-differentiated tumors, also known as "early" HCCs, and distinctly nodular tumors, with histologic features of "classic" HCC. The precancerous lesions include dysplastic foci and DNs (Park and Kim 2011).

As there is progression along this pathway of multistep hepatocarcinogenesis, there is a corresponding decrease in hepatocyte function, Kupffer cell density, decreased biliary function, progressive sinusoidal capillarization, and recruitment of unpaired arterioles (Khatri et al. 2010). Small-sized nodules detected in cirrhotic liver by imaging include large regenerative nodules, DNs (low- or high-grade), and small HCCs (early or progressed). Recently, the clinical detection rate of these nodules has increased by the development of cross-sectional imaging modalities. However, the differential diagnosis of these lesions by imaging studies may be difficult and even the histological interpretation of these nodules may be difficult, especially for the biopsy tissue (Park and Kim 2011).

A DN is a precancerous nodular hepatocellular region that contains dysplastic features without histologic evidence for malignancy (Earls et al. 1996; Hytiroglou 2004; Libbrecht et al. 2005). DNs are subclassified on the basis of the degree of cellular abnormalities: low-grade (containing hepatocytes with mild atypia) and high-grade (when the degree of atypia is moderate, but insufficient for the diagnosis of malignancy). High-grade DNs are more likely to progress to HCC than are low-grade DNs

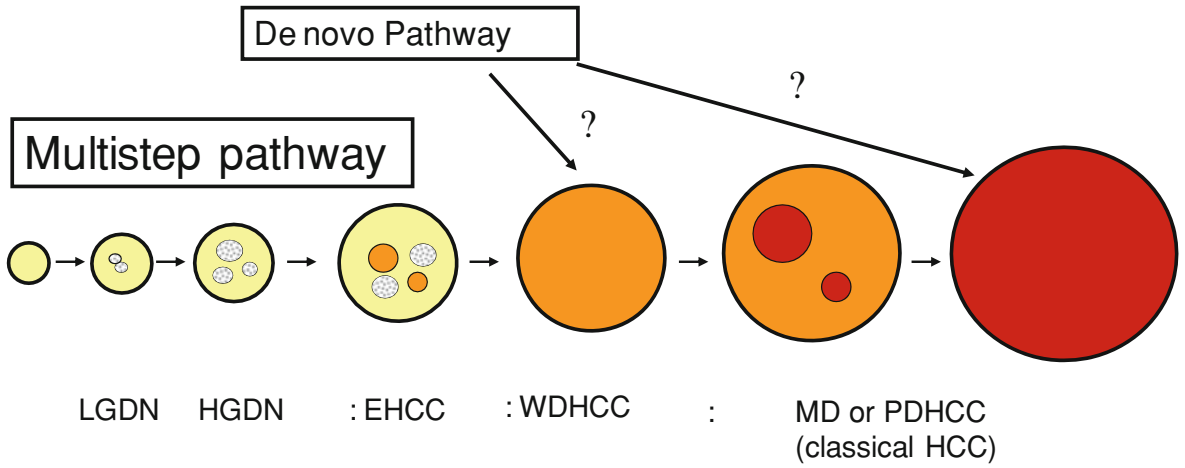

Fig. 5 Hepatocarcinogenesis: there are two pathways of carcinogenesis for hepatocellular carcinoma in cirrhosis: multistep pathway and de novo pathway. One or more regenerative nodules may show a number of changes in shape and size of nuclei and the cytoplasm of the hepatocytes (signs of atypia) and change into dysplastic nodules. Dysplastic nodules show an increased number of cells and cellular density. In addition, atypia within dysplastic nodules can give rise to early hepatocellular carcinoma, which represents an early stage of HCC development with indistinct margin, and finally developed into small and progressed HCC with different degree of differentiation

(Borzio et al. 2003). A DN that contains a microscopic focus of HCC is called "DN with subfocus of HCC" (Earls et al. 1996). DNs may contain cells with features suggestive of a clonal population, such as accumulation of fat, hemosiderin or copper (Terada and Nakanuma 1989; Terada et al. 1989). The high-grade DNs are featured with increased cell density of these lesions, mildly thickened cell plates and foci of increased cell proliferation may be evident, forming subnodules within DNs. DNs usually contain portal tracts, and often contain small numbers of nontriadal (also called "unpaired") arteries, and also demonstrate variable degrees of sinusoidal capillarization, which is detectable by immunohistochemical stains for CD31 and CD34 antigens (Park et al. 2000). On the contrary, the cell density within early HCC is at least two times greater than that of the surrounding parenchyma. The tumor cells grow in a replacing fashion, and portal tracts may be present within these lesions. Tumor-cell invasion into the intralesional portal tracts (stromal invasion) is frequently seen (Nakashima et al. 1999). Detection of heat shock protein-70 and glypican-3 by immunohistochemical stains has been suggested as a useful adjunct in distinguishing early HCC from DNs (Sakamoto et al. 1991; Llovet et al. 2006). Early HCCs receive blood supply from two sources: vessels of entrapped portal tracts (branches of the hepatic artery and portal vein), as well as newly formed (nontriadal) arteries. However, the number of intratumoral portal tracts is less than one-third of that in the surrounding liver tissue, while the nontriadal arteries of these lesions are insufficiently developed (Nakashima et al. 1999; Kojiro and Roskams 2005). Therefore, cell crowding and low blood supply may result in hypoxia (Kutami et al. 2000). Sometimes, nodular aggregates of less differentiated tumor cells are seen to arise within the well-differentiated cell population of early HCCs (Kojiro and Nakashima 1999). Finally, small HCCs of distinctly nodular type are well-demarcated, often encapsulated nodules. Approximately 80% of these lesions are moderately differentiated histologically, the remaining contains both moderately and well-differentiated areas (Nakashima et al. 1995, 1999; Kojiro and Roskams 2005). Portal tracts are not present within small HCCs of distinctly nodular type, whereas nontriadal arteries are often plentiful, and sinusoidal capillarization is well-developed. Therefore, the blood supply of these lesions is basically derived from nontriadal arteries (Ito et al. 1999a, b; Kojiro and Nakashima 1999; Hytiroglou et al. 2007). In addition, a de novo development of HCC can occur, and it has been usually seen on normal liver parenchyma without evidence of cirrhosis or nodules in Europeans and Americans who have the low incidence of chronic liver disease (Freeny et al. 1992;

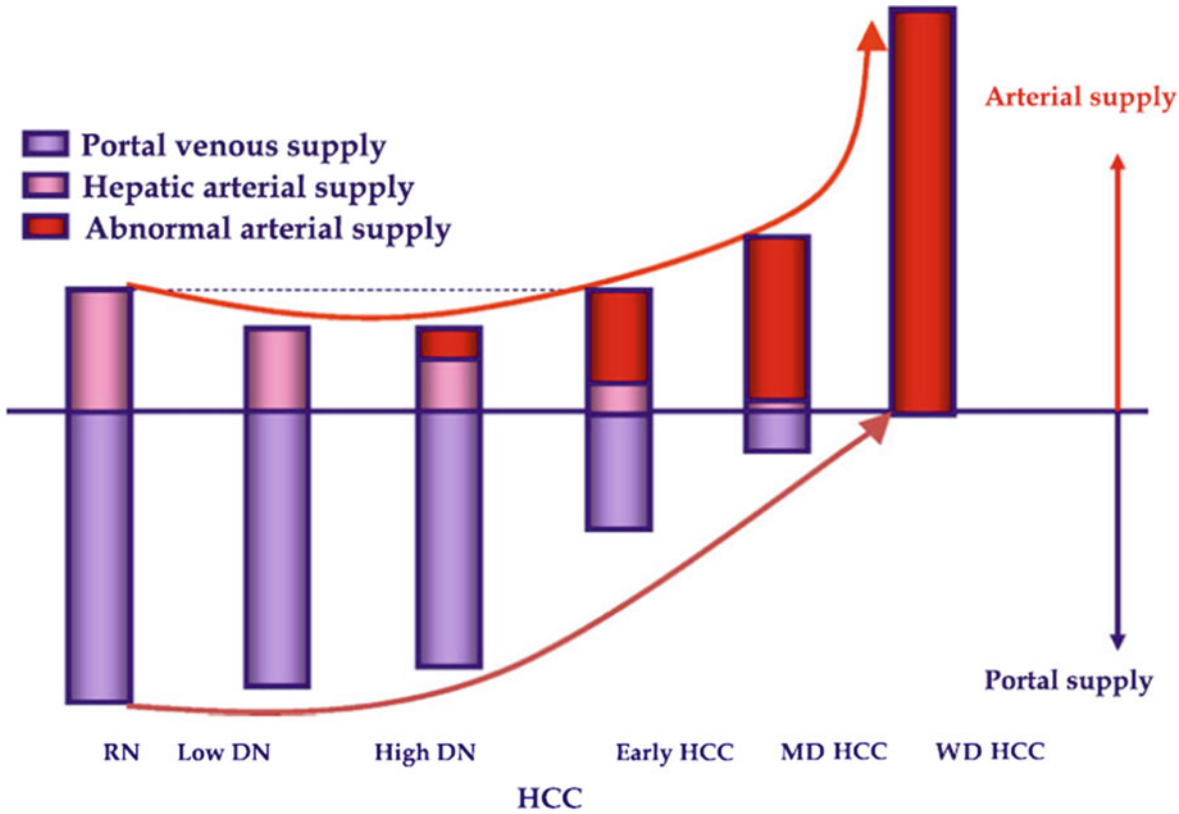

Fig. 6 Multi-step hepatocarcinogenesis and changes of intranodular blood supply. As malignancy grade progresses, intranodular portal supply gradually decreases during early stage of hepatocarcinogenesis and finally disappears in moderately differentiated HCCs. On the contrary, arterial supply first decreases during the early stage of hepatocarcinogenesis and then acutely increases, and finally the entire nodule is fed only by artery in moderately differentiated HCCs (Courtesy of Matsui et al. 2011)

Fernandez and Redvanly 1998; Taguchi et al. 2005). The challenge for the radiologists is to detect premalignant and malignant lesion early, to distinguish HCC from RNs or DNs in patients with liver cirrhosis, and to allocate the patients with HCC properly to the treatment options which are nowadays available (Hytiroglou 2004; Zech et al. 2009).

2.2 Multistep Changes of Intranodular Blood Supply and Drainage Vessels During Hepatocarcinogenesis

As the progression of multistep carcinogenesis from regeneration to HCC, increased arterial neovascularization combined with decreased portal blood flow are the key features of change occurring within the nodules, and these features were reported by some investigators with CT during hepatic arteriography (CTHA) and CT during arterial portography (CTAP) (Hayashi et al. 1999; Matsui 2004). According to the results of previous studies on CTAP and CTHA, it has been suggested that the intranodular portal supply relative to the surrounding liver parenchyma is decreased, whereas the intranodular arterial supply is first decreased during the early stage of hepatocarcinogenesis and then increased in parallel with increasing grade of malignancy of the nodules (Matsui et al. 2011). More specifically, normal hepatic artery decreases in accordance with increasing grade of malignancy and is virtually absent in HCC, but abnormal arteries due to tumor angiogenesis develop in high-grade DN during the course of hepatocarcinogenesis, and are markedly increased in number in moderately differentiated HCCs (Figs. 6, 7) (Kitao et al. 2009). However, there is a fairly wide

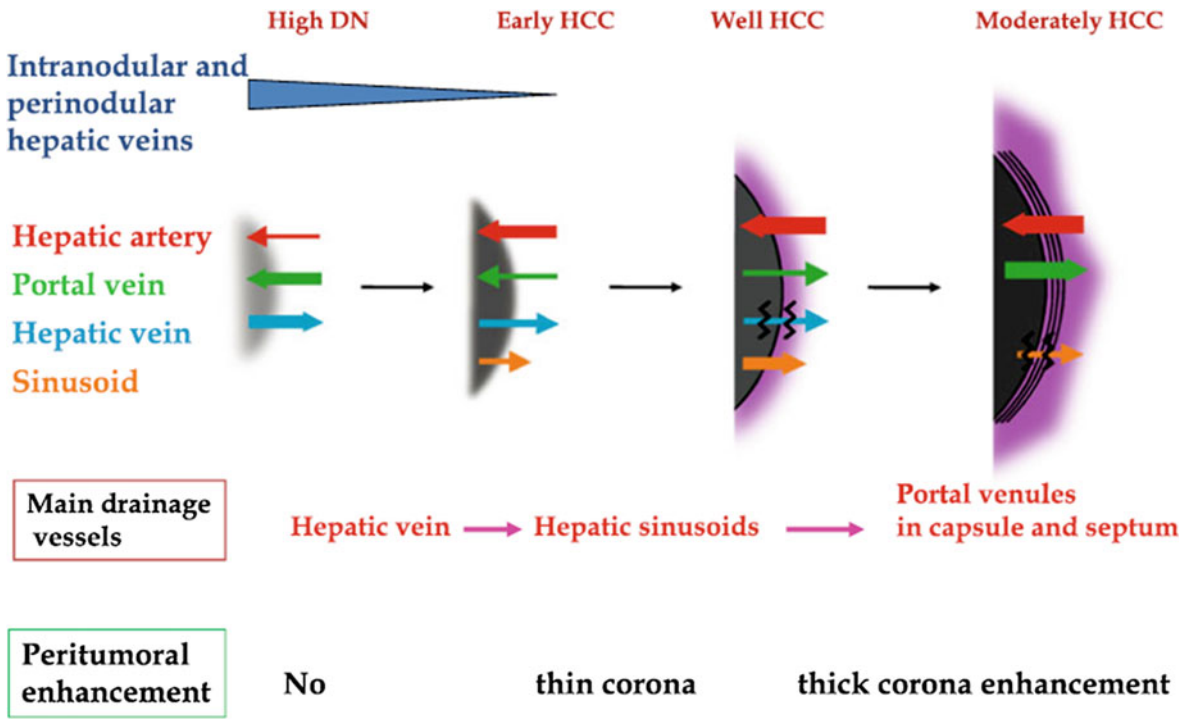

Fig. 7 Multi-step changes of drainage vessels and peritumoral enhancement during hepatocarcinogenesis. In dysplastic nodules or early HCCs, the main drainage route from the tumor is intranodular or perinodular hepatic vein, but during early stage of hepatocarcinogenesis hepatic veins disappear from the tumor, and drainage vessels change to hepatic sinusoids. In moderately differentiated HCC with pseudocapsule formation, the communication between tumor sinusoids and the surrounding hepatic sinusoids are also blocked, and then, the portal venules in the pseudocapsule finally become the main drainage vessel from the tumor. In accordance with the changes of the drainage vessels, thin to thick corona enhancement appears surrounding the tumor (Courtesy of Matsui et al. 2011)

range of overlap in blood supply patterns among the various types of hepatocellular nodules (Nakamura et al. 2007). Nevertheless, small HCCs sometimes display characteristic radiologic features, such as "nodule-in-nodule" configuration (Fig. 8) and "corona enhancement" pattern (Fig. 9) (Efremidis et al. 2007). It should be noted that a lesion demonstrating hypervascularity (throughout the lesion) on any contrast-enhanced arterial phase images should be defined as progressed HCC per the ICGHN criteria, even if the lesion is less than 2 cm in diameter.

Furthermore, according to a recent study using CTAP and CTHA, the main drainage vessels of hepatocellular nodules change from hepatic veins to hepatic sinusoids and then to portal veins during multi-step hepatocarcinogenesis, mainly due to disappearance of the hepatic veins from the nodules (Kitao et al. 2009).

3 Imaging Features of Cirrhotic Nodules

3.1 Regenerative Nodules

In the cirrhotic liver, RNs are macronodular (≥3 mm), as usually seen in chronic hepatitis B, or micronodular (<3 mm), as seen in other causes of cirrhosis. Most RNs are difficult to detect at CT because they are too small or are too similar to surrounding liver parenchyma (Krinsky and Lee 2000; Kamel et al. 2005; Brancatelli et al. 2007). CT detects RNs when they are surrounded by hyperdense fibrotic bands on delayed phase CT (Fig. 10). Siderotic RNs are typically hyperattenuating to liver parenchyma on non-enhanced CT and are isoattenuating to liver, and therefore difficult to detect, after contrast injection

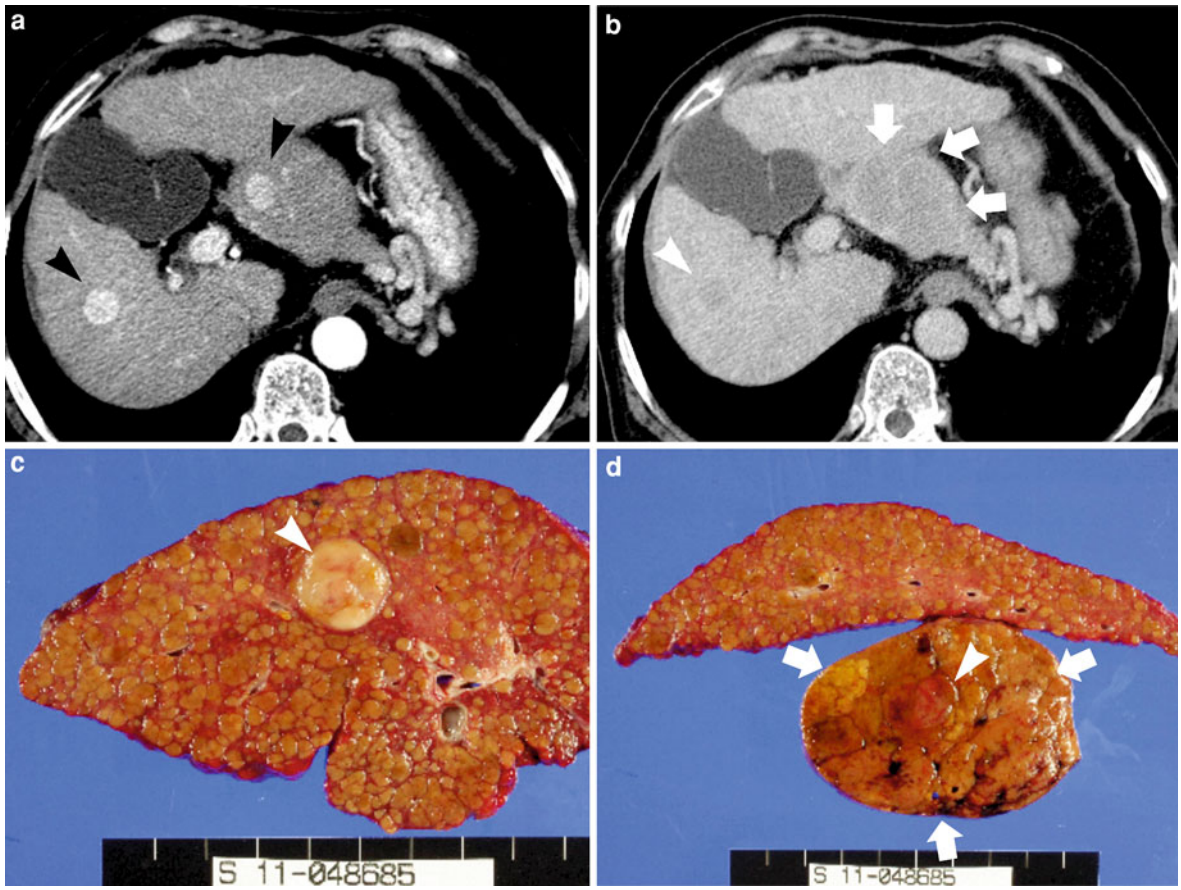

Fig. 8 Small HCC with nodule-in-nodule appearance. **a** Contrast-enhanced arterial phase CT scan shows two enhancing nodules in segment 5 and segment 1 (*arrowheads*). **b** On the portal venous phase CT scan, the lesion in segment 5 becomes hypoattenuated to the adjacent liver parenchyma. In addition, the lesion in segment 1 shows much bigger area with hypoattenuation, which represents so-called "nodule in nodule" appearance (*arrows*). **c** Photograph of the specimen shows a small classic HCC (*arrowhead*) in segment 5. **d** Photograph of segment 1 lesion shows a small HCC (*arrowhead*) developed in the background of dysplastic nodule (*arrows*)

(Ito et al. 1996; Baron and Peterson 2001). However, in the setting of Budd-Chiari syndrome with cirrhosis, RNs can have features suggestive of HCC, including a size larger than 2 cm, and arterial hyperenhancement (Imaeda et al. 1994; Vilgrain et al. 1999; Brancatelli et al. 2002). On portal venous phase images, a hypoattenuated peripheral rim or presence of central scar have also been reported in patients with Budd-Chiari syndrome (Vilgrain et al. 1999). Although HCC and RNs may be difficult to distinguish based on imaging characteristics in the setting of Budd-Chiari, the presence of more than 10 nodules measuring up to 4 cm in diameter, should favor the diagnosis of RNs (Vilgrain et al. 1999).

3.2 Dysplastic Nodules

DNs are seen in 15–25% of patients with cirrhosis (Krinsky and Lee 2000), although are not seen on imaging as frequently, possibly because they appear similar to RNs or the surrounding liver (Baron and Peterson 2001). DNs receive predominantly portal venous flow with decreased hepatic arterial flow and therefore, such low-grade DNs may be indistinguishable from RNs based on enhancement characteristics (Lim et al. 2004). Although there have been some reports that described increased hepatic arterial blood supply of high-grade DNs and consequent arterial hyperenhancement mimicking HCC, most

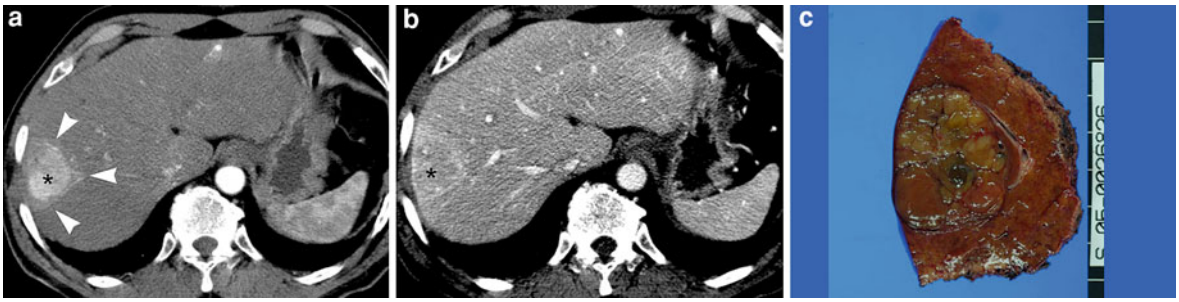

Fig. 9 HCC with corona enhancement. **a** Contrast-enhanced arterial phase CT scan shows hypervascular tumor (*asterisk*) with peritumoral corona enhancement (*arrowheads*). **b** Contrast-enhanced portal phase CT scan shows washout of the tumor (*asterisk*) ith perilesional enhancement. **c** Specimen photograph shows a well encapsulated HCC lesion

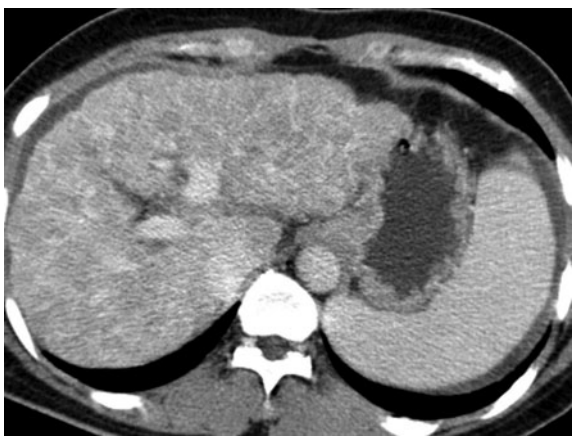

Fig. 10 Regenerative nodule: CT appearance. Delayed phase CT scan also shows multiple nodules which are separated by hyperenhancing fibrous tissues in the liver. Note nodularity of liver contour, splenomegaly and small amount of ascites

DNs show slightly low or similar degree cumulative arterial vascularity due to diminished normal hepatic arterial flow despite of increased neovascularity (Krinsky et al. 2001; Taouli et al. 2004; Efremidis et al. 2007; Willatt et al. 2008). On CT imaging, only 10% of DNs were depicted on CT, and most of them showed hypoattenuation during arterial and/or portal venous phase (Fig. 11) (Lim et al. 2004). This low sensitivity of CT for depiction of dysplastic nodule could be explained by that DNs possess approximately the same amount of arterial supply as the surrounding hepatic parenchyma and a normal or slightly decreased portal venous supply (Ueda et al. 1992). Therefore, in a practical point of view, since most DNs do not usually demonstrate bright enhancement on arterial phase CT, marked arterial phase enhancement should suggest HCC rather than dysplastic nodule. A further distinguishing feature of DNs from HCC is that DNs typically lack a capsule (Willatt et al. 2008). However, there is still much overlap in imaging features among regenerative nodules, DNs and well-differentiated HCC (Brancatelli et al. 2007). The difficulty in distinguishing between high-grade dysplastic nodule and well-differentiated HCC on CT is paralleled in their histologic appearance (Khatri et al. 2010). Therefore, triple phase helical dynamic CT is insensitive for detection of DNs in cirrhotic livers, and DNs are detected and characterized better by MR than by CT; however, accurate diagnosis may be made in only about 15% of cases (Krinsky et al. 2001).

3.3 Small Hepatocellular Carcinoma

By definition, small HCCs measure less than 2 cm in diameter (1995). Careful morphologic studies from Japan have shown that these lesions can be classified into two types: (1) small HCC of indistinctly (vaguely) nodular type (early HCC) (Fig. 12) and (2) small HCC of distinctly nodular type (small progressed HCC) (Figs. 13 and 14) (Sakamoto et al. 1991; Hytiroglou et al. 2007). Microscopic invasion of stroma and portal tracts is the primary diagnostic feature used to differentiate well-differentiated HCC from DNs (Wanless 1995; Kondo et al. 2009). Although early HCCs receive blood supply from both the hepatic artery and portal vein branches, the number of intratumoral portal tracts is less than one-third of that in the surrounding liver tissue and the nontriadal arteries are insufficiently developed (Nakashima et al. 1999; Kojiro and Roskams 2005). Therefore, cell crowding and low blood supply may

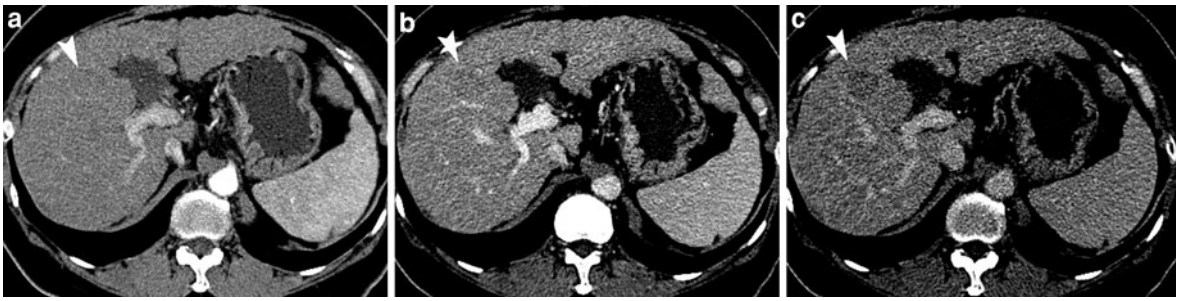

Fig. 11 Dysplastic nodule: CT appearance. **a** Arterial (**a**) and portal (**b**) phase CT scans demonstrate a nodule with subtle hypoenhancement (*arrowhead*). **c** Delayed phase CT scan shows a hypoattenuated nodule compared with the surrounding liver parenchyma (*arrowhead*)

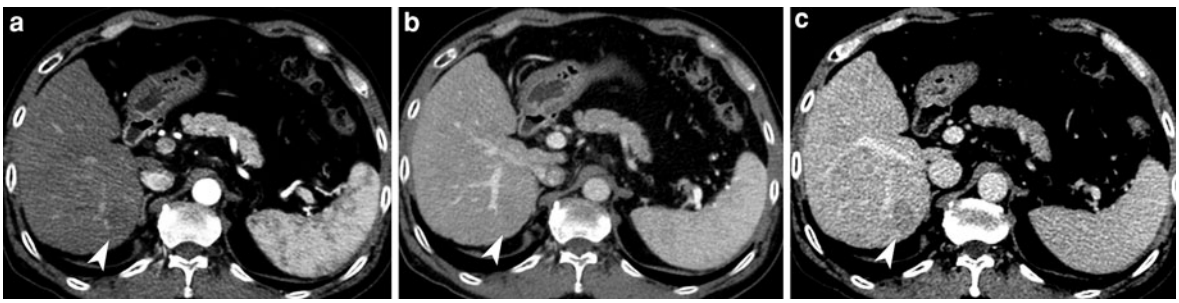

Fig. 12 Small HCC of indistinctly nodular type (early HCC). **a** Arterial phase CT scan demonstrates a nodule with subtle hypoenhancement in segment 6 (*arrowhead*). **b** Portal phase CT scan demonstrates a nodule with isoenhancement (*arrowhead*). **c** Delayed phase CT scan shows a hypoattenuated nodule compared with the surrounding liver parenchyma (*arrowhead*)

result in hypovascularity of those nodules on CT (Bolog et al. 2011; Matsui et al. 2011; Sano et al. 2011). On the contrary, small HCCs of distinctly nodular type are similar to larger examples of classic HCC not only at the macroscopic, but also at the microscopic level. Portal tracts are not present within small HCCs of distinctly nodular type, whereas nontriadal arteries are often plentiful, and sinusoidal capillarization is well-developed. Therefore, the blood supply of these lesions is basically derived from nontriadal arteries (Ito et al. 1999a, b; Kojiro and Nakashima 1999; Hytiroglou et al. 2007).

Distinction among RNs, DNs, and HCC with varying degrees of differentiation requires an assessment of the hemodynamic nature of the mass (arterioportal imbalance). In the diagnosis of HCC in patients with liver cirrhosis using MDCT, the detection of vascular changes within the hepatic nodules is crucial since there are no other reliable criteria to detect or characterize HCC (Zech et al. 2009). The presence of early arterial enhancement with rapid washout during the portal venous phase should be regarded as highly suspicious for the presence of HCC (Luca et al. 2010; Lee et al. 2011). Characteristically, HCC is hypoattenuating to liver on unenhanced CT, and manifests as a heterogeneous, moderately enhancing lesion during the arterial phase, with washout on portal venous and delayed phase (Fig. 15). Other useful characteristics of HCC are heterogeneity, mosaic appearance, multiplicity, encapsulation, and portovenous or hepatovenous invasion (Brancatelli et al. 2007). However, unfortunately, early HCCs are often lack of sufficient arterial neovascularization, and show isoattenuation to hepatic parenchyma on arterial-dominant phase (Takayasu et al. 1995; Bolog et al. 2011; Sano et al. 2011). This feature can cause the difficulty in differential diagnosis of hepatic nodule with the liver cirrhosis patients. As the MDCT images can only show the vascular changes of lesions, differentiation among the simple RNs, high-grade DNs, and well-differentiated early HCC in the cirrhotic liver can be difficult, and this is the main limitation of MDCT (Burrel et al. 2003;

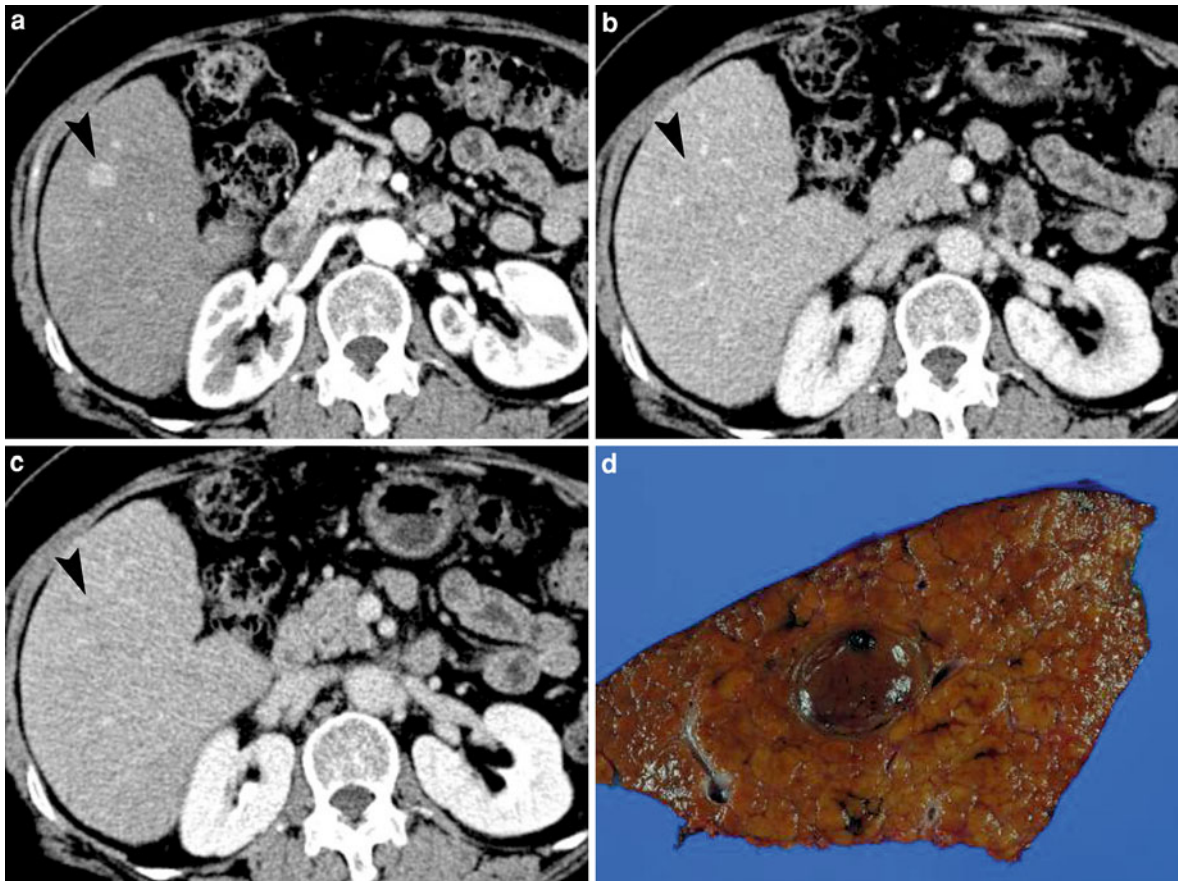

Fig. 13 Small HCC of distinctly nodular type (small progressed HCC) showing atypical enhancement pattern. **a** Arterial phase CT scan shows a small hyperenhancing nodule (*arrowhead*) with distinct margin in segment 5. **b** and **c** Portal phase (**b**) and delayed phase (**c**) CT scans show no washout (*arrowheads*). **d** Specimen photograph shows a well encapsulated HCC lesion

Bartolozzi et al. 2007). This so-called 'grey zone of hepatocarcinogenesis' remains still unclear for imaging [not only MDCT but also magnetic resonance imaging (MRI)] as well as even sometimes for pathology (Bartolozzi et al. 2007). However, radiologic criteria favoring malignancy are as follows: size larger than 2 cm, washout on delayed phase, delayed enhancing tumor capsule, and rapid interval growth (Choi et al. 1993; Krinsky and Lee 2000; Willatt et al. 2008; Lee et al. 2011).

3.4 Classification of Nodules on the Imaging Workup

For de novo 1- to 2-cm nodules in a cirrhotic liver, the specificity and positive predictive power of the typical radiological pattern of HCC, which is characterized by increased contrast enhancement (wash-in) during the late arterial phase and then by wash-out during the portal venous or delayed phase with a single dynamic technique (CT or MRI), have been found to be high in single-center studies, although the negative predictive values have been only 42–50% (Fournier et al. 2004; Luca et al. 2010; Sangiovanni et al. 2010). Therefore, any new nodule that is greater than 1 cm and shows this combination of imaging findings can be considered HCC when it is observed in a cirrhotic liver (Sherman 2010; Lee et al. 2011). The sensitivity of this single-technique policy to the malignancy of tiny lesions is 65%, whereas the sensitivity of the two-technique policy (suggested by the 2005 guidelines from the American Association for the Study of Liver Diseases) is only 35% (Fournier et al. 2004; Bruix and

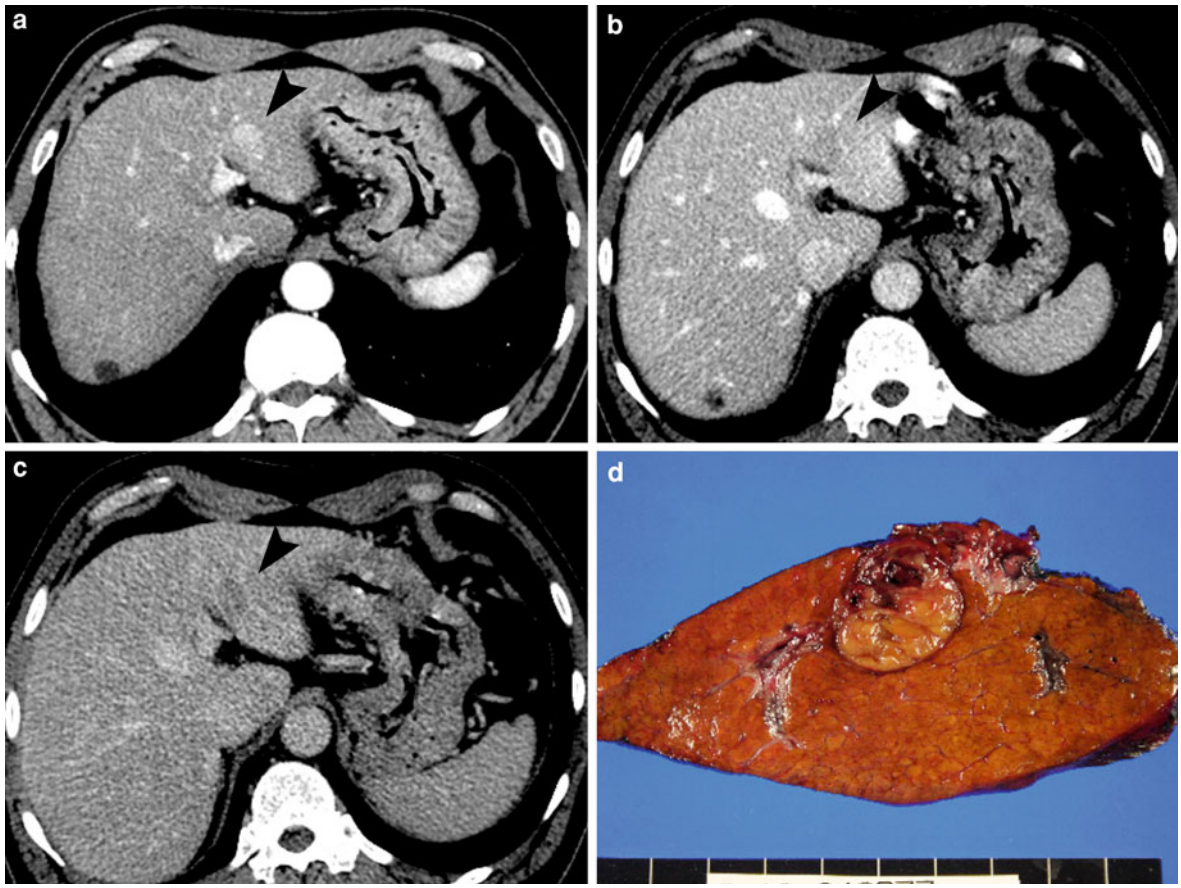

Fig. 14 Small HCC of distinctly nodular type (small progressed HCC) showing typical enhancement pattern. **a** Arterial phase CT scan demonstrates a hyperenhancing nodule in segment 3 (*arrowhead*). **b** and **c** Portal phase (**b**) and delayed phase (**c**) CT scan shows washout of the lesion. **d** Specimen photograph shows a well encapsulated HCC lesion with a small necrotic portion

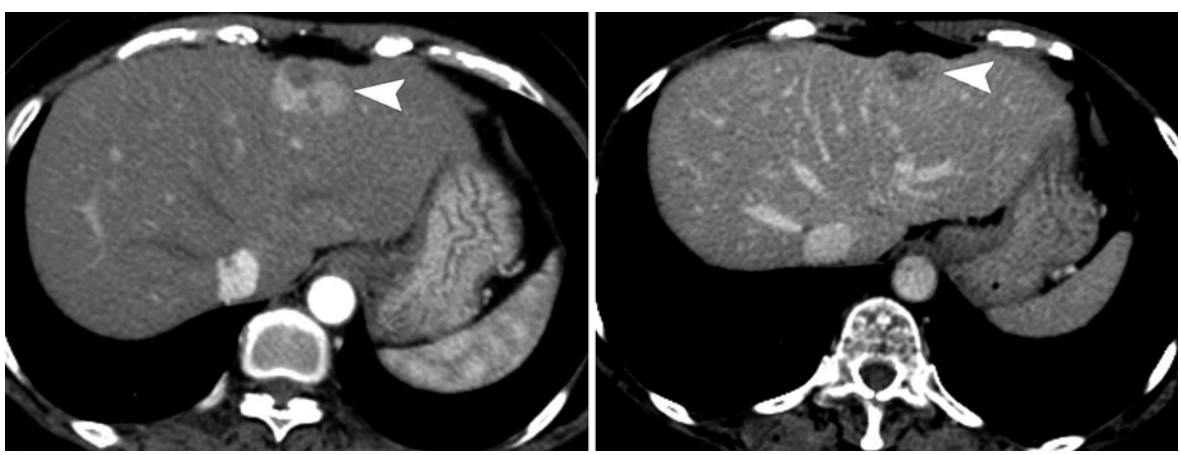

Fig. 15 Small HCC showing heterogeneous arterial hyperenhancement. **a** Arterial phase CT scan shows a heterogeneously enhancing nodule in segment 3. **b** Portal phase CT scan shows washout of the nodule

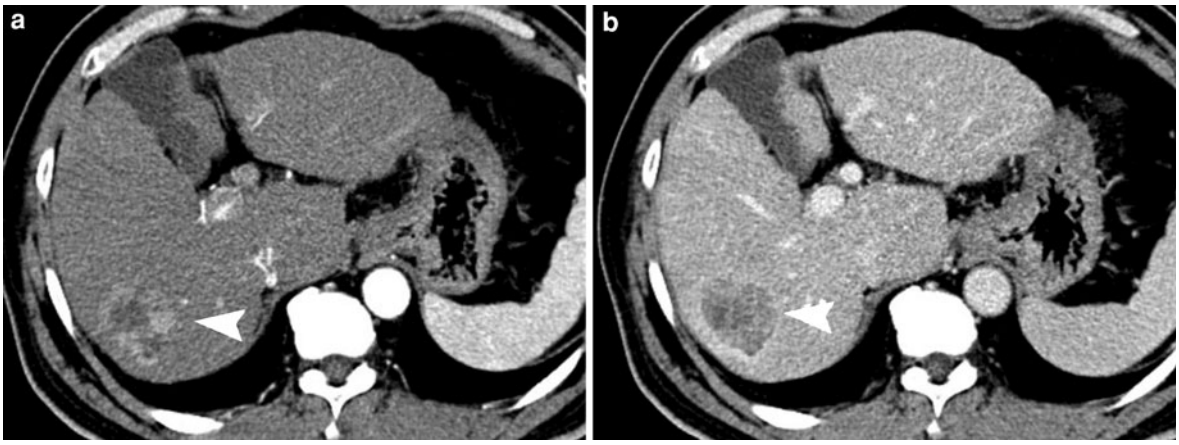

Fig. 16 Advanced HCC: typical appearance. **a** Arterial phase CT scan shows a heterogeneously enhancing nodule in segment 7 (*arrowhead*). **b** Delayed phase CT scan shows washout and a hyperattenuating capsule

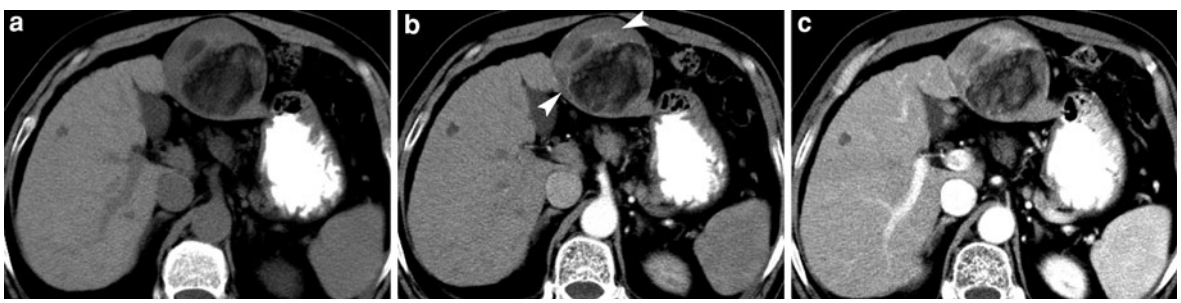

Fig. 17 Hypovascular HCC with fatty metamorphosis. **a** Precontrast CT scan demonstrates an exophytic, fat containing mass lesion in segment 3. **b** Arterial phase CT scan shows faint internal enhancement of the lesion (*arrowheads*). **c** Portal phase CT scan shows similar appearance to the arterial phase image

Sherman 2005); thus, the adoption of the single-technique policy could eliminate the use of fine needle biopsy (FNB) for a final diagnosis in one-third of patients (Sangiovanni et al. 2010). For hypervascular nodules without washout that are greater than 1 cm, the chance of being HCC is as high as 66% (Luca et al. 2010). Hence, this radiological pattern can be considered worrisome for the diagnosis of HCC. In these cases, an additional imaging technique for detecting washout is advisable so that the malignancy can be confirmed without FNB.

Additional imaging observations that are more commonly found in association with HCC include peripheral rim enhancement during the delayed phase (Fig. 16), intralesional fat (Fig. 17), an internal mosaic pattern (Fig. 18), the presence of a tumor capsul (Fig. 18), vascular invasion on any dynamic postcontrast imaging (Fig. 19) and interval growth (maximum diameter increase) of 50% or more on serial MRI or CT images obtained less than 6 months apart (Choi and Lee 2010; Pomfret et al. 2010). The presence of one or several of these features may increase the confidence of the radiological diagnosis of HCC. However, hypovascular or isovascular HCC cannot be diagnosed with the aforementioned radiological criteria. Therefore, image-guided FNB or follow-up imaging needs to be considered for nodules that do not meet the qualitative criteria for HCC but raise concerns about HCC (e.g., there is documented interval growth) (Lee et al. 2011).

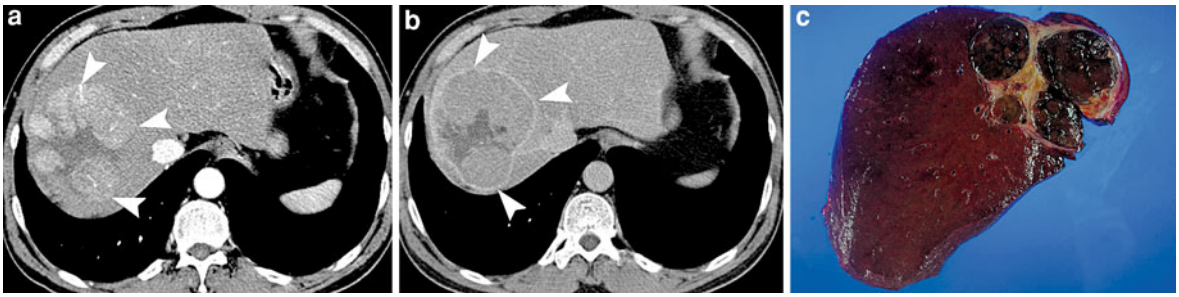

Fig. 18 Hypervascular HCC with a mosaic appearance and a peripheral capsule. **a** Arterial phase CT scan shows a 7-cm lesion that is heterogeneously hyperenhancing to the liver and shows a mosaic appearance (*arrowheads*). **b** Delayed phase CT scan shows washout of the lesion with capsular enhancement, typical of HCC (*arrowheads*). **c** Specimen photograph shows a well encapsulated HCC lesion with necrosis and confluent areas of tumor nodularity separated by fibrous septations and necrotic area

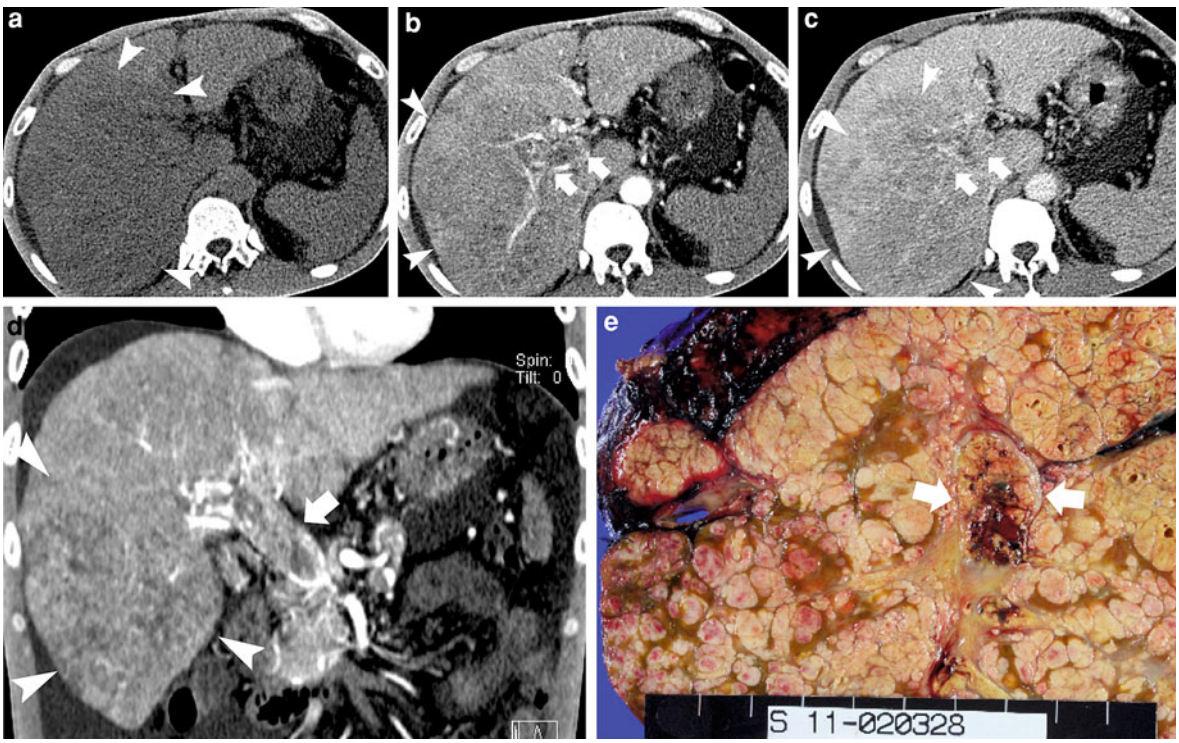

Fig. 19 Diffuse HCC with portal vein thrombosis. **a** Precontrast CT scan shows that the right lobe is hypoattenuated (*arrowheads*) compared with the left lobe. **b** Arterial phase CT scan shows enhancing thrombus (*arrows*) within the portal vein that appears expanded. The presence of tumor thrombus suggests an underlying mass. Patchy enhancement is noted in the right lobe mass lesion (*arrowheads*). *c* Portal phase CT scan shows washout of the diffuse HCC (*arrowheads*), as well as tumor thrombus (*arrows*) within the portal vein. **d** Coronal CT scan that was obtained during arterial phase shows heterogeneous enhancement of the mass (*arrowheads*), and increased vascularity within the tumor thrombus (*arrow*). **e** Specimen photograph shows a diffuse HCC with portal vein invasion (*arrows*)

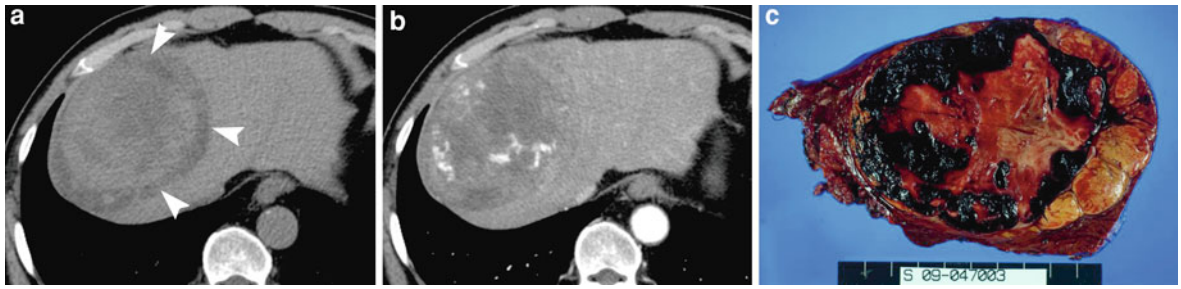

Fig. 20 HCC with intratumoral hemorrhage. **a** Precontrast CT scan demonstrates a large tumor with internal hemorrhage, which resulted in hyperattenuation in the *central portion* of the main tumor with hypoattenuation (*arrowheads*). **b** Arterial phase CT scan shows patchy enhancement of the tumor with dilated tumor vessels. **c** Specimen photograph shows a well encapsulated HCC lesion with intratumoral hemorrhage

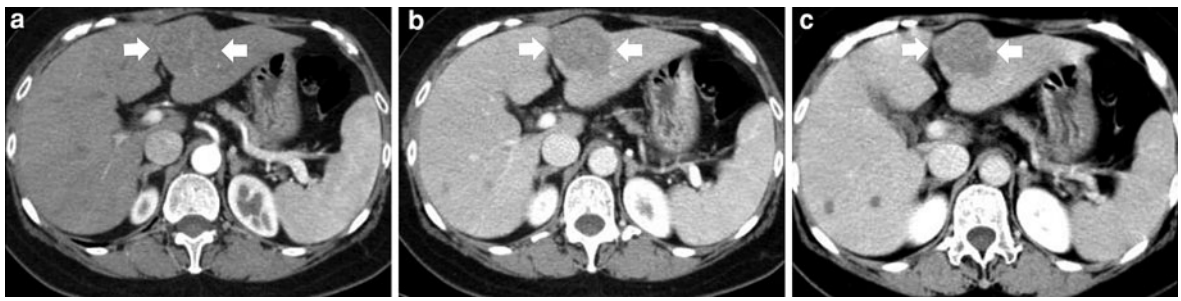

Fig. 21 A poorly differentiated HCC with atypical enhancement. **a** Arterial phase CT scan shows a tumor (*arrows*) with isoenhancement to adjacent liver parenchyma. **b** and **c** Portal phase (**b**) and delayed phase (**c**) CT scans show hypoenhancement of the lesion (*arrows*). Two small nodules in the right lobe were diagnosed as dysplastic nodules

4 MDCT Findings of HCC

4.1 Characteristic CT Features of HCC

Imaging finding of HCC seen on MDCT can be classified as two main categories, i.e. nodular (Figs. 14 and 19) diffuse infiltrative. Although nodular HCCs frequently show well-demarcated, hypoattenuated masses in liver parenchyma on noncontrast image, sometimes tumor-liver contrast is insufficient for the detection of HCC on noncontrast image, and the contour change of hepatic surface is the only clue for the presence of HCC. In the setting of cirrhosis, heterogeneity and nodularity of background liver may make it difficult to detect HCC on precontrast CT images. Intratumoral calcification, hemorrhage or necrosis can also be present, and these may change the attenuation of hepatic nodule on noncontrast image (Fig. 20). However, for imaging of HCC and lesions in the cirrhotic liver, the main diagnostic criterion in CT is the detection of changes in the vascular supply of hepatic nodules due to arterial neovascularization descried on multistep hepatocarcinogenesis.

4.1.1 Arterial Enhancement and Washout

As DNs progress to develop malignant foci, the tumor recruits unpaired arteries and sinusoidal capillaries, with resultant avid arterial enhancement that is best detected on arterial phase (Lee et al. 2000; Hammerstingl and Vogl 2005). Approximately 80–90% of HCCs are hypervascular during the arterial phase (Kim et al. 2011a, b, c, d), whereas approximately 10–20% of HCCs may be hypovascular to the surrounding parenchyma on the arterial phase images and they are generally seen in smaller tumors <2 cm (Honda et al. 1993; Yoon et al. 2009; Matsui et al. 2011). Hypovascularity (or hypovascular enhancement) in small tumors may be related to lack of arterialization of the tumor. However, large HCC can be also hypovascular on the arterial phase and

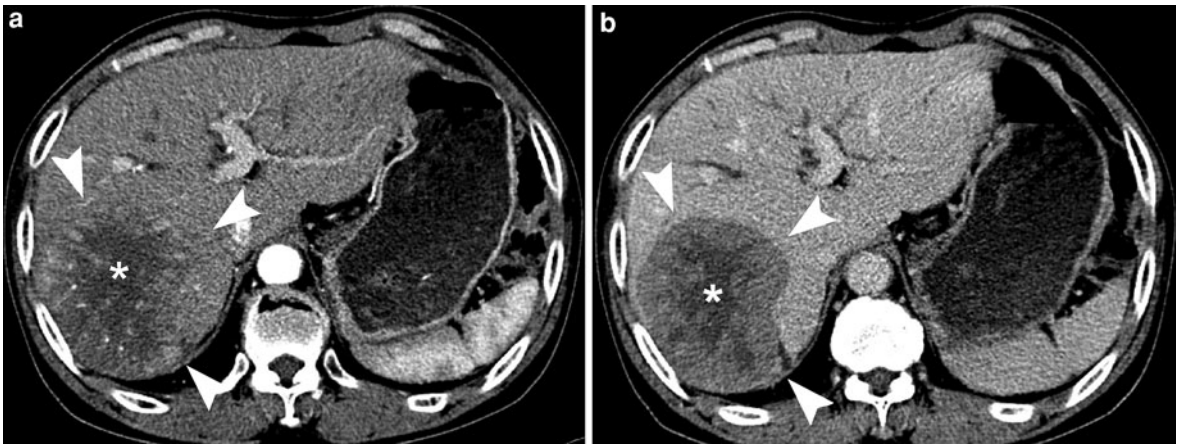

Fig. 22 Poorly differentiated HCC with central necrosis. **a** Arterial phase CT scan shows a heterogeneously enhancing tumor (*arrowheads*) with central necrosis (*asterisk*). **b** Delayed phase CT scan shows non-enhancing, central necrotic area (*asterisk*) as well as washout of peripheral viable portion of the tumor (*arrowheads*)

may appear more heterogeneous in enhancement (Figs. 21 and 22).

HCC typically shows as a hyperattenuated nodular lesion on the arterial-dominant phase with following washout to iso- or mostly low attenuated nodule on portal venous or delayed phase (Figs. 15, 16, and 18) (Choi et al. 1997; Furlan et al. 2011). The presence of pathologic washout can be better shown on delayed phase images than on portal phase images with improved diagnostic accuracy for detecting HCCs (Hwang et al. 1997; Loyer et al. 1999; Iannaccone et al. 2005; Furlan et al. 2011; Serste et al. 2011). Unfortunately, however, in cirrhotic liver, although for de novo 1–2 cm nodules ensuing in a cirrhotic context the specificity and positive predictive power of the "typical" radiological pattern of HCC at *one* dynamic techniques (US, CT, or MRI) were found to be high in single-center studies, the negative predictive value was only 42–50% as there are many HCCs showing atypical enhancement pattern (Figs. 13 and 17) (Forner et al. 2008; Luca et al. 2010; Sangiovanni et al. 2010). Therefore, delayed hypoattenuation (washout) increases diagnostic accuracy for diagnosis of HCC, the lack of washout does not exclude HCC. In a series by Luca et al. (Hayashi et al. 1999), 43% of HCCs were hypoattenuated on the portal or delayed phase images, whereas 45% were iso- or hyperattenuated on the delayed phase images. Indeed, according to a recent study, hypervascular nodules >1 cm without wash-out in cirrhotic liver on CT have a risk of being HCC up to 66% (Fig. 13) (Luca et al. 2010). Hence, this radiological pattern can be considered being worrisome for HCC diagnosis. Arterial enhancing false-positive lesions such as arterioportal shunt are also frequently seen in advanced cirrhotic liver, as the compensatory arterial hyperperfusion can be developed. Therefore, differentiating this atypically hyperenahncing small HCC from early enhancing pseudolesions such as arterioportal shunt is a clinical dilemma (Sun et al. 2010). In such cases of hypervascular nodule >1 cm, an additional imaging technique such as dynamic MRI aimed at detecting the washout is advisable, in order to confirm malignancy without fine needle biopsy (FNB) (Khalili et al. 2011; Lee et al. 2011).

The detection rates of HCC using MDCT reported in the literature are highly variable. One trial with a very strict methodology and whole liver explants correlation showed sensitivity of 49.4% and positive predictive value of 57.9% for detection of HCC using triphasic CT (Lee et al. 2009). A subgroup analysis in this study showed a strong influence of the lesion size to the diagnostic performance of MDCT. While lesions >2 cm showed the detection rate of 74.1%, lesions <2 cm were only detected in 37.3% (Lee et al. 2009). Another trial with a four-row MDCT showed an overall sensitivity of 73% for detecting HCC, with also markedly decreased detection rates (approximately 33%) for lesions lesser than 1 cm in diameter (Kawata et al. 2002). Maetani et al. (2008) reported a sensitivity, positive predictive value, and accuracy for HCC detection using MDCT with 87, 96, and 84%,

respectively. Considering these reports, lesion sizes combined with degree of vascular change within nodule are strongly influenced to the diagnostic performance of MDCT for detecting HCC.

4.1.2 Capsule or Pseudocapsule

A tumor capsule or pseudocapsule is most often seen in large HCCs and may be present in 24–90% of cases in the Asian population and 12–42% of cases in the non-Asian population (Freeny et al. 1992; Stevens et al. 1994). Larger tumors tend to demonstrate thicker capsules which may be hypoattenuated on precontrast CT images (Khatri et al. 2010). Histologically, the capsule consists of an inner fibrous layer and an outer layer composed of compressed vessels and bile duct (Ishigami et al. 2009). The capsule frequently demonstrates persistent or delayed enhancement (Fig. 18) (Freeny et al. 1992). These features are highly specific for HCC and the presence of a capsule or pseudocapsule strongly suggests a diagnosis of HCC (Grazioli et al. 1999; Choi and Lee 2010; Khatri et al. 2010; Matsui et al. 2011). Lower grade tumors are more likely to be encapsulated (Stevens et al. 1994). Extracapsular extension or daughter nodule formation has been shown to be a negative prognostic factor seen pathologically in 43–77% of HCCs (Imaeda et al. 1994).

4.1.3 Mosaic Appearance

HCC can exhibit a mosaic appearance as manifested by variable unenhanced and contrast-enhanced attenuation within a single lesion. Pathologically, the mosaic appearance reflects multiple confluent areas of tumor nodularity interspersed with fibrous septations, necrosis, hemorrhage, copper deposition, and fatty infiltration as well as varying degrees of histologic differentiations (Stevens et al. 1996). The mosaic appearance has been seen in 28–63% of cases and is more common in larger tumors and nodular type tumors (Stevens et al. 1994; Loyer et al. 1999; van den Bos et al. 2007). The mosaic appearance is well seen on contrast-enhanced CT, as some higher grade poorly differentiated HCCs may have decreased arterial blood supply whereas other large atypical well-differentiated HCCs may be characterized by areas of portal perfusion (Kudo 2004; van den Bos et al. 2007; Asayama et al. 2008).

4.1.4 Vascular Invasion

Vascular invasion of the portal vein or hepatic vein by HCC is frequently seen in the setting of HCC and has been reported to occur in as many as 6.5–48% of cases (Freeny et al. 1992; Stevens et al. 1994; Loyer et al. 1999). Vascular invasion has been found to be more common in patients with larger tumors or poorly differentiated HCC or diffuse type HCC (Fig. 18) (Kanematsu et al. 2003; Khatri et al. 2010). Vascular extension involves the portal venous system more frequently than the hepatic veins, and is thought to be related to the portal venous drainage of HCC (Stevens et al. 1994; Hayashi et al. 2002; Kanematsu et al. 2005; Matsui et al. 2011). Extension of HCC into the hepatic veins is often associated with invasion of the portal vein and when tumor thrombus develops in the hepatic vein, it frequently predisposes to tumor thrombus extension into the inferior vena cava and right atrium. However, patients with cirrhosis can also develop benign portal vein thrombosis secondary to portal hypertension and venous stasis (Hall et al. 2011). The distinction between tumor and bland thrombosis is important due to the associated management implications (Tublin et al. 1997; Lee et al. 2008; Poddar et al. 2010). Patients with tumor thrombosis are typically not candidates for surgical resection or transplantation (Piscaglia et al. 2010). Malignant tumor thrombus is typically seen in contiguity with or in close proximity to the primary tumor and characteristically exhibits luminal expansion of the involved vessels, arterial enhancement (neovascularity) with washout, and frequently shows similar imaging features with the primary tumor (Fig. 18) (Tarantino et al. 2006; Piscaglia et al. 2010). On the contrary, benign PVTs show a lack of vascularization of the thrombus on CT and absence of mass-forming features of PVT (near normal caliber) (Fig. 23) (Tarantino et al. 2006; Piscaglia et al. 2010). In some cases of diffuse or infiltrating HCC, the presence of tumor thrombus may be the only clue to suggest that there is an underlying malignancy and is commonly associated marked elevation in serum alpha-fetoprotein levels (Kanematsu et al. 2003; Poddar et al. 2010). While macrovascular invasion can be easily detected at imaging, microvascular invasion is almost impossible to visualize, but fortunately, it does not constitute a contraindication to curative treatment although it is often associated with tumor recurrence

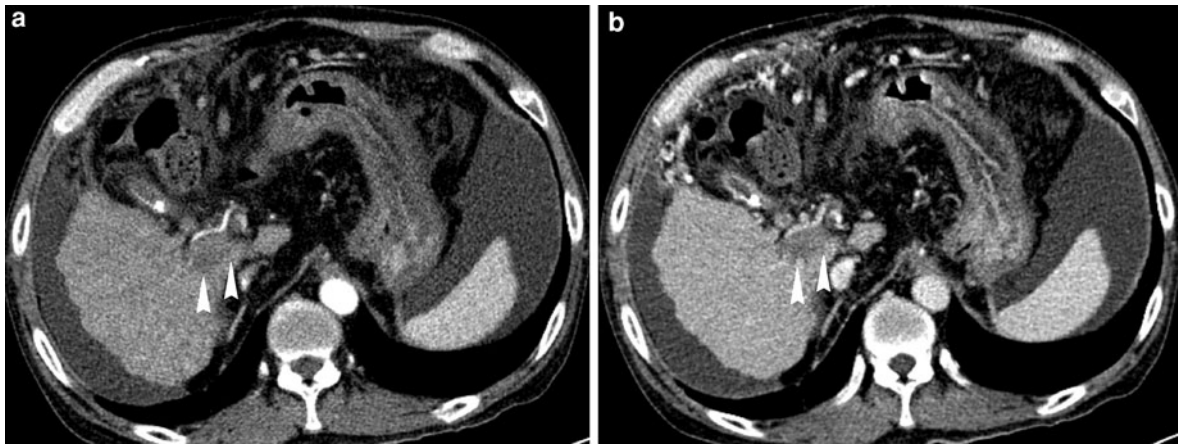

Fig. 23 Liver cirrhosis with benign portal vein thrombosis. **a** Arterial phase CT scan shows a hypoattenuated thrombus in the right lobar branch of the portal vein (*arrowheads*). **b** Portal phase CT scan shows the thrombus (*arrowheads*) in the portal vein with normal caliber, with better conspicuity compared with the arterial phase image

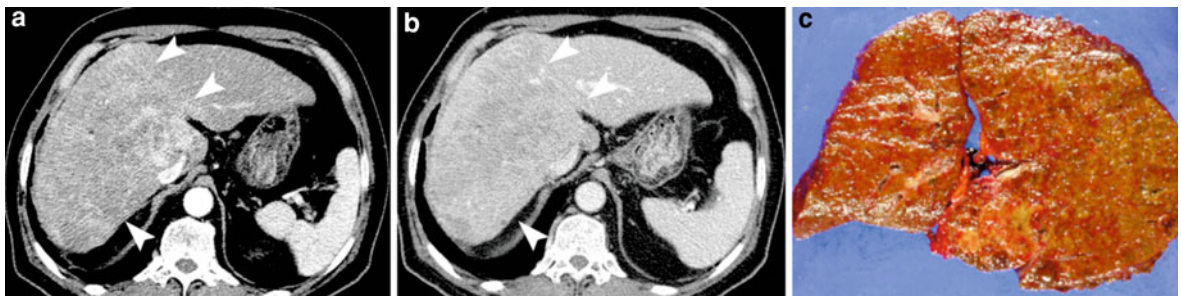

Fig. 24 Diffuse HCC. **a** Arterial phase CT scan shows a very heterogeneously enhancing right hepatic lobe (*arrowheads*). **b** Portal phase CT scan shows an inhomogeneous hypoattenuation of the lesion (*arrowheads*). **c** Specimen photograph shows a diffuse infiltrative type HCC having similar appearance of macronodular cirrhosis

following resection or transplantation (Kim et al. 2008a; Sumie et al. 2008; Chou et al. 2011).

4.2 Uncommon Features of HCC

4.2.1 Diffuse Infiltrative HCC

Diffuse type HCC constitutes up to 13% of cases of HCC and appears as an extensive, heterogeneous, permeative hepatic tumor with portal venous thrombosis, often associated with an elevated serum alpha-fetoprotein level (Kanematsu et al. 2003). These tumors have a patchy or nodular early enhancement pattern and can be difficult to detect on arterial phase, but they become hypoattenuated in the late equilibrium phase images (Fig. 24) (Kanematsu et al. 2003). For the diffuse infiltrative HCCs, margin of the lesions is indistinct in many cases, and it often combines with vascular invasion (i.e. portal vein or hepatic vein). Tumor thrombi within the portal vein or hepatic vein are also present on MDCT images, and these tumor thrombi also show the arterial neovascularization (Fig. 19). Hepatic parenchymal changes secondary to the vascular invasion such as arterioportal shunt in portal vein tumor invasion or hepatic congestion in hepatic vein invasion can also be seen (Freeny et al. 1992; Baron and Peterson 2001).

4.2.2 Nodule Within Nodule Appearance

When foci of HCC develop within a preexisting dysplastic nodule, the typical appearance of an arterially

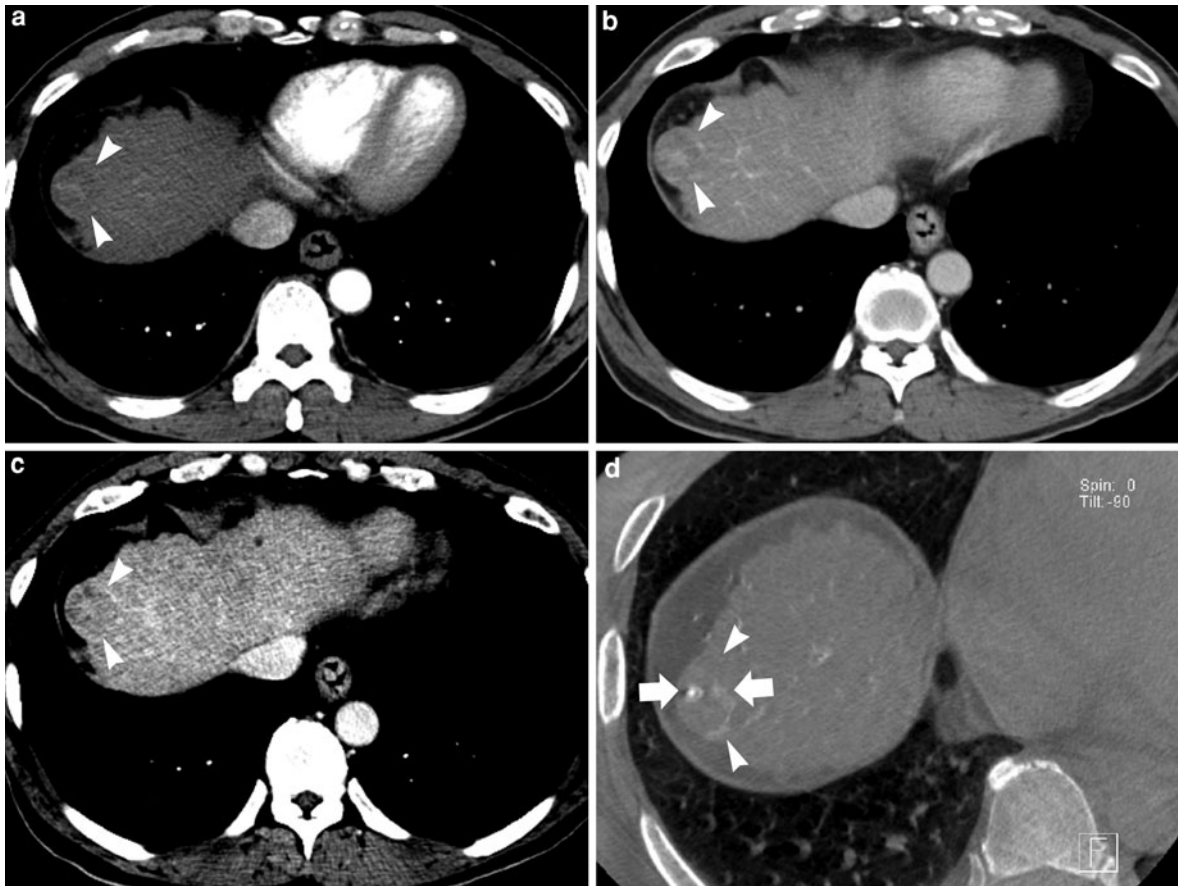

Fig. 25 Small HCC in dysplastic nodule showing "nodule in nodule" appearance. **a** Arterial phase CT scan shows a small enhancing focus with a hypoattenuated nodule in segment 8 (*arrowheads*). **b** and **c** Portal phase (**b**) and delayed phase (**c**) CT scans show a central enhancing focus within a hypoattenuated nodule. **d** Dyna-CT scan shows two enhancing foci (*arrows*) within the hypovascular nodule (*arrowheads*) in segment 8. Note that Dyna-CT scan with contrast injection through the hepatic artery can provide much high spatial resolution and better contrast enhancement of the small HCC foci within the dysplastic nodule compared with MDCT scan

hyperenhancing nodule within a hypoattenuated nodule is termed a "nodule within nodule" appearance (Fig. 8) (Kojiro 1998; Goshima et al. 2004; Zheng et al. 2004; Kim et al. 2007b; Ishida et al. 2008; Kudo and Tochio 2008; Sano et al. 2011). The appearance on CT may be of an overt hypervascular HCC within a hypovascular dysplastic nodule (Fig. 25) (Onaya et al. 2000; Takayasu et al. 2007). HCC that occurs within a preneoplastic focus and exhibits such imaging features has been shown to have potential for rapid growth (Sadek et al. 1995). A different nodule-in-nodule appearance can also be seen on contrast-enhanced CT when necrotic HCCs contain foci of viable enhancing tumor.

4.2.3 Fatty Metamorphosis

HCCs may sometimes contain fat (Stevens et al. 1994). HCCs with fatty metamorphosis show low attenuation with negative Hounsfield units on CT images and the presence of fat within a lesion favors a primary HCC (Fig. 17) (Yoshikawa et al. 1988; Tsunetomi et al. 1989; Martin et al. 1995; Prasad et al. 2005). Although fatty components have been described in regernative nodules and focal nodular hyperplasia, such an observation is quite rare and possibly related with underlying liver steatosis (Valls et al. 2006). Other hepatic lesions that contain fat include adenomas, rare tumors such as angiomyolipomas, lipomas, and certain metastases such as those from

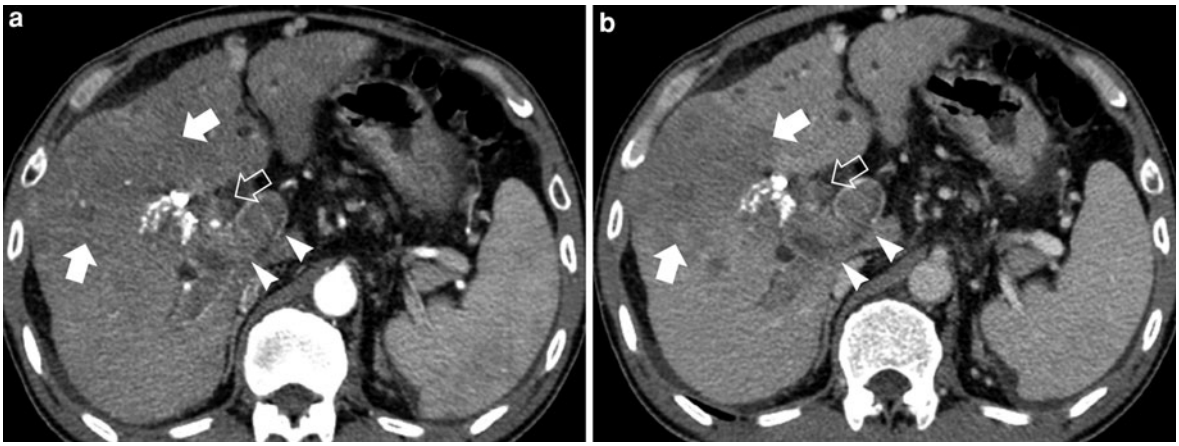

Fig. 26 HCC with bile duct invasion and tumor thrombus in the portal vein. **a** Arterial phase CT scan shows a faintly enhancing HCC lesion (*arrows*) in right anterior segment with lipiodol and enhancing tumor thrombus in the bile duct (*open arrow*) and in the portal vein (*arrowheads*). **b** Portal phase CT scan shows washout of the main tumor (*arrows*) as well as the tumor thrombi in the bile duct (*open arrow*) and the portal vein (*arrowheads*)

liposarcomas, teratomas, ovarian dermoids, Wilms tumors, and certain renal cell carcinomas (Basaran et al. 2005; Prasad et al. 2005). In the cirrhotic liver, a fat containing lesion should raise suspicion for HCC over these other diseases, which are not typically seen in cirrhotic liver (Khatri et al. 2010).

4.2.4 HCC with Bile Duct Invasion

HCC may grow in major bile ducts, causing obstructive jaundice, and is frequently associated with concomitant intraportal tumor growth (Kim et al. 2011d). Tumor growth into the bile duct is found in 6% of cases of HCC at autopsy. The imaging features that help differentiating HCC with bile duct invasion from cholangiocarcinoma of the bile duct include the presence of parenchymal mass, liver cirrhosis, and the hyperattenuating intraductal tumor on the hepatic arterial phase (Fig. 26) (Minagawa et al. 2007; Ikenaga et al. 2009; Liu et al. 2010; Kim et al. 2011d). HCC with bile duct invasion has an infiltrative nature and a high risk of intrahepatic recurrence, resulting in poor prognosis (Ikenaga et al. 2009).

4.2.5 HCC Variants

Classic HCCs with atypical histologic features demonstrate atypical imaging features. These include cancers with marked fatty metamorphosis, massive necrosis, abundant fibrous stroma (scirrhous type), sarcomatous change, and copper accumulation. Pathologically, there are several variant types of HCC: clear cell type HCC, fibrolamellar HCC, sarcomatoid HCC, combined HCC-cholangiocarcinoma, and sclerosing HCC (Ichikawa et al. 1999; McLarney et al. 1999; Okuda 2002; Lao et al. 2007; Kim et al. 2009b). Clinically, sarcomatoid HCC and combined HCC-cholangiocarcinoma show poorer prognosis than classic HCC, whereas fibrolamellar HCC shows better prognosis and sclerosing HCC shows prognosis similar to classic HCC (Ariizumi et al. 2011a, b).

Radiologically, these variants do not share imaging characteristics typical of HCC (Chung et al. 2009). Clear cell HCCs frequently showed decreased attenuation on unenhanced CT and hypovascularity on contrast-enhanced CT, which are non specific. (Monzawa et al. 1999). Sclerosing or scirrhous HCC is a rare hepatic tumor characterized by intense fibrosis which shows very similar CT appearance to cholangiocarcinoma (Fig. 27) (Kim et al. 2009b). Fibrolamellar HCC is a distinctive HCC variant that is not associated with hepatitis or cirrhosis. This tumor occurs in young adults (second or third decade of life) without sex predominance (Ichikawa et al. 1999; McLarney et al. 1999; Okuda 2002). Pathologically, fibrolamellar HCC usually presents as a single, large, well-demarcated, but non-encapsulated tumor with a fibrous band infiltrating throughout. The fibrotic tissue coalesces to form a central scar, which is reported in 20–60% of cases (Ichikawa et al. 1999; McLarney et al. 1999). On unenhanced CT, the tumor is low-attenuating compared with the surrounding liver,

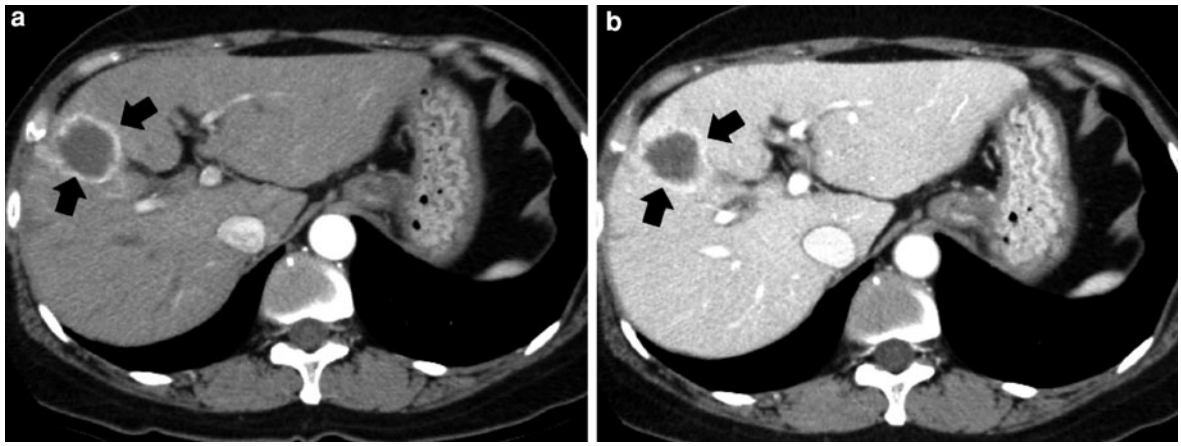

Fig. 27 Schirrhous type HCC showing atypical enhancement pattern. **a** Arterial phase CT scan demonstrates a hypovascular nodule with peripheral rim-like enhancement (*arrows*), which is similar to the typical enhancement pattern of cholangiocarcinoma. **b** Portal phase CT scans demonstrate a tumor with peripheral enhancement (*arrows*), similar to the arterial phase image

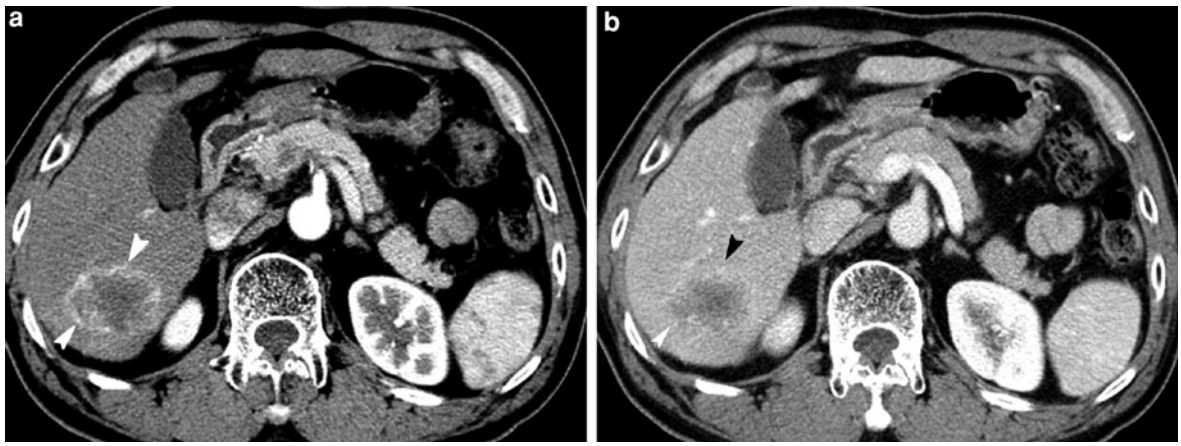

Fig. 28 Combined HCC-cholangiocarcinoma. **a** Arterial phase CT scan shows a heterogeneously enhancing tumor (*arrowheads*) with lobulated margin in segment 6. **b** Portal phase CT scan shows washout of the arterially enhancing portion along the lateral side (*white arrowhead*) as well as centripetal enhancement along the medial side (*black arrowhead*)

whereas on dynamic contrast-enhanced CT it has predominant heterogeneous enhancement. Intratumoral calcification (68%), a central scar (71%), and pseudocapsule (35%) are visible on CT (Ichikawa et al. 1999; McLarney et al. 1999). Sarcomatous HCC is an aggressive variant of HCC with an incidence of 3.9–9.4%, with either a sarcomatous change in part of the HCC or coexistence of a sarcoma and HCC (Honda et al. 1996; Da Ines et al. 2009).

Combined HCC-cholangiocarcinoma is composed of elements from both entities (Fukukura et al. 1997). The characteristics of these tumors, as visualized by contrast-enhanced dynamic imaging, depend on the proportions of tumor components (Shin et al. 2007). On contrast-enhanced CT, the HCC-dominant tumor is well enhanced in the early phase and washed out in the late phase, and the cholangiocarcinoma-dominant tumor shows peripheral and delayed enhancement (Fig. 28) (Murakami et al. 1997). Sometimes, these mixed tumors appear heterogeneously enhanced because the HCC component appears hyperenhanced, whereas the cholangiocarcinoma component appears

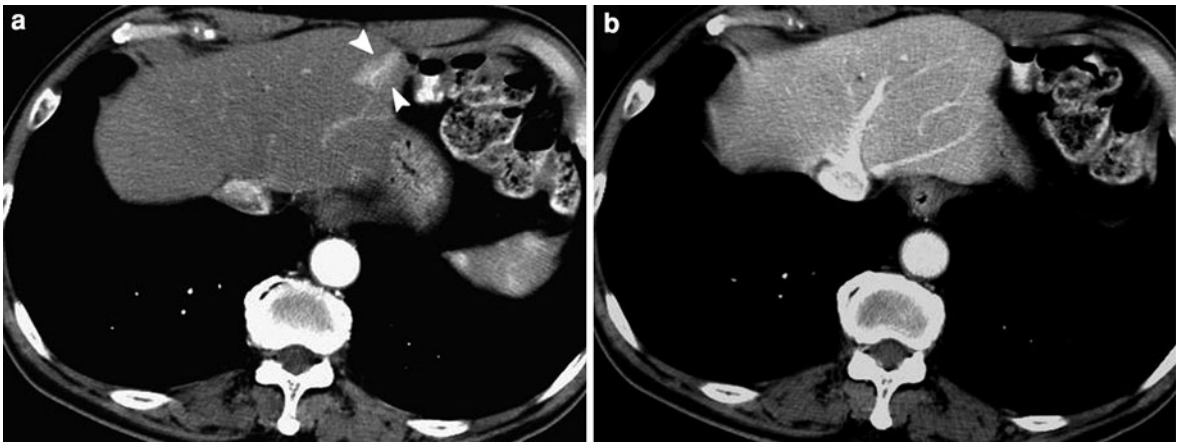

Fig. 29 Transient hepatic attenuation difference. **a** Arterial phase CT scan shows a triangular-shaped hyperenhancing lesion (*arrowheads*) with central enhancing vascular structure and straight margins in segment 3. **b** Portal phase CT scan shows that the lesion becomes isoattenuated

hypoenhanced relative to the surrounding liver (Fukukura et al. 1997; Murakami et al. 1997; Shin et al. 2007; Ariizumi et al. 2011a, b). On dynamic contrast-enhanced CT, sclerosing HCC shows hypervascularity and remarkable progressive and prolonged enhancement (Yamashita et al. 1993). The adjacent liver capsule may retract, especially in highly fibrotic tumors (Kim et al. 2009).

5 Hepatocellular Carcinoma Mimics

While considered the most consistent feature of HCC, arterial enhancement is also a feature of other nonmalignant lesions that can be found in the cirrhotic liver, especially those measuring smaller than 2 cm, which explains the high incidence of false-positive results for HCC (Brancatelli et al. 2003; Wiesner et al. 2004). Enhancing lesions seen only on the hepatic arterial phase on MR imaging are a daily challenge. Common hypervascular liver lesions include hemangioma, focal nodular hyperplasia, hepatocellular adenoma, HCC, fibrolamellar carcinoma, and metastases from primary tumors such as neuroendocrine tumor (Fig. 29), renal cell carcinoma, melanoma, and thyroid carcinoma (Namasivayam et al. 2007). Helical CT screening for HCC in patients with cirrhosis has a substantial false-positive detection rate (Brancatelli et al. 2003). Among several causes of false-positive diagnosis, transient hepatic attenuation differences (THADs) is the most common in cirrhotic liver (Desser 2009). THADs are typically wedge-shaped hypervascular regions visible on the hepatic arterial phase, and fade to isodense on venous and delayed phases. They are commonly seen in the setting of locally diminished portal venous inflow. Familiarity with the characteristic appearance of arterially enhancing liver lesions should permit discrimination of these lesions from true HCCs (Desser 2009).

5.1 Transient Hepatic Attenuation Difference

THADs are the imaging manifestation of regional variations in the balance between hepatic arterial, portal venous, and third inflow sources of hepatic blood flow. THADs due to nontumorous arterioportal shunt or focal obstruction of a distal parenchymal portal vein are a common finding seen in the cirrhotic liver on arterial phase CT images (Baron 1994; Yu et al. 1997, 2000a). They are typically seen as well-defined areas of enhancement only on the arterial phase and not on other phases. Most cases of THADs not usually seen on the noncontrast images, they can occasionally have a corresponding area of hypoattenuation when a focal fat deposit occurs, and associated with mild prolonged parenchymal enhancement (Fig. 31) (Yu et al. 1997). Shunts are usually triangular or fan-shaped, peripherally located, and have straight margins. They may follow the

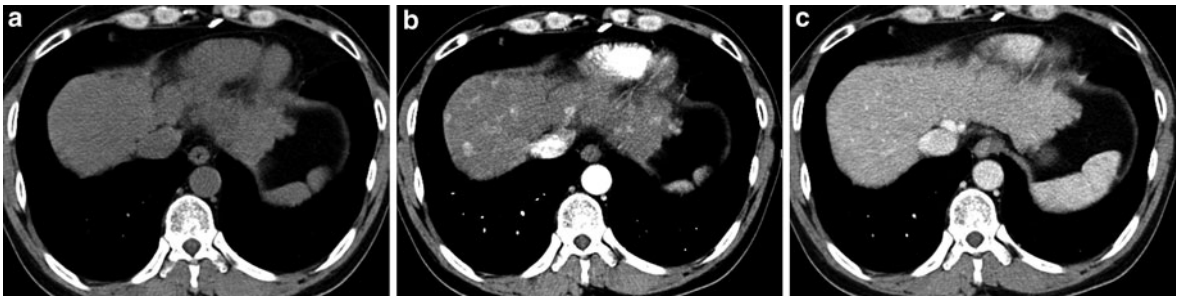

Fig. 30 Nodular-shaped transient hepatic attenuation difference. **a** Precontrast CT scan does not demonstrate any nodular lesions in the liver. **b** Arterial phase CT scan demonstrates multiple, hyperenhancing nodular lesions in both hepatic lobes. **c** On portal phase CT scan, the lesions become isoattenuated. Isoattenuation of the lesions on precontrast as well as absence of washout of those lesions suggest high probability of arterially enhancing pseudolesion rather than small HCC with atypical enhancement

segmental anatomy of the liver. However, occasionally, they can be nodular or irregularly outline and mimic a hypervascular lesion (Fig. 30) (Yu et al. 2000a, b). Shunts characteristically do not demonstrate delayed postcontrast washout, and may have normal vessels coursing through them (Figs. 30 and 31) (Choi et al. 2002; Colagrande et al. 2007a, b). The waxing and waning of the size of a hypervascular lesion in cirrhosis at 2- to 3-month follow-up imaging also favors a pseudolesion (Ahn et al. 2010).

Moreover, THADs may be caused by underlying focal lesions such as hemangioma or HCC because of a siphoning or sump effect of the lesion, from portal hypoperfusion either attributable to compression or thrombosis from the lesion, or because of arterioportal shunting related to the lesion causing diversion of flow (Colagrande et al. 2007a, b). In addition, THADs can also be induced by portal hypoperfusion attributable to nontumoral causes, anomalous blood supply, or arterioportal shunting not related to focal lesions, and inflammation of biliary vessels or adjacent organs (Choi et al. 2002). Because HCC is frequently associated with a THAD, even when an arterially enhancing focus is deemed to be a THAD, in the setting of cirrhosis, the radiologist should look closely for an associated HCC (Choi et al. 2002; Kim et al. 2005; Khatri et al. 2010). Besides shunts and perfusion abnormalities, hemangiomas and high-grade DNs are differential considerations for small arterial phase enhancing lesions (Kim et al. 2005)

However, although small HCCs smaller than or equal to 1.5 cm in size are frequently isoattenuated on precontrast CT images, and may only be seen as diffuse homogeneously enhancing lesions on the arterial enhanced phase, it is important not to consider such arterially enhancing lesions as specific for HCC (Khatri et al. 2010; Sun et al. 2010). Several previous studies of CT or MRI demonstrated that the majority of hepatic arterial phase enhancing lesions that are occult at portal and/or equilibrium phase CT imaging are non-neoplastic, even in patients with pathologically proved HCC (Tsuchiyama et al. 2002; Holland et al. 2005). Several investigators have recommended similar approaches to hepatic lesions seen on the arterial phase which is to check the other phases to confirm that they are only seen on the hepatic arterial phase and do not have other features of HCC such as washout, capsular enhancement, and low attenuation on precontrast suggesting microscopic fat (Willatt et al. 2008; Sano et al. 2011). When the abnormality is peripheral, wedge-shaped, and seen only on the hepatic arterial phase, it is more likely to represent a perfusional phenomenon (Choi et al. 2002). However, if the abnormality is round, oval, or masslike in shape, but small (<2 cm), and seen only on the arterial phase without other features of HCC, close interval follow-up CT examination (3–6 months) may be considered to assess for growth or features more suggestive of HCC on follow-up examination.

5.2 Hemangiomas

Hypervascular HCC must be differentiated from various other hypervascular hepatic lesions. Among them, cavernous hemangioma is the most common. Although common in the general population, hemangiomas occur less frequently in the setting of cirrhosis, probably because the process of cirrhosis

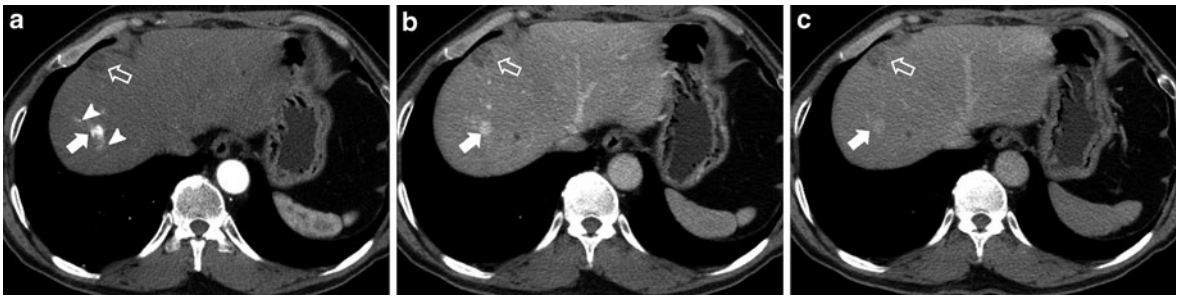

Fig. 31 Flash-filling hemangioma with shunt and dysplastic nodule. **a** Arterial phase CT scan shows a hyperenhancing nodule (*arrow*) with peritumoral shunt (*arrowheads*). Another hypoattenuated nodule (*open arrow*) was detected in segment 8 which was diagnosed as dysplastic nodule. **b**, and **c** Portal phase (**b**) and delayed phase (**c**) CT scans show persistent enhancement of the hemangioma (*arrowhead*), and a hypoattenuated dysplastic nodule (*open arrow*)

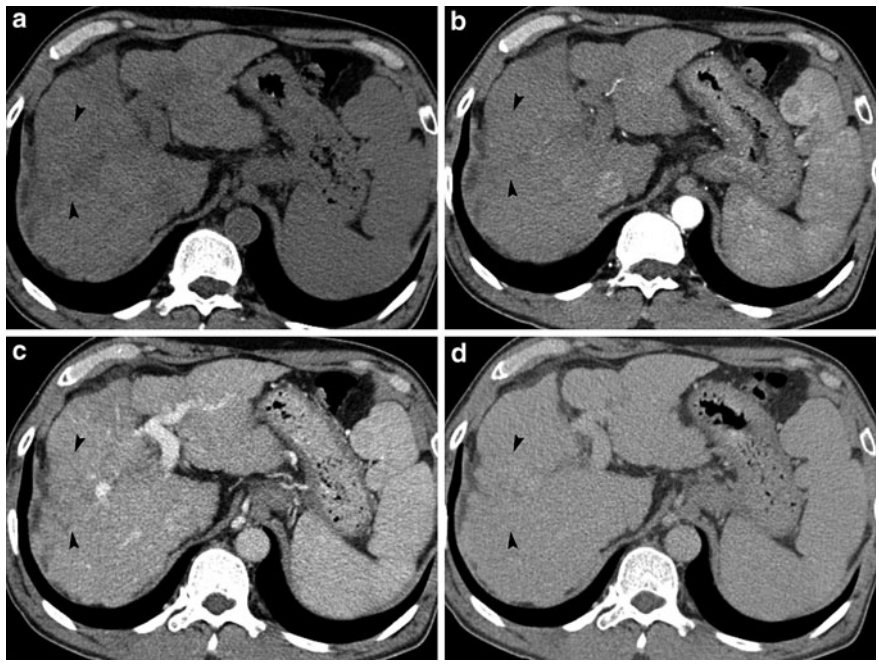

Fig. 32 Confluent Fibrosis: typical appearance. **a** Precontrast CT scan shows a wedge-shaped, hypoattenuated lesion in segment 8 (*arrowheads*). **b** Arterial phase CT scan shows hypoenhancement of the lesion (*arrowheads*). **c** Portal phase CT scan shows hypoenhancement of the lesion (*arrowheads*). **d** Delayed phase CT scan shows subtle delayed enhancement of the lesion (*arrowheads*)

obliterates existing hemangiomas (Khatri et al. 2010). When hemangioma shows typical enhancing features (peripheral globular enhancement and centripetal enhancement) on multiphase CT, it can be easily distinguished from HCC. However, hemangiomas are often atypical in appearance in cirrhotic livers and contain large regions of fibrosis (Dodd et al. 1999a, b). When hemangiomas do occur in the cirrhotic liver, they are commonly solitary, and small in size, and in many contrast-enhanced dynamic CT imaging demonstrates rapid enhancement (Fig. 31) (Yu et al. 2000a, b; Mastropasqua et al. 2004). Preexisting hemangiomas likely undergo obliteration from fibrosis and necrosis (Dodd et al. 1999a, b). Either related to fibrosis (Dodd et al. 1999a, b; Brancatelli et al. 2001) or alterations in blood flow (Mastropasqua et al. 2004) hemangiomas in cirrhotic livers have also been shown to progressively decrease in size and display more atypical imaging characteristics, including loss of the peripheral nodular enhancement (Brancatelli et al. 2001). In addition, hemangiomas in the cirrhotic patients may also be associated with adjacent capsular retraction (Vilgrain et al. 2000; Brancatelli et al. 2001; Blachar et al. 2002).

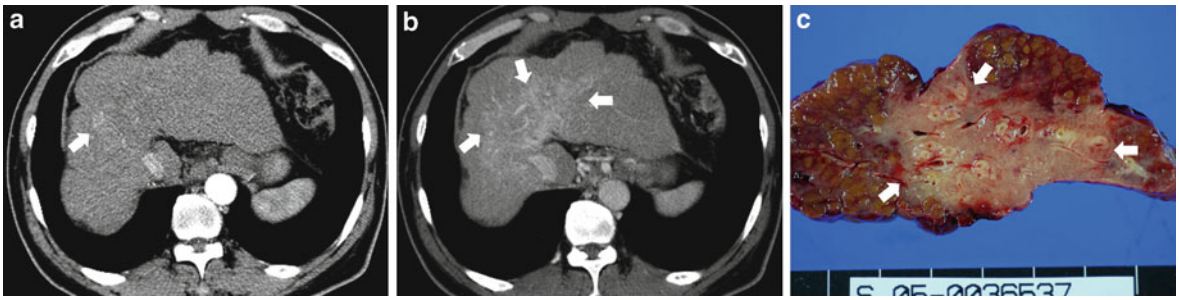

Fig. 33 Confluent fibrosis showing arterial and delayed enhancement. **a** Arterial phase CT scan reveals nodular contour of the liver, and an indistinct, subtle enhancing area (*arrow*) in right anterior segment of the liver. **b** Portal phase CT scan shows a poorly marginated, delayed enhancing central zone (*arrows*) compared with the peripheral zone of the liver. Note hepatic vessels traverse the central enhancing area. **c** Specimen photograph shows an ill-defined, fibrotic area (*arrows*) in central portion of the right hepatic lobe which contains multiple hepatic vessels without luminal obliteration

Among hemangiomas, small flash-filling hemangiomas may simulate HCC, as they demonstrate early homogeneous arterial phase enhancement (Fig. 31) (Semelka et al. 1994; Yu et al. 2000a, b; Baron and Peterson 2001; Mastropasqua et al. 2004). Although persistent enhancement on delayed images rather than washout is suggestive of hemangioma, these may be associated with minimal central enhancement (Semelka et al. 1994; Jang et al. 1998). Therefore, HCC should be considered more likely than hemangioma in cirrhosis if the nodular area of enhancement demonstrates washout. On the contrary, peliotic HCC contains multiple blood-filled sinusoids, which may result persistent peripheral enhancement that progresses centrally (Kadoya et al. 1992; Hoshimoto et al. 2009). Although peliotic change within HCC is rare, it may lead to misdiagnosis as hemangioma. Prior imaging (predevelopment of cirrhosis) showing more typical hemangioma features and stability or sclerosis of the lesion over time facilitates correct diagnosis. Alternatively, if an indeterminate lesion demonstrates interval increase in size in a cirrhotic liver, HCC should be suspected (Khatri et al. 2010).

5.3 Confluent Hepatic Fibrosis

Confluent hepatic fibrosis is typically seen in the setting of advanced cirrhosis, most commonly in cases secondary to PSC (Ohtomo et al. 1993a, b; Dodd et al. 1999a, b; Blachar et al. 2002; Brancatelli et al. 2009). Confluent hepatic fibrosis usually demonstrates low attenuation on precontrast CT images (Fig. 32) (Ohtomo et al. 1993a, b; Dodd et al. 1999a, b; Baron and Peterson 2001). Although it typically exhibits delayed enhancement, (Ohtomo et al. 1993a, b; Dodd et al. 1999a, b; Blachar et al. 2002) hepatic fibrosis can occasionally enhance in the arterial phase (Fig. 33) (Ahn and de Lange 1998). Hepatic fibrosis may present as a confluent mass (Dodd et al. 1999a, b; Baron and Peterson 2001) or may be poorly marginated, mimicking infiltrating HCC (Krinsky et al. 2001). However, imaging features which are helpful for distinguishing hepatic fibrosis from HCC is that confluent hepatic fibrosis is generally wedge-shaped, has linear margins, and is typically seen in the anterior segment of the right lobe and medial segment of the left lobe (segments 8 and 4) (Fig. 32) (Khatri et al. 2010). It characteristically demonstrates volume loss with focal capsular retraction of the adjacent liver surface, unlike HCC, which generally has mass effect and often expands the contour (Ohtomo et al. 1993a, b; Dodd et al. 1999a, b; Baron and Peterson 2001; Blachar et al. 2002). In troublesome cases where confluent mass-like fibrosis simulates a neoplasm, biopsy may be necessary for differentiation (Dodd et al. 1999a, b). Because hepatic fibrosis and cholangiocarcinoma share features such as delayed or persistent enhancement, associated capsular retraction, and common occurrence in patients with PSC, these two entities may also be confused. However, the characteristic location and geographic morphology (Ohtomo et al. 1993a, b; Dodd et al. 1999a, b; Baron and Peterson 2001; Blachar et al. 2002) in conjunction with the absence of biliary duct dilation may help to distinguish confluent fibrosis from cholangiocarcinoma in cirrhosis (Blachar et al. Blachar et al. 2002).

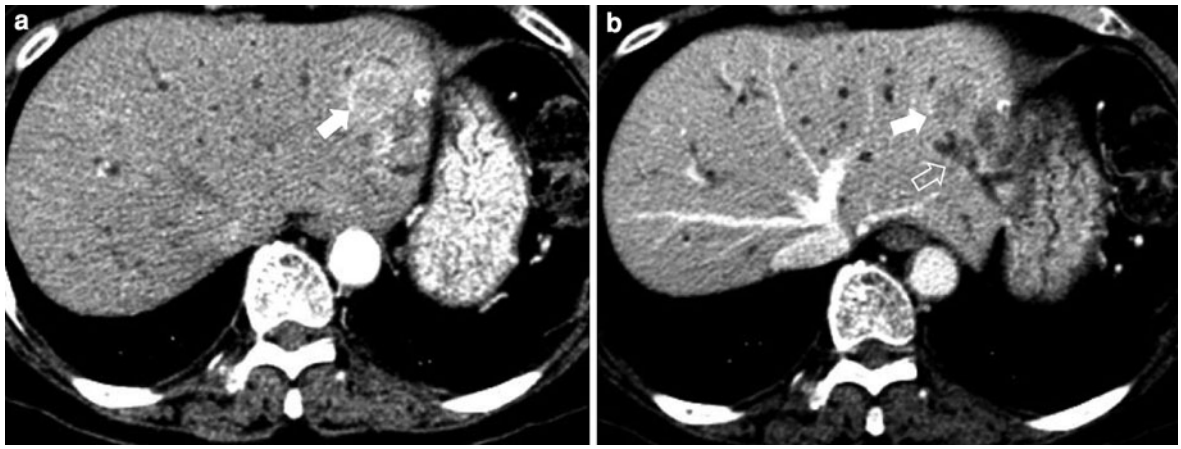

Fig. 34 A small intrahepatic cholangiocarcinoma showing arterial enhancement. **a** Arterial phase CT scan demonstrates a 2 cm, arterially enhancing nodule (*arrow*) in segment 3 of the liver. Note the peripheral intrahepatic ducts are dilated, which suggests a liver fluke infestation. **b** On portal phase CT scan, the nodule (*arrow*) becomes isoattenuated. The tumor involves adjacent bile duct (*open arrow*)

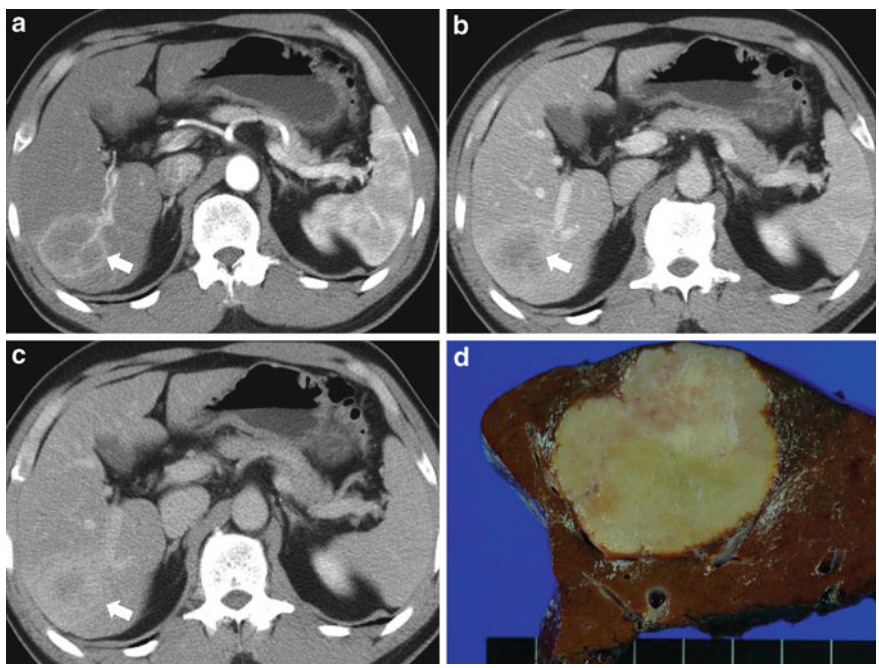

Fig. 35 Intrahepatic cholangiocarcinoma: typical enhancement pattern. **a** Arterial phase CT scan shows a hypovascular mass (*arrow*) with irregular peripheral enhancement. **b** and **c** Portal phase (**b**) and delayed phase (**c**) CT scans show progressive central enhancement of the tumor (*arrow*). **d** Specimen photograph shows a well-defined, firm, whitish tumor with lobulated contour

5.4 Intrahepatic Cholangiocarcinoma

Intrahepatic cholangiocarcinoma (IHC) may sometimes be difficult to distinguish from HCC. Particularly when IHC is smaller than 3 cm, it may mimic HCC as it can show arterial enhancement, while when large, it may mimic diffuse infiltrating HCC (Fig. 33) (Kim et al. 2007a, 2011a, b, c; Ariizumi et al. 2011a, b). Although there is overlap of imaging features, IHC is more likely to appear as a discrete mass than diffuse infiltrating HCC. Contrast enhancement characteristics may provide the strongest differentiation between the two entities. IHCs usually exhibit thick irregular peripheral enhancement with progressive central enhancement on more delayed images, which is a pattern that is rarely seen in HCC (Fig. 34) (Loyer et al. 1999). The persistent enhancement seen with IHC is generally a function of the fibrotic nature of

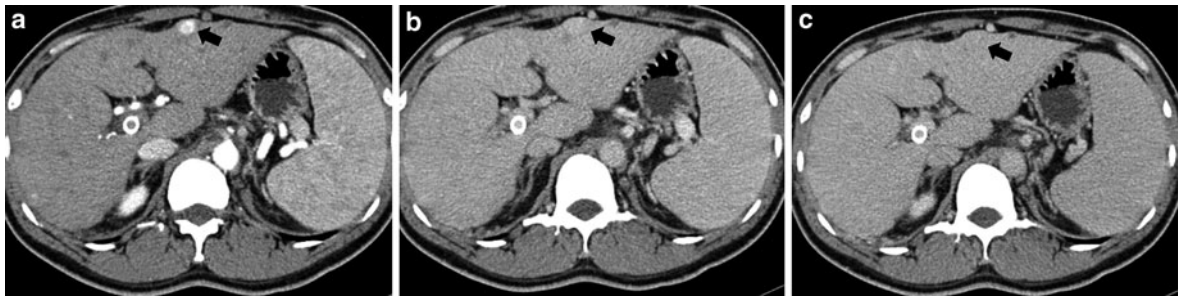

Fig. 36 Focal nodular hyperplasia like nodule in patients with membranous obstruction of the inferior vena cava. **a** Arterial phase CT scan shows a hyperenhancing nodule (*arrow*) in segment 3. **b** Portal phase CT scan shows a slightly hyperenhancement of the nodule (*arrow*). **c** Delayed phase CT scan shows isoenhancement of the lesion (*arrow*) compared with the surrounding parenchyma

the tumor. However, approximately 6–10% of IHC can demonstrate atypical enhancement pattern consisting of arterial enhancement and washout, which is similar appearance to HCC (Kim et al. 2007a, 2011a, b, c). Unlike hemangiomas, the peripheral enhancement of IHCs is not nodular or cloudlike and is not similar to the blood pool enhancement (Kim et al. 2011a, b, c; Sano et al. 2011). As arterially enhancing small IHCs were not rare; thus, enhancement pattern analysis of arterially enhancing IHCs will be helpful in differentiating them from HCC or hemangiomas (Kim et al. 2011a, b, c). In addition, presence of peripheral biliary ductal dilation (Fig. 34), encasement or compression of the portal vein rather than direct invasion or tumor thrombus formation, and associated capsular retraction would suggest higher probability of IHC more than HCC (Kim et al. 2009c). However, when small (<3 cm) IHCs are developed in cirrhotic liver, since stable arterial enhancement pattern without washout also can be registered in small HCC nodules, the evaluation of delayed phase is mandatory for a proper nodule characterization. If washout is not seen on CT, a biopsy should be mandatory for diagnosis, if transplantation is considered for treating cirrhosis (Rimola et al. 2009) (Fig. 35).

5.5 Hyperplastic Nodules or Focal Nodular Hyperplasia Like Nodules

In the setting of Budd-Chiari syndrome with cirrhosis or alcoholic cirrhosis or autoimmune hepatitis, hypervascular hyperplastic nodules or focal nodular hyperplasia like nodules can have features suggestive of HCC, including a size larger than 2 cm, and arterial phase enhancement (Fig. 36) (Vilgrain et al. 1999; Brancatelli et al. 2002; Maetani et al. 2002; Ibarrola et al. 2004; Nakashima et al. 2004; Qayyum et al. 2004; Namasivayam et al. 2007; Kim et al. 2008b; Takahashi et al. 2008). Such hypervascular regenerative nodules have also been shown to have a central scar, and therefore show similar appearance of HCC (Maetani et al. 2002). On portal venous phase of enhancement, the appearance may be variable. A hypointense regenerative nodule rim has also been reported in patients with Budd-Chiari (Vilgrain et al. 1999). The incidence of HCC in patients with Budd-Chiari is approximately 4% (Moucari et al. 2008). Although HCC and regenerative nodules may be difficult to distinguish based on imaging characteristics in the setting of Budd-Chiari, the presence of more than 10 nodules measuring up to 4 cm in diameter should favor the diagnosis of regenerative nodules (Vilgrain et al. 1999). In addition, increased levels of serum AFP were highly accurate in distinguishing HCC from benign nodules (Moucari et al. 2008). However, in alcoholic cirrhosis of autoimmune hepatitis, it is very difficult to differentiate FNH-like nodules radiologically, pathologically, and clinically from HCC (Kobayashi et al. 2007; Lee et al. 2007).

6 New Approaches of MDCT for Evaluation of HCC

Although detection rate of HCC reported in the literature are highly variable, the sensitivity and specificity of HCC detection using multiphasic MDCT in

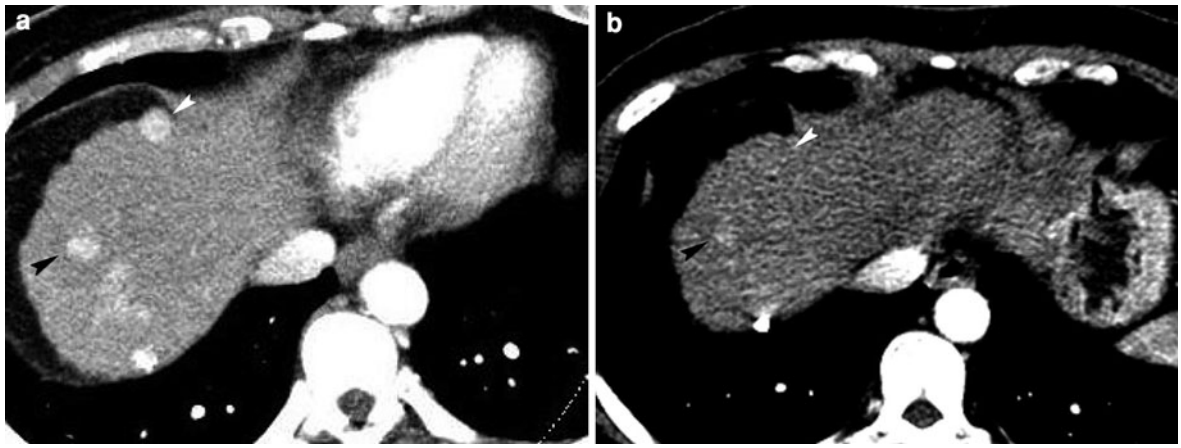

Fig. 37 Low-kVp scanning with high tube current for improving sensitivity for detection of iodine contrast media in hypervascular HCCs. **a** Low-kVp (80 kVp) scan with high tube current (600 mAs) shows two hypervascular HCCs in segment 8 (*arrowheads*) **b** Standard 120 kVp scan shows one of the two lesions(*black arrowhead*) by faint arterial enhancement. The other lesion(*white arrowhead*) is not well depicted

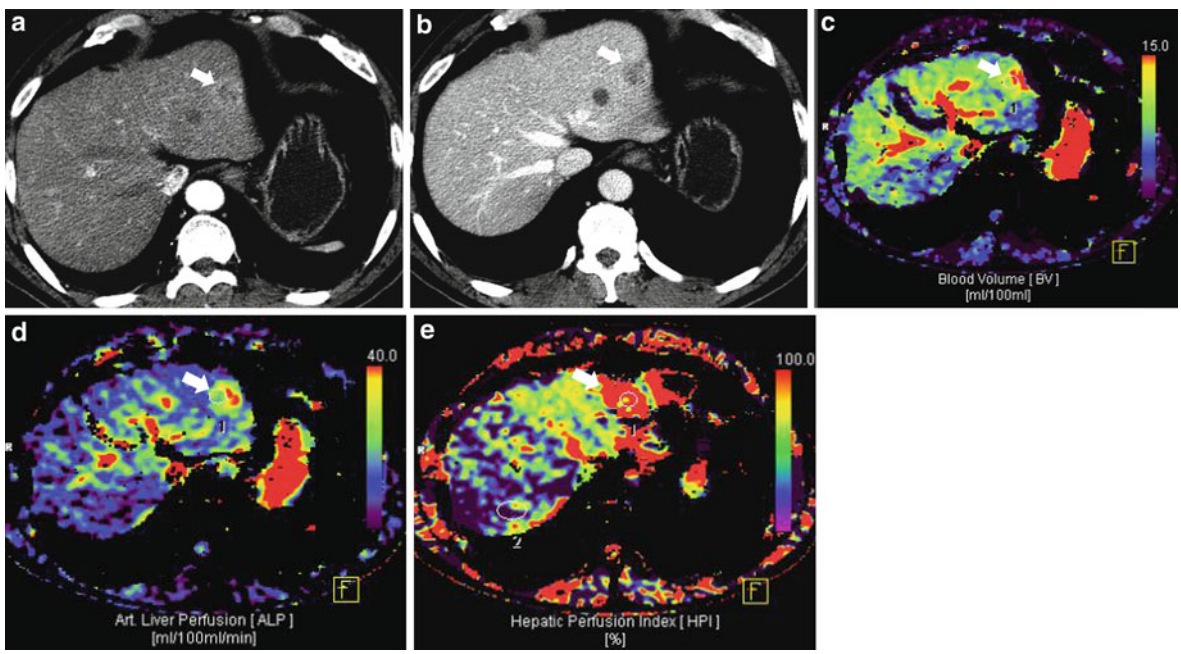

Fig. 38 Perfusion CT for quantification of tissue perfusion in patient with HCC in the left lateral segment of the liver. **a** Arterial phase CT scan shows a 2 cm hyperenhancing HCC (*arrow*) in the left hepatic lobe. **b** Portal phase CT scans washout of the nodule (*arrow*). **c**–**e** Perfusion CT maps indicates increased blood volume, arterial flow, and hepatic perfusion index (ratio of arterial to portal blood flow) of the tumor (*arrow*), which represents hemodynamic change of HCC

cirrhotic patients were reported in the range of 65–75% and 47–88%, respectively, when explanted liver was used as a standard of reference (Burrel et al. 2003; Kim et al. 2008c; Lee et al. 2009; Addley et al. 2011). However, the sensitivity can be decreased to 48–57% for lesions of size <2 cm in diameter (Kim et al. 2008c; Addley et al. 2011) and 10–33% for lesions of size <1 cm (Kawata et al. 2002; Burrel et al. 2003). There have been several approaches to improve diagnostic performance of CT for detection

of HCC. A recent study demonstrated that quantitative color mapping of the arterial enhancement fraction (AEF) using a registration and subtraction of precontrast, arterial, and portal venous phase images, can increase the sensitivity and diagnostic performance of multiphasic MDCT for detecting HCC (Kim et al. 2009a). In addition, multiphasic MDCT scans combined multiplanar reconstruction images are very effective in the detection of HCCs > 1 cm in diameter with a very low false-positive rate: sensitivity, positive predictive value, and accuracy for HCC detection were 87, 96, and 84% for all lesions, respectively, but only 46, 76, and 41% for tumors <1 cm, respectively (Maetani et al. 2008).

Other approaches for increasing sensitivity of CT for detecting hypervascular HCC may include a low-kVp CT scanning technique with high tube current (Fig. 37) and dual energy CT scanning method with iodine map or sigmoidal blending technique (Marin et al. 2009). Several previous studies have demonstrated that low-kVp images are more sensitive in detecting hypervascular liver lesions, despite of lower image quality of low-kVp images (Marin et al. 2009; Kim et al. 2010; Altenbernd et al. 2011).

Recently, Sorafenib (Nexavar_, Bayer Schering Pharma AG, Berlin, Germany), an orally active multikinase inhibitor with effects on tumor-cell proliferation and tumor angiogenesis, is a promising therapy that demonstrates superior survival in advanced HCC (Llovet et al. 2008). Although therapeutic response of solid tumors to chemotherapy has been assessed based on tumor size measurement using the Response Evaluation Criteria in Solid Tumors (RECIST), this assessment for response to Sorafenib therapy, however, has highlighted the limitations associated with morphologic measurement (Kim et al. 2011a, b, c). Perfusion CT quantifies not only tumor biologic behavior, but also changes in liver parenchyma (without tumor) caused by Sorafenib therapy in patients with advanced HCC (Okada et al. 2011), as it can provide non-invasive quantification of tumor blood supply, permeability, leakage space and blood volume related to the formation of new arterial structures (neoangiogenesis) (Fig. 38) (Choi and Lee 2010; Ippolito et al. 2011; International Consensus Group for Hepatocellular NeoplasiaThe International Consensus Group for Hepatocellular Neoplasia 2011; Okada et al. 2011). In the future, although new advanced technologies enable larger volumetric datasets and promising functional data to be obtained using CT, it will be necessary to reduce the radiation dose level of abdominal CT imaging for a variety of diagnostic purposes. Currently, various dose iterative reconstruction techniques have developed (Martinsen et al. 2011; Schindera et al. 2011; Mitsumori et al. 2012), and the use of those techniques for lowering noise and radiation dose will be more widely accepted at many centers.

References

Addley HC, Griffin N et al (2011) Accuracy of hepatocellular carcinoma detection on multidetector CT in a transplant liver population with explant liver correlation. Clin Radiol 66(4):349–356

Ahn IO, de Lange EE (1998) Early hyperenhancement of confluent hepatic fibrosis on dynamic MR imaging. AJR Am J Roentgenol 171(3):901–902

Ahn JH, Yu JS et al (2010) Nontumorous arterioportal shunts in the liver: CT and MRI findings considering mechanisms and fate. Eur Radiol 20(2):385–394

Altenbernd J, Heusner TA et al (2011) Dual-energy-CT of hypervascular liver lesions in patients with HCC: investigation of image quality and sensitivity. Eur Radiol 21(4): 738–743

Ariizumi SI, Kotera Y et al (2011a) Combined hepatocellular-cholangiocarcinoma had poor outcomes after hepatectomy regardless of Allen and Lisa class or the predominance of intrahepatic cholangiocarcinoma cells within the tumor. Ann Surg Oncol

Ariizumi S, Kotera Y et al (2011b) Mass-forming intrahepatic cholangiocarcinoma with marked enhancement on arterial-phase computed tomography reflects favorable surgical outcomes. J Surg Oncol 104(2):130–139

Asayama Y, Yoshimitsu K et al (2008) Arterial blood supply of hepatocellular carcinoma and histologic grading: radiologic-pathologic correlation. AJR Am J Roentgenol 190(1): W28–W34

Awaya H, Mitchell DG et al (2002) Cirrhosis: modified caudate-right lobe ratio. Radiology 224(3):769–774

Baron RL (1994) Understanding and optimizing use of contrast material for CT of the liver. AJR Am J Roentgenol 163(2): 323–331

Baron RL, Peterson MS (2001) From the RSNA refresher courses: screening the cirrhotic liver for hepatocellular carcinoma with CT and MR imaging: opportunities and pitfalls. Radiographics 21 Spec No: S117–132

Bartolozzi C, Crocetti L et al (2007) Biliary and reticuloendothelial impairment in hepatocarcinogenesis: the diagnostic role of tissue-specific MR contrast media. Eur Radiol 17(10): 2519–2530

Basaran C, Karcaaltincaba M et al (2005) Fat-containing lesions of the liver: cross-sectional imaging findings with emphasis on MRI. AJR Am J Roentgenol 184(4): 1103–1110

Blachar A, Federle MP et al (2002) Hepatic capsular retraction: spectrum of benign and malignant etiologies. Abdom Imaging 27(6):690–699

Bolog N, Andreisek G et al (2011) CT and MR imaging of hepatocellular carcinoma. J Gastrointestin Liver Dis 20(2): 181–189

Borzio M, Fargion S et al (2003) Impact of large regenerative, low grade and high grade dysplastic nodules in hepatocellular carcinoma development. J Hepatol 39(2):208–214

Brancatelli G, Federle MP et al (2001) Hemangioma in the cirrhotic liver: diagnosis and natural history. Radiology 219(1):69–74

Brancatelli G, Federle MP et al (2002) Large regenerative nodules in Budd-Chiari syndrome and other vascular disorders of the liver: CT and MR imaging findings with clinicopathologic correlation. AJR Am J Roentgenol 178(4):877–883

Brancatelli G, Baron RL et al (2003) Helical CT screening for hepatocellular carcinoma in patients with cirrhosis: frequency and causes of false-positive interpretation. AJR Am J Roentgenol 180(4):1007–1014

Brancatelli G, Federle MP et al (2007) Cirrhosis: CT and MR imaging evaluation. Eur J Radiol 61(1):57–69

Brancatelli G, Baron RL et al (2009) Focal confluent fibrosis in cirrhotic liver: natural history studied with serial CT. AJR Am J Roentgenol 192(5):1341–1347

Bruix J, Sherman M (2005) Management of hepatocellular carcinoma. Hepatology 42(5):1208–1236

Burrel M, Llovet JM et al (2003) MRI angiography is superior to helical CT for detection of HCC prior to liver transplantation: an explant correlation. Hepatology 38(4):1034–1042

Choi BI, Lee JM (2010) Advancement in HCC imaging: diagnosis, staging and treatment efficacy assessments: imaging diagnosis and staging of hepatocellular carcinoma. J Hepatobiliary Pancreat Sci 17(4):369–373

Choi BI, Takayasu K et al (1993) Small hepatocellular carcinomas and associated nodular lesions of the liver: pathology, pathogenesis, and imaging findings. AJR Am J Roentgenol 160(6):1177–1187

Choi BI, Lee HJ et al (1997) Detection of hypervascular nodular hepatocellular carcinomas: value of triphasic helical CT compared with iodized-oil CT. AJR Am J Roentgenol 168(1):219–224

Choi BI, Lee KH et al (2002) Hepatic arterioportal shunts: dynamic CT and MR features. Korean J Radiol 3(1):1–15

Chopra S, Dodd GD 3rd et al (1999) Mesenteric, omental, and retroperitoneal edema in cirrhosis: frequency and spectrum of CT findings. Radiology 211(3):737–742

Chou CT, Chen RC et al (2011) Prediction of microvascular invasion of hepatocellular carcinoma by pre-operative CT imaging. Br J Radiol [Epub ahead of print]

Chung YE, Park MS et al (2009) Hepatocellular carcinoma variants: radiologic-pathologic correlation. AJR Am J Roentgenol 193(1):W7–W13

Colagrande S, Centi N et al (2007a) Transient hepatic intensity differences: part 1, those associated with focal lesions. AJR Am J Roentgenol 188(1):154–159

Colagrande S, Centi N et al (2007b) Transient hepatic intensity differences: part 2, those not associated with focal lesions. AJR Am J Roentgenol 188(1):160–166

Da Ines D, Bailly A et al (2009) Hepatocellular carcinoma with sarcomatous change: prompt and fatal intraabdominal recurrence after liver transplantation. Gastroenterol Clin Biol 33(6–7):590–593

Desmet VJ (2009) East-West pathology agreement on precancerous liver lesions and early hepatocellular carcinoma. Hepatology 49(2):355–357

Desser TS (2009) Understanding transient hepatic attenuation differences. Semin Ultrasound CT MR 30(5):408–417

Dodd GD 3rd, Baron RL et al (1999a) Spectrum of imaging findings of the liver in end-stage cirrhosis: part I, gross morphology and diffuse abnormalities. AJR Am J Roentgenol 173(4):1031–1036

Dodd GD 3rd, Baron RL et al (1999b) Spectrum of imaging findings of the liver in end-stage cirrhosis: part II, focal abnormalities. AJR Am J Roentgenol 173(5):1185–1192

Earls JP, Theise ND et al (1996) Dysplastic nodules and hepatocellular carcinoma: thin-section MR imaging of explanted cirrhotic livers with pathologic correlation. Radiology 201(1):207–214

Efremidis SC, Hytiroglou P et al (2007) Enhancement patterns and signal-intensity characteristics of small hepatocellular carcinoma in cirrhosis: pathologic basis and diagnostic challenges. Eur Radiol 17(11):2969–2982

Fan R, Chen P et al (2011) Cooperation of deregulated Notch signaling and Ras pathway in human hepatocarcinogenesis. J Mol Histol 42(5):473–481

Fernandez MP, Redvanly RD (1998) Primary hepatic malignant neoplasms. Radiol Clin N Am 36(2):333–348

Ferrell LD, Crawford JM et al (1993) Proposal for standardized criteria for the diagnosis of benign, borderline, and malignant hepatocellular lesions arising in chronic advanced liver disease. Am J Surg Pathol 17(11):1113–1123

Fisher MR, Gore RM (1985) Computed tomography in the evaluation of cirrhosis and portal hypertension. J Clin Gastroenterol 7(2):173–181

Forner A, Vilana R et al (2008) Diagnosis of hepatic nodules 20 mm or smaller in cirrhosis: prospective validation of the noninvasive diagnostic criteria for hepatocellular carcinoma. Hepatology 47(1):97–104

Fournier LS, Cuenod CA et al (2004) Early modifications of hepatic perfusion measured by functional CT in a rat model of hepatocellular carcinoma using a blood pool contrast agent. Eur Radiol 14(11):2125–2133

Freeny PC, Baron RL et al (1992) Hepatocellular carcinoma: reduced frequency of typical findings with dynamic contrast-enhanced CT in a non-Asian population. Radiology 182(1):143–148

Fukukura Y, Taguchi J et al (1997) Combined hepatocellular and cholangiocarcinoma: correlation between CT findings and clinicopathological features. J Comput Assist Tomogr 21(1):52–58

Furlan A, Marin D et al (2011) Hepatocellular carcinoma in cirrhotic patients at multidetector CT: hepatic venous phase versus delayed phase for the detection of tumour washout. Br J Radiol 84(1001):403–412

Gibo M, Murata S et al (2001) Pericaval fat collection mimicking an intracaval lesion on CT in patients with chronic liver disease. Abdom Imaging 26(5):492–495

Giorgio A, Amoroso P et al (1986) Cirrhosis: value of caudate to right lobe ratio in diagnosis with US. Radiology 161(2):443–445

Gomaa AI, Khan SA et al (2008) Hepatocellular carcinoma: epidemiology, risk factors and pathogenesis. World J Gastroenterol 14(27):4300–4308

Gore RM (2008) Diffuse liver disease. In: Gore RM, Levine MS, Laufer I (eds) Textbook of gastrointestinal radiology, vol 2. Saunders, Philadelpia, pp 1685–1730

Goshima S, Kanematsu M et al (2004) Nodule-in-nodule appearance of hepatocellular carcinomas: comparison of gadolinium-enhanced and ferumoxides-enhanced magnetic resonance imaging. J Magn Reson Imaging 20(2):250–255

Grazioli L, Olivetti L et al (1999) The pseudocapsule in hepatocellular carcinoma: correlation between dynamic MR imaging and pathology. Eur Radiol 9(1):62–67

Greenfield V, Cheung O et al (2008) Recent advances in nonalcholic fatty liver disease. Curr Opin Gastroenterol 24(3):320–327

Hall TC, Garcea G et al (2011) Management of acute non-cirrhotic and non-malignant portal vein thrombosis: a systematic review. World J Surg 35(11):2510–2520

Hammerstingl RM, Vogl TJ (2005) Abdominal MDCT: protocols and contrast considerations. Eur Radiol 15(Suppl 5): E78–E90

Harbin WP, Robert NJ et al (1980) Diagnosis of cirrhosis based on regional changes in hepatic morphology: a radiological and pathological analysis. Radiology 135(2):273–283

Hayashi M, Matsui O et al (1999) Correlation between the blood supply and grade of malignancy of hepatocellular nodules associated with liver cirrhosis: evaluation by CT during intraarterial injection of contrast medium. AJR Am J Roentgenol 172(4):969–976

Hayashi M, Matsui O et al (2002) Progression to hypervascular hepatocellular carcinoma: correlation with intranodular blood supply evaluated with CT during intraarterial injection of contrast material. Radiology 225(1):143–149

Holland AE, Hecht EM et al (2005) Importance of small (< or = 20-mm) enhancing lesions seen only during the hepatic arterial phase at MR imaging of the cirrhotic liver: evaluation and comparison with whole explanted liver. Radiology 237(3):938–944

Honda H, Ochiai K et al (1993) Hepatocellular carcinoma: correlation of CT, angiographic, and histopathologic findings. Radiology 189(3):857–862

Honda H, Hayashi T et al (1996) Hepatocellular carcinoma with sarcomatous change: characteristic findings of two-phased incremental CT. Abdom Imaging 21(1):37–40

Hoshimoto S, Morise Z et al (2009) Hepatocellular carcinoma with extensive peliotic change. J Hepatobiliary Pancreat Surg 16(4):566–570

Hwang GJ, Kim MJ et al (1997) Nodular hepatocellular carcinomas: detection with arterial-, portal-, and delayed-phase images at spiral CT. Radiology 202(2):383–388

Hytiroglou P (2004) Morphological changes of early human hepatocarcinogenesis. Semin Liver Dis 24(1):65–75

Hytiroglou P, Park YN et al (2007) Hepatic precancerous lesions and small hepatocellular carcinoma. Gastroenterol Clin N Am 36(4):867–887, vii

Iannaccone R, Laghi A et al (2005) Hepatocellular carcinoma: role of unenhanced and delayed phase multi-detector row helical CT in patients with cirrhosis. Radiology 234(2): 460–467

Ibarrola C, Castellano VM et al (2004) Focal hyperplastic hepatocellular nodules in hepatic venous outflow obstruction: a clinicopathological study of four patients and 24 nodules. Histopathology 44(2):172–179

Ichikawa T, Federle MP et al (1999) Fibrolamellar hepatocellular carcinoma: imaging and pathologic findings in 31 recent cases. Radiology 213(2):352–361

Ikenaga N, Chijiiwa K et al (2009) Clinicopathologic characteristics of hepatocellular carcinoma with bile duct invasion. J Gastrointest Surg 13(3):492–497

Imaeda T, Kanematsu M et al (1994) Extracapsular invasion of small hepatocellular carcinoma: MR and CT findings. J Comput Assist Tomogr 18(5):755–760

International Consensus Group for Hepatocellular Neoplasia-aThe International Consensus Group for Hepatocellular Neoplasia (2011) Perfusion measurement of the whole upper abdomen of patients with and without liver diseases: initial experience with 320-detector row CT. Eur J Radiol

Ippolito D, Capraro C et al (2011) Quantitative assessment of tumour associated neovascularisation in patients with liver cirrhosis and hepatocellular carcinoma: role of dynamic-CT perfusion imaging. Eur Radiolo [Epub ahead of print]

Ishida Y, Nagamatsu H et al (2008) Hepatocellular carcinoma with a "nodule-in-nodule" appearance reflecting an unusual dilated pseudoglandular structure. Intern Med 47(13): 1215–1218

Ishigami K, Yoshimitsu K et al (2009) Hepatocellular carcinoma with a pseudocapsule on gadolinium-enhanced MR images: correlation with histopathologic findings. Radiology 250(2):435–443

Ito K, Honjo K et al (1996) Liver neoplasms: diagnostic pitfalls in cross-sectional imaging. Radiographics 16(2):273–293

Ito K, Mitchell DG et al (1999a) Expanded gallbladder fossa: simple MR imaging sign of cirrhosis. Radiology 211(3): 723–726

Ito K, Mitchell DG et al (1999b) Primary sclerosing cholangitis: MR imaging features. AJR Am J Roentgenol 172(6): 1527–1533

Ito K, Mitchell DG et al (2000) Enlargement of hilar periportal space: a sign of early cirrhosis at MR imaging. J Magn Reson Imaging 11(2):136–140

Ito K, Mitchell DG et al (2003) Right posterior hepatic notch sign: a simple diagnostic MR finding of cirrhosis. J Magn Reson Imaging 18(5):561–566

Ito K, Mitchell DG (2004) Imaging diagnosis of cirrhosis and chronic hepatitis. Intervirology 47(3–5):134–143

Jang HJ, Choi BI et al (1998) Atypical small hemangiomas of the liver: "bright dot" sign at two-phase spiral CT. Radiology 208(2):543–548

Kadoya M, Matsui O et al (1992) Hepatocellular carcinoma: correlation of MR imaging and histopathologic findings. Radiology 183(3):819–825

Kamel IR, Liapi E et al (2005) Multidetector CT of hepatocellular carcinoma. Best Pract Res Clin Gastroenterol 19(1):63–89

Kanematsu M, Semelka RC et al (2003) Hepatocellular carcinoma of diffuse type: MR imaging findings and clinical manifestations. J Magn Reson Imaging 18(2):189–195

Kanematsu M, Goshima S et al (2005) Optimizing scan delays of fixed duration contrast injection in contrast-enhanced biphasic multidetector-row CT for the liver and the detection of hypervascular hepatocellular carcinoma. J Comput Assist Tomogr 29(2):195–201

Kang SE, Lee JM et al (2011) Quantitative color mapping of the arterial enhancement fraction in patients with diffuse liver disease. AJR Am J Roentgenol 197(4):876–883

Kawata S, Murakami T et al (2002) Multidetector CT: diagnostic impact of slice thickness on detection of hypervascular hepatocellular carcinoma. AJR Am J Roentgenol 179(1): 61–66

Khalili K, Kyoung Kim T et al (2011) Indeterminate 1–2-cm nodules found on hepatocellular carcinoma surveillance: Biopsy for all, some, or none? Hepatology 54(6):2048–2054

Khatri G, Merrick L et al (2010) MR imaging of hepatocellular carcinoma. Magn Reson Imaging Clin N Am 18(3):421–450 X

Kim HJ, Kim AY et al (2005) Transient hepatic attenuation differences in focal hepatic lesions: dynamic CT features. AJR Am J Roentgenol 184(1):83–90

Kim SJ, Lee JM et al (2007a) Peripheral mass-forming cholangiocarcinoma in cirrhotic liver. AJR Am J Roentgenol 189(6):1428–1434

Kim SR, Ikawa H et al (2007b) Multistep hepatocarcinogenesis from a dysplastic nodule to well-differentiated hepatocellular carcinoma in a patient with alcohol-related liver cirrhosis. World J Gastroenterol 13(8):1271–1274

Kim BK, Han KH et al (2008a) Prediction of microvascular invasion before curative resection of hepatocellular carcinoma. J Surg Oncol 97(3):246–252

Kim SR, Imoto S et al (2008b) Focal nodular hyperplasia-like lesion with venous washout in alcoholic liver cirrhosis. Intern Med 47(21):1899–1903

Kim SH, Choi BI et al (2008c) Diagnostic accuracy of multi-/single-detector row CT and contrast-enhanced MRI in the detection of hepatocellular carcinomas meeting the milan criteria before liver transplantation. Intervirology 51(Suppl 1): 52–60

Kim KW, Lee JM et al (2009a) Quantitative CT color mapping of the arterial enhancement fraction of the liver to detect hepatocellular carcinoma. Radiology 250(2):425–434

Kim SH, Lim HK et al (2009b) Scirrhous hepatocellular carcinoma: comparison with usual hepatocellular carcinoma based on CT-pathologic features and long-term results after curative resection. Eur J Radiol 69(1):123–130

Kim YK, Han YM et al (2009c) Comparison of diffuse hepatocellular carcinoma and intrahepatic cholangiocarcinoma using sequentially acquired gadolinium-enhanced and Resovist-enhanced MRI. Eur J Radiol 70(1):94–100

Kim KS, Lee JM et al (2010) Image fusion in dual energy computed tomography for detection of hypervascular liver hepatocellular carcinoma: phantom and preliminary studies. Invest Radiol 45(3):149–157

Kim KW, Lee JM et al (2011a) Assessment of the treatment response of HCC. Abdom Imaging 36(3):300–314

Kim SA, Lee JM et al (2011b) Intrahepatic mass-forming cholangiocarcinomas: enhancement patterns at multiphasic CT, with special emphasis on arterial enhancement pattern—correlation with clinicopathologic findings. Radiology 260(1):148–157

Kim SE, Lee HC et al (2011c) Noninvasive diagnostic criteria for hepatocellular carcinoma in hepatic masses >2 cm in a hepatitis B virus-endemic area. Liver Int 31(10):1468–1476

Kim KE, Park MS et al (2011d) Hepatocellular carcinoma: clinical and radiological findings in patients with chronic B viral hepatitis and chronic C viral hepatitis. Abdom Imaging [Epub ahead of print]

Kitao A, Zen Y et al (2009) Hepatocarcinogenesis: multistep changes of drainage vessels at CT during arterial portography and hepatic arteriography–radiologic-pathologic correlation. Radiology 252(2):605–614

Kobayashi S, Matsui O et al (2007) Imaging of benign hypervascular hepatocellular nodules in alcoholic liver cirrhosis: differentiation from hypervascular hepatocellular carcinoma. J Comput Assist Tomogr 31(4):557–563

Kojiro M (1998) Pathology of early hepatocellular carcinoma: progression from early to advanced. Hepatogastroenterology 45(Suppl 3):1203–1205

Kojiro M, Nakashima O (1999) Histopathologic evaluation of hepatocellular carcinoma with special reference to small early stage tumors. Semin Liver Dis 19(3):287–296

Kojiro M, Roskams T (2005) Early hepatocellular carcinoma and dysplastic nodules. Semin Liver Dis 25(2):133–142

Kondo F et al (2009) Pathologic diagnosis of early hepatocellular carcinoma: a report of the international consensus group for hepatocellular neoplasia. Hepatology 49(2): 658–664

Krinsky GA, Lee VS (2000) MR imaging of cirrhotic nodules. Abdom Imaging 25(5):471–482

Krinsky GA, Lee VS et al (2001) Hepatocellular carcinoma and dysplastic nodules in patients with cirrhosis: prospective diagnosis with MR imaging and explantation correlation. Radiology 219(2):445–454

Kudo M (2004) Atypical large well-differentiated hepatocellular carcinoma with benign nature: a new clinical entity. Intervirology 47(3–5):227–237

Kudo M, Tochio H (2008) Intranodular blood supply correlates well with biological malignancy grade determined by tumor growth rate in pathologically proven hepatocellular carcinoma. Oncology 75(Suppl 1):55–64

Kutami R, Nakashima Y et al (2000) Pathomorphologic study on the mechanism of fatty change in small hepatocellular carcinoma of humans. J Hepatol 33(2):282–289

Lafortune M, Matricardi L et al (1998) Segment 4 (the quadrate lobe): a barometer of cirrhotic liver disease at US. Radiology 206(1):157–160

Lao XM, Chen DY et al (2007) Primary carcinosarcoma of the liver: clinicopathologic features of 5 cases and a review of the literature. Am J Surg Pathol 31(6):817–826

Lee KH, Choi BI et al (2000) Nodular hepatocellular carcinoma: variation of tumor conspicuity on single-level dynamic scan and optimization of fixed delay times for two-phase helical CT. J Comput Assist Tomogr 24(2):212–218

Lee YH, Kim SH et al (2007) Focal nodular hyperplasia-like nodules in alcoholic liver cirrhosis: radiologic-pathologic correlation. AJR Am J Roentgenol 188(5):W459–W463

Lee HK, Park SJ et al (2008) Portal vein thrombosis: CT features. Abdom Imaging 33(1):72–79

Lee DH, Kim SH et al (2009) Diagnostic performance of multidetector row computed tomography, superparamagnetic iron oxide-enhanced magnetic resonance imaging, and dual-contrast magnetic resonance imaging in predicting the appropriateness of a transplant recipient based on milan criteria: correlation with histopathological findings. Invest Radiol 44(6):311–321

Lee JM, Trevisani F et al (2011) Imaging diagnosis and staging of hepatocellular carcinoma. Liver Transpl 17(Suppl 2): S34–43

Libbrecht L, Desmet V et al (2005) Preneoplastic lesions in human hepatocarcinogenesis. Liver Int 25(1):16–27

Lim JH, Kim MJ et al (2004) Dysplastic nodules in liver cirrhosis: detection with triple phase helical dynamic CT. Br J Radiol 77(923):911–916

Lim YS, Kim WR (2008) The global impact of hepatic fibrosis and end-stage liver disease. Clin Liver Dis 12(4):733–746 Vii

Liu QY, Huang SQ et al (2010) Small hepatocellular carcinoma with bile duct tumor thrombi: CT and MRI findings. Abdom Imaging 35(5):537–542

Llovet JM, Chen Y et al (2006) A molecular signature to discriminate dysplastic nodules from early hepatocellular carcinoma in HCV cirrhosis. Gastroenterology 131(6): 1758–1767

Llovet JM, Ricci S et al (2008) Sorafenib in advanced hepatocellular carcinoma. N Engl J Med 359(4):378–390

Loyer EM, Chin H et al (1999) Hepatocellular carcinoma and intrahepatic peripheral cholangiocarcinoma: enhancement patterns with quadruple phase helical CT—a comparative study. Radiology 212(3):866–875

Luca A, Caruso S et al (2010) Multidetector-row computed tomography (MDCT) for the diagnosis of hepatocellular carcinoma in cirrhotic candidates for liver transplantation: prevalence of radiological vascular patterns and histological correlation with liver explants. Eur Radiol 20(4):898–907

Maetani Y, Itoh K et al (2002) Benign hepatic nodules in Budd-Chiari syndrome: radiologic-pathologic correlation with emphasis on the central scar. AJR Am J Roentgenol 178(4): 869–875

Maetani YS, Ueda M et al (2008) Hepatocellular carcinoma in patients undergoing living-donor liver transplantation. Accuracy of multidetector computed tomography by viewing images on digital monitors. Intervirology 51(Suppl 1): 46–51

Marin D, Nelson RC et al (2009) Hypervascular liver tumors: low tube voltage, high tube current multidetector CT during late hepatic arterial phase for detection—initial clinical experience. Radiology 251(3):771–779

Martin J, Sentis M et al (1995) Fatty metamorphosis of hepatocellular carcinoma: detection with chemical shift gradient-echo MR imaging. Radiology 195(1):125–130

Martinsen AC, Saether HK et al (2011) Iterative reconstruction reduces abdominal CT dose. Eur J Radiol [Epub ahead of print]

Mastropasqua M, Kanematsu M et al (2004) Cavernous hemangiomas in patients with chronic liver disease: MR imaging findings. Magn Reson Imaging 22(1):15–18

Mathers CD, Lopez AD, Murray CJL (2006) The burden of disease and mortality by condition data, methods, and results for 2001. In: Mathers CD, Lopez AD, Ezzati M et al (eds) Global burden of disease and risk factors. Oxford University Press and the World Bank, Washington (DC), pp 45–93

Matsui O (2004) Imaging of multistep human hepatocarcinogenesis by CT during intra-arterial contrast injection. Intervirology 47(3–5):271–276

Matsui O, Kobayashi S et al (2011) Hepatocelluar nodules in liver cirrhosis: hemodynamic evaluation (angiography-assisted CT) with special reference to multi-step hepatocarcinogenesis. Abdom Imaging 36(3):264–272

McLarney JK, Rucker PT et al (1999) Fibrolamellar carcinoma of the liver: radiologic-pathologic correlation. Radiographics 19(2):453–471

Minagawa M, Ikai I et al (2007) Staging of hepatocellular carcinoma: assessment of the Japanese TNM and AJCC/UICC TNM systems in a cohort of 13,772 patients in Japan. Ann Surg 245(6):909–922

Mitsumori LM, Shuman WP et al (2012) Adaptive statistical iterative reconstruction versus filtered back projection in the same patient: 64 channel liver CT image quality and patient radiation dose. Eur Radiol 22(1):138–143

Monzawa S, Omata K et al (1999) Well-differentiated hepatocellular carcinoma: findings of US, CT, and MR imaging. Abdom Imaging 24(4):392–397

Moubarak E, Bouvier A et al (2011) Portosystemic collateral vessels in liver cirrhosis: a three-dimensional MDCT pictorial review. Abdom Imaging [Epub ahead of print]

Moucari R, Rautou PE et al (2008) Hepatocellular carcinoma in Budd-Chiari syndrome: characteristics and risk factors. Gut 57(6):828–835

Murakami T, Kim T et al (1997) Combined hepatocellular and cholangiocellular carcinoma. Radiat Med 15(4):243–246

Nakashima O, Sugihara S et al (1995) Pathomorphologic characteristics of small hepatocellular carcinoma: a special reference to small hepatocellular carcinoma with indistinct margins. Hepatology 22(1):101–105

Nakashima Y, Nakashima O et al (1999) Vascularization of small hepatocellular carcinomas: correlation with differentiation. Liver 19(1):12–18

Nakashima O, Kurogi M et al (2004) Unique hypervascular nodules in alcoholic liver cirrhosis: identical to focal nodular hyperplasia-like nodules? J Hepatol 41(6): 992–998

Nakamura K, Zen Y et al (2007) Vascular endothelial growth factor, its receptor Flk-1, and hypoxia inducible factor-1alpha are involved in malignant transformation in dysplastic nodules of the liver. Hum Pathol 38(10):1532–1546

Namasivayam S, Salman K et al (2007) Hypervascular hepatic focal lesions: spectrum of imaging features. Curr Probl Diagn Radiol 36(3):107–123

Ohtomo K, Baron RL et al (1993a) Confluent hepatic fibrosis in advanced cirrhosis: appearance at CT. Radiology 188(1): 31–35

Ohtomo K, Baron RL et al (1993b) Confluent hepatic fibrosis in advanced cirrhosis: evaluation with MR imaging. Radiology 189(3):871–874

Okada M, Kim T et al (2011) Hepatocellular nodules in liver cirrhosis: state of the art CT evaluation (perfusion CT/volume helical shuttle scan/dual-energy CT, etc.). Abdom Imaging 36(3):273–281

Okazaki H, Ito K et al (2000) Discrimination of alcoholic from virus-induced cirrhosis on MR imaging. AJR Am J Roentgenol 175(6):1677–1681

Okuda K (2002) Natural history of hepatocellular carcinoma including fibrolamellar and hepato-cholangiocarcinoma variants. J Gastroenterol Hepatol 17(4):401–405

Onaya H, Itai Y et al (2000) Highly enhanced hepatic masses seen on CT during arterial portography: early hepatocellular carcinoma and adenomatous hyperplasia. Jpn J Clin Oncol 30(10):440–445

Ozaki K, Matsui O et al (2010) Selective atrophy of the middle hepatic venous drainage area in hepatitis C-related cirrhotic liver: morphometric study by using multidetector CT. Radiology 257(3):705–714

Park YN, Kim YB et al (2000) Increased expression of vascular endothelial growth factor and angiogenesis in the early stage of multistep hepatocarcinogenesis. Arch Pathol Lab Med 124(7):1061–1065

Park YN, Kim MJ (2011) Hepatocarcinogenesis: imaging-pathologic correlation. Abdom Imaging 36(3):232–243

Parkin DM, Bray F et al (2001) Estimating the world cancer burden: Globocan 2000. Int J Cancer 94(2):153–156

Perez-Johnston R, Lenhart DK et al (2010) CT angiography of the hepatic and pancreatic circulation. Radiol Clin N Am 48(2):311–330 viii

Piscaglia F, Gianstefani A et al (2010) Criteria for diagnosing benign portal vein thrombosis in the assessment of patients with cirrhosis and hepatocellular carcinoma for liver transplantation. Liver Transpl 16(5):658–667

Poddar N, Avezbakiyev B et al (2010) Hepatocellular carcinoma presenting as an incidental isolated malignant portal vein thrombosis. J Gastrointest Cancer [Epub ahead of print]

Pomfret EA, Washburn K et al (2010) Report of a national conference on liver allocation in patients with hepatocellular carcinoma in the United States. Liver Transpl 16(3):262–278

Popper H (1986) General pathology of the liver: light microscopic aspects serving diagnosis and interpretation. Semin Liver Dis 6(3):175–184

Prasad SR, Wang H et al (2005) Fat-containing lesions of the liver: radiologic-pathologic correlation. Radiographics 25(2): 321–331

Qayyum A, Graser A et al (2004) CT of benign hypervascular liver nodules in autoimmune hepatitis. AJR Am J Roentgenol 183(6):1573–1576

Rimola J, Forner A et al (2009) Cholangiocarcinoma in cirrhosis: absence of contrast washout in delayed phases by magnetic resonance imaging avoids misdiagnosis of hepatocellular carcinoma. Hepatology 50(3):791–798

Roncalli M, Terracciano L et al (2011) Liver precancerous lesions and hepatocellular carcinoma: the histology report. Dig Liver Dis 43(Suppl 4):S361–372

Sadek AG, Mitchell DG et al (1995) Early hepatocellular carcinoma that develops within macroregenerative nodules: growth rate depicted at serial MR imaging. Radiology 195(3): 753–756

Sakamoto M, Hirohashi S et al (1991) Early stages of multistep hepatocarcinogenesis: adenomatous hyperplasia and early hepatocellular carcinoma. Hum Pathol 22(2):172–178

Sangiovanni A, Manini MA et al (2010) The diagnostic and economic impact of contrast imaging techniques in the diagnosis of small hepatocellular carcinoma in cirrhosis. Gut 59(5):638–644

Sano K, Ichikawa T et al (2011) Imaging study of early hepatocellular carcinoma: usefulness of gadoxetic acid-enhanced MR Imaging. Radiology 261(3):834–844

Saygili OB, Tarhan NC et al (2005) Value of computed tomography and magnetic resonance imaging for assessing severity of liver cirrhosis secondary to viral hepatitis. Eur J Radiol 54(3):400–407

Schindera ST, Diedrichsen L et al (2011) Iterative reconstruction algorithm for abdominal multidetector CT at different tube voltages: assessment of diagnostic accuracy, image quality, and radiation dose in a phantom study. Radiology 260(2):454–462

Schuppan D, Afdhal NH (2008) Liver cirrhosis. Lancet 371(9615):838–851

Schutte K, Bornschein J et al (2009) Hepatocellular carcinoma—epidemiological trends and risk factors. Dig Dis 27(2):80–92

Semelka RC, Brown ED et al (1994) Hepatic hemangiomas: a multi-institutional study of appearance on T2-weighted and serial gadolinium-enhanced gradient-echo MR images. Radiology 192(2):401–406

Serste T, Barrau V et al (2011) Accuracy and disagreement of CT and MRI for the diagnosis of small hepatocellular carcinoma and dysplastic nodules: role of biopsy. Hepatology

Sherman M (2010) The radiological diagnosis of hepatocellular carcinoma. Am J Gastroenterol 105(3):610–612

Shin CI, Lee JM et al (2007) Recurrence patterns of combined hepatocellular-cholangiocarcinoma on enhanced computed tomography. J Comput Assist Tomogr 31(1):109–115

Stevens WR, Johnson CD et al (1994) CT findings in hepatocellular carcinoma: correlation of tumor characteristics with causative factors, tumor size, and histologic tumor grade. Radiology 191(2):531–537

Stevens WR, Gulino SP et al (1996) Mosaic pattern of hepatocellular carcinoma: histologic basis for a characteristic CT appearance. J Comput Assist Tomogr 20(3):337–342

Sumie S, Kuromatsu R et al (2008) Microvascular invasion in patients with hepatocellular carcinoma and its predictable clinicopathological factors. Ann Surg Oncol 15(5):1375–1382

Sun HY, Lee JM et al (2010) Gadoxetic acid-enhanced magnetic resonance imaging for differentiating small hepatocellular carcinomas (< or = 2 cm in diameter) from arterial enhancing pseudolesions: special emphasis on hepatobiliary phase imaging. Invest Radiol 45(2):96–103

Taguchi K, Aishima S et al (2005) Significance of the relationship between irregular regeneration and two hepatocarcinogenic pathways: "de novo" and so-called "dysplastic nodule-hepatocellular carcinoma" sequence. J Surg Oncol 92(2):100–103

Takahashi S, Miyanishi K et al (2008) Case report of a focal nodular hyperplasia-like nodule present in cirrhotic liver. Hepatol Res 38(5):521–528

Takayasu K, Furukawa H et al (1995) CT diagnosis of early hepatocellular carcinoma: sensitivity, findings, and CT-pathologic correlation. AJR Am J Roentgenol 164(4): 885–890

Takayasu K, Muramatsu Y et al (2007) CT Imaging of early hepatocellular carcinoma and the natural outcome of hypoattenuating nodular lesions in chronic liver disease. Oncology 72(Suppl 1):83–91

Taouli B, Losada M et al (2004) Magnetic resonance imaging of hepatocellular carcinoma. Gastroenterology 127(5 Suppl 1): S144–S152

Tarantino L, Francica G et al (2006) Diagnosis of benign and malignant portal vein thrombosis in cirrhotic patients with hepatocellular carcinoma: color Doppler US, contrast-enhanced US, and fine-needle biopsy. Abdom Imaging 31(5):537–544

Terada T, Nakanuma Y (1989) Survey of iron-accumulative macroregenerative nodules in cirrhotic livers. Hepatology 10(5):851–854

Terada T, Nakanuma Y et al (1989) Fatty macroregenerative nodule in non-steatotic liver cirrhosis. A morphologic study. Virchows Arch A Pathol Anat Histopathol 415(2):131–136

Tsuchiyama T, Terasaki S et al (2002) Tiny staining spots in liver cirrhosis associated with HCV infection observed by computed tomographic hepatic arteriography: follow-up study. J Gastroenterol 37(10):807–814

Tsunetomi S, Ohto M et al (1989) Diagnosis of small hepatocellular carcinoma by computed tomography: correlation of CT findings and histopathology. J Gastroenterol Hepatol 4(5):395–404

Tublin ME, Dodd GD 3rd et al (1997) Benign and malignant portal vein thrombosis: differentiation by CT characteristics. AJR Am J Roentgenol 168(3):719–723

Ueda K, Terada T et al (1992) Vascular supply in adenomatous hyperplasia of the liver and hepatocellular carcinoma: a morphometric study. Hum Pathol 23(6):619–626

Valls C, Andia E et al (2002) CT in hepatic cirrhosis and chronic hepatitis. Semin Ultrasound CT MR 23(1):37–61

Valls C, Iannacconne R et al (2006) Fat in the liver: diagnosis and characterization. Eur Radiol 16(10):2292–2308

van den Bos IC, Hussain SM et al (2007) MR imaging of hepatocellular carcinoma: relationship between lesion size and imaging findings, including signal intensity and dynamic enhancement patterns. J Magn Reson Imaging 26(6):1548–1555

Vilgrain V, Lewin M et al (1999) Hepatic nodules in Budd-Chiari syndrome: imaging features. Radiology 210(2): 443–450

Vilgrain V, Boulos L et al (2000) Imaging of atypical hemangiomas of the liver with pathologic correlation. Radiographics 20(2):379–397

Wanless IR (1995) Terminology of nodular hepatocellular lesions. International working party. Hepatology 22(3): 983–993

Wiesner RH, Freeman RB et al (2004) Liver transplantation for hepatocellular cancer: the impact of the MELD allocation policy. Gastroenterology 127(5 Suppl 1):S261–S267

Willatt JM, Hussain HK et al (2008) MR Imaging of hepatocellular carcinoma in the cirrhotic liver: challenges and controversies. Radiology 247(2):311–330

Yamashita Y, Fan ZM et al (1993) Sclerosing hepatocellular carcinoma: radiologic findings. Abdom Imaging 18(4): 347–351

Yang JD, Roberts LR (2010) Epidemiology and management of hepatocellular carcinoma. Infect Dis Clin N Am 24(4): 899–919 viii

Yoon SH, Lee JM et al (2009) Multiphasic MDCT enhancement pattern of hepatocellular carcinoma smaller than 3 cm in diameter: tumor size and cellular differentiation. AJR Am J Roentgenol 193(6):W482–W489

Yoshikawa J, Matsui O et al (1988) Fatty metamorphosis in hepatocellular carcinoma: radiologic features in 10 cases. AJR Am J Roentgenol 151(4):717–720

Yu JS, Kim KW et al (1997) Small arterial-portal venous shunts: a cause of pseudolesions at hepatic imaging. Radiology 203(3):737–742

Yu JS, Kim KW et al (2000a) Nontumorous hepatic arterial-portal venous shunts: MR imaging findings. Radiology 217(3):750–756

Yu JS, Kim KW et al (2000b) Hepatic cavernous hemangioma in cirrhotic liver: imaging findings. Korean J Radiol 1(4): 185–190

Zech CJ, Reiser MF et al (2009) Imaging of hepatocellular carcinoma by computed tomography and magnetic resonance imaging: state of the art. Dig Dis 27(2):114–124

Zheng RQ, Zhou P et al (2004) Hepatocellular carcinoma with nodule-in-nodule appearance: demonstration by contrast-enhanced coded phase inversion harmonic imaging. Intervirology 47(3–5):184–190

Imaging Findings in Non-Cirrhotic Liver

Daniele Marin and Giuseppe Brancatelli

Contents

Abstract

With the widespread use of cross-sectional imaging examinations, physicians from a wide array of specialties are becoming involved with questions regarding the management of patients with focal liver lesions. To formulate a practical approach to these patients, several factors must be incorporated into a clinical decision-making algorithm, including the clinical setting (e.g., known comorbidities, underlying cirrhosis or a known primary neoplasm), the presence of clinical signs and symptoms, the results of laboratory tests, and the critical information provided by imaging studies. In this chapter, we will briefly review important technical factors for optimization of CT protocols for the evaluation of focal liver lesions in non-cirrhotic liver. We will emphasize key features and common pitfalls of most common liver lesions in the setting of non-cirrhotic liver and provide examples about benign and malignant tumors in non-cirrhotic liver.

D. Marin (✉)
Department of Radiology,
Duke University Medical Center, Durham,
NC 27710, USA
e-mail: danielemarin2@gmail.com

G. Brancatelli
Department of Radiology, University of Palermo,
90127 Palermo, Italy

G. Brancatelli
Radiology Unit, La Maddalena Hospital,
90146 Palermo, Italy

1 MSCT Technique

Multi-slice CT (MSCT) has become the most commonly used modality in the preoperative diagnosis, staging, treatment planning, and follow-up of patients with known or suspected hepatic tumors (Sahani and Kalva 2004). With the recent advent of MSCT

C. J. Zech et al. (eds.), *Multislice-CT of the Abdomen*, Medical Radiology. Diagnostic Imaging,
DOI: 10.1007/174_2011_407, © Springer-Verlag Berlin Heidelberg 2012

scanners, substantial anatomic volumes can be acquired within a short scan time, with submillimeter section thickness and virtually no penalty in increased radiation dose. Clinically, these technologic advances have led to image acquisition during peak vascular enhancement with almost uniform enhancement along the entire scanned volume, reduced motion artifacts, and the capability to generate high resolution reformations in any desired plane. In a single examination, MDCT provides detailed morphologic and hemodynamic information on the number, size, distribution, and vascularity of liver lesions, all of which are vital in guiding the clinical decision-making and therapeutic plan.

To maximize the detection and characterization of liver tumors, the CT protocol must be designed according to the diagnostic task. To increase the attenuation difference (i.e., conspicuity) between the hepatic parenchyma and liver tumors, several injection factors need to be optimized, including the volume and iodine concentration of contrast media, the injection rate (4–5 mL/s), and the scanning delay from the start of contrast media administration. Image acquisition should be obtained during the period of maximum vascular and/or hepatic parenchymal enhancement (Baron 1994). This requires application of contrast agent bolus timing methods—either automatic computer-assisted bolus tracking or test bolus—to correct for differences in circulation times in individual patients.

Unlike hepatic parenchyma, predominantly fed by the portal vein, liver tumors receive blood supply from the hepatic arterial system. Most tumors are best seen during the hepatic venous phase (HVP) (approximately 60–70 s after the start of contrast media injection), when the maximal difference in attenuation is attained between the vividly enhancing hepatic parenchyma and hypo attenuating lesions (Foley et al. 2000).

For certain specific clinical settings, HVP imaging must be preceded by a contrast-enhanced acquisition during the hepatic arterial dominant phase (HAP). This phase is crucial in the detection of those liver tumors (most notably, hepatocellular nodules, hypervascular liver metastases, and hemangiomas) that receive abundant arterial supply (Foley et al. 2000). These lesions manifest as hyperattenuating foci during HAP, but may not be detected during the HVP due to increasing liver enhancement from portal venous blood supply.

By taking advantage of two-dimensional (2D) reformation and three-dimensional (3D) rendering techniques, the HAP images also enable noninvasive preoperative mapping of the normal hepatic arterial anatomy and common anatomic variants. This information is crucial in patients who are candidates for liver surgery (e.g., transplantation, tumor resection or laparoscopic hepatobiliary surgery), transcatheter arterial chemoembolization, or hepatic arterial infusion chemotherapy (Catalano et al. 2008; Kapoor et al. 2003).

In selected cases, CT protocol should include additional acquisitions either before or after contrast material administration, during a more delayed phase of enhancement, approximately 3–10 min after the start of contrast injection. Unenhanced acquisitions are helpful for the characterization of liver lesions with inherently high attenuation due to calcification, hemorrhage, and iron or glycogen increased accumulation. Unenhanced images are also necessary for detection of areas of lower attenuation, such as in the setting of fat deposition, edema, and necrosis. Many institutions recommend acquisition of unenhanced images in addition to post-contrast acquisitions for patients with cirrhosis and during baseline evaluation of oncology patients (Baron and Brancatelli 2004; Oliver et al. 1997).

Delayed phase images plays a key role in the diagnosis of liver lesions with a prominent fibrous component, such as cholangiocarcinoma, focal confluent fibrosis, cavernous hemangioma, and other liver tumors that may manifest with a central scar. On delayed phase images, these lesions demonstrate prolonged enhancement in the fibrous tissue component, which appears relatively hyperattenuating compared to the surrounding liver (Lacomis et al. 1997; Ohtomo et al. 1993).

2 Benign Liver Lesions in Non-Cirrhotic Liver

With the widespread use of sensitive imaging studies, benign hepatic tumors are increasingly reported. Most benign hepatic tumors are an incidental finding in asymptomatic patients during imaging work-up for an

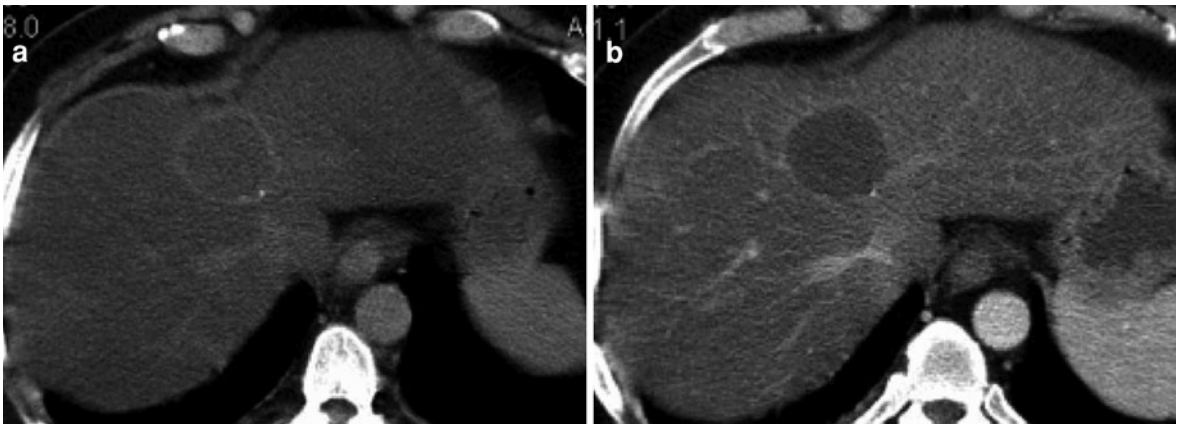

Fig. 1 Simple hepatic cyst in fatty liver. **a** Transverse unenhanced CT image demonstrates a 4 cm lesion in segment 4 showing isoattenuation compared to the surrounding liver. Lesion attenuation measured +9 HU, compatible with simple fluid. Note diffuse low attenuation of the liver relative to the spleen (S), consistent with hepatic steatosis. Also note the peripheral hyperattenuating rim of fatty sparing around the lesion. **b** Corresponding contrast-enhanced CT image shows no enhancement, internal debris, or wall irregularities in the lesion

unrelated medical problem. Notably, even in patients with a known primary malignancy, about 50% of small (<2.0 cm) hepatic lesions are benign (Khalil et al. 2005).

Besides lesion detection, the main goal of CT is to firmly establish a diagnosis of benign hepatic tumors. Mistaking an incidental benign lesion for a malignant tumor may lead to unnecessary, aggressive management, or possibly preclude surgery when benign and malignant lesions coexist within the same liver. In the great majority of cases, imaging provides important clues for a confident diagnosis of frequently encountered benign lesions. Occasionally, imaging findings may remain indeterminate or suggestive of malignancy. In these cases, liver biopsy is often necessary to establish a definite diagnosis.

3 Simple (Nonparasitic) Cysts

Simple (nonparasitic) cyst is the result of a congenital defective development of the intrahepatic biliary ducts. Simple cysts are among the most common liver lesion with an estimated incidence of 3% in the general population. Typically, cysts are an incidental finding in asymptomatic patients. These lesions may be solitary or multiple and manifest as well-defined fluid attenuating lesions, varying in size from few millimeters to several centimeters. When more than ten simple cysts are identified in the liver, fibropolycystic disease should be considered, such as biliary hamartomas or autosomal dominant fibropolycystic liver disease. Cysts do not communicate with the biliary tree and typically contain clear fluid. At histology, the cyst lining consists of a single layer of bile duct epithelium.

At unenhanced CT, cysts manifest as rounded or oval shaped, thin-walled, well-defined, water attenuating (from −10 to +10 HU) lesions (Fig. 1). When cysts are smaller than 1.0 cm, reliable attenuation measurements cannot be obtained and lesions remain indeterminate at imaging (Mortelé et al. 2001). The majority of hepatic cysts are unilocular, although occasionally one or two thin septa may be seen. Rarely, cysts may demonstrate increased attenuation and heterogeneous appearance due to hemorrhage or infection. In these cases, differential diagnosis with hepatic abscess or cystic liver tumors (e.g., biliary cystadenoma or cystadenocarcinoma, and cystic metastases) cannot be made at imaging. Cyst may also show relatively higher attenuation compared to the surrounding liver in the setting of severe fatty liver disease (Fig. 1). At contrast-enhanced CT, no contrast enhancement is demonstrated in both the cystic content and peripheral wall (Mortelé et al. 2001; Fig. 1).

Simple cysts should be managed conservatively. Surgery or percutaneous catheter drainage with alcohol sclerosis may be indicated in rare cases of patients with large, symptomatic cysts.

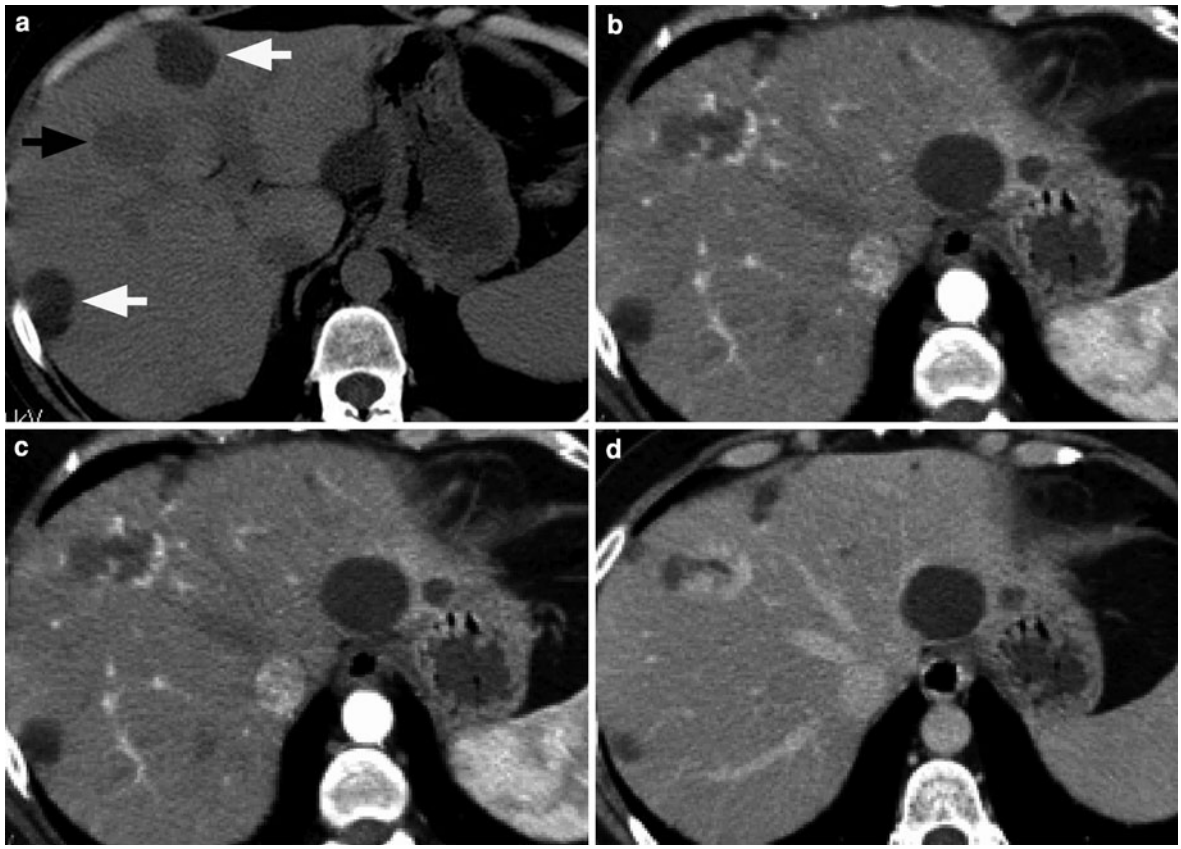

Fig. 2 Hepatic hemangioma and simple hepatic cysts. **a** Transverse unenhanced CT image demonstrates two water density lesions (*white arrows*), consistent with simple hepatic cysts, and a third low attenuation indeterminate lesion (*black arrow*) in the right liver. **b** Corresponding contrast-enhanced CT image during hepatic arterial phase shows lack of enhancement of the two cysts and early, discontinuous, peripheral nodular enhancement of the third lesion, which progresses centripetally toward near complete filling during the (**c**) hepatic venous and (**d**) delayed phases. Findings are characteristic of hepatic cavernous hemangioma

4 Hepatic Cavernous Hemangioma

Hepatic cavernous hemangioma is a common benign congenital lesion. With an estimated incidence of 5–20% in the general population, hemangioma is the most common benign hepatic tumor. This tumor is more frequently encountered in middle-aged women, suggesting a possible causative effect of female sex hormones. In most cases, hemangioma is an incidental finding in asymptomatic patients. Occasionally, larger lesions may cause signs and symptoms related to mass effect, such as upper abdominal mass, abdominal discomfort, and pain. Giant hemangiomas (defined as lesions >10 cm) may also cause thrombocytopenia and consumptive coagulopathy due to blood pooling within the dilated sinusoids of the tumor.

With the exception of patients with fatty liver disease, hemangioma manifests as hypoattenuating lesion relative to the liver at unenhanced CT. Central coarse calcifications may be identified in giant hemangiomas. At contrast-enhanced CT, hemangioma demonstrate a characteristic enhancement pattern with early, discontinuous, peripheral nodular enhancement, which progresses centripetally toward uniform filling (Nelson et al. 1990; Quinn and Radiology 1992; Fig. 2). By definition, the areas of contrast enhancement are

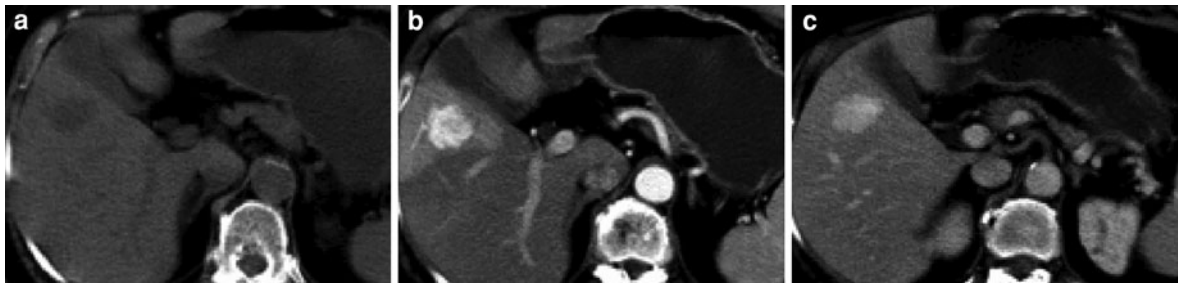

Fig. 3 Capillary (flash filling) hemangioma. **a** Transverse unenhanced CT image demonstrates a low attenuation lesion in segment V, adjacent to the gallbladder fossa. **b** Corresponding contrast-enhanced CT image during hepatic arterial phase shows uniform vivid enhancement of the lesion. Note peripheral wedge-shaped homogeneously hyperattenuating area adjacent to the lesion, consistent with a transient hepatic attenuation difference due to arterioportal shunt. **c** Corresponding contrast-enhanced CT image during hepatic venous phase demonstrates sustained enhancement of the lesion comparable to the vessels. Findings are suggestive of capillary (flash filling) hemangioma. Note the perilesional area of transient hepatic attenuation difference is not discernible on this more delayed contrast-enhanced phase

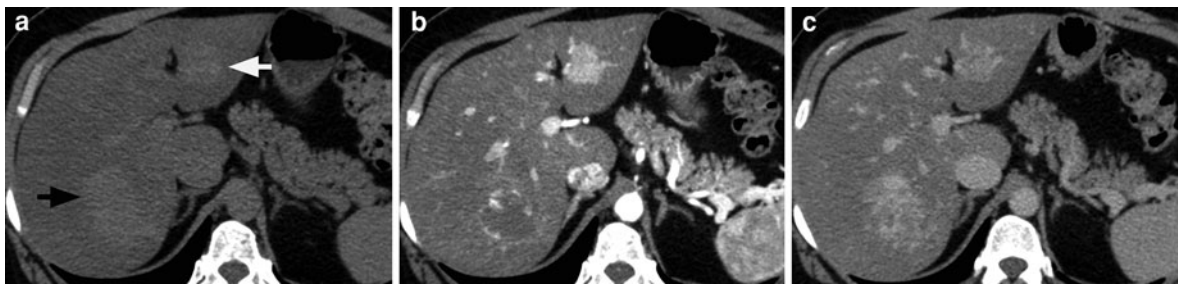

Fig. 4 Focal nodular hyperplasia and hepatic hemangioma. **a** Transverse unenhanced CT image demonstrates two hyperdense lesions, one lesion in the right hepatic lobe (*black arrow*) and the other in the left hepatic lobe (*white arrow*). Note attenuation of the liver is lower than that of the intrahepatic vessels, consistent with hepatic steatosis. **b** Corresponding contrast-enhanced CT image during hepatic arterial phase shows early, discontinuous, peripheral nodular enhancement of the lesion on the right lobe, suggestive of hepatic hemangioma, and uniform vivid enhancement of the lesion on the left lobe. **c** Corresponding contrast-enhanced CT image during hepatic venous phase demonstrates nearly homogenous enhancement of the lesion on the right lobe, which is consistent with hemangioma. The lesion on the left lobe shows sustained enhancement, fading toward isoattenuation compared to the surrounding liver. Findings are suggestive of focal nodular hyperplasia. No central scar is identified likely due to the small size (<3.0 cm) of the tumor. Association of hepatic hemangioma and focal nodular hyperplasia is not uncommon on cross-sectional imaging

isodense to the blood pool vessels. Giant hemangiomas usually lack complete enhancement on delayed phase images due to thrombosis or sclerosis of the central portion of the tumor.

Small hemangiomas (<2.0 cm)—commonly referred to as capillary hemangiomas or flash filling hemangiomas—may enhance rapidly and homogeneously during HAP (Fig. 3), mimicking other either benign or malignant hypervascular liver tumors (Kim et al. 2001). Transient peritumoral enhancement during the HAP is frequently observed due to associated arterio-venous shunt (Byun et al. 2004; Fig. 3).

Hepatic cavernous hemangiomas should be managed conservatively. Larger lesions may require surgery (i.e., enucleation or liver resection) if clinically symptomatic.

5 Focal Nodular Hyperplasia

Focal nodular hyperplasia (FNH) is a hyperplastic response of the hepatic parenchyma to a congenital or acquired anomaly of the arterial blood supply leading to focal hyperperfusion (Wanless et al. 1985). FNH

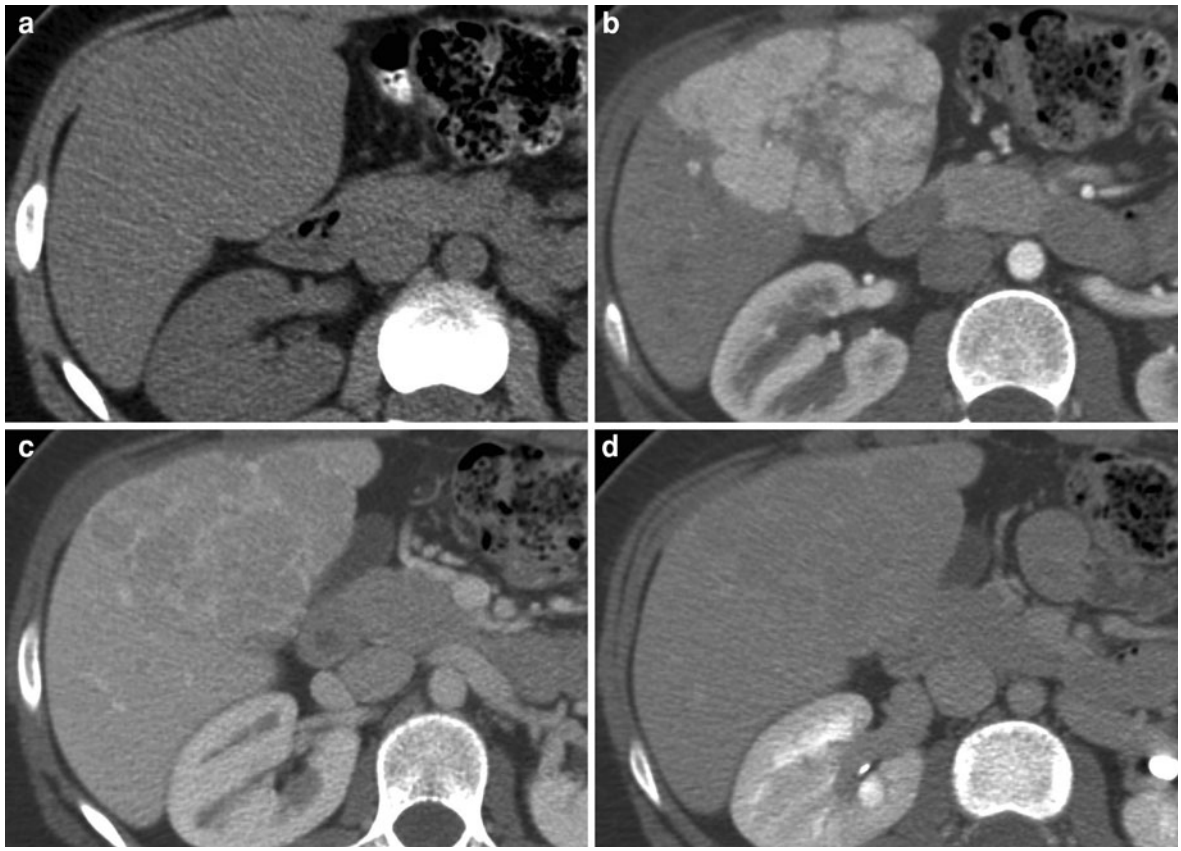

Fig. 5 Classic focal nodular hyperplasia. **a** Transverse unenhanced CT image demonstrates an expanding mass in the inferior tip of the right liver lobe. Lesion shows isoattenuation relative to the surrounding liver. **b** Corresponding contrast-enhanced CT image during hepatic arterial phase shows uniform vivid enhancement of a large hepatic lesion. Note irregular central scar and radiating septa manifesting as linear hypodense areas within the tumor. Corresponding contrast-enhanced CT image during (**c**) hepatic venous and (**d**) delayed phases demonstrate with isoattenuation relative to the surrounding liver, consistent with focal nodular hyperplasia. Note delayed increased enhancement of the central scar relative to the lesion

occurs most frequently in childbearing women (male-to-female ratio is 1:8). After hemangioma, FNH is the second most common benign tumor of the liver with an estimated incidence of 3–8% in the general population. Unlike hepatic adenoma, oral contraceptives do not play a causative role in the development of FNH, although data suggests possible lesion growth in patients taking oral contraceptives or anabolic hormones. Typically, FNH is an incidental finding in asymptomatic patients. Larger lesions may cause abdominal discomfort and pain due to mass effect.

At unenhanced CT, FNH is generally isoattenuating relative to the surrounding liver. In the setting of diffuse fatty liver disease, FNH may show high attenuation due to decreased density of the surrounding liver (Fig. 4). FNH demonstrates a characteristic enhancement pattern with vivid enhancement during the HAP followed by isoattenuation relative to the adjacent liver during the HVP and delayed phase (Brancatelli et al. 2001; Choi et al. 1998; Figs. 4, 5). This enhancement pattern reflects the rich arterial blood supply of FNH and differentiates this benign lesion from common malignant hypervascular liver tumors, which show faster contrast

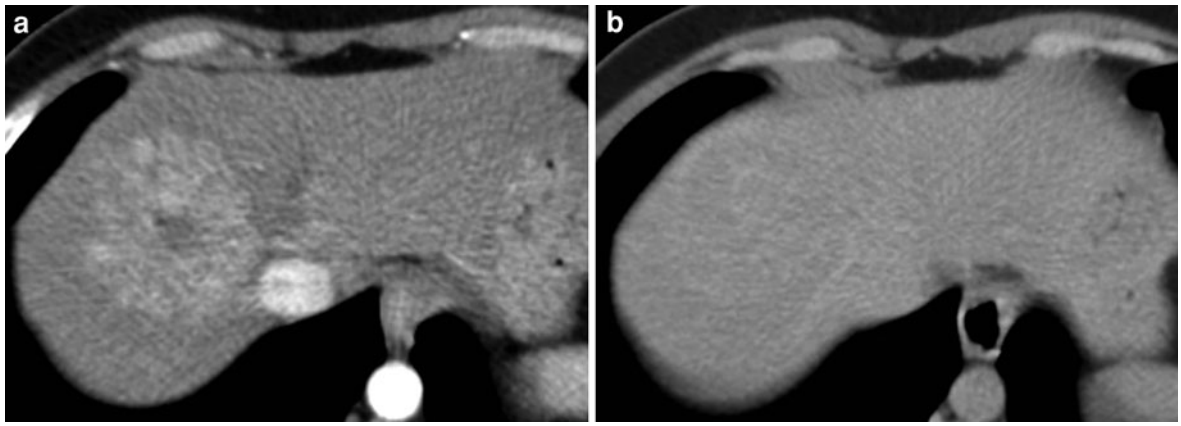

Fig. 6 Atypical focal nodular hyperplasia. **a** Transverse contrast-enhanced CT image during hepatic arterial phase demonstrates a large lesion in the right hepatic lobe, which shows uniform vivid enhancement with the exception of a central scar. **b** Corresponding contrast-enhanced CT image during delayed phase (5 min after intravenous contrast material administration) shows isoattenuation of the lesion relative to the surrounding liver, but no delayed enhancement of the central scar

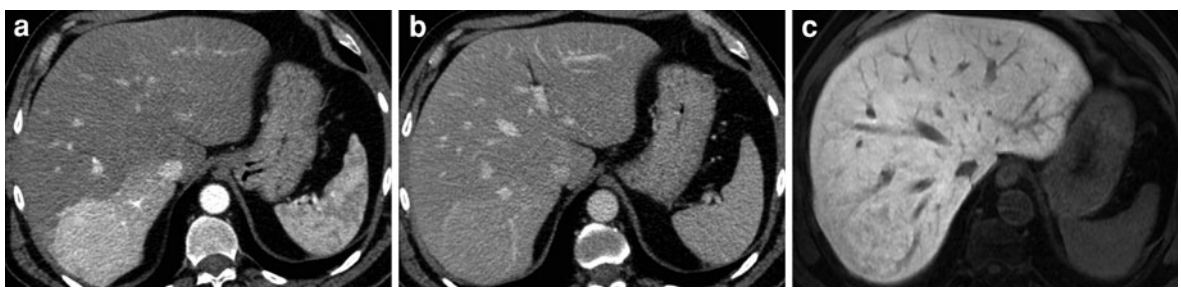

Fig. 7 Atypical focal nodular hyperplasia. **a** Transverse contrast-enhanced CT image during hepatic arterial phase demonstrates a large lesion in the posterior right hepatic lobe, which demonstrates uniform vivid enhancement. No central scar is identified. **b** Corresponding contrast-enhanced CT image during hepatic venous shows isoattenuation of the lesion relative to the surrounding liver and thin peripheral hyperattenuating rim mimicking a pseudocapsule. **c** Transverse gadoexetate dimeglumine-enhanced fat-suppressed T1-weighted gradient-echo image during the liver-specific phase demonstrates homogenous uptake of the hepatobiliary contrast agent by the lesion, which is comparable with that of the surrounding liver. Findings are consistent with focal nodular hyperplasia

washout compared to the liver over time. Delayed enhancement of a central fibrous scar (frequently seen in larger lesions) is another characteristic imaging finding of FNH (Fig. 5).

Although most lesions can be confidently diagnosed based on characteristic imaging appearance, occasionally FNH may show atypical imaging findings, including washout (i.e., hypoattenuating to liver parenchyma) during the PVP and equilibrium phases, peripheral rim enhancement, absence of a central scar (particularly for lesions <3.0 cm), or lack of delayed enhancement of the central scar (Fig. 6). Atypical FNH may simulate either primary or secondary hypervascular malignant liver tumors, thus prompting further investigation with close imaging follow-up or, in some cases, liver biopsy. Recently, liver-specific MR contrast agents have shown the potential to provide additional clues, which may help in the diagnosis of atypical FNH lesions (Grazioli et al. 2001; Fig. 7).

Due to the lack of malignant potential and extremely low complication-rate, FNH is managed conservatively.

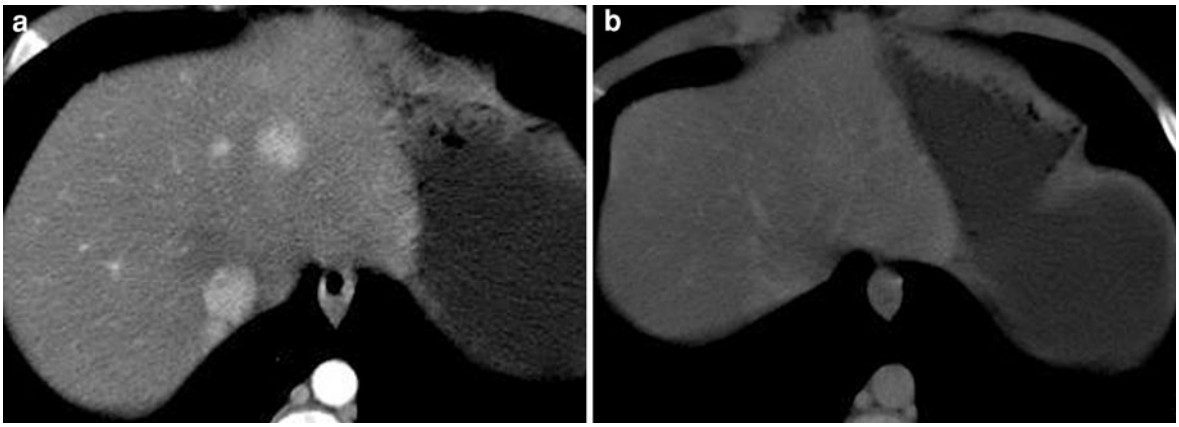

Fig. 8 Large regenerative nodules. **a** Transverse contrast-enhanced CT image during hepatic arterial phase demonstrates two liver lesions showing uniform vivid enhancement. **b** Corresponding contrast-enhanced CT image during hepatic venous shows isoattenuation relative to the surrounding liver. Focal nodular hyperplasia would demonstrate identical appearance on dynamic CT. When imaging findings are typical, no follow-up or aggressive management is warranted

6 Large Regenerative Nodules

Large regenerative nodules (LRN) represent a compensatory response of the liver in the setting of impaired hepatic perfusion. Several hepatic vascular disorders may foster the development of LRN, most notably Budd–Chiari syndrome, hereditary hemorrhagic telangectasia, congenital portosystemic shunt, and congenital hepatic fibrosis (Kondo 2001). Although LRN nodules are relatively rare, their reported frequency is raising as a result of higher-resolution contrast-enhanced CT and MR imaging performed with multiphasic acquisition protocols. Patients with LRN are generally asymptomatic, although portal hypertension and hepatic failure have been reported in rare cases.

Imaging findings of LRN closely overlap with those of FNH. At unenhanced CT, LRN are isoattenuating compared with the surrounding liver. At contrast-enhanced CT, lesions demonstrate vivid, homogeneous enhancement during the HAP with sustained enhancement during HVP and delayed phase (Brancatelli et al. 2002a, c; Vilgrain et al. 1999; Fig. 8). Other common, but less distinctive features of LRN are the tendency to multifocality, well-circumscribed margins, smooth surface, and homogeneous appearance. Another characteristic, although not always identified finding of LRN is a thin perilesional hypointense halo, best seen during HAP. This finding differs from the pseudocapsule of HCC, which manifests as a thin rim of perilesional enhancement, only seen during HVP and delayed phase.

LRN are managed conservatively.

7 Hepatocellular Adenoma and Adenomatosis

Hepatocellular adenoma is a typical lesion of reproductive age women (male-to-female ratio is 1:10). Although the pathogenesis of adenoma remains uncertain, estrogen-containing or androgen-containing medications have shown to play an important in lesion development and growth. The incidence of adenoma is also increased in patients with glycogen storage disease for unknown reasons. Liver adenomatosis is a clinical syndrome characterized by multiple adenomas (by definition more than 10) without known predisposing factors (Grazioli et al. 2000). Although generally asymptomatic, patients with large lesions may present with abdominal pain or, in rare cases, hypovolemic shock secondary to hemorrhage. Malignant degeneration may rarely develop within adenoma. Lesion complications occur more frequently with a subgroup of adenomas, called telangiectatic adenomas.

At precontrast CT, adenoma manifest as a large, heterogeneous mass due to variable extent of hemorrhage, necrosis, and calcification (Ichikawa et al. 2000).

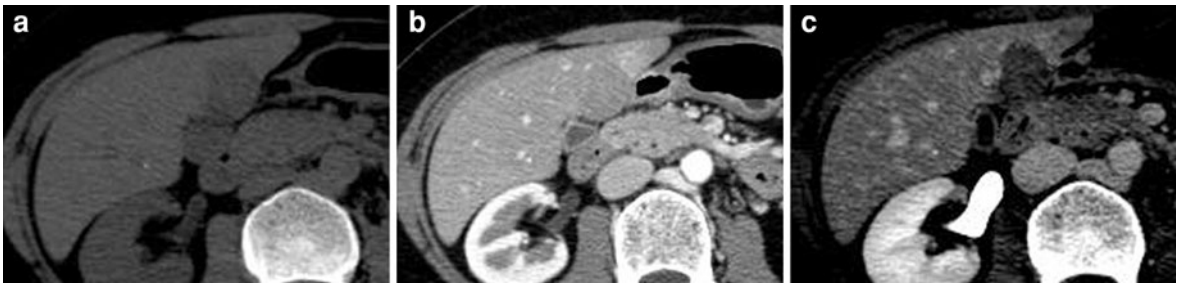

Fig. 9 Hepatic adenoma. **a** Transverse unenhanced CT image demonstrates no definite liver abnormalities. **b** Corresponding contrast-enhanced CT image during hepatic arterial phase shows a small (<3.0 cm) subcapsular lesion in segment 4, which demonstrates mild uniform enhancement. **c** Corresponding contrast-enhanced CT image during delayed phase demonstrates lesion washout with relative hypoattenuation compared to the surrounding liver. The latter findings was concerning for a malignant hypervascular liver tumor and prompted further investigation with biopsy. Hepatic adenoma with no signs of malignant degeneration was demonstrated at histopathological analysis

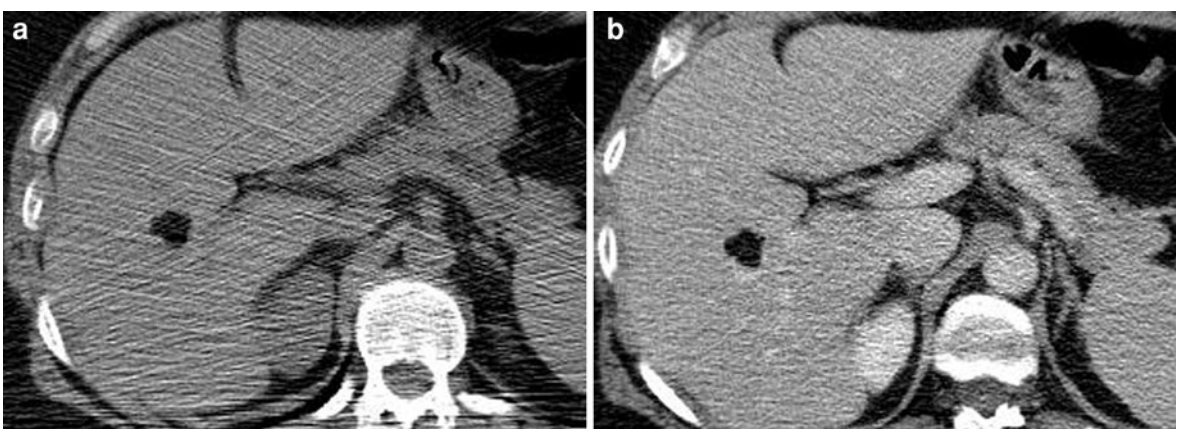

Fig. 10 Hepatic lipoma. **a** Transverse unenhanced CT image demonstrates a small, well-circumscribed, fat density lesion in the right hepatic lobe. **b** Corresponding contrast-enhanced CT image during hepatic venous shows lack of enhancement of the lesion, consistent with lipoma. Purely fat containing angiomyolipoma would have identical appearance on CT

Small lesions tend to be homogeneous in appearance and are commonly iso or slightly hypoattenuating relative to the surrounding normal liver. Lesions may be hyperattenuating in the setting of diffuse fatty liver disease. The presence of internal areas of fat deposition is another distinctive feature of adenoma. MR imaging using in-phase and opposed-phase chemical shift gradient-echo imaging is more sensitive than CT for the detection of intracellular fat. At contrast-enhanced CT, adenomas demonstrate heterogeneously mildly increased enhancement compared with the surrounding liver during HAP with inconsistent washout during PVP and delayed phase (Ichikawa et al. 2000; Fig. 9). Differential diagnosis between adenomas and hepatocellular carcinoma or other malignant hypervascular lesions is not possible based on imaging findings, thus warranting lesion biopsy in most cases.

Discontinuation of steroid medication may be indicated for conservative management of small adenomas. Due to increased risk of complications (i.e., rupture or malignant transformation), surgical resection is warranted for larger lesions.

8 Angiomyolipoma and Lipoma

Angiomyolipoma and lipoma are rare benign mesenchymal tumors of the liver. Angiomyolipoma is composed of variable amounts of smooth muscle, fat,

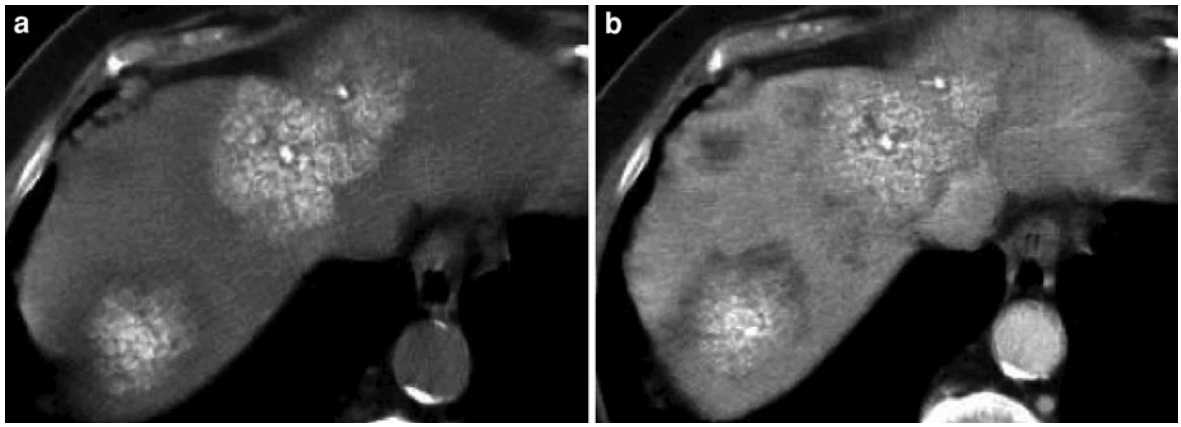

Fig. 11 Calcified metastatic liver lesions from mucinous colorectal cancer. **a** Transverse unenhanced CT image demonstrates two large predominantly calcified masses and a subtle, noncalcified, low attenuation lesion in the right hepatic lobe. **b** Corresponding contrast-enhanced CT image during hepatic venous shows increased conspicuity of the noncalcified lesion and peripheral hypodense rim in the two calcified lesions. Findings are suggestive of metastatic disease from a primary mucinous tumor (e.g., colon or ovarian cancer). Metastatic disease from other primary tumors could also demonstrate a similar appearance after chemotherapy treatment

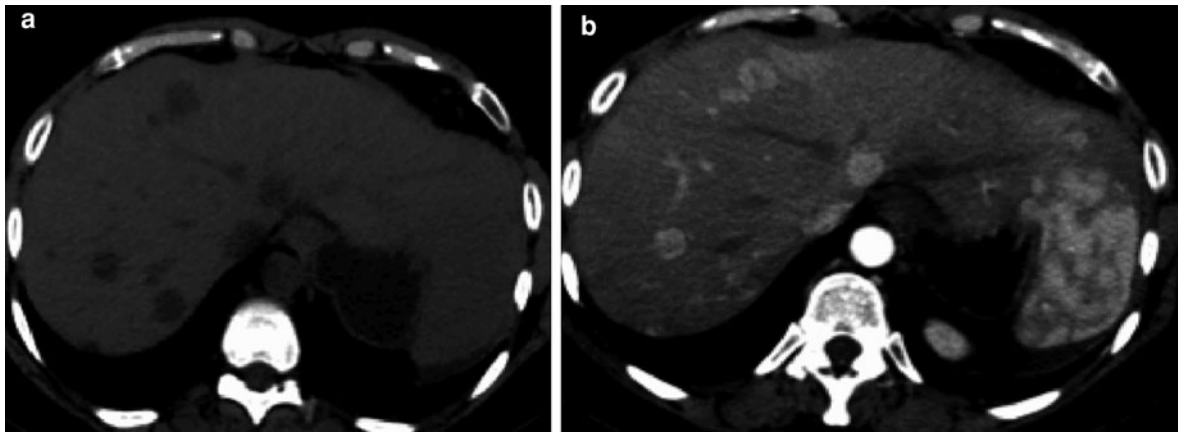

Fig. 12 Hypervascular metastatic liver lesions from neuroendocrine tumor of the pancreas. **a** Transverse unenhanced CT image demonstrates two subtle low attenuation lesions in the right liver lobe. **b** Corresponding contrast-enhanced CT image during hepatic arterial phase shows vivid enhancement of the lesions, as well as a third subcentimeter lesion in the left hepatic lobe

and proliferating blood vessels. Association with tuberous sclerosis is described in 10% of cases.

At unenhanced CT, angiomyolipoma demonstrate coexistence of both fat and soft tissue components that vary in relative extent in different patients. Occasionally, tumor may demonstrate dominance of a single component, mimicking either hepatic lipoma (dominance of fat tissue) or other hypervascular liver tumors (dominance of smooth muscle and blood vessels component) (Fig. 10).

9 Malignant Liver Lesions in Non-Cirrhotic Liver

Thin-section contrast-enhanced MSCT is the preferred imaging modality for the preoperative detection, staging, treatment planning, and follow-up of patients with malignant liver lesions. Furthermore, MSCT plays a pivotal role during imaging follow-up of patients with treated liver tumors, where it allows

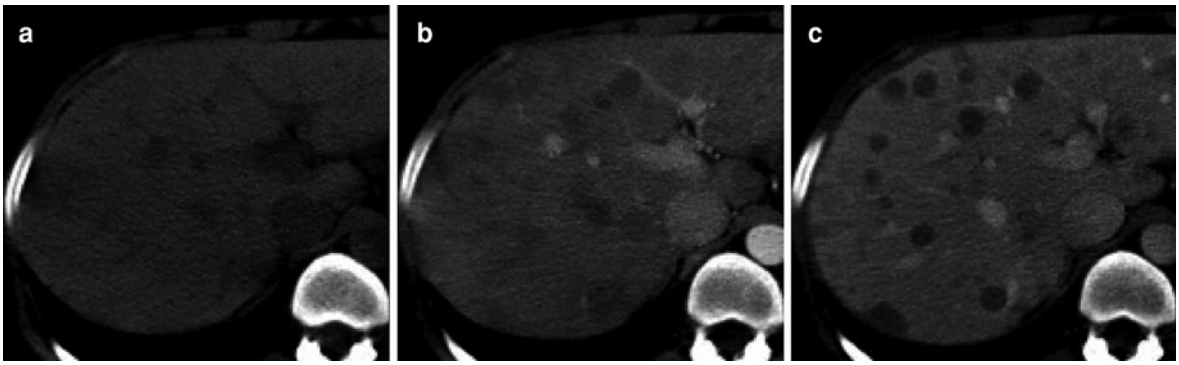

Fig. 13 Hypovascular metastatic liver lesions from cutaneous melanoma. **a** Transverse unenhanced CT image demonstrates subtle heterogeneous appearance of the liver without discrete lesions. **b** Corresponding contrast-enhanced CT image during hepatic arterial phase shows multiple low attenuation lesions in both hepatic lobes, which increase in both number and conspicuity during (**c**) the hepatic venous phase. Findings are consistent with multifocal disseminated hypovascular liver metastases

prompt identification of procedure-related complications, tumor recurrence, and differentiation of therapy responders from nonresponders (Valls et al. 2001). The latter information is critical for timely discontinuation or change of chemotherapy regimen, resulting in improved patient's survival, quality of life, and decreased costs.

10 Hepatic Metastases

Metastases are by far the most common malignant neoplasm of the liver, with an incidence of 40% in cancer patients at the time of death. The most common primary sites for liver metastases include the gastrointestinal tract, pancreas, gallbladder, breast, lung, eye, and carcinoids. Although liver metastases are fed primarily by arterial blood supply, they have been arbitrarily classified as hypervascular or hypovascular according to their enhancement pattern relative to that of the surrounding liver at MSCT (Foley et al. 2000).

At unenhanced CT, metastases are commonly difficult to identify demonstrating variable appearance (Namasivayam et al. 2007; Kanematsu et al. 2006). Two notable exceptions are the presence of prominent areas of calcifications in mucinous adenocarcinoma metastases (i.e., colon-rectum or ovary) (Fig. 11) and the nearly complete cystic degeneration that may occur after chemotherapy, particularly in gastrointestinal stromal tumors treated with new antiangiogenic therapies. At contrast-enhanced CT, hypervascular

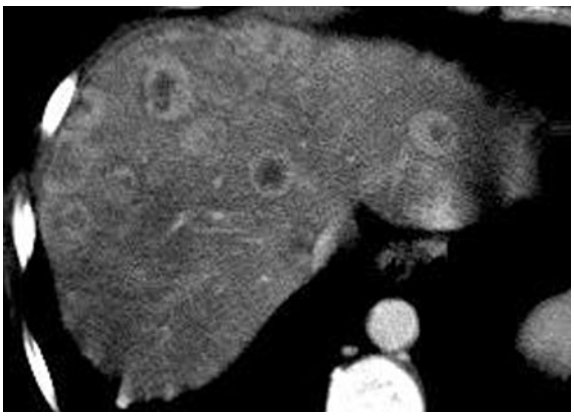

Fig. 14 Ring enhancement of metastatic liver lesions from breast cancer. Transverse contrast-enhanced CT image during hepatic venous demonstrates multiple liver lesions showing continuous peripheral rim of enhancement and hypodense necrotic center, consistent with multifocal metastatic liver disease. This enhancement pattern differs substantially from the discontinuous nodular enhancement pattern of hepatic hemangioma

metastases, such as those from neuroendocrine tumors, thyroid, renal cell carcinoma, pheocromocytoma, and occasionally, breast, melanoma, and gastrointestinal stromal tumors, are best depicted during the HAP as hyperattenuating foci compared with the surrounding liver (Fig. 12). Hypovascular liver metastases, which encompass the vast majority of cases (e.g., colorectal tumor metastases), manifest as hypoattenuating lesions best seen during the HVP when the maximum enhancement of hepatic parenchyma is attained (Fig. 13). An early, continuous,

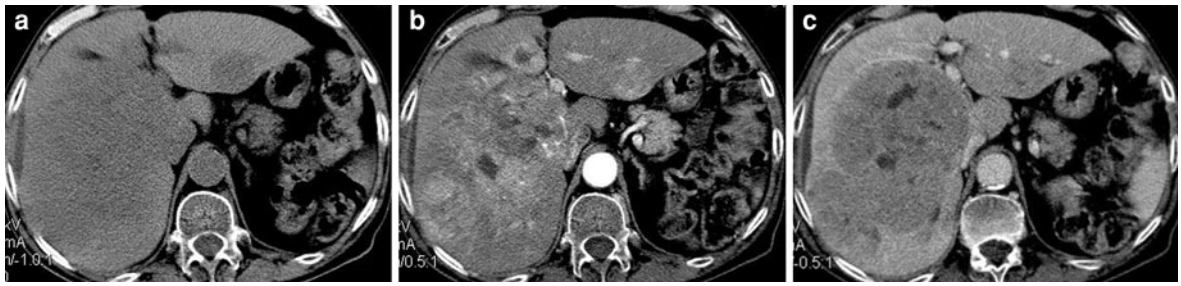

Fig. 15 Hepatocellular carcinoma in noncirrothic liver. **a** Transverse unenhanced CT image demonstrates a large hypodense mass occupying most of the right hepatic lobe as well as a smaller lesion with similar appearance in the left hepatic lobe. **b** Corresponding contrast-enhanced CT image during hepatic arterial phase shows mild heterogeneous enhancement of the tumor due to presence of areas of viable tissue and necrosis. Note smaller hypervascular satellite lesion in the left liver lobe. **c** On hepatic venous phase, both lesions demonstrate unequivocal washout showing hypoattenuation compared to the surrounding liver, a classic finding of hepatocellular carcinoma

peripheral rim of enhancement is also a classic finding of hypovascular liver metastases, reflecting highly vascularised viable tumor at the periphery of the lesion (Yu et al. 2006; Fig. 14). This sign differs from the typically discontinuous nodular peripheral enhancement of hemangiomas.

11 Hepatocellular Carcinoma in Non-Cirrhotic Liver

Hepatocellular carcinoma (HCC) is the most common primary malignant liver tumor. Although HCC develops classically in the setting of cirrhosis, particularly in patients with chronic hepatitis viral infection, recent evidence suggests that in a significant minority of cases (approximately 20%) HCC may arise in an otherwise normal liver (Brancatelli et al. 2002b). The demographic characteristics, imaging manifestations, and prognosis of HCC in non-cirrhotic liver differ substantially from those of HCC in cirrhosis. Patients are generally younger and have a longer survival rate. Since the disease course is generally indolent and tumor surveillance is not performed, HCC in non-cirrhotic liver tend to manifest as large lesions at diagnosis. Abdominal pain due to mass effect, weight loss, and anorexia are common symptoms referred by patients at diagnosis. In a consistent number of patients, HCC may be incidentally discovered at imaging studies for unrelated reasons. Despite the large size, most HCC arising in non-cirrhotic liver are well to moderately differentiated at histopathological analysis, thus explaining the generally favorably prognosis in these patients.

At unenhanced CT, HCC manifest as a large dominant lesion that is hypoattenuating compared with the surrounding liver (Fig. 15; Brancatelli et al. 2002b). Peripheral calcification may be seen. At contrast-enhanced CT, lesions show mild, heterogeneous enhancement during HAP followed by washout during HVP and delayed phase (Fig. 15; Brancatelli et al. 2002). Areas of necrosis or hemorrhage are common findings within these lesions, which are best seen on unenhanced CT images. Tumor invasion of the portal vein, hepatic veins, and biliary ducts are common.

Radical surgery with curative intent is the treatment of choice for HCC in non-cirrhotic liver.

12 Fibrolamellar HCC

Fibrolamellar HCC is a rare primary hepatic malignancy. Although this tumor differs from conventional HCC at histopathological analysis, fibrolamellar HCC demonstrates many overlapping clinical and imaging characteristics with HCC in non-cirrhotic liver (McLarney et al. 1999). Fibrolamellar HCC occurs in young patients without cirrhosis. Although tumor is generally identified at more advanced stages due to its indolent slow growth, it is associated with more favorable prognosis than that of HCC in cirrhosis.

At unenhanced CT, fibrolamellar HCC manifest as hypoattenuating large liver mass (McLarney et al. 1999; Ichikawa et al. 1999). Demonstration of a

central fibrous scar with radiating septa and coarse calcifications is a very distinctive feature of fibrolamellar HCC. At contrast-enhanced CT, fibrolamellar HCC shows well-defined contour and lobulated margins with heterogeneous enhancement (McLarney et al. 1999; Ichikawa et al. 1999). During HVP and delayed phase, tumor demonstrates washout becoming hypoattenuating compared with the surrounding liver. Notably, unlike other benign liver tumors with a central scar (e.g., FNH), there is no delayed enhancement of the central fibrous scar in fibrolamellar HCC (Blachar et al. 2002). Coexistence of multiple bulky lymphadenopathy in the porta hepatis and the anterior cardiophrenic angles is identified in more 50% of patients at the time of diagnosis.

Radical surgery with curative intent is the treatment of choice for fibrolamellar HCC.

13 Hepatocellular Cholangiocarcinoma

Combined hepatocellular cholangiocarcinoma (cHCC-CC) is an uncommon tumor accounting for 1–7% of the primary hepatic cancers. This tumor may occur in the setting of cirrhosis and demonstrates an aggressive course with almost invariably poor outcome (Jarnagin et al. 2002). Diagnosis of cHCC-CC is based on demonstration within the same lesion of areas of both hepatocellular differentiation and cholangiocellular differentiation at histopathological analysis.

At imaging shows nonspecific imaging findings (Ebied et al. 2003). Typically, there is coexistence of areas of arterial enhancement, suggestive of HCC, along with other areas of delayed enhancement and capsular retraction consistent with cholangiocarcinoma. The relative extent of these two components may vary substantially among different patients.

Radical surgery with curative intent is the treatment of choice for cHCC-CC.

14 Epithelioid Haemangioendothelioma

Epithelioid haemangioendothelioma (EHE) is a low-grade malignant vascular neoplasm with an intermediate clinical course between that of cavernous hemangioma and malignant angiosarcoma. EHE shows slight female predominance (male-to-female ratio is 2:3) and peak incidence around 50 years of age. Clinical signs and symptoms are nonspecific, including weakness, anorexia, weight loss, and upper abdominal discomfort.

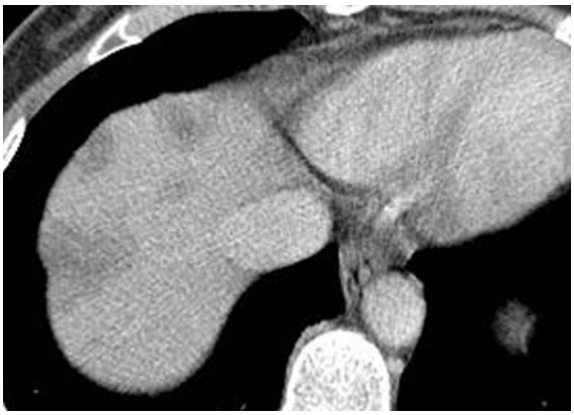

Fig. 16 Epithelioid haemangioendothelioma. Transverse contrast-enhanced CT image during the hepatic venous demonstrates multiple peripheral liver lesions showing characteristic target-type enhancement pattern (the so-called, bull's eye appearance), with central hypoattenuating area surrounded by a peripheral thick enhancing ring and outer hypoattenuating halo

At unenhanced CT, EHE manifests as multiple hypoattenuating masses compared with the liver (Miller et al. 1992; Mermuys et al. 2004; Fig. 16). With increasing size, lesions may become partially confluent. Capsular retraction is a common distinctive finding of EHE that occur when lesions abut the liver surface. At contrast-enhanced CT, EHE shows characteristic target-type enhancement pattern (the so-called, bull's eye appearance) with a central hypoattenuating area, corresponding to central fibrous core, surrounded by a peripheral thick enhancing ring and outer hypoattenuating halo, corresponding to peripheral viable tumor and avascular transition zone, respectively (Miller et al. 1992; Mermuys et al. 2004).

Liver transplantation is sometimes offered to patients with EHE.

15 Angiosarcoma

Angiosarcoma is the most common sarcoma of the liver. The peak age incidence is in the sixth and seventh decades, with a male-to-female ratio of 3:1.

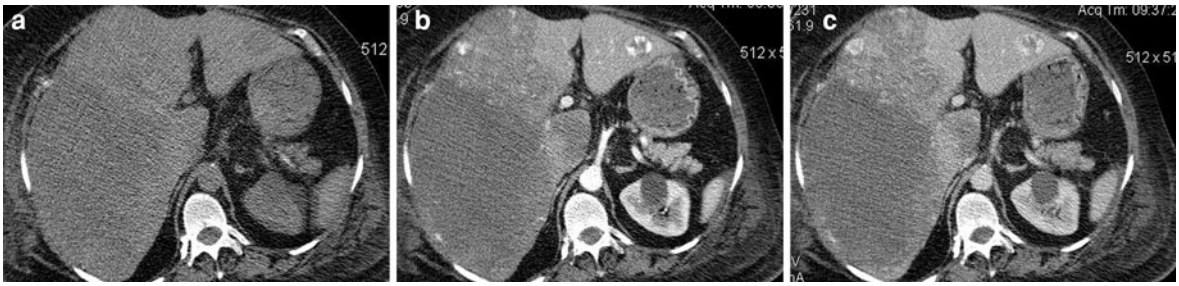

Fig. 17 Hepatic angiosarcoma. **a** Transverse unenhanced CT image during the hepatic venous demonstrates a large hypodense mass occupying most of the right hepatic lobe. Corresponding contrast-enhanced CT image during (**b**) hepatic arterial and (**c**) hepatic venous phases shows minimal enhancement of the lesion. Findings are nonspecific and lesion biopsy was performed demonstrating angiosarcoma at histopathological analysis

Several conditions have been associated with the development of angiosarcoma of the liver, including hemochromatosis, von Recklinghausen's disease, and environmental carcinogens (i.e., vinyl chloride thorium dioxide and arsenic). However, tumor develops in patients without known associated risk factors.

At unenhanced CT, angiosarcoma demonstrates isoattenuation to the abdominal vessels. Focal hyperattenuating areas can be seen due to hemorrhage. At contrast-enhanced CT, tumor shows variable, nonspecific enhancement patterns (Peterson et al. 2000; Koyama et al. 2002; Fig. 17). Diagnosis is rarely suggested at imaging, thus prompting further evaluation with lesion biopsy.

Surgery can be performed with curative intent when tumor involves one hepatic lobe. Involvement of both liver lobes precludes any surgical intervention making the patient a candidate for palliative therapies including, systemic or hepatic arterial chemotherapy. Note small hepatic hemangioma in the left liver lobe (curved arrow).

References

Baron RL (1994) Understanding and optimizing use of contrast material for CT of the liver. Am J Roentgenol 163:323–331

Baron RL, Brancatelli G (2004) Computed tomographic imaging of hepatocellular carcinoma. Gastroenterology 127:S133–S143

Blachar A et al (2002) Radiologists' performance in the diagnosis of liver tumors with central scars by using specific CT criteria. Radiology 223:532–539

Brancatelli G et al (2001) Focal nodular hyperplasia: CT findings with emphasis on multiphasic helical CT in 78 patients. Radiology 219:61–68

Brancatelli G, Federle MP, Grazioli L, Golfieri R, Lencioni R (2002a) Benign regenerative nodules in Budd–Chiari syndrome and other vascular disorders of the liver: radiologic-pathologic and clinical correlation. Radiographics 22: 847–862

Brancatelli G et al (2002b) Hepatocellular carcinoma in noncirrhotic liver: CT, clinical, and pathologic findings in 39 U.S. residents. Radiology 222:89–94

Brancatelli G, Federle MP, Grazioli L, Golfieri R, Lencioni R (2002c) Large regenerative nodules in Budd–Chiari syndrome and other vascular disorders of the liver: CT and MR imaging findings with clinicopathologic correlation. Am J Roentgenol 178:877–883

Byun JH, Kim TK, Lee CW et al (2004) Arterioportal shunt: prevalence in small hemangiomas versus that in hepatocellular carcinomas 3 cm or smaller at two-phase helical CT. Radiology 232:354–360

Catalano OA, Singh AH, Uppot RN, Hahn PF, Ferrone CR, Sahani DV (2008) Vascular and biliary variants in the liver: implications for liver surgery. Radiographics 28:359–378

Choi CS et al (1998) Triphasic helical CT of hepatic focal nodular hyperplasia: incidence of atypical findings. Am J Roentgeol 170:391–395

Ebied O, Federle MP, Blachar A et al (2003) Hepatocellular-cholangiocarcinoma: helical computed tomography findings in 30 patients. J Comput Assist Tomogr 27:117–124

Foley WD, Mallisee TA, Hohenwalter MD, Wilson CR, Quiroz FA, Taylor AJ (2000) Multiphase hepatic CT with a multirow detector CT scanner. Am J Roentgenol 175: 679–685

Grazioli L et al (2000) Liver adenomatosis: clinical, histopathologic, and imaging findings in 15 patients. Radiology 216:395–402

Grazioli L et al (2001) Focal nodular hyperplasia: morphologic and functional information from MR imaging with gadobenate dimeglumine. Radiology 221:31–39

Ichikawa T et al (1999) Fibrolamellar hepatocellular carcinoma: imaging and pathologic findings in 31 recent cases. Radiology 213:352–361

Ichikawa T et al (2000) Hepatocellular adenoma: multiphasic CT and pathologic findings in 25 patients. Radiology 214: 861–868

Jarnagin WR, Weber S, Tickoo SK et al (2002) Combined hepatocellular and cholangiocarcinoma: demographic, clinical, and prognostic factors. Cancer 94:2040–2046

Kanematsu M et al (2006) Imaging liver metastases: review and update. Eur J Radiol 58:217–228

Kapoor V, Brancatelli G, Federle MP, Katyal S, Marsh JW, Geller DA (2003) Multidetector CT arteriography with volumetric three-dimensional rendering to evaluate patients with metastatic colorectal disease for placement of a floxuridine infusion pump. Am J Roentgenol 181:455–463

Khalil HI, Patterson SA, Panicek DM (2005) Hepatic lesions deemed too small to characterize at CT: prevalence and importance in women with breast cancer. Radiology 235:872–878

Kim T, Federle MP, Baron RL, Peterson MS, Kawamori Y (2001) Discrimination of small hepatic hemangiomas from hypervascular malignant tumors smaller than 3 cm with three-phase helical CT. Radiology 219:699–706

Kondo F (2001) Benign nodular hepatocellular lesions caused by abnormal hepatic circulation: etiological analysis and introduction of a new concept. J Gastroenterol Hepatol 16:1319–1328

Koyama T et al (2002) Primary hepatic angiosarcoma: findings at CT and MR imaging. Radiology 222:667–673

Lacomis JM, Baron RL, Oliver JH 3rd, Nalesnik MA, Federle MP (1997) Cholangiocarcinoma: delayed CT contrast enhancement patterns. Radiology 203:98–104

McLarney JK et al (1999) Fibrolamellar carcinoma of the liver: radiologic-pathologic correlation. Radiographics 19:453–471

Mermuys K et al (2004) Epithelioid hemangioendothelioma of the liver: radiologic–pathologic correlation. Abdom Imaging 29:221–223

Miller WJ et al (1992) Epithelioid hemangioendothelioma of the liver: imaging findings with pathologic correlation. AJR 159:53–57

Mortelé KJ et al (2001) Cystic focal liver lesions in the adult: differential CT and MR imaging features. Radiographics 21:895–910

Namasivayam S et al (2007) Imaging of liver metastases: MRI. Cancer Imaging 7:2–9

Nelson RC et al (1990) Diagnostic approach to hepatic hemangiomas. Radiology 76:11–13

Ohtomo K, Baron RL, Dodd GD 3rd et al (1993) Confluent hepatic fibrosis in advanced cirrhosis: appearance at CT. Radiology 188:31–35

Oliver JH 3rd, Baron RL, Federle MP, Jones BC, Sheng R (1997) Hypervascular liver metastases: do unenhanced and hepatic arterial phase CT images affect tumor detection? Radiology 205:709–715

Peterson MS et al (2000) Hepatic angiosarcoma: findings on multiphasic contrast-enhanced helical CT do not mimic hepatic hemangioma. Am J Roentgeol 175:165–170

Quinn SF et al (1992) Hepatic cavernous hemangiomas: simple diagnostic sign with dynamic bolus CT. Radiology 182: 545–548

Sahani DV, Kalva SP (2004) Imaging the liver. Oncologist 9:385–397

Valls C et al (2001) Hepatic metastases from colorectal cancer: preoperative detection and assessment of resectability with helical CT. Radiology 218:55–60

Vilgrain V, Lewin M, Vons C et al (1999) Hepatic nodules in Budd–Chiari syndrome: imaging features. Radiology 210:443–450

Wanless IR et al (1985) On the pathogenesis of focal nodular hyperplasia of the liver. Hepatology 5:1194–2000

Yu JS et al (2006) Hepatic metastases: perilesional enhancement on dynamic MRI. Am J Roentgeol 186: 1051–1058

Liver and Biliary System: Postoperative Findings

Magaly Zappa, Annie Sibert, and Valérie Vilgrain

Contents

Abstract

Liver resection consists of the removal of a lobe or segment of the liver, and is usually followed by subsequent regeneration of the remnant parenchyma. Liver resection is mostly indicated not only in malignant tumors, but also in some benign liver conditions. Most of liver resections are "anatomical" which means that they are ruled by vascular landmarks such as portal and hepatic veins. Imaging, especially multiphasic CT, plays a major role in diagnosing and staging the liver disease, helping in surgical treatment planning, and in evaluating postoperative regeneration. CT is also crucial in the postoperative course for diagnosing complications. Most common complications are fluid collections (hematoma, biloma), and vascular complications. Postoperative imaging of the bile ducts is nowadays primarily based on non-invasive imaging modalities and invasive approach should be restricted to interventional procedures. CT scan has several advantages: complete overview of the abdomen, excellent vessels analysis, and pneumobilia depiction. Laparoscopic cholecystectomy is the most common biliary surgery, usually for acute or chronic calculous disease. Bile leakages are the most common complications, usually due to an incomplete cystic duct stump or to an injury because of an anatomical biliary duct variant. They may be revealed early with biliary collection, or lately with bile duct stenosis. Other common biliary surgical procedures are gallbladder resection and bile duct resection for cancer, inflammatory or traumatic lesions. Most early complications are biliary or enteric leaks or hemorrhage, all of them easily diagnosed by CT scan. Most late

M. Zappa · A. Sibert · V. Vilgrain (✉)
Department of Radiology, Hôpital Beaujon,
Hôpital Beaujon, 92118 Clichy, France
e-mail: valerie.vilgrain@bjn.aphp.fr

C. J. Zech et al. (eds.), *Multislice-CT of the Abdomen*, Medical Radiology. Diagnostic Imaging,
DOI: 10.1007/174_2011_408, © Springer-Verlag Berlin Heidelberg 2012

complications are secondary cholangitis due to stenosis, reflux, or dysfunction, for which CT plays an important role in assessing changes in liver morphology and searching vascular complications.

1 Postoperative Liver

Liver resection consists of the removal of a lobe or segment of a liver. It is usually followed by subsequent regeneration of the residual parenchyma within a few weeks which allows resection up to 80% of the liver volume in healthy livers. Liver resection is still considered as one of the most difficult and challenging operations in general surgery. The explosion in liver resection over the last 20 years has been due to refinements of surgical techniques, appropriate patient selection, optimal anesthesia and proper postoperative care leading to significant reduction of mortality and morbidity. Despite the advances in non-surgical ablative treatments, surgery is still the curative treatment for metastatic liver tumors combined with perioperative chemotherapy. In hepatocellular carcinoma, there are more therapeutic options from non-surgical treatments, the most common being radiofrequency tumor ablation and chemoembolization to liver transplantation. Liver resection is best indicated in large tumors developing in patients with no or minimal liver insufficiency. Liver resection is also widely performed in resectable peripheral cholangiocarcinomas and in some benign liver tumors. The most current indications of liver resection in benign liver neoplasms are hepatocellular adenomas at risk of complications and hydatid cyst. Liver resection could also be indicated in symptomatic patients with polycystic liver disease. Conversely, there are no indications for liver resection in patients with asymptomatic hemangioma or focal nodular hyperplasia. Imaging plays a major role in diagnosing and staging the liver disease and helping in treatment planning. It is also crucial in the postoperative course for diagnosing complications.

1.1 Anatomical Versus Non-Anatomical Resection

Developments in the understanding of hepatic anatomy have been of vital importance in liver resection. It is now well known that the external morphology of the liver does not correspond to the functional anatomy. Thanks to Couinaud who has been a pioneer in this field by showing two major advances (Couinaud 1957). First, liver can be subdivided in hemilivers, sectors and segments using venous landmarks: portal branches and hepatic veins. Second, each segment has its own hepatic artery, portal vein and biliary drainage and therefore can be removed or kept safely. Resection of liver lesions can thus be planned and carried out according to the segmental distribution. This carries the advantage of less bleeding as it avoids major vessels and also reduces the likelihood of leaving ischemic liver tissues behind, since the blood supply to the remnants is preserved. Non-anatomical or wedge-resection has a place for peripheral or superficial lesions, or when the lesion crosses the boundary of multiple segments, or in situations where the preservation of liver substance is of paramount importance.

A resection of less than three liver segments is regarded as a minor hepatectomy while resection of three or more liver segments is termed major hepatectomy. Resections involving five or more liver segments are regarded as extended hepatectomy (Huynh-Charlier et al. 2009).

1.2 Preoperative Imaging

The role of preoperative imaging is not only to give diagnostic clues but also to give all the information for safe surgery including anatomical landmarks, abnormal variants that could make the resection difficult and assess the future liver remnant volume in major resection. Ultrasound, CT and MR imaging are the most useful tools. Multiphasic CT is really the key imaging by showing 2D and 3D high resolution images. Liver volume can be measured easily either automatically or semi-automatically from CT and MR images. The minimal future liver remnant volume varies with the liver function. Twenty-five to 30% are sufficient in normal livers whereas 40–50% are needed in cirrhotic livers (Tanaka et al. 1993). Presence of portal hypertension in cirrhotic patients should also be searched and often contra-indicates liver resection. When future liver remnant volume is insufficient, portal vein embolization of the future resected liver can be performed. It induces significant increase of the future liver remnant allowing safer surgery (Abdalla 2010).

1.3 Surgical Techniques

Basically, there are two approaches in anatomical resections. In the conventional approach, hepatectomy starts by mobilizing the liver to be resected. This consists of division of the falciform ligament, the right or left triangular ligament. An alternate anterior approach has been advocated especially in right hepatectomy. It starts with hilar dissection, ligation and division of the right hepatic artery and portal vein. Liver transection then begins over the anterior surface of the liver, toward the IVC along the principal plane using the hanging maneuvre (Belghiti et al. 2001). Bleeding remains the major problem associated with liver resection. Bleeding and the subsequent blood transfusion have been shown to increase postoperative morbidity and mortality (Kooby et al. 2003). Thus, reducing blood loss and avoidance of transfusion are the primary objectives of most liver surgeons. Hepatic vascular control (Pringle maneuvre and other more recent techniques) is an effective way to achieve these goals.

Intra-operative ultrasound is an essential tool for hepato-biliary surgeons. It is used to locate knownliver lesions, to detect further liver lesions on-table, to guide the line of transection and to mark important vascular patterns. Intraoperative contrast-enhanced ultrasound may help to visualize poorly visible lesions on conventional intra-operative ultrasound either to resect them or to perform combined ablation procedures.

Liver resection can be performed laparoscopically however the development of laparoscopic techniques for liver resection has been relatively slow. The best indications for laparoscopic liver resection nowadays are that tumors located at segment II, III, IVb, V or VI, of size 5 cm or less; lesions which are not close to major vascular trunks; and when there is no need for vascular or biliary reconstruction (Gagner et al. 2004).

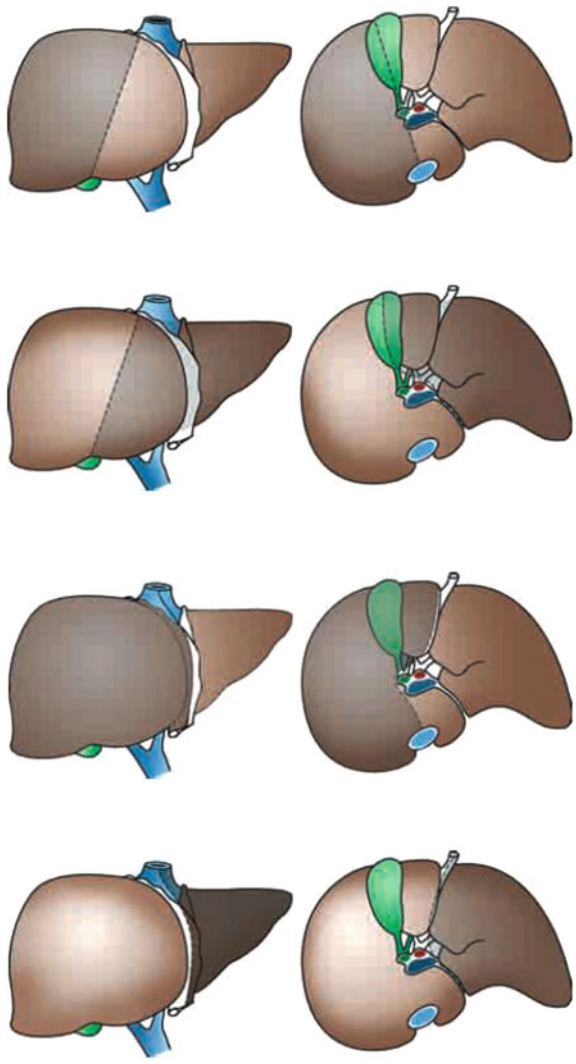

Fig. 1 *Top* Right hepatectomy (anterior and inferior view): The section plane courses parallel to the middle hepatic vein. *Below* Left hepatectomy (anterior and inferior view): The section plane courses parallel to the middle hepatic vein. *Below* Extended right hepatectomy (anterior and inferior view): The section plane is the umbilical fissure. *Bottom* Left lobectomy (anterior and inferior view): The section plane is the umbilical fissure

1.3.1 Most Common Anatomical Liver Resections

The majority of hepatic resections involve the right or left hemiliver and the inflow of the resected hemiliver must be ligated at some point during the resection (Fig. 1). The same is true of resections of a sector or of a segment. The outflow must also be controlled and divided at some point. Right hepatectomy involves the resection of segment V, VI, VII and VIII which approximately represents 65% of the total liver volume (Chen et al. 1991). The right pedicles are ligated. The section plane courses parallel to the middle hepatic vein which might be preserved.

Left hepatectomy involves the resection of segment II, III and IV which approximately represents 35% of the total liver volume (Chen et al. 1991). The left pedicles are ligated. The section plane courses parallel to the middle hepatic vein which might be preserved.

Extended right hepatectomy involves the resection of segments IV to VIII and can include resection of the

caudate lobe (segment I). This resection is necessary to treat right-sided tumors that extend into segment IV. The umbilical fissure is opened, and all vascular and biliary branches to segments IVa and IVb are ligated. This resection represents approximately 80% of the total liver volume (Chen et al. 1991). The outflow is maintained via the left hepatic vein.

Left lobectomy involves the resection of segment II and III which approximately represents 20% of the total liver volume (Chen et al. 1991). The section plane is the umbilical fissure. The left pedicles are ligated at the left side of the umbilical fissure while preserving the left branch of the portal vein.

1.3.2 Other Surgical Procedures

Caudate lobe (segment I) resection: The caudate lobe represents less than 5% of the total liver volume and is deeply located between the inferior vena cava, the hepatic hilum and the distal portion of the middle and left hepatic veins. This explains why isolated resection of the caudate lobe is rarely performed (Katsihuko et al. 1994). Right or left hepatectomy may be associated to resection of the caudate lobe.

Right anterior hepatectomy involves the resection of segment II, III, IV, V and VIII which approximately represents 65% of the total liver volume (Chen et al. 1991). The section plane courses parallel to the right hepatic vein which has to be preserved.

Central hepatectomy involves the resection of segment IV, V and VIII which approximately represents 50% of the total liver volume (Chen et al. 1991). This resection might be indicated in central tumors that do not invade primary biliary confluence. The middle hepatic vein is removed. The drawback of this surgical procedure is to have two liver sections which potentially increase the postoperative complications.

Posterior sectorectomy involves the resection of segment VI and VIII which approximately represents 35% of the total liver volume (Chen et al. 1991). This resection is mainly performed when liver volume should be preserved as much as possible especially in patients with chronic liver disease.

1.4 Normal Postoperative Course

Liver regeneration allows restoration of the liver function within two or three weeks. During the first week, prothrombin time and serum bilirubin can be profoundly altered. The "50–50 Criteria" on postoperative day 5 (defined by the association of prothrombin time <50% and serum bilirubin >50 μml/L) have been shown an accurate predictor of liver failure and death after hepatectomy (Balzan et al. 2005). After right hepatectomy, the liver remnant at day 7 shows a mean increase in the volume of 64% from the future liver remnant. The most important factors that significantly alter liver regeneration are the presence of liver fibrosis or cirrhosis and disturbance of the outflow. Patients with harvesting of the middle hepatic vein have volume and segmental regeneration index significantly lower than in other patients, for both the caudate lobe and segment IV (Zappa et al. 2009).

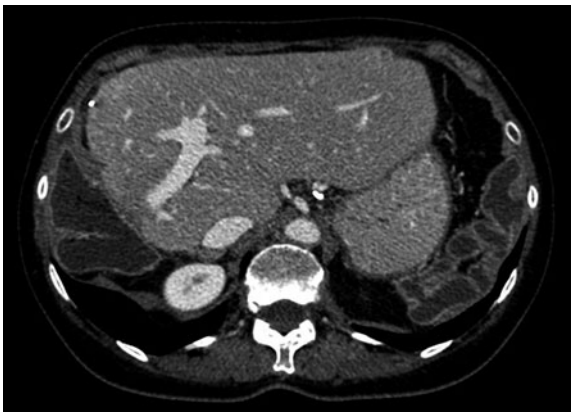

Fig. 2 Contrast-enhanced CT after right hepatectomy: the left hepatic lobe extends in the epigastrium and becomes ovoid with round contours. Inferior vena cava is displaced posteriorly. Right colon occupies the right hypocondrium

Shape and location of the postoperative liver depends on the type of liver resection. After right hepatectomy, the left hepatic lobe extends in epigastrium and becomes ovoid with round contours. The caudate lobe may increase in volume or not. The umbilical fissure is displaced to the right, whereas inferior vena cava is displaced posteriorly. Right colon and ileum may occupy the right hypocondrium (Fig. 2). After extended right hepatectomy, findings are similar but the segment IV is no longer visible (Couanet et al. 1984).

After left hepatectomy, right liver becomes hypertrophic extending below the costal skeleton and has round contours. The caudate lobe may enlarge or not. The portal vein is displaced to the left. The stomach and transverse colon are next to the right liver (Couanet et al. 1984) (Fig. 3).

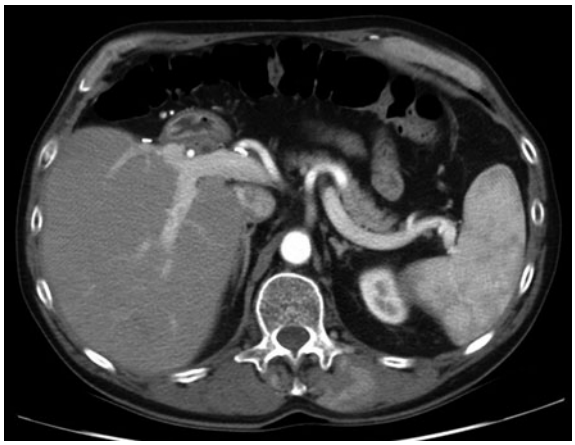

Fig. 3 Contrast-enhanced CT after left hepatectomy: the right liver becomes hypertrophic extending below the costal skeleton and has round contours. The portal vein is displaced to the left. The duodenum and the transverse colon are next to the right liver

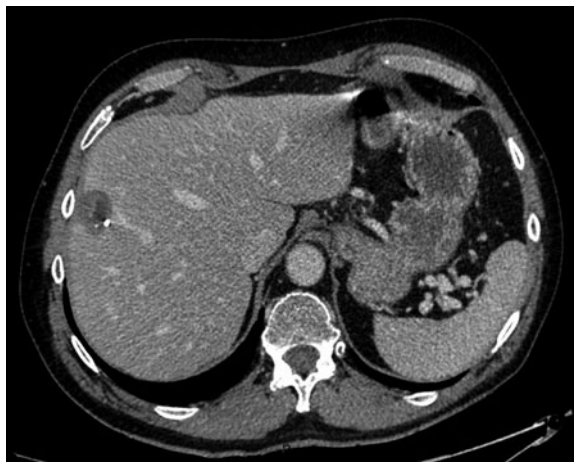

Fig. 4 Contrast-enhanced CT after wedge-resection: a peripheral capsular retraction is seen at the site of the resection. Note the presence of metallic clips and of a small amount of fluid in the resection site

After left lobectomy, the left portal branch is the inner border of the liver. The left portal branch usually decreases in size over time. Morphologic changes of the remnant liver are minimal (Couanet et al. 1984).

After wedge-resection, a peripheral capsular retraction may be seen at the site of the resection. Surgeons may use or not metallic clips (Couanet et al. 1984) (Fig. 4).

Some findings are common to all liver resections: presence of air or fluid collection may be depicted in the early postoperative course up to two months; hypoattenuating linear band adjacent to the liver resection is seen in 30–50% of the cases and corresponds to bile or blood accumulation, fibrous infiltration, focal steatosis or devascularized parenchyma. This abnormality disappears over time; fat-density area related to epiploplasty can be seen next to the liver. Last, pleural effusion is noticed in 50–80% of the cases, in particular after right hepatectomy (Letourneau et al. 1988; Quinn et al. 1988).

1.5 Early Complications

The most common complications encountered after liver resection are liver insufficiency, fluid collections and vascular complications. Diagnosis of liver insufficiency is based on clinical and biological findings such as ascites and abnormal blood liver tests. Imaging in this setting is performed to exclude any other complication.

Conversely, imaging plays a major role in detecting the other early complications. Imaging is indicated in early postoperative course in patients who present with fever, abdominal pain, jaundice or suspicion of bleeding. Doppler ultrasound is the first step in intensive care unit because it is easily performed at bedside. Multiphasic CT is more accurate than Doppler ultrasound for showing active bleeding, hematoma and abscess. Indeed, CT protocol includes unenhanced and contrast-enhanced acquisitions with one obtained at the arterial-dominant phase and the other at the portal venous-phase.

1.5.1 Fluid Collections

Fluid collections are mostly due to vessel or bile leaks along the liver section. If they do not stop, they may lead to large fluid collections that can be either hematoma, biloma or mixed (Fig. 5). Detection of fluid collections is easy on imaging, but conversely fluid characterization is often difficult. Findings suggestive of hematoma are heterogeneous collections containing septa and hyperattenuating fluid collections on unenhanced CT scan. Bilomas are typically more homogeneous. Presence of a peripheral hyperenhancing rim or large amount of air should raise the possibility of abscesses. Ponction aspiration is indicated if the fluid collection is poorly tolerated. Drainage of the

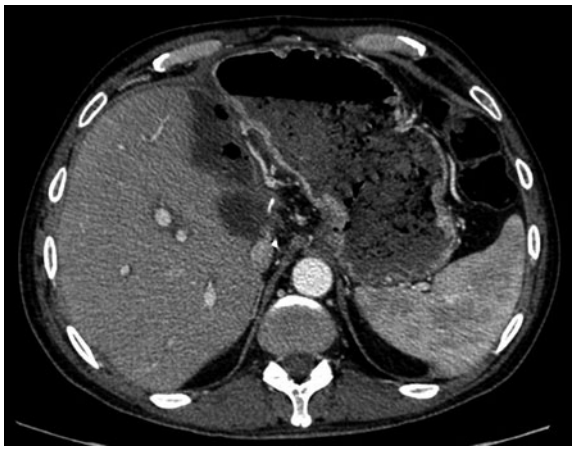

Fig. 5 Contrast-enhanced CT after left hepatectomy. Presence of a fluid collection. On CT the collection appears hypoattenuating and heterogeneous with gas formation on the section plane

collection will be performed in abscesses or bilomas (Letourneau et al. 1988). In bilomas, MR imaging could be helpful to look for biliary confluence abnormality that could require biliary drainage.

1.5.2 Vascular Complications

Liver surgery increases the risk of portal vein thrombosis and Budd-Chiari syndrome. Portal vein thrombosis appears as an echogenic vessel with absence of flow on Doppler ultrasound. Contrast-enhanced CT shows lack of enhancement of the obstructed vessel. Budd-Chiari syndrome is mostly observed after right hepatectomy. As the remnant liver is displaced to the right, middle or left hepatic veins may be compressed or have kinking appearance (Pitre et al. 1992) (Fig. 6). Postoperative Budd-chiari syndrome is suspected by persistent blood liver tests abnormalities and ascites. Doppler ultrasound is the modality of choice for diagnosing hepatic venous abnormalities and demonstrates flow demodulation in the remnant hepatic veins as well as decreased portal vein flow velocity. Incidence of pulmonary embolism is known to be increased after general abdominal surgery, reported from 1% to 5% (Geerts et al. 2004). In our experience, the risk of pulmonary embolism after liver surgery has an incidence of 2.4% (personal data). Three factors were strongly associated with this risk in multivariate analysis: BMI of 27 kg/m^2, patients with benign liver disease, and resections performed on liver with a fibrosis score no more than F2 (healthy liver parenchyma).

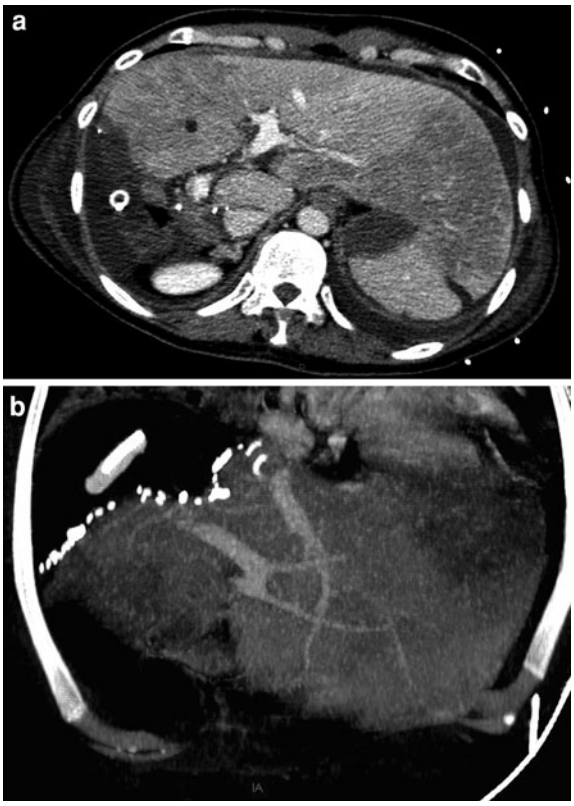

Fig. 6 Contrast-enhanced CT after right hepatectomy: Postoperative Budd-Chiari syndrome. **a** axial view at the portal venous-phase; note the left liver congestion because of compromise of hepatic venous outflow. **b** coronal MIP view at the portal venous-phase; note the stenosis of the distal part of the left hepatic vein

1.6 Late Complications

Late complications are mostly related to tumor recurrence in patients with liver malignancies. Diagnosis of recurrence is based on clinical, biological and imaging findings. If the diagnosis remains difficult after extensive imaging work-up, biopsy of the lesion is indicated (Letourneau et al. 1988; Abir et al. 2006).

2 Postoperative Bile Ducts

For years, postoperative imaging of the bile ducts was invasive. It is nowadays primarily based on non-invasive imaging modalities and invasive approach shoud be restricted to interventional procedures. Knowledge of normal postoperative findings is

mandatory to avoid misdiagnosis. The choice of one imaging modality is guided by symptoms, patient disease and surgical procedure (Laurent et al. 2009). Ultrasound has been considered as a key imaging for bile ducts diseases but appears insufficient in post-operative context. CT has three main advantages: first, CT allows complete overview of the abdomen; second, vessel analysis is excellent; third, CT easily depicts pneumobilia. CT technique includes multi-phasic contrast-enhanced acquisitions performed in the late arterial, portal venous and delayed phases. Contrast-enhanced images should provide details on the liver vasculature. Delayed phase imaging is interesting when looking for wall enhancement of the bile ducts or bilioenteric anastomosis (Laurent et al. 2009). When active bleeding is suspected, it is recommended to perform an early arterial phase.

MR cholangiography is used without any contrast agent administration. 2D and 3D acquisitions are complementary tools. MR cholangiography is also accurate when bile ducts are not dilated. In patients with bile ducts stenosis, both downstream and upstream bile ducts can be seen. MR imaging can also be performed after intravenous administration of hepatospecific contrast agents such as Gadoxetic acid (Primovist, Bayer). One of the leading indications of contrast-enhanced MR cholangiography is the diagnosis of biliary leaks (Laurent et al. 2009).

Surgical procedures of the bile ducts are various from simple cholecystectomy to complex treatment of the extrahepatic or hilar tumors. Normal postoperative imaging findings and complications depend upon the surgical procedure

2.1 Cholecystectomy

Cholecystectomy is one of the most common operations in general surgery. Cholecystectomy was first performed in 1882 and has traditionally been done by the conventional open technique. Laparoscopic cholecystectomy was developed in the 80ties and has become the surgical procedure of choice, now being employed in over 80% of cases. The advantages of laparoscopic over open cholecystectomy include a significant reduction in hospitalization time and recovery period, less pain and minimal scarring. Overall postoperative complications rates for laparoscopic approach are comparable to those for open cholecystectomy, although there is a slightly higher incidence of biliary injury with laparoscopic approach (Walker 2008).

Cholecystectomy is mostly performed for acute or chronic calculous diseases and their complications. Other indications include gallbladder polyps and porcelain gallbladder. This surgical procedure includes a gallbladder dissection from the liver and dissection of the cystic artery and cystic duct toward the porta hepatis. Cystic artery, veins and cystic duct are then ligated. Last the gallbladder bed and porta hepatis are checked for haemostasis and bile leaks.

2.1.1 Normal Postoperative Findings

Imaging is not indicated in asymptomatic patients. On early ultrasound or CT, it is usual to observe a small fluid collection in the gallbladder bed that could mimic the gallbladder itself "pseudogallbladder sign". Free fluid effusion may be seen as well. These findings disappear in less than two weeks (Thurley and Dhingsa 2008). Such fluid may result from interruption of accessory cystohepatic ducts, which are persistent embryological remnants between the liver and the gallbladder. Pneumoperitoneum is also common and can be observed up to 3 weeks (Gayer et al. 2000). However, after laparoscopic cholecystectomy, pneumoperitoneum disappears more quickly and should not be seen after day 2 (Feingold et al. 2003). Similarly, increased density in the abdominal wall fat at the site of the laparoscopic ports is also often present after laparoscopic cholecystectomy (Thurley and Dhingsa 2008). Another potential pitfall is the use of hemostatic agents in the gallbladder bed. Surgicel is a bio absorbable hemostatic agent with bactericidal properties that is used in laparoscopic cholecystectomy and other surgical procedures to control hemorrhage. When imaging is performed on postoperative patients, the appearances of Surgicel can mimic those of hematoma that is a mass of 40–55 HU containing foci of air (Laurent et al. 2009).

Lately, the gallbladder bed appears empty and may have surgical clips (Fig. 7).

2.1.2 Complications

The reported overall complication rate after cholecystectomy ranges from 4.5 to 21% (Gilliland and Traverso 1990). Early complications are mostly fluid collections and hemorrhage whereas late complications are essentially of biliary origin.

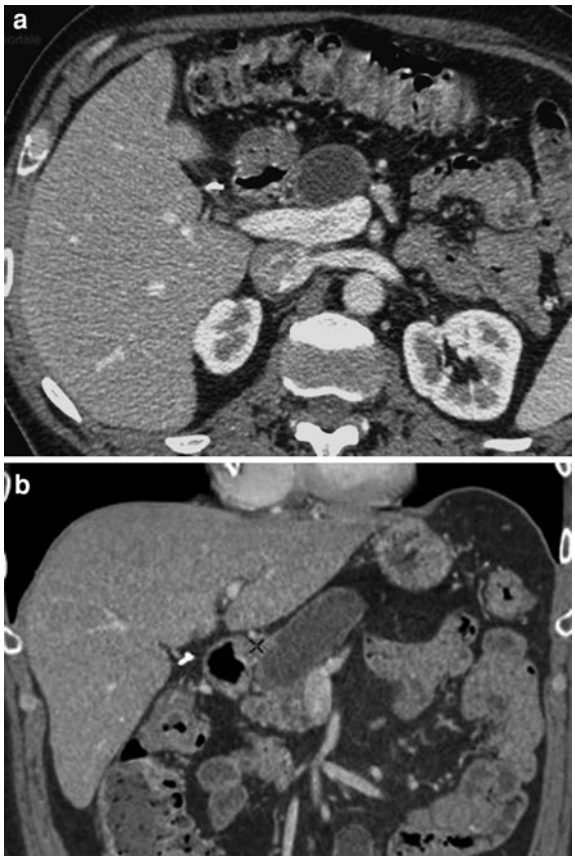

Fig. 7 Contrast-enhanced CT after cholecystectomy: normal appearance. Axial view (**a**) and coronal view (**b**). Note the metallic clips on the right side of the hepatoduodenal ligament (cystic duct and cystic artery ligation)

2.1.2.1 Early Complications

Fluid collections are equivocal and are considered abnormal if they extend beyond the gallbladder bed. Presence of free fluid effusion should raise the possibility of biliary leak and therefore be related to intraoperative bile duct injury, yet fortunately most fluid collections are not bilomas. Most of them are seromas. Free fluid may also be due to clinical decompensation of chronic liver disease (McAlister 2000).

Imaging findings are nonspecific. Among imaging modalities, CT should be performed widely when a fluid collection is suspected clinically because CT is more sensitive than ultrasound and a normal ultrasound does not rule out fluid collections in particular when conditions are difficult. (Lee et al. 2000). The diagnosis is made by biochemical analysis of the fluid including bilirubin and amylase after ultrasound-guided ponction of the collection. The ponction is completed by a drainage in infected collections or in patients with bilomas (Sibert 2010).

Hemorrhagic complications are rare. A review of 14,243 laparoscopic procedures showed a rate of hemorrhage of 4.1%, with bleeding rates of 2.3% intraoperatively and 1.8% postoperatively (Schäffer et al. 2000). They are related to direct trocar injury or insufficient hemostasis. They might appear as hematomas which predominate in the abdominal wall or in the gallbladder bed. On imaging, hematomas are usually heterogeneous and have characteristic patterns: hyperechoic on ultrasound and areas of higher attenuation on unenhanced CT phase. In some patients, the bleeding is clinically severe and multiphasic CT is required in emergency looking for active bleeding or pseudoaneurism (Fig. 8). These arterial complications usually occur in the right hepatic artery or the cystic artery stump and may result from thermal or mechanical injury of these arteries, which are occasionally associated with bile duct injury (Thurley and Dhingsa 2008; Lohan et al. 2005). If present, selective embolization of the artery should be performed (Kim et al. 2008).

2.1.2.2 Biliary Complications

Biliary complications are more common after laparoscopic than after open cholecystectomy. They should be suspected when patients are referred with symptoms of abdominal pain, sepsis, or jaundice soon after cholecystectomy (Lohan et al. 2005).

Bile leakage is the most common complication of laparoscopic cholecystectomy. Most leaks occur from the cystic duct stump or from the gallbladder bed. Bile leaks at the cystic duct may occur when clips on the cystic duct remnant become dislodged or do not encompass the entire duct. Leaks from the gallbladder bed are observed when small accessory right hepatic ducts or ducts of Luschka, which connect the gallbladder directly to the right lobe of the liver are injured (Laurent et al. 2009; Hoeffel et al. 2006). These bile leaks can nearly always be treated successfully with endoscopic sphincterotomy.

Other bile leaks are due to inadvertent ligation of an aberrant right hepatic duct or common bile duct injury which varies from a tear in the common bile duct to complete section of the common bile duct (Hoeffel et al. 2006). More rarely, the ductal confluence, the right hepatic duct and the left hepatic duct

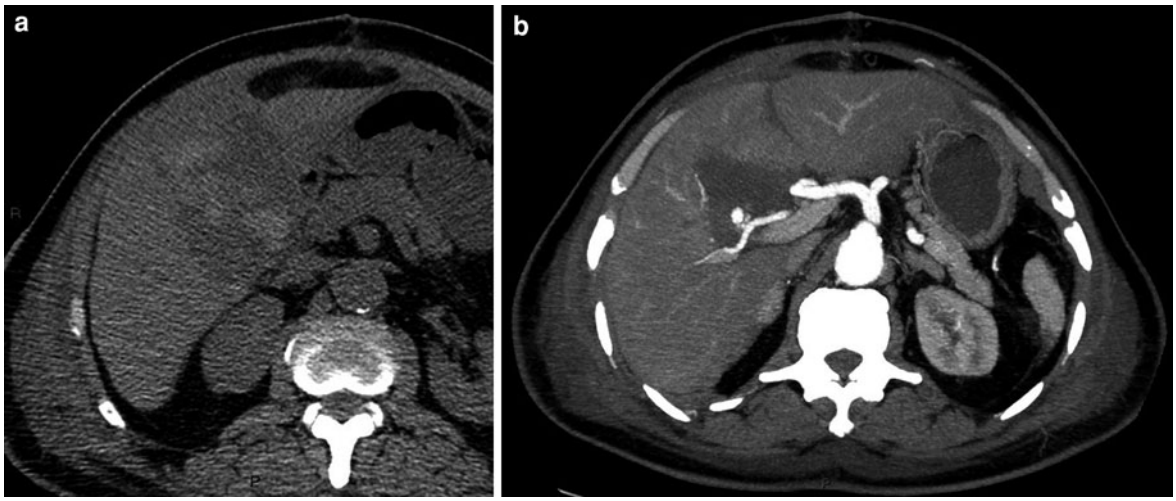

Fig. 8 CT scan after laparoscopic cholecystectomy. **a** areas of higher attenuation on unenhanced CT in the gallbladder bed. **b** CT during the arterial phase demonstrating a pseudoaneurism of the cystic artery

may be involved. Indeed, treatment will be different. As most tears are partial and may be treated with endoscopic stent placement, treatment of complete section of the common bile duct often requires surgery (Fig. 9).

Clinically, bile leaks usually present with shoulder pain, abdominal pain, leukocytosis and fever with mildly elevated bilirubin and transaminase levels, or bilious drainage from a drain, if present. In bile leaks, CT can show fluid collections but identification of the biliary origin and the precise site is often difficult. Bile collections are usually close to the site of the leak, and the presence of free fluid on the right side of the abdomen, with or without a fluid collection adjacent to the injured bile duct, should be considered suggestive of bile leakage. When bile leakage is rapid and is not contained by peritoneal adhesions, the bile spreads in the peritoneum "Bile peritonitis" and can be a cause of postoperative mortality. MR cholangiography is mandatory but may fail to demonstrate biliary communication. Contrast-enhanced MR cholangiography can be very helpful for the diagnosis of biliary leaks (Vitellas et al. 2001). In some countries, hepatobiliary scintigraphy is part of the workup. Endoscopic retrograde cholangiography and/or percutaneous transhepatic cholangiography are often necessary for the staging and treatment planning.

Biliary complications may be revealed lately. Late strictures of extrahepatic ducts are often due to mild injury which results in fibrosis months or years after cholecystectomy. Clinical findings vary from abnormal blood liver tests to obstructive jaundice. CT shows dilatation of intrahepatic bile ducts (defined as a diameter of more than 3 mm) with stenosis of the common bile duct. It is interesting to note that the stenosis often extends to the primary biliary confluence. MR cholangiography is needed for accurate diagnosis and staging according to the Bismuth classification system. This system relates to the level of the stricture. Bismuth type I is a stricture in the common duct >2 cm from the hepatic bifurcation, a type II is a stricture in the common hepatic duct <2 cm from the bifurcation, a type III is at the bifurcation, a type IV is above the bifurcation of the right and left hepatic ducts and a type V is a stricture of a right sectorial duct that comes off the common hepatic duct before the main hepatic duct bifurcation. This classification has proven useful in determining the difficulty of the reconstruction and comparing surgical results. CT has an additional role in identifying vascular complications (Fig. 10); the most common being portal vein thrombosis and thrombosis of the right hepatic artery (Alves et al. 2003). Arterial supply is then provided by the left hepatic artery at the hilum.

Some patients may suffer from complications associated with the long cystic duct remnant such as stasis and stones that tend to re-form.

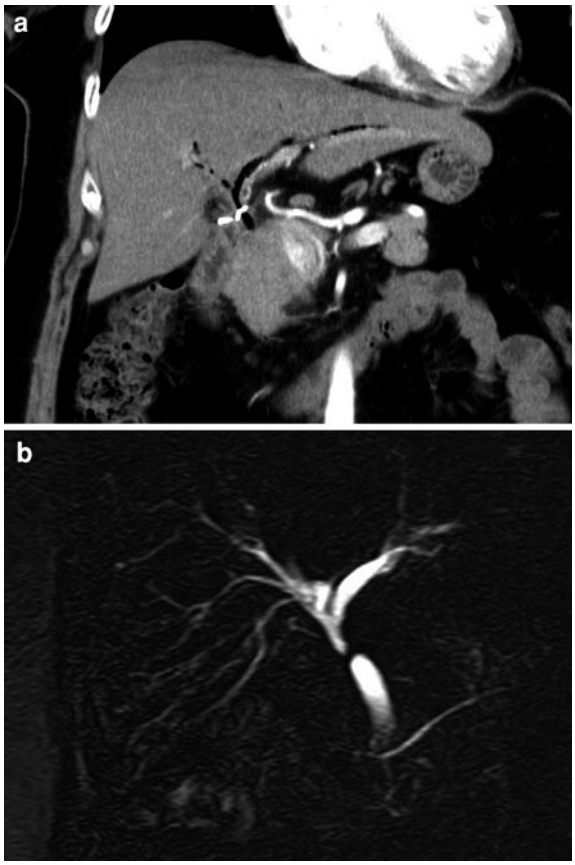

Fig. 9 **a** contrast-enhanced CT scan (coronal plane): pneumobilia post ERCP; note the metallic clip postcholecystectomy just below the primary biliary confluence, responsible for the stenosis. **b** MR cholangiography: Complete stenosis of the common bile duct below the primary biliary confluence which occured lately after a postcholecystectomy bile duct leak

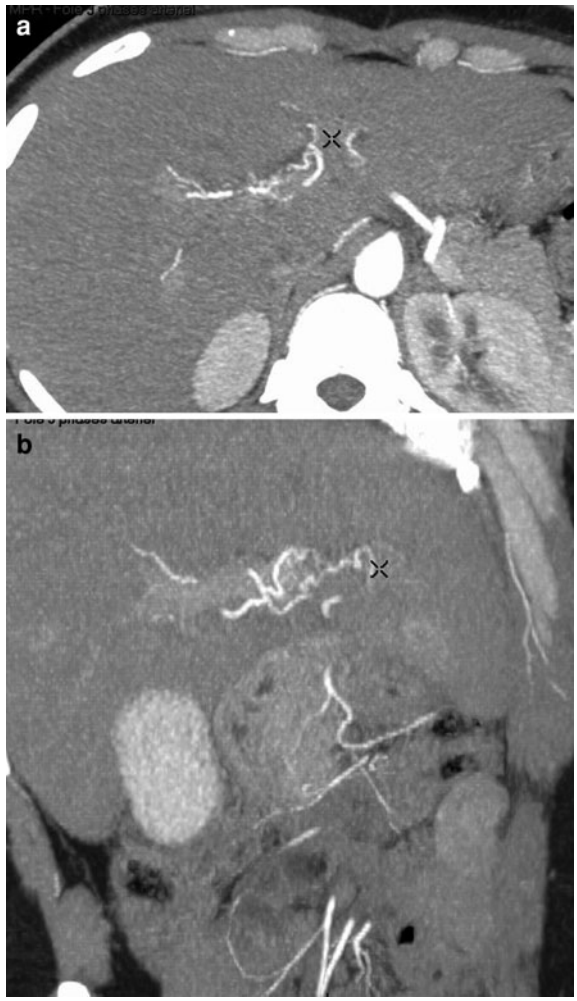

Fig. 10 CT scan postcholecystectomy obtained during arterial phase. Inadvertent ligation of the right hepatic during cholecystectomy which has not been diagnosed intraoperatively. Axial (**a**) and coronal CT images (**b**) show arterial supply provided by the left hepatic artery to the intrahepatic right hepatic arteries

Retained stones are another cause of biliary obstruction. They may be identified on CT if the stones are of a differing density from bile. If CT is equivocal, MRCP is indicated and can show stones as small as 2 mm in the biliary tree (Laurent et al. 2009).

Dropped gallstones occur commonly during laparoscopic cholecystectomy, with a reported incidence of 0.1–20% (Brockmann et al. 2002). Fortunately, most of these stones do not cause symptoms, yet the most common complication is abscess formation which can occur after a period of months to years after the laparoscopic cholecystectomy, making diagnosis challenging. Spilled gallstones are mostly seen in the subdiaphragmatic or subhepatic spaces but they may occur anywhere in the peritoneal cavity. If they are calcified, gallstones may also be visible on CT as hyperattenuating areas. Abscess formation has also been described in the abdominal wall (Fig. 11). The diagnosis of abscess formation complicating dropped gallstones should be raised when a central or eccentric nidus with calcific or metallic density is observed on CT (Morrin et al. 2000).

2.1.2.3 Other Complications

Several less common complications of cholecystectomy have been reported that may be diagnosed on

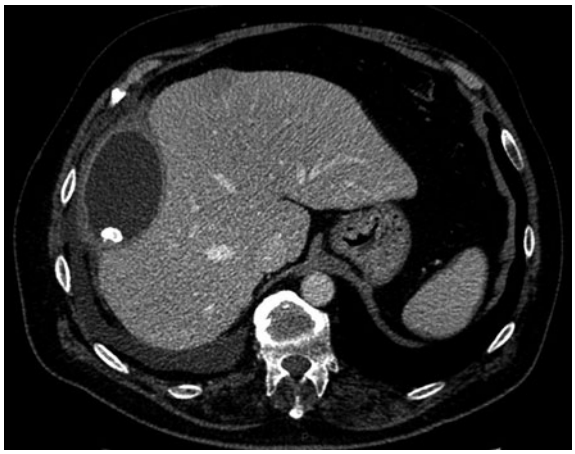

Fig. 11 Contrast-enhanced CT scan 4 years after cholecystectomy: Calcified dropped gallstones in the perihepatic space, with abscess formation

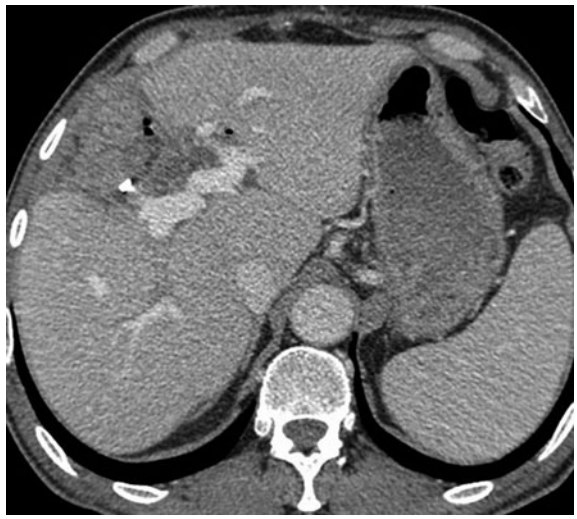

Fig. 12 Contrast-enhanced CT scan after surgery for gallbladder cancer. Normal appearance showing resection of the gallbladder and the segments 4 and 5. Filling of the gallbladder bed by small bowel

imaging. Indeed, laparoscopic cholecystecomy favors the incidence of port site hernia. Although hernias can be clinically suspected, the diagnosis can be confirmed using CT. Diaphragmatic hernias are less common and CT is helpful by depicting a defect in the diaphragm or herniation of peritoneal fat into the chest (Thurley and Dhingsa 2008). Other complications are very unusual such as portal vein thrombosis, splenic rupture, intestinal ischemia and delayed bowel perforation due to thermal injury after laparoscopic cholecystectomy.

2.2 Other Surgical Techniques of the Biliary Tree

In this section, we will only consider the most common surgical techniques for the biliary tree (Clavien et al. 2007). Simple choledochotomy and sphincterotomy will not be covered.

2.2.1 Resection of Gallbladder Cancer

The extent of resection of gallbladder cancer varies according to stage. Patients with N2 or M1 are not eligible to curative surgery but may have palliation by biliary or gastric bypass. The curative resection includes a radical cholecystectomy (including segments 4b and 5) and lymph node dissection (Fig. 12). An extended lobectomy can be necessary because of the bulk of the tumor or because of vascular invasion. With gallbladder cancer, when an extended resection is necessary, it is usually an extended right lobectomy. The resection of the common duct is usually performed and allows dissection and inspection of the portal vein and hepatic arteries behind the tumor and in the hilar area. A Roux-en-Y jejunal loop is lifted and anastomosed to the left and right hepatic ducts. Portal vein can be reconstructed when the portal vein is encased or to facilitate the resection (Fong et al. 2006).

2.2.2 Resection of Bile Duct

Resection of tumors at the bifurcation of the left and right hepatic duct is one of the most difficult operations. The surgical procedure requires not only a portal lymphadenectomy and bile duct resection, but almost always a liver resection. This surgical procedure is indicated in primary malignancies (intrahepatic cholangiocarcinoma involving the hepatic hilus, hilar cholangiocarcinoma, gallbladder carcinoma involving the hepatic hilus, or diffuse carcinoma of the extrahepatic bile duct), benign diseases (such as primary sclerosing cholangitis, inflammatory pseudotumor) or traumatic lesion at the hepatic hilus.

The goals of this operation are threefold: resection of the primary tumor (including removal of the entire supraduodenal bile duct, gallbladder, cystic duct and

extrahepatic hepatic ducts), resection of the lymphatic drainage of the liver and reestablishment of biliary continuity. The distal bile duct is dissected down to the head of the pancreas and divided above the pancreas. Roux-en-Y jejunal loop is lifted and anastomosed to the remnant hepatic ducts.

Concomitant hepatectomy including caudate lobectomy is often necessary to achieve negative margins. In most patients, there is intrahepatic extension of the tumor, and right or left portal vein involvement. In these cases, en bloc liver resection, often with caudate lobectomy, is necessary to achieve tumor clearance (Igami et al. 2010).

2.2.3 Resection of Mid Bile Duct

True mid bile duct tumors are very rare. Indications for this surgical procedure are biliary strictures without confirmed malignancy, diagnosis of suspected benign disease or confirmed malignant disease confined to mid common bile duct in patients unfit for more extensive resection (pancreaticoduodenectomy or liver resection). Roux-en-Y hepaticojejunostomy has the best success rate (80–99%) for the repair of an injury of the common duct or common hepatic duct (Clavien et al. 2007).

The gallbladder is dissected free from its liver bed. The distal common bile is ligated above the superior edge of the pancreas. The proximal duct is transected at the confluence of the right and left hepatic ducts. The biliary-enteric continuity is restored with a Roux-en-Y hepaticojejunostomy. This procedure requires the preparation of a segment of the gastro-intestinal tract and a direct end-to-side mucosa to mucosa anastomosis between the bile duct and the bowel. The blind end of the jejunal loop is closed and kept in the abdominal cavity. In some cases and especially when patients have extensive calculi formation within the common bile duct or within intrahepatic bile ducts, the blind end is kept long and brought to abdominal wall and can be further used as an avenue for subsequent interventional maneuvres (Clavien et al. 2007).

2.2.4 Normal Postoperative Findings

Imaging is not indicated in asymptomatic patients with no or minimal liver resection. On CT, it is usual to observe pneumobilia in the non dependent liver segments (Fig. 13). It may not be easy to identify the jejunal loop. Multiplanar reconstructions that can follow extrahepatic bile ducts joining the biliary-enteric anastomosis are helpful. Some teams have proposed CT using biliary contrast medium in order to improve visibility of the jejunal loops (Stumpp et al. 2005). Analysis should also look at the remnant common bile duct in the head of the pancreas. Associated liver resection is detailed above (see Sect. 1.3). Extensive lymph node dissection may cause densification of the porta hepatis.

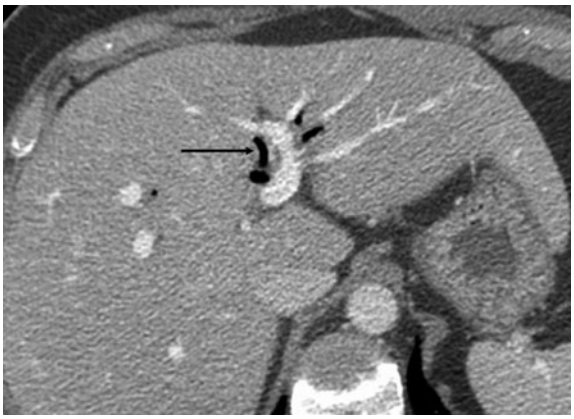

Fig. 13 Contrast-enhanced CT scan after biliary-enteric anastomosis demonstrating pneumobilia in the left bile ducts (*arrow*)

2.2.5 Early Complications

Early complications are mostly biliary or enteric leaks or hemorrhage. As in other postoperative settings, CT is accurate in diagnosing fluid collections but precise diagnosis often requires direct ponction. In patients with liver resection, fluid collections may come from resection site or from bilioenteric anastomosis. In patients with extensive lymph node resection, lymphocele may occur. They predominate in the hepatoduodenal ligament and around the pancreatic head. They usually do not require any treatment. Presence of spontaneous hyperattenuating collection on unenhanced CT is synonymous of hematoma and multiphasic CT is indicated for excluding acute bleeding.

Patients with extensive liver resection may have liver insufficiency (see Sect. 1.3). Notably, liver parenchyma is often abnormal in those patients either cholestatic or fibrotic explaining that liver regeneration might be altered (Hirano et al. 2010).

Portal vein thrombosis is a rare complication which can be favored by extensive dissection of the portal hepatis and/or portal vein reconstruction.

Color Doppler ultrasound and multiphasic examination are the modalities of choice for diagnosing this complication which requires prompt anticoagulation.

2.2.6 Late Complications

The most typical complications are secondary cholangitis. Although biliary-enteric patency should be checked, cholangitis may be observed without any stenosis due to reflux, or dysfunction. Imaging is difficult because bile duct dilatation may be absent even in patients with stenosis. Furthermore, pneumobilia may still be seen in patients with stenosis. Beside the biliary dilatation, CT plays an important role in assessing changes in liver morphology and searching vascular complications. It also may show complications such as marked enhancement of the bile duct wall on enhanced CT images, abscess formation within the liver, and upstream bile duct calculi (Sibert 2010).

Late complications in patients with history of gallbladder or bile duct cancer are dominated by recurrence which is commonly seen close to the surgical resection (Kitagawa et al. 2001).

Sump syndrome in an uncommon (0.14–1.30%) complication of side-to-side choledochoduodenostomy (Hawes et al. 1992). The segment of common bile duct between the anastomosis and the ampulla of Vater may act as a stagnant reservoir or sump. When debris, stones or infected bile accumulate in the sump, usually because of malfunction of the ampulla of Vater, recurrent abdominal pain or symptoms of cholangitis, pancreatitis or biliary obstruction may develop. Although, very rare, sump syndrome has also been described after hepaticojejunostomy. CT may show debris or stones in the common bile duct. Upstream dilated bile or pancreatic ducts may be seen. Complications of sump syndrome are pancreatitis, cholangitis and liver abscess. Endoscopic treatment is the primary therapeutic approach in those patients.

References

Abdalla EK (2010) Portal vein embolization (prior to major hepatectomy) effects on regeneration, resectability, and outcome. J Surg Oncol 102(8):960–967

Abir F, Alva S, Longo WE et al (2006) The postoperative surveillance of patients with colon cancer and rectal cancer. Am J Surg 192:100–108

Alves A, Farges O, Nicolet J, Watrin T, Sauvanet A, Belghiti J (2003) Incidence and consequence of an hepatic artery injury in Patients with postcholecystectomy bile duct strictures. Ann Surg 238:93–96

Balzan S, Belghiti J, Farges O (2005) The "50–50 Criteria" on Postoperative Day 5: An Accurate Predictor of Liver Failure and Death After Hepatectomy et al. Ann Surg 242:824–829

Belghiti J, Guevara OA, Noun R, Saldinger PF, Kianmanesh R (2001) Liver hanging manoeuvre: A safe approach to right hepatectomy without liver mobilization. J Am Coll Surg 193:109–111

Brockmann JG, Kocher T, Senninger NJ, Schürmann GM (2002) Complications due to gallstones lost during laparoscopic cholecystectomy. Surg Endosc 16:1226–1232

Chen MF, Hwang TL, Hing CF (1991) Human liver regeneration after major hepatectomy. A study of liver volume by computed tomography. Ann Surg 213:227–229

Clavien PA, Sarr MG, Fong Y (2007) Atlas of upper gastrointestinal and hepato-pancreato-biliary surgery. Springer, Berlin Heidelberg

Couanet D, Shirkhoda A, Wallace S (1984) Computed tomography after partial hepatectomy. J Comput Assist Tomogr 8:453–457

Couinaud C (1957) Le foie: Etudes anatomiques et chirurgicales. Masson, Paris

Feingold DL, Widmann WD, Calhoun SK et al (2003) Persistent post-laparoscopy pneumoperitoneum. Expected or cause for alarm? Surg Endosc 17:296–299

Fong Y, Wagman L, Gonen M et al (2006) Evidence-based gallbladder cancer staging: changing cancer staging by analysis of data from the national Cancer database. Ann Surg 243:767–774

Gagner M, Rogula T, Selzer D (2004) Laparoscopic liver resection: Benefits and controversies. Surg Clin North Am 84:451–462

Gayer G, Jonas ST, Apter S, Amitai M, Shabtai M, Hertz M (2000) Popstoperative pneumoperitoneum as detected by CT: prevalence, duration, and relevant factors affecting its possible significance. Abdom Imaging 25:301–305

Geerts WH, Pineo GF, Heit JA et al (2004) Prevention of venous thromboembolism: the seventh ACCP Conference on antithrombotic and thrombolytic therapy. Chest 126(Suppl 3): S388–S400

Gilliland TM, Traverso LW (1990) Modern standards for comparison of cholecystectomy with alternative treatments for symptomatic cholelithiasis with emphasis on long-term relief of symptoms Surg Gynecol Obstet 170(1):39–44

Hawes DR, Pelsang RE, Janda RC, Lu CC (1992) Imaging of the biliary sump syndrome. Am J Roentgenol 158:315–319

Hirano S, Kondo S, Tanaka E et al (2010) Outcome of surgical treatment of hilar cholangiocarcinoma: a special reference to postoperative morbidity and mortality. J Hepatobiliary Pancreat Sci. 17(4):455–462

Hoeffel C, Azizi L, Lewin M et al (2006) Normal and pathologic features of the postoperative biliary tract at 3D MR Cholangiography and MR Imaging. Radiographics 26:1603–1620

Huynh-Charlier I, Taboury J, Charlier P, Vaillant JC, Grenier P, Lucidarme O (2009) Imagerie du foie opéré. J Radiol 90: 888–904

Igami T, Nishio H, Ebata T et al (2010) Surgical treatment of hilar cholangiocarcinoma in the "new era": the Nagoya University experience. J Hepatobiliary Pancreat Sci. 17(4):449–454

Katsihuko Y, Takashi M, Hirochi H et al (1994) Isolated hepatic caudate lobectomy. Surg 115:757–761

Kim JY, Kim KW, Ahn CS et al (2008) Spectrum of biliary and nonbiliary complications after laparoscopic cholecystectomy: radiologic findings. Am J Roentgenol. 191(3): 783–789

Kitagawa Y, Nagino M, Kamiya J et al (2001) Lymph node metastasis from hilar cholangiocarcinoma : Audit of 110 patients who underwent regional and paraaortic node dissection. Ann Surg 233:385–392

Kooby DA, Stockman J, Ben-Porat L, Gonen M, Jarnagin WR, Dematteo RP et al (2003) Influence of transfusions on perioperative and long-term outcome in patients following hepatic resection for colorectal metastases. Ann Surg 237: 860–870

Laurent V, Ayav A, Hoeffel C et al (2009) Imagerie des voies biliaires opérées. J Radiol 90:905–917

Lee CM, Stewart L, Way LW (2000) Postcholecystectomy abdominal bile collections. Arch Surg 135:538–544

Letourneau JG, Steely JW, Crass JR et al (1988) Upper abdomen: CT finding following partial hepatectomy. Radiology 166:139–141

Lohan D, Walsh S, McLoughlin R, Murphy J (2005) Imaging of the complications of laparoscopic cholecystectomy. Eur Radiol 15:904–912

McAlister VC (2000) Abdominal fluid collection after laparoscopic cholecystectomy British Journal of Surgery 87: 1126–1127

Morrin MM, Kruskal JB, Hochman MG, Saldinger PF, Kane RA (2000) Radiologic features of complications arising from dropped gallstones in laparoscopic cholecystectomy patients. Am J Roentgenol 174:1441–1445

Pitre J, Panis Y, Belghiti J (1992) Left hepatic vein kinking after right hepatectomy: a rare cause of acute Budd Chiari syndrome. Br J Surg 79:798–799

Quinn SF, Bodne DJ, Clark RA et al (1988) Upper abdomen: CT finding following partial hepatectomy. Radiology 168: 879–880

Schäffer M, Lauper M, Krähenbühl L (2000) A nation's experience of bleeding complications during laparoscopy. Am J Surg 180:73–77

Sibert A (2010) Aspect post opératoire des voies biliaires. In Imagerie de l'abdomen, Vilgrain V and Regent D, Flammarion Paris

Stumpp P, Kloppel R, Kahn T (2005) Imaging after a Whipple operation. Improving visibility of the afferent jejunal loop in spiral Computed Tomography using biliary contrast medium. J Comput Assist Tomogr 29:394–400

Tanaka K, Uemoto S, Tokunaga Y et al (1993) Surgical techniques and innovations in living related liver transplantation. Ann Surg 217:82–91

Thurley PD, Dhingsa R (2008) Laparoscopic cholecystectomy: Postoperative Imaging, Am J Roentgenol 191:794–801

Vitellas KM, El-Dieb A, Vaswani KK et al (2001) Detection of bile duct leaks using MR cholangiography with IV mangafodipir trisodium (Teslascan). J Comput Assist Tomogr 25:102–105

Walker T (2008) Biliary injury after laparoscopic cholecystectomy: why still a problem? Gastroenterology 134: 894–895

Zappa M, Dondero F, Sibert A, Vullierme MP, Belghiti J, Vilgrain V (2009) Liver Regeneration at Day 7 after Right Hepatectomy: Global and Segmental Volumetric Analysis by Using CT. Radiology 252:426–432

Inflammatory Processes in the Liver and Biliary Tract

Wesley C. Chan and Benjamin M. Yeh

Contents

Abstract

The liver and bile ducts and gallbladder are common organs to be affected by inflammatory processes. This chapter summarizes the range of common benign disease processes that involve these organs. The most common of these diseases involve biliary stones, which may lodge in the gallbladder or intra- or extra-hepatic ducts. Bile duct and gallbladder obstruction lead to inflammation and infection. Ascending or idiopathic causes of biliary inflammation are also not uncommon and typically affect characteristic populations. Infection of the liver parenchyma is most commonly related to viral hepatitis, but can also be related to bacterial, fungal, and parasitic infection. Idiopathic causes, such as autoimmune hepatitis may also occur. Most of these benign entities predispose the patient to develop hepatobiliary malignancies, and so the evaluation of CT scans for these patients should include a search for possible tumor.

1 General Considerations

This chapter will summarize the major benign inflammatory conditions of the liver and biliary tract which cover a wide range of entities, from hepatitis to abscesses to cholangitis. A critical consideration is

W. C. Chan · B. M. Yeh (✉)
Department of Radiology and Biomedical Imaging,
University of California San Francisco,
San Francisco, CA 94143-0628, USA
e-mail: ben.yeh@ucsf.edu

C. J. Zech et al. (eds.), *Multislice-CT of the Abdomen*, Medical Radiology. Diagnostic Imaging,
DOI: 10.1007/174_2012_545, © Springer-Verlag Berlin Heidelberg 2012

that many of these benign hepatobiliary conditions are risk factors for the development of hepatobiliary malignancy, and so a search for possible malignancy should be made if an inflammatory process is noted. Hepatobiliary malignancies are covered in "Imaging Findings of Cirrhotic Liver" and "Neoplastic Processes in Biliary System".

1.1 Normal Appearance of the Liver and Biliary Tract

At unenhanced CT, the normal liver parenchyma shows a homogeneous CT attenuation between approximately 35–60 Hounsfield units when imaged at a tube potential of 120 kVp. The contour of the liver is smooth and regular, particularly along the dome of the diaphragm, although muscular slips of the diaphragm may cause indentations, and mild irregularity may be normal along the undersurface of the liver. With intravenous contrast material enhancement, the parenchyma of the liver should be homogeneous in attenuation without regional variation in any phase of CT contrast enhancement. The intrahepatic bile ducts almost always are parallel the portal veins and normal ducts should be imperceptible or only barely visible as scattered, noncontinuous low attenuation foci. The common hepatic and common bile ducts in most cases measure less than 7 mm in diameter and the bile duct wall either imperceptible or less than 1.5 mm thick without associated fat stranding.

The normal common bile duct usually is less than 7 mm in diameter, though larger diameters may be seen in some patients with a prominent cystic duct in close apposition with the common bile duct and in some patients with prior cholecystectomy. Regardless of size, a normal common bile duct should gradually taper just as it approaches the ampulla. The wall of the extrahepatic bile duct while often imperceptible can be visualized up to 1.5 mm thick, usually on intravenous contrast enhanced CT (Schulte et al. 1990).

The gallbladder is a cystic structure which sits in the gallbladder fossa between the right and left lobes of the liver. The wall of the normal gallbladder should either be nonvisible or, if seen, should enhance to a similar degree as liver parenchyma and be less than 3 mm in thickness. The gallbladder should not be larger than 5 cm in diameter. There should be no surrounding fat stranding and the internal contents (bile) should be of fluid attenuation (between −10 and 20 HU).

1.2 Effect of Inflammation and Bile Duct Obstruction on Appearances

While occasionally inflammation of the liver parenchyma and biliary tract may occur in the absence of visible findings at CT, in the majority of cases CT findings are evident. Geographic or heterogeneous hyperenhancement of the associated liver parenchyma, particularly during the late arterial phase of contrast enhancement, may be identified due to increased arterial and decreased portal venous fractional flow. These transient hepatic attenuation differences may be related to increased overall vascular flow related to the inflammation, or may be due to edema-related local increased hepatic interstitial pressure which limits low pressure portal venous inflow. Intraparenchymal gas or pneumobilia may be seen due to the presence of gas forming organisms, but such findings are most commonly related to prior instrumentation. Periportal edema may be seen with biliary disease or with vascular processes. Affected bile duct segments may be dilated and show a visibly thickened enhancing bile duct wall.

1.3 MSCT Technique

CT is often the first imaging study performed on patients with abnormal liver function tests or upper quadrant pain. Unenhanced CT may be helpful for the identification of biliary stones, but the use of intravenous iodinated contrast is required for optimal assessment of the liver parenchyma and biliary tract. Portal venous phase imaging (obtained after a 60–90 s delay following injection of contrast) is often adequate for preliminary assessment of possible hepatobiliary pathology. The use of high attenuation oral contrast is usually unnecessary and may result in image artifacts or limited evaluation of the distal duct and associated bowel wall perfusion abnormalities. The use of near water attenuation contrast agents which distend the duodenum can be helpful to evaluate the distal duct. Coronal and sagittal reformats are often useful for delineating anatomy and to problem solve questionable abnormalities seen on the axial source images.

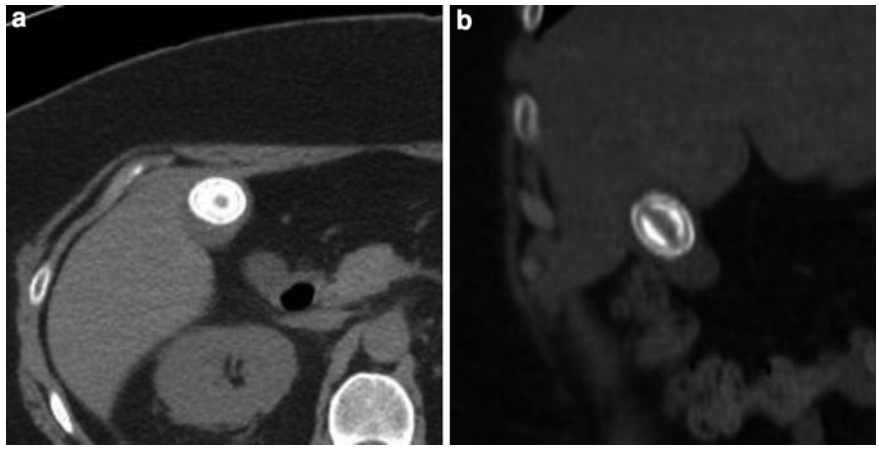

Fig. 1 **a** Axial image of a lamellated gallstone. **b** Coronal view

Thin section (2.5 mm or thinner) imaging with multiplanar reformations assists in the evaluation of the biliary tract. In particular, coronal reformations assist with common bile and common hepatic duct visualization. High tube potential settings (140 kVp) may improve the visualization of biliary stones.

2 Biliary Stone Disease

2.1 Epidemiology

Cholelithiasis affects approximately 25 million adults in the United States, particularly in women. Higher rates of cholelithiasis occur in Caucasian, Hispanic, and Native American populations while lower rates have been reported in African American, eastern European, and Japanese populations. Roughly 70% of gallstones are predominantly cholesterol and 30% pigment.

2.2 Appearance of Stones

Ultrasonography is the imaging technique of choice for detection of gallstones in the gallbladder. However, the sensitivity markedly decreases for the direct depiction of stones in the common bile duct (as low as 25%). Endoscopic retrograde cholangiopancreatography (ERCP) remains the gold standard for detecting biliary stones outside of the gallbladder, but is invasive and associated with major complication rates of 1.4% or higher. MRCP provides outstanding sensitivity for biliary stones, but may miss small stones <3 mm and may be limited when pneumobilia is present.

Reports of CT sensitivity have varied from 25 to 88% for direct depiction of gallstones. Biliary stones are more conspicuous on noncontrast than on intravenous contrast enhanced CT of the abdomen (Neitlich et al. 1997). Biliary stones can have a surprisingly varied appearance at CT, though for any given patient stones tend to resemble each other. Occasionally stones may have markedly different imaging features even within the same patient. Non-calcified pure cholesterol stones can appear slightly hypodense when compared to the surrounding bile, particularly when low kVp settings are used. Pigment stones and calcified stones usually appear hyperdense to bile. Stones containing a mixture of cholesterol and calcium carbonate/bilirubinate often demonstrate a laminated appearance with alternating low and high density rings (Fig. 1). Occasionally, stones can dehydrate and become internally filled with nitrogen gas which can be depicted on CT imaging (Fig. 2). The gas often has a stellate configuration and may be the only finding to indicate the presence of stones. Gallstones almost always appear in the dependent portion of the gallbladder, but occasionally adherent stones may be nondependent.

Potential mimics of stones at CT include gallbladder sludge, blood clots, and dense proteinaceous mucus can simulate multiple small stones on CT. Ultrasound or MRCP can be used to problem solve in cases where accurate determination of gallbladder content is needed.

Choledocholithiasis, which is the presence of stones in the common bile duct, is frequently a delayed diagnosis and should be considered for any patient with recurrent colicky upper abdominal pain.

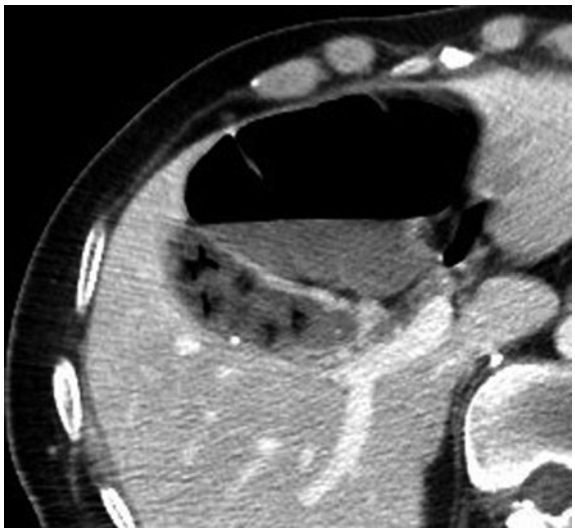

Fig. 2 Multiple nitrogen-gas-containing gallstones. Note the stellate configuration of the gas in the gallstones

Choledocholithiasis may be missed at US owing to the poor acoustic window for the common bile duct and the fact that up to 50% of cases of choledocholithiasis occur in the setting of nondilated bile ducts. For this reason, careful evaluation of the common bile duct for stones should be made. In particular, the observation of a dependent focus that may be less or more dense than bile and that shows an anterior crescent of bile or gas should prompt further work up by MRCP or possibly ERCP to confirm the presence of a common duct stone. With careful observation, CT has a sensitivity of up to 75–88% for choledocholithiasis.

3 Inflammatory Biliary Conditions

3.1 Acute Cholecystitis

Cholecystitis refers to inflammation of the gallbladder and can occur in both acute and chronic forms. In acute cholecysitis, patients often present with right upper quadrant pain, tenderness over the gallbladder fossa, and a positive Murphy's sign. Approximately 90–95% of all cases of acute cholecystitis are related to gallstone disease, where classically, a stone becomes impacted at the gallbladder neck or cystic duct causing obstruction of the normal bile drainage of the gallbladder. Trapped concentrated bile has an inflammatory effect on the gallbladder, and gallbladder distension itself may cause increased translocation of bacteria into the wall. Cholecystitis ranges in severity from mild inflammation to gangrene.

CT findings of cholecystitis are similar to that seen with ultrasound. An inflamed and obstructed gallbladder will appear distended (>10 cm in long axis), demonstrate a thickened wall (>3 mm), and show evidence of pericholecytic fat stranding (Fig. 3). Pericholecytic fluid may be present and internal bile can show increased attenuation (>20 HU) (Fidler et al. 1996). Gallbladder wall hyperenhancement is an unreliable finding. Adjacent inflammation to the liver (perihepatitis) can manifest as ill-defined low attenuation in the liver adjacent to the gallbladder fossa at unenhanced or portal venous phase imaging. On arterial phase imaging, this area may demonstrate increased hepatic attenuation around the gallbladder fossa due to increased arterial flow. An obstructing gallstone within the gallbladder neck or cystic duct may not be directly visualized on CT but should be sought as a cause of acute cholecystitis.

Gallbladder wall thickening can be sometimes difficult to distinguish from pericholecystic fluid. In these cases, one should look for the presence of a crossing vessel through the area of low density "thickening" which is more indicative of gallbladder wall thickening. It is important to remember that isolated gallbladder wall thickening is nonspecific and may be caused by many non-inflammatory etiologies such as portal hypertension, hence other signs of local inflammation should be sought. A nondistended gallbladder virtually excludes a diagnosis of acute cholecystitis, with the exception being perforated acute cholecystitis leading to a decompressed gallbladder.

Acute cholecystitis can rarely be complicated by the presence of gas forming bacteria and/or ischemia of the gallbladder wall may result in emphysematous cholecysitits. Up to 38% of such cases are associated with diabetes and are more common in men than women (7:3). Cholelithiasis is often absent. There is a much higher (five times) risk for development of gangrenous cholecysitis and/or perforation when compared to conventional acute cholecytitis. Mortality is high (approximately 15%), therefore accurate and timely diagnosis is important.

On CT, the main finding is the presence of gas either in the gallbladder wall or lumen (Fig. 4). Gas in the gallbladder wall often has a curvilinear appearance similar to that of bowel pneumatosis. Gas may also extend out of the gallbladder and track along fistulas.

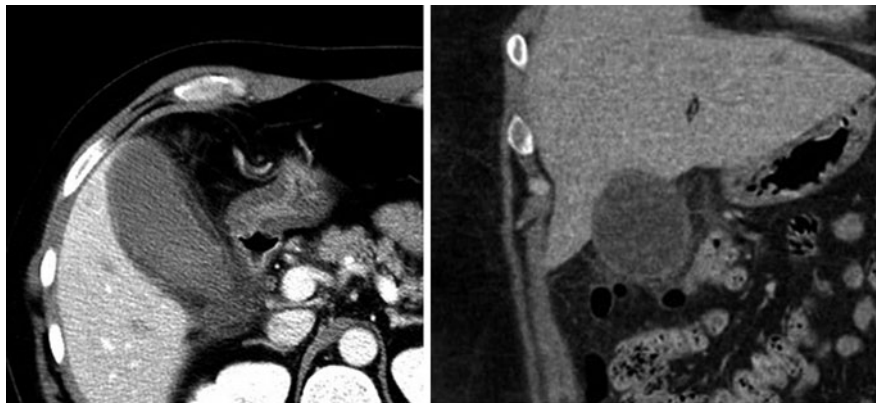

Fig. 3 Axial and coronal views of acute cholecystitis

3.2 Acalculous Cholecystitis

Acalculous cholecystitis comprises up to 15% of all cases of acute cholecystitis and 47% of all post-operative cholecystitis. It occurs most commonly in critically ill, burned, traumatic, and post-surgical patients who are chronically fasted. Other risk factors include vasculitis, total parenteral nutrition, and diabetes mellitus. The exact etiology is unknown but it may be related to overdistension of the gallbladder which may lead to reduced mural perfusion or other causes of reduced resistance to infection.

CT findings are similar to those of acute cholecystitis associated with stone disease and include gallbladder wall thickening, gallbladder distention, and pericholecystic inflammatory changes.

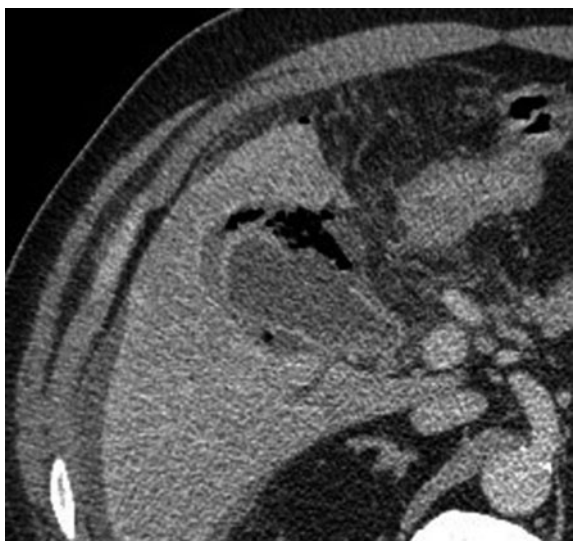

Fig. 4 Axial view of emphysematous cholecystitis. Note the presence of gas in the gallbladder wall. There is also evidence of rupture with a locule of free air at the anterior liver tip

3.3 Gangrenous Cholecystitis

Gangrenous cholecystitis, where the gallbladder wall becomes ischemic and necrotic, may complicate both acute and chronic cholecystitis. There is an increased rate of perforation with an associated mortality ranging from 15 to 40%. It occurs in 2–38% of all acute cholecystitis cases.

A critical CT finding is absence of or markedly decreased gallbladder wall enhancement compared to that of the liver parenchyma in the presence of gallbladder wall thickening. Other suggestive findings include the presence of gas in the gallbladder wall or lumen, irregular gallbladder wall thickening, the presence of intraluminal sloughed membranes, and pericholecystic collections (Fig. 5). The degree of gallbladder distention and wall thickening tends to be greater than that seen with uncomplicated acute cholecystitis. Clinically, the patient's symptoms often will shift away from the right upper quadrant and gallbladder fossa.

Rarely, bleeding may occur into the gallbladder wall and lumen resulting in a variant of gangrenous cholecystitis termed hemorrhagic cholecysititis. On CT, the presence of mural or luminal high density compatible with acute blood product suggests the presence of hemorrhagic cholecytitis. Both gangrenous and hemorrhagic cholecysititis require urgent surgical intervention as they are at high risk for perforation.

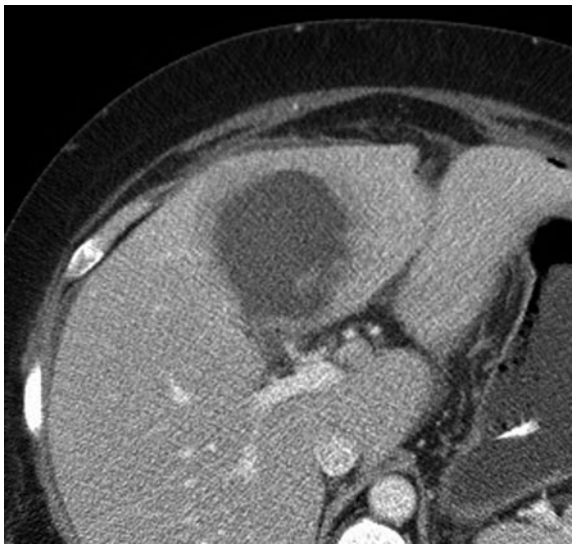

Fig. 5 Axial image of gangrenous cholecystitis. Note lack of mural enhancement and intraluminal membranes

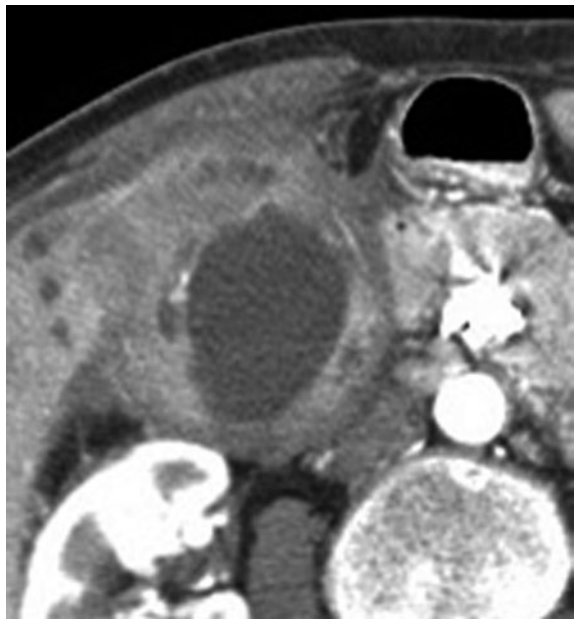

Fig. 6 Axial view of xanthogranulomatous cholecystitis. Note the marked gallbladder wall thickening and presence of low density foci in the wall. Gallbladder carcinoma can have a similar appearance

3.4 Gallbladder Perforation

If untreated, acute cholecystitis may progress to perforation. There is a higher rate of perforation in the setting of gangrenous and emphysematous cholecystitis. Perforation occurs in approximately 5–10% of all cases of acute cholecystitis with an associated mortality of 19–24%. Acute perforation often presents as generalized peritonitis. On CT, the gallbladder may appear decompressed with a marked amount of pericholecytic fluid. Extraluminal gallstones may also been seen outside of the gallbladder in the peritoneal cavity. If untreated, abscesses may occur locally around the gallbladder, liver, colon, or small bowel. In chronic perforation, biliary fistulas cause abnormal communication between the biliary system/gallbladder and the GI tract and rarely to the abdominal wall. On CT, a fistulous tract may be seen connecting the gallbladder and stomach or right colon.

3.5 Chronic Cholecystitis

Chronic cholecystitis refers to repeated transient gallbladder obstruction by gallstones which, over time, leads to low-grade chronic inflammation and fibrosis. CT findings are nonspecific demonstrating gallbladder wall thickening with cholelithiasis. The clinical history of long-standing symptomology would point toward chronic over acute cholecystitis.

Xanthogranulomatous cholecystitis is a rare disease related to chronic cholecystitis with a pathogenesis similar to xanthogranulomatous pyelonephritis. In this entity, chronic gallbladder inflammation leads to infiltration of the gallbladder by multiple lipid-laden inflammatory cells. On CT, the gallbladder wall is often markedly thickened and deformed. The wall may contain multiple low density areas caused by foci of fatty inflammation or abscesses (Fig. 6). The appearance can mimic that of gallbladder carcinoma.

3.6 Porcelain Gallbladder

Porcelain gallbladder is a rare disorder related to chronic cholecystitis causing gallbladder wall calcification. On CT, there will be varying amounts of high density calcification in the gallbladder wall (Fig. 7). Special care should be made to look for any underlying soft tissue mass as there is a controversial reported association with gallbladder carcinoma. For this

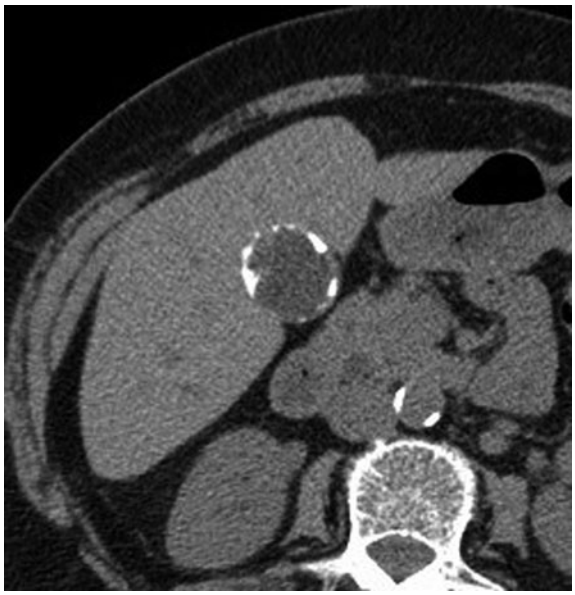

Fig. 7 Axial unenhanced image of porcelain gallbladder

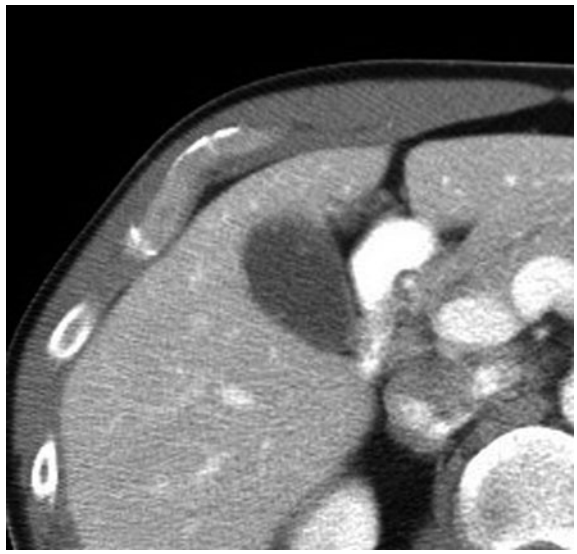

Fig. 8 Multiple small gallbladder polyps. Note the non-dependent polyps along the anterior gallbladder wall

reason, prophylatic cholecystectomy has been advocated in cases of porcelain gallbladder, though more recent studies show the risk of malignancy may not be substantially greater than for the general population.

3.7 Mirrizi Syndrome

Mirrizi syndrome is rare and occurs when extrinsic obstruction of the common hepatic duct is caused by an impacted gallstone in the cystic duct or gallbladder neck. In the majority of cases, the distal cystic duct and common hepatic duct are parallel and encased in a common sheath. On CT, careful assessment of the hepatic duct may demonstrate an area of extrinsic narrowing by an adjacent gallstone with upstream duct dilation.

3.8 Choledocholithiasis

Choledocholithiasis refers to the presence of a stone in the intra or extrahepatic bile ducts and represents the most common cause for biliary obstruction. This can occur from the passage of gallstones from the gallbladder to the common bile duct or from stone development directly within the biliary tract. This can lead to obstruction and cholangitis. Stones lodged in the distal bile duct near the ampulla can also obstruct the main pancreatic duct and cause pancreatitis.

On CT, stone visualization has been reported between 75 and 88% (Neitlich, Anderson). Several signs have been described for choledocholithiasis (Baron et al. 1983; Baron 1987; Baron 1991). The target sign refers to a stone visible as a central density surrounded by a complete halo of hypodense bile. The rim sign refers to a complete rim of increased density around the periphery of a low density stone. A cresent sign is seen when a high density calculus is eccentrically and dependently located within the duct with an anterior cresent of hypodense bile. Indirect signs of choledocholithiasis include bile duct dilation and abrupt termination of the bile duct. Indirect findings on their own are nonspecific and are not definitive of stone disease. MRCP and ERCP are often the imaging modality of choice in the setting of suspected choledocholithiasis. Notably, even with these modalities, small stones < 3 mm in diameter may be missed by imaging.

3.9 Gallbladder Polyps

Gallbladder polyps are small enhancing soft tissue lesions projecting from the gallbladder wall into the lumen (Fig. 8). Most are cholesterol polyps which are

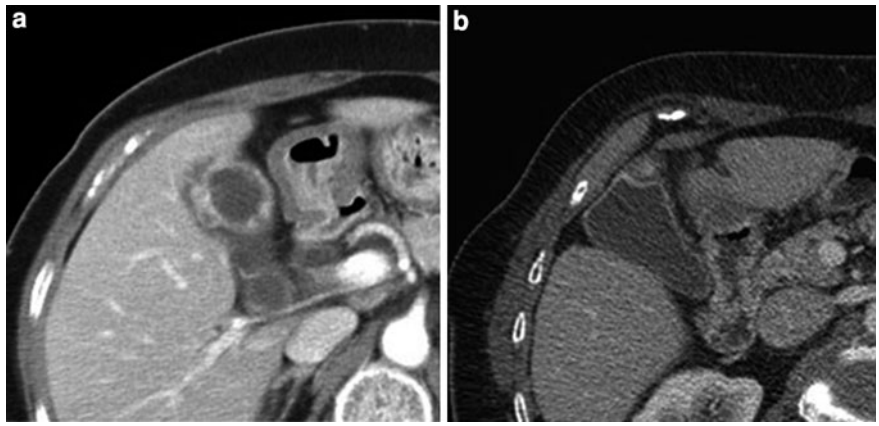

Fig. 9 Axial images of adenomyomatosis. **a** diffuse type **b** focal fundal type

often multiple. A single polyp is often a benign adenoma. There is a slight associated malignant degeneration of polyps and cholecystectomy is often advocated for polyps larger than 10 mm in size. Polyps between 5 and 10 mm are often followed by ultrasound. When seen in the dependent portion of the gallbladder, they can be difficult to be distinguished from small gallstones by CT.

3.10 Adenomyomatosis

Adenomyomatosis of the gallbladder is a benign hyperplastic cholecystosis marked by tiny macroscopic diverticula (dilated Rokitansky-Aschoff sinuses) and thickening of the gallbladder wall. Adenomyomatosis is relatively common, found in up to 8.7% of cholecystectomy specimens (Williams et al. 1986) and is associated with gallstones. Often, it is an incidental finding with surgery only indicated if the patient is symptomatic.

Most commonly, adenomyomatosis is localized to the gallbladder fundus and may appear to be mass-like with characteristic small ~ 5 mm cystic spaces representing the dilated sinuses (Fig. 9a). More extensive involvement of the gallbladder fundus may result in an "hourglass" configuration of the gallbladder. In the diffuse form, there is global gallbladder wall thickening and hyperenhancement (Fig. 9b). The presence of small cystic spaces in the thickened area of gallbladder wall helps distinguish benign adenomyomatosis from malignant disease (Ching et al. 2007).

4 Bile Duct Inflammation

4.1 Acute Cholangitis

Acute cholangitis refers to acute infection of the biliary tract, usually by gram negative bacteria, and is usually associated bile duct obstruction from strictures or stone disease. Acute cholangitis classically presents with right upper quadrant pain, jaundice, and fever.

The diagnosis of acute cholangitis relies heavily on clinical signs and symptoms. CT may show intra and extra-hepatic bile ductal dilation with mural enhancement of the intra and extrahepatic bile ducts. Periportal hyperenhancement may occur and reflect local hyperemia. Advanced cases can be complicated by the formation of hepatic biliary absesses which are often multiple. Chronic infection can also lead to secondary sclerosing cholangitis.

4.2 Sclerosing Cholangitis

Sclerosing cholangitis refers to an inflammatory disease of the biliary tract that results in stricturing of the affected ducts. There are two major forms: primary sclerosing cholangitis (PSC) refers to idiopathic inflammation of the biliary system. Primary sclerosing cholangitis is seen mostly in young adult men and has a high association with inflammatory bowel disease. Up to 75% of cases are associated with ulcerative colitis. However, only a minority of patients with

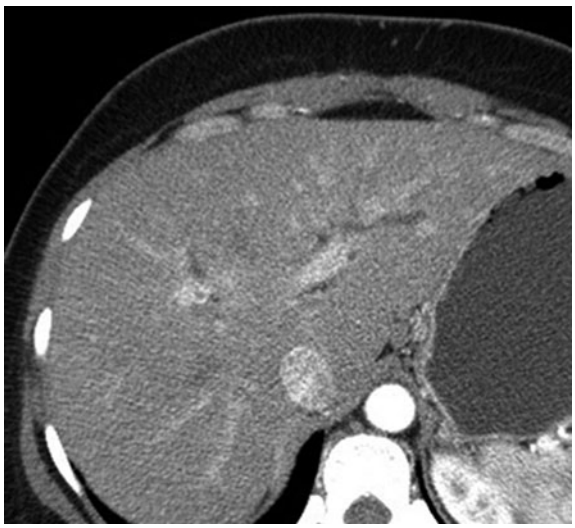

Fig. 10 Primary sclerosing cholangitis. There is irregular and discontinuous dilatation and structuring of the intrahepatic biliary tract

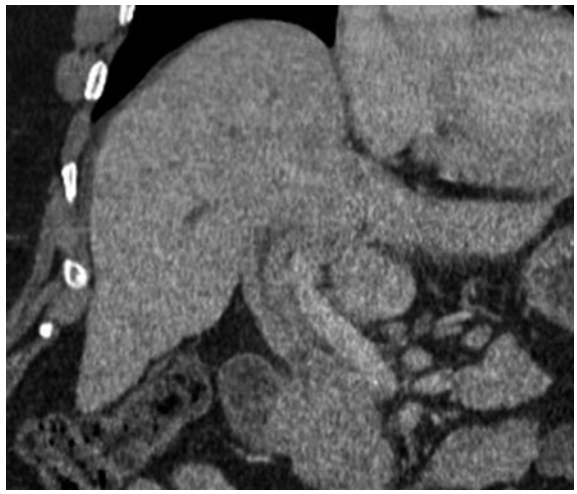

Fig. 11 Primary sclerosing cholangitis changes in the CBD. On this coronal contrast enhanced image, there is marked nodular mural thickening of the CBD with irregular luminal narrowing

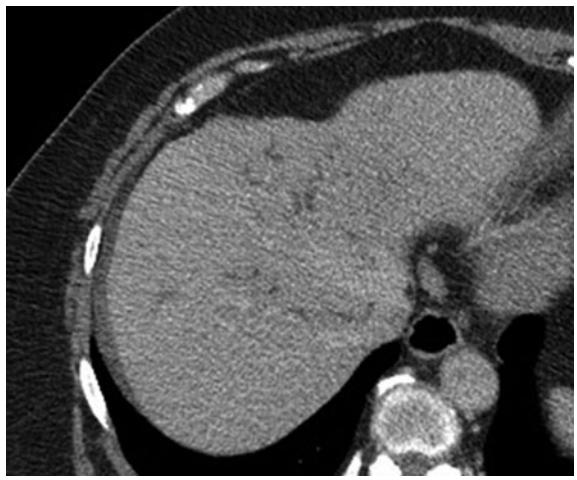

Fig. 12 Chronic primary sclerosing cholangitis. Irregular dilated intrahepatic ducts are seen most prominently in segments 8 and 4a. There is atrophy of the affected segments with nodularity to the liver contour due to fibrosis

ulcerative colitis show clinical sclerosing cholangitis. This disease is eventually leads to cirrhosis and liver failure over a period of 5–10 years. Secondary sclerosing cholangitis occurs due to an identifiable cause and may be related to chronic infection from bile duct strictures or stones, previous surgery, drug use, or congenital biliary anomalies. Typically, involvement of both the intra- and extrahepatic ducts is seen, though rarely only one of these sites may be involved. The cystic duct is also less commonly involved (18% or less).

At ERCP, highly suggestive findings of sclerosing cholangitis are diffuse irregularity of the biliary tract with alternating areas of structuring and mild bile duct dilatation. Findings at CT are nonspecific and include focal, discontinuous areas of mild or moderate bile duct dilation without an obvious underling mass (Rahn et al. 1983) (Fig. 10). If the inflammation is advanced, CT may show marked biliary mural thickening, nodularity, and hyperenhancement, particularly of the common bile duct wall (Fig. 11). Lymphadenopathy may also be seen, but is nonspecific. As the inflammatory process progresses into the more chronic phase, secondary findings can be seen in the adjacent liver with fibrosis and atrophy of affected segments of the liver and more pronounced dilation of the intra and extrahepatic bile ducts (Fig. 12). Cholangiocarcinoma is a feared complication of sclerosing cholangitis and special care should be taken to evaluate for the presence of soft tissue masses in these patients or for secondary signs of focal areas of increasing focal bile duct dilatation suggesting evolving stricutres.

Mimics of sclerosing cholangitis include AIDS cholangitis and ischemic biliary stricture. AIDS cholangitis may be related to opportunistic infection in the AIDS population that cause biliary inflammation and can lead to biliary structuring and obstruction. Common organisms

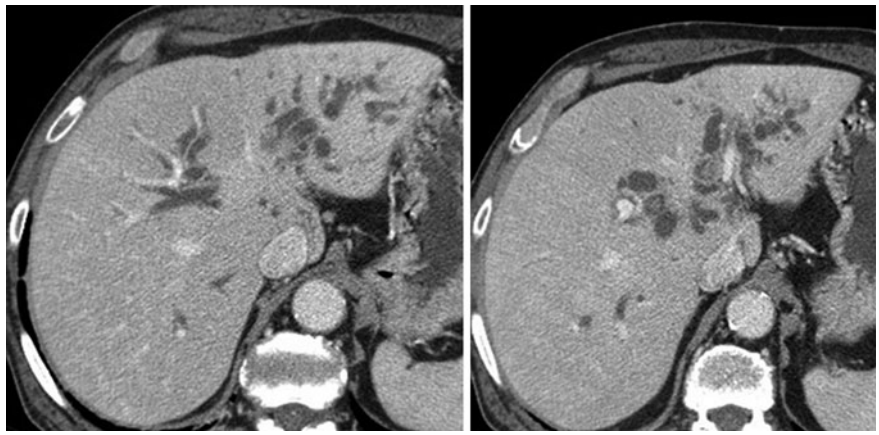

Fig. 13 Recurrent pyogenic cholangitis. Axial contrast enhanced images from the same patient demonstrate marked intrahepatic biliary ductal dilation, predominantly in the *left* lobe. There are also multiple hyperdense intraductal filling defects (*arrows*) seen in keeping with pigment stones

include *Cryptosporidium* and *Cytomegalovirus (CMV)*. AIDS cholangitis can have an identical appearance to sclerosing cholangitis on all imaging modalities, but papillary stenosis is distinctly more common in AIDS cholangitis. Ischemic biliary strictures typically occur only after hepatobiliary surgery, hepatic arterial chemoembolization, or trauma.

4.3 Primary Biliary Cirrhosis

Primary biliary cirrhosis (PBC) describes an idiopathic progressive destruction of intrahepatic bile ducts leading to portal fibrosis and hepatic scarring. Typically it affects middle aged women and leads inexhorably to liver failure, at times as quickly as in two years. PBC is associated with a number of systemic autoimmune disorders including rheumatoid arthritis and thyroiditis.

The diagnosis of PBC is made by biopsy. Imaging findings serve to help stage the severity of disease and to assess for complications. Initially, the liver may be enlarged and smooth in contour. As disease progresses, the liver begins to atrophy and becomes more nodular. Asymmetric hypertrophy and hyperattenuation of the caudate lobe may be seen in the majority of cases. As disease progresses to cirrhosis, liver parenchymal heterogeneity with lacelike low density areas of fibrosis are seen (Blachar et al. 2001). Lymphadenopathy can be very prominent with multiple enlarged enhancing lymph nodes seen in the upper abdomen. In advanced disease, there will be CT findings of portal hypertension such as splenomegaly, ascites, and varices. As with other chronic liver diseases, patients with PBC have an increased risk of hepatocellular cancer, but with a lower frequency when compared to that of alcoholic and viral cirrhosis.

4.4 Recurrent Pyogenic Cholangitis

Recurrent pyogenic cholangitis (RPC) is a chronic inflammatory disorder characterized by a cycle of intra- and extrahepatic bile duct pigment stone formation leading to biliary obstruction that causes bile stasis and pyogenic cholangitis. RPC is almost always associated with Gram negative bacterial infections and may also be related to chronic parasitic infection such as by *Ascaris* or *Clonorchis sinesis*. This disease is endemic in Southeast Asia, and relatively rare elsewhere. Repeated mechanical extraction of recurrent putty-like stones is often required, and partial hepatectomy may be considered for intractable disease. Over time, repeated cholangitis can lead to liver failure and patients are at an increased risk for developing cholangiocarcinomas.

The classic CT finding of RPC is intrahepatic biliary ductal dilation with hyperdense intrahepatic ductal stones, which can be seen in up to 75% of cases (Fig. 13). The common bile duct may also demonstrate dilation and increased tortuosity. In contrast to PSC, bile duct stricture is relatively rare in RPC (22%) (Chan et al. 1989). Fibrosis and lobar atrophy can be seen in advanced cases, reportedly more commonly affecting the left lobe. When RPC is a diagnostic consideration, special care should be made to assess for any associated soft tissue masses which may indicate cholangiocarcinoma.

5 Inflammatory Hepatic Conditions

5.1 Hepatitis

Inflammation of the liver most commonly occurs as result of viral infection, alcohol, or acetaminophen overdose. The CT findings of acute hepatitis are nonspecific and clinical history and liver function tests are often the key to making the accurate diagnosis. CT findings include hepatomegaly, heterogenous parenchymal enhancement, periportal edema, and marked gallbladder wall thickening (Fig. 14). The liver is often diffusely hypodense in alcoholic hepatitis due to fatty infiltration. Lymphadenopathy in the porta hepatis is also often seen. In chronic hepatitis, regenerative nodules maybe seen and can progress to cirrhosis. Careful assessment should be made to identify possible hepatocellular carcinoma in patients with chronic hepatitis, particularly when cirrhosis is present.

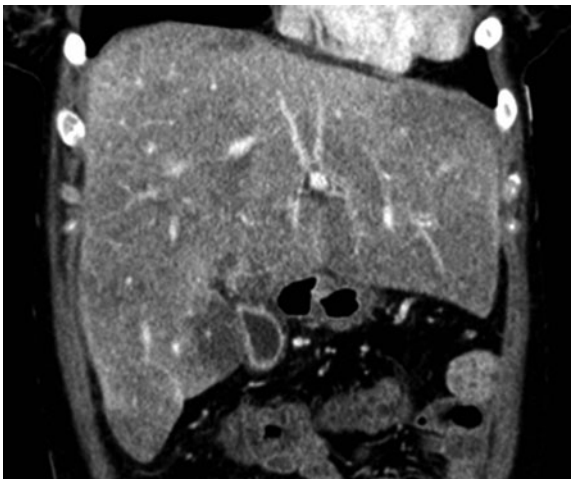

Fig. 14 Acute hepatitis. Coronal CT demonstrating hepatomegaly, heterogenous parenchymal enhancement, and gallbladder wall thickening

5.2 Autoimmune Hepatitis

Autoimmune hepatitis is a rare and poorly understood chronic inflammatory disease that may have systemic manifestations. It affects women more frequently than men and is associated with primary biliary cirrhosis and sclerosing cholangitis. As there is no definite diagnostic test, the diagnosis is often made by combining clinical, biochemical, and pathologic findings. CT findings are nonspecific with a wide number of findings which overlap with that of conventional hepatitis.

5.3 Intrahepatic Abscess

Infections of the liver can lead to localized collections damaging parenchyma. Bacterial abscesses account for the majority of liver abscess with *Clostidium* and *E. Coli* being the most common offending organisms. Fungal, mycobacterial, and amebic abscesses represent other, less common, causes of intrahepatic abscess. Organisms may migrate into the liver parenchyma from the biliary tract, portal vein, hepatic artery, or by direct extension. Abscesses may be clustered and multiloculated ("cluster sign"), or may be unilocular.

On CT, hepatic pyogenic abscesses are often well defined, round, hypodense parenchymal masses. They will often demonstrate peripheral wall enhancement and may also have internal enhancing septations. A second peripheral rim of different enhancement in the surrounding liver parenchyma may create a 'double target' appearance (Mathieu et al. 1985). The presence of internal air within a cavity occurs in 20% of all cases and, in the absence of instrumentation, is highly suggestive of infection by gas-producing bacteria and often diagnostic for pyogenic abscess (Fig. 15). Occasionally, a cluster of smaller abscesses can coalesce into a single large collection resulting in a multiseptated cystic mass which can mimic a cystic neoplasm. Secondary edema in the surrounding liver parenchyma can be seen manifesting as ill-defined hypodensity surrounding an abscess. Secondary signs include right sided pleural effusions and ascites. When a pyogenic liver abscess is seen, special care should be made to interrogate the remainder of the abdomen for a source of infection such as appendicitis, diverticulitis, or biliary obstruction.

Amoebic abscesses are similar in CT appearance to pyogenic abscess. One differentiating feature is the presence of gas which should not be present in amoebic infection unless a fistula is present. Clinical and biochemical markers are helpful to confirm amebic infection.

Fungal microabscesses are often small and multiple, and are seen in the setting of immunocompromised

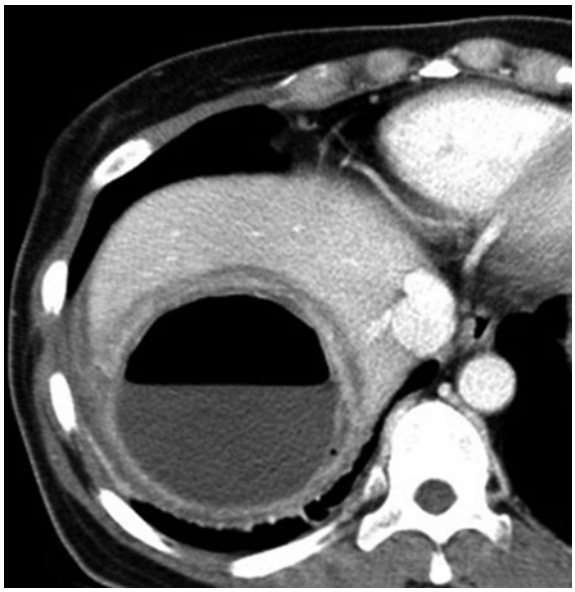

Fig. 15 Intrahepatic abscess. Large round rim enhancing cavity containing an air-fluid level in the dome of the liver

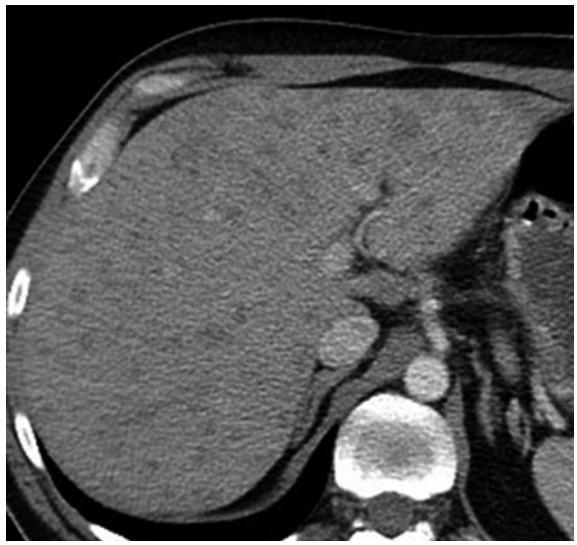

Fig. 16 Fungal abscesses. Multiple small hypodense lesions throughout all segments of the liver in this patient with candidiasis. Note that many lesions contain a pinpoint focus of central high attenuation, representing the *central dot* sign

patients. On CT, they may be imperceptible, but larger abscesses appear as multiple small hypodense lesions thoughout the liver which may or may not have peripheral rim enhancement (Fig. 16). They may contain a central small focus of high density due to accumulation of hyphae, termed the central dot sign. Simultaneous involvement of the spleen is often seen. Chronic healed abscesses may calcify.

5.4 Hydatid Disease

Hydatid disease refers to parasitic infection by the larval form of *Echinococcus granulosis or multilocularis* with *E. granulosis* seen more commonly in the western hemisphere. While the disease is rare in the developed world, it should always be considered, especially in areas with large immigrant populations exposed to sheep and dogs. Liver involvement is seen in up to 60% of cases (lungs are involved in 20%). Humans are accidental intermediate hosts and are infected by oral ingestion of food contaminated with eggs, usually from feces.

CT findings of hydatid disease differ according to the stage of infection. The right liver lobe is most often involved. Initially, hydatid cysts appear as well-defined fluid-density lesions which do not demonstrate any internal enhancement. There may be mild

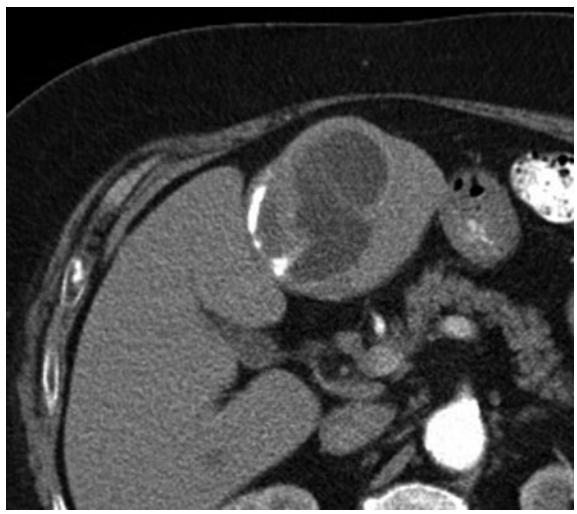

Fig. 17 Hydatid cyst. Multiloculated cystic lesions in the *left* lobe of the liver with peripheral calcification

enhancement of the cyst wall. Curvilinear crescentic peripheral calcification can be seen in up to 50% of cases (Fig. 17). As the cyst matures, internal septations can develop and the internal contents can become slightly increased in density due to the presence of internal debris. The pericyst membranes can detach and float within the cyst visualized as linear

areas of high density. The presence of multiple smaller 'daughter' cysts located peripherally within the larger 'mother' cyst is a characteristic finding and highly suggestive of hydatid disease when present. The daughter cysts often have a lower density than that of the mother cyst. As the cyst heals, dense calcification of the entire cyst may occur and imply death of the parasite.

It is important to note that biopsy of hydatid cysts should be performed with caution as leakage of the cyst contents into the peritoneal cavity can result in life-threatening anaphylaxis.

5.5 Peliosis

Peliosis hepatis is a rare disorder where multiple blood-filled cavities are seen throughout the liver. It is a benign entity and is thought to be related to sinusoidal damage and dilation. It is often asymptomatic and can affect other organs such as the spleen and lymph nodes. There are multiple associations including AIDS, renal transplantation, and drug use (including anabolic steroids).

On CT, peliosis appears as multiple small areas of low density throughout the liver. If the cavities are smaller than 1 cm in diameter, CT images may be normal. On unenhanced CT, some of the cavities may be hyperdense to liver due to internal hemorrhage. On arterial phase, the lesions may have central globular enhancement similar in attenuation to that of blood pool. The enhancement radiates outward on portal venous phase and eventually fills the cavity on delayed phase (Gouya et al. 2001). However, peripheral globular enhancement may occasionally be seen. Over time following an acute inflammation these lesions evolve and fibrose, with appropriate evolving CT characteristics.

5.6 Hepatic Sarcoidosis

Sarcoidosis is a systemic illness that can cause multiple noncaseating granulomas throughout the liver parenchyma. The most common CT finding of sarcoidosis is that of hepatomegaly with diffuse heterogeneity to the liver. Nonenhanced CT may show innumerable small low density lesions (less than 2 cm in diameter) throughout the liver which become isodense to liver after intravenous contrast administration. The spleen is often similarly affected and lymphadenopathy is very common.

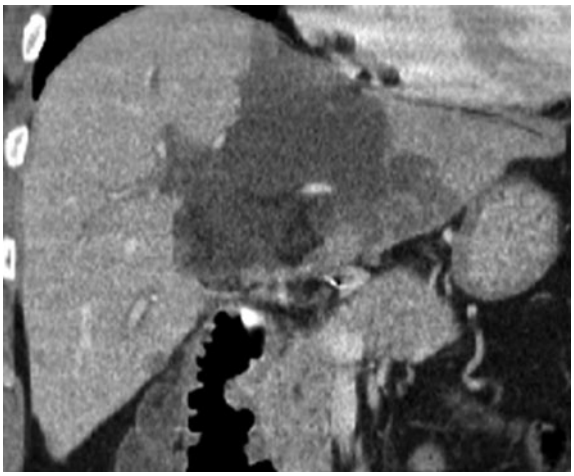

Fig. 18 Hepatic infarct. Coronal reformat in portal venous phase demonstrating a large well-defined geographic area of hypodensity in the *left* hepatic lobe in keeping with infarct. The patient was post liver transplantation

5.7 Hepatic Infarct

Infarcts of the liver are rare due to dual blood supply to the liver from the hepatic artery and portal vein. The liver also has a rich network of collateral pathways which help to maintain perfusion. Liver infarction can occur after hepatic instrumentation or surgery, including cholecystectomy, placement of a transjugular intrahepatic portosystemic shunt (TIPS), chemoembolization, partial hepatectomy, blunt trauma, and liver transplantation.

On CT, infarcts can have multiple appearance, including wedge-shaped, irregular geographic distribution or rounded (oval) areas, of low density or poor enhancement. Acutely, infarcts show ill-defined borders and these borders become more distinct as the infarct evolves. It has been shown that the varied appearances of infarcts is due to their evolution from wedge-shaped or irregular geographic zones of low attenuation with poor perfusion to round or oval collections, often cystic (Holbert et al. 1996). Infarcts are more apparent on contrast enhanced CT when compared to unenhanced, and the infracted tissue remains hypodense to normal perfused liver on all phases. Blood vessels within an infarct are non-enhancing and

may appear iso- or hypodense. Gas can be occasionally seen within the area of infarct due to necrosis and does not necessarily indicate superinfection. Rarely, infarcts can appear rounded, mimicking intrahepatic abscess (Lev-Toaff et al. 1987).

5.8 Venoocclusive Disease

Venocclusive disease is a life-threatening complication of bone marrow transplantation. Small hepatic veins become clotted/obstructed leading to liver failure. Clinically, patients present with painful hepatomegaly, ascites, and jaundice often four to five weeks after transplantation. The CT findings include narrowing of the hepatic veins, periportal edema, ascites, and heterogeneous liver enhancement. The presence of small bowel thickening should raise the possibility of graft-versus-host disease rather than venoocclusive disease (Erturk et al. 2006).

6 Conclusion

The liver and bile ducts may be affected by a range of inflammatory processes that may be focal, diffuse, or systemic. Clinical correlation complements radiological signs for the accurate diagnosis and treatment monitoring of these diseases. A continued search for possible hepatobiliary malignancy must be performed at each cross-sectional scan of the liver when benign inflammatory disease is suspected.

References

Baron RL (1987) Common bile duct stones: reassessment of criteria for CT diagnosis. Radiology 162(2):419–424

Baron RL (1991) Computed tomography of the biliary tree. Radiol Clin North Am 29(6):1235–1250

Baron RL, Stanley RJ, Lee JK, Koehler RE, Levitt RG (1983) Computed tomographic features of biliary obstruction. AJR Am J Roentgenol 140(6):1173–1178

Blachar A, Federle MP, Brancatelli G (2001) Primary biliary cirrhosis: clinical, pathologic, and helical CT findings in 53 patients. Radiology 220(2):329–336

Chan FL, Man SW, Leong LL, Fan ST (1989) Evaluation of recurrent pyogenic cholangitis with CT: analysis of 50 patients. Radiology 170(1 Pt 1):165–169

Ching BH, Yeh BM, Westphalen AC, Joe BN, Qayyum A, Coakley FV (2007) CT differentiation of adenomyomatosis and gallbladder cancer. AJR Am J Roentgenol 189(1):62–66

Erturk SM, Mortele KJ, Binkert CA, Glickman JN, Oliva MR, Ros PR et al (2006) CT features of hepatic venoocclusive disease and hepatic graft-versus-host disease in patients after hematopoietic stem cell transplantation. AJR Am J Roentgenol 186(6):1497–1501

Fidler J, Paulson EK, Layfield L (1996) CT evaluation of acute cholecystitis: findings and usefulness in diagnosis. AJR Am J Roentgenol 166(5):1085–1088

Gouya H, Vignaux O, Legmann P, de Pigneux G, Bonnin A (2001) Peliosis hepatis: triphasic helical CT and dynamic MRI findings. Abdom Imaging 26(5):507–509

Holbert BL, Baron RL, Dodd GD (1996) Hepatic infarction caused by arterial insufficiency: spectrum and evolution of CT findings. AJR 166:815–820

Lev-Toaff AS, Friedman AC, Cohen LM, Radecki PD, Caroline DF (1987) Hepatic infarcts: new observations by CT and sonography. AJR Am J Roentgenol 149(1):87–90

Mathieu D, Vasile N, Fagniez PL, Segui S, Grably D, Larde D (1985) Dynamic CT features of hepatic abscesses. Radiology 154(3):749–752

Neitlich JD, Topazian M, Smith RC, Gupta A, Burrell MI, Rosenfield AT (1997) Detection of choledocholithiasis: comparison of unenhanced helical CT and endoscopic retrograde cholangiopancreatography. Radiology 203(3):753–757

Rahn NH 3rd, Koehler RE, Weyman PJ, Truss CD, Sagel SS, Stanley RJ (1983) CT appearance of sclerosing cholangitis. AJR Am J Roentgenol 141(3):549–552

Schulte SJ, Baron RL, Teefey SA et al (1990) CT of the extrahepatic bile ducts: Wall thickness and contrast enhancement in normal and abnormal ducts. AJR 154:79–85

Williams I, Slavin G, Cox A, Simpson P, de Lacey G (1986) Diverticular disease (adenomyomatosis) of the gallbladder: a radiological-pathological survey. Br J Radiol 59(697):29–34

Neoplastic Processes in Biliary System

Tae Kyoung Kim, Korosh Khalili, and Hyun-Jung Jang

Contents

Abstract

Cholangiocarcinoma (CC) is a malignant tumor arising from biliary epithelium. Clinical manifestations vary depending on the location of the tumor. Understanding of different morphologic types of CC is useful for accurate staging and predicting prognosis. Gallbladder carcinoma usually presents with advanced disease because of the absence of specific symptoms. Multislice CT (MSCT) is presently the most commonly used imaging modality for the diagnosis and staging of the neoplasms involving the biliary system by demonstrating the tumor and abdominal vessels on any desired imaging planes with high spatial resolution. This chapter reviews imaging findings of neoplasms in the biliary system, focusing on typical imaging findings of biliary neoplasms and clinical applications of MSCT.

1 Introduction

Most neoplasms that arise from the bile duct and Gallbladder (GB) are malignant and have a poor prognosis. Clinical symptoms vary depending on the location and morphologic types of the tumor. Intrahepatic Cholangiocarcinoma (CC) or GB carcinomas usually present with a large, advanced tumor because clinical symptoms do not appear until the tumor progresses to an advanced stage. Hilar and distal extrahepatic CC, on the other hand, are relatively small at the time of detection as they typically present with symptoms of biliary obstruction.

T. K. Kim (✉) · K. Khalili · H.-J. Jang
Department of Medical Imaging,
Toronto General Hospital, 585 University Avenue,
Toronto, ON M5G 2N2, Canada
e-mail: TaeKyoung.Kim@uhn.on.ca

C. J. Zech et al. (eds.), *Multislice-CT of the Abdomen*, Medical Radiology. Diagnostic Imaging,
DOI: 10.1007/174_2011_409, © Springer-Verlag Berlin Heidelberg 2012

Radiological imaging is performed for the diagnosis and staging of the tumor. The most important role of imaging is to determine the exact location, extent, and spread of the tumor, thereby differentiating resectable and unresectable tumors. Resectability is limited by extent of the tumor in the liver and bile duct, and tumor invasion of the major hilar vessels, distant metastases to the lymph nodes and peritoneum, and underlying liver or biliary tract disease.

Multislice CT (MSCT) is presently the most commonly used imaging modality for the diagnosis and staging of neoplasms in the biliary system. With the advent of MSCT, abdominal CT scanning has become remarkably faster and the results of multiplanar reformat (MPR) images have remarkably improved. MSCT can accurately provide the tumor extent and provide detailed information of the vascular anatomy and relationship between the tumor and major abdominal vessels which is crucial for surgical planning.

2 Prevalence and Etiology

2.1 Cholangiocarcinoma

The incidence of CC varies greatly depending on the geographic regions, with the highest reported in Southeast Asia (Charbel and Al-Kawas 2011). Recent studies from most world regions have shown the incidence and mortality rate of intrahepatic CC are continuously increasing whereas those of extrahepatic CC remain constant or decreasing. Large differences in incidence and mortality between intrahepatic and extrahepatic CC suggest that these two types of CC develop from largely different etiologic factors (Cardinale et al. 2010).

Risk factors for CC include primary sclerosing cholangitis (PSC), chronic hepatolithiasis, recurrent pyogenic cholangitis (RPC), choledocholithiasis, parasitic biliary infestation, viral hepatitis, bile duct adenoma, biliary papillomatosis, Caroli's disease, choledochal cyst, thorotrast, smoking, and chronic typhoid carrier state. However, no risk factor can be identified in a large number of cases. There are substantial differences between the risk factors for both Western and Eastern geographic regions and also with respect to the anatomic location of the tumor. PSC is a major risk factor for CC in the West where the lifetime risk is 7–20% with an annual incidence of 0.6–1.5% (Burak et al. 2004). On the other hand, liver fluke infestation by *Clonorchis sinensis* and *Opisthorchis viverrini*, is a major risk factor for both intrahepatic and extrahepatic CC in the East and Southeast Asia (Choi et al. 2006; Marcos et al. 2008). Chronic hepatitis C and B virus infection has recently been reported as a risk factor for intrahepatic CC in both East and West (Malhi and Gores 2006).

2.2 Gallbladder Carcinoma

GB carcinoma affects women three times more commonly than men, and the vast majority patients are older than 40 years of age (Miller and Jarnagin 2008). GB carcinoma has a worldwide geographic distribution that correlates with the prevalence of gallstone disease. High prevalence has been reported in South America, Northern India, Japan, and Central European countries (Reid et al. 2007).

Cholelithiasis is the most important risk factor for GB carcinoma. The vast majority of patients with GB carcinoma have gallstones. The risk of GB carcinoma is 2.3–34.4 times higher in patients with gallstones than in individuals without gallstones (Lowenfels et al. 1999; Miller and Jarnagin 2008). Factors associated with gallstone disease, such as obesity, a high fat and carbohydrate diet, multiple pregnancies, and the use of estrogens, correlate with an increased risk of GB carcinoma. The mechanism by which cholelithiasis predisposes to GB carcinoma has not been clarified. Chronic inflammation of the GB mucosa by gallstones may predispose to malignant transformation through a sequence evolving from atypia to dysplasia to carcinoma in situ and, finally, to invasive carcinoma (Reid et al. 2007). Other risk factors of GB carcinoma include porcelain GB (Stephen and Berger 2001), anomalous junction of the pancreaticobiliary duct (Elmer et al. 2001), gallbladder polyps, chronic typhoid fever, adenomyomatosis, and inflammatory bowel disease (Reid et al. 2007).

3 Pathology and Clinical Features

3.1 Cholangiocarcinoma

CC can be classified as intrahepatic and extrahepatic CC by anatomic location. Extrahepatic CC can be further divided into hilar CC and distal extrahepatic

CC (Cardinale et al. 2010). Morphologic classification of CC is useful for interpreting images as well as predicting tumor behavior, prognosis and planning appropriate surgery. The morphologic classification proposed by the Liver Cancer Study Group of Japan (Yamasaki 2003) classifies intrahepatic CC as mass-forming, periductal-infiltrating, and intraductal-growing types. Lim (Lim and Park 2004) suggested that the classification can be used for both intrahepatic and extrahepatic CC. The most common histologic type of mass-forming and periductal-infiltrating CC is a well to poorly differentiated tubular adenocarcinoma which is often accompanied by abundant fibrous stroma. On the other hand, the majority of intraductal-growing CC are papillary adenocarcinomas.

Mass-forming CC is the most common type in intrahepatic CC. The tumor easily invades and penetrates the bile duct wall and grows outward to form a nodular mass in the liver parenchyma. Bile duct narrowing is common and obstructive jaundice occurs when the tumor involves the hepatic hilum. periductal-infiltrating CC is the most common type in hilar CC. The tumor grows along the bile duct wall, resulting in concentric thickening of the bile duct wall to form an elongated, spiculated appearance. The involved bile ducts are narrowed or obstructed and the upstream bile ducts are dilated. The tumors are usually small because they are discovered early due to obstructive jaundice. intraductal-growing CC is characterized by intraluminal papillary tumors anywhere in the biliary system associated with partial bile duct obstruction or dilatation. The tumors are usually small and often spread along the mucosal surface of the bile duct resulting in multiple tumors (papillomatosis). The tumor produces a variable amount of mucin which may impede the file flow causing biliary dilatation because of viscous mucin (Lim and Park 2004).

Clinical presentation of CC primarily depends on anatomic location. Intrahepatic mass-forming CC frequently presents with nonspecific right upper quadrant abdominal pain. Obstructive symptoms are uncommon. Fever, night sweats, and weight loss may occur. On the contrary, extrahepatic CC present with symptoms of biliary obstruction, cholangitis and right upper quadrant pain. Other symptoms may coexist, related to hepatitis, cirrhosis, or systemic metastases (Malhi and Gores 2006). intraductal-growing CC is usually less invasive and shows better prognosis than mass-forming or periductal-infiltrating CC.

3.2 Gallbladder Carcinoma

The vast majority of GB carcinomas are adenocarcinomas. Less common variants include papillary, mucinous, squamous, and adenosquamous subtypes. Papillary carcinomas tend to fill the lumen of the gallbladder before invading the gallbladder wall; therefore, they are associated with a better prognosis than other variants (Levy et al. 2001). The majority (60%) of GB carcinomas arise in the fundus, whereas 30% occur in the body and 10% in the neck (Reid et al. 2007). Invasion to adjacent organs, metastatic lymphadenopathy, and distant metastases are common.

The majority of patients with GB carcinoma present with advanced disease because of the absence of specific symptoms. GB carcinomas usually present with nonspecific symptoms that include abdominal pain, nausea, vomiting, jaundice, anorexia, and weight loss. As a result, the prognosis for GB carcinoma remains poor, with the curative resection rate less than 30% (Miller and Jarnagin 2008).

4 MSCT Imaging Techniques

For diagnosis and staging of neoplasms in the biliary system with MSCT, unenhanced and dual-phase contrast-enhanced scanning in the arterial phase (AP) and portal venous phase (PVP) is most commonly used. Unenhanced CT scan is helpful to differentiate between an intraductal tumor and calculi. AP scan is performed 25–40 s after the initiation of a contrast bolus or using a bolus-triggering technique. Scan delay should be optimized depending on the type of MSCT scanners and the amount and rate of contrast injection (Johnson and Fishman 2006). AP imaging is useful for understanding the arterial anatomy and evaluating the relationship between the arteries and tumor. PVP images are typically obtained at 70–80 s after initiation of a contrast bolus. It is important to ensure hepatic veins as well as portal veins are adequately enhanced as hepatic veins function as an important landmark for planes of liver resection. PVP images are most important to determine the tumor extent, venous invasion, and metastases. Delayed phase scanning at 3–5 min may be performed to demonstrate typical late enhancement of CC, but it is not widely used as dual-phase scanning (i.e. AP and

PVP) is sufficient for characterization and staging of the tumor in most cases.

Thin slice thickness of 1–2.5 mm with a variable degree of scan overlaps (typically 50%) is important for accurate tumor staging. High-end MSCT scanners, such as 32- or 64-slice MSCT scanners, are preferred for preoperative staging as they have an advantage of larger anatomic coverage during a single breath-hold. MPR images with coronal and sagittal planes are helpful to evaluate the tumor extent and relationship between the tumor and adjacent important anatomic structures. Three-dimensional (3D) reconstructions by using a maximum intensity projection or volume-rendering technique can be easily performed on various commercially available 3D workstations. 3D images provide a comprehensive delineation of hepatic vascular architecture that is particularly helpful for surgical planning, thereby reducing the risk of vascular injury during tumor resection (Catalano et al. 2008; Sahani et al. 2002, 2008).

5 MSCT Imaging Findings

5.1 Intrahepatic CC

Mass-forming intrahepatic CC usually presents with a large mass because it does not cause any symptoms when the mass is small. However, small mass-forming CC is occasionally found during the imaging surveillance for HCC in cirrhotic liver or imaging tests for other abdominal indications (Fig. 1) (Kim et al. 2007). The mass typically shows marked hypoattenuation in the AP and PVP with or without thin rim-like enhancement (Kim et al. 1997). The central portion of the tumor shows substantial enhancement in the delayed phase (>4–6 min after contrast injection) (Fig. 2) that may persist for hours due to abundant fibrous stroma and large interstitial spaces of the tumor (Asayama et al. 2006). Mass-forming CC infrequently shows hypervascularity in the AP which mimics the appearance of HCC (Fig. 2) (Kim et al. 2007, 1997). The absence of washout (negative enhancement) and persistent positive enhancement of CC may help to differentiate it from HCC that typically shows later washout.

Small intrahepatic metastases are frequently seen adjacent to the main mass, but they can be seen in other parts of the liver. Capsular retraction is an uncommon, but a unique feature of mass-forming CC which typically has a prominent desmoplastic reaction (Fig. 1). Dilatation of intrahepatic bile ducts peripheral to the tumor is occasionally seen. Diffuse mild dilatation of the intrahepatic bile ducts is often seen because of associated liver fluke infection in endemic areas (Choi et al. 1998, 2006). If the tumor invades the hilar bile duct confluence, the intrahepatic ducts in both lobes of the liver are severely dilated (Fig. 3). Narrowing or obstruction of the portal or hepatic vein by tumor invasion or extrinsic compression or arterial encasement by infiltrative tumor is often seen when the tumor is centrally located. Careful and detailed evaluation of axial and MPR images is crucial to detect vascular invasion. Metastatic lymphadenopathy in the hepatoduodenal ligament or retroperitoneum or peritoneal metastasis is commonly seen (Fig. 3).

CC is a serious complication of primary sclerosing cholangitis (PSC). It is often difficult to diagnose because of preexisting bile duct strictures and thickening. CC in PSC is most commonly seen as a hepatic parenchymal mass associated with progressive biliary dilatation or a dominant stricture of the bile duct on MSCT (Fig. 4). Less common manifestations include focally thickened bile duct or a polypoid mass (Campbell et al. 1998). It is important to carefully assess any interval changes of the degree of biliary dilatation and thickening between follow-up imaging studies.

Recurrent pyogenic cholangitis (RPC) is characterized by intrahepatic biliary calculi, bile duct dilatation and strictures, segmental hepatic atrophy, and recurrent episodes of cholangitis and liver abscesses. CC in RPC most commonly manifests as a mass-forming intrahepatic CC and predominantly localizes in segments with severe atrophy (Fig. 5). CC can be easily misdiagnosed as an abscess or inflammatory mass because the mass typically shows marked hypoattenuation on CT scan. Hilar or distal extrahepatic CC is less commonly associated with RPC (Kim et al. 2006a, b, c)

Preoperative staging of intrahepatic mass-forming CC with MSCT should primarily focus on determining tumor extent in the liver and extrahepatic metastases that are best demonstrated on PVP images. It becomes important to assess the relationship between the tumor and perihilar vessels and bile ducts using axial and MPR images if the tumor invades the hepatic hilum.

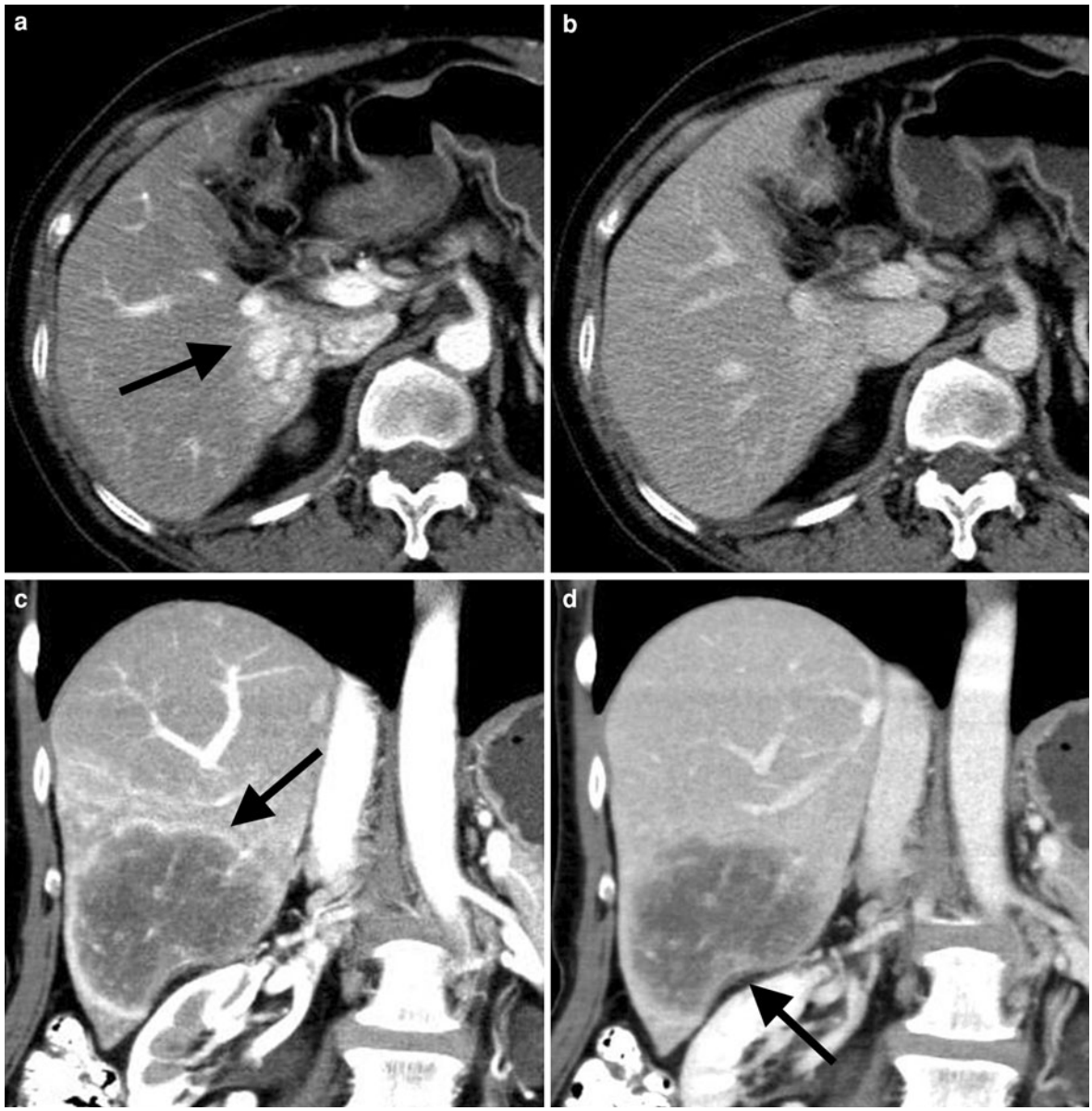

Fig. 1 Spectrum of MSCT findings of mass-forming intrahepatic CC. **a**, **b** Small hypervascular tumor discovered during surveillance in patient with hepatitis B induced cirrhosis. **a** A homogeneously enhancing tumor (I) is seen in the arterial phase. **b** Tumor becomes isoattenuating to the liver parenchyma during the portal venous phase. **c**, **d** Common appearance of tumor, presenting as a large, hypoattenuating mass with thin peripheral rim of enhancement in the arterial phase (**c**, *arrow*) and capsular retraction shown in the portal venous phase (**d**, *arrow*)

5.2 Hilar and Distal Extrahepatic Cholangiocarcinoma

Hilar CC most commonly has a periductal-infiltrating morphologic type. Distal extrahepatic CC most commonly manifests as a small (1–2 cm in size) mass-forming type although other morphologic types can be seen (Seo et al. 2009). MSCT is excellent to localize the tumor by demonstrating a focal bile duct thickening or a mass with substantial enhancement accompanied by upstream biliary dilatation. The mucosal/submucosal component of the tumor is often

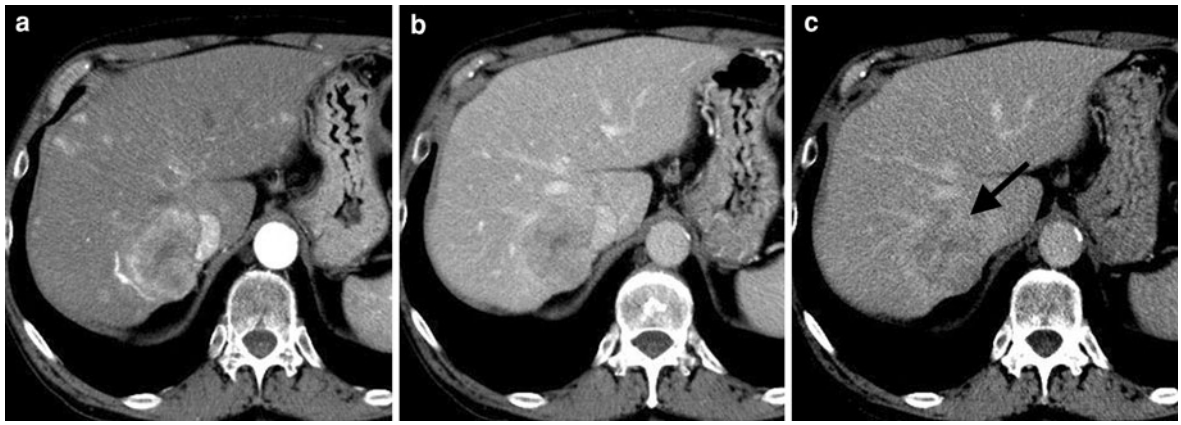

Fig. 2 Enhancement pattern of mass-forming CC. Variable degree of enhancement of the tumor is seen in the arterial phase. The tumor is heterogeneously hypervascular in this particular case (**a**) with the tumor becoming hypoattenuating in the portal venous phase (**b**). During the delayed phase (**c**) the tumor shows progressive hyperenhancement in its central portion (*arrow*) due to abundant fibrous stroma and large interstitial spaces

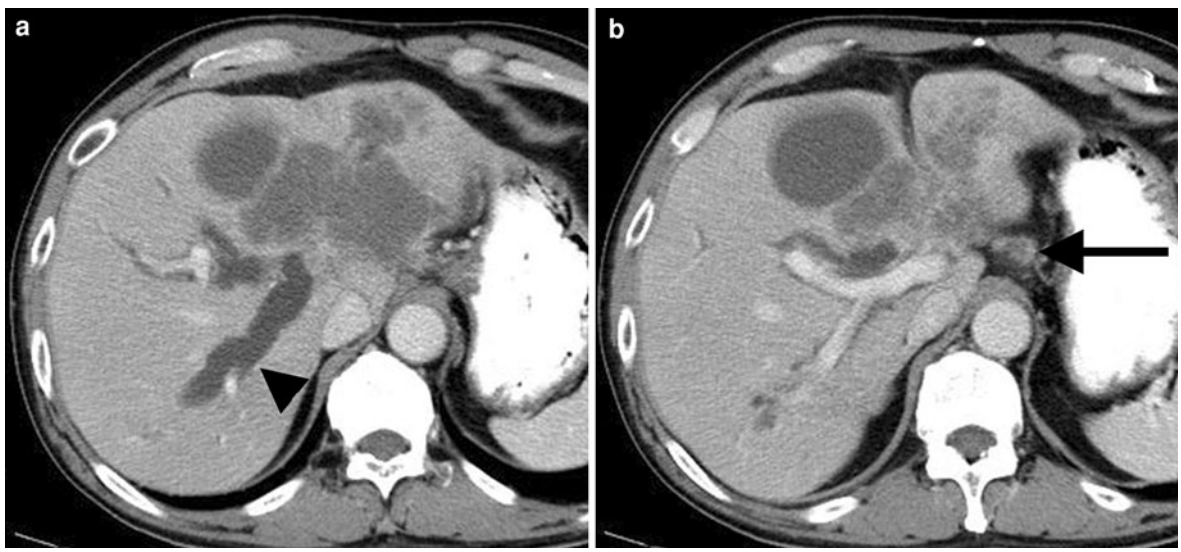

Fig. 3 Biliary obstruction in mass-forming CC. **a** Central invasion of the tumor results in obstruction of the biliary tree (*arrowhead*). **b** Nodal metastases are seen in the gastrohepatic ligament (*arrow*)

slightly hyperattenuating or isoattenuating relative to the liver on both AP and PVP images (Fig. 6) (Han et al. 2002). MSCT is also useful to assess the relationship between the tumor and perihilar structures that can be best evaluated on thin-section images facilitated by MPR images and 3D reconstructions (Chen et al. 2006; Uchida et al. 2005). Hepatic arterial anatomic variations and arterial tumor invasion can be better evaluated in the AP than PVP (Fig. 6).

The evaluation of MSCT of hilar and distal extrahepatic CC should focus on tumor resectability because surgical resection with histologically negative resection margin can offer the best chance of long-term survival. Resection of hilar CC includes a partial

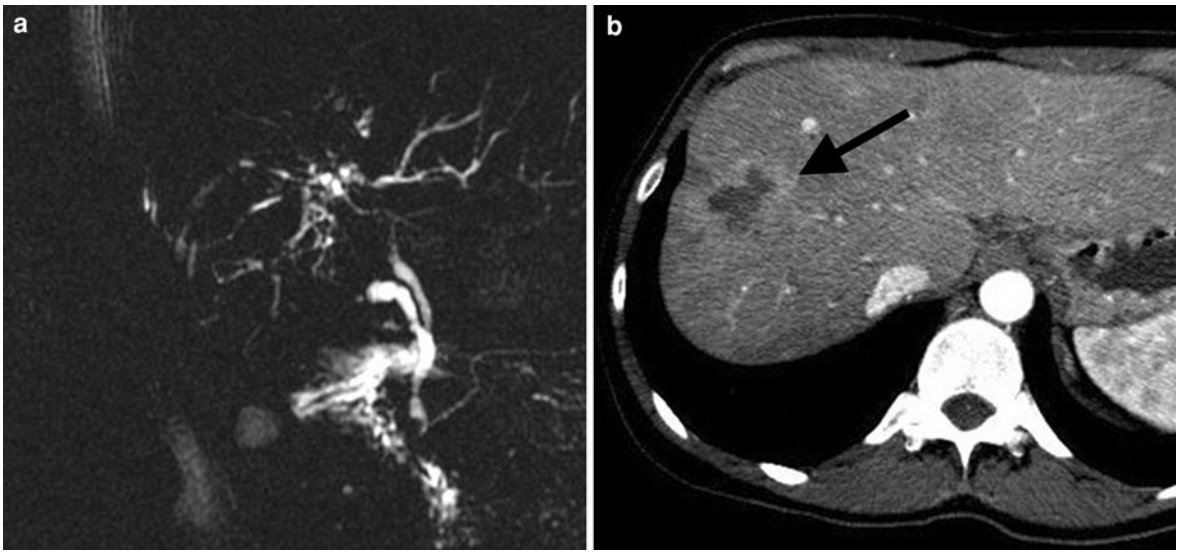

Fig. 4 Mass-forming CC in primary sclerosing cholangitis. **a** Coronal thick-slab MRCP sequence depicts the typical diffuse ductal changes of primary sclerosing cholangitis with numerous alternating areas of strictures and dilatations. **b** Axial arterial phase CT scan shows a hypoattenuating mass with faint rim enhancement (*arrows*)

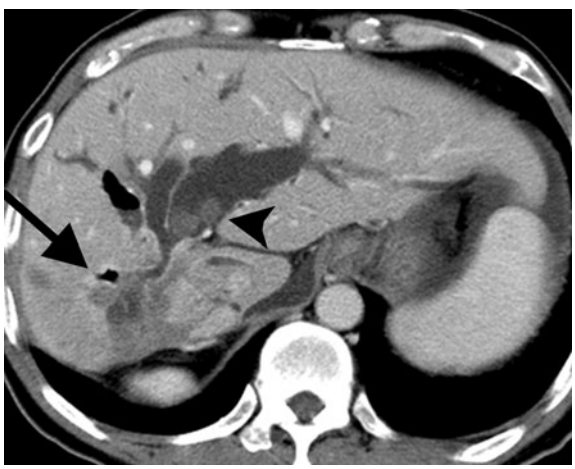

Fig. 5 CC in recurrent pyogenic cholangitis. Note the typical changes of the underlying disease, including right lobar atrophy, ductal dilatation, and intraductal stones (*arrowhead*). Mass-like areas (*arrow*) in these patients should be viewed with high suspicion for CC

hepatectomy of the predominantly involved lobe of the liver. Tumor extension to the bilateral secondary biliary confluence or tumor invasion to bilateral hilar vessels had been considered unresectable. However, a curative resection is now often performed depending on the remaining liver volume, the length of vascular invasion, and anatomic configurations of the bile ducts with successful outcome (Chung et al. 2008; Lee et al. 2006). A longitudinal tumor extent of the distal extrahepatic CC is critical to determine the surgical planning and is best evaluated by coronal or oblique coronal MPR images (Fig. 7). Tumor involvement of intrapancreatic segment of bile duct indicates pancreaticoduodenectomy whereas a tumor close to the hepatic hilum may indicate partial liver resection.

MSCT might be limited to determine the exact tumor extent of hilar CC within the bile duct especially after insertion of biliary drainage or stent. However, it is often possible to determine the level and extent of obstruction by a careful tracing of the individual segmental bile ducts and identifying a focal wall thickening with enhancement which obliterates the lumen. A detailed evaluation of axial and coronal thin-section CT images enables a reliable evaluation of the tumor involvement of the primary and secondary bile duct confluence (Fig. 8). MSCT tends to underestimate the longitudinal tumor extent of distal extrahepatic CC due to submucosal tumor extension along the bile duct (Seo et al. 2009). Additional imaging with MR cholangiopancreatography or percutaneous transhepatic cholangiography is often performed for a comprehensive visualization of the tumor extent in the bile duct (Choi et al. 2008; Lee et al. 2002). MSCT cholangiography using an

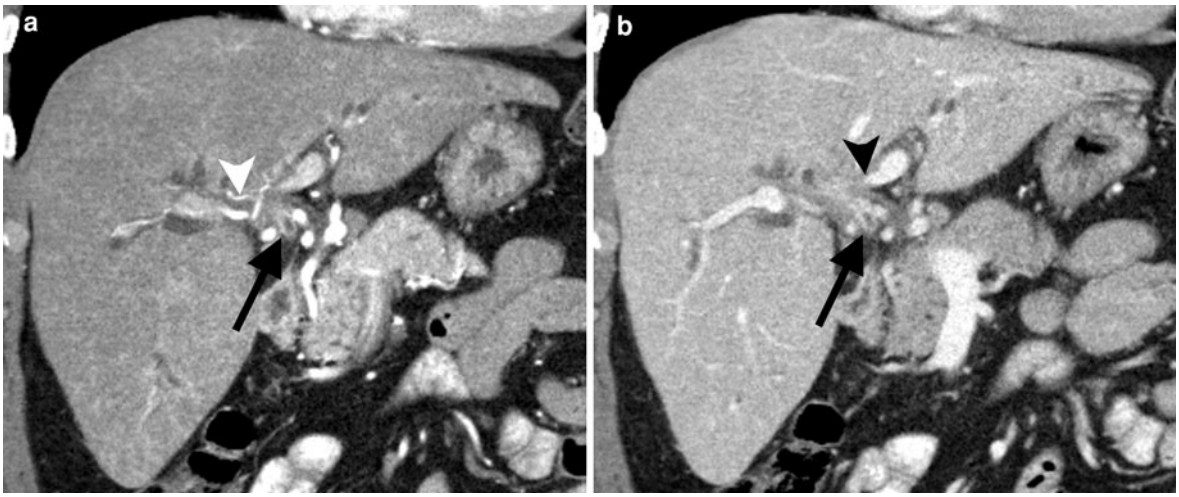

Fig. 6 Periductal-infiltrating hilar CC. The encasement of both right and left hepatic arteries (*white arrowhead*) is best seen during the arterial phase (**a**). Similarly, the portal venous phase (**b**) allows for improved assessment of the portal veins, the left portal vein being narrowed by tumor (*black arrowhead*). In both phases, the mucosal/submucosal component of the tumor appears as hyperattenuating to the liver parenchyma (*black arrow*)

injection of contrast material through biliary drainage tubes is an excellent imaging method; however, this technique is only available when percutaneous biliary drainage tubes are placed (Kim et al. 2006a, b, c).

Vascular invasion is diagnosed when there is vessel occlusion (Fig. 9), stenosis, or contour deformity associated with tumor contact, or greater than 50% perimeter contact with the tumor (Lee et al. 2006). It is important to estimate the length of involved hilar portal vein as it is important for surgical planning including resection and anastomosis of the portal vein (Sugiura et al. 2008). MSCT tends to underestimate nodal metastasis and peritoneal metastasis which is less common in extrahepatic CC than intrahepatic mass-forming CC. The presence of equivocal lymph nodes on CT scan cannot be used as a criterion for unresectability as the lymph node status cannot be reliably determined on current imaging system (Chung et al. 2008). The use of MSCT has markedly improved the detection and staging of hilar CC compared with conventional CT scan (Cha et al. 2000; Chen et al. 2006; Lee et al. 2006). Lee et al. (2006) recently reported an overall accuracy of 74.5% for prediction of resectability for hilar HCC. The main causes of inaccuracies were underestimation of biliary and vascular invasion.

5.3 Intraductal-growing Cholangiocarcinoma

Intraductal-growing CC is the least common morphologic type and occurs in both intrahepatic and extrahepatic bile ducts. The tumors are usually small papillary or polypoid lesions, often spreading superficially along the mucosal surface. The tumors are often confined within the bile duct without invasion to adjacent liver parenchyma. A large amount of mucin is occasionally produced and excreted to the bile duct, resulting in partial biliary obstruction and aneurysmal biliary dilatation due to thick mucin (Lim 2003).

Intraductal-growing CC may show various imaging patterns on CT scan determined by the location, size, and the presence or absence of mucin hypersecretion. Diagnosis of the tumor may be difficult if the tumor is small and located in the peripheral intrahepatic bile duct without mucin hypersecretion. MSCT may show a nonspecific hypoattenuating tubular structure in the liver that can be easily dismissed or misdiagnosed as biliary calculi (Fig. 10) (Lee et al. 2000). It is important to carefully assess any lesional enhancement on contrast-enhanced scan by comparing with unenhanced images. When the tumor produces mucin, a focally dilated intrahepatic bile duct that harbors multiple

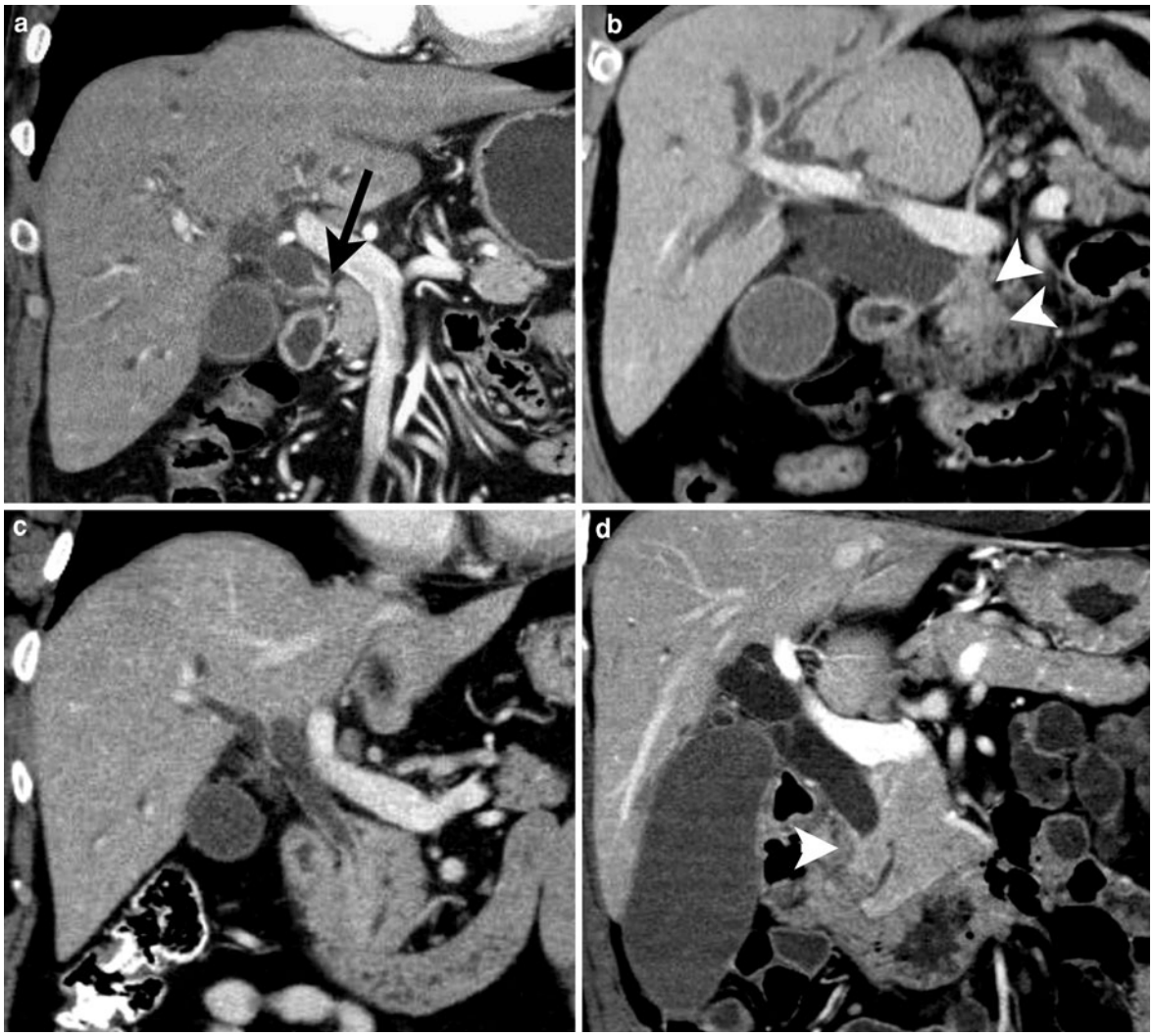

Fig. 7 Spectrum of MSCT findings of extrahepatic CC. **a** A periductal-infiltrating tumor (*arrow*) in mid common bile duct causing short-length stricture which ends cranial to the pancreas. **b** Larger mass-forming tumor affecting the mid and distal common bile duct with invasion of the pancreas (*arrowheads*). **c** Periductal-infiltrating tumor affecting the entire intrapancreatic portion of common bile duct. **d** Distal common bile duct tumor (*arrowhead*) causing short-length high-grade stricture

polypoid enhancing nodules is visualized. An aneurysm-like cystic biliary dilatation can be misdiagnosed as a biliary cystic neoplasm (Fig. 11). A tubular appearance and identification of communication with the bile duct may help to lead to a correct diagnosis. A diffuse dilatation of the entire biliary system occurs if the tumor produces a profuse amount of mucin. Papillary tumors are occasionally very small in size and may not be clearly seen even on the state-of-the-art MSCT scan, resulting in a diagnostic dilemma in cases with diffuse or focal dilatation of the bile duct without visible mass or obstruction (Chung et al. 2009; Lim et al. 2008). Careful evaluation of thin-section contrast-enhanced axial and MPR images is critical to detect any tiny polypoid lesions or focally thickened bile duct wall that may represent small papillary tumors. Vascular invasion or distant metastasis is not common in intraductal growing type of CC.

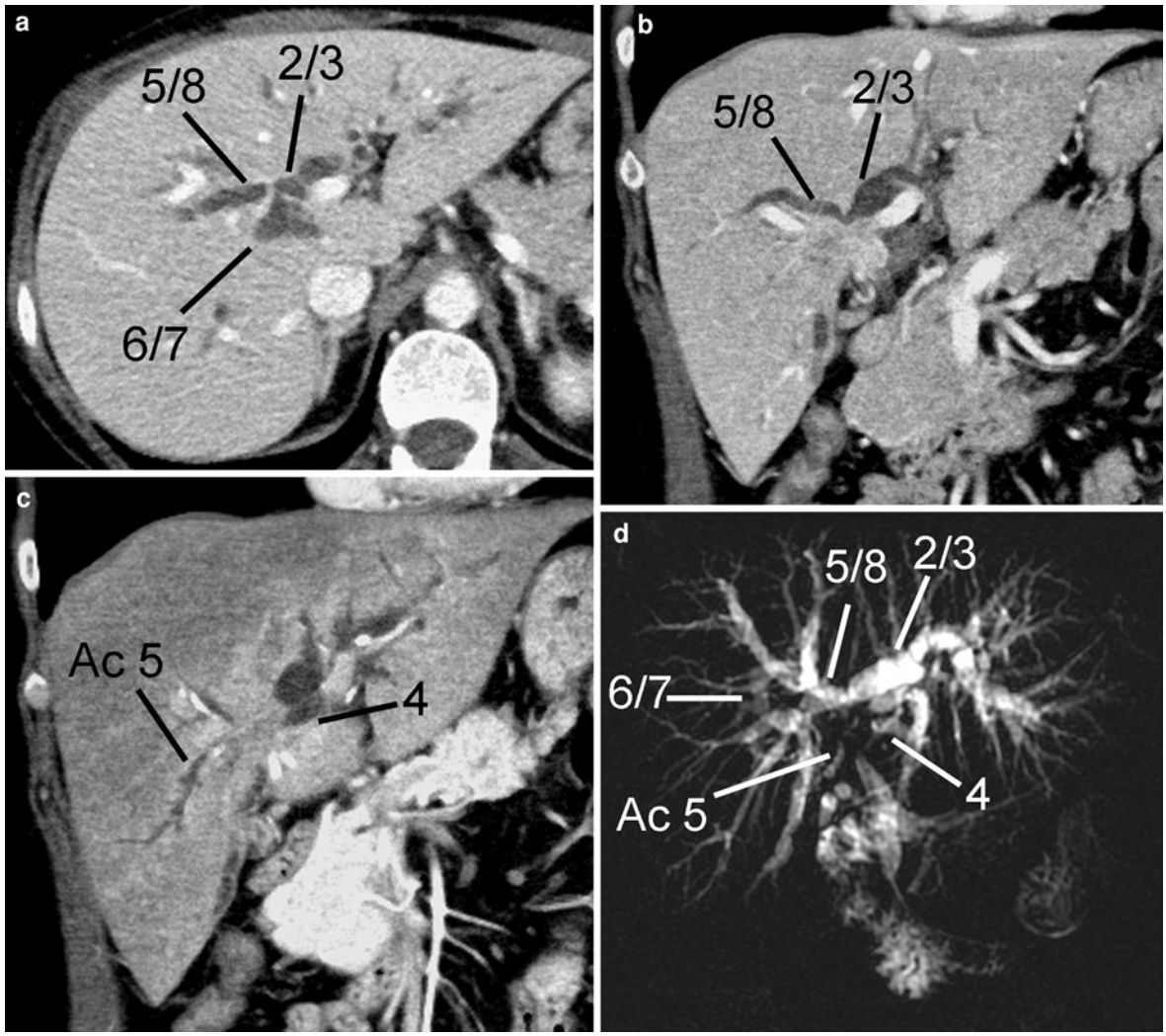

Fig. 8 MSCT assessment of bile ducts in hilar CC. **a** Axial image shows the confluence of right anterior (segment 5/8), right posterior (segment 6/7) ,and left hepatic ducts. Note the anomalous insertion of the right posterior duct into the left hepatic duct. **b** Coronal image showing the confluence of the right anterior and left hepatic ducts. **c** However, on a more anterior coronal image, obstruction of both an accessory segment 5 duct (Ac 5) and anomalous segment 4 duct (4) are noted indicating bilateral second-order branch involvement. **d** Thick-slab MRCP image with annotations confirms the complex ductal anatomy showed by the high-resolution MSCT

5.4 Gallbladder Carcinoma

Imaging patterns of gallbladder carcinoma of CT scan have been described as a mass replacing the GB in 40–65% of cases (Fig. 12), focal or diffuse GB wall thickening in 20–30% (Fig. 13), and an intraluminal polypoid mass in 15–25% (Fig. 14) (Levy et al. 2001). In the imaging pattern of a mass replacing the GB, contrast-enhanced CT scan shows a heterogeneous solid mass replacing the GB fossa often associated with soft-tissue extension to the adjacent liver, pericholecystic fat, and porta hepatis as well as metastatic lymphadenopathy. The mass frequently contains gallstones and areas of hypoattenuating necrosis. After regional lymph nodes, the most common sites of distant metastasis are the peritoneum and liver. Local staging of GB carcinoma by MSCT scan is somewhat limited with overall T-staging accuracy of 71% reported by Kim (Kim et al. 2002). MSCT has an important benefit to provide MPR images in any axis that can improve the

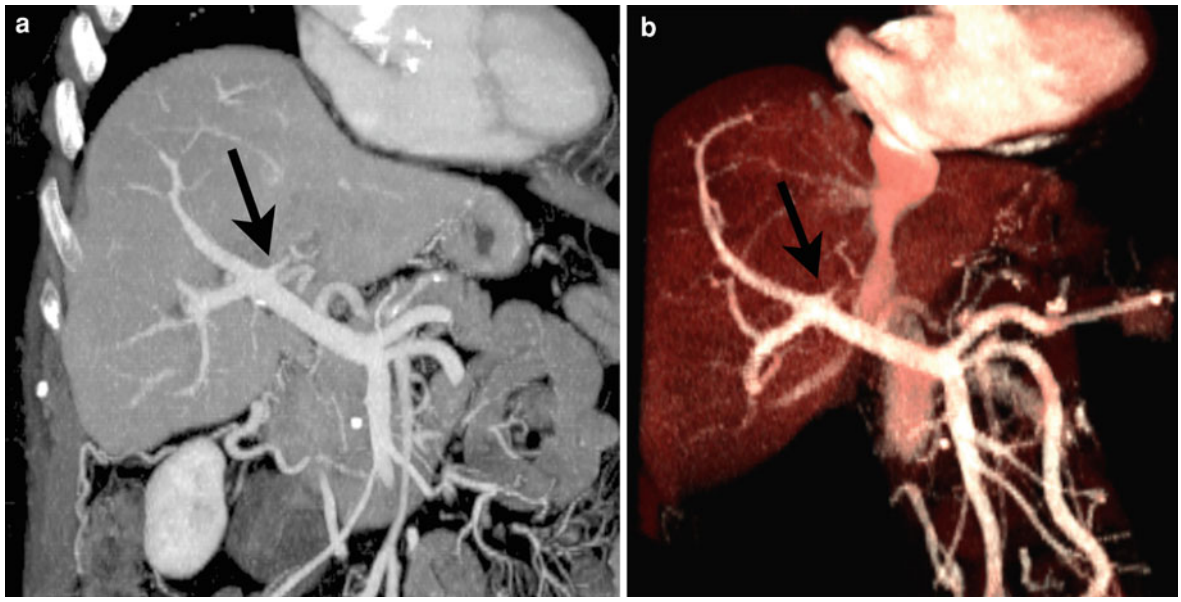

Fig. 9 Vascular invasion in hilar CC. Thick-slab maximum intensity projection (**a**) and volume-rendering (**b**) images of portal venous phase MSCT scan show an obstruction of the left portal vein (*arrow*) by tumor invasion

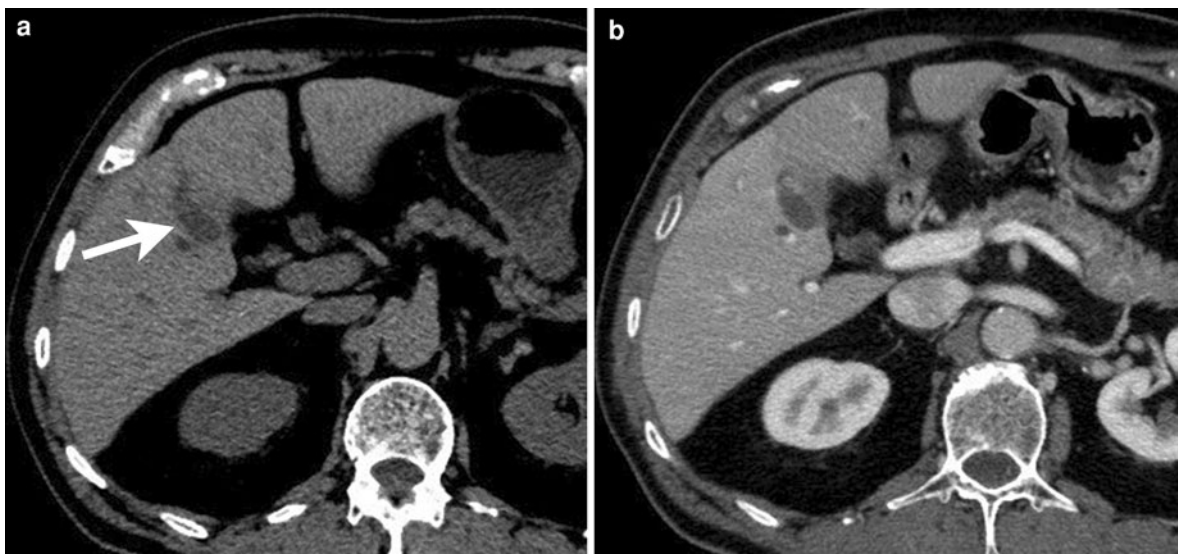

Fig. 10 Intraductal-growing intrahepatic CC. **a** A tubular hypoattenuating lesion is noted in segment 5 (*arrow*) on unenhanced scan. **b** The lesion remains hypoattenuating to the liver parenchyma in the portal venous phase. Only by measurement of the attenuation of the lesion can enhancement, from 22 HU in the precontrast to 45 HU in the portal venous phase, be appreciated

T-staging accuracy of GB carcinoma compared with axial images alone (Fig. 12) (Kim et al. 2008a, b). MSCT with MRP images and 3D volume-rendering techniques is also useful to evaluate the relationship between the tumor and major hilar vessels which is critical to determine resectability and surgical planning (Kalra et al. 2006). MSCT can demonstrate anatomic variation of the hepatic vessels which is needed to

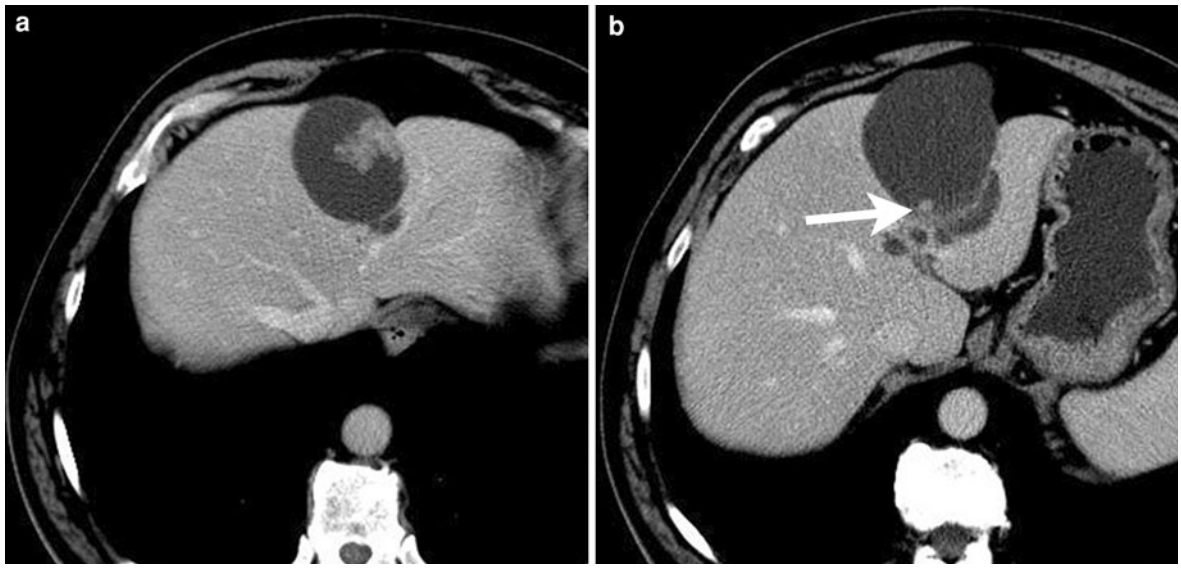

Fig. 11 Intraductal-growing intrahepatic CC. **a**, **b** Axial CT images show multiple papillary tumors (*arrow*) that aneurysmally distend the affected duct due to excess mucin production. This can be mistaken for a biliary cystadenoma which does not communicate with the bile ducts

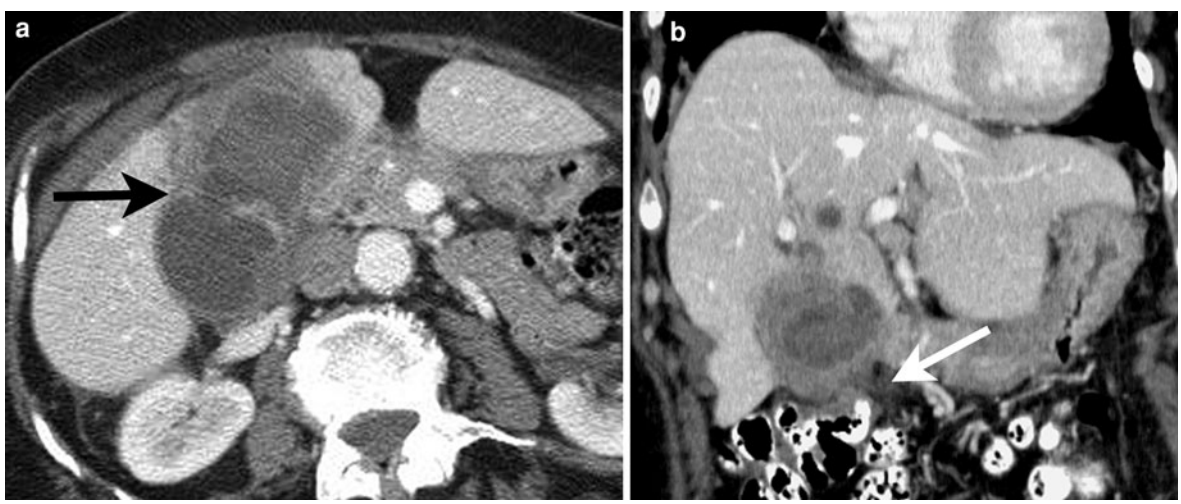

Fig. 12 Mass-forming gallbladder carcinoma. **a** An axial image shows a large hypoattenuating mass and irregular thickening of the gallbladder wall which is disrupted (*arrow*) and in contiguity with the mass. **b** Coronal image shows extension of the tumor inferiorly through Gleason's capsule and invasion of the colon (*arrow*)

provide a vascular road map before surgery. The anatomy of the hepatic veins helps surgeons determine the plane of partial hepatectomy.

Diagnosis of focal or diffuse wall thickening pattern of GB carcinoma can be challenging because benign GB wall thickening such as cholecystitis or adenomyomatosis can show similar findings. Enhancement pattern of thickened GB wall on MSCT may help to differentiate the two conditions (Fig. 13). A recent study by Kim (Kim et al. 2008a, b) reported that a strongly enhancing thick inner layer and weakly enhancing outer layer are typical for GB carcinoma.

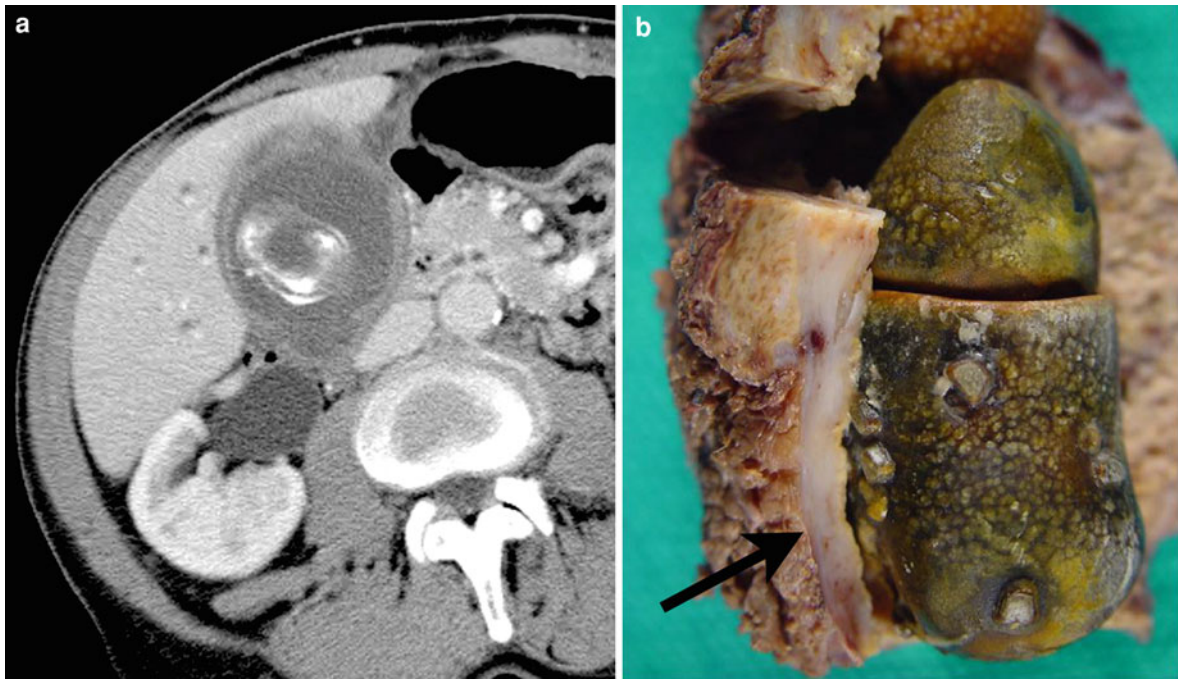

Fig. 13 Gallbladder carcinoma with diffuse wall thickening. **a** Axial image through the gallbladder shows an irregularly thickened and enhancing gallbladder wall and gallstones. **b** The corresponding image of the gross specimen shows diffuse infiltration of the wall with fleshy white tumor (*arrow*)

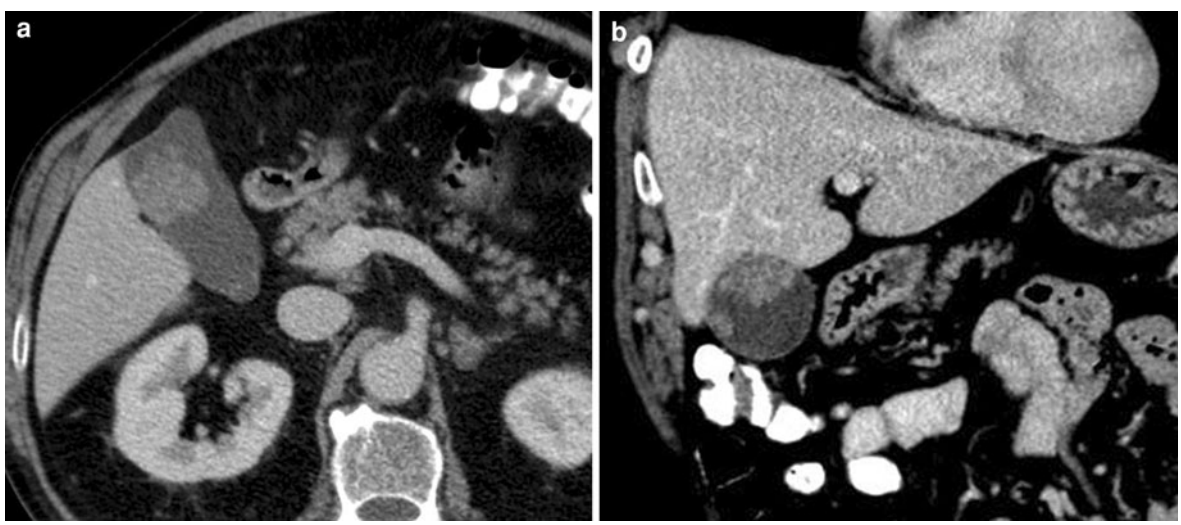

Fig. 14 Intraluminal polypoid gallbladder carcinoma. Axial (**a**) and coronal images (**b**) show a polypoid mass within the gallbladder with no evidence of gross invasion of the adjacent liver parenchyma

Intraluminal polypoid GB carcinoma is least common and is seen as a well-defined mass with round or oval shape on CT scan (Fig. 14). The presence of contrast enhancement of the mass can distinguish tumor mass from tumefactive sludge or stones. MSCT scan with MRP images is helpful to

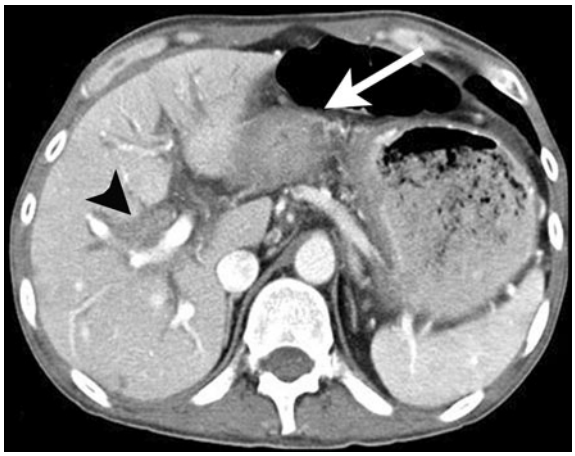

Fig. 15 Gastric carcinoma metastasis to the bile ducts. Axial image shows marked thickening and obstruction of the central right hepatic duct (*black arrowhead*), identical to hilar CC. Note the diffusely thickening gastric pylorus (*white arrow*) and posterior wall, hinting at the origin of the tumor

demonstrate extension of the tumor beyond the wall of the GB. Vascular invasion or distant metastasis is uncommon (Kim et al. 2006a, b, c).

5.5 Other Neoplastic Processes in Biliary System

Biliary obstruction is frequently caused by metastatic disease. Frequent primary cancers include carcinomas from the stomach, colon, lung, and breast. The level of biliary obstruction is most commonly at the proximal extrahepatic bile duct or hepatic hilum. Obstruction is mostly caused by periductal nodal masses that are readily visualized on MSCT scan; however, biliary metastasis infrequently manifests as a focal thickening and enhancement of the bile duct or a nodular intraductal mass that is indistinguishable from primary CC (Fig. 15) (Moon et al. 2003). History of primary malignancy is the key to the differential diagnosis.

Hepatocellular carcinoma (HCC) infrequently invades into the bile duct and develops an intraductal polypoid mass that can mimic the appearance of intraductal-growing CC on CT scan. The presence of a parenchymal mass that is contiguous with the intraductal mass, liver cirrhosis, and hyperattenuation of the tumor in the AP are typical imaging findings on CT scan that help to diagnose HCC (Fig. 16) (Jung et al. 2006).

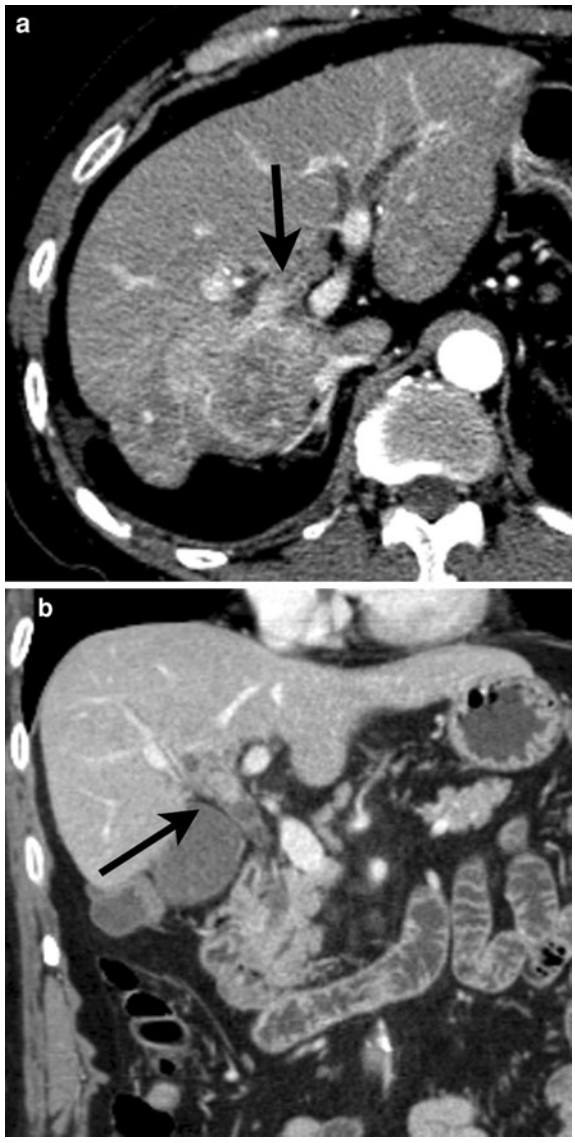

Fig. 16 Hepatocellular carcinoma with bile duct invasion. **a** Axial arterial phase image shows a hyper-enhancing right lobe mass with central extension (*arrow*). **b** Coronal portal venous phase image shows extension of the tumor into the common bile duct (*arrow*)

Intraductal metastasis in the liver is an uncommon manifestation of colorectal carcinoma (Riopel et al. 1997). The intraductal tumor usually shows an expansile, tubular lesion within the bile duct (Fig. 17), mimicking the appearance of intraductal-growing CC, and is often associated with parenchymal mass that is contiguous with the intraductal tumor (Lee et al. 2009).

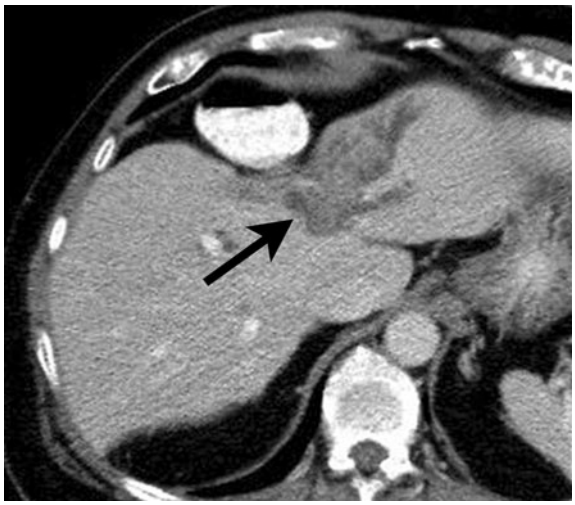

Fig. 17 Colorectal metastases to bile ducts. Axial CT image shows a large tubular branching intraductal tumor (*arrow*) causing ductal obstruction

6 Conclusion

MSCT enables thin-section multiphasic contrast-enhanced images with any desired imaging planes, which improve the diagnosis and staging of CC and GB carcinoma. Detailed evaluation of high-resolution axial and MPR MSCT images is important to assess tumor extent, vascular invasion, and distant metastases that are critical for surgical planning. Understanding of morphologic types of CC and GB carcinoma and their biological behaviors is useful to determine tumor extent, tumor staging, and predicting prognosis.

References

Asayama Y, Yoshimitsu K, Irie H, Tajima T, Nishie A, Hirakawa M, Nakayama T, Kakihara D, Taketomi A, Aishima S, Honda H (2006) Delayed-phase dynamic CT enhancement as a prognostic factor for mass-forming intrahepatic cholangiocarcinoma. Radiology 238:150–155

Burak K, Angulo P, Pasha TM, Egan K, Petz J, Lindor KD (2004) Incidence and risk factors for cholangiocarcinoma in primary sclerosing cholangitis. Am J Gastroenterol 99:523–526

Campbell WL, Ferris JV, Holbert BL, Thaete FL, Baron RL (1998) Biliary tract carcinoma complicating primary sclerosing cholangitis: evaluation with CT, cholangiography, US, and MR imaging. Radiology 207:41–50

Cardinale V, Semeraro R, Torrice A, Gatto M, Napoli C, Bragazzi MC, Gentile R, Alvaro D (2010) Intra-hepatic and extra-hepatic cholangiocarcinoma: New insight into epidemiology and risk factors. World J Gastrointest Oncol 2:407–416

Catalano OA, Singh AH, Uppot RN, Hahn PF, Ferrone CR, Sahani DV (2008) Vascular and biliary variants in the liver: implications for liver surgery. Radiographics 28:359–378

Cha JH, Han JK, Kim TK, Kim AY, Park SJ, Choi BI, Suh KS, Kim SW, Han MC (2000) Preoperative evaluation of Klatskin tumor: accuracy of spiral CT in determining vascular invasion as a sign of unresectability. Abdom Imaging 25:500–507

Charbel H, Al-Kawas FH (2011) Cholangiocarcinoma: Epidemiology, Risk Factors, Pathogenesis, and Diagnosis. Curr Gastroenterol Rep13(2):182–187

Chen HW, Pan AZ, Zhen ZJ, Su SY, Wang JH, Yu SC, Lau WY (2006) Preoperative evaluation of resectability of Klatskin tumor with 16-MDCT angiography and cholangiography. Am J Roentgenol 186:1580–1586

Choi BI, Kim TK, Han JK (1998) MRI of clonorchiasis and cholangiocarcinoma. J Magn Reson Imaging 8:359–366

Choi D, Lim JH, Lee KT, Lee JK, Choi SH, Heo JS, Jang KT, Lee NY, Kim S, Hong ST (2006) Cholangiocarcinoma and Clonorchis sinensis infection: a case–control study in Korea. J Hepatol 44:1066–1073

Choi JY, Kim MJ, Lee JM, Kim KW, Lee JY, Han JK, Choi BI (2008) Hilar cholangiocarcinoma: role of preoperative imaging with sonography, MDCT, MRI, and direct cholangiography. Am J Roentgenol 191:1448–1457

Chung YE, Kim MJ, Park NY, Lee YL, Choi JY (2008) Staging of extrahepatic cholangiocarcinoma. Euro Radial 18:2182–2195

Chung YE, Kim MJ, Park NY, Choi JY, Po JY, Kim IC, Cho HE, Kim KA, Choi SEE (2009) Varying appearances of cholangiocarcinoma: radiologic-pathologic correlation. Radiographic 29:683–700

Elmer A, Oath T, Kalahari M, Kitagawa H, Yoshimoto K, Tain T, Shimizu K, Nishimura G, Terada T, Miwa K (2001) Anomalous pancreaticobiliary ductal junction without bile duct dilatation in gallbladder cancer. Hepatogastroenterology 48:382–386

Han JK, Choi BI, Kim AY, An SK, Lee JW, Kim TK, Kim SW (2002) Cholangiocarcinoma: pictorial essay of CT and cholangiographic findings. Radiographics 22:173–187

Johnson PT, Fishman EK (2006) IV contrast selection for MDCT: current thoughts and practice. Am J Roentgenol 186:406–415

Jung AY, Lee JM, Choi SH, Kim SH, Lee JY, Kim SW, Han JK, Choi BI (2006) CT features of an intraductal polypoid mass: differentiation between hepatocellular carcinoma with bile duct tumor invasion and intraductal papillary cholangiocarcinoma. J Comput Assist Tomogr 30:173–181

Kalra N, Suri S, Gupta R, Natarajan SK, Khandelwal N, Wig JD, Joshi K (2006) MDCT in the staging of gallbladder carcinoma. Am J Roentgenol 186:758–762

Kim BS, Ha HK, Lee IJ, Kim JH, Eun HW, Bae IY, Kim AY, Kim TK, Kim MH, Lee SK, Kang W (2002) Accuracy of CT in local staging of gallbladder carcinoma. Acta Radiol 43:71–76

Kim TK, Choi BI, Han JK, Jang HJ, Cho SG, Han MC (1997) Peripheral cholangiocarcinoma of the liver: two-phase spiral CT findings. Radiology 204:539–543

Kim HJ, Kim AY, Hong SS, Kim MH, Byun JH, Won HJ, Shin YM, Kim PN, Ha HK, Lee MG (2006a) Biliary ductal evaluation of hilar cholangiocarcinoma: three-dimensional direct multi-detector row CT cholangiographic findings versus surgical and pathologic results–feasibility study. Radiology 238:300–308

Kim JH, Kim TK, Eun HW, Byun JY, Lee MG, Ha HK, Auh YH (2006b) CT findings of cholangiocarcinoma associated with recurrent pyogenic cholangitis. Am J Roentgenol 187:1571–1577

Kim MJ, Kim KW, Kim HC, Kim SY, Park SH, Kim AY, Ha HK, Byun JH, Won HJ, Shin YM, Kim PN, Lee MG (2006c) Unusual malignant tumors of the gallbladder. Am J Roentgenol 187:473–480

Kim SJ, Lee JM, Han JK, Kim KH, Lee JY, Choi BI (2007) Peripheral mass-forming cholangiocarcinoma in cirrhotic liver. Am J Roentgenol 189:1428–1434

Kim SJ, Lee JM, Lee JY, Choi JY, Kim SH, Han JK, Choi BI (2008a) Accuracy of preoperative T-staging of gallbladder carcinoma using MDCT. Am J Roentgenol 190:74–80

Kim SJ, Lee JM, Lee JY, Kim SH, Han JK, Choi BI, Choi JY (2008b) Analysis of enhancement pattern of flat gallbladder wall thickening on MDCT to differentiate gallbladder cancer from cholecystitis. Am J Roentgenol 191:765–771

Lee JW, Han JK, Kim TK, Kim YH, Choi BI, Han MC, Suh KS, Kim SW (2000) CT features of intraductal intrahepatic cholangiocarcinoma. Am J Roentgenol 175:721–725

Lee SS, Kim MH, Lee SK, Kim TK, Seo DW, Park JS, Hwang CY, Chang HS, Min YI (2002) MR cholangiography versus cholangioscopy for evaluation of longitudinal extension of hilar cholangiocarcinoma. Gastrointest Endosc 56:25–32

Lee HY, Kim SH, Lee JM, Kim SW, Jang JY, Han JK, Choi BI (2006) Preoperative assessment of resectability of hepatic hilar cholangiocarcinoma: combined CT and cholangiography with revised criteria. Radiology 239:113–121

Lee YJ, Kim SH, Lee JY, Kim MA, Lee JM, Han JK, Choi BI (2009) Differential CT features of intraductal biliary metastasis and double primary intraductal polypoid cholangiocarcinoma in patients with a history of extrabiliary malignancy. Am J Roentgenol 193:1061–1069

Levy AD, Murakata LA, Rohrmann C–A, Jr. (2001) Gallbladder carcinoma: radiologic-pathologic correlation. Radiographics 21:295-314; questionnaire, 549–255

Lim JH (2003) Cholangiocarcinoma: morphologic classification according to growth pattern and imaging findings. Am J Roentgenol 181:819–827

Lim JH, Park CK (2004) Pathology of cholangiocarcinoma. Abdom Imaging 29:540–547

Lim JH, Jang KT, Choi D (2008) Biliary intraductal papillary-mucinous neoplasm manifesting only as dilatation of the hepatic lobar or segmental bile ducts: imaging features in six patients. Am J Roentgenol 191:778–782

Lowenfels AB, Maisonneuve P, Boyle P, Zatonski WA (1999) Epidemiology of gallbladder cancer. Hepatogastroenterology 46:1529–1532

Malhi H, Gores GJ (2006) Cholangiocarcinoma: modern advances in understanding a deadly old disease. J Hepatol 45:856–867

Marcos LA, Terashima A, Gotuzzo E (2008) Update on hepatobiliary flukes: fascioliasis, opisthorchiasis and clonorchiasis. Curr Opin Infect Dis 21:523–530

Miller G, Jarnagin WR (2008) Gallbladder carcinoma. Eur J Surg Oncol 34:306–312

Moon SG, Han JK, Kim TK, Kim AY, Kim TJ, Choi BI (2003) Biliary obstruction in metastatic disease: thin-section helical CT findings. Abdom Imaging 28:45–52

Reid KM, Ramos-De la Medina A, Donohue JH (2007) Diagnosis and surgical management of gallbladder cancer: a review. J Gastrointest Surg 11:671–681

Riopel MA, Klimstra DS, Godellas CV, Blumgart LH, Westra WH (1997) Intrabiliary growth of metastatic colonic adenocarcinoma: a pattern of intrahepatic spread easily confused with primary neoplasia of the biliary tract. Am J Surg Pathol 21:1030–1036

Sahani D, Saini S, Pena C, Nichols S, Prasad SR, Hahn PF, Halpern EF, Tanabe KK, Mueller PR (2002) Using multidetector CT for preoperative vascular evaluation of liver neoplasms: technique and results. Am J Roentgenol 179:53–59

Sahani NI, Catalano OA, Holalkere NS, Zhu AX, Hahn PF, Sahani DV (2008) Cholangiocarcinoma: current and novel imaging techniques. Radiographics 28:1263–1287

Seo H, Lee JM, Kim IH, Han JK, Kim SH, Jang JY, Kim SW, Choi BI (2009) Evaluation of the gross type and longitudinal extent of extrahepatic cholangiocarcinomas on contrast-enhanced multidetector row computed tomography. J Comput Assist Tomogr 33:376–382

Stephen AE, Berger DL (2001) Carcinoma in the porcelain gallbladder: a relationship revisited. Surgery 129:699–703

Sugiura T, Nishio H, Nagino M, Senda Y, Ebata T, Yokoyama Y, Igami T, Oda K, Nimura Y (2008) Value of multidetector-row computed tomography in diagnosis of portal vein invasion by perihilar cholangiocarcinoma. World J Surg 32:1478–1484

Uchida M, Ishibashi M, Tomita N, Shinagawa M, Hayabuchi N, Okuda K (2005) Hilar and suprapancreatic cholangiocarcinoma: value of 3D angiography and multiphase fusion images using MDCT. Am J Roentgenol 184:1572–1577

Yamasaki S (2003) Intrahepatic cholangiocarcinoma: macroscopic type and stage classification. J Hepatobiliary Pancreat Surg 10:288–291

Assessment of the Hepatic Vessels with MDCT

Rocio Perez-Johnston, Dipti K. Lenhart, Daniella F. Pinho, and Dushyant V. Sahani

Contents

R. Perez-Johnston · D. K. Lenhart · D. F. Pinho · D. V. Sahani (✉)
Division of Abdominal Imaging and Intervention, Radiology, Harvard Medical School,
Massachusetts General Hospital,
55 Fruit Street, White 270,
Boston, MA 02114, USA
e-mail: dsahani@partners.org

Abstract

Multidetector computed tomography angiography (MDCTA) is an established, noninvasive and effective imaging method to evaluate the liver primarily for neoplasm staging and presurgical planning. However, its role has also extended into variety of other clinical indications. Technological advances in MDCT scanners and post processing now offer new opportunities with CTA but the challenges of protocol optimization should be confronted. In this article, we will focus on the technical details with MDCTA protocols for the liver and discuss the common pathologic conditions where CTA is now considered integral to patient management.

1 Introduction

The technological development of multidetector scanner (MDCT) allows not only a more rapid acquisition of axial images but also volumetric scanning in a desired anatomical area during a phase of contrast enhancement. MDCT angiography (MDCTA) has become an established noninvasive imaging method to define vascular anatomy, pathology affecting vascular structures and for presurgical treatment planning (Frenchel et al. 2003; Kamel et al. 2005). The liver is part of the mesenteric circulation and has an inherently complex vascular anatomy. Therefore, to facilitate the treatment decisions for tumors and minimizing inadvertent surgical complications, adequate definition of the vascular structures of the hepatic circulation is crucial.

C. J. Zech et al. (eds.), *Multislice-CT of the Abdomen*, Medical Radiology. Diagnostic Imaging,
DOI: 10.1007/174_2011_461, © Springer-Verlag Berlin Heidelberg 2012

Table 1 Major Indications of MDCTA of the liver

Indications for MDCTA of the liver
Surgical Planning: Hepatic transplant and neoplasms
Vascular pathology: Arterial (aneurysms), Portal venous (thrombosis), Hepatic venous (Budd-Chiari Syndrome)
Pseudolesions: arterial and venous shunts
Neoplasms: HCC

HCC hepatocellular carcinoma

The MDCT technology itself is constantly evolving and to exploit the full potential of these new developments in MDCT, protocol optimization has become paramount. This article will focus on technical factors to MDCT protocols for CTA applications in the liver (Table 1).

2 MDCT Techniques

Recent advances in MDCT scanners have improved its capabilities in multiphasic acquisition of larger territories in optimal phases of organ enhancement with improved 2D and 3D image display. In general, faster acquisition with reasonably thinner slices and appropriate scanning delay are crucial components of an optimal MDCTA protocol.

2.1 Imaging Techniques

Distention of the stomach and duodenum is usually beneficial. In our practice patients drink from 500 to 1000 ml of water 20–30 min prior to the scan, and an additional 300–500 ml should be administered immediately before the scan.

In order to sustain a fast injection, a good intravenous access with an 18–20 gauge catheter is recommended. Typically 100–120 ml of nonionic iodinated contrast material (CM) (300–370 mg of iodine/ml) is bolus-injected at a rate of 4–5 ml/s in order to obtain optimal vascular enhancement (Pannu et al. 2001; Horton and Fishman 2000; Tanikake et al. 2003).

In specific patients, the rate of injection and the volume should be adjusted. In patient with large body size and weight (over 300 pounds) the CM injection rate is increased by 0.5–1 ml/s faster than the existing rate of injection.

In order to minimize the risk of CM induced nephropathy in patients with an estimated glomerular filtration rate (eGFR) under 45 ml/min/m^2, volume load of contrast should be decreased by 20–30% of the calculated dose and adequate intravenous hydration before and after the injection should be administered.

Irrespective of the use rate of CM injection, it is generally agreed that a saline chaser/flush of 30–40 ml improves the iodine flux and provides more uniform vascular enhancement (Tatsugami et al. 2006).

The technical parameters of acquisition are listed in Table 2.

An empiric delay that is fixed based on the organ circulation time for the given CM injection rate is the most commonly used approach (as in our institution) (Table 3).

However, the rate of CM injection and patient cardiac output variability are not always factored into the equation by fixed delay and as a result, in select patients this can impact the quality of vascular/organ enhancement. In order to avoid this variability, many centers with high volume MDCTA practice a test bolus or automated scanning trigger technique. With automated bolus-tracking technique, the acquisition of the scan is performed during the plateau of attenuation, which offers a more homogenous enhancement in the main branches of the aorta (Thomas and Bernhard 2005).

The use of dual-energy acquisition has recently been introduced for hepatic and MDCTA studies. The advantage of this dual-acquisition (usually 80 and 140 kVp) is the use of the lower energy images to provide better vascular enhancement and also better detection of hypervascular lesions of the liver (Marin et al. 2009; Nakayama et al. 2005). This effect occurs because iodine is more attenuating at lower energies (closer to the iodine k-edge) than at higher energies, and therefore gives better vascular enhancement (Fig. 1).

2.1.1 Image Acquisition

The dual blood supply of the liver must be taken into consideration for protocol optimization, acknowledging that the liver typically derives around 20–25% of its supply from arterial circulation and the remaining dominant 75–80% of blood flow from the portal venous system.

Table 2 Technical parameter for scanning of MDCTA used in our institution

	Slice thickness (mm)	Slice interval (mm)	kV	mA/mAs	Pitch-Tube rotation (s)
Unenhanced	5–10	5–10	100–120	150–250	1–1.5
MDCTA	1–3	0.5–1	80–100	300–600	1–1.5
Venous phase	2.5–5	2.5–5	100–120	150–250	1–1.5

Table 3 Fixed scanning delays according to vascular phases at MDCT

Injection rate (ml/s)	Arterial phases (s)		Portal venous phase (s)
	Vascular mapping	Liver parenchyma arterial phase	
3	30	45	70
4	25	40	65
5	20	35	60

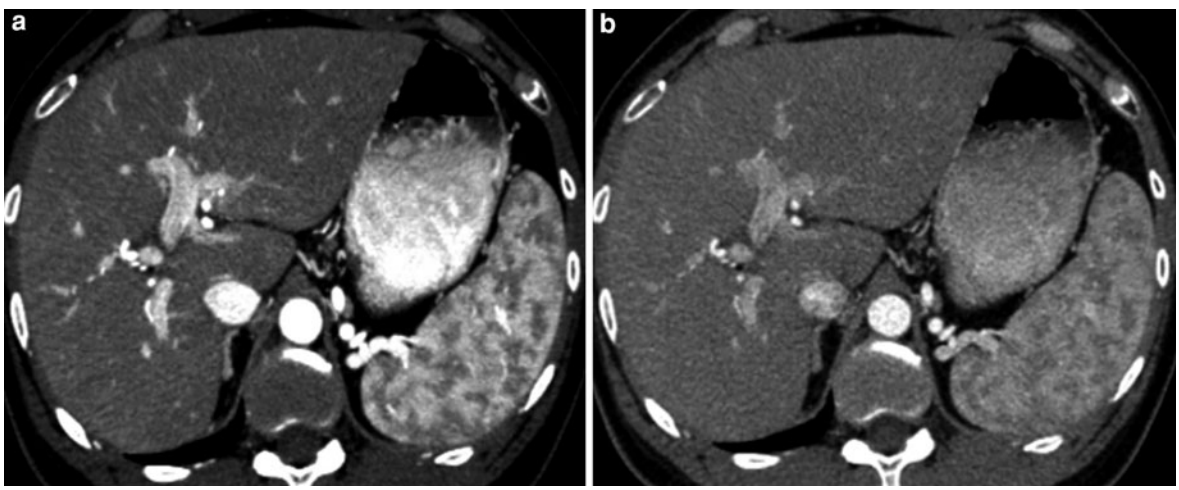

Fig. 1 Virtual monochromatic images generated from an abdominal MDCTA performed with dual-energy acquisition. Image **a** (70 keV) shows better vascular enhancement than image **b** (100 keV)

In our institution, unenhanced images are acquired first, using 5–10 mm slice thickness to cover the organ of interest. The role of unenhanced CT is controversial but usually helps with selecting the coverage for the CTA portion. It is agreed that it has a limited diagnostic role.

Early or true arterial phase images are generally preferred for vascular/arterial imaging to map vascular anatomy. A late arterial phase is advocated when hypervascular lesions of the liver are suspected.

The maximal enhancement of the liver parenchyma occurs in the portal phase, approximately 40–50 s after aortic enhancement or approximately 65–75 s after start of injection.

A delayed/equilibrium phase at 3–5 min after injection can complement the previous phases improving the characterization and differentiation of certain liver lesions such as hepatocellular carcinomas and vascular shunts.

The different phases for the liver acquisitions are summarized in Fig. 2.

2.2 PostProcessing Techniques

The liver has complex diagnostic and management needs; therefore imaging postprocessing is now integral to all MDCTA applications in these organs. Although a variety of postprocessing protocols have been advocated, the most frequently used approaches include multiplanar reconstruction (MPR), maximum intensity projections (MIP), minimum intensity

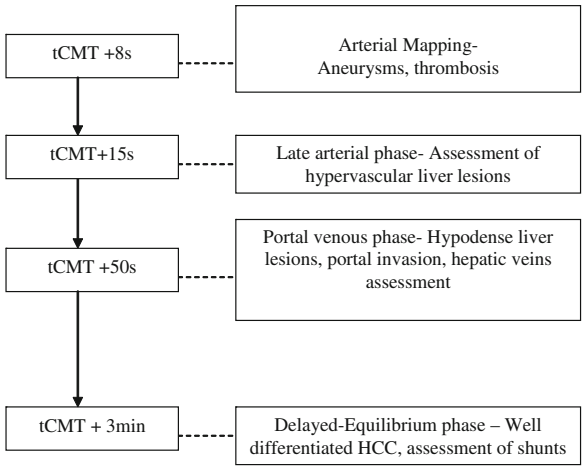

Fig. 2 Phases of imaging acquisition with bolus tracking for liver MDCTA. tCMT is the time interval needed for the contrast material to arrive in the arterial territory of interest tCMT + 8 s: scan starts 8 s after CM arrives in the aorta, as established with automated bolus triggering

Table 4 Postprocessed views for liver MDCTA

Liver	Best postprocessing view
Hepatic artery	3D vascular maps
Portal pedicle	Coronal MPR and VR
Hepatic veins and IVC	Axial and coronal MPR and MIP

projections (MinIP), volume rendering (VR), and 3D and curved planar reformation (CPR). Each of these processing protocols has a specific role for assessing regional anatomy and the relationship of lesions to vascular structures. The postprocessing protocols used in our institution are listed in Table 4.

The post processing techniques applied to dual-energy acquisitions have been shown to add value for liver imaging. It is possible to generate from set acquisitions of 80 and 140 kVp, an additional set of virtual monochromatic images of lower energies (50–80 keV), which have shown to improve contrast of vascular structures and detection of hypervascular lesions (Lv et al. 2011).

3 Anatomy

Modern hepatic surgery is based on knowledge of the distribution and variations of vasculature. Preoperative MDCTA has provided essential information for planning the surgical procedures and routes of access.

3.1 Branches of the Aorta

The celiac trunk is the first major branch of the aorta below the level of the diaphragm. In the majority of patients, the celiac artery gives rise to three vessels: common hepatic artery, splenic artery, and left gastric artery. The superior mesenteric artery is the next major branch of the aorta, followed by the inferior mesenteric artery.

3.2 Liver Vasculature

The hepatic artery originates from the celiac trunk and divides into right and left branches; its branches classically follow the portal vein and bile duct distribution (Fig. 3). The most frequent anatomical variation of the arterial hepatic system is a replaced right hepatic artery (arising from the superior mesenteric artery), present in up to 18% of patients (Fig. 4).

The portal vein is formed by the confluence of the superior mesenteric vein (SMV) and splenic vein posterior to the neck of the pancreas. Most commonly, it divides into the right and left portal veins at the porta hepatis (Fig. 1). The right portal vein first branches within the caudate lobe into anterior and posterior branches and both subdivide into superior and inferior branches to supply the segments of the right lobe. The left portal vein initially has a horizontal course to the left and then turns medially toward the ligamentum teres, supplying the lateral segments of the left lobe. It courses anteriorly in a concave curve to end in the superior and inferior branches supplying the medial segments of the left lobe.

In the hepatic venous anatomy, three main hepatic veins drain into the inferior vena cava (IVC). The right hepatic vein drain segments V, VI and VII; the middle hepatic vein drains segments IV, V and VIII; and the left vein drains segments II and III. In over 60% of the population, the middle and left hepatic veins form a common vessel, which drains directly into the IVC. This anatomical variant is important to acknowledge prior to hepatic transplantation.

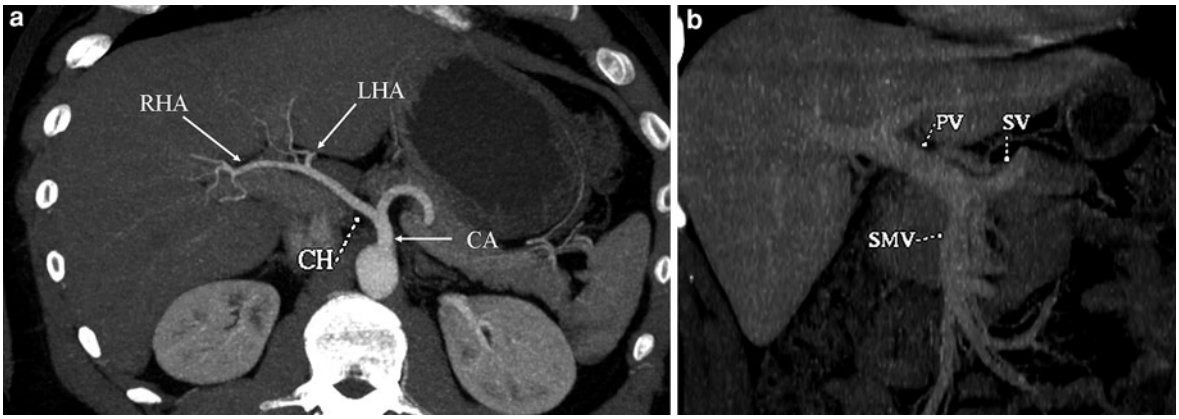

Fig. 3 Normal anatomy of hepatic vessels. **a** Arterial anatomy: the common hepatic artery (*CH*) is a branch of the celiac artery (*CA*) and bifurcates in right (*RHA*) and left (*LHA*) hepatic arteries. **b** Portal anatomy: the portal vein is formed by the union of superior mesenteric vein (*SMV*) and splenic vein (*SV*). The portal vein bifurcates in right portal (*RPV*) and left portal vein (*LPV*)

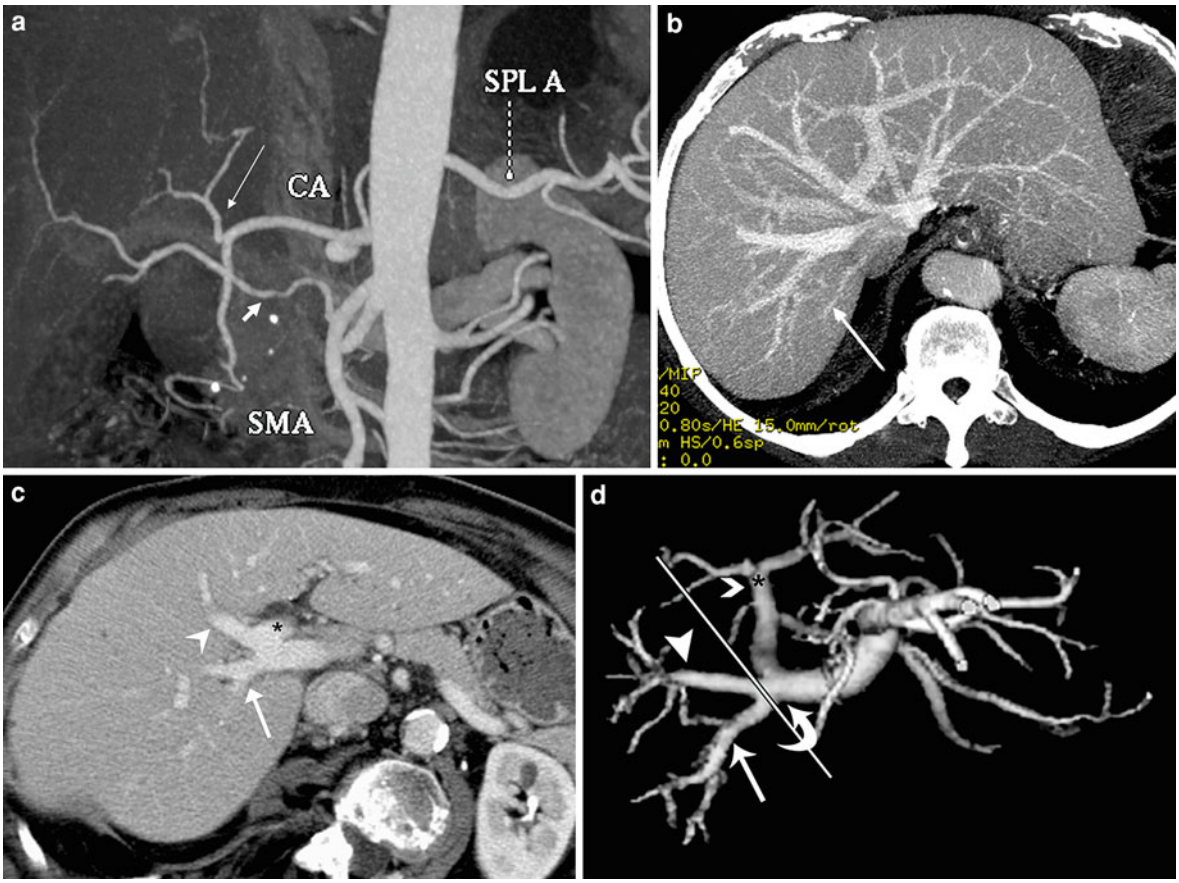

Fig. 4 Anatomic variants of hepatic vasculature. **a** Right replaced hepatic artery (*short arrow*) originating from the superior mesenteric artery. The left hepatic artery (*long arrow*) originates from the celiac axis (*CA*) **b** Accessory hepatic vein in segment VII (*long arrow*) drains directly to the inferior vena cava. **c** Trifurcation of the portal vein, formed by the left portal vein (*LPV,* *) and by the anterior (*RAPV*, *arrowhead*) and posterior (*LPPV*, *arrow*) left portal veins. **d** 3D reformat image showing the trifurcation (*curved arrow*), LPV (*), RAPV (*arrowhead*) and LPPV (*arrow*)

Table 5 Relevant anatomical variants of hepatic vasculature for pretransplant assessment and tumor resection planning

	Transplant donor	Transplant recipient	Liver neoplasms
Hepatic arterial variants	MHA from RHA	Short RHA	Replaced LHA and RHA
	CHA trifurcation into RHA, LHA and SDA	Replaced LHA	Accessory RHA and LHA
		Replaced hepatic trunk arising from SMA	Origin of hepatic trunk from SMA or LGA
Hepatic venous variants	Accessory inferior RHV	Accessory inferior RHV	Segment VIII drainage into MHV
		Early confluence of hepatic veins	Accessory MHV draining directly into IVC
		Anomalous drainage of segments V and VII into MHV	Accessory inferior hepatic veins of segments V and VI draining directly into IVC
Portal variants	Trifurcation of portal vein	Trifurcation of portal vein	-Trifurcation of portal vein
		Short portal vein	Right and left portal veins supplying segment VIII
		Acute angle of portal vein branching	

CHA common hepatic artery, *RHA* and *LHA* right and left hepatic arteries, *RHV*, *MHV* and *LHV* right, middle and left hepatic veins, *SMA* superior mesenteric artery, *IVC* inferior vena cava, *LGA* left gastric artery

4 Surgical Planning and Outcome Evaluation

4.1 Hepatic Transplant

Liver transplantation is a last resource surgical procedure in end-stage liver disease and acute liver failure when no alternative treatment options are available. Advanced chronic liver disease, acute liver failure, unresectable hepatic malignancy and inherited metabolic disease are the major categories for which liver transplantation is performed in adult patients. The most common indications for liver transplantation in adults are chronic hepatitis C and alcoholic cirrhosis, accounting for approximately 40–50% of the cases.

MDCTA is now the standard of care in the evaluation and surgical planning of living liver donors, where part of the liver along with its vascular structures and ducts are removed for transplantation in the recipient. Defining the liver anatomy for the benefit of surgical planning as well as acknowledging the anatomic variants is of immense clinical significance both for better outcome in the recipient as well as minimizing risk to the donor (Table 5; Fig. 4). It is paramount that the residual liver in the donor has an intact vascular supply and drainage to sustain its metabolic needs (Catalano et al. 2008).

In addition, the assessment of the total and segmental volumes is important in order to assure appropriate graft size, which is one of the predictor factors for a successful outcome in the donor and the recipient. It is established that a remnant measuring 30–40% of the original liver is required for donor survival (Lo et al. 1997). MDCT is an accurate non-invasive tool for volumetric assessment, either with manual or automated techniques (Suzuki et al. 2011) (Fig. 5).

In addition to the pretransplant assessment of the hepatic vasculature, in recent year MDCTA has been used to evaluate complications from the surgical procedure. Vascular complications occur in around 9% of all orthotopic liver transplantations being the most common cause of graft loss. The most common complication is hepatic artery thrombosis occurring in 2–12% of transplants, followed by hepatic artery stenosis reported in 5% of cases and portal vein thrombosis 1–3% (Glockner and Forauer 1999; Tzakis et al. 1985; Legmann et al. 1995) (Fig. 6).

Most authors routinely perform Doppler ultrasonography as initial imaging study to evaluate graft vessels since it can be performed at the bedside and it is widely available, but carries significant incidence of false negative results (Platt et al. 1997).

Hence, MDCTA has become a valuable technique in patients with suspected vascular complication, avoiding the need for diagnostic angiography

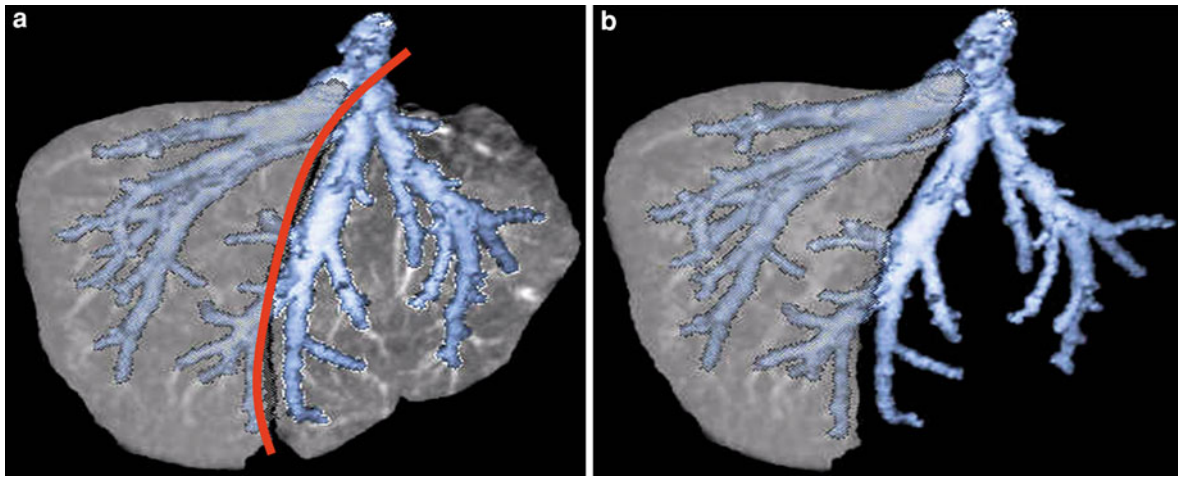

Fig. 5 Volumetric assessment of liver for surgical planning. 3D images displaying manual processing of the volumetric images for planning a left lobe resection of liver metastasis in a 45 year-old male with a primary colon cancer

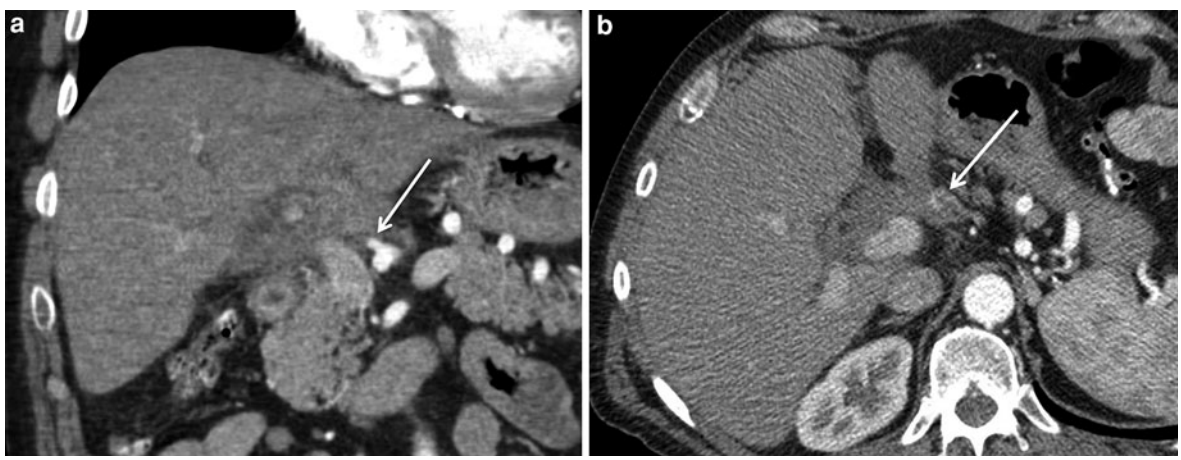

Fig. 6 MDCT coronal (**a**) and axial (**b**) images of a 57-year-old patient who underwent a hepatic transplant 2 months prior to this study. There is abrupt cut-off the hepatic artery (**a**, *long arrow*) in the coronal reformats, which correlates with a filling defect on axial images (**b**, *long arrow*) resulting from a thrombosed hepatic artery

(Katyal et al. 2000; Kim et al. 2007). In addition to the vascular evaluation, it also reveals parenchymal abnormalities and to a lesser extent bile ducts.

4.2 Other Surgical Procedures

In patients requiring major hepatectomies for primary neoplasms or metastatic disease, detailed assessment of the tumor and its relationship to critical vascular structures and the biliary tree are often needed to facilitate successful liver resection and obviate inadvertent injury to remaining liver parenchyma (Sahani et al. 2004).

Few metastatic cancers are treated successfully by surgery. Different techniques of hepatic resection have been reported, which include wedge resection, segmentectomy, lobectomy and extended lobectomy (e.g. trisegmetnectomy), all of which need adequate presurgical evaluation of the vasculature.

Surgical therapy for isolated hepatic metastasis from colorectal cancer has been proposed to be a safe and potentially curable treatment. However controversy exists on which factors predict the outcome.

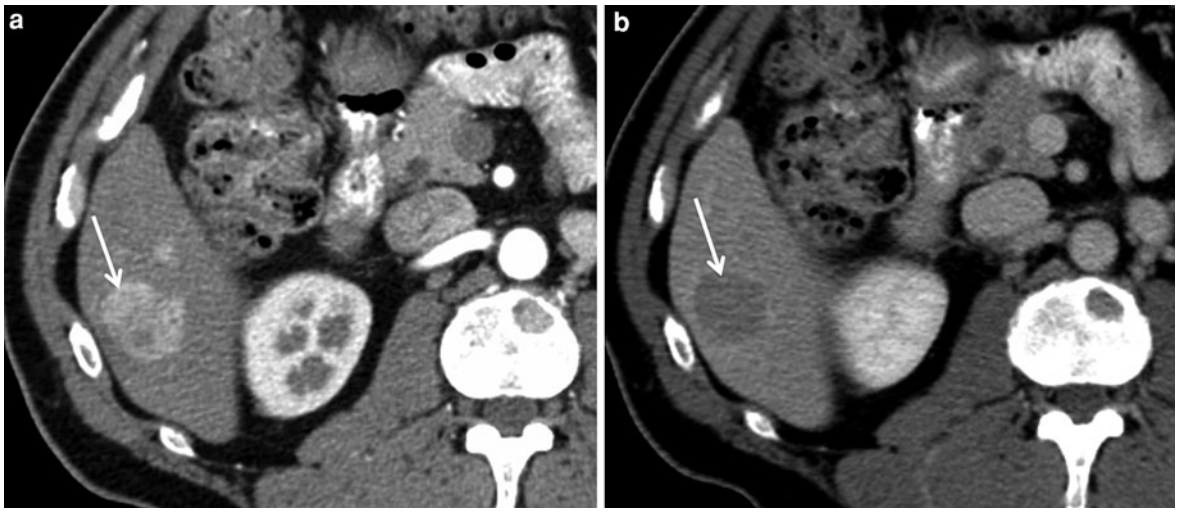

Fig. 7 Axial MDCT images from a 63-year-old male patient with cirrhosis. **a** Arterial phase image shows a well-circumscribed hypervascular lesion in segment VI of the liver (*long arrow*). **b** Delayed phase image shows wash-out in the lesion (*long arrow*) highly suspicious for a hepatocelullar carcinoma. The imaging diagnosis was posteriorly confirmed after a hepatectomy

The significant prognostic factors are surgical margins, number of metastases, and preresection CEA. With accurate selection of patients, the 5 year disease free survival rate ranges from 25–35% for surgical treated metastases (Cady et al. 1998; Wagner et al. 1984).

In the setting of unresectable liver metastases, another therapeutic alternative is hepatic artery chemotherapy, which has demonstrated response rates of 50–70% (Buyse 1996). In patients considered for intraarterial (IA) chemotherapy pump placement, arterial anatomy is required for optimal placement of the chemotherapy pump catheter in the hepatic artery to maximize the success of chemotherapy (Allen et al. 2005). Anomalous arteries may require ligation/embolization or might render a patient unsuitable for IA pump placement.

4.3 Hepatocellular Carcinoma

Hepatocellular carcinoma (HCC) is the most frequent liver malignancy. Although not a prerequisite, the majority of HCCs develop in the setting of chronic liver disease or cirrhotic livers. HCC may be present as a solitary mass, multifocal nodules or diffuse disease throughout the liver. When infiltrative, HCCs usually have irregular borders and indistinct margins with invasion of the portal or hepatic veins.

Recent studies have reported an overall sensitivity of dual-phase MDCT for HCC detection of about 86%. However, the MDCT performance is dependent on tumor size, as sensitivity decreases to about 60% for tumors with a diameter of 2 cm or smaller (Murakami et al. 2001; Lim et al. 2000).

On MDCT, an early arterial phase enhancement with a rapid washout in the portal venous phase with or without a pseudocapsule is a typical presentation. (Fig. 7). However the tumor's vascularity is dependent on the grade of malignancy and neoangiogenesis. (Tajima et al. 2002). Small low-grade tumors (>2 cm) may have poor arterial blood supply and receive portal venous blood supply, demonstrating a delayed enhancement in the early portal phase. Some authors advocate routinely utilizing delayed images, since it increases the diagnostic performance and helps differentiate HCC from arterioportal shunts, especially in cirrhotic livers (Iannaccone et al. 2005).

Twenty percent of patients develop HCC in the absence of cirrhosis or known risk factors. However, they are present in younger patients and have been described as larger, solitary and encapsulated tumors or as a dominant lesion with satellite tumors (Brancatelli et al. 2002a).

Hepatic resection is widely accepted as the mainstay of curative therapy for localized HCC. MDCTA is the first line imaging modality for assessing candidates for hepatic resection by demonstrating the relationship of the tumor to major intrahepatic vessels, tumor invasion of the inferior vena cava or main portal vein, and the presence of satellite tumor nodules.

In recent years, liver transplantation has evolved as the main treatment for early-stage HCC because it can be curative, minimize the risk of recurrence and avoid the complications of cirrhosis (Befeler et al. 2005).

The United Network of Organ Sharing (UNOS) has adopted criteria proposed by the Milan group as a selection guideline for orthotopic liver transplantation in patient with HCC. In order to be a candidate according to the Milan criteria, the patient should have a solitary tumor $\leq$5 cm or three or fewer lesions none >3 cm (Mazzaferro et al.1996; UNOS 2011). If the size and number of HCC exceeds that of the Milan criteria, the patient is considered ineligible for transplant. In the case of a single lesion which is <2 cm in size, it is usually followed by imaging until it meets the UNOS requirement.

While a pre-listing biopsy is not mandatory, it is required that candidates meet certain CT or MRI imaging criteria, which in addition to the criteria detailed above regarding tumor size and number, also include the absence of extrahepatic spread and of macrovascular invasion UNOS (2011).

Other studies have proposed an expanded version of the Milan criteria, the so-called UCSF criteria, in which a single tumor $\leq$ 6.5 cm, 3 or fewer tumors with the largest being 4.5 cm, or a total tumor burden $\leq$ 8.0 cm without gross vascular involvement, achieving the same long-term results as the Milan criteria Yao et al. (2001).

5 Vascular Liver Pathology

5.1 Hepatic Artery Aneurysm

Hepatic artery aneurysms are the second most common visceral artery aneurysms. The most common causes reported are medial degeneration, trauma, iatrogenic and mycotic aneurysms (Shanley et al. 1996) (Fig. 8). Up to 80% of spontaneous hepatic artery aneurysms are solitary and have an extrahepatic location at the level of the common hepatic or right hepatic artery. Often, these are incidentally detected on imaging studies, but when symptomatic they are frequently present due to rupture or bleed in the bowel as right upper quadrant/epigastric pain or GI bleeding. Intrahepatic aneurysms may rupture into the hepatobiliary system leading to the classic triad of biliary colic, hematobilia and jaundice (Pasha et al. 2007). On MDCTA, aneurysms of the hepatic artery may be viewed as fusiform dilatation of the vessel or as a sacular arterial enhancing structure connecting with the hepatic artery.

The management is usually dependent on the size of the lesion and the regional vascular anatomy. Catheter-based endovascular approaches including embolization and endograft exclusion, are increasingly being used over surgical intervention (Rossi et al. 2008). Large proximal aneurysms may require liver resection. On the other hand, extrahepatic aneurysm may undergo aneurysmorrhaphy, resection and interposition or bypass grafting.

Pseudoaneurysms, are a rare but potentially fatal complication of liver transplant, reported in up to 0.6% of cases. Pseudoaneurysms usually occur at the sites of vascular anastomosis but can also be intrahepatic (Stange et al. 2000) (Fig. 8).

5.2 Portal Vein Thrombosis

Thrombosis of the portal vein is frequently a complication of preexisting abdominal malignancy (such as hepatocellular carcinoma or pancreatic carcinoma) or abdominal inflammation such as pancreatitis, diverticulitis, or appendicitis (Choen et al. 1992).

On MDCTA, in an acute setting, recently formed thrombus can be hyperdense and obscured on contrast enhanced images. More chronic thrombus can be iso or hypodense relative to adjacent soft tissues, presenting as a filling defect within the lumen of the portal vein. The hepatic segment supplied by the occluded venous branch appears hyperdense on arterial phase due to compensatory arterial flow, and more hypodense on the portal venous phase compared to the rest of the parenchyma (Parvey et al. 1994).

Diagnosing portal venous invasion by tumor thrombus is thought to be one of the most important prognostic factors regulating recurrence and survival after surgical resection of hepatic malignancies (Ikai et al. 2004). In order to diagnose neoplastic

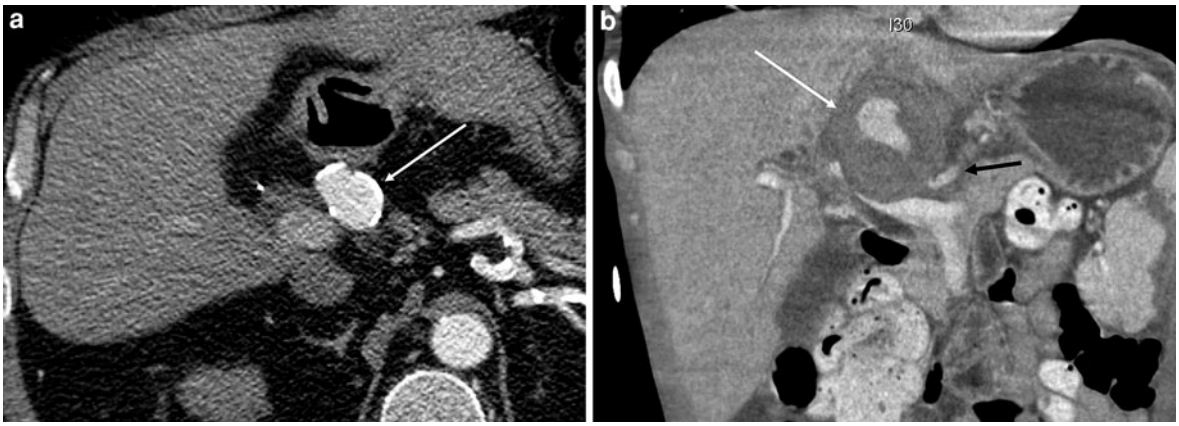

Fig. 8 Hepatic artery aneurysms. **a** MDCT axial image of a 65-year-old male asymptomatic patient, who had undergone liver transplant 7 years prior to this study. On follow-up imaging, the patient demonstrated a chronic aneurysm of the common hepatic artery with calcified walls (*arrow*). **b** Mycotic aneurysm in a 36-year-old male patient, with history of IV drug abuse. Coronal MDCT image shows a large sacular, partially thrombosed aneurysm (*white arrow*) arising from the common hepatic artery (*black arrow*)

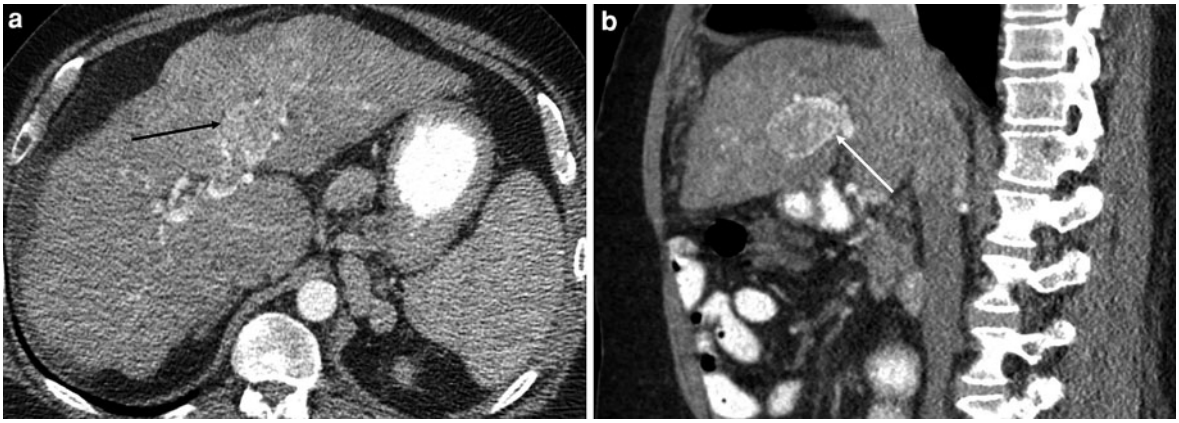

Fig. 9 Tumoral thrombus in the portal vein. Axial (**a**) and sagittal (**b**) images of a 67-year-old male patient with history of chronic hepatitis C infection and cirrhosis. On both images, expansion of the left portal vein and an intraluminal arterial enhancing thrombus (*arrows*) is observed. The patient underwent percutaneous biopsy of the thrombosed portal vein, which proved to be secondary to hepatocellular carcinoma invasion (*arrows*)

invasion, expansion of the main portal vein (diameter over 25 mm), as well as thrombus enhancement and neovascularity should be observed (Tublin et al. 1997). Intense enhancement is more associated with HCC over other malignancies (Shah et al. 2007) (Fig. 9).

When segmental occlusion of the portal venous system occurs, local collateral pathways of flow arise to bypass the obstruction. Cavernous transformation of the portal vein is defined as a mass-like network of intertwined veins in the hepatoduodenal ligament and porta hepatis that provide an alternative pathway around an occluded main portal vein or lobar branch. In these patients, increased arterial flow to the portions deprived of portal venous flow is depicted, showing hyperattenuation of the periphery of the parenchyma in the arterial phase. The central portion of the liver demonstrates normal enhancement because the cavernous collateral vessels provide adequate flow.

Other than in the setting of portal venous thrombosis, cavernous transformation has also been reported as a congenital malformation in a nondeveloped portal vein and as a hemangioma of the portal vein (De Gaetano et al. 1995).

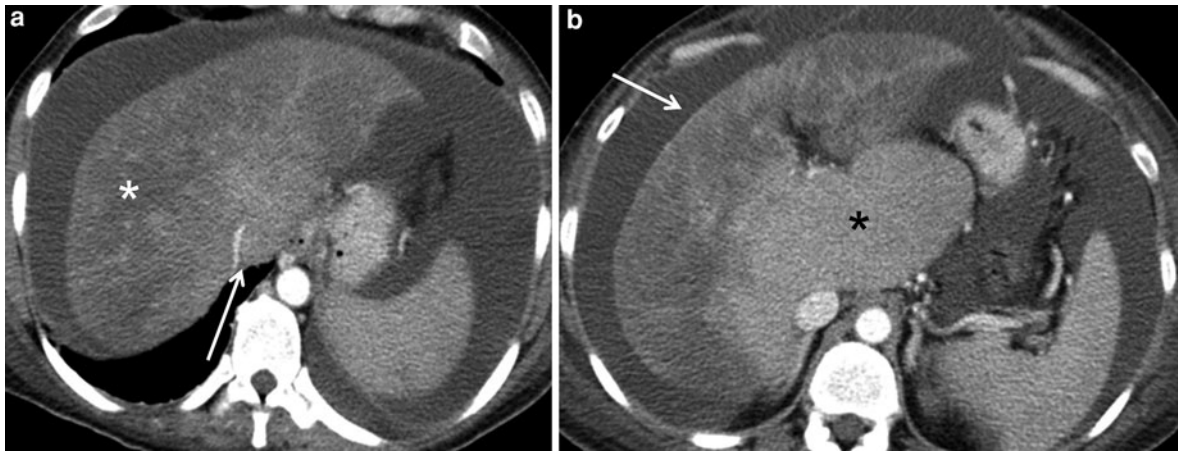

Fig. 10 Budd-Chiari Syndrome. Axial images from a 46-year-old female patient with history of leukemia. **a** There is heterogeneous hypoenhancement of the periphery of the liver (*). Note a filling defect in the inferior vena cava in the dome of the liver (*arrow*). In lower slices **b**, there is hypertrophy of the caudate lobe (*). Note the mild subcapsular enhancement (*arrow*) and moderate amount of ascitis

5.3 Budd-Chiari Syndrome

Budd-Chiari syndrome represents a spectrum of disease resulting from hepatic venous outflow obstruction, which can occur at the level of the hepatic veins, IVC or right atrium. The most common causes are myeloproliferative disorders such as polycythemia vera and use of oral contraceptives. Other less common associated pathologies are hepatitis, hepatic abscesses, trauma, polycystic liver disease and idiopathic (Denninger et al. 2000).

The MDCTA imaging findings of Budd-Chiari syndrome depend on whether the disease is acute or chronic. In acute presentation, the parenchyma is enlarged and diffusely hypodense in the unenhanced phase. The IVC and hepatic veins can be hyperdense due to the presence of thrombus and on contrast enhanced images inadequate opacification or an intraluminal filling defect can be observed.

On arterial phase, there is early enhancement of the caudate lobe and central portion of the liver, as well as decreased peripheral enhancement. On portal venous phase, no collateral veins are present and there is a reverse pattern of enhancement, in which the central area of the liver is hypodense and the periphery displays increased attenuation with accumulation of contrast material in the subcapsular veins (Fig. 10).

In chronic Budd-Chiari syndrome, the liver appears irregular, with caudate lobe hypertrophy and atrophy of the peripheral segments, resulting in a caudate lobe to right lobe ratio of >0.55 (Kim et al. 1999). On arterial phase, there is heterogeneous enhancement of the parenchyma, with regenerative macronodules (ranging from 1 to 4 cm) which enhance homogenously with or without a hypoattenuating rim (Brancatelli et al. 2002b).

Collateral circulatory portosystemic and intrahepatic pathways develop, with obliteration of the IVC, hepatic veins or both. Other extrahepatic findings are ascites and splenomegaly.

In the setting of chronic disease, it is important to distinguish macronodules from small HCC, which usually enhance heterogeneously in the arterial phase and demonstrate washout in the portal venous phase. The morphological characteristics of the liver and the clinical setting should help in differentiating them (Brancatelli et al. 2002).

It is critical to adequately diagnose Budd-Chiari syndrome, since if untreated, it has a mortality rate of 80%, with liver failure as the primary cause of death (Valla 2003). If patients with Budd-Chiari deteriorate despite medical treatment, decompressive portosystemic transjugular or surgical shunting must be considered. Prior to these procedures, patients need accurate vascular mapping and evaluation with MDCTA or magnetic resonance angiography to evaluate patency of hepatic, portal and splachnic veins (Mancuso et al. 2003).

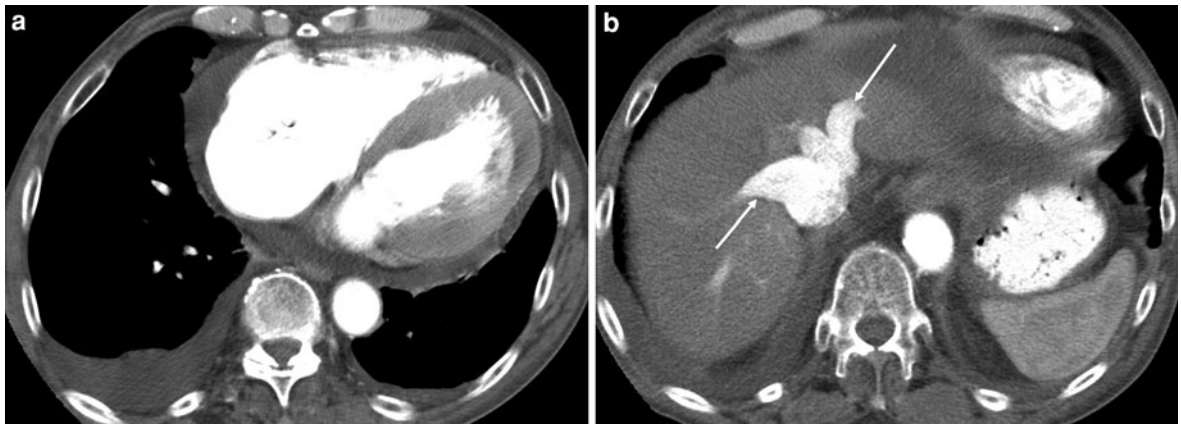

Fig. 11 Hepatic congestion secondary to cardiac heart failure. **a** Axial images of the lower thorax show cardiomegaly and right pleural effusion (*). **b** Dilation of the inferior vena cava and hepatic veins (*arrows*) with early opacification due to retrograde flow from the right atrium

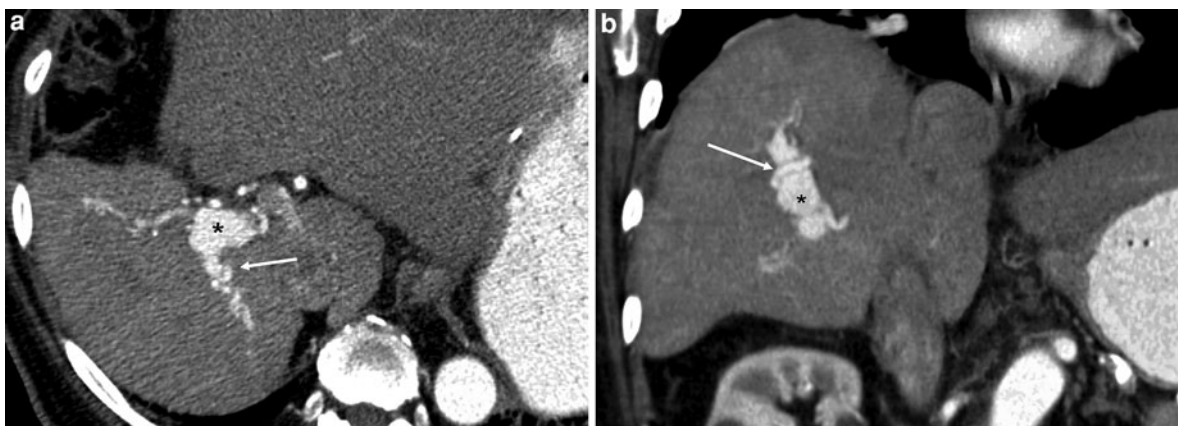

Fig. 12 Arterioportal shunt. Axial (**a**) and coronal (**b**) MDCT images from a 75-year-old male patient who underwent a percutaneous radiofrequency ablation of small hepatocellular carcinoma. The images are acquired during the arterial phase, in which early enhancement of the right portal vein (*) is noted. Adjacent to the right portal vein there is a branch of the right hepatic artery (*arrow*), suggesting an arterioportal communication

5.4 Passive Hepatic Congestion

The clinical condition of right heart failure effectively produces a degree of hepatic venous outflow obstruction. While there is no thrombus within the venous circulation such as in Budd-Chiari syndrome, the diminished pumping activity of the heart prevents normal outflow of hepatic venous blood from the liver into the hepatic veins, IVC and right heart.

The MDCT appearance of passive hepatic congestion is termed "nutmeg" liver, due to the heterogeneous perfusion in the liver, which resembles the cut surface of a nutmeg. On MDCT exam, the findings of acute passive congestion include a diffusely mottled appearance of the liver involving all segments including the caudate, and early opacification of the hepatic veins and IVC due to retrograde flow from the right atrium into these vessels rather than into the failing right ventricle (Moulton et al. 1988). Additional features may include hepatomegaly, cardiomegaly, pleural effusions and ascites (Fig. 11).

It is important to recognize these findings and correctly attribute them to right heart failure as the heterogeneous appearance may be mistaken for pseudolesions or a diffuse infiltrative process. In chronic passive congestion, the liver can develop cirrhosis (termed "cardiac cirrhosis") (Gore et al. 1994).

Table 6 Clinical Implications of vascular abnormalities

Vascular abnormality	Imaging findings	Clinical impact	Management
Anatomical variants	Multiple variants of:	Presurgical assessment to avoid prolonged surgical time and complications	Adequate vascular mapping
	hepatic arteries		
	hepatic veins		
	portal veins		
Hepatic artery aneurysms	Fusiform or sacular arterial enhancing dilatation originating from hepatic artery	Rupture	Endovascular
		GI bleed	Embolization
		Jaundice	Surgical resection
Shunts	Arterio-portal:	Differentiate from HCC	If definitive diagnosis and small: none
	small peripheral arterial enhancing focus		
	wedge shaped		If diagnostic uncertainty: follow-up or evaluate with MRI
	early enhancement of portal vein		
		When large can cause portal hypertension	If large: transarterial embolization, surgical resection
	Porto-systemic:	Low flow shunt: asymptomatic	None
	early enhancement of hepatic vein	High flow: encephalopathy	Medical treatment, surgical resection
	TIPS: assess patency	Recurrence of symptoms of portal hypertension	Balloon angioplasty
			Insertion of new stent or parallel TIPS
Hypervascular tumor- HCC	Arterial enhancing mass with portal venous phase washout	Assess portal vein invasion	Presurgical planning
		Satellite nodules	Assess transplant candidate
		Milan criteria/UCSF criteria	
Portal vein thrombosis	Bland thrombus: Filling defect in portal vein; Cavernous transformation	Assess cause: cirrhosis, pancreatitis, diverticulitis, appendicitis	Medical or surgical treatment according to specific etiology
	Malignant thrombosis: enhancing thrombus with expansion of vein	Prognostic factor	Prognostic factor for recurrence after surgical resection
Budd chiari	Acute: hyperdense IVC and hepatic veins on non contrast images; filling defect in IVC or hepatic veins; early enhancement of caudate lobe Chronic: irregular liver; hypertrophy of caudate lobe; macronodules	Liver failure	Medical treatment Surgical or transjugular shunt

5.5 Pseudolesions/Shunts

5.5.1 Arterioportal Shunts

An arterioportal (AP) shunt is defined as a direct communication between a hepatic arterial branch and a portal vein. It can occur at the level of trunk, sinusoids, or peribiliary venules (Quiroga et al. 2001).

AP shunts can occur following trauma, instrumentation, in association with a liver lesion, or can be congenital (as in Rendu-Osler-Weber disease). Spontaneous small arterioportal shunts may occur in a cirrhotic liver. In the setting of a liver lesion, they are associated usually with hepatocellular carcinoma and small hemangiomas.

On MDCTA, the arterial phase shows small, peripheral, enhancing foci, occasionally wedge-shaped, displaying early enhancement of the portal vein prior to the opacification of the main portal vein

(Fig. 12). The shunt then becomes isoattenuating to the liver and vasculature in the portal venous phase (Quiroga et al. 2001). The most important role of imaging when an early enhancing focus is observed, is to differentiate it from a small hepatocellular carcinoma, which tend to be more hypodense when compared to the parenchyma on portal venous phases. When doubt persists, either a follow-up CT in 6 months or complementary imaging with MR is recommended (Torabi et al. 2008).

5.5.2 Portosystemic Shunts

Intrahepatic portosystemic venous shunt is a rare condition defined as communication between a systemic vein and a portal vein via an anomalous channel. It may be congenital or acquired from trauma or portal hypertension. The most frequent portosystemic shunt occurs between the right portal vein and the inferior vena cava (Lane et al. 2000).

Clinical manifestation depends on the shunt flow: a low flow shunt can be asymptomatic, whereas a high-flow shunt can cause encephalopathy and hypoglycemia. On MDCTA, the most common finding on a portal venous phase is early enhancement of the involved hepatic vein compared with the other hepatic veins, and in some cases the communication between the portal vein branch and the hepatic vein can be observed.

Transjugular intrahepatic postosystemic shunt (TIPS) is a percutaneous interventional procedure used to control symptomatic complications of portal hypertension, such as variceal bleeding and refractory ascitis. In most cases TIPS is created between the right portal vein and the right or middle hepatic vein. Regular shunt surveillance allows detection of early shunt failure as stenosis or thrombosis. There is no established consensus of what is the optimal surveillance protocol for TIPS. Ultrasound is widely accepted as the imaging modality of choice for TIPS surveillance, but the use of MDCTA has been described with high sensitivity for depicting significant shunt abnormalities (Chopra et al. 2000).

6 Conclusion

In summary, MDCTA is an effective, high resolution, noninvasive imaging technique, which readily demonstrates the presence of vascular and neoplastic pathology in the liver, with a direct impact on treatment decision and patient selection for medical or surgical management (Table 6).

References

Allen PJ, Nissan A, Picon AI et al (2005) Technical complications and durability of hepatic artery infusion pumps for unresectable colorectal liver metastases: an institutional experience of 544 consecutive cases. J Am Coll Surg 201(1): 57–65

Befeler AS, Hayashi PH, Bisceglie AM (2005) Liver transplantation for hepatocellular carcinoma. Gatroenterology 128:1752–1764

Brancatelli G, Federle MP, Grazioli L et al (2002a) Hepatocellular carcinoma in noncirrhotic liver: CT, clinical, and pathologic findings in 39 US residents. Radiology 222:89–94

Brancatelli G, Federle MP, Grazioli L et al (2002b) Large regenerative nodules in Budd-Chiari syndrome and other vascular disorders of the liver: CT and MR imaging findings with clinico-pathologic correlation. Am J Roentgenol 178: 877–883

Buyse M (1996) Reappraisal of hepatic arterial infusion in the treatment of nonresectable liver metastases from colorectal cancer: Meta-Analysis Group in Cancer. J Natl Cancer Inst 88:252–258

Cady B, Jenkins RL, Steele GD, Lewis D et al (1998) Surgical Margin in Hepatic resection for colorectal metastasis. Ann Surg 227:566–571

Catalano O, Singh A, Uppot R et al (2008) Vascular and biliary variants in the liver: implications for liver surgery. Radiographics 28:359–378

Choen J, Edelman RR, Chopra S (1992) Portal vein thrombosis: a review. Am J Med 92:173–182

Chopra S, Dodd GD 3rd, Chintapalli KN et al (2000) Transjugular intrahepatic portosystemic shunt: accuracy of helical CT angiography in the detection of shunt abnormalities. Radiology 215:115–122

De Gaetano AM, Lafotune M, Patriquin H et al (1995) Cavernous transformation of the portal vein: patterns of intrahepatic and splachnic collateral circulation detected with Doppler Sonography. Am J Roentgenol 165: 1151–1155

Denninger MH, Chait Y, Casadevall N et al (2000) Causes of portal or hepatic venous thrombosis in adults: the role of multiple concurrent factors. Hepatology 31:587–591

Frenchel S, Boll DT, Fleiter TR et al (2003) Multislice helical CT of the pancreas and spleen. Eur J Radiol 45(suppl 1): S59–S72

Glockner JF, Forauer AR (1999) Vascular or ischemic complications after liver transplantation. AJR 173: 1055–1059

Gore RM, Mathieu DG, White EM et al (1994) Passive hepatic congestion: cross-sectional imaging features. Am J Roentgenol 162:71–75

Horton KM, Fishman EK (2000) 3D CT angiography of the celiac and superior mesenteric arteries with multidetector

CT data sets: preliminary observations. Abdom Imaging 25:523–525
Iannaccone R, Laghi A, Catalano C et al (2005) Hepatocellular carcinoma: role of unenhanced and delayed phase multidetector row helical CT in patients with cirrhosis. Radiology 234:460–467
Ikai I, Arii S, Kojiro M et al (2004) Reevaluation of prognostic factors for survival after liver resection in patients with hepatocellular carcinoma in a Japanese nationwide survey. Cancer 101:769–802
Kamel IR, Liapi E, Fishman EK (2005) Liver and biliary system: evaluation by multidetector CT. Radiol Clin N Am 43:977–997
Katyal S, Oliver JH, Buck DG, Federle MP (2000) Detection of vascular complications after liver transplantation: early experience in multislice CT angiography volume rendering. Am J Roentgenol 175:1735–1739
Kim TK, Chung JW, Han JK et al (1999) Hepatic changes in benign obstruction of the hepatic inferior vena cava: CT findings. Am J Roentgenol 173:1235–1242
Kim SY, Kim KW, Kim MJ, Shin YM et al (2007) Multidetector row CT of various hepatic artery complications after living donor liver transplantation. Abdom Imaging 32: 635–643
Lane MJ, Jeffrey RB Jr, Katz DS (2000) Spontaneous intrahepatic vascular shunts. Am J Roentgenol 174:125–131
Legmann P, Costes V, Tudoret L et al (1995) Hepatic artery thrombosis after liver transplantation: diagnosis with spiral CT. AJR Am J Roentgenol 164:97–101
Lim JH, Kim CK, Lee WJ et al (2000) Detection of hepatocellular carcinomas and dysplastic nodules in cirrhotic livers: accuracy of helical CT in transplant patients. Am J Roentgenol 175:693–698
Lo CM, Fan ST, Liu CL et al (1997) Adult-to-adult donor liver transplantation using extended right lobe grafts. Ann Surg 226:261–269
Lv P, Lin XZ, Li J, Li W, Chen K (2011) Differentiation of small hepatic hemangioma from small hepatocellular carcinoma: recently introduced spectral CT method. Radiology 259(3):720–729
Mancuso A, Fung K, Mela M et al (2003) TIPS for acute and chronic Budd-Chiari syndrome: a single center experience. J Hepatol 38:751–754
Marin D, Nelson RC, Samei E et al (2009) Hypervascular liver tumors: low tube voltage, high tube current multidetector CT during late hepatic arterial phase for detection—initial clinical experience. Radiology 251(3):771–779
Mazzaferro V, Regalia E, Doci R et al (1996) Liver transplantation for the treatment of small hepatocellular carcinomas in patients with cirrhosis. N Engl J Med 334(11): 693–699
Moulton JS, Miller BL, Dodd GD III, Vu DN (1988) Passive hepatic congestion in heart failure: CT abnormalities. Am J Roentgenol 151:939–942
Murakami T, Kim T, Takamura M et al (2001) Hypervascular hepatocellular carcinomas: detection with double arterial phase multi-row helical CT. Radiology 218:763–767
Nakayama Y, Awai K, Funama Y, Hatemura M, Imuta M, Nakaura T, Ryu D et al (2005) Abdominal CT with low tube voltage: preliminary observations about radiation dose, contrast enhancement, image quality, and noise (No. 3). Radiology 237:945–951
Pannu HK, Maley WR, Fishman EK (2001) Liver transplantation: preoperative CT. Radiographics 21:S133–S146
Parvey R, Raval B, Sandler C (1994) Portal vein thrombosis: imaging findings. Am J Roentgenol 162:77–81
Pasha SF, Gloviczki P, Stanson AW et al (2007) Splanchnic artery aneurysms. Mayo Clin Proc 82(4):472–479
Platt JF, Yutzy GG, Bude RO, Ellis JH, Rubin JM (1997) Use of Doppler sonography for revealing hepatic artery stenosis in liver transplant recipients. AJR 168:473–476
Quiroga S, Sebastia C, Pallisa E et al (2001) Improved diagnosis of hepatic perfusion disorders: value of hepatic arterial phase imaging during helical CT. Radiographics 21:65–81
Rossi M, Rebonato A, Greco L et al (2008) Endovascular exclusion of visceral artery aneurysms with stent-grafts: technique and long-term follow-up. Cardiovasc Intervent Radiol 31(1):36–42
Sahani D, Mehta A, Blake M et al (2004) Preoperative hepatic vascular evaluation with CT and MR angiography: implications for surgery. Radiographics 24:1367–1380
Shah Z, McKernan MG, Hahn P, Sahani D (2007) Enhancing and expansile portal vein thrombosis value in the diagnosis of hepatocellular carcinoma in patients with multiple hepatic lesions. Am J Roentgenol 188:1320–1323
Shanley CJ, Shah NL, Messina LM (1996) Common splanchnic artery aneurysms: splenic, hepatic and celiac. Ann Vasc Surg 10(3):315–322
Stange B, Settmacher U, Glanemann M et al (2000) Aneurysms of the hepatic artery after liver transplantation. Transplant Proc 32:533–534
Suzuki K, Epstein ML, Kohlbrenner R et al (2011) Automated CT liver volumetry compared with interactive volumetry and manual volumetry. AJR 197:W706–W712
Tajima T, Honda H, Taguchi K et al (2002) Sequential hemodynamic change in hepatocellular carcinoma and dysplastic nodules: CT angiography and pathologic correlation. Am J Roentgenol 178:885–897
Tanikake M, Shimizu T, Narabayashi I et al (2003) Three-dimensional angiography of the hepatic artery: use of multidetector row helical CT and contrast agent. Radiology 227: 883–889
Tatsugami F, Matsuki M, Kani H et al (2006) Effect of saline pushing after contrast material injection in abdominal multidetector computed tomography with the use of different iodine concentrations. Acta Radiol 47(2): 192–197
Thomas A, Bernhard M (2005) New trends in multidetector computed tomography angiography of peripheral arteries. Advances in MDCT—an international literature review service 2(2):1–6
Torabi M, Hosseinzadeh K, Federle M (2008) CT of nonneoplastic hepatic vascular and perfusion disorders. Radiographics 28:1967–1982
Tublin M, Dodd GD, Baron R (1997) Benign and malignant portal vein thrombosis: differentiation by CT characteristics. Am J Roentgenol 168:719–723

Tzakis AG, Gordon RD, Shaw BW Jr, Iwatsuki S, Starzl TE (1985) Clinical presentation of hepatic artery thrombosis after liver transplantation in the cyclosporine era. Transplantation 40:667–671

United Network for Organ Sharing (UNOS). Policy 3.6.4.4. Allocation of livers: liver transplant candidates with hepatocellular carcinoma.http://optn.transplant.hrsa.gov/PoliciesandBylaws2/policies/pdfs/policy_8.pdf. Accessed 8 Mar 2011

Valla DC (2003) The diagnosis and management of the Budd-Chiari syndrome: consensus and controversies. Hepatology 38:793–803

Wagner S, Adson MA, van Heerden JA et al (1984) The natural history of hepatic metastases from colorectal cancer. Ann Surg 199:502–507

Yao FY, Ferrell L, Bass NM et al (2001) Liver transplantation for hepatocellular carcinoma: expansion of the tumor size limits does not adversely impact survival. Hepatology 33:1394–1403

MSCT Imaging of Acute and Chronic Pancreatitis

Shelby Fishback, David H. Kim, and Perry J. Pickhardt

Contents

Abstract

Multi-slice computed tomography (MSCT) has improved evaluation in a variety of abdominal applications over the older single slice era. Multi-slice technology allows for large volumetric acquisition of data which in turn leads to faster imaging with thinner collimation during optimal contrast enhancement. Regarding the pancreas, it has allowed improved depiction of this gland and the various processes that can affect it. For example, whereas the development of pancreatic necrosis complicating acute pancreatitis may have been less apparent with single slice scanner protocols, MSCT can more accurately detect this important complication for confident diagnosis by the interpreting radiologist. This chapter discusses the current capabilities and role of MSCT imaging in the evaluation of acute and chronic pancreatitis. In particular, the manner in which MSCT integrates within the clinical evaluation to affect management for acute pancreatitis will be stressed. In addition, autoimmune pancreatitis and the evolving views of this disease process will be covered.

Abbreviations

APFCs	Acute pancreatic/peripancreatic fluid collections
PNPFCs	Post necrotic pancreatic/peripancreatic fluid collections
WOPN	Infected necrosis and walled off pancreatic necrosis

S. Fishback · D. H. Kim · P. J. Pickhardt (✉)
Department of Radiology,
University of Wisconsin School of Medicine
and Public Health, E3/311 Clinical Science Center,
600 Highland Avenue, Madison,
WI 53792-3252, USA
e-mail: ppickhardt2@uwhealth.org

C. J. Zech et al. (eds.), *Multislice-CT of the Abdomen*, Medical Radiology. Diagnostic Imaging,
DOI: 10.1007/174_2011_410, © Springer-Verlag Berlin Heidelberg 2012

1 Acute Pancreatitis

Acute pancreatitis is a disease process characterized by acute inflammation and autodigestion of the pancreatic gland, resulting from premature activation of pancreatic exocrine enzymes. It can be limited to the gland proper or extend considerably beyond the pancreas via the retroperitoneal interfascial planes, subperitoneal ligaments, and mesenteries. Likewise, the clinical spectrum may range from a mild presentation where the process is largely self limited with little or no long term sequelae to severe outcomes complicated by a prolonged hospital course with multi-system organ failure, pancreatic necrosis, pseudocysts, and vascular aneurysms/thrombosis. Although most episodes of acute pancreatitis result in recovery, overall mortality is not insignificant and has been reported at 5% (Banks and Freeman 2006). Due to this wide spectrum of outcomes, many clinically-based (i.e., Ranson criteria—Ranson et al. 1974, Apache score—Knaus et al. 1985, Bisap—Singh et al. 2009) and imaging-based (i.e., the CT severity index; Balthazar et al. 1990) classification systems have been develop to help predict the future clinical course. The clinically-based systems are typically more useful in the first days of an acute pancreatitis episode where the presence of organ failure is a major determinant in future prognosis, whereas the imaging-based systems may be more helpful later in the disease as structural complications become of primary importance to determine clinical course (and treatment; Acute pancreatitis classification working group 2008).

The Atlanta classification (Atlanta, Ga, International Symposium on acute pancreatitis 1992; Bradley 1993) has helped to standardize the terminology regarding acute pancreatitis as well as help summarize the current views and theories on this disease. More recently, this classification scheme has undergone a suggested revision by the Acute Pancreatitis Classification Working Group (2008). Severity is defined in terms of the absence or presence of persistent organ failure (greater than 48 h in duration). *Mild* (*nonsevere*) *acute pancreatitis* is characterized by the absence of organ failure and leads to an uneventful recovery, while *severe pancreatitis* is defined as pancreatitis in association with organ failure. Overall, most presentations are mild in severity, as approximately 20% are categorized as severe pancreatitis (Swaroop et al. 2004; Russo et al. 2004). Within this classification, *interstitial* (*edematous*) *pancreatitis* is a specific diagnosis that is defined in terms of contrast-enhanced CT imaging as focal or diffuse enlargement of the pancreas with homogenous enhancement of the parenchyma without necrosis. Mild soft tissue stranding extending into the peripancreatic tissues may be seen (Fig. 1). On the other end of the spectrum is *necrotizing pancreatitis* which is also defined by imaging criteria. Necrosis is defined as the presence of nonenhancing parenchyma (categorized by <30, 30–50 and >50% of gland involvement; Fig. 2). CT-confirmed interstitial pancreatitis typically equates to mild (nonsevere) acute pancreatitis, although a small percentage may manifest with severe presentation, whereas necrotizing pancreatitis almost always occurs in the setting of severe acute pancreatitis. Overall, mortality in interstitial pancreatitis is low at 3% whereas necrosis holds an overall mortality of 17% (Banks and Freeman 2006). The Atlanta classification also standardized definitions for terms of *acute pancreatic/peripancreatic fluid collections* (*APFCs*), *pseudocysts*, *pancreatic abscesses*, *post necrotic pancreatic/peripancreatic fluid collections* (*PNPFCs*), *infected necrosis*, *and walled off pancreatic necrosis* (*WOPN*).

Imaging in acute pancreatitis is predominantly undertaken by computed tomography. Multi-slice computed tomography (MSCT) has improved the ability over single slice scanners to delineate the various findings in pancreatitis to help aid in clinical decision making. The advantages are related to the faster volumetric acquisition of data with MSCT, which allows for imaging during the optimal contrast enhancement of the pancreas. The imaging appearance of acute pancreatitis at computed tomography is dependent on the severity of the disease process. In mild acute pancreatitis, the pancreas may appear normal, maintaining a characteristic parenchymal texture without enlargement, edema, or surrounding soft tissue stranding. Thus, a normal appearing gland should not dissuade the diagnosis of acute pancreatitis in the face of suggestive clinical presentation and corroborating laboratory values (i.e., elevated serum amylase and lipase levels). As the intensity of the inflammatory process increases, the pancreas will demonstrate evidence of edema, with enlargement, low attenuation infiltration of the parenchyma, and decreased enhancement. The borders of the pancreas

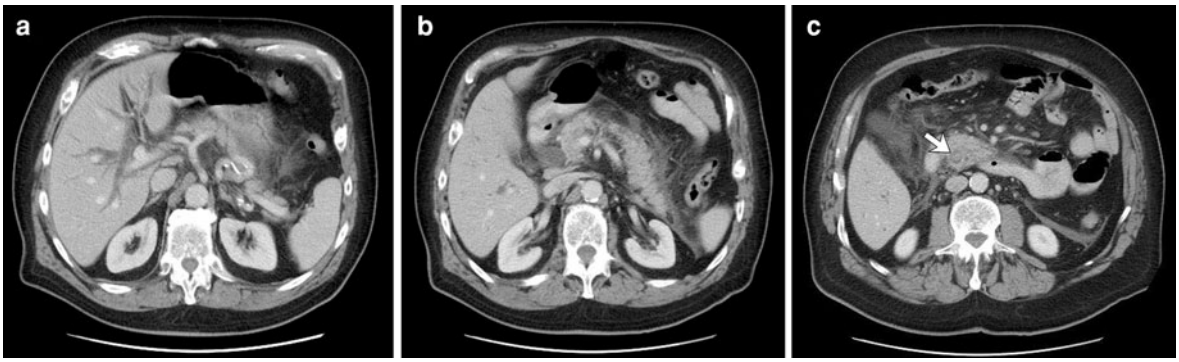

Fig. 1 Gallstone pancreatitis. **a**–**c** Axial CECT images in a patient with edematous (*interstitial*) pancreatitis secondary to choledocholithiasis (**c**, *arrow*). Note the intrahepatic biliary ductal dilatation (**a**, **b**) and moderate peripancreatic inflammation and associated thickening of the adjacent fascial planes (518761)

may become indistinct with hazy soft tissue stranding related to the inflammatory exudate (Fig. 1). Such an appearance would be consistent with the image-defined diagnosis of interstitial (edematous) pancreatitis. The appearance of homogenous but decreased enhancement is indicative of an intact capillary network and argues against necrosis. In more severe cases, the inflammatory stranding and fluid may extend from the pancreas along predefined retroperitoneal interfascial planes (Fig. 1), dissect into the lesser sac, small bowel and transverse colon mesenteries, and various subperitoneal ligaments (Molmenti et al. 1996; Meyers and Evans 1973). The inflammatory products may break through tissue planes into the peritoneal cavity as well as traverse across the layers of the body wall. Typically in the setting of severe pancreatitis, gland necrosis can result related to thrombosis of the microcirculation of the pancreas. Necrosis can present as zones of low attenuation representing nonenhancing parenchyma or fluid-filled areas replacing the expected position of pancreatic parenchyma, which represent liquefied necrosis (Fig. 2).

CT imaging of acute pancreatitis can typically be accomplished by a standard abdomino-pelvic protocol for MSCT. Although thinner collimation (i.e., 2.5 mm or less) may be employed, thicker reading slices typically used in generic protocols (i.e., 5 mm) are more than adequate from a diagnostic standpoint. Thicker slices also allow for potential dose reduction relative to thinner slices; a consideration not insignificant as this patient population may receive numerous exams during recurrent bouts of pancreatitis. Intravenous contrast administration should be undertaken as a rule whenever possible. Many important complications such as pancreatic necrosis or vascular sequelae may be difficult to detect without the use of contrast. The historic concern of intravenous contrast use exacerbating pancreatic necrosis if present has been largely discounted. Such a phenomenon was suggested in one animal model (Foitzik et al. 1994) but has not been seen in other animal models nor is clinically evident in people (Uhl et al. 2002a). The timing of image acquisition during contrast administration can be at a standard abdominal delay of 70–90 s. However, imaging at an earlier time frame of 40–45 s can optimize pancreatic enhancement (i.e., "pancreatic phase"; Balthazar et al. 1994; McNulty et al. 2001; Fletcher et al. 2003) and may improve detection of subtle presentations of developing pancreatic necrosis.

Awareness of the clinical course and pathophysiology of pancreatitis is helpful to understand how MSCT may best impact decision making and treatment choice. There are two apparent clinical phases with a bimodal distribution of mortality (Acute pancreatitis classification working group 2008; Uhl et al. 2002b). In the first phase of the disease which covers the first week, mortality is determined by the systemic response to the inciting inflammatory pancreatic and peripancreatic process; the development of persistent organ failure leads to increased mortality. This is in distinction to the second phase which occurs over the next weeks to months where mortality is related to the sequelae of pancreatic necrosis, particularly in regards to subsequent superinfection.

In the first phase, there are variable degrees of pancreatic and peripancreatic inflammation, ischemia, and fluid collection development. The process either

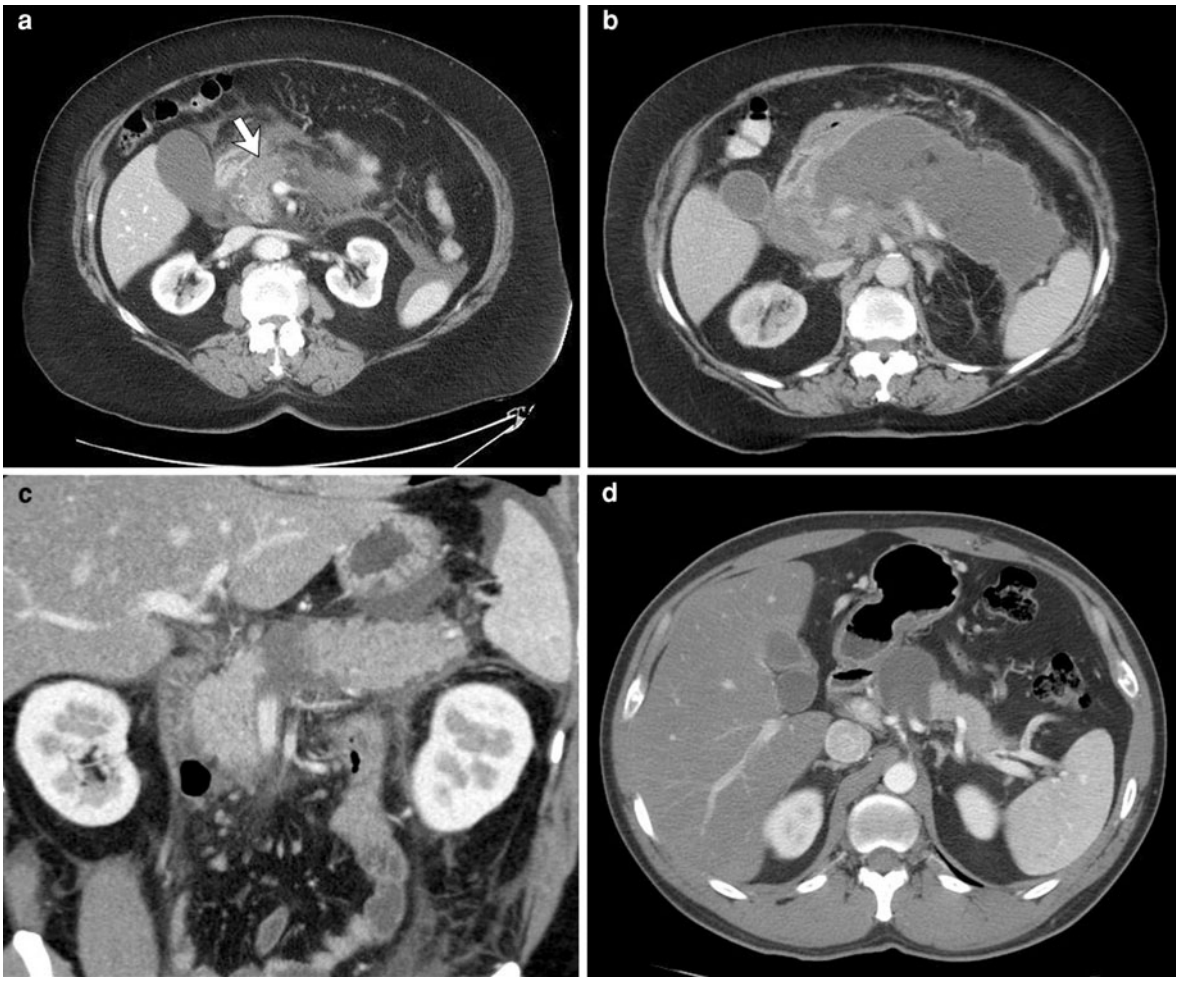

Fig. 2 Necrotizing pancreatitis. **a** Axial CECT image shows areas of non-enhancing pancreatic parenchyma consistent with pancreatic necrosis, most notably involving the neck (*arrow*) and body regions. There is peripancreatic inflammation and fluid extending along the anterior left pararenal fascia plane and surrounding the inferior spleen; **b** CECT obtained 3 weeks later shows progressive pancreatic necrosis with an organized, rim-enhancing fluid collection now encompassing the pancreatic bed (1540631007); coronal (**c**) and axial (**d**) CECT images in a different patient initially show pancreatic necrosis (HU < 30) within the neck/proximal body (**c**). Later image (**d**) shows a circumscribed rim-enhancing fluid collection in the region of pancreatic necrosis, consistent with an intrapancreatic pseudocyst (1928397)

resolves or may progress into necrosis. When organ failure has occurred, it typically resolves by the first week or becomes more severe. In general, the severity and extent of the inflammatory process correlates to the severity of the organ failure although this is not absolute. In the second phase, the disease process may improve and resolve, as in the case of interstitial (edematous) pancreatitis, or enter a more protracted course over weeks to months related to necrosis and subsequent complications. Mortality is largely determined by whether necrosis becomes superinfected (Fig. 3).

Thus, the roles for CT imaging are dependent on when the exam is acquired in relation to disease presentation. Early in the first week, the major purpose is not so much to assess the location and extent of the inflammatory process but for the detection of pancreatic necrosis. The extent of the inflammatory process can be assessed at imaging but generally, the severity (and presumed extent) can be judged fairly well on clinical grounds; mortality is largely influenced by the presence or absence of organ failure. However, whether or not the inflammatory process

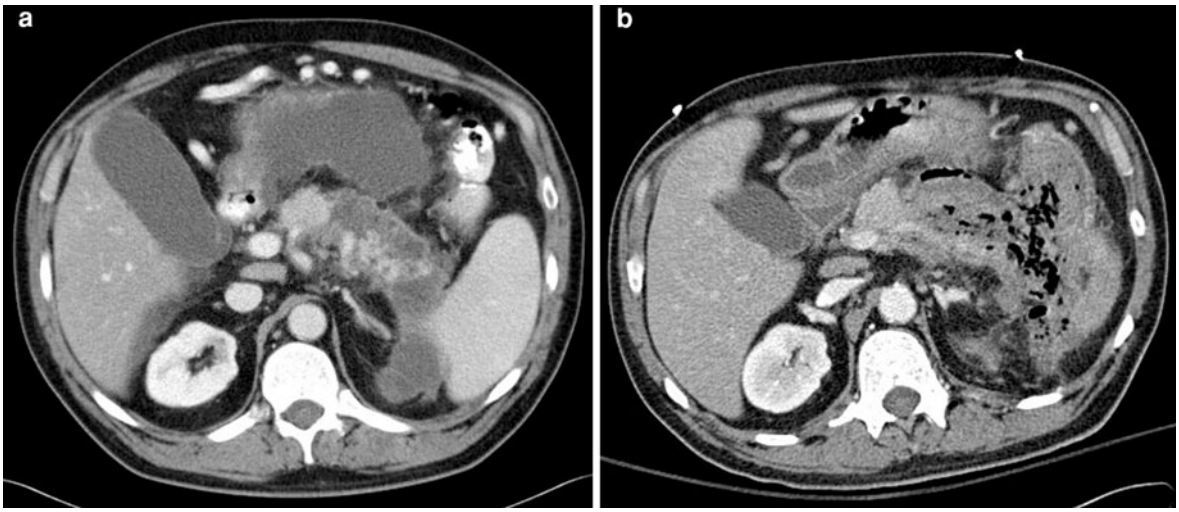

Fig. 3 Infected pancreatic necrosis. **a** Axial CECT image shows multifocal areas of non-enhancing pancreatic parenchyma consistent with pancreatic necrosis; **b** image of the same patient obtained 2 months later shows superinfection of the necrotic pancreas with associated gas formation (Rotzoll WG)

and ischemia has progressed into irreversible necrosis is an important finding that holds important prognostic information regarding future disease course. The presence of pancreatic necrosis significantly increases the likelihood of significant morbidity and mortality, whereas its absence suggests a more benign clinical course. One series showed rates of 23% mortality and 82% morbidity in necrotizing pancreatitis, whereas patients without necrosis had rates of 0% mortality and 6% morbidity (Balthazar et al. 1990).

Pancreatic necrosis typically occurs within the first 24–48 h of the disease course and is well established at 96 h; the extent of pancreatic involvement is usually defined at this point without significant delayed progression (Isenmann et al. 1993). The appearance at CT is characterized by zones of nonenhancing parenchyma and may evolve over time to fluid-filled spaces in the expected region of the pancreas (Fig. 2). Hounsfield unit measurements in necrotic areas are typically $\leq$30. Ischemia and necrosis may be difficult to detect within the first 12 h and are much more evident on delayed imaging after the first 24–48 h. If equivocal on the initial CT, it may be helpful to reassess several days later for confirmation, at which time any necrosis will likely be more apparent.

The development of infected necrosis is a serious finding. It has been reported to occur in approximately one-third of patients with necrotizing pancreatitis (Perez et al. 2002) with a typical time frame toward the end of the second week (Swaroop et al. 2004). The presence of superinfection raises mortality from 12% in sterile necrosis to 30% with infected necrosis (Banks and Freeman 2006). This is often mediated by the associated organ failure in these patients which has been reported to occur in half of infected cases (Perez et al. 2002). Infection may be suggested at CT by the development of gas bubbles within the necrotic parenchyma (Fig. 3) although fistulous connection between the pancreatic bed and bowel may give a similar appearance (Fig. 4). Treatment of choice for infected necrosis is surgical debridement; percutaneous drainage is ineffective unless the necrosis is completely liquefied which is typically not the case.

Another potential contribution for imaging during early presentation can be to confirm the diagnosis of acute pancreatitis. In the setting of straightforward clinical presentation and laboratory studies, imaging confirmation is not required. However, MSCT can be helpful when the diagnosis is unsuspected or the presentation is confusing. In this clinical scenario, the diagnosis can potentially be established at cross-sectional imaging or an alternative condition may be offered. At times, duodenal ulceration or perforation, ruptured aortic aneurysm or mesenteric ischemia can be mistaken for acute pancreatitis on clinical grounds.

After the first few days and extending into weeks, MSCT is helpful to assess for a variety of structural complications that may arise from the inflammatory

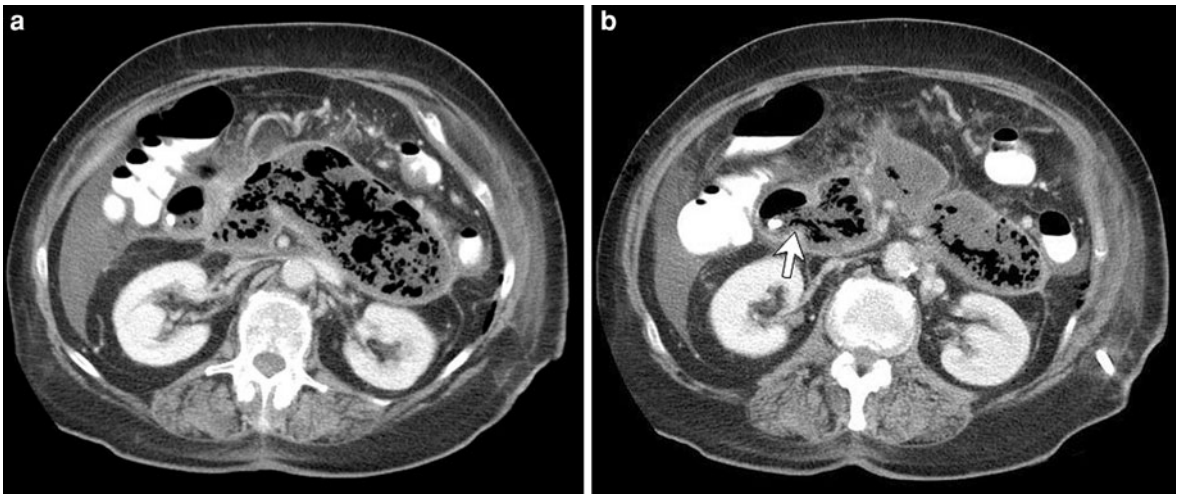

Fig. 4 Pancreatic necrosis with duodenal fistula formation. **a**, **b** Axial CECT images show diffuse pancreatic necrosis with a large amount of gas throughout the necrotic parenchyma; **b** shows a direct communication with the adjacent proximal duodenum (*arrow*) consistent with fistula formation. As opposed to patients with infected necrosis, this patient was relatively asymptomatic (2502477)

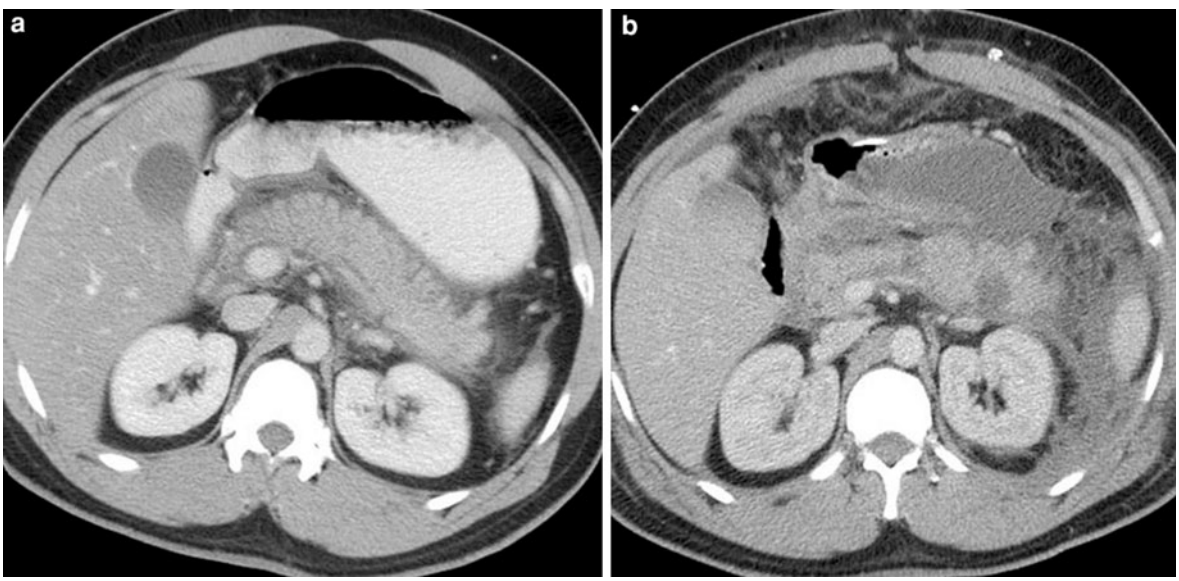

Fig. 5 Acute peripancreatic fluid collections. **a** Axial CECT image shows edematous (*interstitial*) pancreatitis with peripancreatic inflammation; **b** short term follow-up shows acute intrapancreatic and peripancreatic fluid collections

process and necrosis (if present). Identification of these complications is important in the subacute setting as they impact on the overall disease course. Alongside the presence of pancreatic necrosis (particularly with infection), these processes impact overall mortality. As defined in the revised Atlanta classification, they include APFCs, pseudocysts, pancreatic abscesses, PNPFCs, infected necrosis, WOPN, and vascular complications such as splenic vein thrombosis and arterial pseudoaneurysm formation (Acute pancreatitis classification working group 2008).

Acute peripancreatic fluid collections represent collections of pancreatic fluid and enzymes without any necrotic components. These collections may also consist of nonspecific inflammation and hemorrhage.

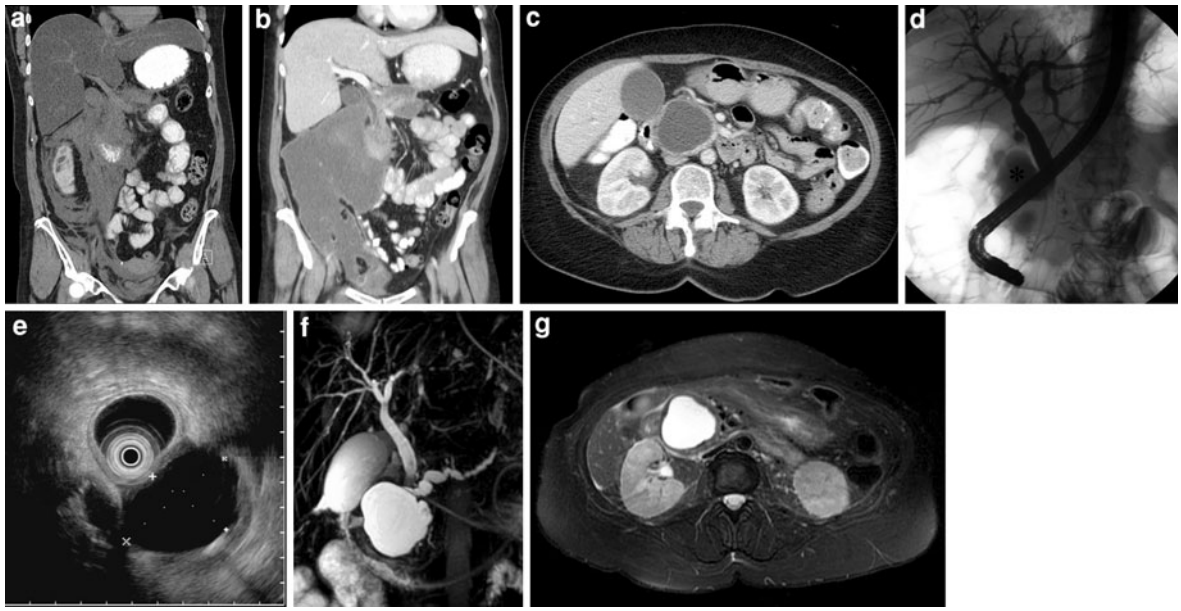

Fig. 6 Pseudocysts. **a** Coronal CECT image at initial presentation shows a large amount of ill-defined inflammatory exudate throughout the right abdomen and pelvis. Note marked hepatic steatosis; **b** coronal CECT obtained 7 weeks later, shows interval evolution of large complex pseudocyst. (1610164); **c**–**g** axial CECT image (**a**) in a different patient shows a pseudocyst in the region of the pancreatic head. ERCP (**d**) and EUS (**e**) images from the same patient show contrast filling the pseudocyst (*asterisk*), which has a simple sonographic appearance (*calipers*). MRCP (**f**) and axial T2-weighted MR (**g**) images in the same patient show the T2 hyperintense pseudocyst. Note the pancreatic ductal dilatation on MRCP (**f**; 1969484)

Phlegmon represents an older, discarded term for APFC (Bradley 1993). APFC typically are sterile and resolve spontaneously in the majority of cases (Lenhart and Balthazar 2008). Those that persist develop into a pseudocyst (Balthazar et al. 1985). At CT, they present as low attenuation collections about the pancreas without a discrete border (Fig. 5). Typical locations include the anterior pararenal space or lesser sac (Fig. 5). Potentially, they may dissect through various subperitoneal ligaments (including the gastrohepatic, gastrosplenic and gastrocolic ligaments), as well as along predetermined retroperitoneal fascial planes. APFC can also dissect into the root of the small bowel mesentery. These fluid collections and associated inflammation may cause pain as well as mass effect resulting in biliary obstruction or mechanical bowel obstruction.

Pseudocysts represent persistent APFCs which have developed a surrounding non-epithelialized capsule. This capsule forms as a result of the inflammatory process at its periphery and typically occurs over a time frame of about four weeks. Pseudocysts are seen in approximately 10–20% of cases of pancreatitis (Memis and Parildar 2002). At CT, they present as low attenuation fluid collections with a definable wall, typically rounded or ovoid in shape (Fig. 6). The wall of the pseudocyst can be barely perceptible or have a thick enhancing rind (Balthazar et al. 1994). Pseudocysts are usually located in a peripancreatic location but can dissect into the same retroperitoneal planes, subperitoneal ligaments, and mesenteries that acute fluid collections can. Over time, approximately one-half of all pseudocysts resolve. Of the remainder, the majority are stable in appearance and asymptomatic. A few may progress with clinical sequelae including pain, hemorrhage, infection, or even gastrointestinal obstruction requiring intervention (Yeo et al. 1990). A pancreatic abscess is defined as an infected pseudocyst. Percutaneous drainage with imaging guidance has become a viable treatment option in addition to surgical debridement and endoscopic drainage (Fig. 7). It is important to note that the prognosis of an infected pseudocyst ("pancreatic abscess") is much better than infected post necrotic fluid collections/infected necrosis (Baril et al. 2000).

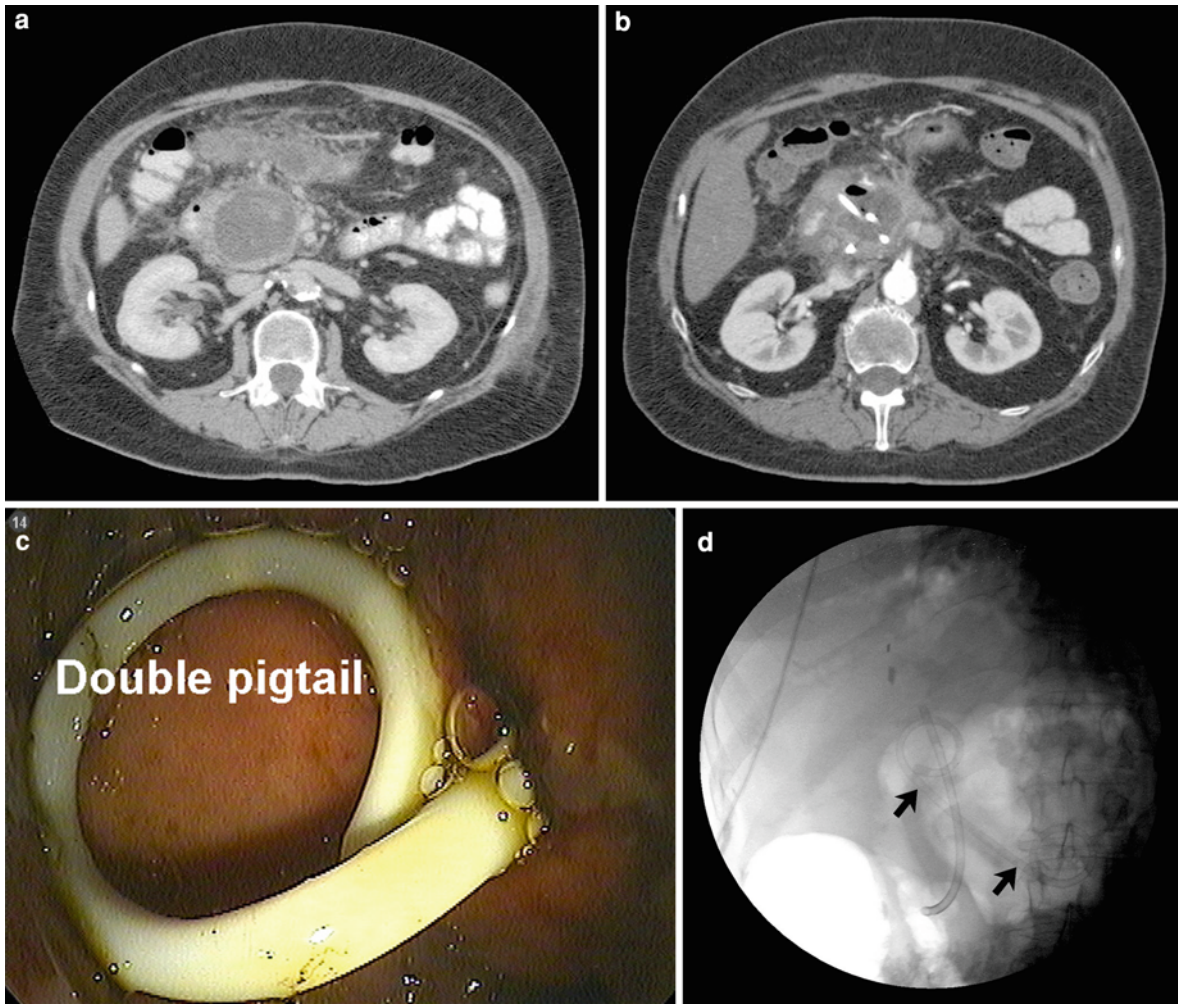

Fig. 7 Endoscopic drainage of pseudocyst. **a**, **b** Axial CECT images show a pseudocyst in the region of the pancreatic head before (**a**) and after (**b**) endoscopically-guided pigtail drain placement; **c** endoscopic image showing endoluminal pigtail in the proximal duodenum; **d** corresponding fluoroscopic image following drain placement. Note indwelling biliary drain (*arrows*; 2380258)

PNPFCs represent fluid collections in the setting of necrotizing pancreatitis (Acute pancreatitis classification working group 2008). They represent evolving collections of fluid, liquefying necrosis, and necrotic debris. Often, they occur in the setting of necrosis of a portion of the main pancreatic duct and can communicate with the ductal system. Superinfection ("infected necrosis") is an ominous complication and increases mortality. Over time, PNPFC may develop a non-epithelialized wall (akin to the process of APFC to pseudocysts) to form WOPN. Other previous terms for WOPN include organized necrosis, necroma, and pancreatic sequestration. Again, superinfection is a poor prognostic complication, leading to a doubling of mortality rates (Beger et al. 1986). Even sterile WOPN may lead to a persistently ill and debilitated patient.

Vascular complications in acute pancreatitis include venous thrombosis and arterial pseudoaneurysm formation. Both entities can result in significant morbidity and even mortality in the case of a ruptured pseudoaneurysm. Venous thrombosis may result from the intense inflammatory process associated with acute pancreatitis. The splenic vein is a commonly affected venous structure given its proximity to the pancreas (Mortele et al. 2004), which then can lead to collateral formation and gastric varices (Fig. 8).

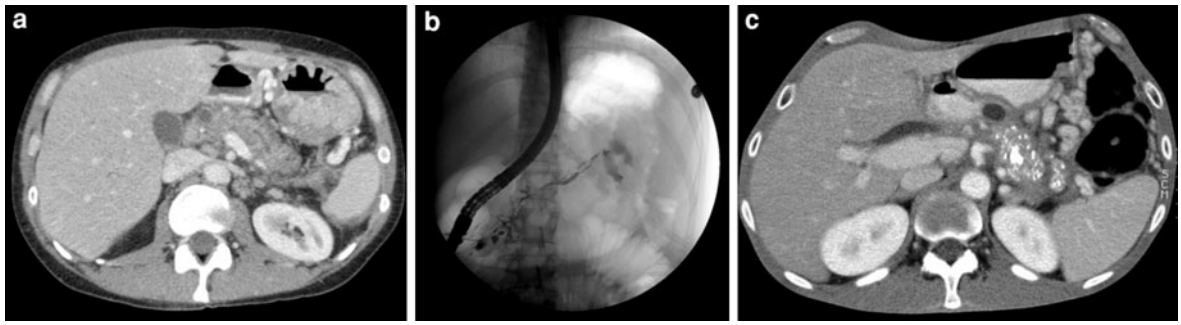

Fig. 8 Chronic pancreatitis with associated splenic vein thrombosis. Axial CECT (**a**) and ERCP (**b**) images show irregular pancreatic ductal dilatation with dilated side-branches. CT demonstrates isolated gastric varices in the setting of splenic vein thrombosis. Note filling of a pseudocyst near the pancreatic tail on the ERCP image. (1769462); **c** axial CECT image in a different patient with chronic pancreatitis and splenic vein thrombosis shows punctate calcifications throughout the visualized pancreas, as well as biliary and pancreatic ductal dilatation. Again, numerous isolated gastric varices secondary to splenic vein thrombosis are present

Other affected venous structures include the superior mesenteric vein. On the arterial side, pseudoaneurysms can result from vessel damage from extravasated activated pancreatic enzymes. Typical vessels of involvement include the splenic artery or branches of the pancreatico-duodenal arcade. Rupture can be catastrophic with mortality rates of 20%, even with treatment (Bergert et al. 2005). At CT, the pseudoaneurysm presents as a focal, rounded enhancing collection, often with crescentic mural thrombus, in communication with the adjacent artery (Fig. 9). With rupture, adjacent stranding and high-attenuation intraperitoneal fluid (hemoperitoneum) can be seen.

2 Chronic Pancreatitis

Chronic pancreatitis is a progressive pancreatic disease characterized by increasing fibrosis with an end-stage result of exocrine and endocrine insufficiency. Chronic pancreatitis has been postulated to represent a distinct clinical entity separate from acute pancreatitis where acute episodes do not lead to a chronic presentation (Singer et al. 1985). However, there is growing evidence that indeed chronic pancreatitis results from repeated episodes of acute necroinflammation (Witt et al. 2007). There is a variable subclinical phase, after which the disease is marked by recurrent bouts of severe abdominal pain and ultimately with disease manifestations related to exocrine and endocrine insufficiency. Alcohol is the most common cause of chronic pancreatitis in the US (Etemad and Whitcomb 2001).

Because of the variable clinical presentations, the diagnosis of chronic pancreatitis can be difficult to establish, particularly in the early stages of the disease. Random pancreatic biopsies are rarely performed and thus, the diagnosis is established by a combination of clinical factors, imaging appearance, and functional studies. From an imaging standpoint, although the morphologic changes present in chronic pancreatitis are often evident in advanced disease, they are variably so in early disease, decreasing the sensitivity during the time when the clinical presentation may be equivocal or not suspected. Also, the structural changes with chronic pancreatitis have not been shown to correlate with the level of gland functioning (Bozkurt et al. 1994). Thus, it requires a synthesis of the specific clinical presentation, the imaging findings, and other functional studies (not discussed here) to establish this diagnosis.

The imaging findings reflect the pathologic processes of this disease. Histopathologic features of chronic pancreatitis include acinar atrophy, pancreatic fibrosis, distorted ducts with eosinophilic protein plugs and calcium deposits. The process is typically diffuse in distribution but at times can be more focal. Thus, at CT, the pancreas may appear atrophic with parenchymal stippling of calcifications in a focal or diffuse pattern. The calcifications represent inspissated intraductal protein plugs which subsequently calcify (Figs. 8, 10; Luetmer et al. 1989; Owens and

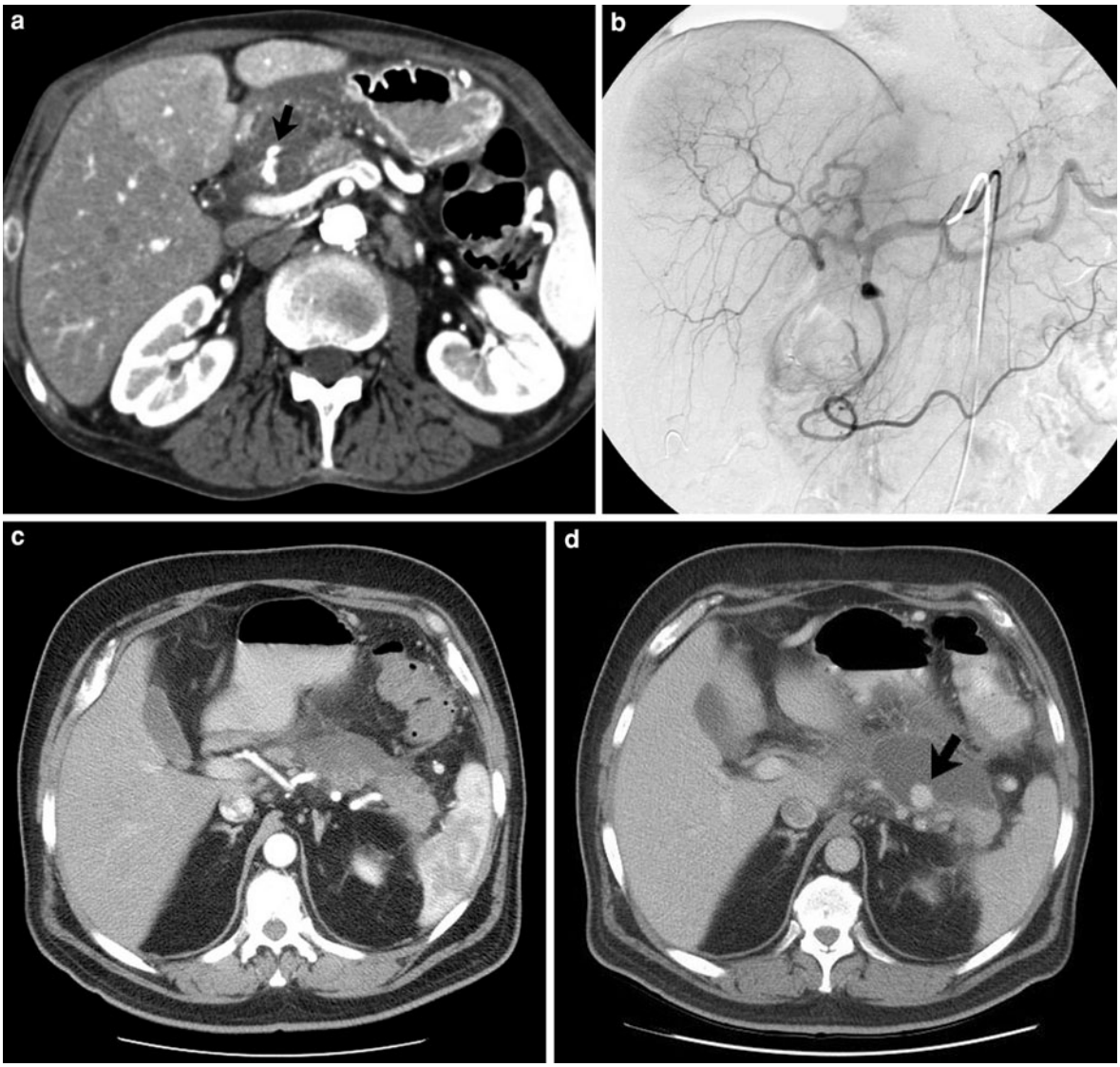

Fig. 9 Pseudoaneurysm formation following pancreatitis. Axial arterial phase CECT image (**a**) and corresponding DSA image (**b**) show dense focus of enhancement in the pancreatic head region (*arrow* in **a**), consistent with a pseudoanerysm of the gastroduodenal artery (GDA); initial axial CECT image (**c**) in a different patient demonstrates areas of pancreatic necrosis without evidence of pseudoaneuysm. CECT image of the same patient obtained 3 months later (**d**) shows development of a splenic artery pseudoaneurysm (*arrow*) surrounded by a pseudocyst (1823745)

Howard 1958). These intraductal calcifications strongly suggest the diagnosis of chronic pancreatitis but unfortunately present late in the disease course (Luetmer et al. 1989; Remer and Baker 2002). Due to the ongoing fibrosis, there is also worsening dilation and distortion of the pancreatic ducts over time. In general, there is first beading and ectasia of the side branches, then ultimately enlargement of the main pancreatic duct (Figs. 8, 10). These ductal abnormalities can be detected at CT; the ability is certainly improved with MSCT protocols over the single slice versions. However, ERCP and MRCP hold considerable advantages and are considered the main imaging methods in this area of assessment.

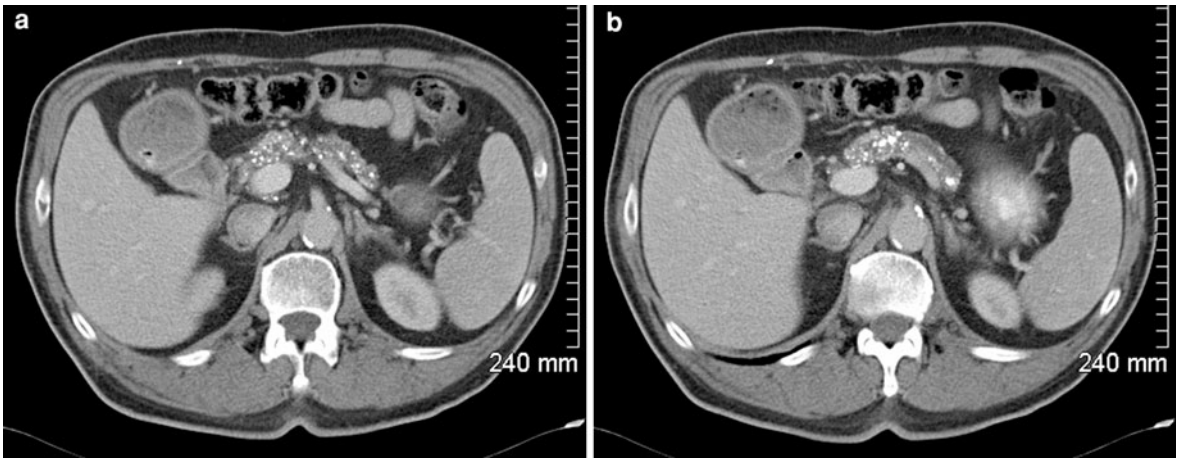

Fig. 10 Chronic pancreatitis. **a**, **b** Axial CECT images shows punctuate calcifications throughout a diffusely atrophic pancreas. Pancreatic ductal dilatation is seen within the pancreatic body and tail (2412938)

As stated above, the imaging findings in chronic pancreatitis are usually distributed diffusely throughout the gland. However, at times, they can manifest as a more focal abnormality that can mimic the appearance of a carcinoma. Patients with chronic pancreatitis hold a higher risk for cancer, with an overall lifetime risk of 4% (Lowenfels et al. 1993). Distinguishing between focal chronic pancreatitis and adenocarcinoma can be difficult at imaging and ultimately a biopsy may be needed to differentiate between the two. There is also some degree of overlap in CT imaging findings between chronic pancreatitis and main duct IPMN.

Imaging is also utilized to gauge the severity of chronic pancreatitis by assessing the degree of abnormality of the ductal anatomy. Currently, CT is typically not utilized but rather ERCP or MRCP is employed given their improved abilities to evaluate the ducts. The Cambridge classification grades the severity of chronic pancreatitis based on structural changes to the main pancreatic duct and side branches (Axon et al. 1984). As the number of involved side branches and as the main pancreatic duct is involved, severity grade increases. Although generally helpful, the scoring system may not correlate with disease severity in all cases.

CT is useful in assessing the complications seen in chronic pancreatitis which mirror those that may occur in acute pancreatitis. These include pseudocyst formation, pseudoaneurysms of the visceral arteries, and splenic vein thrombosis.

3 Autoimmune Pancreatitis

Autoimmune pancreatitis (AIP) is a distinct subtype of chronic pancreatitis that is pathologically characterized by a lymphoplasmocytic infiltrate, storiform fibrosis, and an obliterative phlebitis. In contrast to standard chronic pancreatitis, there is a differing clinical presentation, course, and treatment. It has become apparent in recent years that AIP is one end organ manifestation of a larger systemic process now termed IgG4-related systemic disease (IgG4-RSD).

AIP is a heterogeneous disease with two separate subtypes (Deshpande et al. 2011; Notohara et al. 2003). AIP type 1 represents the classically described disease which can include extrapancreatic manifestations (i.e., IgG4-RSD) while type 2 is limited to the pancreas only (with differing demographics and clinical course). Although imaging characteristics of the pancreatic process may overlap, histology between the two types differs. Type 1 exhibits a periductal lymphoplasmocytic inflammation with a preserved duct epithelium, while type 2 shows a prominent intraepithelial granulocytic infiltration with a damaged epithelium (Smyrk 2011). Much more is known in regards to AIP type 1 as opposed to type 2. The remainder of the section will address AIP type 1 ("classic form").

AIP is at least twice as common in men, with most patients older than 50 years (Chari et al. 2006; Finkelberg et al. 2006). Severe abdominal pain in AIP

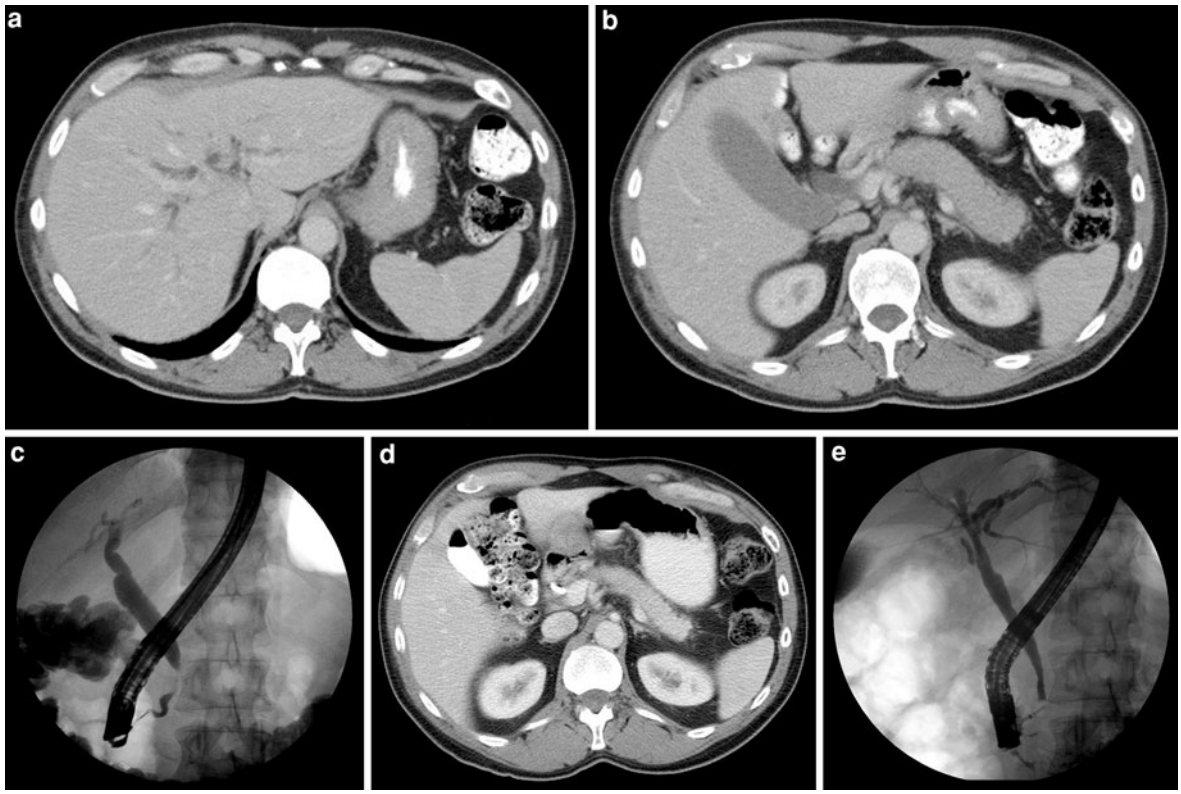

Fig. 11 Classic appearance of autoimmune pancreatitis (AIP) with positive response to treatment. Axial CECT images show intrahepatic (**a**) and extrahepatic (**b**) biliary ductal dilatation secondary to downstream obstruction related to the patient's AIP. There is diffuse homogeneous enlargement of the pancreas demonstrating the classic "sausage shape" seen with AIP (**b**); **c** ERCP image from the same patient shows narrowing of the distal common bile duct; axial CECT (**d**) and ERCP (**e**) images obtained after treatment show return of the pancreas to normal size (**d**) and near-total resolution of the distal common bile duct stricture (**e**; 1203076)

is unusual, although individuals with AIP typically report mild abdominal pain, often in association with acute obstructive jaundice (Chari et al. 2006). Recurrent bouts of acute pancreatitis are uncommon. Weight loss over a few weeks to months can be seen in up to 40% of patients (Raina et al. 2009).

Extrapancreatic manifestations, which can occur in over a half of AIP cases, affect a variety of organs including bile ducts (inflammatory strictures), mediastinum (adenopathy, pericarditis), salivary/lacrimal glands, thyroid, retroperitoneum, lung (inflammatory pseudotumor, interstitial pneumonias), liver (inflammatory pseudotumor, portal inflammation), and kidney (pseudotumors, tubulointerstitial nephritis; Smyrk 2011; Forcione and Brugge 2010). Of these, the most common extrapancreatic manifestation involves the biliary system resulting in steroid-responsive strictures where the imaging appearance can mimic primary sclerosing cholangitis. In the past, these extrapancreatic presentations have been considered separate disease entities (i.e., Mikulicz's disease, Sjogren's-like syndrome, Riedel's thyroiditis, orbital pseudotumor, retroperitoneal fibrosis, sclerosing cholangitis, etc.) but more recent evidence suggests that they may in part represent differing organ manifestations of the systemic disease process of IgG-4 RSD (Khosroshahi and Stone 2011). As with the pancreatic lesions, these manifestations typically respond to steroid treatment.

Imaging can be critical in the diagnosis of autoimmune pancreatitis. For both diagnostic classification schemas currently in use (the Asian Consensus Criteria—Otsuki et al. 2008) and the Mayo clinic HISORt—Chari et al. 2006), imaging is one of the major diagnostic categories in addition to serologic and pathologic information. The classic appearance

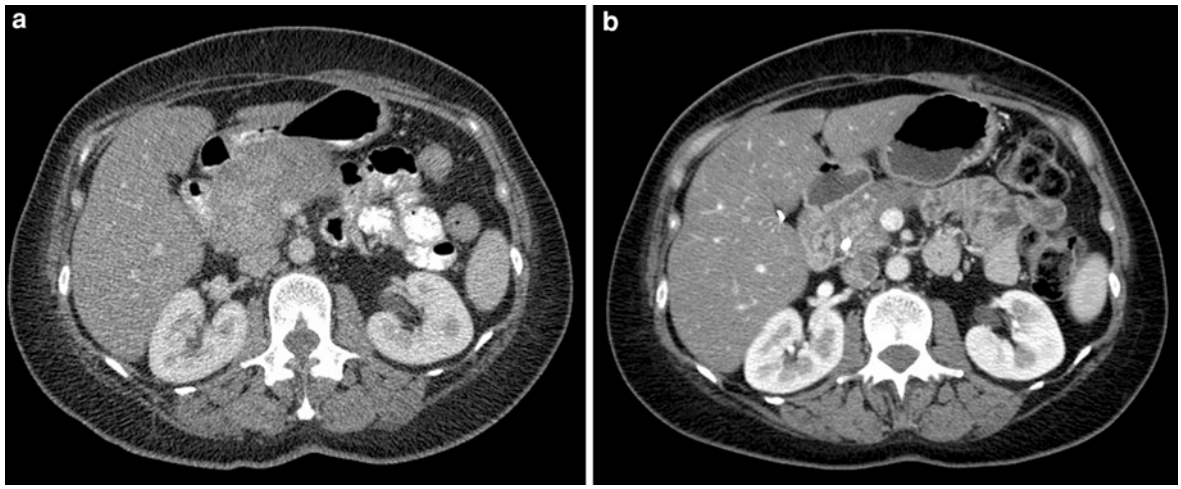

Fig. 12 Focal AIP mimicking pancreatic adenocarcinoma. Initial axial CECT image (**a**) shows heterogeneous enlargement of the pancreatic head and neck that was concerning for malignancy. CECT image (**b**) obtained after treatment shows near complete resolution of the mass-like enlargement with persistence of low attenuation. There has been interval placement of a biliary stent (2605446)

on CT is sausage-shaped enlargement and homogeneous attenuation of the pancreas with a peripheral rim ("halo") of low attenuation (Fig. 11). The enhancement of the pancreatic parenchyma may be decreased and the peripheral rim halo may demonstrate increased enhancement on delayed images. Loss of the normal pancreatic lobulations is frequently seen and in extreme examples can result in a "featureless" pancreas (Fig. 11). In addition, a foreshortened or retracted pancreatic tail can be seen. Important diagnostic clues include lack of significant peripancreatic inflammatory stranding and nearly universal involvement of the pancreatic tail in the more chronic form.

A focal form of AIP can mimic pancreatic adenocarcinoma where the pancreatic head is more commonly involved and can contain a low attenuating or isoattenuating mass (Fig. 12). It is important to note that marked improvement or complete resolution of the mass is needed after medical treatment for the diagnosis of AIP to exclude pancreatic adenocarcinoma which can respond to steroid treatment. A key diagnostic clue involves the diffuse narrowing of the pancreatic duct resulting from the swelling of the surrounding pancreatic parenchyma. Extrinsic mass effect on the distal common bile duct can also result from swelling at the level of the pancreatic head, sometimes necessitating the need for biliary stent placement (Fig. 11). Another clue signaling AIP is resolution of the other sites of involvement with the administration of corticosteroids.

Given the rapid and profound improvement that can be seen by initiating corticosteroid treatment, several advocate the timely use of CT to evaluate the response to treatment. It has been suggested that the range of appearances of AIP on imaging and the variable response to therapy indicate different stages of AIP (Sahani et al. 2009). Furthermore, certain CT features can be used to predict response to medical treatment. The early, inflammatory stage of the disease presents with pancreatic swelling and peripancreatic changes such as the hypoattenuating halo. It is thought that these acute findings are more amenable to corticosteroid treatment. CT features seen with fibrotic changes in the later stages of the disease include focal mass-like swelling, persistent pancreatic tail retraction, and ductal strictures (Sahani et al. 2009).

Diagnosis of AIP by other imaging modalities are less established. The classic appearance on ERCP includes focal, segmental or diffuse attenuation of the main pancreatic duct and the loss of right-angled branches (Finkelberg et al. 2006). Diagnosis can be achieved with endoscopic ultrasound and fine needle aspiration. However, surgical exploration is sometimes needed to make the diagnosis.

4 Summary

MSCT plays an important role in the assessment of acute and chronic pancreatitis. In acute pancreatitis, the most important contribution involves the evaluation for pancreatic necrosis and for other potential complications. When appropriately integrated with the clinical data, MSCT can help to optimally direct care and treatment. In chronic pancreatitis, MSCT is helpful in assessing morphologic changes associated with this disease process, both in diagnosis and assessment of disease severity. Unfortunately, many of the pancreatic changes are more evident late in the disease course as opposed to early when the diagnosis is equivocal or unsuspected. MSCT remains a useful modality to assess for potential complications including the development of adenocarcinoma. Finally, radiologists should be familiar with both the clinical and CT features of autoimmune pancreatitis, as recognition could significantly change patient management and outcome.

References

Acute pancreatitis classification working group (2008) Revision of the Atlanta classification of acute pancreatitis. http://www.pancreasclub.com/resources/AtlantaClassification.pdf. Accessed Apr 2011

Axon AT, Classen M, Cotton PB et al (1984) Pancreatography in chronic pancreatitis: international definitions. Gut 25:1107–1112

Balthazar EJ, Ranson JHC, Naidich DP, Megibow AJ, Caccavale R, Cooper MM (1985) Acute-pancreatitis—prognostic value of CT. Radiology 156:767–772

Balthazar EJ, Robinson DL, Megibow AJ, Ranson JHC (1990) Acute-pancreatitis—value of CT in establishing prognosis. Radiology 174:331–336

Balthazar EJ, Freeny PC, Vansonnenberg E (1994) Imaging and intervention in acute-pancreatitis. Radiology 193:297–306

Banks PA, Freeman ML (2006) A practice parameters committee of the American college of gastroenterology: practice guidelines in acute pancreatitis. Am J Gastroenterol 101:2379–2400

Baril NB, Ralls PW, Wren SM et al (2000) Does an infected peripancreatic fluid collection or abscess mandate operation? Ann Surg 231:361–367

Beger HG, Bittner R, Block S, Buchler M (1986) Bacterial-contamination of pancreatic necrosis—a prospective clinical-study. Gastroenterology 91:433–438

Bergert H, Hinterseher I, Kersting S, Leonhardt J, Bloomenthal A, Saeger HD (2005) Management and outcome of hemorrhage due to arterial pseudoaneurysms in pancreatitis. Surgery 137:323–328

Bozkurt T, Braun U, Leferink S, Gilly G, Lux G (1994) Comparison of pancreatic morphology and exocrine functional impairment in patients with chronic-pancreatitis. Gut 35:1132–1136

Bradley EL (1993) A clinically based classification-system for acute-pancreatitis—summary of the international-symposium on acute-pancreatitis, Atlanta, 11–13 Sept 1992. Arch Surg 128:586–90

Chari ST, Smyrk TC, Levy MJ et al (2006) Diagnosis of autoimmune pancreatitis: the Mayo clinic experience. Clin Gastroenterol Hepatol 4:1010–1016

Deshpande V, Gupta R, Sainani N et al (2011) Subclassification of autoimmune pancreatitis: a histologic classification with clinical significance. Am J Surg Pathol 35:26–35

Etemad B, Whitcomb DC (2001) Chronic pancreatitis: diagnosis, classification, and new genetic developments. Gastroenterology 120:682–707

Finkelberg DL, Sahani D, Deshpande V, Brugge WR (2006) Current concepts—autoimmune pancreatitis. N Engl J Med 355:2670–2676

Fletcher JG, Wiersema MJ, Farrell MA et al (2003) Pancreatic malignancy: value of arterial, pancreatic, and hepatic phase imaging with multi-detector row CT. Radiology 229:81–90

Foitzik T, Bassi DG, Schmidt J et al (1994) Intravenous contrast-medium accentuates the severity of acute necrotizing pancreatitis in the rat. Gastroenterology 106:207–214

Forcione DG, Brugge WR (2010) New kid on the block? autoimmune pancreatitis. Best Pract Res Clin Gastroenterol 24:361–378

Isenmann R, Buchler M, Uhl W, Malfertheiner P, Martini M, Beger HG (1993) Pancreatic necrosis—an early finding in severe acute-pancreatitis. Pancreas 8:358–361

Khosroshahi A, Stone JH (2011) A clinical overview of IgG4-related systemic disease. Curr Opin Rheumatol 23:57–66

Knaus WA, Draper EA, Wagner DP, Zimmerman JE (1985) Apache-II—a severity of disease classification-system. Crit Care Med 13:818–829

Lenhart DK, Balthazar EJ (2008) MDCT of acute mild (nonnecrotizing) pancreatitis: abdominal complications and fate of fluid collections. Am J Roentgenol 190:643–649

Lowenfels AB, Maisonneuve P, Cavallini G et al (1993) Pancreatitis and the risk of pancreatic-cancer. N Engl J Med 328:1433–1437

Luetmer PH, Stephens DH, Ward EM (1989) Chronic-pancreatitis—reassessment with current CT. Radiology 171:353–357

McNulty NJ, Francis IR, Platt JF, Cohan RH, Korobkin M, Gebremariam A (2001) Multi-detector row helical CT of the pancreas: effect of contrast-enhanced multiphasic imaging on enhancement af the pancreas, peripancreatic vasculature, and pancreatic adenocarcinoma. Radiology 220:97–102

Memis A, Parildar M (2002) Interventional radiological treatment in complications of pancreatitis. Eur J Radiol 43:219–228

Meyers MA, Evans JA (1973) Effects of pancreatitis on small bowel and colon—spread along mesenteric planes. Am J Roentgenol 119:151–165

Molmenti EP, Balfe DM, Kanterman RY, Bennett HF (1996) Anatomy of the retroperitoneum: observations of the distribution of pathologic fluid collections. Radiology 200:95–103

Mortele KJ, Mergo PJ, Taylor HM et al (2004) Peripancreatic vascular abnormalities complicating acute pancreatitis: contrast-enhanced helical CT findings. Eur J Radiol 52:67–72

Notohara K, Burgart LJ, Yadav D, Chari S, Smyrk TC (2003) Idiopathic chronic pancreatitis with periductal lymphoplasmacytic infiltration—clinicopathologic features of 35 cases. Am J Surg Pathol 27:1119–1127

Otsuki M, Chung JB, Okazaki K et al (2008) Asian diagnostic criteria for autoimmune pancreatitis: consensus of the Japan–Korea symposium on autoimmune pancreatitis. J Gastroenterol 43:403–408

Owens JL, Howard JM (1958) Pancreatic calcification: a late sequel in the natural history of chronic alcoholism and alcoholic pancreatitis. Ann Surg 147:326–338

Perez A, Whang EE, Brooks DC et al (2002) Is severity of necrotizing pancreatitis increased in extended necrosis and infected necrosis? Pancreas 25:229–233

Raina A, Yadav D, Krasinskas AM et al (2009) Evaluation and management of autoimmune pancreatitis: experience at a large US center. Am J Gastroenterol 104:2295–2306

Ranson JH, Rifkind KM, Roses DF et al (1974) Prognostic signs and the role of operative management in acute pancreatitis. Surg Gyncol Obstet 139:69–81

Remer EM, Baker ME (2002) Imaging of chronic pancreatitis. Radiol Clin North Am 40:1229-1242

Russo MW, Wei JT, Thiny MT et al (2004) Digestive and liver diseases statistics, 2004. Gastroenterology 126:1448–1453

Sahani DV, Sainani NI, Deshpande V, Shaikh MS, Frinkelberg DL, Fernandez-del Castillo C (2009) Autoimmune pancreatitis: disease evolution, staging, response assessment, and CT features that predict response to corticosteroid therapy. Radiology 250:118–129

Singer MV, Gyr K, Sarles H (1985) Revised classification of pancreatitis—report of the 2nd international-symposium on the classification of pancreatitis in Marseille, France, 28–30 Mar 1984. Gastroenterology 89:683–685

Singh VK, Wu BU, Bollen TL et al (2009) A prospective evaluation of the bedside index for severity in acute pancreatitis score in assessing mortality and intermediate markers of severity in acute pancreatitis. Am J Gastroenterol 104:966–971

Smyrk TC (2011) Pathological features of IgG4-related sclerosing disease. Curr Opin Rheumatol 23:74–79

Swaroop VS, Chari ST, Clain JE (2004) Severe acute pancreatitis. J Am Med Assoc 291:2865–2868

Uhl W, Roggo A, Kirschstein T et al (2002a) Influence of contrast-enhanced computed tomography on course and outcome in patients with acute pancreatitis. Pancreas 24:191–197

Uhl W, Warshaw A, Imrie C et al (2002b) IAP guidelines for the surgical management of acute pancreatitis. Pancreatology 2:565–73

Witt H, Apte MV, Keim V, Wilson JS (2007) Chronic pancreatitis: Challenges and advances in pathogenesis, genetics, diagnosis, and therapy. Gastroenterology 132:1557–1573

Yeo CJ, Bastidas JA, Lynchnyhan A, Fishman EK, Zinner MJ, Cameron JL (1990) The natural-history of pancreatic pseudocysts documented by computed-tomography. Surg Gynecol Obstetrics 170:411–417

Solid Pancreatic Masses

Alec J. Megibow

Contents

Abstract

There is a wide variety of solid neoplasms that affect the pancreas. The vast majority of them will be ductal adenocarcinoma and neuroendocrine tumors. MSCT has significantly increased both the detection and improved preoperative staging of pancreatic adenocarcinoma. Volume acquisitions facilitate the creation of high-quality 3D images that provide superior depiction of peripancreatic extension of disease allowing appropriate therapeutic decision making; however pancreas specific multiphase MSCT protocols are required to achieve these results. Additionally, multiphase MSCT has increased the detection of small neuroendocrine tumors. Finally, although there are several much more unusual pancreatic tumors, both primary and secondary that may be infrequently encountered in clinical practice, a more detailed discussion of metastases to the pancreas and non-neoplastic focal pancreatic masses is offered.

1 MSCT Technique

1.1 Clinical Indications for Specialized Pancreatic MSCT Technique

CT scanning is established as the imaging procedure of choice for the investigation of patients suspected of pancreatic cancer (Callery et al. 2009; Tempero et al. 2010). MSCT affords significant advantages compared with single slice CT for the detection and assessment of suspected pancreatic neoplasms. Optimal utilization

A. J. Megibow (✉)
NYU-Langone Medical Center, 560 First Avenue, New York, NY 10016, USA
e-mail: Alec.megibow@nyumc.org

C. J. Zech et al. (eds.), *Multislice-CT of the Abdomen*, Medical Radiology. Diagnostic Imaging,
DOI: 10.1007/174_2011_411, © Springer-Verlag Berlin Heidelberg 2012

of MSCT technology requires protocol modifications from standard approaches. Protocol modifications result from (a) differing times of peak pancreatic enhancement versus other solid abdominal organs, most notably liver; (b) differential enhancement of peripancreatic arteries versus veins. Protocols that are designed to acquire isotropic voxels allow 3D evaluation of the relation of a pancreatic tumor to adjacent vessels, organs and ducts maximizing therapeutic decision making in individual cases. This is achieved by using multiphase acquisitions combined with thin detectors.

Because a multiphase protocol is required (and hence some additional radiation), routine use is inappropriate, therefore clinical history is critical. At our institution, we perform "pancreatic protocols" on all patients referred with the following indications: (a) jaundice; (b) recent onset of diabetes; (c) gallstones/cholecystitis. Our experience, and that of others, suggests that because referring clinicians may not wish to alarm patients by telling them they suspect pancreatic cancer, the clinical indication supplied by the referring physician is indirect. Therefore, when we receive a referral for a patient with either severe epigastric pain or weight loss we will also utilize the pancreatic protocol.

1.2 Acquisition Timing and Parameters

The pancreatic phase (phase 1) is directed at evaluation of the pancreas and peripancreatic arteries; the portal phase (phase 2) is directed at the peripancreatic veins other abdominal viscera, including the liver. The phases are related to the timing of data acquisition in relation to the initiation of the intravenous contrast bolus. We administer 1.25 of 370 mgI/ml of non-ionic iodinated medium delivered through a power injector. The higher concentration of contrast medium provides improved depiction of peripancreatic arteries and higher parenchymal enhancement when compared with lower concentrations. Assuming venous integrity, we administer the contrast at 4–5 ml/sec, although improved parenchymal to tumor attenuation differences have been reported with flow rates as high as 8 ml/sec (Schueller et al. 2006). We acquire pancreatic phase images at approximately 45 s following initiation; portal phase images are acquired at 75 s from initiation of the bolus. This timing has been shown to result in maximal pancreatic parenchymal and arterial enhancement in the pancreatic phase, whereas peak hepatic enhancement and homogeneous venous filling is obtained in the portal phase, optimizing tumor detection and staging (McNulty et al. 2001; Fletcher et al. 2003) (Fig. 1). At the time of this writing, early experience with dual energy MSCT documents increased parenchymal to

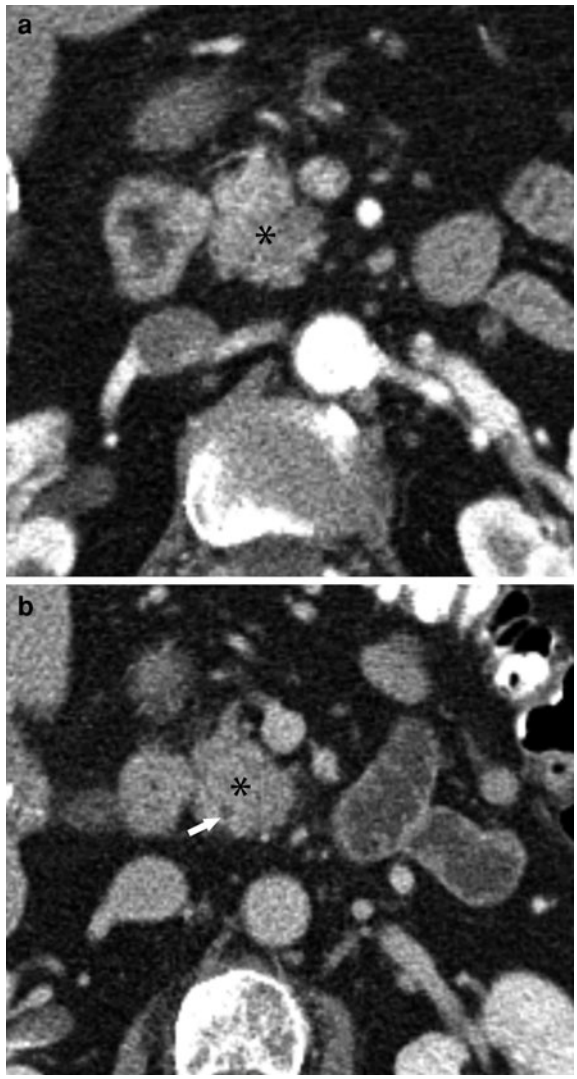

Fig. 1 **a** Importance of pancreatic phase: an infiltrating tumor (*asterisks*) is recognized in the pancreatic head on this pancreatic phase acquisition. **b** Importance of pancreatic phase: Same patient, same examination but images acquired 30 s later (*portal phase*). The tumor (*asterisks*) is barely visible. Despite the fact that the tumor is located in the head of the pancreas, the common bile duct (*arrow*) is unaffected

tumor attenuation differences by using data from the lower kVp acquisition (Macari et al. 2010).

We utilize the thinnest available detector configuration for each acquisition. For most clinical systems this will mean using a 0.6–0.625 mm detector. The pancreatic phase extends from the xiphoid through the transverse duodenum and the portal phase extends from the xiphoid through the pubic symphisis.

For each acquisition we create two separate sets of images, a "thin section" data set and a "thick section" data set. The thin sections are reconstructed as contiguous 0.75 mm slices with a 20% overlap. Two data sets (one from the pancreatic and the second from the portal phase) are sent to either a dedicated work station or to a server that supports thin-client 3D analysis. The thick sections are reconstructed as 3 mm continuous sections in the axial and coronal plane for the pancreatic phase and as 4 mm continuous sections for the portal phase data set. These "thick section" images are sent to PACS for viewing and reading. This supports the basic workflow by having "traditional" multiplanar slice data presented for reading with thin section data available for 3D evaluation (Ichikawa et al. 2006).

1.3 Angiographic and Ductal Displays

The major benefit of MSCT is the ability to rapidly acquire images composed of isotropic voxels with virtually no limits in *z*-axis coverage. This facilitates high-quality 3D displays without loss of spatial resolution (Dalrymple et al. 2007). Combined with post-processing capabilities such as multiplanar reformatting (MPR), maximal intensity projection (MIP), minimum intensity projection (MinIP) and volume rendering (VRT) the radiologist has the ability to extend the diagnostic utility of the CT study. MPR imaging is most widely used technique; all of the CT gray scale data can be preserved but the display is constrained to within a 2D representation. High-quality CT angiograms can be created from pancreatic phase data that can display normal and variant arterial anatomy as well as reproduce radiologic signs of vessel involvement as depicted by catheter angiography (Fishman and Horton 2001; Kalra et al. 2003) (Fig. 2), similarly high-quality venograms can be created from the portal phase data. MIP images provide the highest quality angiographic displays at the sacrifice of soft tissue detail. VRT can be used to visualize the pancreas in 3D with preserved soft tissue contrast. By projecting the lowest attenuation pixel along the ray of sight, MinIP is excellent for displaying the main pancreatic duct and biliary tree (Salles et al. 2007) (Fig. 3). Angiographic and ductal displays can be further enhanced by the use of curved multiplanar reformatting (Prokesch et al. 2002a, b; Fukushima et al. 2006). Radiologists who are familiar with all of these techniques will find

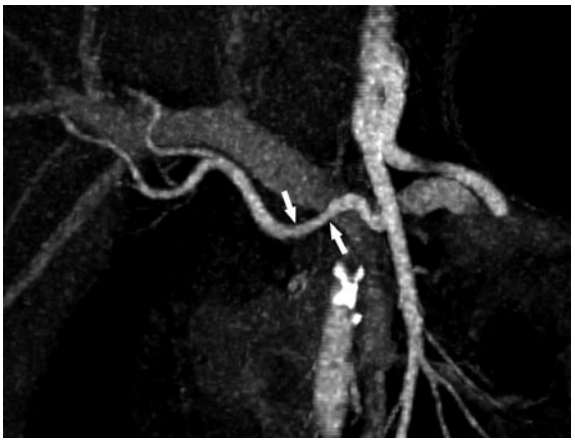

Fig. 2 MIP MSCT angiogram in patient with carcinoma of pancreatic head reveals smooth encasement of a replaced right hepatic artery (*arrows*)

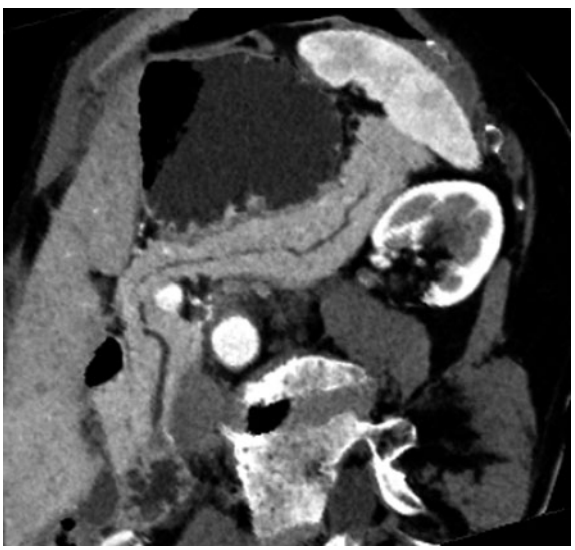

Fig. 3 MinIP MSCT pancreatogram reveals a uniform caliber main pancreatic duct. Volume rendering displays allow the entire duct to be visualized

themselves to be valued consultants in the care of patients with pancreatic diseases.

2 Ductal Adenocarcinoma

2.1 Epidemiology

Pancreatic adenocarcinoma is the fourth leading cause of cancer death; the five-year survival rate remains at 5%, most patients dying within 2 years of diagnosis. In the United States, 43,000 new cases and 37,000 deaths were expected in 2010 (Jemal et al. 2010). In 2005, 32,000 new cases were suspected (Jemal et al. 2005). Multiple risk factors have been identified including smoking, chronic pancreatitis, hereditary pancreatitis, familial history, long standing diabetes, BRCA2 gene mutations, Peutz–Jehgers syndrome among others (Tempero and Brand 2008; Raimondi et al. 2009).

Ductal adenocarcinoma accounts for 85–90% of all pancreatic tumors. About 60–70% of them arise in the head (defined as that portion of the pancreas to the right of the portal confluence), 5–10% in the body and 15% in the tail. Based on autopsy series, pancreatic head tumors average between 2.5 and 3 cm, whereas tumors in the body and tail average between 5 and 7 cm (Jimenez and Fernandez-del Castillo 2010).

2.2 MSCT Imaging Features

2.2.1 Primary Tumor

The classic MSCT appearance of ductal adenocarcinoma is that of a poorly marginated mass, hypodense to surrounding enhanced pancreatic parenchyma. Images acquired in the pancreatic phase will assure that there is maximal enhancement of normal pancreatic parenchyma maximizing lesion conspicuity. The differences in tumor to parenchymal attenuation will decrease or may disappear in the portal phase. It is estimated that between 5 and 13% of pancreatic tumors will be isoattenauting with background pancreas even on MSCT studies performed with optimized protocols (Prokesch et al. 2002a, b; Kim et al. 2010). The frequency of isoattenauting, better differentiated tumors is higher when masses are <2 cm (27%) as opposed to larger lesions (13%). Not unexpectedly, secondary signs are more prevalent when the tumor is small, isoattenauting and otherwise undetectable (Yoon et al. 2010, 2011) (Fig. 4).

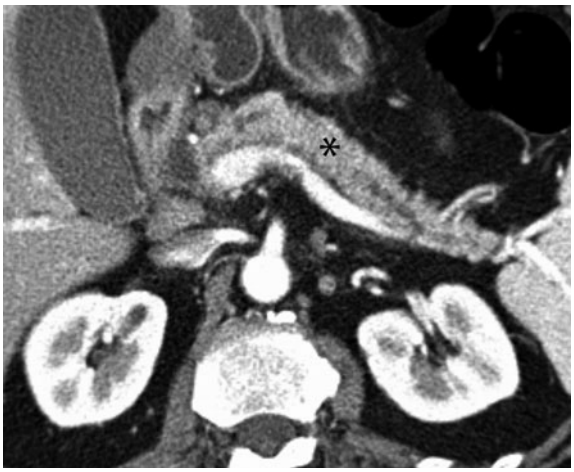

Fig. 4 Isodense pancreatic adenocarcinoma. The tumor (*asterisks*) is recognized because it has led to pancreatic duct obstruction and obliterated the lobular parenchymal architecture

Secondary imaging features of pancreatic adenocarcinoma include: textural parenchymal alterations with loss of the lobular architecture; upstream parenchymal atrophy, usually associated with a dilated pancreatic duct; rounding of the normal pointed appearance of the uncinate process for tumors located in that area (Stephens 1997) (Fig. 5). Biliary dilatation is not invariable when the tumor is within the head of the gland, biliary dilatation does not exclude a pancreatic neoplasm. When the common bile duct is dilated, mural enhancement can be seen on high-quality contrast-enhanced studies. If the common duct is narrowed as a result of a stricture within the intrapancreatic portion in the absence of visible mass, differentiation between a primary tumor arising for the pancreas or common bile duct cannot be differentiated by imaging.

2.2.2 Pancreatic Duct

Earliest CT descriptions of CT assessment of the pancreatic duct suggested that visualization was always a result of pathologic dilatation, although it was realized that there were technological limitations to visualizing a normal duct (Berland et al. 1981). With current MSCT technology, the main pancreatic duct (MPD) can be seen in the majority of cases. Itoh reported 94–95% a normal duct seen in 94–95% of

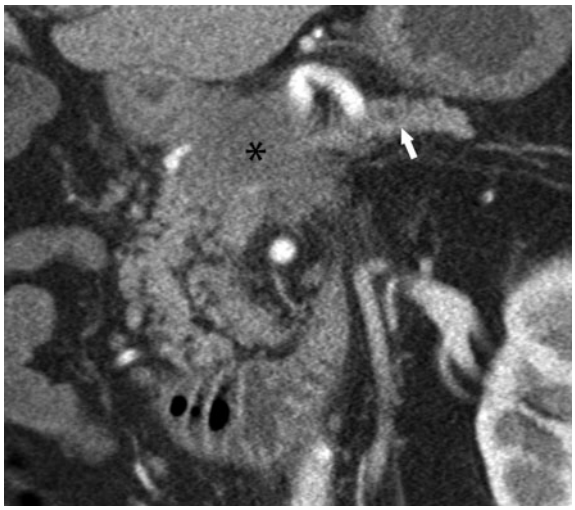

Fig. 5 Ductal pancreatic adenocarcinoma. The tumor (*asterisks*) obliterates the lobular pancreatic architecture. There is upstream parenchymal atrophy (*arrow*). The tumor surrounds the splenic artery and extends into the peripancreatic fat along the inferior margin

cases in the head and body of the gland, with 75% visualization in the tail. This improvement was the direct result of the ability to acquire sub-millimeter isotropic slices coupled with MPR and curved-MPR visualization (Itoh et al. 2003).

The pancreatic duct should be specifically evaluated in any patient suspected of pancreatic disease. This is best done by viewing thin slice images on a workstation or thin-client 3D imaging server. The normal duct is <6 mm in width, although in the vast majority of normal patients, the duct will be <3 mm. The normal duct should be of uniform caliber. The finding of a dilated duct must be explained. In cases where the entire duct is dilated differential diagnosis includes age-related atrophy, chronic pancreatitis, main duct IPMN or small periampullary neoplasm. When there is segmental duct obstruction, the etiology is frequently neoplastic, either from a pancreatic neoplasm or from segmental main duct IPMN. Isolated duct strictures may occur in patients with autoimmune pancreatitis or following pancreatic trauma. Strictures from chronic pancreatitis will frequently be associated with a dilated downstream MPD.

Despite the wide number of possible causes of an isolated MPD stricture, the majority will be neoplastic (Uehara et al. 2009). The presence of an isolated stricture may predate the development of a macroscopic pancreatic mass. In a series of patients presenting with advanced pancreatic adenocarcinoma from whom prior imaging studies were available, 50% had imaging findings suggestive of pancreatic cancer on those prior examinations. Most studies reviewed were obtained up to 18 months prior to diagnosis; although in one patient findings were present even longer than 18 months. Unfortunately, these findings were recognized in a small percentage of cases (Gangi et al. 2004). Similar results were reproduced in a study of 16 patients who presented with pancreatic cancer in whom prior CT studies were available for review (Ahn et al. 2009) (Fig. 6). In a study of 1,058 patients with mean follow-up time of 75.5 months, the presence of MPD dilatation >2.5 mm was predictive of development of pancreatic cancer, with the likelihood significantly increased when there was an associated cyst (Tanaka et al. 2010). As stated in Sect. 2.1, tumors <2 cm (those having greater likelihood of improved survival) will most likely be isodense on optimized imaging studies, and therefore only recognized by visualizing segmental pancreatic duct dilatation.

When CT findings of acute pancreatitis are present in combination with an isolated duct stricture, a comprehensive workup should be initiated to exclude the presence of an underlying cancer (Imamura et al. 2002). Underlying pancreatic cancer may also be suspected in acute pancreatitis patients with soft tissue attenuation extrapancreatic masses, lymphadenopathy or focal CT findings restricted to a portion of the gland (Balthazar 2005).

2.2.3 Extrapancreatic Extension

The presence or absence of extrapancreatic extension is a critical component of the interpretation of the MSCT study. Locally advanced pancreatic cancer is defined by the presence of major arterial or peripancreatic venous extension. In most cases, the tumor will extend to the surrounding vessels, contacting but not encasing them. Larger tumors (>2 cm) are more likely to have extended beyond the pancreatic margin than smaller lesions, although small aggressive lesions are frequently encountered. Pancreatic adenocarcinoma extends through lymphatics (Sai et al. 2010) and along extrapancreatic nerve plexi (Deshmukh et al. 2010; Mochizuki et al. 2010). Knowledge of the anatomic relationships of these

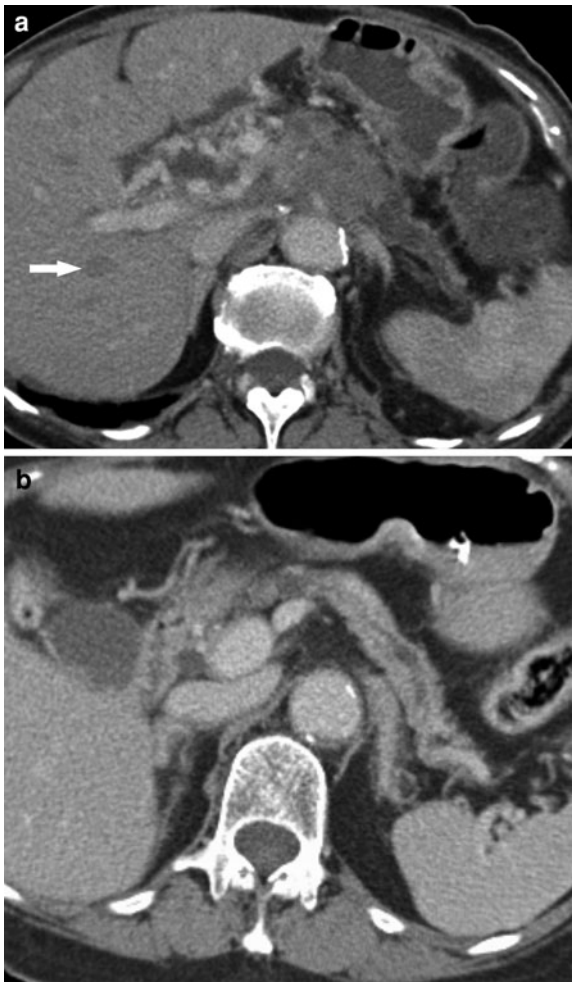

Fig. 6 **a** Stage IV pancreatic adenocarcinoma. The tumor is in the body of the pancreas resulting in upstream duct obstruction and parenchymal atrophy. It extends into the SMA and the aorta. Portal venous thrombosis has resulted in cavernous transformation. Hepatic metastasis (*arrow*) is seen. **b** Same patient as in (**a**) 2 years earlier. Segmental main pancreatic duct obstruction was present. There was no other evidence of extrapancreatic disease

pathways increases the radiologist's specificity in determining extra-glandular extension (Fig. 7).

Arterial involvement is diagnosed when soft tissue attenuating tissue makes direct contact with a peripancreatic artery. Based on correlation with surgical confirmation of imaging findings, the likelihood of arterial involvement is graded as follows: 0 = normal, with a fat plane or normal pancreas between tumor and vessel (no tumor contiguity); 1 = loss of fat plane between tumor and vessel, with or without smooth (<quarter circumference); 2 = flattening and/

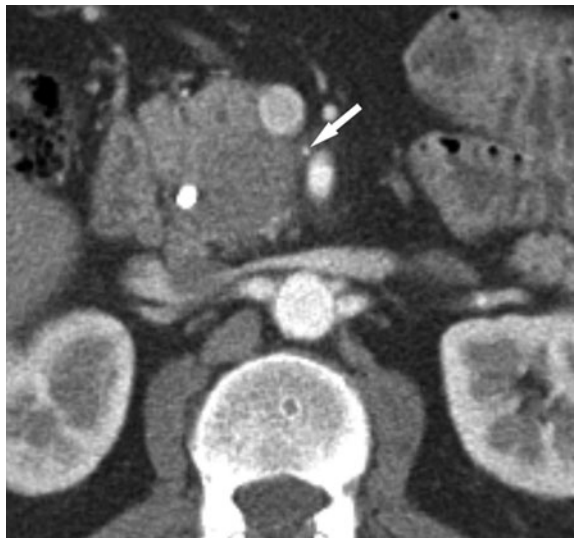

Fig. 7 Perineural invasion. A mass is present in the pancreatic head. Although there is no distortion of the SMV, nor any contact with the SMA, tongue of tissue has surrounded a pancreaticoduodenal arterial branch (*arrow*). This mode of spread has been shown to occur along peripancreatic nerve plexi. CBD stent is present

or slight irregularity of one side of the vessel (25–50% circumferential involvement); 3 = encased vessel with tumor extending around at least two sides altering its contour and producing concentric or eccentric lumen narrowing (50–75% circumferential involvement); 4 = at least one major occluded vessel (or >75% circumferential involvement) (Lu et al. 1997; Zamboni et al. 2007). Use of CT angiographic displays has significantly increased the sensitivity while preserving specificity (Manak et al. 2009).

Involvement of major peripancreatic veins, most frequently the superior mesenteric vein (SMV), may be seen without detectable arterial involvement. Venous involvement is best detected on portal phase images because the veins are more homogeneously enhanced (Fletcher et al. 2003). SMV involvement as depicted by MSCT is graded as follows: I = normal; II = smooth shift; III = narrowing along pancreatic border; IV = circumferential narrowing; V = circumferential narrowing with collaterals (Ishikawa et al. 1992). Grade IV or V SMV involvement demonstrates flattening of the vein circumference or a "teardrop" configuration (Hough et al. 1999; O'Malley et al. 1999). The pattern of venous collaterals, particularly distended posterior pancreatico–duodenal veins, has been shown to be significant in

predicting venous involvement even when the SMV itself appears normal (Hommeyer et al. 1995, Yamada et al. 2000).

Pancreatic carcinoma can metastasize to regional or distant lymphnodes, liver, other abdominal viscera and peritoneal cavity. MSCT is poor in predicting lymphnode involvement. Peripancreatic nodes are not important in the imaging evaluation of these patients as they will be resected in the surgical field. Particular care should be directed at the porta hepatis and retroperitoneum as both are frequent sites of lymphnode involvement that will not be seen at the time of surgical resection, however as with peripancreatic lymphnodes, disease can only be recognized in them when they become enlarged (Roche et al. 2003). Hepatic metastases are evaluated on portal phase images. Hepatic metastases are frequently quite small <1.5 cm), raising the index of suspicion for small hepatic lucencies that are difficult to characterize. Peritoneal implants are estimated to be present in 20% of patients in whom CT assessment suggests locally advanced disease. Their presence upstages patients to stage IV disease. They are often microscopic, present only in peritoneal washings; therefore most pancreatic centers will perform diagnostic laparoscopy prior to undertaking formal pancreatic resection even when no implants are detected on the preoperative imaging study (Callery et al. 2009; Clark and Traverso 2010). The combination of pancreatic dedicated MSCT and diagnostic laparoscopy is the most cost-effective strategy for imaging patients who may be surgical candidates (McMahon et al. 2001).

2.3 Assessment of Surgical Resectability

The relationship between small tumor size and successful therapy is established (Ariyama et al. 1998). By current AJCC staging criteria, tumors <2 cm in diameter are considered as T1 lesions, those >2 cm are considered as T2 lesions when confined to the pancreas, with increasing T stage based on extrapancreatic extension (Byrd et al. 2010). The 5-year survival rates are sharply different between T1 (27–31%) and T2 tumors (8–16%) (Bilimoria et al. 2007), highlighting the critical need to optimize imaging protocols in all patients suspected of pancreatic cancer.

National comprehensive cancer network (NCCN) guidelines define resectable pancreatic tumors as those with no distant metastases; no SMV, portal venous abutment, distortion or encasement; clear fat planes surrounding peripancreatic arteries. The tumor is borderline resectable when there are: no distant metastases; venous involvement with suitable normal vein proximal and distal to site allowing for safe reconstruction; (Tempero et al. 2010) involvement of SMA. The tumor is unresectable when there are distant metastases; any celiac abutment; unsalvageable venous involvement, greater than 180° SMA involvement, aortic invasion; lymphnode disease beyond the field of resection (Tempero et al. 2010). MSCT is recommended as the imaging procedure of choice for the initial assessment of a patient suspected with pancreatic cancer. Most guidelines that are followed in the United States go further in advising the study be performed with a "specialized pancreatic protocol" (Callery et al. 2009; Simianu et al. 2010; Tempero et al. 2010).

The sensitivity of CT for diagnosis of pancreatic adenocarcinoma (89–97%) and its positive predictive value for predicting unresectability (89–100%) are high. The positive predictive value of CT for predicting resectability (45–79%) is low because the diagnostic criteria for diagnosing vascular invasion by tumor favors specificity over sensitivity to avoid denying surgery to patients with potentially resectable tumor (Wong and Lu 2008). In a meta-analysis looking at pooled data from 18 studies revealed a pooled sensitivity and specificity of CT in diagnosing vascular invasion of 77 and 81%. Since CT technology improved over the period of the analysis, when only studies published between 2004 and 2008 were considered, the pooled sensitivity and specificity increased to 85 and 82%, respectively (Zhao et al. 2009). When studies are equivocal, accuracy is improved if interpreted as unresectable as opposed to resectable (Kaneko et al. 2010). Analysis of resectability may be more difficult in patients who are being re-evaluated following neoadjuvant chemotherapy (Morgan et al. 2010).

3 Neuroendocrine Tumors

Pancreatic neuroendocrine tumors (PNET) can be divided into either non-functioning (non-secreting, inactive) and functioning (secreting, active) types. Benign or malignant tumors can exist within each

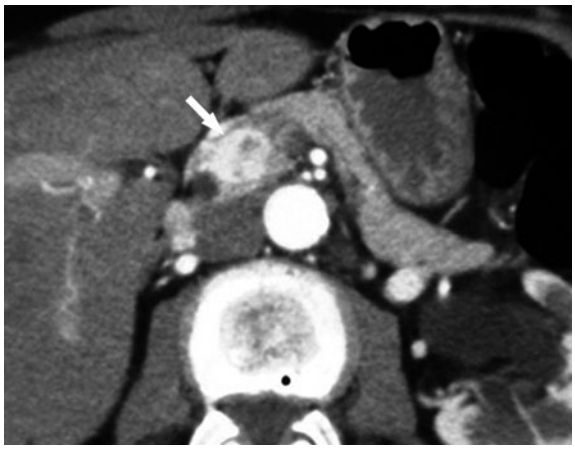

Fig. 8 Typical PNET. Arterial enhancing mass in pancreatic neck (*arrow*) is seen adjacent to CBD. No associated endocrinopathy was detected by laboratory or clinical evaluation

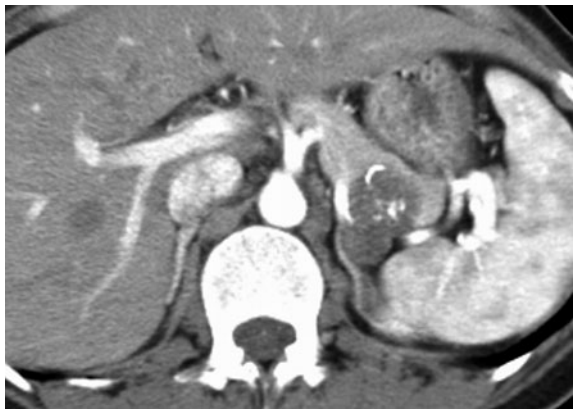

Fig. 9 Non-functioning PNET. Tumor mass in the tail of the pancreas is hypodense compared with pancreatic parenchyma. The presence of dense calcification should raise the suspicion of PNET

group. PNET accounts for 1–2% of all pancreatic neoplasms. They occur with equal frequency in men and women, peak age in the 50 and 60s, and they can be located anywhere within the gland (Solcia et al. 1997). They can occur sporadically or be inherited as in patients with the autosomal dominant multiple endocrine neoplasia (MEN I) syndrome.

PNET have similar imaging features regardless of their secretory activity (Fig. 8). The typical appearance is that of a hypervascular focus best seen in the arterial phase of enhancement on MSCT. Current imaging techniques will detect up to 90% of functioning PNET.

3.1 Functioning Tumors

Insulinoma is the most common PNET occurring with a yearly frequency of approximately 1/100,000 cases. About 50% of the lesions are found in the head of the pancreas; 85% are solitary; 0.5% of the lesions are extrapancreatic. Most lesions are 1–2 cm and 10% are malignant; malignant insulinomas are larger (measuring up to 8 cm) which produce extremely high levels of insulin or pro-insulin. When the lesion is solitary and localized, enucleation is sufficient for treatment. In advanced cases, surgery must attempt to completely remove the tumor and debulk metastases for adequate control of the hypoglycemia. Arterial phase images obtained during multiphase MSCT significantly improves detection (Fidler et al. 2003; Liu et al. 2009).

Gastrinoma is the second most common functioning PNET. Most are located in the anatomic region between the pancreatic head and common bile duct and within the first or second portion of the duodenum, the so-called "gastrinoma triangle" (Stabile et al. 1984). About 50–70% of sporadic cases of Z–E syndrome are usually the result of tumors within the pancreas whereas the remaining cases are secondary to tumors located within the duodenum. At diagnosis, 60% of gastrinomas already have metastasized to peripancreatic lymphnodes or, less frequently, the liver.

3.2 Non-Functioning Tumors

These lesions have a peak incidence in the 50 and 60s with an equal distribution between men and women. They can be sporadic, seen in MEN I or von Hippel–Lindau syndrome. The masses are usually larger than seen in functioning PNET; 60–83% of lesions are malignant at the time of diagnosis. Five-year survival rates are significantly better than for ductal adenocarcinoma with 5-year survival rates approaching 70% and 10-year survival rates approaching 50% of patients. Non-functioning islet cell tumors display a wide variety of imaging appearances, but the most common appearance is that of a hyperdense

pancreatic mass with hypervascular hepatic metastases. Calcifications can be present in as many as 20% of masses; the presence of calcification in a solid pancreatic mass makes PNET as the primary diagnostic consideration (Fig. 9). Approximately 3% of PNET will be "cystic", indistinguishable from other cystic neoplasms (Procacci et al. 2001; Lee et al. 2009). Non-functioning PNET may be clinically silent but do secrete hormones; these hormones may: (a) be secreted in tiny amounts; (b) be substances which are rapidly degraded; (c) be biologically inactive. Some patients with so-called non-functioning PNET come to attention due to MPD obstruction. It has been shown that these tumors will often produce serotonin (Powell et al. 2008; Shi et al. 2010).

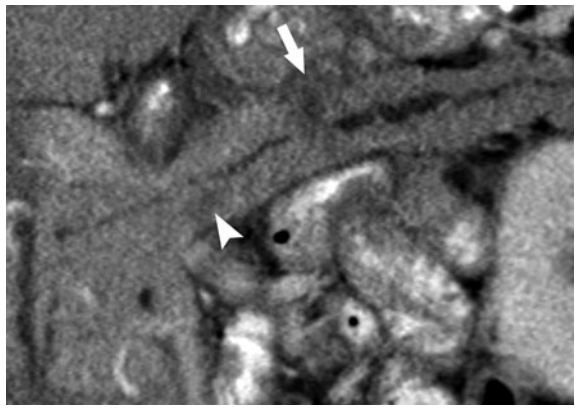

Fig. 10 Lung cancer metastasis to pancreas. Curved MinIP image reveals segmental pancreatic duct obstruction secondary to a low attenuation mass in the pancreatic body (*arrow*). A second mass in the pancreatic neck is partially visible (*arrowhead*)

4 Other Solid Pancreatic Tumors

More than 95% of pancreatic neoplasms arise from or within the exocrine pancreas, ductal adenocarcinoma accounting for 85–90%. A wide variety of "other" solid neoplasms can be encountered in clinical practice, each individual histologic type accounting for approximately 1–2% of pancreatic tumors, therefore extremely rare (Jimenez and Fernandez-del Castillo 2010). These include such rare tumors as acinar cell carcinoma, primary pancreatic lymphoma, adenosquamous carcinoma. They cannot be reliably distinguished from ductal pancreatic adenocarcinoma at MSCT or with other imaging methods (Megibow and Francis 2003). Two of these "other" types of pancreatic tumors will be encountered in clinical practice and are discussed in more detail below.

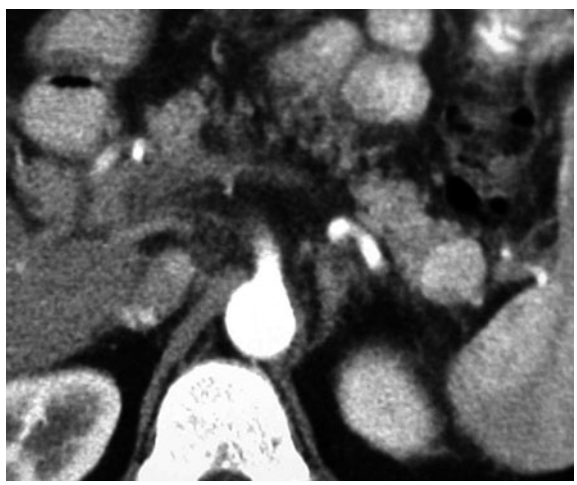

Fig. 11 IPAS, pancreatic tail. Distinguishing a lesion such as this hypervascular mass in the pancreatic tail from PNET or metastasis is difficult. Location and enhancement mimicking spleen are suggestive. We have found MRI helpful in these cases

4.1 Metastatic Disease to the Pancreas

The pancreas can be secondarily involved by neoplasm by either (i) direct extension from a contiguous primary tumor (e.g. gastric carcinoma); (ii) invasion from local metastatic lymphnodes (e.g. invasion of the pancreatic head by metastatic peripancreatic lymphnodes draining a primary tumor of the right colon); and (iii) by hematogenous dissemination.

Renal cell cancer is the most likely primary tumor to metastasize to the pancreas, followed by colorectal, lung, breast, melanoma and carcinoid. Renal cell cancer is widely reported to metastasize several years following nephrectomy (Moussa et al. 2004). Renal cell metastases to the pancreas present as hyperenhancing nodules simulating PNET. They can obstruct the pancreatic duct. They rarely extend into the peripancreatic fat or vessels. Surgical resection is reported to improve survival (Ghavamian et al. 2000). The imaging appearance of other metastases from other primary tumors is variable. As with any pancreatic tumor they may obstruct the pancreatic duct. Multiple foci are not infrequent (Fig. 10).

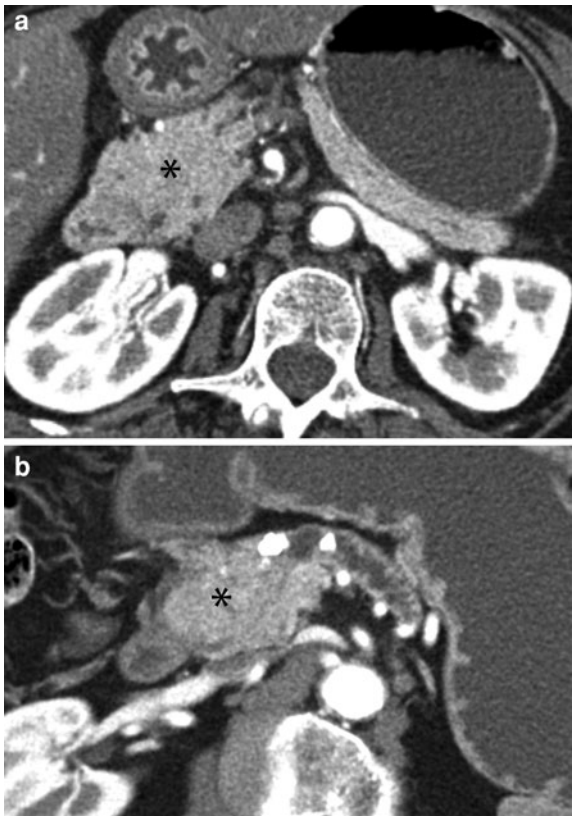

Fig. 12 **a** Focal pancreatitis. There is a focal mass (*asterisks*) in the pancreatic head simulating a neoplasm. This mass has been stable over 8 years. **b** In a different patient with chronic calcific pancreatitis, the focal mass (*asterisks*) in the pancreatic head was resected. Pathology revealed a PNET

4.2 Non-Neoplastic Solid Pancreatic Masses

Two types of non-neoplastic solid pancreatic masses are likely to be encountered in clinical practice; the intrapancreatic accessory spleen and pancreatitis-related masses.

The tail of the pancreas is the most common site of intrapancreatic accessory spleen (IPAS). An IPAS has similar characteristics to those of the spleen on the precontrast and contrast-enhanced images of all the imaging modalities, displaying inhomogeneous (moiré type) enhancement on early phases may be a diagnostic clue (Kim et al. 2008) (Fig. 11). In our practice, we rely on MR imaging to characterize this lesion when detected on MSCT. The multi-sequence protocols used in MR are sufficient to confirm that the lesion "tracks" with spleen on all sequences.

Focal masses in patients with pancreatitis, especially chronic pancreatitis are much more difficult to distinguish from solid neoplasms. Focal pancreatitis masses account for a significant percentage of pathologies that are resected in large surgical series (Yeo et al. 1997). From early descriptions, this imaging issue is not yet definitively resolved (Lammer et al. 1985). No single test can stand alone in differentiating benign from malignant masses in these patients. When a mass is detected in a patient with chronic pancreatitis, MRCP to evaluate for duct penetration is recommended (Ichikawa et al. 2001). If there is no duct penetration, EUS with FNA is recommended to confirm diagnosis of malignancy. If this is equivocal, PET-CT is utilized (Gerstenmaier and Malone 2011). In patients with autoimmune pancreatitis, the pancreatic parenchyma and the suspicious mass will demonstrate a reversal of the typical enhancement pattern, specifically, the pancreas and the mass will be relatively hypodense in the pancreatic phase with a rise in attenuation in the portal phase (Takahashi et al. 2009) (Fig. 12).

References

Ahn SS, Kim MJ et al (2009) Indicative findings of pancreatic cancer in prediagnostic CT. Eur Radiol 19(10):2448–2455

Ariyama J, Suyama M et al (1998) Imaging of small pancreatic ductal adenocarcinoma. Pancreas 16(3):396–401

Balthazar EJ (2005) Pancreatitis associated with pancreatic carcinoma. Preoperative diagnosis: role of CT imaging in detection and evaluation. Pancreatology 5(4–5):330–344

Berland LL, Lawson TL et al (1981) Computed tomography of the normal and abnormal pancreatic duct: correlation with pancreatic ductography. Radiology 141(3):715–724

Bilimoria KY, Bentrem DJ et al (2007) Validation of the 6th edition AJCC pancreatic cancer staging system: report from the national cancer database. Cancer 110(4):738–744

Byrd SB, Compton CC et al (eds) (2010) AJCC cancer staging manual, Springer, New York

Callery MP, Chang KJ et al (2009) Pretreatment assessment of resectable and borderline resectable pancreatic cancer: expert consensus statement. Ann Surg Oncol 16(7):1727–1733

Clark CJ, Traverso LW (2010) Positive peritoneal lavage cytology is a predictor of worse survival in locally advanced pancreatic cancer. Am J Surg 199(5):657–662

Dalrymple NC, Prasad SR et al (2007) Price of isotropy in multidetector CT. Radiographics 27(1):49–62

Deshmukh SD, Willmann JK et al (2010) Pathways of extrapancreatic perineural invasion by pancreatic adenocarcinoma: evaluation with 3D volume-rendered MDCT imaging. Am J Roentgenol 194(3):668–674

Fidler JL, Fletcher JG et al (2003) Preoperative detection of pancreatic insulinomas on multiphasic helical CT. Am J Roentgenol 181(3):775–780

Fishman EK, Horton KM (2001) Imaging pancreatic cancer: the role of multidetector CT with three-dimensional CT angiography. Pancreatology 1(6):610–624

Fletcher JG, Wiersema MJ et al (2003) Pancreatic malignancy: value of arterial, pancreatic, and hepatic phase imaging with multi-detector row CT. Radiology 229(1):81–90

Fukushima H, Itoh S et al (2006) Diagnostic value of curved multiplanar reformatted images in multislice CT for the detection of resectable pancreatic ductal adenocarcinoma. Eur Radiol 16(8):1709–1718

Gangi S, Fletcher JG et al (2004) Time interval between abnormalities seen on CT and the clinical diagnosis of pancreatic cancer: retrospective review of CT scans obtained before diagnosis. Am J Roentgenol 182(4):897–903

Gerstenmaier JF, Malone DE (2011) Mass lesions in chronic pancreatitis: benign or malignant? An "evidence-based practice" approach. Abdom Imaging 36(5):569–577

Ghavamian R, Klein KA et al (2000) Renal cell carcinoma metastatic to the pancreas: clinical and radiological features. Mayo Clin Proc 75(6):581–585

Hommeyer SC, Freeny PC et al (1995) Carcinoma of the head of the pancreas: evaluation of the pancreaticoduodenal veins with dynamic CT–potential for improved accuracy in staging. Radiology 196(1):233–238

Hough TJ, Raptopoulos V et al (1999) Teardrop superior mesenteric vein: CT sign for unresectable carcinoma of the pancreas. Am J Roentgenol 173(6):1509–1512

Ichikawa T, Sou H et al (2001) Duct-penetrating sign at MRCP: usefulness for differentiating inflammatory pancreatic mass from pancreatic carcinomas. Radiology 221(1):107–116

Ichikawa T, Erturk SM et al (2006) MDCT of pancreatic adenocarcinoma: optimal imaging phases and multiplanar reformatted imaging. Am J Roentgenol 187(6):1513–1520

Imamura M, Asahi S et al (2002) Minute pancreatic carcinoma with initial symptom of acute pancreatitis. J Hepatobiliary Pancreat Surg 9(5):632–636

Ishikawa O, Ohigashi H et al (1992) Preoperative indications for extended pancreatectomy for locally advanced pancreas cancer involving the portal vein. Ann Surg 215(3):231–236

Itoh S, Ikeda M et al (2003) Assessment of the pancreatic and intrapancreatic bile ducts using 0.5-mm collimation and multiplanar reformatted images in multislice CT. Eur Radiol 13(2):277–285

Jemal A, Murray T et al (2005) Cancer statistics, 2005. CA Cancer J Clin 55(1):10–30

Jemal A, Siegel R et al (2010) Cancer statistics, 2010. CA Cancer J Clin 60(5):277–300

Jimenez RE, Fernandez-del Castillo C (2010) Tumors of the pancreas. Sleisenger and Fordtran's gastrointestinal and liver disease. Feldman M, Friedman LS, Brandt LJ (eds) Philadelphia 2:1017–1027 Elsevier

Kalra MK, Maher MM et al (2003) State-of-the-art imaging of pancreatic neoplasm. Br J Radiol 76(912):857–865

Kaneko OF, Lee DM et al (2010) Performance of multidetector computed tomographic angiography in determining surgical resectability of pancreatic head adenocarcinoma. J Comput Assist Tomogr 34(5):732–738

Kim SH, Lee JM et al (2008) Intrapancreatic accessory spleen: findings on MR Imaging, CT, US and scintigraphy, and the pathologic analysis. Korean J Radiol 9(2):162–174

Kim JH, Park SH et al (2010) Visually isoattenuating pancreatic adenocarcinoma at dynamic-enhanced CT: frequency, clinical and pathologic characteristics, and diagnosis at imaging examinations. Radiology 257(1):87–96

Lammer J, Herlinger H et al (1985) Pseudotumorous pancreatitis. Gastrointest Radiol 10(1):59–67

Lee DS, Jeffrey RB et al (2009) Islet-cell tumors of the pancreas: spectrum of MDCT findings. A pictorial essay. Applied Radiology 38(11):10–28

Liu Y, Song Q et al (2009) The value of multidetector-row CT in the preoperative detection of pancreatic insulinomas. Radiol Med 114(8):1232–1238

Lu DS, Reber HA et al (1997) Local staging of pancreatic cancer: criteria for unresectability of major vessels as revealed by pancreatic-phase, thin-section helical CT. Am J Roentgenol 168(6):1439–1443

Macari M, Spieler B et al (2010) Dual-source dual-energy MDCT of pancreatic adenocarcinoma: initial observations with data generated at 80 kVp and at simulated weighted-average 120 kVp. Am J Roentgenol 194(1):W27–W32

Manak E, Merkel S et al (2009) Resectability of pancreatic adenocarcinoma: assessment using multidetector-row computed tomography with multiplanar reformations. Abdom Imaging 34(1):75–80

McMahon PM, Halpern EF et al (2001) Pancreatic cancer: cost-effectiveness of imaging technologies for assessing resectability. Radiology 221(1):93–106

McNulty NJ, Francis IR et al (2001) Multi–detector row helical CT of the pancreas: effect of contrast-enhanced multiphasic imaging on enhancement of the pancreas, peripancreatic vasculature, and pancreatic adenocarcinoma. Radiology 220(1):97–102

Megibow AJ, Francis IR (2003) Unusual pancreatic neoplasms: imaging. Imaging of the Pancreas: cystic and rare tumors. In: Procacci C, Megibow AJ (eds) Springer**,** Heidelberg, pp 249–267

Mochizuki K, Gabata T et al (2010) MDCT findings of extrapancreatic nerve plexus invasion by pancreas head carcinoma: correlation with en bloc pathological specimens and diagnostic accuracy. Eur Radiol 20(7):1757–1767

Morgan DE, Waggoner CN et al (2010) Resectability of pancreatic adenocarcinoma in patients with locally advanced disease downstaged by preoperative therapy: a challenge for MDCT. Am J Roentgenol 194(3):615–622

Moussa A, Mitry E et al (2004) Pancreatic metastases: a multicentric study of 22 patients. Gastroenterol Clin Biol 28(10 Pt 1):872–876

O'Malley ME, Boland GW et al (1999) Adenocarcinoma of the head of the pancreas: determination of surgical unresectability with thin-section pancreatic-phase helical CT. Am J Roentgenol 173(6):1513–1518

Powell AC, Hajdu CH et al (2008) Nonfunctioning pancreatic endocrine neoplasm presenting as asymptomatic, isolated pancreatic duct stricture: a case report and review of the literature. Am Surg 74(2):168–171

Procacci C, Carbognin G et al (2001) Nonfunctioning endocrine tumors of the pancreas: possibilities of spiral CT characterization. Eur Radiol 11(7):1175–1183

Prokesch RW, Chow LC et al (2002a) Isoattenuating pancreatic adenocarcinoma at multi-detector row CT: secondary signs. Radiology 224(3):764–768

Prokesch RW, Chow LC et al (2002b) Local staging of pancreatic carcinoma with multi-detector row CT: use of curved planar reformations initial experience. Radiology 225(3):759–765

Raimondi S, Maisonneuve P et al (2009) Epidemiology of pancreatic cancer: an overview. Nat Rev Gastroenterol Hepatol 6(12):699–708

Roche CJ, Hughes ML et al (2003) CT and pathologic assessment of prospective nodal staging in patients with ductal adenocarcinoma of the head of the pancreas. Am J Roentgenol 180(2):475–480

Sai M, Mori H et al (2010) Peripancreatic lymphatic invasion by pancreatic carcinoma: evaluation with multi-detector row CT. Abdom Imaging 35(2):154–162

Salles A, Nino-Murcia M et al (2007) CT of pancreas: minimum intensity projections. Abdom Imaging 27: 27

Schueller G, Schima W et al (2006) Multidetector CT of pancreas: effects of contrast material flow rate and individualized scan delay on enhancement of pancreas and tumor contrast. Radiology 241(2):441–448

Shi C, Siegelman SS et al (2010) Pancreatic duct stenosis secondary to small endocrine neoplasms: a manifestation of serotonin production? Radiology 257(1):107–114

Simianu VV, Zyromski NJ et al (2010) Pancreatic cancer: progress made. Acta Oncol 49(4): 407–417

Solcia E, Capella C et al (eds) (1997) Tumors of the Pancreas. AFIP atlas of tumor pathology. Washington, DC, Armed Forces Institute of Pathology

Stabile BE, Morrow DJ et al (1984) The gastrinoma triangle: operative implications. Am J Surg 147(1):25–31

Stephens DH (1997) CT of pancreatic neoplasms. Part I: adenocarcinoma. Curr Probl Diagn Radiol 26(2):59–80

Takahashi N, Fletcher JG et al (2009) Autoimmune pancreatitis: differentiation from pancreatic carcinoma and normal pancreas on the basis of enhancement characteristics at dual-phase CT. Am J Roentgenol 193(2):479–484

Tanaka S, Nakao M et al (2010) Slight dilatation of the main pancreatic duct and presence of pancreatic cysts as predictive signs of pancreatic cancer: a prospective study. Radiology 254(3):965–972

Tempero M, Brand R (2008) Pancreatic Cancer. Cecil Medicine Goldman L, Ausiello D (eds). Philadelphia, Elsevier, pp 1479–1482

Tempero MA, Arnoletti JP et al (2010) Pancreatic adenocarcinoma. J Natl Compr Canc Netw 8(9):972–1017

Uehara H, Tatsumi K et al (2009) Scraping cytology with a guidewire for pancreatic-ductal strictures. Gastrointest Endosc 70(1):52–59

Wong JC, Lu DS (2008) Staging of pancreatic adenocarcinoma by imaging studies. Clin Gastroenterol Hepatol 6(12):1301–1308

Yamada Y, Mori H et al (2000) CT assessment of the inferior peripancreatic veins: clinical significance. Am J Roentgenol 174(3):677–684

Yeo CJ, Cameron JL et al (1997) Six hundred fifty consecutive pancreaticoduodenectomies in the 1990s: pathology, complications, and outcomes. Ann Surg 226(3):248–57, discussion 257–260

Yoon SH, Lee JM et al (2010) Small (<=20 mm) Pancreatic adenocarcinomas: analysis of enhancement patterns and secondary signs with multiphasic multidetector CT. Radiology 2011:15

Yoon SH, Lee JM et al (2011) Small (<=20 mm) Pancreatic adenocarcinomas: analysis of enhancement patterns and secondary signs with multiphasic multidetector CT. Radiology 259(2):442–452

Zamboni GA, Kruskal JB et al (2007) Pancreatic adenocarcinoma: value of multidetector CT angiography in preoperative evaluation. Radiology 245(3):770–778

Zhao WY, Luo M et al (2009) Computed tomography in diagnosing vascular invasion in pancreatic and periampullary cancers: a systematic review and meta-analysis. Hepatobiliary Pancreat Dis Int 8(5):457–464

Cystic Pancreatic Masses

A. Oto

Contents

Abstract

Cystic neoplasms of the pancreas have been recognized for almost two centuries. In 1830, Becourt described the first cystic neoplasm of the pancreas as a tumor, "with the size of a child's head and composed of very strong walls" (Verbesey and Munson in Surg Clin North America 90(2): 411–425, 2010). Especially after 1990s, cystic lesions of the pancreas are being increasingly identified primarily due to wide-spread use of CT and other state-of-the-art imaging methods. It is now estimated that they can be detected in approximately 1.2% of abdominal CT scans with increasing prevalence with age and up to 24% of patients have pancreatic cystic lesions at autopsy (Spinelli et al. in Ann Surg 239(5):651–657, 2004; Kimura et al. in Int J Pancreatol 18(3):197–206, 1995). As they encompass a variety of processes of neoplastic, developmental and inflammatory in origin, their discovery prompts management concerns and their accurate characterization is necessary for appropriate patient triage. Many patients with a pancreatic cystic neoplasm (PCN) present with no relevant signs or symptoms and most of these lesions are incidentally diagnosed (Bassi et al. in World J Surg 27:319–323, 2003; Kerlin et al. in Surg Gynecol Obstet 165: 475–478, 1987). The proportion of pancreatic resections that were performed for PCN has doubled in the last two decades (Fernandez-del Castillo and Warshaw in Adv Surg 34:237–248, 2000). Multidetector row CT (MDCT) is the most commonly utilized imaging modality for pancreas imaging and has the capability to provide high resolution images of the pancreas and can depict even small pancreatic

A. Oto (✉)
Chief of Abdominal Imaging and Body MRI
Department of Radiology, University of Chicago,
5841 S Maryland Ave, MC 2026,
Chicago, IL 60637, USA
e-mail: aoto@radiology.bsd.uchicago.edu

C. J. Zech et al. (eds.), *Multislice-CT of the Abdomen*, Medical Radiology. Diagnostic Imaging,
DOI: 10.1007/174_2011_425, © Springer-Verlag Berlin Heidelberg 2012

cysts. MDCT can also provide information about characterization of pancreatic cystic lesions, their follow-up and staging (Curry et al. in Am J Roentgenol 175(1):99–103, 2000). In this chapter, we will provide an overview of pancreatic cystic lesions and their clinical management and then describe the CT imaging features of common PCN.

1 Cystic Lesions of Pancreas

Cysts of the pancreas constitute a broad spectrum of entities from non-neoplastic to malignant cysts (Verbesey and Munson 2010; Spinelli et al. 2004; Kimura et al. 1995; Bassi et al. 2003; Kerlin et al. 1987; Fernandez-del Castillo and Warshaw 2000; Curry et al. 2000; Pitman et al. 2010). Despite the increasing number of intraductal papillary mucinous neoplasms (IPMN), the large majority of pancreatic cystic lesions remain to be pseudocysts. Other non-neoplastic cysts of the pancreas include retention cysts, congenital cysts, foregut cysts and endometriotic cysts and constitute a relatively small percentage of pancreatic cystic lesions.

The World Health Organization (WHO) classification system divided pancreatic cystic neoplasms into three categories: benign (adenomas), low grade malignant (borderline) and malignant (carcinoma in situ and invasive cancer) (Hamilton and Aaltonen 2000). Microcystic, serous tumors are almost universally benign (other than case reports of malignant variants) and mucinous neoplasms are accepted as either premalignant or malignant. In addition to the truly cystic pancreatic neoplasms, some of the solid pancreatic lesions can demonstrate cystic degeneration or may have cystic components. Necrosis within some of the solid neoplasms may also mimic a cystic lesion on CT.

In the absence of systemic cystic disease such as von Hippel-Lindau disease, polycystic kidney disease or cystic fibrosis, true epithelial cysts are considered rare and are assumed to be neoplasms (Handrich et al. 2005). However, morbidity and mortality due to small cysts ≤ 3 cm is very unlikely and observation appears to be a safe management option (Handrich et al. 2005). Sahani et al. (2006a) showed that majority (87%) of the small pancreatic cysts in their series of 111 pathologically verified cysts were benign (Sahani et al. 2006).

2 Clinical Overview

More than 70% of PCN are found in asymptomatic patients, usually as an incidental finding on scans obtained for another reason (Verbesey and Munson 2010). In an autopsy study, it was found that almost 25% o f the 300 cadavers had small cystic lesions (Kimura et al. 1995). Increasing age was directly related to the probability of finding a lesion. Most published studies agree that the ratio of benign to malignant lesions is approximately 2:1 and cystic neoplasms are more common in females at a ratio of 2:1 to 3:1 (Verbesey and Munson 2010). Identification of a pancreatic cyst requires the clinician to focus on the main clinical challenge of determination of benign or malignant nature of the cyst. Differentiation of pseudocyst from neoplastic cystic lesions, mucinous cystic neoplasms (MCN) from serous cystic neoplasms (SCN) and branch type IPMN from main duct or combined IPMN are the common crucial questions that need to be answered in patients with pancreatic cystic lesions. The approach to the patient with a pancreatic cystic lesion begins with a detailed history seeking for previous episodes of pancreatitis or abdominal trauma, which may predispose the patient for a pseudocyst.

Imaging is usually the first step in detection and characterization of PCN's; however, most of the time it cannot provide a definite answer regarding the benign or malignant nature of the lesions. When cross-sectional imaging is not conclusive, depending on the lesion size, appearance, patient symptoms and age, follow-up with imaging or a more aggressive approach to characterize the lesion is pursued.

Endoscopic US (EUS) and EUS-guided fine needle aspiration of the cystic lesion is usually the next step for lesion characterization. EUS is very sensitive for detecting small cysts, however, EUS morphology alone has limitations in differentiating between mucinous and non-mucinous as well as benign and malignant lesions (Stelow et al. 2003; Ahmad et al. 2001). Detection of focal nodules and invasive lesions on EUS may facilitate the diagnosis of a malignant lesion by directing the fine needle aspiration biopsy to these suspicious areas. Aspirated fluid from the cyst is sent for chemical and cytological analysis. A large prospective study concluded that carcinoembryonic antigen (CEA) was the most useful tumor marker for

differentiating mucinous from non-mucinous lesions (Brugge et al. 2004a). CEA, however, does not distinguish benign from malignant mucinous neoplasms (Pitman et al. 2010). Amylase may be another helpful marker as it is typically very high (in thousands) in pseudocysts but low in serous cysts. In the same prospective, multicentre study, the accuracy of cytology was found to be poor (59%) in differentiation of benign and malignant cystic lesions (Brugge et al. 2004a). Only inflammatory cells should be present in fluid aspirated from pseudocysts (Nguyen et al. 1997). Molecular testing can be considered to look for the presence of KRAS, p53 mutations and loss of p16 and SMAD4 in malignant lesions (Pitman et al. 2010; Brugge et al. 2004b).

Endoscopic retrograde cholangiopancreatography (ERCP) can be useful in detection of IPMN's. On endoscopy, visualization of mucin coming out from a widely patent ampulla is pathognomonic for IPMN.

In the past, resection was the recommended treatment for all PCN's. With the increasing number of incidentally discovered PCN's and recent data suggesting that many tumors are benign or have a low malignant potential, other treatment strategies such as follow-up with imaging have started to be commonly utilized (Verbesey and Munson 2010). Age, female gender, weight loss, jaundice and elevated aminotransferase levels were found to be significant predictors of malignancy (Gomez et al. 2008; Javle et al. 2007). The presence of symptoms is another critical factor in deciding appropriate therapy. The frequency of malignancy in small cysts is significantly higher in symptomatic patients. Imaging findings and cyst fluid analysis also contribute in risk stratification process. If a lesion is determined to be a pseudocyst, based on its size, it can be drained or followed up with imaging (usually if less than 6 cm). Serous lesions can be followed up with imaging if the patient is asymptomatic. MCN, on the other hand, require resection. In 2006, the International Association of Pancreatology working group consensus guidelines were established to help guide the management of PCN's (Tanaka et al. 2006). Unless there is a contraindication for surgery, all MCN's and main duct and combined type IPMN's should be resected. Small ($\leq$3 cm) branch type IPMN's can be followed up by imaging. There is no universally accepted follow-up protocol. Surveillance interval can be increased if the lesions remain stable in size after two years of follow-up. A cost analysis using the consensus guidelines suggested that although immediate surgical resection was the most effective method, its cost was prohibitive (Huang et al. 2010). Imaging surveillance was found to be a cost-effective option when compared with no surveillance.

3 Imaging of Cystic Pancreatic Lesions

The characterization of cystic pancreatic lesions relies heavily on imaging. Main aims of the imaging are to differentiate pseudocysts from true cysts, MCN from non-MCN and benign lesions from malignant lesions. Sahani et al. 2005 proposed a simple but useful imaging-based classification system differentiating pancreatic cystic lesions into four different types: (1) unilocular (pseudocysts, MCN, lymhoepithelial cysts, small IPMN's and small serous tumors), (2) microcystic (serous cystadenomas and lymhoepithelial cysts), (3) macrocystic (MCN, oligocystic serous tumors and IPMN's) and (4) cysts with solid components (solid appearing tumors, solid-pseudopapillary neoplasms (SPEN) and cystic islet cell tumors). MDCT is the most commonly utilized imaging test for their detection and characterization by visualizing the calcification of the cyst wall, septa, mural nodules and findings suggestive of pancreatitis (Curry et al. 2000; Minami et al. 1989). Two-dimensional curved reformations can provide additional imaging details of IPMN which include display of the ductal anatomy and of the communication between the cystic lesion and pancreatic ductal system (Sahani et al. 2006b). Two-dimensional curved reformation is a very valuable, comprehensive evaluation tool for analysis of MDCT data to characterize pancreatic cystic lesions.

MRCP is becoming increasingly popular for the diagnosis of pancreatic cystic lesions. MRCP offers better depiction of pancreatic duct and displays the relation between the pancreatic duct and the cystic lesion (Berland et al. 2010). Secretin administration may facilitate the visualization of the communication between a cystic lesion and pancreatic duct (Carbognin et al. 2007). In the ACR white paper, the Incidental Findings Committee suggested dedicated MRI as the imaging procedure of choice to characterize a pancreatic cyst (Berland et al. 2010). Superior contrast resolution of MRI facilitates the recognition

of septae, nodules, and duct communication (Waters et al. 2008). Sainani et al. (2009) compared the performance of MDCT with MRCP in a retrospective analysis of 30 patients with 38 pathologically confirmed cysts. They concluded that MRI enabled more confident assessment of the morphology of small cysts than MDCT, but the accuracy of the two imaging techniques for cyst characterization was comparable. Although, there is no clear consensus among pancreatic experts regarding the optimal imaging test for follow-up of pancreatic cysts, a limited MRI examination relying exclusively on T2-weighted images has been proposed as a practical follow-up strategy (Macari et al. 2009).

Regardless of the imaging test, large size and presence of mural nodules, dilatation of the common bile duct, and lymphadenopathy are accepted as worrisome features for malignancy (Berland et al. 2010). Morphologic features that aid in a diagnosis of a mucinous tumor include (Verbesey and Munson 2010) the presence or absence of septae (MCN's are multilocular, with large cysts), (Spinelli et al. 2004) the location of calcification (MCN's typically have peripheral calcification, whereas SCN's have central calcification), (Kimura et al. 1995) location within the pancreas, and (Bassi et al. 2003) the presence of main duct involvement (Procacci et al. 1997, 1999, 2001; Rautou et al. 2008). MCN can also be suspected when a cyst is present in the tail of pancreas in a premenopausal woman (Sperti et al. 2001).

Despite some promising results, the role of PET/CT in the evaluation of pancreatic cystic lesions is still investigational and not established. Sperti et al. (2007) showed that Positive criteria of increased uptake on 18-FDG PET was absent in 13 of 13 adenomas and 7 of 8 borderline IPMNs, but was present in 4 of 5 carcinoma in situ (80%) and in 20 of 21 invasive cancers (95%). Pitfalls include false-positive 18-FDG uptake of pseudocysts due to inflammation and lack of uptake in some of the malignant PCN's.

4 CT Findings of Common PCN

4.1 Serous Cystic Neoplasms

Serous tumors represent approximately 1–2% of all pancreatic neoplasms and almost 25% of PCN (Phillips et al. 2008). They predominantly occur in middle aged woman (average age: 61 years) and are distributed evenly throughout the pancreas. They are almost always incidentally discovered and can cause symptoms (such as abdominal pain or jaundice) only if they reach a large size. Especially large cystadenomas may demonstrate progressive enlargement at serial follow-up imaging examinations (Tseng et al. 2005). Multiple serous cystadenomas may occur in von Hippel-Lindau disease (Mohr et al. 2000). Serous cystadenomas are typically benign tumors. However, there are several case reports in the literature describing serous cystadenomas that presented with metastases (Verbesey and Munson 2010).

Serous cystadenomas have characteristic imaging and histologic features that may differentiate them from other potentially malignant CPN (Colonna et al. 2008; Kim et al. 2008). In 90% of cases, (Fig. 1) serous cystadenomas are characterized by a polycystic pattern (70%, multiple cysts measuring 2 cm or smaller) or honey comb pattern (20%, subcentimeter cysts that are difficult to be individually distinguished by imaging). On MDCT, the appearance of serous cystadenoma is similar to gross pathology. In the polycystic form, multiple large cysts separated by enhancing fibrous septa can easily be identified. In the honeycomb pattern, due to the small size of the cysts, the lesion may appear as well-marginated with soft tissue or mixed attenuation and a sharp interface with vascular structures (Fig. 1) (Choi et al. 2009). This pattern can be difficult to differentiate from solid tumors on MDCT. Fine, external surface lobulations are considered to be suggestive of serous cystadenoma (Cohen-Scali et al. 2003; Kim et al. 2006). Enhancement of the septae and central scar can be best appreciated on delayed images (Choi et al. 2009). The presence of central scar is considered to be pathognomonic for SCN, even when there is no distinct microcystic appearance (Curry et al. 2000). It was observed from 30–45% of SCN with the percentage increasing with increasing size (Curry et al. 2000; Yasuhara et al. 2002). Central scar may also demonstrate calcifications which can be easily depicted on MDCT.

Various atypical manifestations of SCN may lead incorrect diagnosis. These include oligocystic (macrocystic) pattern (seen in 10% of SCN) (Fig. 2), giant tumors with ductal dilatation, intratumoral hemorrhage, solid variants, unilocular cystic tumors and disseminated form (Choi et al. 2009). Oligocystic

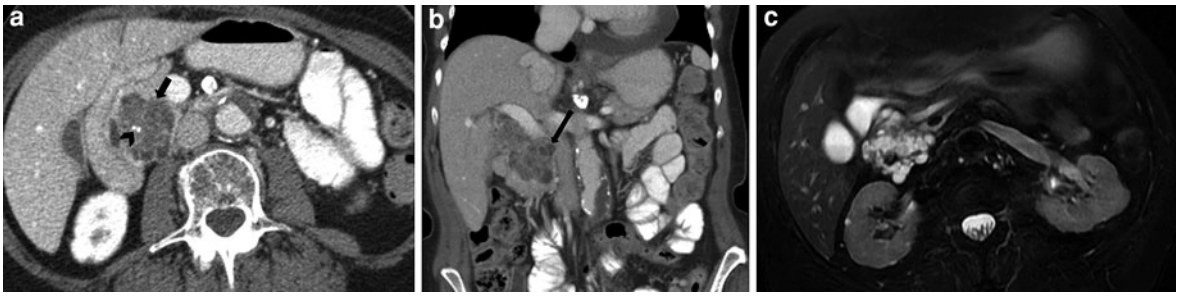

Fig. 1 Serous cystadenoma. Axial (**a**) and coronal (**b**) MDCT images show a cystic mass in the head of pancreas (*arrow*) with central stellate calcifications (*arrowhead*). Multiple, small cysts within the lesion are better delineated on the T2W Axial MRI image (**c**) compared to CT images. Calcification on MR image appears hypointense (*arrowhead*)

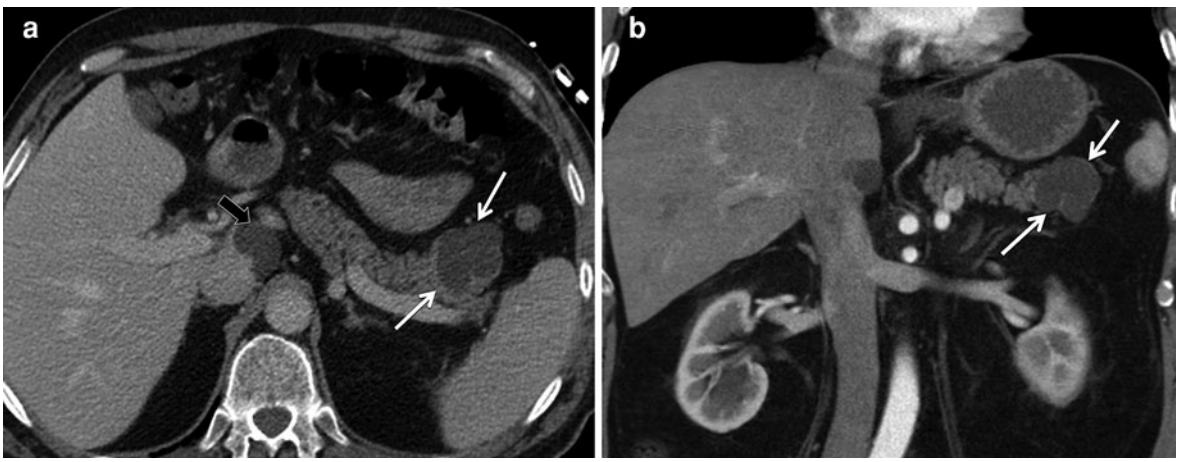

Fig. 2 Macrocystic serous cystadenoma. Axial (**a**) and coronal (**b**) MDCT images show a multiloculated cystic mass (*white arrows*) in the tail of pancreas with internal septations. The size of the individual cysts is larger than 2 cm; however, the wall is very thin and there are external lobulations suggestive of macrocystic variant of serous cystadenoma. Note the incidental hepatic cyst in the caudate lobe (*black arrow*)

pattern exhibits fewer, large (>2 cm) cysts. It may appear as a multicystic or lobulated cystic lesion with septations in the head of the pancreas, whereas, MCN have either a pleomorphic or a clubbed, finger-like, cystic shape (Yasuhara et al. 2002). These lesions can be differentiated from pseudocysts by external lobulations and from a SPEN by its lack of a thick, peripheral wall and hemorrhage in the cystic component (Cohen-Scali et al. 2003; Choi et al. 2006). However, its differentiation from other PCN can be sometimes difficult due to an overlap of morphology. The accuracy of CT in diagnosis of SCN was shown to be better than MCN (Procacci et al. 1999).

Surgical treatment is not indicated for serous neoplasms unless the patient has symptoms secondary to compression of the surrounding structures by the mass (Verbesey and Munson 2010). For tumors 4 cm or larger, which can grow as much as 2 cm per year, surgical resection can be a reasonable option.

4.2 Mucinous Cystic Neoplasms

Before the description of IPMN's, MCN's were accepted as the most common PCN's and account for 10–45% of all PCN (Kalb et al. 2009; Balcom et al. 2000). They occur much more commonly in women (80%) in their fifth or sixth decade of life (Balcom et al. 2000). MCN's are located in the body and tail of the pancreas in more than two-thirds of the cases. They are increasingly discovered incidentally but can also present with abdominal pain, mass or weight

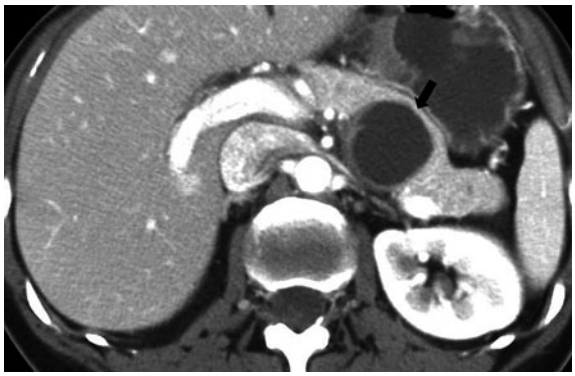

Fig. 3 Mucinous cystadenoma. Axial contrast-enhanced MDCT image shows a unilocular, nonlobulated cystic mass (*arrow*) in the body of pancreas with a thick wall characteristic of unilocular MCN. No communication with pancreatic duct can be seen

loss. MCN are well-circumscribed unilocular or multilocular cysts with no communication with the pancreatic duct. Their content may be hemorrhagic, necrotic or watery (Garcea et al. 2008). It is suspected that MCN may arise from ovarian rests in pancreas. Tanaka et al. reported the presence of ovarian type stroma in MCN of both women and men and ovarian type stroma is accepted as a histologic requirement for diagnosis of MCN (Tanaka et al. 2006). MCN are lined by columnar cells staining positive for mucin and with a spectrum ranging from normal to varying degrees of dysplasia to in situ or invasive carcinoma. Since the separation between benign, borderline and malignant lesions may be indistinct, these tumors are collectively considered as MCN with the understanding that most will develop malignant characteristics if left untreated (Balcom et al. 2000). Malignancy risk is directly related to an increase in size and duration of existence (Verbesey and Munson 2010). Since all MCN's are considered premalignant and can undergo malignant transformation at any time, the general recommendation is to resect MCN, given the patient poses an acceptable surgical risk (Verbesey and Munson 2010).

On MDCT, MCN present as well-encapsulated multilocular, macrocystic (>2 cm) lesions with apparent wall enhancement (Fig. 3) (Scott et al. 2000). Enhancing internal septations may be visualized. Peripheral, "egg shell" calcifications (as opposed to central stellate calcifications of SCN) have been reported in 10–25% of these tumors (Scott et al. 2000) but are specific finding for MCN's and predictive of malignancy. Other CT findings suggestive of malignancy are presence of solid components, thick wall, mural nodules and papillary projections (Fig. 4) (Procacci et al. 2001; Bassi et al. 2008; Biankin et al. 2004). Mucinous cystadenocarcinoma can be locally aggressive and may present with liver metastases, ascites or peritoneal carcinomatosis. The most important differential diagnosis of MCN is pseudocyst. Differentiation of pseudocyst from MCN or malignant MCN from benign MCN can be difficult based on imaging findings alone. FNAB of cystic fluid may be helpful in these cases. While levels of amylase are elevated in pseudocysts, CEA levels are elevated in MCN. The presence of mucinous cyst is often confirmed when thick, viscous mucus is aspirated. Cytology, on the other hand, may underestimate the final histologic grade of neoplastic mucinous cyst (Pitman et al. 2010).

4.3 Intraductal Papillary Mucinous Neoplasms

In 2000, World Health Organization classified cystic mucin producing pancreatic neoplasms into two distinct entities: IPMN and mucinous cystic neoplasms. IPMN was first described by Ohashi et al. (1982). They are characterized by cystic dilatation of the main and/or branches of the pancreatic duct. They originate from the epithelium surrounding the pancreatic ducts and can evolve all the biological stages from slight dysplasia to carcinoma that can be simultaneously present in the same lesion (Gourgiotis et al. 2007). They should be considered premalignant in all clinical situations. Communication of the neoplasm with the pancreatic ductal system is an important feature that differentiates IPMN from MCN. Thick mucin produced by the tumor cells causes obstruction of the pancreatic duct and can be seen pouring from a patulous ampulla by the endoscopist. It mainly occurs in the sixth and seventh decades of life, affecting males slightly more than females and is more commonly located in the head (Gourgiotis et al. 2007).

IPMNs are classified into three types according to the site and extent of involvement: main duct, branch duct and combined type (Kobari et al. 1999). This classification is based on imaging findings and has prognostic implications. Malignancy is reported

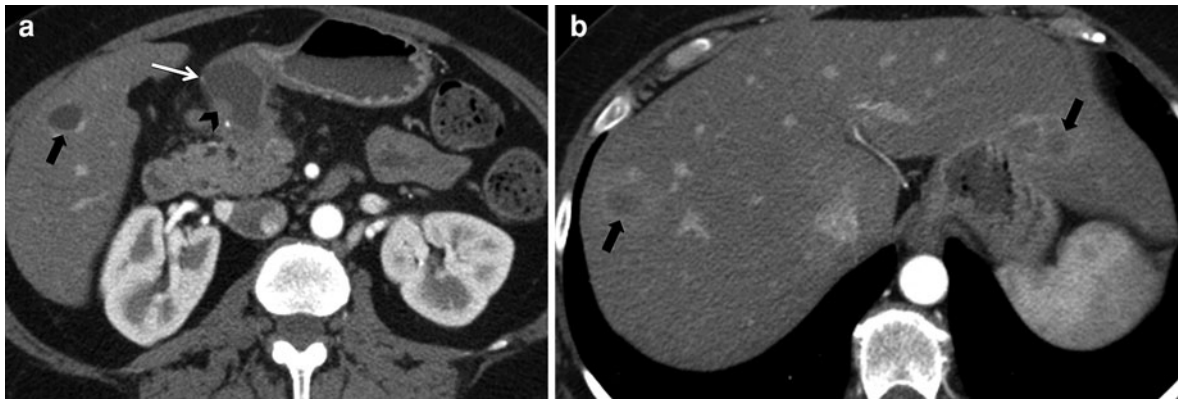

Fig. 4 Mucinous cystadenocarcinoma. Axial contrast-enhanced MDCT images (**a**, **b**) show an exophytic cystic pancreatic mass (*white arrow*) with enhancing mural solid nodular component (*black arrowhead*). Multiple hypodense lesions in the liver (*black arrows*) represent metastatic disease

in 57–92% of main duct tumors but only in 6–46% of branch duct tumors (Gourgiotis et al. 2007). Main duct type IPMN is characterized by diffusely dilated main pancreatic duct filled with mucin. The duct can be partially ectatic in some cases. The branch type IPMN affects one or more of the branches of the pancreatic duct and the dilated duct may contain solitary or multiple tumors or mucin (Gourgiotis et al. 2007). It is most commonly located in the uncinate process and can be multiple. Any combination of the above types is considered as combined type and is considered as main duct type for the purpose of prognosis and treatment.

Histologically, there is papillary hyperplasia and neoplasia of the involved ductal epithelium, often with large quantities of intracellular and intraductal mucin (Balcom et al. 2000). Depending on the degree of atypia, IPMNs are classified into various categories such as adenoma, borderline, carcinoma in situ or invasive carcinoma. With the exception of the cases with invasive carcinoma, it is uncommon for the other histologic types of IPMN to exhibit radial pancreatic or peripancreatic extension or invasion (Azar et al. 1996). An association between IPMN and non-pancreatic malignancies has been reported with a rate range from 23–32% (Sugiyama and Atomi 1999).

Majority of the patients with IPMN do not present with symptoms related to the tumor. Common presenting symptoms are acute pancreatitis, abdominal pain, weight loss, diabetes and jaundice (Salvia et al. 2004; D'Angelica et al. 2004). In addition to radiological imaging methods, ERCP, EUS and EUS-guided fine needle aspiration biopsy are commonly utilized in the diagnosis of IPMN's. Management options range from watchful waiting to radical pancreatectomy depending on the malignancy risk and patient-related factors (symptoms, age, surgery risk etc.). Clinical variables indicating malignancy risk include tumor size, sex, diabetes, pancreatitis, steatorrhea, abdominal mass, weight loss, serum CA 19-9 level and serum CEA level (Gourgiotis et al. 2007). Sugiyama et al. found with multivariate analysis that the size >30 mm and presence of mural nodules were the strongest predictors of malignancy in branch type IPMN's (Sugiyama et al. 2003).

In main duct type IPMN, CT shows diffuse or segmental dilatation of the main pancreatic duct without a transition point, bulging papilla and proportional atrophy of the pancreas (Figs. 5, 6, 7; Taouli et al. 2000). Differential diagnosis of this appearance includes chronic pancreatitis. Although presence of calcifications suggest chronic pancreatitis, it is important to note that they can also be encountered in IPMN and sometimes, differential diagnosis between these two entities may not be possible. Branch type IPMN's present as lobulated or septated cystic lesions communicating with the pancreatic duct (Fig. 8). Communication of IPMN with main pancreatic duct is one of the most reliable imaging finding for the diagnosis of IPMN (Sahani et al. 2006b). Two-dimensional curved reformations are useful for establishment of a clear communication which is not obvious on the axial images. MDCT was shown to provide useful information for prediction of

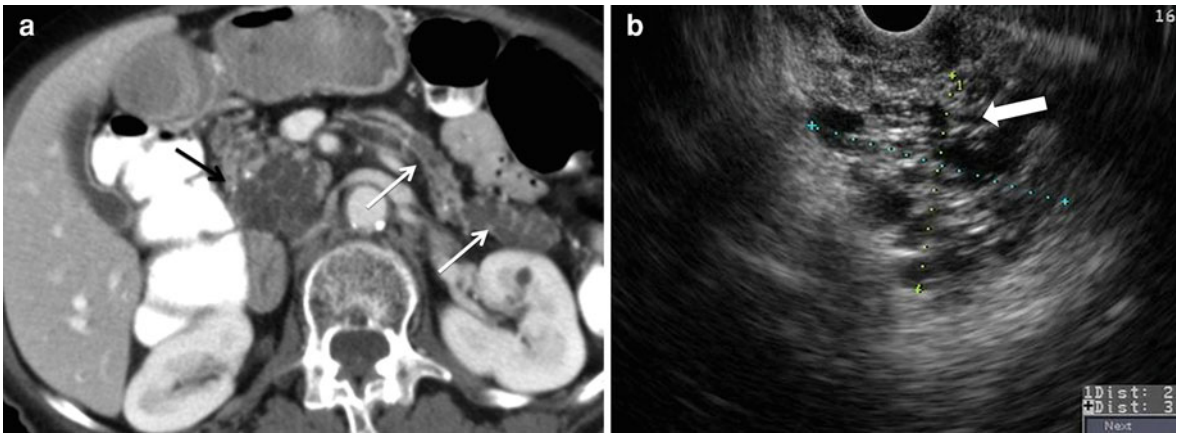

Fig. 5 Main duct type IPMN. Contrast-enhanced axial MDCT image shows a cystic mass in the head of pancreas (*black arrow*) with diffuse dilation of main pancreatic duct (*white arrows*) and atrophy of pancreatic parenchyma. On EUS (**b**), the mass in the pancreatic head appears multicystic (*arrow*)

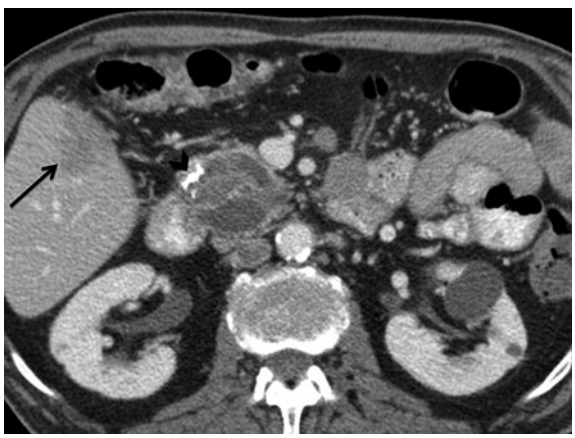

Fig. 6 Axial MDCT image showing calcification (*arrow head*) within main duct IPMN. A hypoattenuating lesion in the liver represents metastasis (*black arrow*)

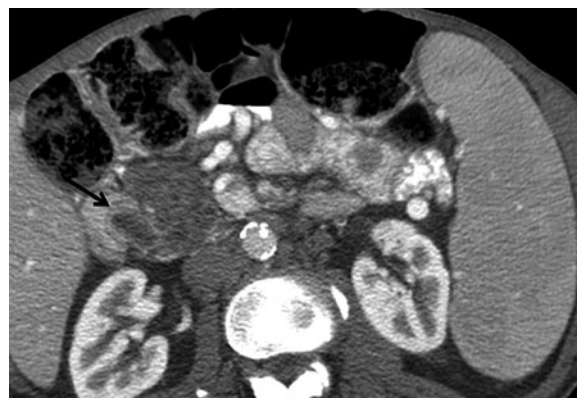

Fig. 7 Axial MDCT image shows bulging papilla (*black arrow*) in a patient with main duct type IPMN

malignancy in IPMN (Kawamoto et al. 2006). Predictive features for the presence of invasive carcinoma at preoperative CT and other imaging studies include involvement of the main pancreatic duct, marked dilatation of the main pancreatic duct, diffuse or multifocal involvement, the presence of a large mural nodule or solid mass, large size of the mass, calcified intraluminal contents, and obstruction of the common bile duct (Taouli et al. 2000; Kawamoto et al. 2005, 2006; Ogawa et al. 2008). Recently, Vuillerme et al. (2007) reported that most solid masses are associated with invasive carcinomas and most intraductal nodules correspond to in situ carcinomas. Ogawa et al. (2008) reported that abnormal attenuating area in the surrounding parenchyma may reflect the earlier feature of parenchymal invasion. Multiphase, contrast-enhanced MDCT is currently the primary imaging modality for evaluation of candidates for surgical resection of pancreas. Locally recurrent IPMN of the pancreas tend to be either extrapancreatic and solid at the resection margin or intrapancreatic and cystic (Christensen et al. 2004). MDCT can detect most recurrent IPMN of the pancreas with moderate to substantial interobserver agreement (Christensen et al. 2004).

MRI with MRCP can potentially provide better depiction of ductal communication with CT (Kalb et al. 2009). Secretin administration may enhance the

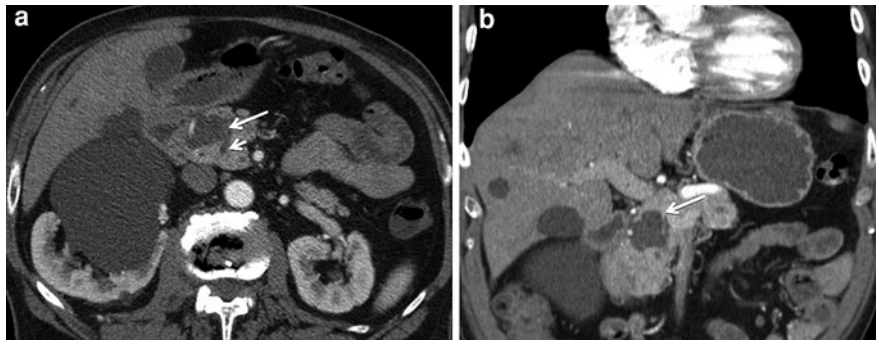

Fig. 8 Branch type IPMN. Axial (**a**) and coronal (**b**) contrast-enhanced MDCT images show a cystic mass in the head of pancreas (*long arrow*), communicating with the pancreatic duct (*small arrow*). The pancreatic duct is normal in size. These features are representative of Branch duct IPMN

ability of MRI to visualize this communication. Lack of exposure to ionizing radiation makes MRI a more suitable test for the follow-up of IPMN's.

4.4 Solid and Pseudopapillary Epithelial Neoplasms

Solid-pseudopapillary tumors of the pancreas are uncommon neoplasms with low malignant potential and which most frequently occur in young women (Papavramidis and Papavramidis 2005). SPEN constitutes 1–3% of pancreatic neoplasms and 10–15% of cystic tumors of the pancreas (Butte et al. 2011). This neoplasm is also known by other names including solid and papillary epithelial neoplasm, solid and cystic tumor, papillary–cystic neoplasm of the pancreas, Frantz tumor and Hamoudi tumor (Hamoudi et al. 1970). In 1996, the World Health Organization renamed this tumor as solid-pseudopapillary and this name is now uniformly accepted (Kloppel et al. 1996). A more aggressive course has been reported in approximately 10–20% of patients with locally advanced tumors at the time of presentation, distant metastases and local or distant recurrence (Papavramidis and Papavramidis 2005; Reddy and Wolfgang 2009). In recent years, there has been a reported increase in the number of cases of SPEN. This increase probably reflects an increase in incidental diagnosis associated with better quality imaging studies (Machado et al. 2008). Most common symptoms are abdominal pain and jaundice. Some patients are asymptomatic and SPEN is discovered incidentally. On histopathology, SPENs are well-circumscribed, large masses with a pseudocapsule of compressed pancreatic tissue and fibrous change. They frequently show extensive hemorrhage and necrotic changes that result in its inhomogeneous texture (Buetow et al. 1996). A mixture of solid, cystic and necrotic areas can be found in the tumor. Treatment is surgical resection and there is a low chance of recurrence following surgery (Butte et al. 2011).

CT findings reflect the histopathologic features of the tumor and include a well-defined mass with varying degrees of solid and cystic components depending on the degree of necrosis and degeneration of the tumor (Fig. 9) (Kawamoto et al. 2011). Less commonly, they can be mostly cystic or mostly solid and may mimic MCN and pancreatic adenocarcinoma (Kawamoto et al. 2011). The attenuation of the cystic areas is usually higher in SPEN compared to other cystic neoplasms (Kawamoto et al. 2011). Solid areas are usually located in the periphery of the tumor, and cystic areas are usually located centrally (Buetow et al. (1996); Friedman et al. 1985; Dong et al. 1996). CT numbers in cystic regions vary from fluid attenuation equal to that of water to soft tissue attenuation in areas rich in blood (Buetow et al. 1996; Friedman et al. 1985). Fluid-debris levels corresponding to cystic hemorrhagic cavities have been reported on CT, MR imaging and ultrasound. In a study by Buetow et al. 1996 16 of 56 patients (29%) had calcifications. There may be dense, peripheral rim calcifications or central stippled calcifications (Buetow et al. 1996; Friedman et al. 1985; Dong et al. 1996; Ohtomo et al. 1992). Some SPENs may demonstrate atypical manifestations such as upstream pancreatic ductal dilatation mimicking pancreatic adenocarcinoma (Kawamoto et al. 2011). Liver metastases can be seen in a small number of cases (Choi et al. 2006). Invasion into the adjacent normal pancreatic parenchyma, adjacent organs or vascular structures, may also be seen on CT (Choi et al. 2006). Rarely, SPEN of the

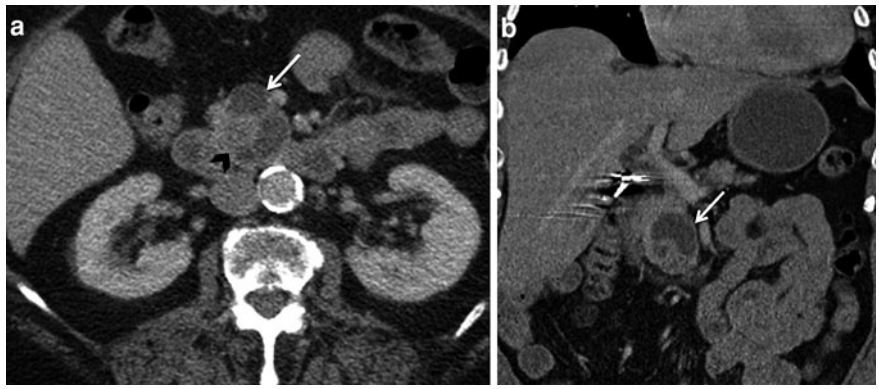

Fig. 9 SPEN. Contrast-enhanced axial (**a**) and coronal (**b**) MDCT images show a heterogeneous, predominantly cystic mass (*arrow*) with solid component (*arrowhead*) in the head of pancreas

pancreas may present acutely with rupture of the capsule and resulting hemoperitoneum, and those patients may require urgent surgery (Mao et al. 1995). Compared with large solid-pseudopapillary tumors, small SPENs (≤3 cm in diameter) have different imaging features; small SPENs usually appear as completely solid tumors with a sharp margin and gradual enhancement (Baek et al. 2010).

4.5 Cystic Pancreatic Neuroendocrine Tumors

Cystic pancreatic neuroendocrine tumors (CPNT) are typically considered as an uncommon subgroup of pancreatic neuroendocrine tumors; however, recent data shows that they are more common than previously thought and should be included in the differential diagnosis of the cystic lesions of the pancreas (Bordeianou et al. 2008). CPNT's are usually nonfunctional although cystic gastrinomas, insulinomas and glucagonomas are occasionally reported (Goh et al. 2006; Ligneau et al. 2001). These tumors are associated with hereditary multiple endocrine neoplasia syndrome (most commonly MEN-1). Suspicion of CPNT should be very high in a patient with a personal or family history of MEN-1 Syndrome. They are usually well described and exhibit either a unilocular cyst or a multilocular cystic pattern (Basturk et al. 2009). The cysts are lined with neoplastic endocrine cells and filled with serosanguineous fluid instead of necrotic debris (Basturk et al. 2009). Cyst formation in neuroendocrine tumors is believed to be secondary to tumor degeneration. Their malignant behavior is not as high as their solid counterparts despite their large size. Treatment includes surgical resection and the prognosis of patients with CPNT is usually good with overall five year survival of 87% (Bordeianou et al. 2008).

On CT, CPNT's appear as well-defined mixed solid-cystic or purely cystic tumors (Fig. 10) (Bordeianou et al. 2008; Goh et al. 2006; Ligneau et al. 2001). They can be unilocular or multilocular cysts with thick walls and internal septations. Solid portion of the tumor (when present) demonstrates intense contrast enhancement. Due to their non-specific imaging features, they are difficult to differentiate from other CPN and pseudocysts, especially if they are not hormonally functional (Ahrendt et al. 2002). Preoperative diagnosis of CPNT could only be made in 3/13 patients (23%) with CT (Bordeianou et al. 2008). In this series, one patient presented with ductal obstruction without a visible mass and all other CT scans revealed neoplasms which are partially cystic with or without a solid component (Bordeianou et al. 2008; Goh et al. 2006; Ligneau et al. 2001). Calcifications were rarely present.

4.6 Solid Tumors Mimicking PCN

Solid tumors such as pancreatic adenocarcinoma and acinar cell carcinoma can present as cystic or mixed solid-cystic lesions Three mechanisms have been suggested for the development of this uncommon phenomenon in pancreatic adenocarcinoma: Necrosis of the tumor, cystic dilatation of the obstructed ducts by the tumor and an uncommon variant of ductal adenocarcinoma referred to as large duct type (Fig. 11). (Adsay and Klimstra 2000). This variant is characterized by microcystic ectasia of the invasive gland, sometimes achieving the size of grossly visible

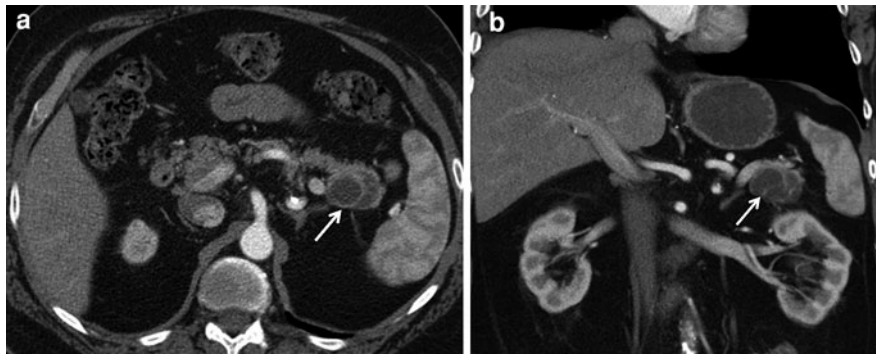

Fig. 10 Non-functional cystic neuroendocrine neoplasm. Contrast-enhanced MDCT axial (**a**) and coronal (**b**) images demonstrate a complex cystic mass (*arrows*) in the tail of the pancreas with thick internal septations

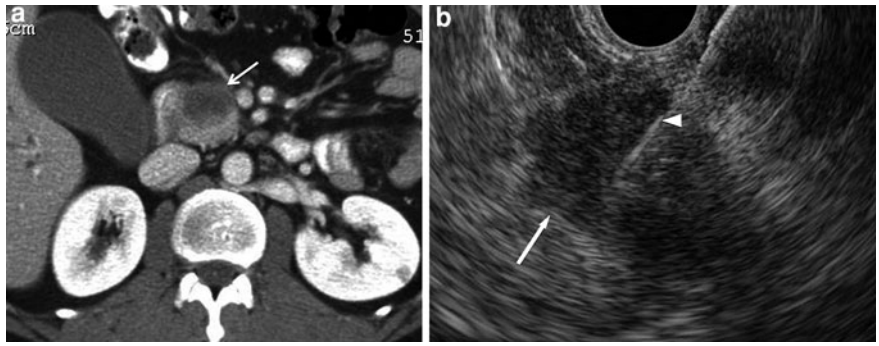

Fig. 11 Adenocarcinoma of the pancreas. Axial MDCT image (**a**) shows a hypoattenuating mass lesion in head of pancreas mimicking a cystic lesion (*arrow*). The mass was biopsied under EUS guidance (**b**). *Arowhead* shows the needle within the mass. The cytology confirmed the diagnosis of adenocarcinoma

cysts (Park et al. 2005). Mucinous adenocarcinoma is another, uncommon variant of (about 2% of non-endocrine pancreatic malignancies) of pancreatic duct cell origin (Cohen-Scali et al. 2003). It is characterized by large amount of mucin and histologically is composed of large cystic spaces filled with mucin and surrounded by connective tissue (Park et al. 2005). It is important to differentiate central necrosis of pancreatic adenocarcinoma from a cystic neoplasm since treatment options can be different and delay in diagnosis may lead to an important delay in the surgical treatment of pancreatic adenocarcinoma.

Acinar cell carcinomas are rare pancreatic tumors characterized by pancreatic enzyme production by the tumor cells. It occurs more often in women, with peak incidence in seventh decade (Solcia et al. 1997). They represent approximately 1% of exocrine pancreatic tumors (Solcia et al. 1997). They are relatively aggressive tumors with prognosis better than adenocarcinoma but worse than neuroendocrine tumors (Klimstra et al. 1992). Surgery is the treatment of choice. Pure acinar cell carcinoma of the pancreas is usually an exophytic, oval or round, well-marginated and hypovascular mass on CT and MRI (Fig. 12) (Tatli et al. 2004). Typically, it is completely solid when small and contains cystic areas due to necrosis when large (Tatli et al. 2004). Partial or complete enhancing capsules were also reported surrounding these tumors (Hsu et al. 2010). Central necrosis is common and may be responsible for the cystic appearance of the tumor. Occasional central hemorrhage and calcifications have also been reported (Hsu et al. 2010).

4.7 Pseudocysts and Other Rare Benign Mimicks of PCN

A number of non-neoplastic cystic lesions can mimic PCN. Pseudocysts are the most common cystic lesions of the pancreas accounting for approximately 75% of pancreatic cysts (Kloppel 2000). They are fully encapsulated pancreatic fluid collections, usually located within or adjacent to the pancreas and require at least four weeks to develop following acute pancreatitis (Balthazar 2002). Histologically, the pseudocyst wall is non-epithelialized, and composed of granulation or fibrotic tissue and contains amylase-rich,

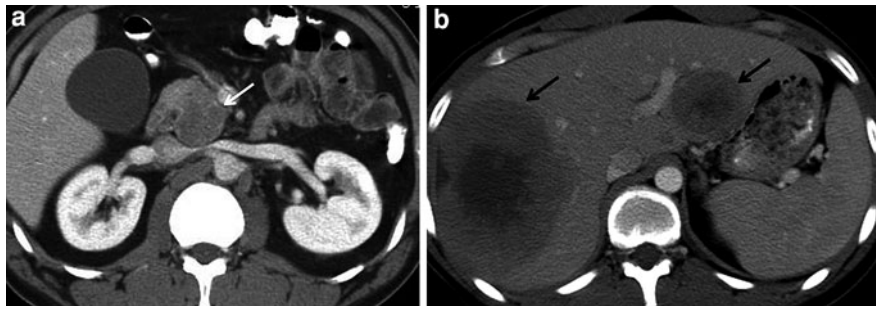

Fig. 12 Acinar cell carcinoma. Contrast-enhanced MDCT axial images (**a** and **b**) show a low density mass in head of pancreas mimicking a cystic mass (*white arrow*) with multiple liver metastasis (*black arrows*). It was confirmed to be an acinar cell carcinoma on histopathology

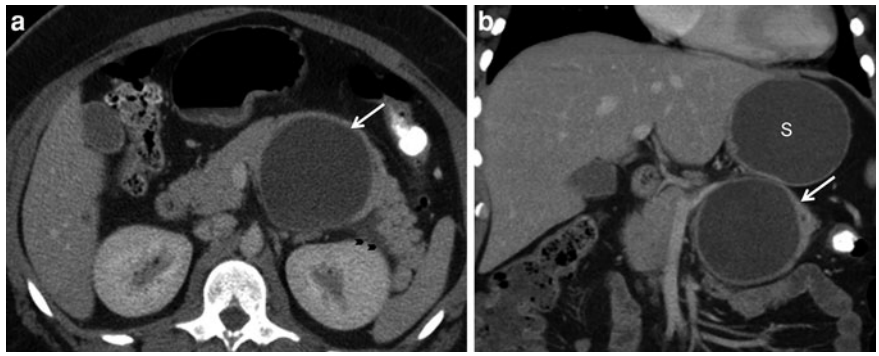

Fig. 13 Pseudocyst. Contrast-enhanced MDCT axial (**a**) and coronal (**b**) images reveal a well-circumscribed, unilocular, thick walled pseudocyst (*arrows*) in the body of the pancreas. Stomach is designated by "s" on the coronal view

possibly hemorrhagic debris (Balthazar 2002). Previous or ongoing history of acute pancreatitis is very helpful for diagnosis. They develop as a complication of alcoholic, biliary or traumatic acute pancreatitis. The clinical diagnosis of pseudocyst is straightforward; however, occasionally, they have to be differentiated from neoplastic cysts. The primary mimic of pseudocyst is mucinous cystadenoma and there may be significant overlap of imaging features between two entities, especially when pseudocyst is intrapancreatic in location (Kalb et al. 2009). Pancreatic pseudocysts may dissect along abdominopelvic fascia remote from pancreas and fistulization may occur between a pseudocyst and organs or vascular structures (Kalb et al. 2009). Typical symptoms include epigastric pain and an abdominal mass, along with clinical sequela of gastric outlet and biliary obstruction (Balthazar 2002). On CT, pseudocysts are round or oval in shape and have a relatively thin or thick capsule, which can calcify (Fig. 13). They contain fluid which is less than 15 Hounsfield units (HU); higher fluid attenuation values of 40–50 HU indicate intracystic hemorrhage (Balthazar 2002). Macari et al. reported that detection of internal, dependent debris within a cystic lesion on MR imaging is a very specific finding for diagnosis of a pseudocyst (Sahani et al. 2006b). Pseudocysts vary significantly in size and may communicate with the pancreatic duct. Surgical or percutaneous drainage is preformed on pseudocysts larger than 5 cm and older than six weeks, along with enlarging, symptomatic or infected pseudocysts (Balthazar 2002).

Other non-neoplastic cystic lesions include retention cysts, benign epithelial cysts, abscesses, duodenal wall cysts, duodenal diverticuli, lymphoepithelial cysts, foregut cyts and mucinous non-neoplastic cyst (Kosmahl et al. 2004). Lymphoepithelial cysts are rare lesions, constituting about 0.5% of pancreatic cysts, which predominately occur in middle age men (mean age, 55; M/F: 4:1) (Adsay et al. 2002). On CT, pancreatic lesions are well-circumscribed low-attenuation masses with a thin enhancing rim; septations and focal calcification are often present (Fig. 14) (Kim et al. 1998). Intracystic contents usually measure 20–30 HU due to high levels of keratin (Kim et al. 1998). No recurrences or malignant degeneration of lymphoepithelial cysts are reported in the literature (Adsay et al. 2002). However, given the difficulty in making a confident preoperative

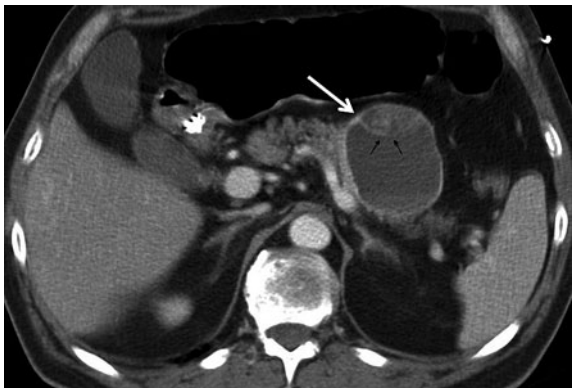

Fig. 14 Lymphoepithelial cyst. Contrast-enhanced MDCT axial view shows a cystic mass (*arrow*) in the body/tail of pancreas with internal septations and soft tissue component (*small black arrows*). This lesion was found to be a lymhoepithelial cyst after resection

diagnosis most are treated with surgical resection (Adsay et al. 2002). Mucinous non-neoplastic cysts are a recently described entity by Kosmahl et al. (2002). Microscopically, these cysts are characterized by mucinous differentiation of lining epithelium, lack of cellular atypia or increased proliferation, and a thin rim of supporting, almost acellular, stroma (Kosmahl et al. 2002). On imaging, MNCs appear as circumscribed unilocular or multilocular fluid collections, which do not communicate with the pancreatic duct. Cysts range in size from 3–12 cm and usually occur in the pancreatic head (Kosmahl et al. 2002).

References

Adsay NV, Klimstra DS (2000) Cystic forms of typically solid pancreatic tumors. Semin Diagn Pathol 17(1):81–88

Adsay NV, Hasteh F, Cheng JD et al (2002) Lymphoepithelial cysts of the pancreas: a report of 12 cases and a review of the literature. Mod Pathol 15:492–501

Ahmad NA, Kochman ML, Lewis JD, Ginsberg GG (2001) Can EUS alone differentiate between malignant and benign cystic lesions of the pancreas? Am J Gastroenterol 96:3295–3300

Ahrendt SA, Komorowski RA, Demeure MJ, Wilson SD, Pitt HA (2002) Cystic pancreatic neuroendocrine tumors: is preoperative diagnosis possible? J Gastrointest Surg 6(1):66–74

Azar C, Van de Stadt J, Rickaert F et al (1996) Intraductal papillary mucinous tumours of the pancreas. Clinical and therapeutic issues in 32 patients. Gut 39(3):457–464

Baek JH, Lee JM, Kim SH et al (2010) Small (< or =3 cm) solid pseudopapillary tumors of the pancreas at multiphasic multidetector CT. Radiology 257(1):97–106

Balcom JH IV, Fernandez-Del Castillo C, Warshaw AL (2000) Cystic lesions in the pancreas: when to watch, when to resect. Curr Gastroenterol Rep 2(2):152–158

Balthazar EJ (2002) Complications of acute pancreatitis: clinical and CT evaluation. Radiol Clin North Am 40:1211–1227

Bassi C, Salvia R, Molinari E, Biasutti C, Falconi M, Pederzoli P (2003) Management of 100 consecutive cases of pancreatic serous cystadenoma: wait for symptoms and see at imaging or vice versa? World J Surg 27:319–323

Bassi C, Sarr MG, Lillemoe KD, Reber HA (2008) Natural history of intraductal papillary mucinous neoplasms (IPMN): current evidence and implications for management. J Gastrointest Surg 12:645–650

Basturk O, Coban I, Adsay NV (2009) Pancreatic cysts: pathologic classification, differential diagnosis, and clinical implications. Arch Pathol Lab Med 133(3):423–438

Berland LL, Silverman SG, Gore RM, Mayo-Smith WW et al (2010) Managing incidental findings on abdominal CT: white paper of the ACR incidental findings committee. J Am Coll Radiol 7(10):754–773

Biankin AV, Kench JG, Biankin SA et al (2004) Pancreatic intraepithelial neoplasia in association with intraductal papillary mucinous neoplasms of the pancreas: implications for disease progression and recurrence. Am J Surg Pathol 28:1184–1192

Bordeianou L, Vagefi PA, Sahani D et al (2008) Cystic pancreatic endocrine neoplasms: a distinct tumor type? Am Coll Surg 206(3):1154–1158

Brugge WR, Lewandrowski K, Lee-Lewandrowski E et al (2004a) Diagnosis of pancreatic cystic neoplasms: a report of the cooperative pancreatic cyst study. Gastroenterology 126:1330–1336

Brugge WR, Lauwers GY, Sahani D, Fernandez-del Castillo C, Warshaw AL (2004b) Cystic neoplasms of the pancreas. MDN Engl J Med 351:1218–1226

Buetow PC, Buck JL, Pantongrag-Brown L, Beck KG, Ros PR, Adair CF (1996) Solid and papillary epithelial neoplasm of the pancreas: imaging-pathologic correlation on 56 cases. Radiology 199(3):707–711

Butte JM, Brennan MF, Gönen M et al (2011) Solid pseudopapillary tumors of the pancreas. Clinical features, surgical outcomes, and long-term survival in 45 consecutive patients from a single center. J Gastrointest Surg 15(2):350–357

Carbognin G, Pinali L, Girardi V, Casarin A, Mansueto G, Mucelli RP (2007) Collateral branches IPMTs: secretin-enhanced MRCP. Abdom Imag 32:374–380

Choi JY, Kim MJ, Kim JH et al (2006) Solid pseudopapillary tumor of the pancreas: typical and atypical manifestations. AJR Am J Roentgenol 187(2):W178–W186

Choi JY, Kim MJ, Lee JY, Lim JS, Chung JJ, Kim KW, Yoo HS (2009) Typical and atypical manifestations of serous cystadenoma of the pancreas: imaging findings with pathologic correlation. Am J Roentgenol 193(1):136–142

Christensen JA, Fletcher JG, Fidler JL et al (2004) Intraductal papillary mucinous neoplasms of the pancreas: CT patterns of recurrence and multiobserver performance in detecting recurrent neoplasm after surgical resection. Am J Roentgenol 183(5):1367–1374

Cohen-Scali F, Vilgrain V, Brancatelli G et al (2003) Discrimination of unilocular macrocystic serous cystadenoma from

pancreatic pseudocyst and mucinous cystadenoma with CT: initial observations. Radiology 228(3):727–733

Colonna J, Plaza JA, Frankel WL, Yearsley M, Bloomston M, Marsh WL (2008) Serous cystadenoma of the pancreas: clinical and pathological features in 33 patients. Pancreatology 8:135–141

Curry CA, Eng J, Horton KM, Urban B, Siegelman S, Kuszyk BS, Fishman EK (2000) CT of primary cystic pancreatic neoplasms: can CT be used for patient triage and treatment? Am J Roentgenol 175(1):99–103

D'Angelica M, Brennan MF, Suriawinata AA, Klimstra D, Conlon KC (2004) Intraductal papillary mucinous neoplasms of the pancreas: an analysis of clinicopathologic features and outcome. Ann Surg 239:400–408

Dong PR, Lu DS, Degregario F, Fell SC, Au A, Kadell BM (1996) Solid and papillary neoplasm of the pancreas: radiological–pathological study of five cases and review of the literature. Clin Radiol 51:702–705

Fernandez-del Castillo C, Warshaw AL (2000) Current management of cystic neoplasms of the pancreas. Adv Surg 34:237–248

Friedman AC, Lichtenstein JE, Fishman EK, Oertel JE, Dachman AH, Siegelman SS (1985) Solid and papillary epithelial neoplasm of the pancreas. Radiology 154:333–337

Garcea G, Ong SL, Rajesh A, Neal CP, Pollard CA, Berry DP, Dennison AR (2008) Cystic lesions of the pancreas. A diagnostic and management dilemma. Pancreatology 8(3): 236–251

Goh BK, Ooi LL, Kumarasinghe MP et al (2006) Clinicopathological features of patients with concomitant intraductal papillary mucinous neoplasm of the pancreas and pancreatic endocrine neoplasm. Pancreatology 6(6): 520–526

Gomez D, Rahman SH, Wong LF et al (2008) Predictors of malignant potential of cystic lesions of the pancreas. Eur J Surg Oncol 34:876–882

Gourgiotis S, Ridolfini MP, Germanos S (2007) Intraductal papillary mucinous neoplasms of the pancreas. Eur J Surg Oncol 33(6):678–684

Hamilton SR, Aaltonen LA (2000) Pathology and genetics of tumours of the digestive system. World Health Organization classification of tumours, vol 2. IARC Press, Lyon

Hamoudi AB, Misugi K, Grosfeld JL, Reiner CB (1970) Papillary epithelial neoplasm of pancreas in a child. Report of a case with electron microscopy. Cancer 26: 1126–1134

Handrich SJ, Hough DM, Fletcher JG, Sarr MG (2005)The natural history of the incidentally discovered small simple pancreatic cyst: long-term follow-up and clinical implications. Am J Roentgenol 184(1):20–23

Hsu MY, Pan KT, Chu SY, Hung CF, Wu RC, Tseng JH (2010) CT and MRI features of acinar cell carcinoma of the pancreas with pathological correlations. Clin Radiol 65(3):223–229

Huang ES, Gazelle GS, Hur C (2010) Consensus guidelines in the management of branch duct intraductal papillary mucinous neoplasm: a cost-effectiveness analysis. Dig Dis Sci 55(3):852–860

Javle M, Shah P, Yu J et al (2007) Cystic pancreatic tumors (CPT): predictors of malignant behavior. J Surg Oncol 95:221–228

Kalb B, Sarmiento JM, Kooby DA, Adsay NV, Martin DR (2009) MR imaging of cystic lesions of the pancreas. Radiographics 29(6):1749–1765

Kawamoto S, Horton KM, Lawler LP, Hruban RH, Fishman EK (2005) Intraductal papillary mucinous neoplasm of the pancreas: can benign lesions be differentiated from malignant lesions with multidetector CT? Radiographics 25(6): 1451–1468

Kawamoto S, Lawler LP, Horton KM, Eng J, Hruban RH, Fishman EK (2006) MDCT of intraductal papillary mucinous neoplasm of the pancreas: evaluation of features predictive of invasive carcinoma. Am J Roentgenol 186(3): 687–695

Kawamoto S, Scudiere J, Hruban RH, Wolfgang CL, Cameron JL, Fishman EK (2011) Solid-pseudopapillary neoplasm of the pancreas: spectrum of findings on multidetector CT. Clin Imaging 35(1):21–28

Kerlin DL, Frey CF, Bodai BI, Twomey PL, Ruebner B (1987) Cystic neoplasms of the pancreas. Surg Gynecol Obstet 165:475–478

Kim YH, Auh YH, Kim KW et al (1998) Lymphoepithelial cysts of the pancreas: CT and sonographic findings. Abdom Imag 23:185–187

Kim SY, Lee JM, Kim SH et al (2006). Macrocystic neoplasms of the pancreas: CT differentiation of serous oligocystic adenoma from mucinous cystadenoma and intraductal papillary mucinous tumor. Am J Roentgenol 187(5): 1192–1198

Kim HJ, Lee DH, Ko YT, Lim JW, Kim HC, Kim KW (2008) CT of serous cystadenoma of the pancreas and mimicking masses. Am J Roentgenol 190:406–412

Kimura W, Nagai H, Kuroda A, Muto T, Esaki Y (1995) Analysis of small cystic lesions of the pancreas. Int J Pancreatol 18(3):197–206

Klimstra DS, Heffess CS, Oertel JE, Rosai J (1992) Acinar cell carcinoma of the pancreas: a clinicopathologic study of 28 cases. Am J Surg Pathol 16:815–837

Kloppel G (2000) Pseudocysts and other non-neoplastic cysts of the pancreas. Semin Diagn Pathol 17:7–15

Kloppel G, Solcia E, Longnecker DS, Capella C, Sobin LH (1996) Histological typing of tumours of the exocrine pancreas, World Health Organization, International histological classification of tumours, 2nd edn. Springer, Berlin

Kobari M, Egawa S, Shibuya K et al (1999) Intraductal papillary mucinous tumors of the pancreas comprise 2 clinical subtypes: differences in clinical characteristics and surgical management. Arch Surg 134:1131–1136

Kosmahl M, Egawa N, Schroder S et al (2002) Mucinous nonneoplastic cyst of the pancreas: a novel nonneoplastic cystic change? Mod Pathol 15:154–1583

Kosmahl M, Pauser U, Peters K et al (2004) Cystic neoplasms of the pancreas and tumor-like lesions with cystic features: a review of 418 cases and a classification proposal. Virchows Arch 445:168–178

Ligneau B, Lombard-Bohas C, Partensky C et al (2001) Cystic endocrine tumors of the pancreas: clinical, radiologic, and histopathologic features in 13 cases. Am J Surg Pathol 25(6):752–760

Macari M, Finn ME, Bennett GL, Cho KC, Newman E, Hajdu CH, Babb JS (2009) Differentiating pancreatic cystic

neoplasms from pancreatic pseudocysts at MR imaging: value of perceived internal debris. Radiology 251(1):77–84
Machado MC, Machado MA, Bacchella T, Jukemura J, Almeida JL, Cunha JE (2008) Solid pseudopapillary neoplasm of the pancreas: distinct patterns of onset, diagnosis, and prognosis for male versus female patients. Surgery 143(1):29–34
Mao C, Guvendi M, Domenico DR, Kim K, Thomford NR, Howard JM (1995) Papillary cystic and solid tumors of the pancreas: a pancreatic embryonic tumor? Studies of three cases and cumulative review of the world's literature. Surgery 118:821–828
Minami M, Itai Y, Ohtomo K, Yoshida H, Yoshikawa K, Iio M (1989) Cystic neoplasms of the pancreas: comparison of MR imaging with CT. Radiology 171:53–56
Mohr VH, Vortmeyer AO, Zhuang Z, Libutti SK et al (2000) Histopathology and molecular genetics of multiple cysts and microcystic (serous) adenomas of the pancreas in von Hippel-Lindau patients. Am J Pathol 157(5):1615–1621
Nguyen GK, Suen KC, Villanueva RR (1997) Needle aspiration cytology of pancreatic cystic lesions. Diagn Cytopathol 17:177–182
Ogawa H, Itoh S, Ikeda M, Suzuki K, Naganawa S (2008) Intraductal papillary mucinous neoplasm of the pancreas: assessment of the likelihood of invasiveness with multisection CT. Radiology 248(3):876–886
Ohashi K, Mirukami Y, Muruyama M et al (1982) Four cases of mucus secreting pancreas cancer. Prog Dig Endosc 20:348–351
Ohtomo K, Furui S, Onoue M, Okada Y, Kusano S, Shiga J, Suda K (1992) Solid and papillary epithelial neoplasm of the pancreas: MR imaging and pathologic correlation. Radiology 184:567–570
Papavramidis T, Papavramidis S (2005) Solid pseudo papillary tumors of the pancreas: review of 718 patients reported in English literature. J Am Coll Surg 200(6):965–972
Park MS, Kim KW, Lim JS et al (2005) Unusual cystic neoplasms in the pancreas: radiologic-pathologic correlation. J Comput Assist Tomogr 29(5):610–616
Phillips K, Fleming JB, Tamm EP et al (2008) Unusual pancreatic tumors. In: Cameron JL (ed) Current surgical therapy, 9th edn. Moby Elsevier, Philadelphia, pp 524–529
Pitman MB, Lewandrowski K, Shen J, Sahani D, Brugge W, Fernandez-del Castillo C (2010) Pancreatic cysts: preoperative diagnosis and clinical management. Cancer Cytopathol 118(1):1–13
Procacci C, Graziani R, Bicego E et al (1997) Serous cystadenoma of the pancreas: report of 30 cases with emphasis on the imaging findings. J Comput Assist Tomogr 21:373–382
Procacci C, Biasiutti C, Carbognin G et al (1999) Characterization of cystic tumors of the pancreas: CT accuracy. J Comput Assist Tomogr 23:906–912
Procacci C, Carbognin G, Accordini S et al (2001) CT features of malignant mucinous cystic tumors of the pancreas. Eur Radiol 11:1626–1630
Rautou PE, Levy P, Vullierme MP et al (2008) Morphologic changes in branch duct intraductal papillary mucinous neoplasms of the pancreas: a midterm follow-up study. Clin Gastroenterol Hepatol 6:807–814
Reddy S, Wolfgang CL (2009) Solid pseudopapillary neoplasms of the pancreas. Adv Surg 43:269–282
Sahani DV, Kadavigere R, Saokar A, Fernandez-del Castillo C, Brugge WR, Hahn PF (2005) Cystic pancreatic lesions: a simple imaging-based classification system for guiding management. Radiographics 25(6):1471–1484
Sahani DV, Saokar A, Hahn PF, Brugge WR, Fernandez-Del Castillo C (2006a) Pancreatic cysts 3 cm or smaller: how aggressive should treatment be? Radiology 238(3):912–919
Sahani DV, Kadavigere R, Blake M, Fernandez-Del Castillo C, Lauwers GY, Hahn PF (2006b) Intraductal papillary mucinous neoplasm of pancreas: multi-detector row CT with 2D curved reformations—correlation with MRCP. Radiology.238(2):560–9
Sainani NI, Saokar A, Deshpande V, Fernández-del Castillo C, Hahn P, Sahani DV (2009) Comparative performance of MDCT and MRI with MR cholangiopancreatography in characterizing small pancreatic cysts. Am J Roentgenol 193:722–731
Salvia R, Fernandez-del Castillo C, Bassi C et al (2004) Main-duct intraductal papillary mucinous neoplasms of the pancreas: clinical predictors of malignancy and long-term survival following resection. Ann Surg 239:678–687
Scott J, Martin I, Redhead D, Hammond P, Garden OJ (2000) Mucinous cystic neoplasms of the pancreas: imaging features and diagnostic difficulties. Clin Radiol 55(3):187–192
Solcia E, Capella C, Kloppel G (1997) Tumors of the exocrine pancreas. In: Rosai J, Sorbin L (eds) Atlas of tumor pathology, 3rd series, fasc. 20 Armed Forces Institute of Pathology, Washington, pp 31–144
Sperti C, Pasquali C, Chierichetti F, Liessi G, Ferlin G, Pedrazzoli S (2001) Value of 18-fluorodeoxyglucose positron emission tomography in the management of patients with cystic tumors of the pancreas. Ann Surg 234:675–680
Sperti C, Bissoli S, Pasquali C, Frison L, Liessi G, Chierichetti F, Pedrazzoli S (2007) 18-fluorodeoxyglucose positron emission tomography enhances computed tomography diagnosis of malignant intraductal papillary mucinous neoplasms of the pancreas. Ann Surg 246(6):932–937
Spinelli KS, Fromwiller TE, Daniel RA, Kiely JM, Nakeeb A, Komorowski RA, Wilson SD, Pitt HA (2004) Cystic pancreatic neoplasms: observe or operate. Ann Surg 239(5):651–657. Discussion 657–659
Stelow EB, Stanley MW, Bardales RH et al (2003) Intraductal papillary-mucinous neoplasm of the pancreas. The findings and limitations of cytologic samples obtained by endoscopic ultrasound-guided fine needle aspiration. Am J Clin Pathol 120:398–404
Sugiyama M, Atomi Y (1999) Extrapancreatic neoplasms occur with unusual frequency in patients with intraductal papillary mucinous tumors of the pancreas. Am J Gastroenterol 94:470–473
Sugiyama M, Izumisato Y, Abe N, Masaki T, Mori T, Atomi Y (2003) Predictive factors for malignancy in intraductal papillary-mucinous tumours of the pancreas. Br J Surg 90(10):1244–1249
Tanaka M, Chari S, Adsay V et al (2006) International consensus guidelines for management of intraductal papillary mucinous neoplasms and mucinous cystic neoplasms of the pancreas. Pancreatology 6:17–32

Taouli B, Vilgrain V, Vullierme MP et al (2000) Intraductal papillary mucinous tumors of the pancreas: helical CT with histopathologic correlation. Radiology 217(3):757–764

Tatli S, Yucel EK, Lipton MJ (2004) CT and MR imaging of the thoracic aorta: current techniques and clinical applications. Radiol Clin North Am 42(3):565–585

Tseng JF, Warshaw AL, Sahani DV, Lauwers GY, Rattner DW, Fernandez-del Castillo C (2005) Serous cystadenoma of the pancreas: tumor growth rates and recommendations for treatment. Ann Surg 242(3):413–419

Verbesey JE, Munson JL (2010) Pancreatic cystic neoplasms. Surg Clin North Am 90(2):411–425

Vullierme MP, Giraud-Cohen M, Hammel P et al (2007) Malignant intraductal papillary mucinous neoplasm of the pancreas: in situ versus invasive carcinoma surgical resectability. Radiology 245(2):483–490

Waters JA, Schmidt CM, Pinchot JW et al (2008) CT vs MRCP: optimal classification of IPMN type and extent. J Gastrointest Surg 12:101–109

Yasuhara Y, Sakaida N, Uemura Y, Senzaki H, Shikata N, Tsubura A (2002) Serous microcystic adenoma (glycogen-rich cystadenoma) of the pancreas: study of 11 cases showing clinicopathological and immunohistochemical correlations. Pathol Int 52:307–312

Imaging CT of the Spleen

Giovanni Morana and Christian Cugini

Contents

G. Morana (✉) · C. Cugini
Radiological Department,
General Hospital Ca' Foncello,
Piazza Ospedale 1,
31100 Treviso, Italy
e-mail: gmorana@ulss.tv.it

Abstract

The spleen is an intraperitoneal organ which is composed of a trabecular network of vessels, nerves and lymphatic tissue. Anatomical variants with regard to the shape and accessory spleens are seen. Systemic lymphatic diseases often result in splenomegaly. There are a number of different focal cystic or solid lesions, which can be found in the spleen in various pathological conditions. These are often inflammatory, but also neoplastic or developmental lesions are found. The following chapter will present the most common focal and diffuse pathologies of the spleen with special emphasis on their CT appearance.

1 Normal Anatomy and Variant

The spleen is an intraperitoneal organ with a smooth serosal surface normally located in the left upper quadrant of the abdomen, supported by the gastrosplenic ligaments. The capsule is penetrated at the hilus by blood vessels, lymphatics, and nerves. Branches of arteries, veins, nerves, and lymphatics travel through the spleen in the trabecular network (Weiss 1983). The spleen contains two distinct tissues: red pulp and white pulp. There is a large volume of erythrocytes within the red pulp owing to the four types of vascular structures within the pulp. The red pulp is composed of slender and nonanastomosing arterial vessels, thin-walled venous vessels called splenic sinuses, plates of cells called splenic cords that lie between sinusoids, and red pulp veins that drain the sinusoids (Warnke et al. 1995).

C. J. Zech et al. (eds.), *Multislice-CT of the Abdomen*, Medical Radiology. Diagnostic Imaging,
DOI: 10.1007/174_2011_426, © Springer-Verlag Berlin Heidelberg 2012

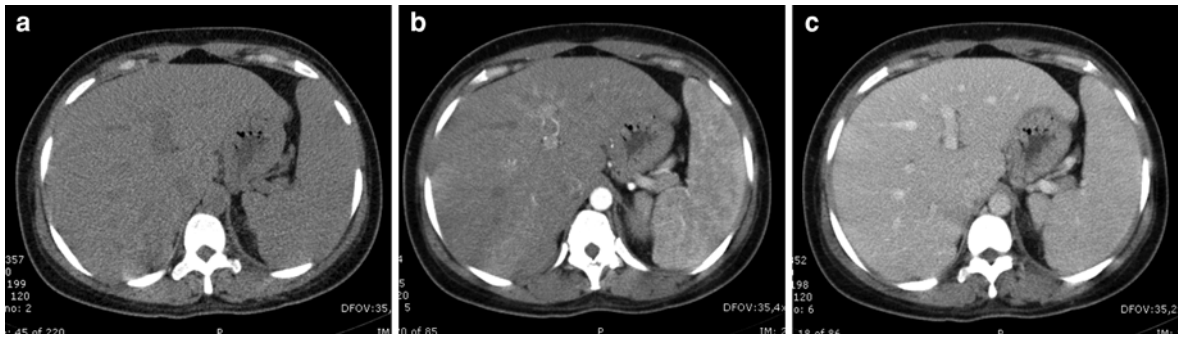

Fig. 1 Normal spleen. MDCT, arterial (**a**), venous (**b**) and distribution phase (**c**). During arterial phase (**a**), the spleen shows an inhomogeneous pattern of splenic attenuation, reflecting variable blood flow within different compartments of the spleen; during the venous (**b**) and distribution phase (**c**), the spleen shows an homogeneous enhancement

The white pulp is composed of lymphatic tissue. The organization of lymphoid cells within the white pulp is similar to that found in the cortex of a lymph node. T cells are usually found in the periarteriolar sheath, and B cells are found in primary and secondary follicles. Lymphoid follicles (malpighian corpuscles) have a central artery that is surrounded by a germinal center, mantle zone, and marginal zone. The marginal zone is the transition between the red and white pulp. In normal condition the spleen measures approximately 12 cm in length, 7 cm in AP diameter, and 4 cm in thickness. However, due to high variability in the shape of the spleen, these measurements are not useful in evaluating splenic size. A more accurate approach to the assessment of splenic volume is the splenic index, a product of length, width and thickness of the spleen, expressed in centimeters. Length is determined by summing the number of contiguous sections on which the spleen is visible or more simpler the caudo-cranial length in coronal reconstruction. Width is the longest splenic diameter in the transverse image. Thickness is the distance between the inner and outer borders of the spleen, as measured at the level of the splenic hilum (normal splenic size corresponds to an index of 120–480 cm^3) (Koehler 1989).

On precontrastographic CT images the normal spleen appears homogeneous in attenuation, with values slightly less than those of a normal liver. With rapid intravenous injection of iodinated contrast media, most patients initially exhibit an inhomogeneous pattern of splenic attenuation, reflecting variable blood flow within different compartments of the spleen. Care must be taken not to misinterpret the early postinjection inhomogeneity of splenic attenuation as an indication of focal abnormality. Only after a minute or more does the splenic parenchyma achieve a uniform, homogeneous appearance (Fig. 1).

2 Splenomegaly

Is a condition characterized by a pathological enlargement of the spleen. Can result from congestion (portal hypertension, splenic vein occlusion or thrombosis), infiltrative disease (Gaucher's disease), hematologic disorders (polycitemia vera, myelofibrosis), inflammatory disease (CMV or mycobacterial infections), rheumatic disease, cyst or tumours (leukemia, lymphoma, metastases).

3 Congenital Variations

3.1 Accessory Spleen

An accessory spleen refers to a congenital focus of normal splenic tissue that is separate from the main body of the spleen. Accessory spleens are found in 10–30% of cases at autopsy examination, and their size varies from a few millimeters to several centimeters in diameter. They occur most frequently in the hilar region and usually have no clinical significance. However, if the location is atypical, an accessory spleen may be mistaken for a tumor. After splenectomy, an accessory spleen may enlarge dramatically, sometimes appearing as a left upper quadrant mass or causing recurrence of problems in patients who have

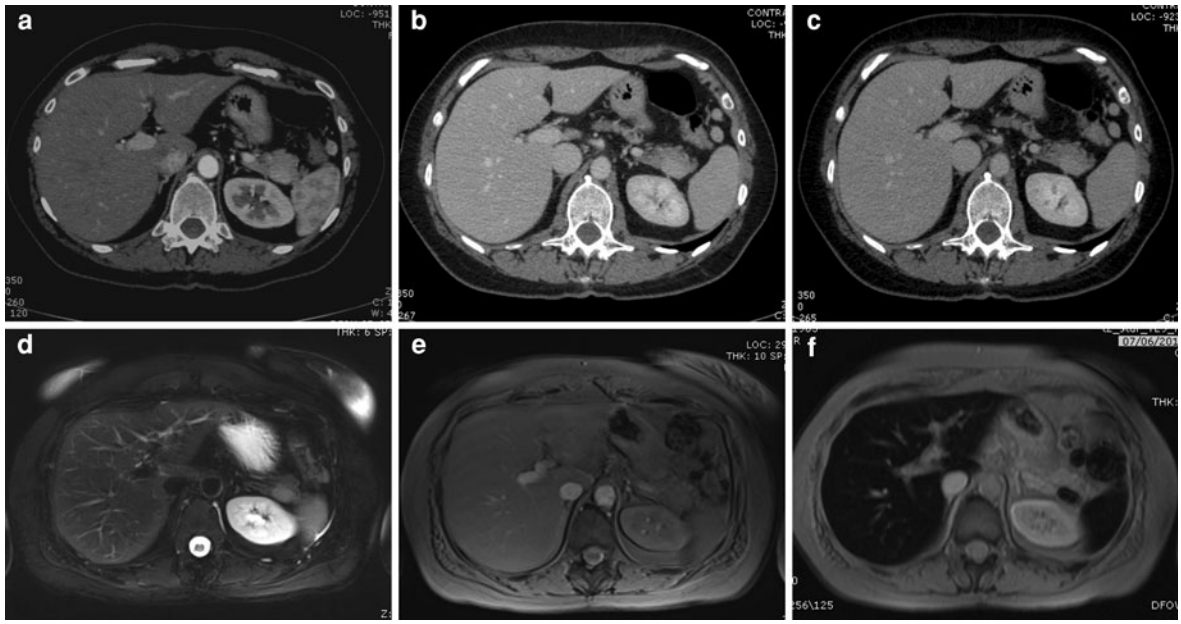

Fig. 2 Intrapancreatic spleen. MDCT, arterial (**a**), venous (**b**) and distribution phase (**c**). During arterial phase (**a**) a hypervascular lesion in the tail of the pancreas can be appreciated, which shows the same contrast enhancement behaviour of the spleen in the different phases. (**d**) MRI, T2w TSE sequence. The lesion has the same signal intensity of the spleen. GRE T2w before (**e**) and after (**f**) SPIO administration. After superparamagnetic CM administration a dramatic signal drop can be appreciated either in the liver and in the spleen and intrapancreatic lesion

undergone splenectomy for hematologic or other disorders. CT is useful in the accurate diagnosis of accessory spleens. Around or ovoid mass near the splenic hilum, with the same attenuation as that of a normal spleen both before and after intravenous administration of contrast material, is virtually pathognomonic. Intrapancreatic location of an accessory spleen can simulate an hypervascular tumor of the pancreas; a CT pattern of contrast enhancement similar to that of the spleen can lead to the suspicious of an accessory spleen: in these cases nuclear scintigraphy with technetium-99 sulfur colloid is useful diagnostically, demonstrating functioning splenic tissue in the area of concern (Rolfes and Ros 1990a, b) or MRI with superparamagnetic contrast media, which demonstrate a decrease of signal intensity of the lesion after contrast media administration (Fig. 2).

3.2 Wandering Spleen

Wandering spleen refers to a normal spleen that does not have its fixed ligamentous attachments and therefore can change position within the abdomen. It may be noticed clinically as an unexplained abdominal mass or as acute abdominal pain secondary to splenic torsion. The etiology is controversial. In many case the origin is related to a congenital abnormal fusion of the posterior mesogastrium (Costello et al. 1985). This condition may be acquired as in multiparous women is described a higher incidence, which suggest an etiologic role of hormonal effects and abdominal laxity associated with pregnancy. Wandering spleen has also been reported in "Prune-belly" syndrome, malaria, Hodgkin's disease and lymphangiomatosis (Solbiati et al. 1983; Balthazar et al. 1985). In patients with a wandering spleen, imaging CT show a change of splenic location or apparent changes in shape. CT scans have also shown an enlarged wandering spleen in a normal position. Torsion may produce a whorled appearance to the splenic pedicle (Warshauer et al. 1995). In case of infarction of the spleen a portion or the entire organ may become hypodense after administration of contrast media. Ascites or necrosis of pancreatic tail can also be detected (Parker and Mittelstaeedt 1984). The chronic torsion with venous congestion may cause splenomegaly and gastric varices.

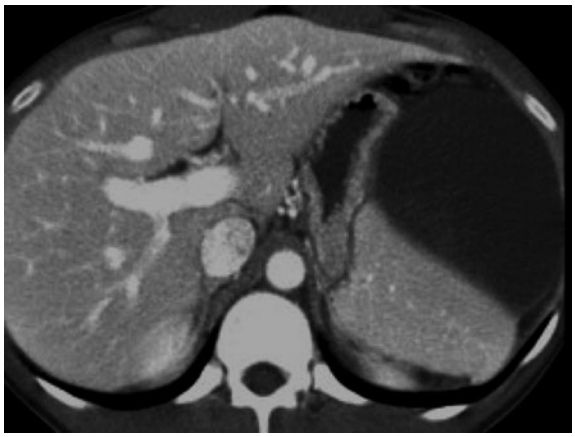

Fig. 3 Splenic cyst. MDCT, venous phase. A large homogeneous hypodense lesion with thin walls can be appreciated in the anterior aspect of the spleen (Courtesy of Ruedi F. Thoeni, M.D., Department of Radiology and Biomedical Imaging, UCSF, San Francisco, CA, USA)

3.3 Splenic Cystic Lesions

Many focal lesions may appear to be cystic on cross-sectional imaging. Cystic lesions can be classified as primary ('true') or secondary ('false'), based on the presence of a cellular or fibrous lining. Primary cysts can be divided into non-parasitic or parasitic (i.e. echinococcal). True non-parasitic cysts include congenital (i.e. epithelial) and neoplastic (lymphangioma, metastases, haemangioma) cysts. False cysts may develop secondary to trauma, haemorrhage, infarction-degeneration and inflammation (Andrea et al. 2005).

3.3.1 Congenital or Epithelial Splenic Cysts (True Cyst)

Congenital or epithelial splenic cysts comprise approximately 25% of true cysts of the spleen. They are mainly seen in children and young adults and are usually solitary, but can be multiple. The exact mechanism of the aetiology, pathogenesis and development of congenital splenic cysts is unknown. Generally, congenital splenic cysts are asymptomatic and the prognosis is good. Occasionally, congenital cysts may become symptomatic because of enlargement (Fig. 3) which may be secondary to trauma, hemorrhage from the cyst wall, an increase in the osmolality of the cystic fluid. Associated complications include infection, rupture and hemorrhage. The therapy of choice for a symptomatic splenic cyst is an interventional procedure such as partial or total splenectomy. On CT, splenic cysts are typically spherical, well defined lesions with an attenuation value near water and a thin or imperceptible wall which demonstrates no enhancement after injection of contrast medium (Dachman et al. 1986a, b). Internal debris, haemorrhage and peripheral cyst wall calcifications may contribute to a more complex picture. Epidermoid cyst has a complex pattern with irregularity and thickening of the posterior wall because of epithelial peripheral trabeculation, and internal blood clots.

3.3.2 False (Pseudo) Cyst

False (pseudo) cysts account for approximately 75% of the non-parasitic cysts of the spleen. They are secondary to trauma, infarction or infection. Trauma is the most probable etiologic factor. The majority of these cysts are solitary and asymptomatic. Microscopically, the wall of these cysts is composed of dense, often calcified fibrous tissue with no epithelial lining. They contain a mixture of blood and necrotic debris. It is often impossible to distinguish radiologically between primary and secondary cysts (Fig. 4). The clinical presentation and patient history may help to narrow the differential diagnosis.

4 Inflammatory Masses

4.1 Pyogenic Abscess

Splenic abscess is an uncommon condition, whose frequency has grown as a result of an increasing number of immunosuppressed patients because of aggressive chemotherapy, bone marrow transplants and AIDS. A splenic abscess is a localized collection of pus that most commonly is caused by the hematogenous spread of infection (75% of cases). This infections are due to aerobic organism, with *Staphylococcus*, *Streptococcus*, *Escherichia coli* and *Salmonella* being the predominant flora. Other causes include penetrating trauma (15%) and prior splenic infarction (10%) (Freeman et al. 1993a, b). Pyogenic abscesses can be single or multiple. The clinical findings of fever, chills, and left-upper-quadrant pain and tenderness arc seen in less than half of the cases. The factors leading to involvement of the spleen are metastatic infection (bacterial endocarditis, sepsis),

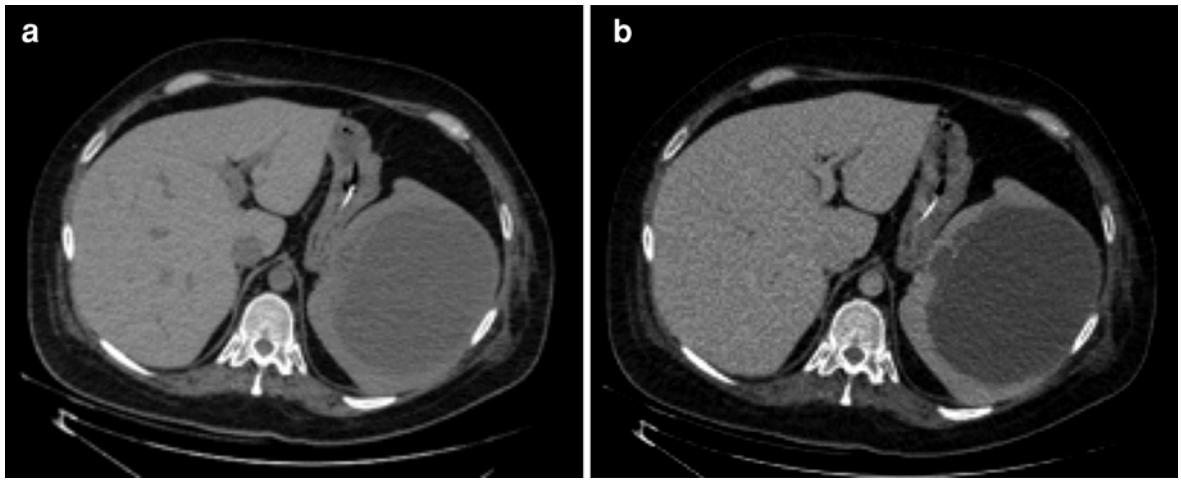

Fig. 4 Pseudocyst (surgical resection). MDCT, unenhanced (**a**) and late venous phase (**b**). A large cyst with lobulated margins, better seen after contrast media administration (**b**), is appreciated in the context of the spleen with thin walls and no mural nodules

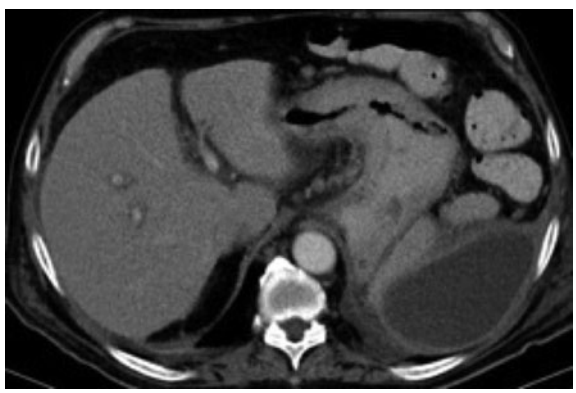

Fig. 5 Splenic abscess. MDCT, venous phase. A unilocular solitary well-defined lesion with thick peripheral rim with internal hypodense content can be appreciated in the context of the spleen (Courtesy of Rita Golfieri, M.D.. Radiology Unit, St. Orsola-Malpighi University Hospital, Bologna, Italy)

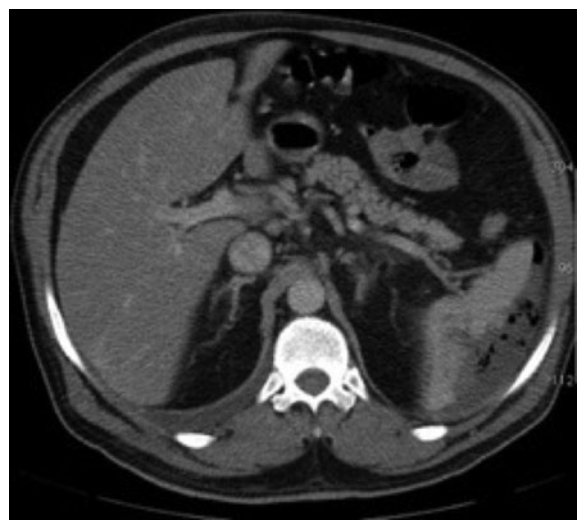

Fig. 6 Splenic abscess. MDCT, venous phase. A subcapsular ill-defined lesion with internal gas can be appreciated (Courtesy of Grazia Bitti, M.D., Brotzu Hospital, Cagliari, Italy)

contiguous infection (pancreatitis, periphrenic abscess), embolic non-infection events causing ischemia and superinfection, trauma and immunodeficiency (Ooi and Leong 1997).

CT can be used for a precise localization of the lesions and for giving information about the perisplenic area and contiguous viscera to guide any interventional and surgical procedures (Van der Lanan et al. 1989). CT scans show a unilocular or multilocular well-defined lesion, solitary or multiple. Bacterial abscess is suggested by thick, irregular, dense peripheral rim with internal nonenhancing area (Fig. 5). Attenuation measurements range from 20 to 40 HU; layers of different attenuation values, secondary to layering of the proteinaceous material within the abscess, are frequently noted. Rim enhancement after contrast administration, may be shown, in venous phase, although it is seen less often than in hepatic abscesses; small amounts of gas can be found (Dachman et al. 1986a, b; Rabushka et al. 1994) (Fig. 6). In the differential diagnosis the splenic lymphoma, in particular diffuse histiocityc or immunoblastic types, may appear as ill-defined masses of

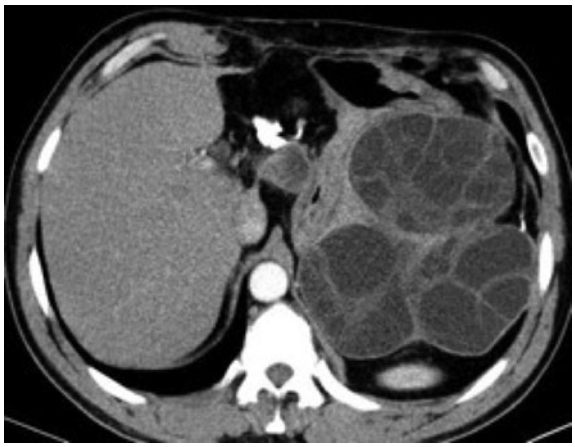

Fig. 7 Hydatid disease. MDCT, venous phase. Three large mass with low attenuation values with multilocular apperance due to the presence of daughter cysts (Courtesy of Rita Golfieri, M.D., Radiology Unit, St. Orsola-Malpighi University Hospital, Bologna, Italy)

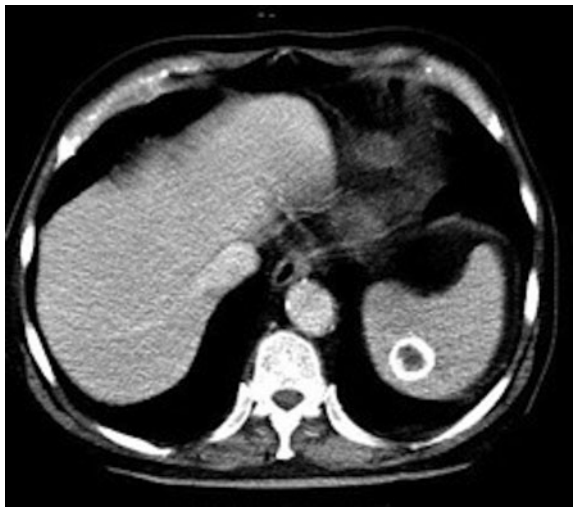

Fig. 8 Hydatid disease. CT, venous phase. A small lesion with low attenuation values and thick calcified walls (Courtesy of Charikleia C Triantopoulou, M.D., Department of Radiology, Konstantopouleion General Hospital, Athens, Greece)

low density with or without a thick rim mimicking an abscess.

4.2 Fungal Microabscess

Fungal abscesses are lesions that occur mainly in immunocompromised patients. Renal transplantation, neoplasms, abdominal surgery, leukemia and lymphoproliferative disorders are risk factor in adult patients. In children is most often associated with leukemia or chronic granulomatous disease. The most frequently encountered pathogens are *Candida albicans, Aspergillus fumigatus,* and *Cryptococcus neoformans* (Chew et al. 1991). Because the lesions are small, fungal abscesses in neutropenic patients may not be detectable by any imaging modality, even in the presence of disseminated infection. Small, low-attenuation areas that are usually well demarcated and that range from a few millimeters to 2 cm in size are shown at CT (Judy et al. 1993a, b, c). Rim enhancement is not seen. Occasionally CT may demonstrate a central focus of higher attenuation or a wheel within a wheel pattern corresponding to ultrasound findings (echoic lesion with central hypoechoic nidus due to necrosis containing fungal elements). The differential diagnosis includes metastases, lymphoma and disseminated mycobacterial infection.

4.3 Hydatid Disease

Splenic involvement of hydatid disease is uncommon, most frequent in endemic areas. It is almost always caused by *Echinococcus granulosus* (Freeman et al. 1993a, b). Clinical findings are nonspecific and frequently include abdominal pain, fever and splenomegaly. CT demonstrates a sharply marginated, round or ovoid mass with attenuation values in the range of that of water. The presence of daughter cysts give a multilocular apperance (Fig. 7). Higher attenuation within the lesion is frequently encountered and may occur secondary to the formation of daughter cysts or as a result of the collection of dense debris (hydatid sand) within the cyst. Ringlike calcifications may be seen in the periphery, within the pericyst (Fig. 8). The differential diagnosis includes prior trauma, intrasplenicic aneurysm and infection.

5 Other Inflammatory Disease

5.1 Inflammatory Pseudotumor

Is a rare condition characterized by well-circumscribed, solitary mass composed of area of inflammatory and reparative fibroblastic changes around foci of necrosis and hemorrhage with a peripheral

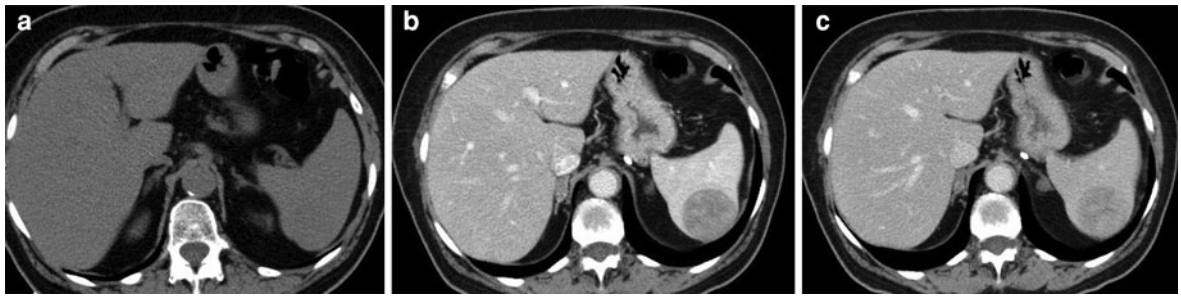

Fig. 9 Inflammatory pseudotumor. MDCT unenhanced (**a**), venous (**b**) and distribution phase (**c**). On unenhanced CT a bulging of the margin of the spleen slightly hypodense can be observed. After contrast administration (**b**) a hypondense aspect of the lesion with progressive opacification, better seen in distribution phase (**c**). (Courtesy of Giulia Zamboni, M.D., Department of Radiology, University of Verona, Italy)

granulomatous component. On unenhanced CT this lesion reveal a rounded mass with low attenuation with or without calcification. After contrast administration observed progressive opacification of the lesion and may persist within the mass central, stellate, low-density areas, corresponding hystologically to focal areas of fibrosis (Fig. 9) (Franquet et al. 1989).

5.2 Sarcoidosis

Although histologic evidence of sarcoidosis involving the liver and spleen is seen in 50–80% of autopsy specimens, dysfunction of these organs is uncommon. The most frequent finding is splenomegaly. On CT low-density intrasplenic lesions is rare. At CT or MR imaging, hepatic sarcoidosis usually manifests with minimal organomegaly. In only 5–15% of patients, coalescing granulomas become apparent as multiple hypointense or hypoattenuating nodules (Fig. 10). Multisistemic involvement makes more confident the diagnosis with splenic nodules larger and more common than hepatic lesions (Koyama et al. 2004) (Fig. 11).

5.3 Splenosis

Splenosis is a post-traumatic autotransplantation and proliferation of splenic tissue in ectopic sites. These implants may mimic malignancy in healthy patients or peritoneal metastases in oncological patients. When a previous history of splenic injury is known, the finding of soft tissue nodules in many thoracic and abdominal locations might raise the suspicion of the benign condition of splenosis, in order to avoid unnecessary surgery or chemotherapy. If the splenic implant is intra-hepatic, CT imaging may show hypodense masses with strong enhancement at the early phase and pooling enhancement at delayed phase (Nakajima et al. 2008; Grande et al. 2008; Imbriaco et al. 2008).

5.4 Splenic Infarction

Splenic infarct is an uncommon form of pathology. It is the result of arterial or venous damage and is associated with a heterogeneous group of disease including thromboembolic disorders, atrial fibrillation, myocardial infarction hematological malignant diseases, sepsis and coagulation disorders. Unenhanced CT show heterogeneous, poorly marginated, hypodense areas, which appear sharply demarcated wedge-shaped after contrast agent administration (Fig. 12).

The shape and size of infarct show a temporal evolution: in the hyperacute phase, CT may show areas of increased attenuation, representing the hemorrhagic infarcts, in the acute (days 2–4) and subacute (days 4–8) phases, there are focal well-demarcated areas of decreased attenuation that become progressively more defined and demonstrate no contrast enhancement. In the chronic phase (2–4 weeks), the infarct gradually decreases in size, and attenuation may return to normal on scans obtained both before and after contrast enhancement (Judy et al. 1993a, b, c).

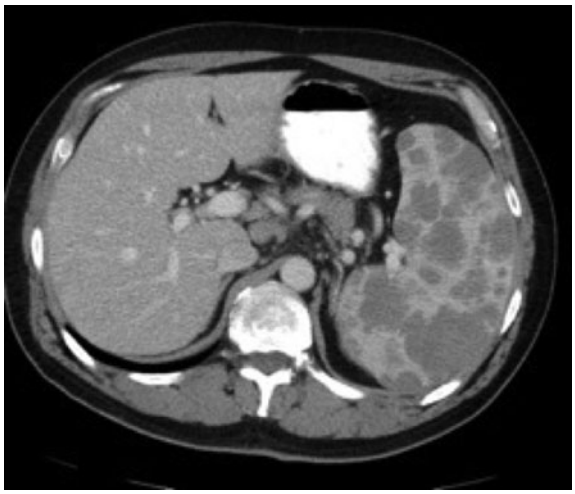

Fig. 10 Sarcoidosis. MDCT, venous phase. Multiple hypoattenuating nodules secondary to coalescing granulomas can be seen (Courtesy of Chitra Viswanathan, M.D., Department of Diagnostic Radiology, University of Texas MD Anderson Cancer Center, Houston, TX, USA)

5.5 Hamartoma

Hamartomas, also known as splenomas, splenadenomas or nodular hyperplasia of the spleen, are rare benign malformations composed of an anomalous mixture of normal splenic red pulp elements. The hamartoma is thought to be congenital in origin, reflecting a focal developmental disturbance in the spleen. Some Authors consider a splenic hamartoma to be a neoplasm (a form of hemangioma or lymphangioma) or possibly a posttraumatic lesion (Silverman and LiVolsi 1978). Others Authors believe that splenic hamartoma might arise from an acquired proliferative process, a theory that supports the association of hamartoma with malignancy (Steinberg et al. 1991). At CT, hamartomas appear as well-demarcated, solid, hypodense or isodense masses, although a hyperattenuating appearance due to haemosiderin deposition has been reported. In large lesions is evident a central area of low attenuation which represent a region of necrosis with focal calcification. It demonstrates inhomogeneous and moderate contrast enhancement in arterial and portal phases of the lesions but the pattern is variable (Fig. 13). In many cases is evident a uniform contrast enhancement in late phase (Ohtomo et al. 1992; Giovagnoni 2005).

5.6 Hemangioma

Splenic hemangioma is a rare disorder, but still the most common benign neoplasm of the spleen (Bailez 2004). Splenectomy can be indicated if large because spontaneous rupture with massive hemorrhage can occur (Disler and Chew 1991). They are mostly solitary but may be multiple or associated with haemangiomas of other sites (Klippel-Trenaunay-Weber syndrome). Hemangioma ranges from solid to cystic and may appear as complex masses corresponding to solid and cystic areas (Urrutia et al. 1996). CT demonstrates homogeneously solid masses or multiple cystic masses with slight hypodensity on unenhanced scans. In some cases it may be demonstrated a central, punctuate, peripheral or curvilinear calcification (Ferrozzi et al. 1996). On unenhanced CT scans, capillary hemangiomas appear as hypoattenuating or isoattenuating, well-marginated masses with homogeneous and marked contrast enhancement occuring after intravenous contrast administration (Fig. 14). Cavernous hemangiomas instead have a combination of solid and cystic components. The lesions with a predominant solid component appear isoattenuating or hypoattenuating relative to normal spleen, with tipical enhancement. They demonstrate early peripheral nodular enhancement with progressive fill-in and are homogeneous on delayed images (with a similar behavior to hemangioma of the liver) (Fig. 15). Howewer, the behavior after contrast administration is often nonspecific and other lesions appear cystic or heterogeneous depending on the extent of cystic and relatively avascular components (Robert 2004).

5.7 Lymphangioma

Cystic lymphangioma is a very rare condition. It is usually seen in children in whom it is frequently discovered incidentally. Most splenic lymphangiomas occur in children, more frequently in female and 80–90% are detected before the end of the second year of life (Wadsworth et al. 1997). The neck (75%) and axillary regions (20%) are the most common locations of lymphangioma, but it can occur in the retroperitoneum, mediastinum, mesentery, omentum, colon, pelvis, groin, bone, skin, scrotum and spleen.

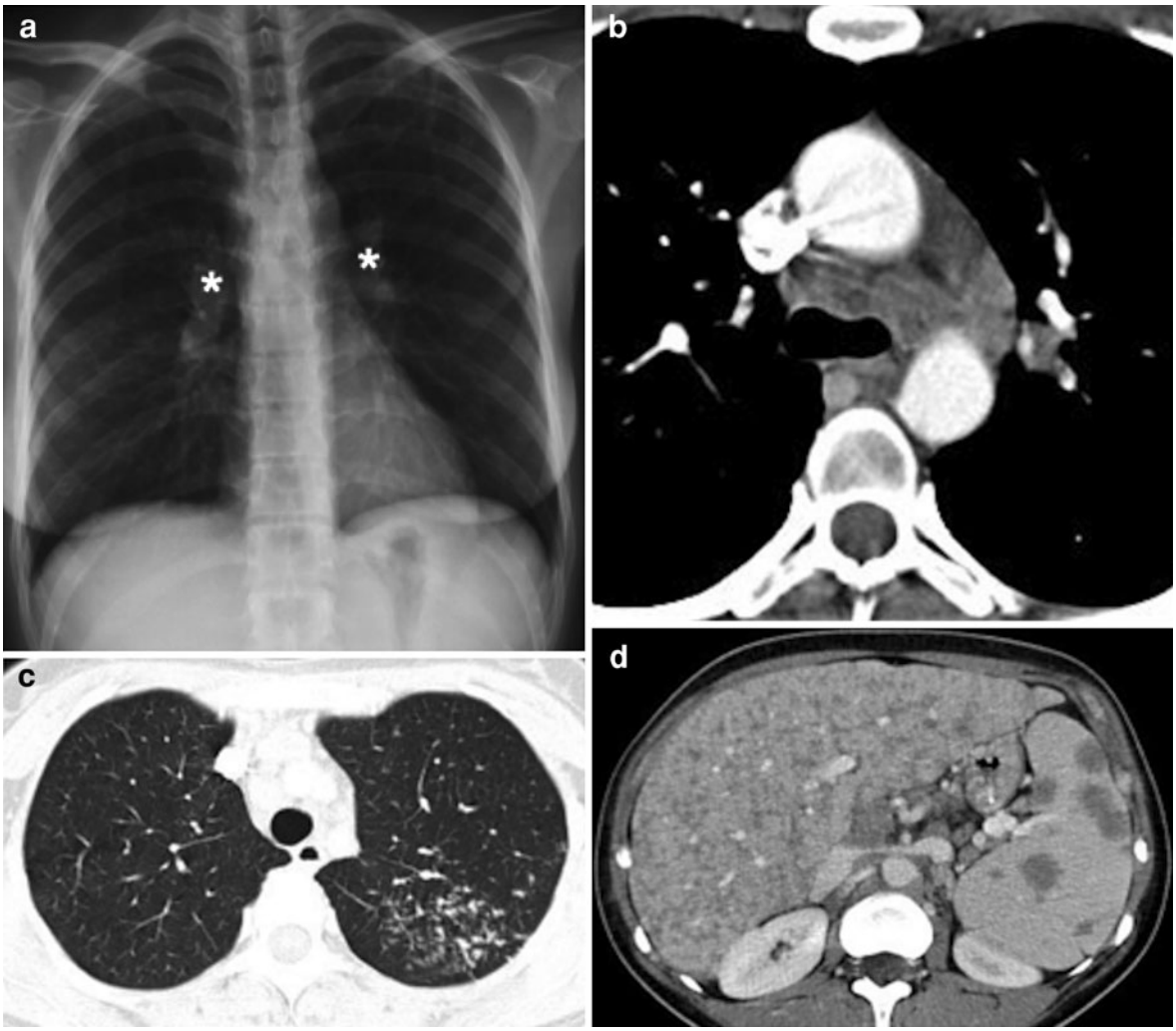

Fig. 11 Sistemic sarcoidosis. (**a**) Chest X-ray. Enlarged ilar lymphnodes (*). MDCT of the thorax. Multiple hypoattenuating lymphnodes can be appreciated in the mediastinum (**b**) with small peribronchial nodules in the lung (**c**). In the abdomen (**d**) several hypoattenuating nodules can be appreciated both in the liver and spleen, with splenic nodules larger than hepatic lesions (Courtesy of Borut Marinchek, M.D., Department of Radiology, Zurich University Hospital, Switzerland)

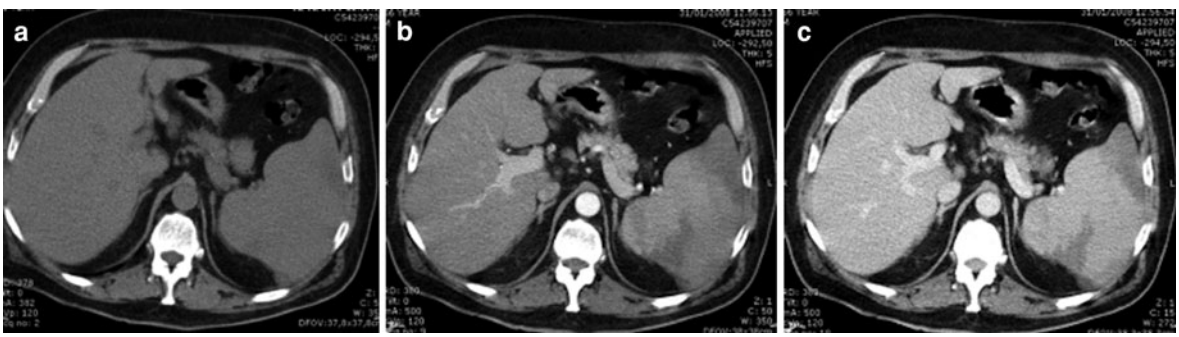

Fig. 12 Splenic infarction. MDCT, unenhanced (**a**), later arterial (**b**) and venous (**c**) phase. Unenhanced CT show heterogeneous, poorly marginated, slightly hypodense areas, which appear sharply demarcated wedge-shaped after contrast agent administration

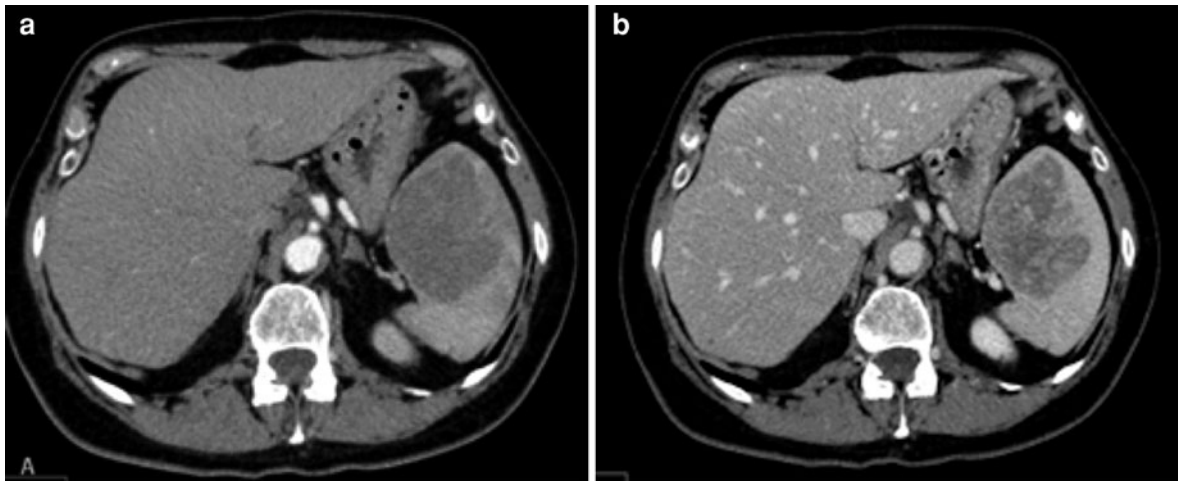

Fig. 13 Hamartoma. MDCT, arterial (**a**) and venous (**b**) phase. A large well-demarcated, solid, hypodense mass with inhomogeneous and moderate contrast enhancement in arterial and portal phases is evident (Courtesy of Orlando Catalano, M.D., Computed Tomography Unit, Department of Radiology, Pascale Hospital, Naples, Italy)

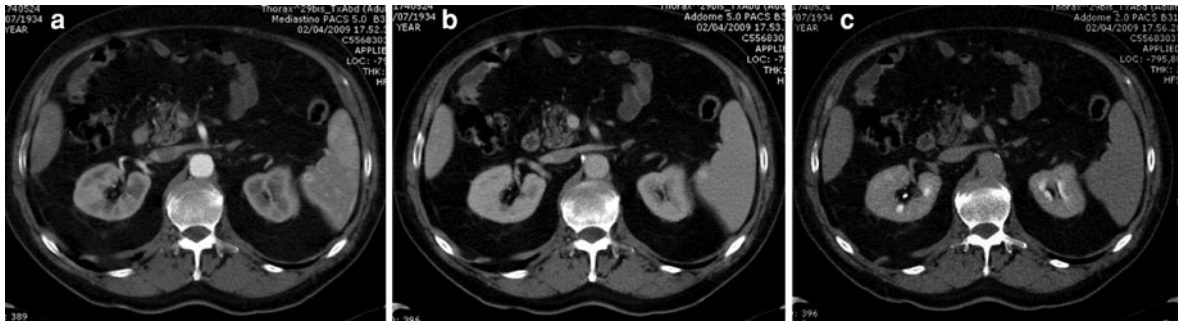

Fig. 14 Capillary hemangioma. MDCT, arterial (**a**) venous (**b**) and distribution (**c**) phase. A small hyperattenuating well-marginated lesion with no washout during the venous (**b**) and distribution (**c**) phase can be appreciated in the lower pole of the spleen

Lymphangioma of the spleen can involve the spleen alone, or it can be a part of multivisceral involvement; when diffuse it is termed systemic cystic angiomatosis (Seckler et al. 1964). Patients with splenic lymphangioma may be asymptomatic or symptomatic at diagnosis. CT typically reveal splenic cysts of various sizes, ranging from a few millimeters to several centimeters in diameter. On CT scans, lymphangiomas appear as single (lymphangioma) or multiple (lymphangiomatosis) thin-walled low-attenuation masses with sharp margins typically subcapsular in location with no contrast enhancement (Fig. 16). The presence of curvilinear peripheral mural calcifications suggests the diagnosis of cystic lymphangioma (Robert 2004; Pyatt et al. 1981).

5.8 Littoral Cell Angioma

Littoral cell angioma is a rare primary vascular neoplasm of the spleen, as described by Falk et al. (1991). This neoplasm is composed of anastomosing vascular channels resembling splenic sinuses and it is thought to arise from littoral cells, which normally line the splenic sinuses of the red pulp, because it has morphologic and immunophenotypic features that reflect the dual endothelial and histiocytic potential of splenic sinus-lining cells. The clinical presentation of LCA ranges from being completely asymptomatic and discovered incidentally, to presenting with a constellation of signs and symptoms such as abdominal pain, vague constitutional symptoms,

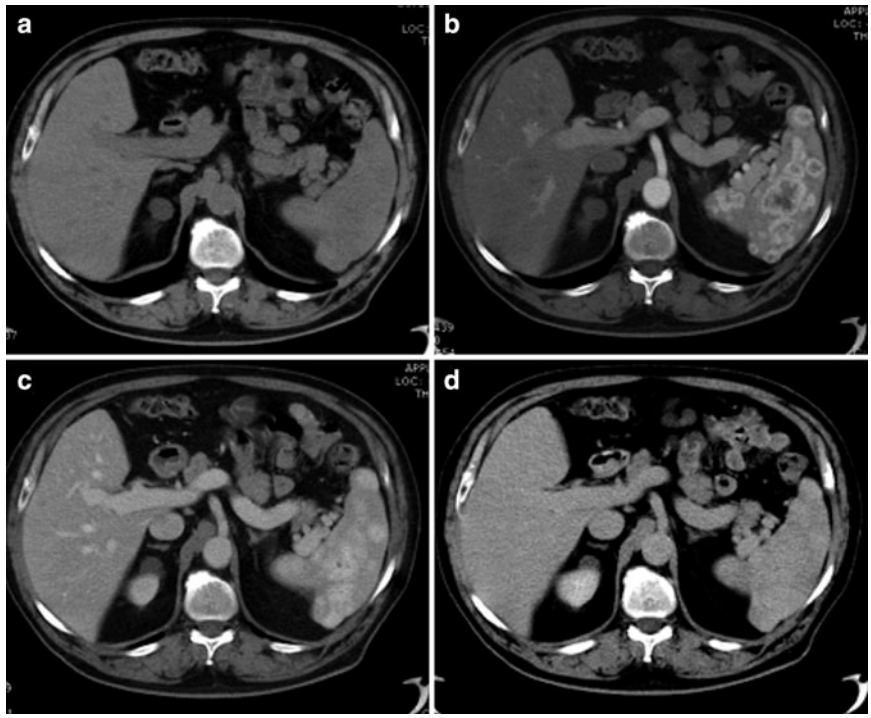

Fig. 15 Cavernous hemangiomas. MDCT, unenhanced (**a**), arterial (**b**) venous (**c**) and distribution (**d**) phase. In unenhanced phase (**a**) no lesions can be appreciated. During arterial phase (**b**) multiple hypervascular lesions with peripheral enhancement and progressive centripetal fill-in at venous (**c**) and distribution (**d**) phase can be seen

splenomegaly, and hypersplenism (Dascalescu and Wendum 2001; Ben-Izhak et al. 2001). Although first described as benign, LCA has recently been shown to exhibit malignant potential (May et al. 2008) and may also be associated with other visceral malignancies. On abdominal CT scans obtained without contrast material, littoral cell angioma typically manifests as multiple hypoattenuating lesions (Fig. 17). Lesions with this appearance have a broad differential diagnosis, including other primary vascular tumors of the spleen, other neoplastic entities, infection and systemic diseases such as sarcoidosis. However, on delayed contrast-enhanced images, this lesions homogeneously enhance and become isoattenuating relative to the remaining splenic parenchyma, a finding that may help in the differential diagnosis (Angela 2004). Rarely, littoral cell angioma may present as a solitary large mass of the spleen, making correct diagnosis more difficult (Tatli et al. 2008) (Fig. 18).

5.9 Hemangiopericytoma

Hemangiopericytoma is a perivascular tumor originating from pericytes located along capillaries and venules. Tumor may have a benign or malignant behavior. Hemangiopericytoma of the spleen is rare and may be single or multifocal. Reported CT findings in hemangiopericytoma include a large splenic mass with polylobular contours and smaller disseminated lesions throughout the spleen. In addition, speckled calcification may be seen on CT scans, and contrast-enhanced studies show discrete hyperattenuation of solid portions and septations (Mortele 2000).

5.10 Hemangioendothelioma

Hemangioendothelioma is a very rare primary vascular tumor of the spleen and has variable malignant potential. The diagnosis of splenic hemangioendothelioma is not likely to be made on the basis of imaging characteristics alone, since these findings are nonspecific. The typical CT appearance is that of a low attenuation mass with enhancement of the solid portions of the tumor that may appear hypovascular relative to the normal splenic parenchyma. Findings suggestive of malignancy, such as areas of necrosis and hemorrhage, may be present and will not show evidence of enhancement. Signs of infiltration of the surrounding splenic parenchyma and evidence of

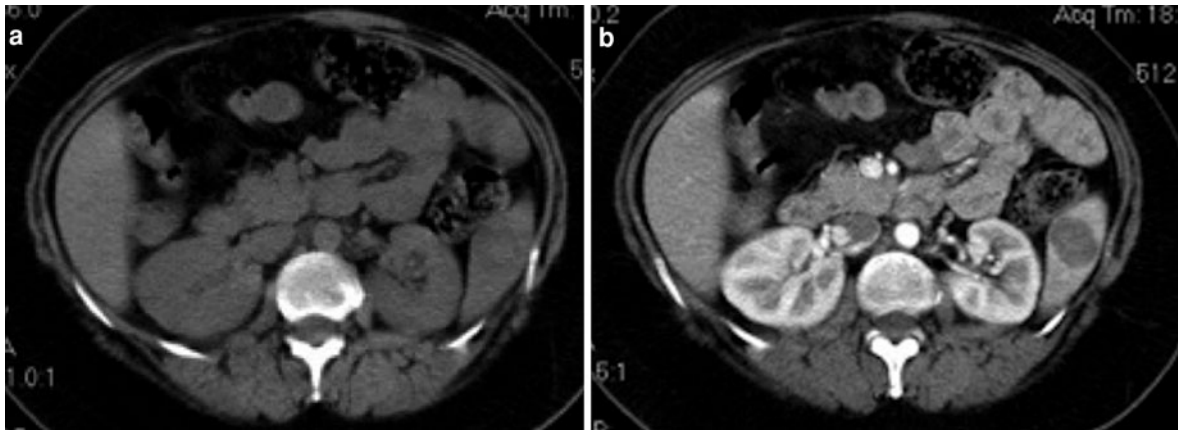

Fig. 16 Lymphangioma. MDCT, unenhanced (**a**) and late arterial (**b**) phase. A subcapsular single thin-walled low-attenuation mass with sharp margins and no contrast enhancement can be appreciated (Courtesy of Giuseppe Brancatelli, M.D., Radiological Department, University of Palermo, Italy)

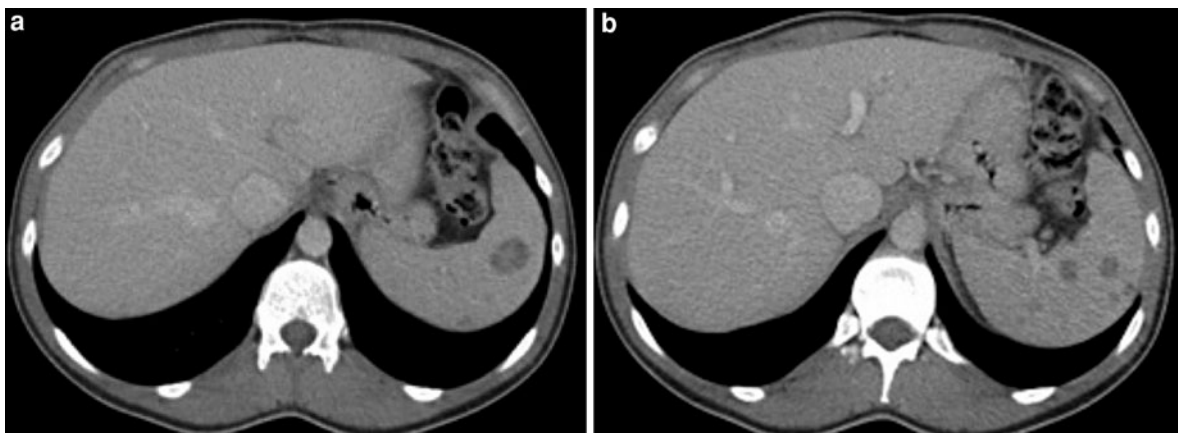

Fig. 17 Multiple littoral cell angiomas. MDCT, venous phase, two different levels. Multiple hypoattenuating lesions in the spleen (Courtesy of Harriet C. Thoeny, M.D., University of Bern, Switzerland)

metastatic disease may also be identified on CT scans. Calcification has not been described as a specific feature of this tumor (Miller et al. 1992).

5.11 Hemolymphangiomiomatosis

Hemolynphangioma is a tumor composed of lymphatic and hematic cells. Many different localizations are described (orbit, tongue, esophagus, neck, heart, liver, pancreas, uterine cervicx and adrenal glands) but involvement of the spleen is a rare condition. In this cases more frequently the lesions is solitary and only one case of diffuse pattern has been described (Santoro et al. 2005) (Fig. 19). In pre-contrastographic phases CT the spleen is increased of volume with the inhomogeneous density in relation to the presence of diffuse hypodense areas with variable diameters (from 1 mm to 4−5 cm). After intravenous administration these lesions appears hypodense in venous phase in relation of enhancement of the surrounding parenchyma and isodense with the normal spleen in the late phase.

5.11.1 Angiosarcoma

Primary splenic angiosarcoma is a rare but highly malignant vascular neoplasm and it represents the most common nonlymphoid malignant tumor of the

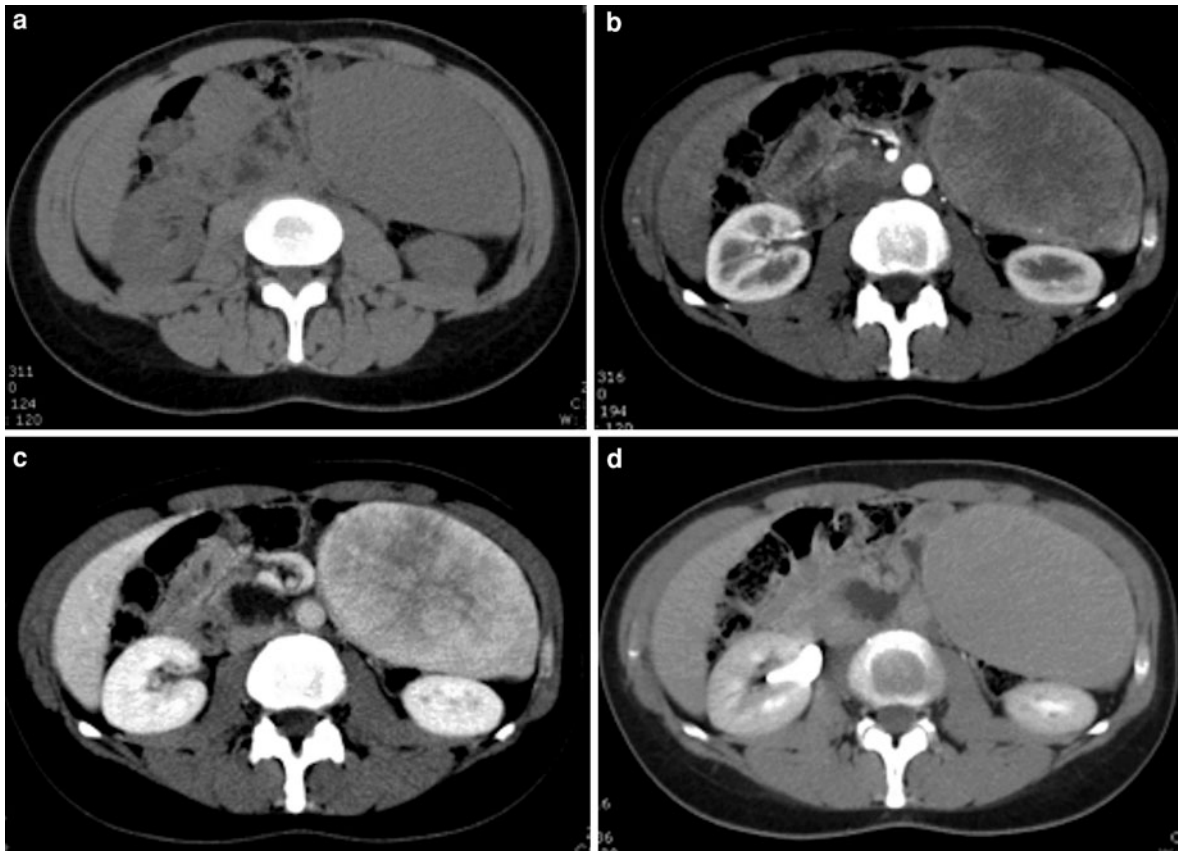

Fig. 18 Solitary littoral cell angioma. MDCT, unenhanced (**a**), arterial (**b**) venous (**c**) and distribution (**d**) phase. A large well-defined mass with inhomogeneous progressive peripheral enhancement and late homogeneous appearance

spleen. It is a highly aggressive malignancy with a poor prognosis. Distant metastases occur most frequently in the liver (70% of cases), lung, pleura, lymph nodes, bone, and brain (Neuhauser et al. 2000). There have been case reports of splenic angiosarcoma associated with previous chemotherapy for lymphoma and radiation therapy for breast cancer (Zwi et al. 1986).

This lesions appear as either solitary (Fig. 20) or multiple nodular masses in enlarged spleen. Some of these masses show peripheral enhancement, and the margins of the lesions are often irregular or poorly marginated. On precontrast CT scans, the tumors may appear hyperattenuating, which corresponds to acute hemorrhage. On dynamic contrast-enhanced CT scans, the lesions may exhibit substantial peripheral contrast enhancement similar to that of hepatic hemangiomas (Rabushka et al. 1994; Mortele et al. 2000), although only minimal contrast enhancement, with areas of decreased attenuation suggesting necrosis has been described (Fig. 20) (William et al. 2005). Calcifications are not frequent but possible (Fig. 20).

5.12 Lymphoma

Lymphoma is the most common malignant tumor of the spleen. Lymphomatous involvement of the spleen as a manifestation of systemic lymphoma is quite common, whereas primary splenic lymphoma is relatively uncommon. CT has not been proved to be an accurate modality in the diagnosis of splenic lymphoma because of the variety of appearances and the possibility of a normal-appearing spleen despite the presence of tumor cells. Moreover, splenomegaly is not a reliable sign of lymphomatous involvement: although splenomegaly in most patients with nonHodgkin lymphoma indicates splenic involvement, up to one-third of patients with

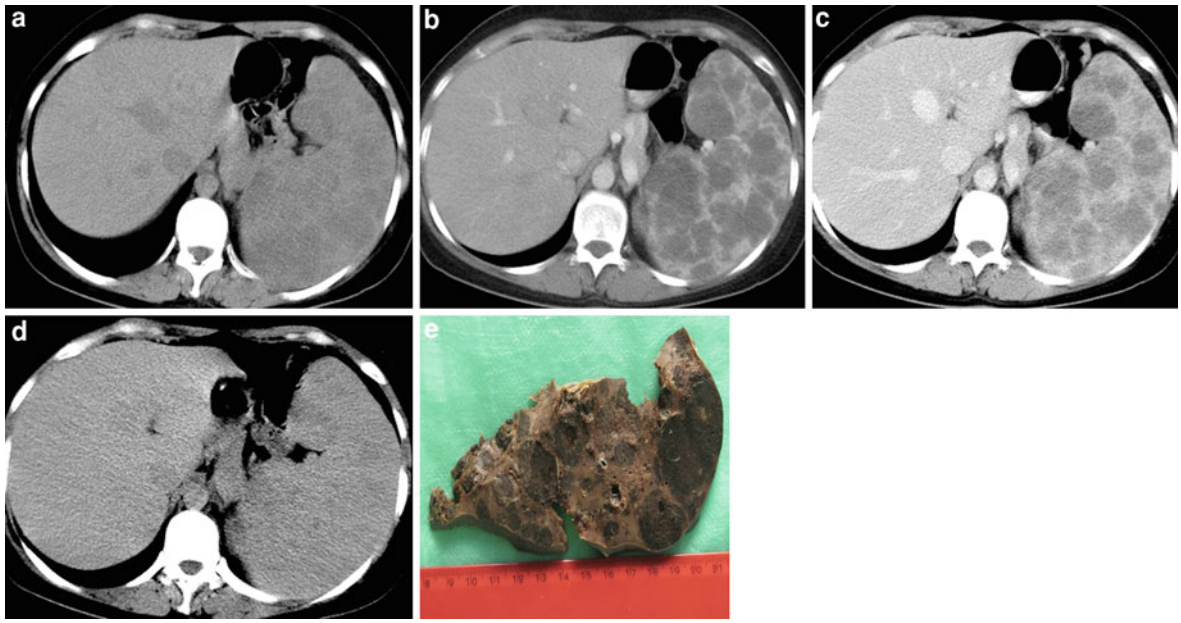

Fig. 19 Hemolymphangiomiomatosis. MDCT, unenhanced (**a**), arterial (**b**) venous (**c**) and distribution (**d**) phase. In pre-contrastographic phases (**a**) the spleen is increased of volume with the inhomogeneous density due to the presence of multiple hypodense areas. After intravenous administration these lesions appears hypodense both in arterial (**b**) and venous phase (**c**) and isodense with the normal spleen in the late phase (**d**). (**e**) surgical specimen (Courtesy of Stefano Colagrande, M.D., Radiological Department, University of Florence, Italy)

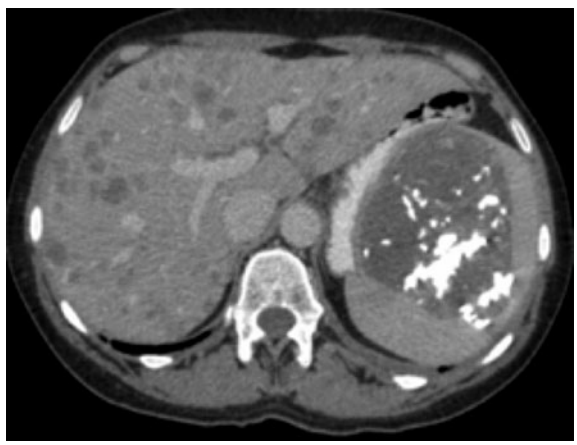

Fig. 20 Angiosarcoma. MDCT, venous phase. A large hypondense mass with huge calcifications can be appreciated in the spleen. Multiple secondary hypodense lesions are visible in the liver (Courtesy of Harriet C. Thoeny, M.D., University of Bern, Switzerland)

splenomegaly have no evidence of splenic lymphoma at histologic examination. In addition, up to one-third of patients with lymphoma of any kind have histologic involvement of the spleen without splenomegaly (Rolfes and Ros 1990a, b). The accuracy of CT in diagnosing splenic lymphoma is related to demonstrating a inhomogeneous splenic enhancement (Fig. 21a) and adenopathy in the splenic hilum in addition to splenomegaly (Fig. 21b). Focal lesions can be solitary or multiple of decreased attenuation and variable size (Fig. 22). Calcification are occasionally detected and considered secondary to necrosis or hemorrhage with subsequent fibrosis (Dachman et al. 1998; Rini et al. 2003; Judy et al. 1993a, b, c).

5.13 Metastatic Disease

The incidence of splenic metastases is between 2.3 and 7.1%. Solitary metastasis to the spleen is secondary to hematogenous dissemination and is confined to the splenic parenchyma. The most common primary sources include breast, lung, stomach, ovarian, colorectal cancers, melanoma and prostate (Berge 1974). Skin melanoma has the highest rate of splenic metastases per primary tumor. More than 30% of patients with skin melanoma have splenic metastasis at autopsy (Lam 2000).

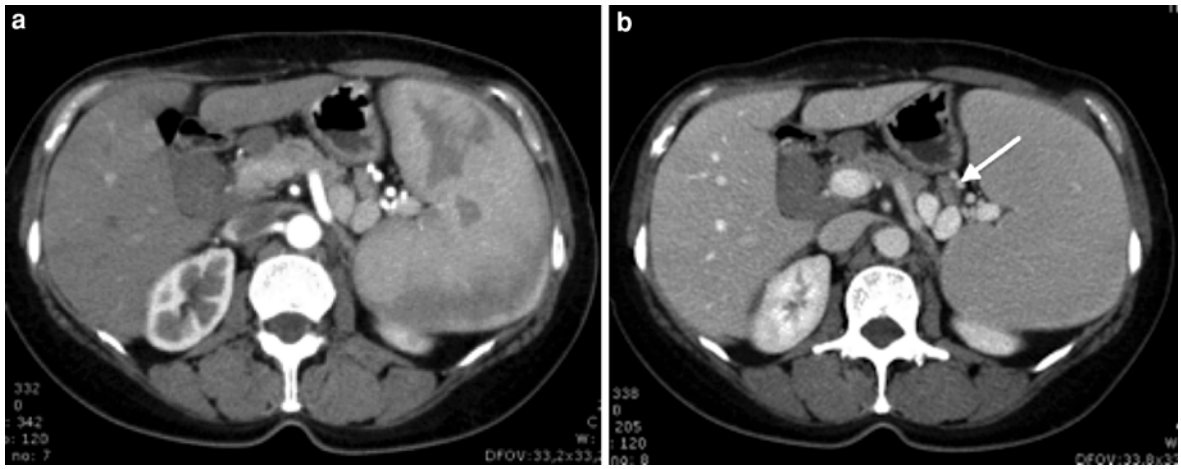

Fig. 21 Non Hodgkin lymphoma. MDCT, arterial (**a**) and venous (**b**) phase. A large spleen in a patient with NH lymphoma with inhomogeneous arterial enhancement (**a**) and a enlarged lymph node at the hilum (*arrow* in b)

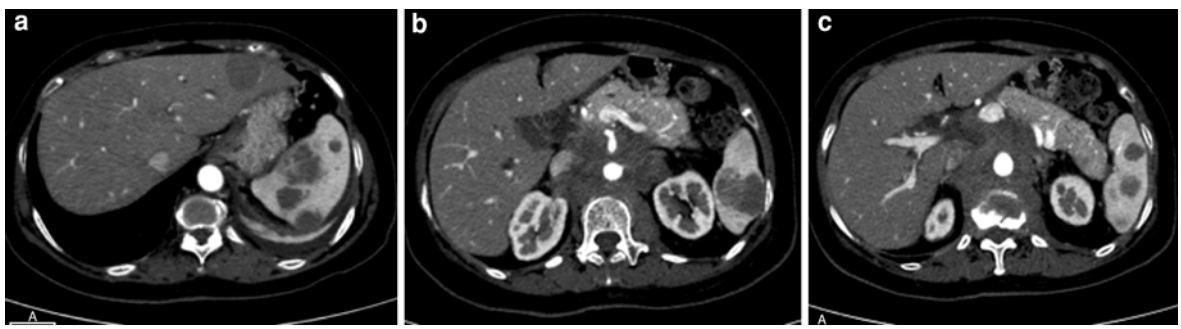

Fig. 22 Non Hodgkin lymphoma. MDCT, late arterial phase, different levels. Multiple hypodense lesions can be appreciated in the spleen. A severe periaortic lymph node involvement can be appreciated (Courtesy of Orlando Catalano, M.D., Computed Tomography Unit, Department of Radiology, Pascale Hospital, Naples, Italy)

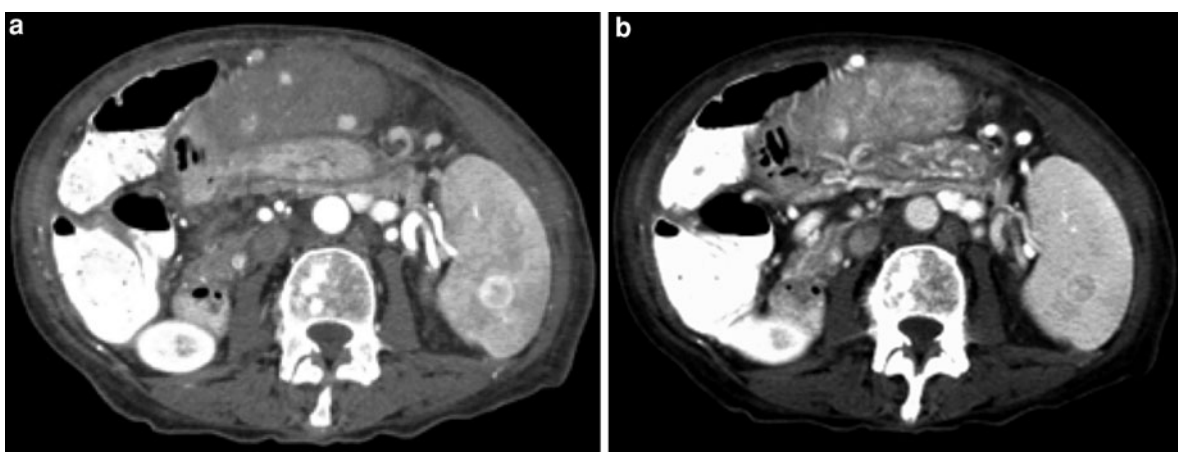

Fig. 23 Metastases from carcinoid. MDCT, arterial (**a**) and venous (**b**) phase. Multiple hypervascular lesions can be appreciated either in the spleen and in the abdomen (**a**); during the venous phase (**b**), the lesion in the spleen shows a washout (Courtesy of Paul M. Silverman, M.D., Department of Diagnostic Radiology, University of Texas MD Anderson Cancer Center, Houston, TX, USA)

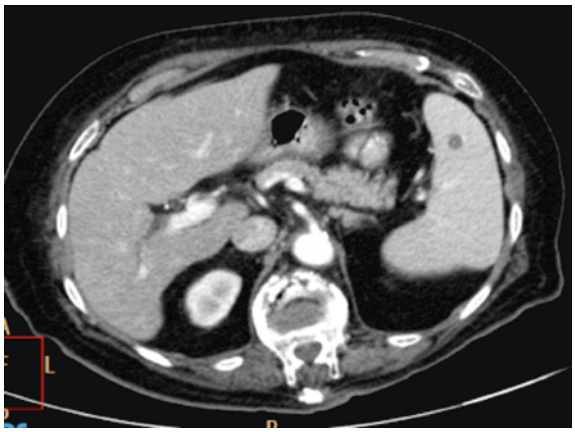

Fig. 24 Metastasis from uterine tumor. MDCT, venous phase. A small hypovascular lesion can be appreciated in the spleen (Courtesy of Orlando Catalano, M.D., Computed Tomography Unit, Department of Radiology, Pascale Hospital, Naples, Italy)

At CT, splenic metastases typically appear as hypodense lesions which may be solid or cystic with inhomogeneous contrast enhancement indicating a mixture of vascularisation and necrosis (Freeman et al. 1993a, b). Enhancement pattern is dependent on the primitive tumor, with either hypervascular (Fig. 23) and hypovascular appearance (Fig. 24) (Thompson et al. 2005).

References

Andrea G, Chiara G, Gaia G (2005) Tumours of the spleen. Cancer Imaging 5:73−77

Angela DL, Robert MA, Susan LA et al (2004) Littoral Cell Angioma of the Spleen: CT Features with Clinicopathologic Comparison. Radiology 230:485–490

Balthazar EJ, Hilton S, Naidich D et al (1985) CT of splenic and perisplenic abnormalities in septic patients. Am J Roentgenol 144: 53−56

Bailez M, Elmo G (2004) Laparoscopic partial splenectomy for a hemangioma of the spleen. Pediatric Endosurgery and Innovative Techniques 8(2):147–151

Ben-Izhak O, Bejar J, Ben-Eliezer S, Vlodavsky E (2001) Splenic littoral cell hemangioendothelioma: a new low-grade variant of malignant littoral cell tumour. Histopathology 39:469–475

Berge T (1974) Splenic metastases: frequencies and patterns. Acta Pathol Microbiol Scand A 82:499–506

Chew FS, Smith PL, Barboriak D (1991) Candidal: splenic abscesses. Am J Roentgenol 156:474

Costello P, Kane RA, Oster J et al (1985) Focal splenic disease demonstrated by ultrasound and computed tomography. J Can Assoc Radiol 36:22−28

Dachman MI, Ros PR, Murari PJ (1986a) Non parasitic splenic cysts: a report of 52 cases with pathologic-radiologic correlation. Am J Roentgenol 147:537–542

Dachman MI, Ros PR, Murari PJ (1986b) Non parasitic splenic cysts: a report of 52 cases with pathologic-radiologic correlation. Am J Roentgenol 147:537–542

Dachman AH, Buck JL, Krishnan J et al (1998) Primary non-Hodgkin's splenic lymphoma. Clin Radiol 53:137–142

Dascalescu CM, Wendum D, Gorin NC (2001) Littoral cell angioma as a cause of splenomegaly. New Engl J Med 345(10):772–777

Disler DG, Chew FS (1991) Splenic hemangioma. Am J Roentgenol 157(1):4

Falk S, Stutte HJ, Frizzera G (1991) Littoral cell angioma: a novel splenic vascular lesion demonstrating histiocytic differentiation. Am J Surg Pathol 15:1023–1033

Freeman JL, Jafri SZH, Roberts JL, Mezwa DG, Shirkhoda A (1993a) CT of congenital and acquired abnormalities of the spleen. RadioGraphics 13:597–610

Freeman JL, Jafri SZH, Roberts JL, Mezwa DG, Shirkhoda A (1993b) CT of congenital and acquired abnormalities of the spleen. RadioGraphics 13:597–610

Ferrozzi F, Bova D, Draghi F, Garlaschi G (1996) CT findings in primary vascular tumors of the spleen. Am J Roentgenol 166:1097–1101

Franquet T, Montes M, Aizcorbe M et al (1989) inflammatory pseudotumor of the spleen: ultrasound and computer tomographic findings. Gastrointest Radiol 14: 181−183

Giovagnoni A, Chiara G, Gaia G (2005) Tumours of the spleen. Cancer Imaging 5:73–77

Grande M, Lapecorella M, Ianora AA, Longo S, Rubini G (2008) Intrahepatic and widely distributed intraabdominal splenosis: multidetector CT, US and scintigraphic findings. Intern Emerg Med 3:265–267

Imbriaco M, Camera L, Manciuria A, Salvatore M (2008) A case of multiple intra-abdominal splenosis with computed tomography and magnetic resonance imaging correlative findings. World J Gastroenterol 14:1453–1455

Judy L, Freeman, S. Zafar H et al (1993a) CT of Congenital and acquired abnormalities ofthe spleen. RadioGraphics 13:597–610

Judy L, Freeman, MD, S. Zafar H. et al (1993b) CT of Congenital and acquired abnormalities of the spleen. RadioGraphics 13:597–610

Judy L, Freeman, S. Zafar H. Jafri, John L. Roberts et al (1993c) CT of congenital and acquired abnormalities ofthe spleen. RadloGraphics 13:597–610

Koehler RE. Spleen. In: LeeJKT, Sagel 55, Stanley RJ (eds) (1989) Computed body tomography with MR correlation, 2nd edn. Raven, New York, pp 521−541

Koyama T, Ueda H, Togashi K, Umeoka S, Kataoka M, Nagai S (2004) Radiologic manifestations of sarcoidosis in various organs. Radiographics. 24(1):87–104

Lam KY, Tang V (2000) Metastatic tumors to the spleen: a 25-year clinicopathologic study. Arch Pathol Lab Med 124:526–530

May T, Patrick V, Peter Z, Sam MW (2008) Case report Incidental littoral cell angioma of the spleen. World J Surg Oncol 6:87

Miller WJ, Dodd GD, Federle MP, Baron RL (1992) Epithelioid hemangioendothelioma of the liver: imaging findings with pathologic correlation. Am J Roentgenol 15:53–57

Mortele KJ (2000) Imaging of tumoral conditions of the spleen. JBR-BTR 83:213–215

Mortele KJ, Mergo PJ, Kunnen M, Ros PR (2000) Tumoral pathology of the spleen. In: De-Schepper AM, Vanhoenacker F (eds) Medical imaging of the spleen. Springer, Berlin, pp 115–116

Nakajima T, Fujiwara A, Yamaguchi M, Makiyama A, Wakae T, Fujita K, Yoshikawa K, Shiomi T, Ohishi T, Nakashima T, Konishi E (2008) Intrahepatic splenosis with severe iron deposition presenting with atypical magnetic resonance images. Intern Med 47:743–746

Neuhauser TS, Derringer GA, Thompson LD et al (2000) Splenic angiosarcoma: a clinicopathologic and immunophenotypic study of 28 cases. Mod Pathol 13:978–987

Ohtomo K, Fukuda H, Mori K, Minami M, Itai Y, Inoue Y (1992) CT and MR appearances of splenic hamartoma. J Comput Assist Tomogr 16:425

Ooi LL, Leong SS (1997) splenic abscesses from 1987 to 1995. Am J Surg 174:87–93

Parker LA, Mittelstaeedt CA, Mauro MA et al (1984) Ttorsion of a wandering spleen: CT appearance. J comput Assist Tomogr 8:1201–1204

Pyatt RS, Williams ED, Clark M, Gaskins R (1981) Case report: CT diagnosis of splenic cystic lymphangiomatosis. J Comput Assist Tomogr 5:446–448

Rabushka LS, Kavashima A, Fishman EK (1994) Imaging of the spleen: CT with supplemental MR examination. Radiographics 14:307–332

Rini JN, Leonidas JC, Maria B, Tomas et al (2003) 18F-FDG PET versus CT for evaluating the spleen during initial staging of lymphoma. J Nucl Med 44:1072–1074

Robert MA, Angela DL et al (2004) From the archives of the AFIP primary vascular neoplasms of the spleen: radiologic-pathologic correlation. RadioGraphics 24:1137–1163

Rolfes RJ, Ros PR (1990a) The spleen: an integrated imaging approach. Crit Rev Diagn Imaging 30:41–83

Rolfes RJ, Ros PR (1990b) The spleen: an integrated imaging approach. Crit Rev Diagn Imaging 30:41–83

Santoro L, Santini V, Lollo SD, Valeri A, Colagrande S (2005) Hemolymphangiomatosis of the spleen: imaging features. J Comput Assist Tomogr 29(6):831–833

Seckler SG, Rubin H, Rabinowitz JC (1964) Systemic cystic angiomatosis. Am J Med 37:976–86

Silverman ML, LiVolsi VA (1978) Splenic hamartoma. Am J Clin Pathol 70:224–229

Solbiati L, Bossi MC, Bellotti E et al (1983) Focal lesions in the spleen: sonographic patterns and guided biopsy. Am J Roentgenol 140:59−65

Steinberg JJ, Suhrland M, Valensi Q (1991) The spleen in the spleen syndrome: the association of splenoma with hematopoietic and neoplastic disease-compendium of cases since 1864. J Surg Oncol 47:193–202

Tatli S, Cizginer S, Wieczorek TJ, Ashley SW, Silverman SG (2008) Solitary littoral cell angioma of the spleen: computed tomography and magnetic resonance imaging features. J Comput Assist Tomogr 32(5):772–775

Thompson WM, Levy AD, Nadine S, Aguilera et al (2005) Angiosarcoma of the spleen: imaging characteristics in 12 patients. Radiology 235:106–115

Urrutia M, Mergo PJ, Ros LH, Torres GM, Ros PR (1996) Cystic masses of the spleen: radiologic-pathologic correlation. RadioGraphics 16:107–129

Van der Lanan RT, Verbeeten BJ, Smits NJ et al (1989) Computed tomography in the diagnosis and treatment of solitary splenic abscesses. J Comput Assist Tomogr 13:71−74

Wadsworth DT, Newman B, Abramson SJ, Carpenter BL, Lorenzo RL (1997) Splenic lymphangiomatosis in children. Radiology 202:173

Warnke R, Weiss LM, Chan JK, Clearly ML, Dorfman RF (1995) Tumors of the lymph nodes and spleen. Armed Forces Institute of Pathology, Washington

Warshauer DM, Molina PL, Hamman SM et al (1995) Nodular sarcoidosis of the liver and spleen: analysis of 32 cases. Radiology 195:757−762

Weiss L (1983) Histology: cell and tissue biology. Elsevier Biomedical, New York

Zwi LJ, Evans DJ, Wechsler AL, Catovsky D (1986) Splenic angiosarcoma following chemotherapy for follicular lymphoma. Hum Pathol 17:528–530

Imaging of Post Pancreatic Surgery

R. Graziani, S. Mautone, M. C. Ambrosetti, M. Barillari,
R. Manfredi, and R. Pozzi Mucelli

Contents

Abstract

Imaging plays an important role in pancreatic post-surgery patients. Because of its high spatial resolution, Multi Detector-row Computed Tomography (MDCT) is the most appropriate Imaging modality for evaluation of the normal aspects of pancreas and pancreatic region after surgery, for detection of post-surgery complications in early post-operative period and disease progression in neoplastic patients submitted to surgery treatment in delayed post-operative period. For these reasons, MDCT examination is performed routinely in pancreatic post-surgical patients. Magnetic Resonance (MR) alternatively can be used in case of hypersensibility reaction to CT intravenous iodinated contrast medium, renal insufficiency or when biliary ducts examination is necessary. MDCT study is performed in patients who have undergone pancreatic surgery in early post-surgery period, when there is clinical, laboratory and/or ultrasound suspicion of complications and later, for follow-up imaging, generally at 3–6 months intervals in neoplastic patients depending on their clinical situation. Thin detector collimation thickness (ideally 1 mm), axial, multiplanar (coronal, sagittal, curve) and 3D reconstruction images analysis is recommended to extensively evaluate post-surgery normal vascular anatomy, site of gastro-intestinal and biliary anastomosis and complications.

R. Graziani · S. Mautone · M. C. Ambrosetti · M. Barillari ·
R. Manfredi (✉) · R. Pozzi Mucelli
Department of Radiology,
Policlinico G.B. Rossi, University of Verona,
P.le Scuro, 10, 37134 Verona, Italy
e-mail: rmanfredi@univr.it

C. J. Zech et al. (eds.), *Multislice-CT of the Abdomen*, Medical Radiology. Diagnostic Imaging,
DOI: 10.1007/174_2011_462,

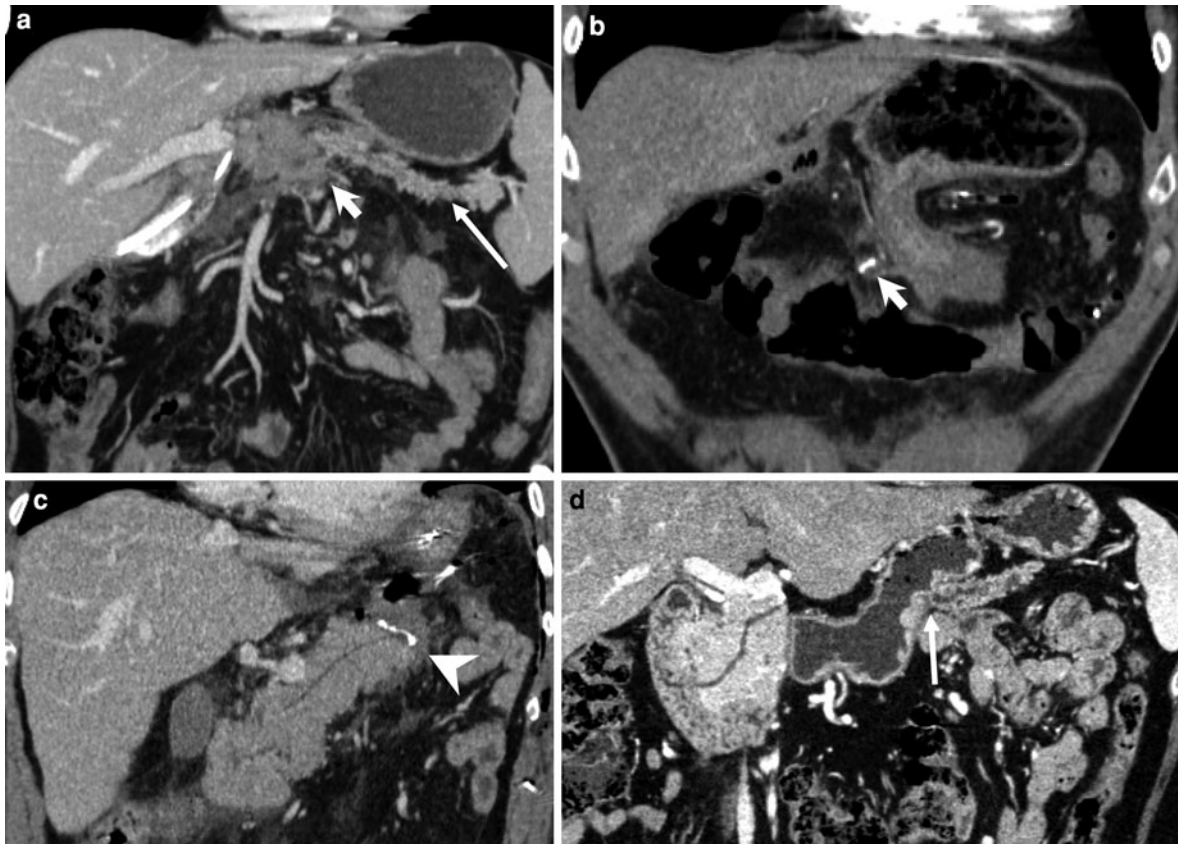

Fig. 1 Normal anatomy post pancreatic surgery. MDCT technique. Coronal (**a**–**c**) and curved (**d**) multiplanar reconstruction images after intravenous contrast medium administration during pancreatic phase. After Pancreaticoduodenectomy with Whipple procedure (**a**, **b**) the atrophic pancreatic parenchyma (*arrow*) and collapsed jejunal loop (*short arrow*), anastomized to pancreatic remnant and hepatic duct at the level of porta hepatis, are visible. In more anterior coronal plane (**b**) usually on the right of gastric remnant, the gastrojejunostomy (*short arrow*) with metallic staples, can be seen. After Spleno-Pancreatectomy (**c**), pancreatic tail and spleen are absent. The cut edge of pancreatic remnant is sutured with metallic staples (*arrowhead*). After Central Pancreatectomy (**d**), pancreatic body and neck are resected. The atrophic distal pancreatic remnant is anastomized to jejunal loop (*arrow*)

1 Normal Anatomic Post-Surgery Imaging Findings of the Pancreas

The knowledge of different surgical procedures, identification of post-surgery normal new anatomy and anastomosis are important for a correct detection of complications and pattern of recurrent diseases in neoplastic patients.

The Pancreaticoduodenectomy (PD) with Whipple procedure (Lepanto et al. 1994; Mortele et al. 2000; Johnson et al. 2002; Singh et al. 2004; Scialpi et al. 2005; Graziani et al. 2007, 2008; Tani et al. 2005; Coombs et al. 1990; Bluemke et al. 1992; Smith et al. 2008) is the most common pancreatic surgical procedure considering the standard surgical resection for pancreatic head and periampullary region lesions. PD is primarily indicated in two disease entities: neoplastic lesions in the periampullary region (cancer of the pancreatic head, of Ampulla of Vater, of the common bile duct and of the duodenum) and some form of chronic pancreatitis involving the pancreatic head and the uncinate process.

In PD with Whipple procedure (Fig. 1a, b), surgical dissection consists of resection of pancreatic head, duodenum, gastric antrum, gallbladder and intrapancreatic bile duct. Surgical reconstruction of this procedure involves the multiple anastomoses:

pancreaticojejunostomy (PJ), hepaticojejunostomy (HJ) and gastrojejunostomy (GJ).

In axial, coronal or curved multiplanar reconstructions MDCT images, PJ appears as tubular loop with endoluminal fluid or unopacified and frequently collapsed jejunal loop, attached to remnant, atrophic pancreatic body-tail (Fig. 1a). This anastomosis is located anterior to superior mesenteric artery, at the level of splenic vein. On the right side, at the level of porta hepatis, the jejunal loop is anastomized to hepatic duct (HJ: Fig. 1a). More anteriorly, the gastro-jejunostomy (GJ) is usually visible to the right of gastric remnant (Fig. 1b). Automated staple devices using metallic staples are frequently used for gastrojejunostomy.

The Whipple procedure has some technical variations, depending on extension of dissection or surgical modality of gastrointestinal tract reconstruction.

Pylorus-preserving—PD with Traverso and Longmires technique (Trerotola et al. 1989) is proposed as alternative to Whipple procedure in selective cases because it has been demonstrated to lead to a long-term improvement in gastrointestinal function. It involves preservation of the pylorus and the first portion of duodenum. In this type of pancreatic surgery, a duodenum-jejunal anastomosis is performed.

Other technical variation of Whipple procedure is PD with Pancreo-Gastro anastomosis (Tamm et al. 1995), that allows easy endoscopic follow–up of the anastomosis, particularly useful to identify recurrence in pancreatic intraductal papillary mucinous neoplams (IPMNs).

Several MDCT non-pathological appearances may be commonly present in asymptomatic patients undergoing PD procedure (Mortele et al. 2000), such as pneumobilia (70–80%), perivascular cuffing or increased attenuation of fat tissue around vascular structure (60%), probably due to inflammatory or fibrotic changes, reactive enlarged lymph nodes (32%), transient fluid film or fluid collections in pancreatic bed and adjacent to the anastomosis (28%). MDCT alone is unable to distinguish transient, reactive fluid from infected fluid collections: in septic patients, percutaneous aspiration is useful to confirm the diagnosis.

The post-surgical anatomy is more simple in other types of pancreatic surgery procedures than PD because the anatomic changes are less complicated.

Spleno-Pancreasectomy (SP) consists in open distal pancreatectomy and splenectomy and it is performed for pancreatic body-tail's neoplasms. In SP surgical procedure, MDCT easily recognizes the absence of the pancreatic tail and spleen (Fig. 1c). After removal of pancreatic tail, the cut edge of the pancreatic parenchyma is often sutured with metallic staples to prevent leakage of pancreatic juice in this area. In Distal Pancreatectomy only the pancreatic tail is resected whereas the spleen is preserved.

In Central Pancreatectomy (CP) the body and the neck of the pancreas are resected and a Roux-en-Y pancreaticojejunostomy to the distal pancreatic remnant is performed (Fig. 1d). This surgical procedure is indicated to treat lesions of the pancreatic body and neck, preserving endocrine and exocrine pancreatic function; however it has a higher incidence of post-surgical complications compared to other types of pancreatic surgery (Christein et al. 2002).

Total Pancreatectomy (TP), is most frequently performed in cases of diffuse central Intraductal Papillary Mucinous Neoplasms (IPMNs). In these cases, the entire pancreatic gland, the spleen, part of the stomach and of the small intestine, the common bile duct and the gallbladder are removed.

Few anatomic changes follow the surgical procedures of Anastomosis between main pancreatic duct and intestinal loops, indicated in Chronic Pancreatitis (Pancreaticojejunostomy or Main pancreatic duct jejunostomy), between Pseudocyst and gastrointestinal structure, indicated in Pancreatic Pseudocysts (Pseudocysto-gastro or Pseudocysto-duodenum, or Pseudocysto-jejuno anastomosis) and of Surgical toilette with Necrosectomy, indicated in the sequelae of Severe Acute Pancreatitis (Zins et al. 2009).

2 Early Post-Surgery Imaging Findings of the Pancreas

In the early post-surgery period, within 30 days after surgical procedure, imaging findings of the pancreas are represented by some MDCT pattern of post-operative complications that may follow pancreatic surgery treatment. These MDCT findings depend on clinical presentation of patients submitted to pancreatic surgery: infective, acute abdominal bleeding, biliary and gastrointestinal functional presentation. All complications are more frequent in the elderly and in

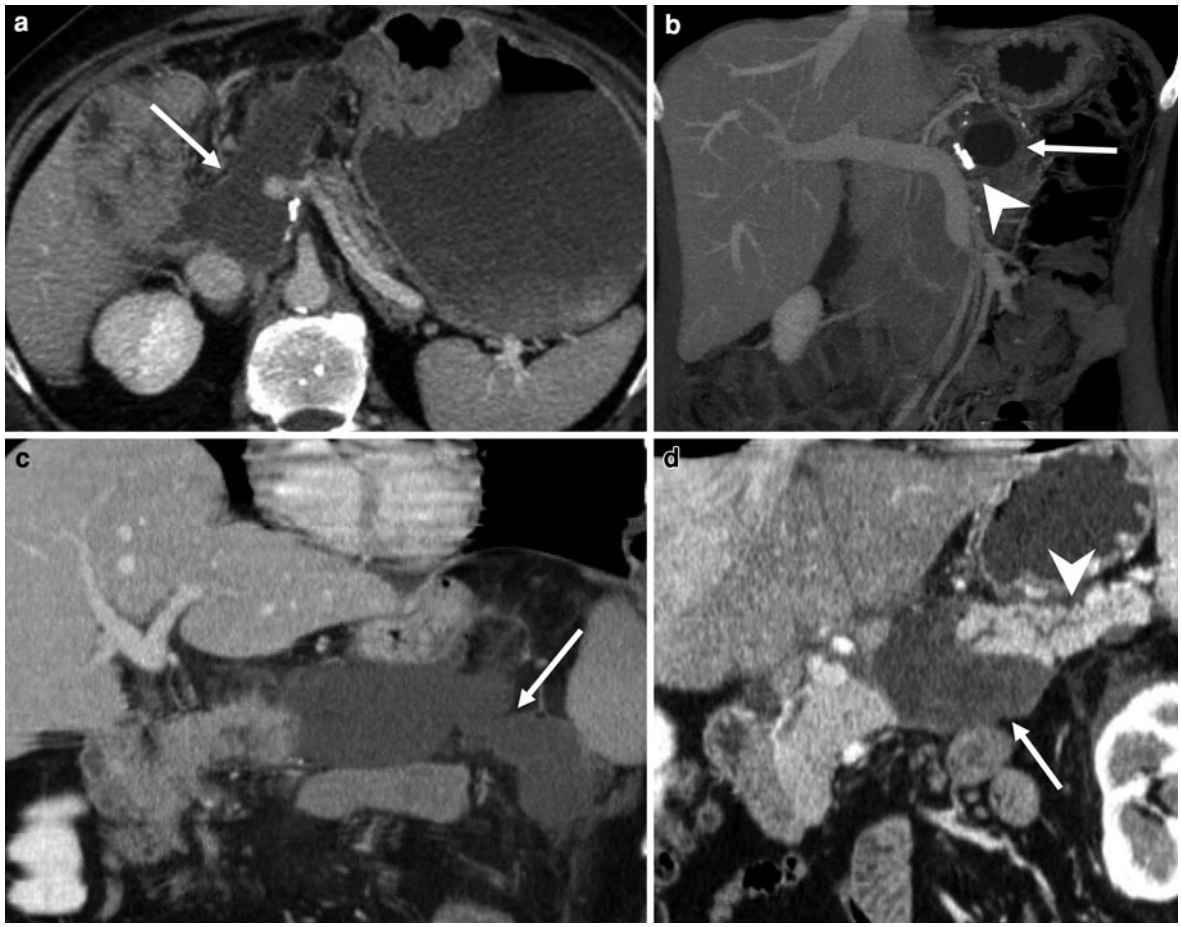

Fig. 2 Early post-surgical pancreatic findings. Infective fluid collections or abscess in patients with infective clinical presentation 6 days after pancreatic surgical resection. MDCT technique. Axial (**a**), coronal (**b**, **c**) and curved (**d**) multiplanar reconstruction images after intravenous contrast medium administration during pancreatic phase. After Pancreatico-duodenectomy with Whipple procedure (**a**) fluid collection, homogeneously hypodense, with thin peripheral wall is present in right anterior pararenal retroperitoneal space (*arrow*). After Spleno-Pancreatectomy (**b**) little rounded fluid collection (*arrow*), homogeneously hypodense, with thin peripheral wall is present on the *left* anterior pararenal retroperitoneal space, near surgery metallic staples of pancreatic remnant cut edge (*arrowhead*). After Distal Pancreatectomy with spleen preserving (**c**), a large homogeneous fluid collection on *left* anterior pararenal retroperitoneal space, near the spleen and along *left* colon fascial plane is present (*arrow*). After Central Pancreatectomy (**d**) fluid collection (*arrow*) between pancreatic remnant (*arrowhead*) and pancreatic head is visible

patients with a prolonged surgery time and high volume intraoperative blood loss (Smith et al. 2008; Miedema et al. 1992).

2.1 Infective Clinical Presentation

It is the most frequent clinical presentation in the early period after surgical pancreatic procedure, with persistent fever, symptoms of sepsis and increase of laboratory inflammatory markers.

The most common complication in this period in patients with infective clinical presentation is the presence of *infected fluid collections or abdominal abscess*, due to bacterial infection of retroperitoneal fluid film. Infected collections are frequently localized in pancreatic bed, near the site of pancreatic gland resection and in subphrenic spaces, but they can occur anywhere in abdomen and pelvis, sometimes localized also in intraperitoneal abdomen when the abdominal infective process is very extensive.

MDCT identifies this complication (Lepanto et al. 1994; Mortele et al. 2000; Johnson et al. 2002; Singh et al. 2004; Scialpi et al. 2005; Graziani et al. 2007, 2008; Tani et al. 2005; Coombs et al. 1990; Bluemke et al. 1992; Smith et al. 2008; Tamm et al. 1995; Zins et al. 2009; Miedema et al. 1992; Gervais et al. 2001; Butturini et al. 2006; DeOliveira et al. 2006; Cheng et al. 2007; Topal et al. 2007; Poon et al. 2007) as collections with fluid density, hypodense before and after intravenous contrast medium administration, (Fig. 2), with presence of gas bubbles in case of infection by anaerobic bacterial agents.

These infected fluid collections are typically localized in retroperitoneum on the right site (in anterior or posterior right pararenal space, near the right mesentery) after PD procedure (Fig. 2a), on the left site (in the anterior or posterior left pararenal space, in the splenic region, near the gastro-splenic ligament) after SP (Fig. 2b) or SP with spleen preservation (Fig. 2c) and in the peri-pancreatic space, after CP (Fig. 2d).

If infective reactions reach the intraperitoneal abdomen, causing peritonitis, MDCT technique shows presence of fluid in the subphrenic spaces, in Morrison's and in Douglas pouch. Frequently multiple abscesses in different abdominal areas are present.

In infective early post-surgery pancreatic patients, because of wound infection and/or dehiscence, with negative Ultrasound examination for abdominal collections, MDCT can easily shows superficial, extraperitoneal abdominal infected fluid collections, frequently missed by Ultrasound (Scialpi et al. 2005; Smith et al. 2008; Gervais et al. 2001).

MDCT is also able to correctly evaluate intraabominal abscesses because it easily depicts abdominal extension, number and intraparenchymal collections (hepatic abscess, biloma and splenic abscess).

MDCT is useful in the follow-up of patients suffering from this type of complications because it can demonstrate their progression or reduction after surgery or percutaneous TC-guided drainage (Singh et al. 2004; Scialpi et al. 2005; Graziani et al. 2007, 2008; Tani et al. 2005; Trerotola et al. 1989; Tamm et al. 1995; Christein et al. 2002; Gervais et al. 2001).

In early post-surgery period of septic patients, especially 7–10 days after PD (with Whipple procedure or Piloro-preserving) and CP, in presence of retroperitoneal infected fluid collections demonstrated by MDCT, a *surgical anasthomosis leakage or dehiscence* may be present (Lepanto et al. 1994; Mortele et al. 2000; Johnson et al. 2002; Singh et al. 2004; Scialpi et al. 2005; Graziani et al. 2007, 2008; Tani et al. 2005; Coombs et al. 1990; Bluemke et al. 1992; Smith et al. 2008; Tamm et al. 1995; Zins et al. 2009; Gervais et al. 2001; Butturini et al. 2006; DeOliveira et al. 2006; Cheng et al. 2007; Topal et al. 2007; Poon et al. 2007; Buchler et al. 2000). The leakage from pancreaticojejunostomy or from pancreatic remnant consequently causes retroperitoneal and/or intraperitoneal infected fluid collections. MDCT technique can demonstrates some indirect findings, that coupled with clinical symptoms and laboratory data, can be suggestive of anastomosis dehiscence. An increase of abdominal free gas, the presence of perianastomotic fluid and ascites should suggest diagnosis of this complications (Smith et al. 2008). MDCT technique directly identifies a dehiscence of surgical pancreojejunostomy (Graziani 2007, 2008; Smith et al. 2008) only after diluted iodinate contrast medium administration through percutaneous drainage catheters positioned in the retroperitoneal space. In this case axial, coronal and curved multiplanar reconstruction MDCT images show iodinate contrast medium inside the retroperitoneal fluid collection, thin fistulous tract and, at the same time, inside lumen of jejunal loop anastomosis and distal small bowel loops (Fig. 3a, b).

In about 20% of surgery procedure of PD (Buchler et al. 2000) and CP (Christein et al. 2002), 10–20 days after resection, infected patients may have *pancreatic fistula*. Diagnosis of pancreatic fistula is clinical. It is defined as concentration of amylase in the drainage output in the 3 days following surgery larger than 50 ml/die and drainage volume larger than 10 ml/die. MDCT study is indicated to exclude infected fluid collections. In 80% of cases medical treatment is sufficient to resolve post-surgery pancreatic fistula.

In 5% of complications in early period of post-pancreatic surgery especially after PD procedure, septic patients may be affected by *acute pacreatitis of remnant pancreas* (Lepanto et al. 1994; Mortele et al. 2000; Johnson et al. 2002; Singh et al. 2004; Scialpi et al. 2005; Graziani 2007, 2008; Tani et al. 2005; Coombs et al. 1990; Bluemke et al. 1992; Smith et al. 2008; Tamm et al. 1995; Zins et al. 2009; Miedema et al. 1992; Gervais et al. 2001; Butturini et al. 2006; DeOliveira et al. 2006; Cheng et al. 2007; Topal et al. 2007; Poon et al. 2007). This disease is clinically suspected when more than threefold increase in serum

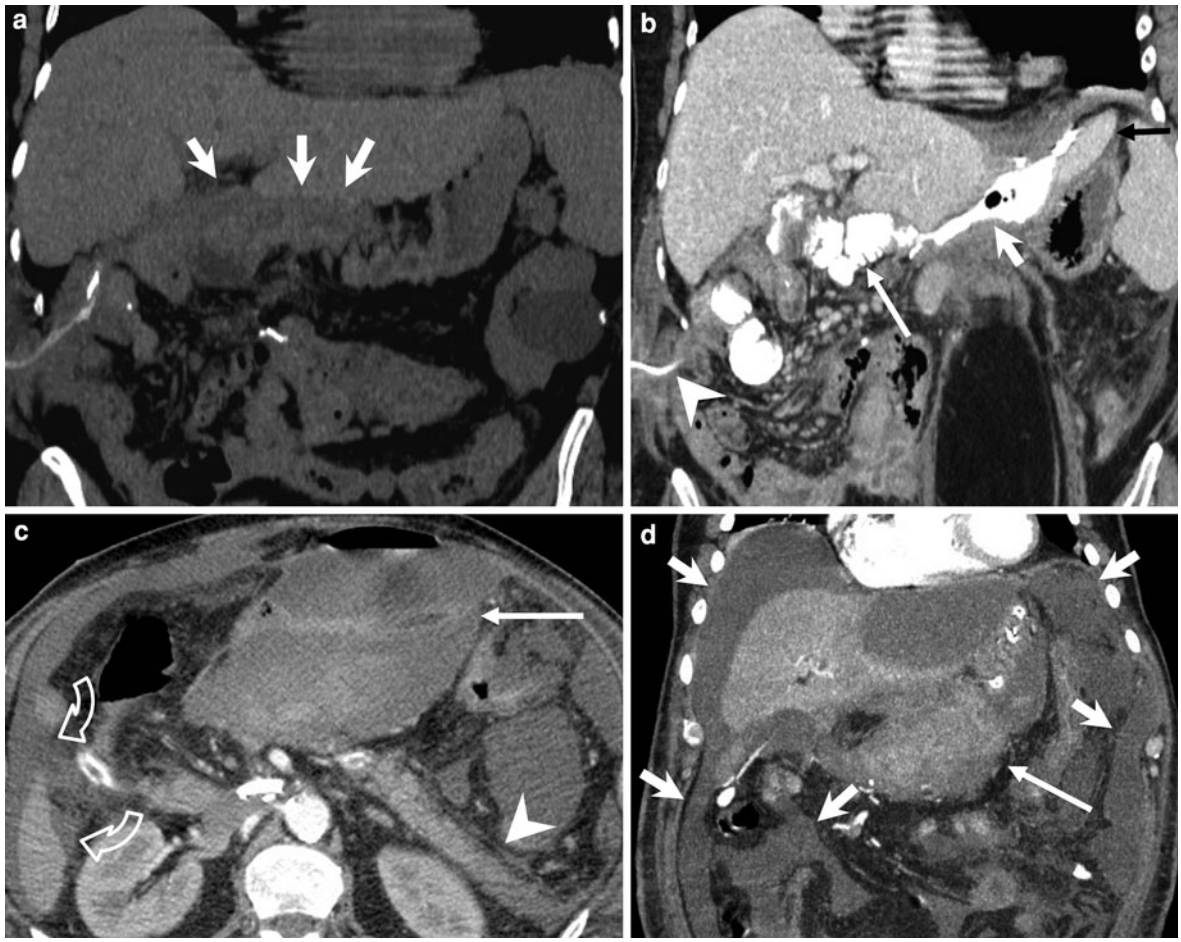

Fig. 3 Early post-surgical pancreatic findings. Pancreatic anastomosis dehiscence (**a**, **b**). Acute pancreatitis of the residual parenchyma (**c**, **d**) in patients with infective and septic clinical presentation after pancreatic surgery resection. MDCT technique. Axial (**c**), and coronal multiplanar reconstruction (**a**, **b** ,**d**) images, before (**a**) and after intravenous contrast medium administration during pancreatic (**c**, **d**) and portal venous (**b**) phases. Pancreatic anastomosis dehiscence (**a**, **b**) 10 days after Pancreaticoduodenectomy with Whipple procedure, a thin fluid film near pancreaticojejunostomy appears (**a** *short arrows*). Gas bubbles are not visible. After diluted iodinate contrast medium administration into retroperitoneal drainage catheters (**b** *arrowhead*), iodinate contrast medium appears inside the lumen of pancreo-jejunostomy (*long arrow*) and fluid collection (*short arrow*) between pancreojejunostomy and pancreatic remnant (*black arrow*). It indirectly demonstrates presence of surgical pancreojejunostomy dehiscence. Acute pancreatitis of the remaining pancreatic parenchyma (**c**, **d**). Six days after Pancreaticoduodenectomy with Whipple procedure a septic patient shows a threefold increase in serum amylase and lipase. Amylase also appears in the drenaige output. MDCT images show pancreatic stranding or fluid film around the remaining pancreatic parenchyma (*arrowhead*), extensive retroperitoneal fluid collections, (*short arrows*) large hemorrhagic collection (*arrow*) with hyperdense areas due to blood clots and perihepatic peritoneal fluid (*curve arrows*)

amylase and lipase is present three days following surgery. MDCT is the best imaging modality to rule out this complication because it demonstrates remnant parenchyma necrosis and typical peripancreatic and left pararenal retroperitoneal fluid collections (Fig. 3c, d).

2.2 Abdominal Acute Bleeding Clinical Presentation

Abdominal bleeding is suspected when in early period after surgical pancreatic procedure, patients present signs and symptoms of hypovolemic shock,

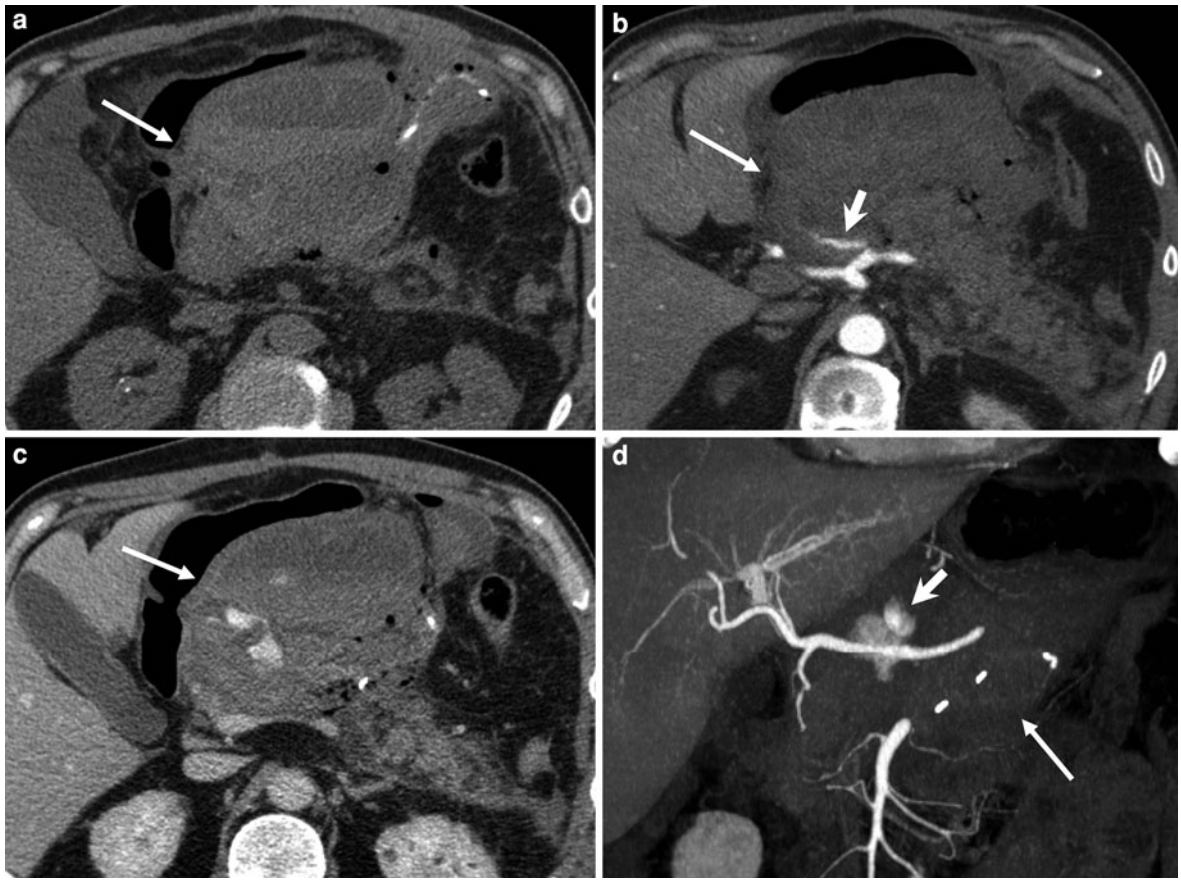

Fig. 4 Early findings post pancreatic surgery. Abdominal acute bleeding in patients with clinical presentation of hypovolemic shock and fresh blood comparing in the drainage catheters output. MDCT technique. Axial (**a**, **c**) and maximum intensity projection (MIP: **d**) reconstruction images, before (**a**) and after intravenous contrast medium administration during pancreatic (**b**, **d**) and portal venous phases (**c**). Forty-eight hours after Pancreaticoduodenectomy with Whipple procedure, MDCT study shows a large abdominal hemorrhagic collection (*arrows*) with hyperdense areas due to blood clots presence. During pancreatic phase of MDCT study in axial images a small hyperdense, vascular lesion compares near the splenic artery, inside the hemorrhagic collection, due to arterial leakage (**b** *short arrow*). MIP reconstruction image better demonstrates the presence of splenic artery Pseudoaneurysm with arterial leakage (**d** *short arrow*). The output of vascular contrast medium (**c**) is visible also during portal venous phase (arterial abdominal bleeding in Pseudoaneurysm of splenic artery)

hemoglobin and hematocrit decrease, fresh blood comparing in drainage catheters fluid and replacement of more than three units of blood is necessary in the 24 h following the end of surgery.

If fresh blood compares in drains catheters fluid before 24–48 h after surgical procedure, bleeding is generally caused by leakage of venous vessels or little arteries, localized in abdominal wound or superficial tissue of abdominal wall or in mesenteric fat tissue, especially along drains catheters. Frequently this complication is self-limiting. MDCT technique recognizes the presence of abdominal hematomas, that appear like fluid collections with increase of attenuation, hyperdense before and after intravenous iodinate contrast medium administration. Vascular acute bleeding during arterial phase of MDCT study is absent.

If fresh blood compares in drains catheters fluid after 48 h of end of surgical procedure, bleeding is caused by "arterial disruption" or pseudoaneurysm formation. Frequently from the gastro-duodenal artery, the superior mesenteric artery or the pancreaticoduodenal arteries. Both these pathological situations are due to previous Acute Pancreatitis of

remnant pancreas and/or pancreaticojejunostomy dehiscence. This hemorrhagic complication, following pancreatic surgery that occurs approximatively in 7% of the cases, is easily and quickly demonstrated by axial, multiplanar and 3D reconstruction MDCT images (Lepanto et al. 1994; Mortele et al. 2000; Johnson et al. 2002; Singh et al. 2004; Scialpi et al. 2005; Graziani et al. 2007, 2008; Tani et al. 2005; Coombs et al. 1990; Bluemke et al. 1992; Smith et al. 2008; Tamm et al. 1995; Zins et al. 2009; Miedema et al. 1992; Gervais et al. 2001), before and after intravenous contrast medium administration with quadriphasic study (Fig. 4a–d). When MDCT arterial phase recognizes acute bleeding from arterial vessels (Fig. 4b, d), Angiography is the modality of choice in defining arterial anatomy, site of bleeding and trying non-invasive treatment of this hemorrhage complication with vascular embolization.

2.3 Biliary Ducts Lesion Clinical Presentation

In 10–30% DP, patients may clinically present signs and symptoms of a biliary tract lesion, most frequently caused by leakage of hepaticojejunostomy or stenosis of bilio-digestive anastomosis, during the early post-surgery period.

MDCT can try to recognize these complications only using multiplanar with MinIP technique and coronal 3D reconstruction images (Lepanto et al. 1994; Mortele et al. 2000; Johnson et al. 2002; Singh et al. 2004; Scialpi et al. 2005; Graziani et al. 2007, 2008; Tani et al. 2005; Coombs et al. 1990; Bluemke et al. 1992; Smith et al. 2008; Tamm et al. 1995; Zins et al. 2009; Miedema et al. 1992; Gervais et al. 2001; Butturini et al. 2006). Imaging modalities of choice for biliary complication study are Magnetic Resonance (MR) and MR-Cholangiopancreatography (MRCP).

2.4 Abdominal Functional Clinical Presentation

During early post-surgical period 10–30% of patients undergoing DP, especially with Whipple technique, suffer of delayed gastric emptying, defined as gastric tube presence, for more than 10 days after the end of surgery procedure.

MDCT is not an useful Imaging technique for diagnosis of this complication because distension of gastric remnant is just visible with X-ray film of Abdomen. Oral-contrast X-ray study may be needed to differentiate a mechanical from a dynamic obstruction disease. This complication may be transient but frequent medical treatment with motility-enhancing agents is necessary (Smith et al. 2008).

3 Delayed Post-Surgery Imaging Findings of the Pancreas

Delayed post-surgery Imaging findings of the pancreas are represented by neoplastic disease progression after complete or not-radical (palliative) resective surgery procedure for presence of tumor recurrence, liver metastasis or peritoneal carcinomatosis. Imaging modality of choice to identify, characterize and follow-up of these lesions is MDCT, associated in some neoplastic forms to MR.

In *ductal adenocarcinoma*, the survival rate of patients who undergo PD is about 4–5% at 5 years. In patients with small adenocarcinoma (<2 cm of maximum diameter), localized disease with no extension beyond pancreatic capsule, no lymph node metastasis, five-year survival rate after complete surgical resection is reported in about 26% (Ferrone et al. 2008). In patients submitted to pancreatic surgery for ductal adenocarcinoma, disease progression occurs in 60% of cases locally (Lepanto et al. 1994; Scialpi et al. 2005; Graziani et al. 2007, 2008; Smith et al. 2008; Bluemke et al. 1997; Dalla Valle et al. 2006). The risk of tumor recurrence is thought to be depending on tumor diameter (inferior or superior to 2 cm), absence or presence of malignancy in pancreatic resection margins, absence or presence of lymph node metastasis and presence or absence of K-ras mutation that seems to be correlated with micro-metastasis.

Detection of recurrent pancreatic carcinoma after surgery and liver metastasis is important for assessing patients' prognosis, and selecting patients who may be candidate to adjuvant and additional treatment.

At imaging follow-up, performed by MDCT (Fig. 5a) and MR techniques, local pancreatic recurrent disease appears as infiltrating soft-tissue mass, hypovascular after intravenous contrast

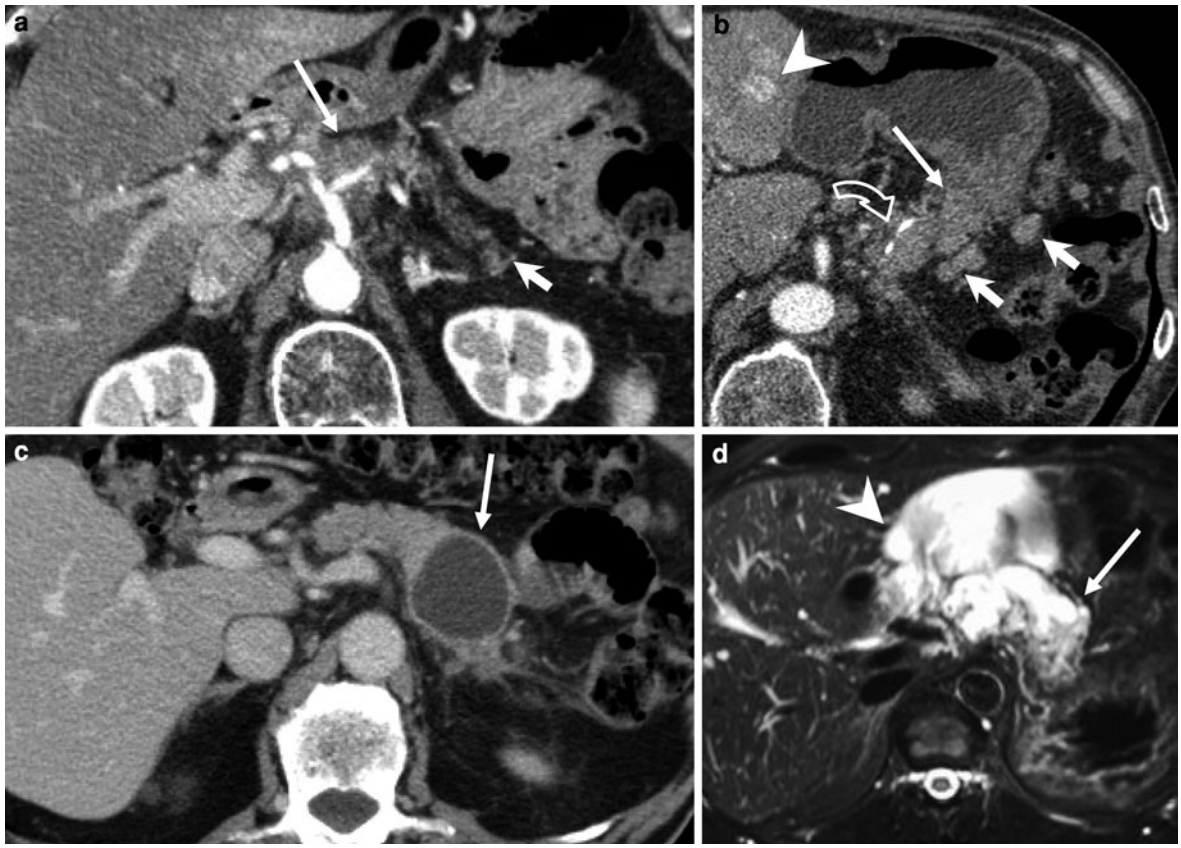

Fig. 5 Findings of delayed recurrent disease post- pancreatic surgery MDCT technique: axial images after intravenous contrast medium administration during pancreatic (**a**, **b**) and portal venous (**c**) phases. MR imaging: T2-weighted axial image before intravenous contrast medium administration (**d**). **a** Seven months after Pancreaticoduodenectomy with Whipple procedure for pancreatic head adenocarcinoma, MDCT imaging follow-up shows hypovascular infiltrating soft-tissue mass (*arrow*) with encasement of celiac artery, localized on pancreatic bed, on the *right* side of atrophic residual pancreatic parenchyma (*short arrow*). **b** One year after Spleno-Pancreasectomy for Non-Functioning Neuroendocrine tumor of pancreatic tail, MDCT imaging follow-up shows irregular soft-tissue mass (*arrow*) with gastric infiltration, near metallic staples of pancreatic remnant cut edge (*curve arrow*). Hypervascular liver metastasis (*arrowhead*) and retroperitoneal lymph nodes (*short arrows*) are visible. **c** Two years after Spleno-Pancreasectomy for IPMN of pancreatic tail, MDCT imaging follow-up shows fluid cystic lesion (*arrow*) at the level of pancreatic remnant cut edge, with thickened peripheral wall, and posterior parietal solid nodule. **d** Five years after Spleno-Pancreasectomy for IPMN of pancreatic tail, MR imaging follow-up shows abnormal dilatation of pancreatic remnant main duct that appears like large fluid cystic lesion (*arrow*), with high signal intensity on T2-weighted sequence and some small endoluminal filling defects due to neoplastic nodules. Abnormal distention of a intestinal loop (*arrowhead*) near the pancreatic lesion, showing high signal intensity on T2-weighted sequence, is visible (malignant IPMN pancreatic recurrent with neoplastic intestinal diffusion)

medium administration, with irregular morphology, generally localized near the surgical margins, with encasement of mesenteric and/or splenic vessels, celiac artery or portal vein and invasion of mesenteric fat tissue. Also intestinal loops and hepaticojejunostomy may be infiltrated by recurrent neoplasm with intestinal occlusion and upstream biliary ducts dilatation respectively (Smith et al. 2008; Zins et al. 2009; Bluemke et al. 1997; Dalla Valle et al. 2006).

In 20% of patients submitted to pancreatic surgery for ductal adenocarcinoma, disease progression is represented by liver metastasis. In the remaining 20% of the patients, disease progression after surgery is due to both local recurrence and liver metastasis (Bluemke et al. 1997).

The MDCT accuracy in disease recurrence detection is reported to be 93% (Bluemke et al. 1997; Dalla Valle et al. 2006). This accuracy values decrease in patients undergoing to Radio- and Chemo-therapy after surgery treatment because the differential diagnosis between tumor recurrence and post-Radio-therapy fibrosis may be difficult on diagnostic imaging. PET–TC seems more useful in addressing this issue (Bares et al. 1994; Delbeke et al. 1999; Ruf et al. 2005).

In *malignant pancreatic neuroendocrine tumors*, functioning or nonfunctioning, the disease progression after surgery treatment is usually suspected by clinical presentation and laboratory tests. It is usually detected by Nuclear Medicine technique.

MDCT (Fig. 5b) and MR are imaging modalities useful to demonstrate site and dimension of recurrent lesions, liver metastasis and abdominal metastatic lymph nodes.

In *malignant pancreatic cystic neoplasms* (mucinous cystoadenoma/cystadenocarcinoma and IPMN) diagnostic accuracy of MR is superior than MDCT because MR has a better tissue contrast resolution than CT.

Imaging techniques identify disease progression after surgery treatment because it recognizes fluid–solid lesions, compared to adjacent pancreas, at level of pancreojejunostomy or in distal retroperitoneum. These lesions are small post surgery showing a large solid-cystic mass appearance (Fig. 5c, d), and tend to enlarge with time.

References

Bares R, Klever P, Hauptmann S et al (1994) F-18 fluorodeoxyglucose PET in vivo evaluation of pancreatic glucose metabolism for detection of pancreatic cancer. Radiology 192:79–86

Bluemke DA, Fishman EK, Kuhlman J (1992) CT evaluation following Whipple procedure: potential pitfalls in interpretation. J Comput Assist Tomogr 16:704–708

Bluemke DA, Abrams RA, Yeo CJ, Cameron JL, Fishman EK (1997) Recurrent pancreatic adenocarcinoma: spiral CT evaluation following the Whipple procedure. Radiographics 17:303–313

Buchler MW, Friess H, Wagner M, Kulli C, Wagener V, Z'Graggen K (2000) Pancreatic fistula after pancreatic head resection. Br J Surg 87:883–889

Butturini G, Marcucci S, Molinari E et al (2006) Complications after pancreaticoduodenectomy: the problem of current definitions. J Hepatobiliary Pancreat Surg 13:207–211

Cheng Q, Zhang B, Zhang Y et al (2007) Predictive factors for complications after pancreaticoduodenectomy. J Surg Res 139:22–29

Christein JD, Kim AW, Jakate S, Deziel DJ (2002) Central pancreatectomy for a pancreatic ganglioneuroma in a patient with previous neuroblastoma. Pancreatology 2:557–560

Coombs RJ, Zeiss J, Howard JM, Thomford NR, Merrick HW (1990) CT of the abdomen after the Whipple procedure: value in depicting postoperative anatomy, surgical complications, and tumor recurrence. AJR Am J Roentgenol 154:1011–1014

Dalla Valle R, Mancini C, Crafa P, Passalacqua R (2006) Pancreatic carcinoma recurrence in the remnant pancreas after a pancreaticoduodenectomy. JOP 7:473–477

Delbeke D, Rose DM, Chapman WC et al (1999) Optimal interpretation of FDG PET in the diagnosis, staging and management of pancreatic carcinoma. J Nucl Med 40:1784–1791

DeOliveira ML, Winter JM, Schafer M et al (2006) Assessment of complications after pancreatic surgery: a novel grading system applied to 633 patients undergoing pancreaticoduodenectomy. Ann Surg 244:931–937(discussion 937–939)

Ferrone CR, Brennan MF, Gonen M et al (2008) Pancreatic adenocarcinoma: the actual 5-year survivors. J Gastrointest Surg 12:701–706

Gervais DA, Fernandez-del Castillo C, O'Neill MJ, Hahn PF, Mueller PR (2001) Complications after pancreatoduodenectomy: imaging and imaging-guided interventional procedures. Radiographics 21:673–690

Graziani R, Cicero C, Casagranda G, Mehrabi S et al (2007) Pancreas. In: Pozzi Mucelli R (eds) TC Multistrato dell'addome. Idelson-Gnocchi, Napoli, pp 193–262

Graziani R, Cicero C, Casagranda G, Contro A et al (2008) Pancreas operato. In: Graziani R, Pozzi Mucelli R (eds) TC multistrato del pancreas. Idelson-Gnocchi, Napoli, pp 217–245

Johnson PT, Curry CA, Urban BA, Fishman EK (2002) Spiral CT following the Whipple procedure: distinguishing normal postoperative findings from complications. J Comput Assist Tomogr 26:956–961

Lepanto L, Gianfelice D, Dery R, Dagenais M, Lapointe R, Roy A (1994) Postoperative changes, complications, and recurrent disease after Whipple's operation: CT features. AJR Am J Roentgenol 163:841–846

Miedema BW, Sarr MG, van Heerden JA, Nagorney DM, McIlrath DC, Ilstrup D (1992) Complications following pancreaticoduodenectomy. Current management. Arch Surg 127:945–949 (discussion 949–950)

Mortele KJ, Lemmerling M, de Hemptinne B, De Vos M, De Bock G, Kunnen M (2000) Postoperative findings following the Whipple procedure: determination of prevalence and morphologic abdominal CT features. Eur Radiol 10:123–128

Poon RT, Fan ST, Lo CM et al (2007) External drainage of pancreatic duct with a stent to reduce leakage rate of pancreaticojejunostomy after pancreaticoduodenectomy: a prospective randomized trial. Ann Surg 246:425–433 (discussion 433–425)

Ruf J, Lopez Hanninen E, Oettle H et al (2005) Detection of recurrent pancreatic cancer: comparison of FDG-PET with CT/MRI. Pancreatology 5:266–272

Scialpi M, Scaglione M, Volterrani L et al (2005) Imaging evaluation of post pancreatic surgery. Eur J Radiol 53: 417–424

Singh AK, Gervais D, Mueller P (2004) Pancreatoduodenectomy: imaging and image-guided interventional treatment. Semin Ultrasound CT MR 25:252–260

Smith SL, Hampson F, Duxbury M, Rae DM, Sinclair MT (2008) Computed tomography after radical pancreaticoduodenectomy (Whipple's procedure). Clin Radiol 63:921–928

Tamm EP, Jones B, Yeo CJ, Maher MM, Cameron JL (1995) Pancreaticogastrostomy and the Whipple procedure: radiographic appearance and complications. Radiology 196: 251–255

Tani M, Onishi H, Kinoshita H et al (2005) The evaluation of duct-to-mucosal pancreaticojejunostomy in pancreaticoduodenectomy. World J Surg 29:76–79

Topal B, Aerts R, Hendrickx T, Fieuws S, Penninckx F (2007) Determinants of complications in pancreaticoduodenectomy. Eur J Surg Oncol 33:488–492

Trerotola SO, Jones B, Crist DW, Cameron JL (1989) Pylorus-preserving Whipple pancreaticoduodenectomy: postoperative evaluation. Radiology 171:735–738

Zins M, Loriau J, Boulay-Coletta I, Julles M, Petit E, Sauvanet A (2009) Postoperative imaging of the pancreas and duodenum. J Radiol 90:918–936

Renal Masses

Anno Graser and Ullrich G. Mueller-Lisse

Contents

Abstract

The widespread use of diagnostic ultrasound and MDCT for a variety of clinical entities has led to an increase in the detection of renal masses (Smith et al. in Radiology 170(3 Pt 1):699–703, 1989). The earlier a mass is detected on imaging, the higher the likelihood of it being early stage and low grade (Tsui et al. in J Urol 163(4):1090–1095, 2000), and therefore amenable to nephron-sparing surgery as opposed to total nephrectomy. Various therapeutic options exist for treatment of localized renal cell carcinoma: Open or laparoscopic total or partial nephrectomy, laparoscopic and percutaneous ablational therapies such as radiofrequency ablation (RFA) and cryotherapy, or minimally invasive catheter techniques like super selective chemoembolization. Against this background, the imaging-based selection of the right therapeutic strategy for each individual patient becomes more and more important. Furthermore, prognosis and outcome are influenced by tumor stage and grade at the time of diagnosis. Because of its high diagnostic power, MDCT can be applied as the primary and definitive diagnostic imaging method in differentiation of renal masses that are indeterminate or suspicious at IVU or ultrasound, e.g., cystic lesions, tumors, pseudotumors, calcifications, or arteriovenous malformations. Recent advances in MDCT technology, namely the introduction of dual energy CT (DECT), iterative reconstruction of image data, and associated advanced dose reduction strategies have a great impact on the routine use of MDCT for the workup of patients with renal masses. This chapter will

A. Graser (✉) · U. G. Mueller-Lisse
Department of Clinical Radiology, University of Munich, Marchioninistrasse 15, 81377 Munich, Germany
e-mail: Anno.Graser@med.uni-muenchen.de

C. J. Zech et al. (eds.), *Multislice-CT of the Abdomen*, Medical Radiology. Diagnostic Imaging,
DOI: 10.1007/174_2011_494, © Springer-Verlag Berlin Heidelberg 2012

focus on both state-of-the-art MDCT applications and recent developments in patients with renal tumors. Furthermore, the TNM staging system will be reviewed.

1 MDCT Technology and Radiation Exposure

MDCT provides the ability to detect, characterize, and stage renal tumors in one single fast high resolution examination, if a specially tailored multiphasic examination protocol is used (Catalano et al. 2003). To allow for multiplanar reformatting of raw data, a narrow detector collimation should be employed, which is typically going to be 64, 128, or up to 320 × 0.5–0.625 mm, depending on the number of the detector rows and detector configuration of the scanner.

2 Post Processing Techniques

State-of-the-art MDCT scanners provide isotropic volume element (voxel) sizes of less than 0.4 mm, enabling high quality sagittal and coronal multiplanar reformats (MPR) as well as reconstruction of three-dimensional volume rendering technique (VRT) images. These different displays of image data sets of the kidneys facilitate large data volume handling and communication of findings to the urologist. In our institution, coronal MPR views are routinely obtained in all scans performed for assessment of renal pathologies; VRT views are helpful for evaluation of renal vasculature and detection of extrarenal tumor spread. In addition, they can be useful for visualization of the relationship between a tumor and the renal vessels and pelvis. If there is suspicion of renal vein invasion, loading the thin-slice dataset into a dedicated 3-D viewing software often facilitates diagnosis. Delayed phase (excretory phase) scans can be displayed using coronal multiplanar reformations (MPR) at a slice thickness of 2–3 mm (Dillman et al. 2008). This display is not useful for detection of small lesions within the renal pelvis and ureters as these may be masked by bright contrast within the renal collecting system.

3 Radiation Dose Considerations

As a renal mass examination protocol should consist of at least two or even three different phases (unenhanced, nephrographic, and delayed phases), radiation exposure is of concern. It can be kept to a minimum using low-dose techniques for unenhanced and delayed phases. In modern scanners, further decrease of radiation dose can be achieved by means of sophisticated dose modulation algorithms that adjust the X-ray tube current to the patient's individual anatomy in x and y plane as well as the patient's length axis (z-axis). Furthermore, the delivery of several contrast agent boluses to the patient leads to inclusion of several phases of contrast media excretion by the kidneys in just one CT scan. Although this technique elegantly saves radiation dose, it decreases contrast between renal arteries, parenchyma, and renal pelvis when compared to multiphasic imaging. Also, it may impair image interpretation whenever renal function deviates from the expected normal range or when the two kidneys differ functionally. Therefore, indications should be carefully evaluated; generally, if benign conditions like hydronephrosis of benign causes or congenital anomalies are assumed, a combined nephrographic-excretory phase approach should be chosen, while suspected TCC in patients with macroscopic hematuria should be evaluated by consecutive nephrographic and excretory phase scans (Van Der Molen et al. 2008).

For multiphasic examinations, there are new ways of reducing radiation exposure to the patient. By means of iterative reconstruction of image data, image quality can be kept constant at significantly reduced tube current–time product values ("reference mAs") when tube current modulation techniques are used. The technology was only recently introduced and since had a significant impact on abdominal CT protocols. Several studies show that an up to 45% dose reduction can be achieved without negative effects on image quality (Lee et al. 2011; Winklehner et al. 2011). Furthermore, new scanner software allows for abdominal MDCT scanning at lower kVp values; the scanner will—based on the attenuation profile of the patient on the topogram scan—suggest to acquire images at 80 or 100 kVp rather than at 120 kVp, thereby dramatically reducing dose and better exploiting contrast characteristics of iodine.

4 Dual Energy CT of the Kidneys

A recent technological advance in CT has been the introduction of different technical approaches to dual energy CT scanning, namely using a dual source CT scanner (Siemens Healthcare), rapid kV switching (GE Healthcare), and use of a dual layer detector (Philips Healthcare). On this scanner, two X-ray tubes can be operated at different tube potentials, making "dual energy" scanning possible. Dual energy scanning implies simultaneously acquiring data sets at two different photon spectra in a single CT acquisition (Chiro et al. 1979; Cann et al. 1982). By scanning at different photon energies, differences in material composition can be detected based on differences in photon absorption. This technique exploits attenuation differences of materials with large atomic numbers like iodine. For example, the attenuation of iodine will be much greater at 80 or 100 kVp than at 140 kVp. Importantly, based on the reconstruction of complete 80 and 140 kVp image data sets from the raw data, "virtual non contrast" data sets and "virtual angiographic" data sets can be generated utilizing various dual energy post processing algorithms which are based on three-material decomposition principles. In the abdomen, the three materials usually analyzed are soft tissue, fat, and iodine (Johnson et al. 2007).

Generation of virtual non-contrast images obviates the routine need for non-contrast acquisitions. That is, a single contrast-enhanced acquisition can yield both contrast-enhanced and non-contrast CT data. This is of great importance when evaluating the adrenal glands and kidneys and can be utilized to decrease radiation exposure to patients.

Dual energy scanning can be used for the differentiation of high density cysts from solid renal masses (Fig. 1). Using dual energy post processing software, the contrast agent can be digitally subtracted from the image. This can be done because the dual energy index of iodine is significantly different from the dual energy index of soft tissue and fat. The dual energy data can also be used to generate a color coded image that shows the distribution of iodine within the scan field. This color coded display is sensitive to subtle enhancement and can aid in detecting enhancement in solid lesions, see Fig. 2. In our experience, high density renal cysts with a density greater than the renal parenchyma (e.g., 60 HU for a hemorrhagic cyst) will be reliably identified and characterized based on measured HU values as those correlate well between true non-contrast and virtual non-contrast datasets (Graser et al. 2009).

A study comparing a dual energy to a single energy approach showed that renal masses can be reliably characterized as being cystic or solid using a single-phase DECT acquisition, thereby reducing radiation exposure to the patient by almost 50% (Graser et al. 2010).

5 Examination Protocols

5.1 Patient Preparation

To guarantee optimal excretion of contrast media during renal CT, sufficient hydration of the patient is essential. This can be achieved by oral or intravenous administration of fluid volume. However, concomitant disease, such as cardiac or renal insufficiency, has to be considered. Hydration may also minimize nephrotoxic effects of intravenous contrast media. Simultaneous filling of the gastro-intestinal tract with negative or neutral oral contrast media may be useful. Interfering effects may occur with CT arteriography or CT urography and the application of positive oral contrast media which is therefore not recommended (Coppenrath and Mueller-Lisse 2006).

5.2 Phases of Renal Contrast

Unenhanced CT can be used for the detection of stones within the urinary tract. A low-dose technique may be applied for this indication. In CT protocols including different phases of contrast enhancement (e.g., protocols for tumor characterization) an unenhanced scan is helpful for verification of fat (for instance, in angiomyolipoma or adenoma), detection of blood (increased CT density and lack of contrast enhancement), and detection of calcifications (e.g., complex cystic lesions or renal cell carcinoma) (Coppenrath and Mueller-Lisse 2006).

Fast modern MDCT scanning requires exact timing of contrast bolus injection and acquisition of images in adequate contrast phases. Usually, about 80–150 ml of non-ionic, iodinated contrast media are injected into a large antecubital vein with a power injector. The delivery rate is set to 2–4 ml/s, and the contrast media is

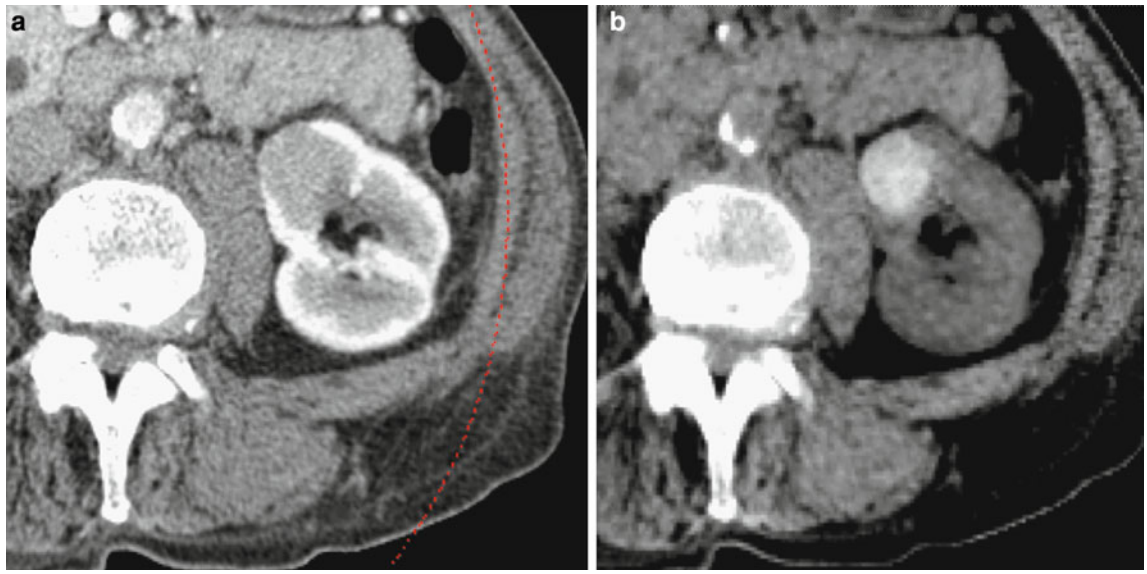

Fig. 1 Intraparenchymal mass on the anterior aspect of the left kidney. The nephrographic phase contrast-enhanced image (**a**) shows the mass as isoattenuated to the renal medulla. The virtual nonenhanced (VNE) image from this dual energy CT scan clearly shows that the lesion is hyperdense, a finding that is consistent with a complex cyst

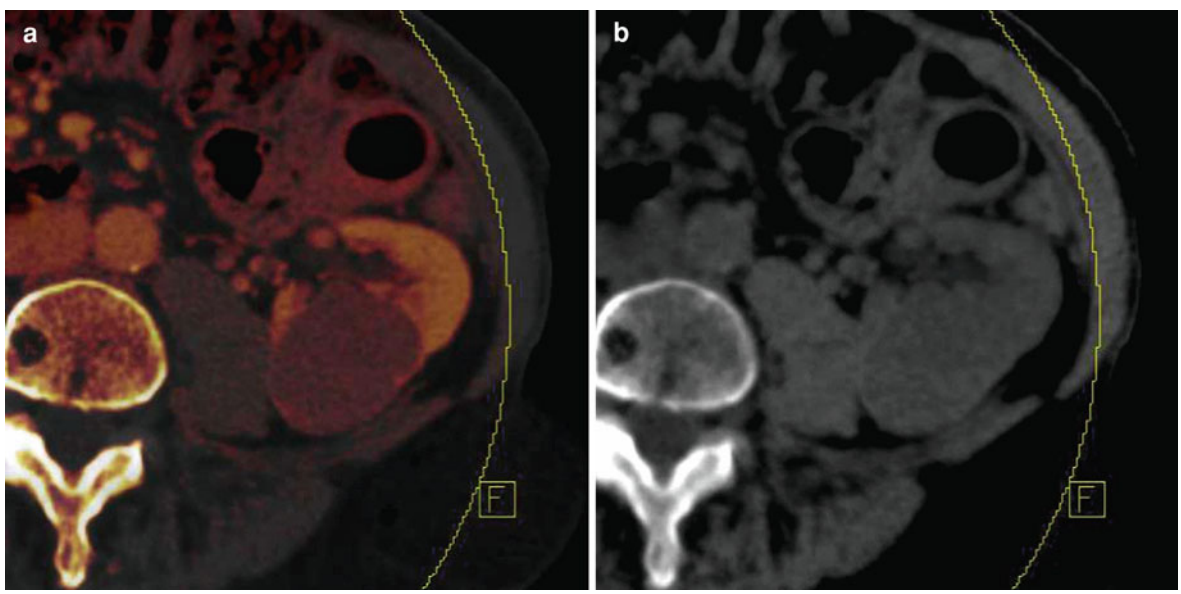

Fig. 2 Visualization of enhancement on single-phase DECT. The color coded iodine map shows orange color, representative of iodine, with a 3.5 cm mass on the dorsal left kidney. The virtual nonenhanced image (**b**) demonstrates the mass to be isoattenuating to renal parenchyma. Note intravertebral hemangioma at the same level

administered as a single bolus. The phases of dynamic, contrast-enhanced renal CT are the same that account for the quality and appearance of renal angiography and of the nephrogram and pyelogram during IVU. In principle, radio-opaque contrast media passes through the three renal compartments: blood vessels, interstitium, and tubules. Since the renal interstitial space is very small, contrast in the kidney at each time point after bolus administration of contrast media is primarily a function of renal perfusion and renal excretion.

Table 1 The Bosniak classifiation system for cystic renal masses (Coppenrath et al. 2006)

Bosniak category	Malignancy	Features
I	Benign	Hair thin wall, no septa, no calcification, no contrast enhancement, no solid components, cyst content with water density
II	Probably benign	Hair thin wall, few hairline thin septa, fine calcification, no contrast enhancement, no solid components, cyst content >20 HU
II F	Probably benign	More hairline thin septa, minor contrast enhancement, nodular calcification, no solid components, cyst content >20 HU
III	Malignant in approximately 30% of cases = potentially malignant	Indeterminate cystic masses, irregular thickened wall, irregular septa, contrast enhancement, no solid components
IV	Malignant	Clearly malignant cystic lesions, contrast enhancement, solid components

Imaging of the kidneys in different phases after intravenous contrast media administration depends on sequential arrival of blood carrying contrast media in different parts of the renal parenchyma. Imaging phases have to be selected carefully in accordance with clinical indication (Table 1).

Protocols concentrating on macroscopic renal arteries (e.g., to rule out renovascular disorders in patients with arterial hypertension, or to rule out anatomic variants of renal vascular anatomy in living kidney donors) will start scanning early after commencement of intravenous contrast injection (Yuh and Cohan 1999). Depending on circulation time, heart rate, ejection volume, circulating blood volume, and other parameters, peak renal arterial enhancement is variable. Frequently, it occurs 10–25 s after injection, but a test bolus imaging series that covers the abdominal aorta at the level of the renal artery take-offs may be necessary to precisely determine the most appropriate delay for CT angiography.

While the renal cortex enhances strongly between 40 and 70 s after intravenous bolus adminstration of contrast media as described above, the renal medulla usually trails behind (cortico-medullary phase of enhancement) (Yuh and Cohan 1999). Contrast equilibrium between cortex and medulla can be expected between 80 and 100 s after commencement of bolus injection of contrast media (nephrographic phase of contrast enhancement). At longer delays, bright contrast from excreted contrast media is first demonstrated in the excretory tubules within the renal medulla (excretory phase). After approximately 120 s, the renal calices and pelvis start to fill with excreted contrast media. As in IVU, contrast in the renal collecting system is usually strongest within 3–5 min after bolus injection when renal excretory function is normal and post renal transport of excretory products is unimpeded. The ureters may be best visualized after 7–10 min, while it may take up to 20 min until the bladder fully opacifies with contrast media (Mueller-Lisse 2004). It has been suggested to follow the injection of intravenous contrast media with 250 ml of normal saline solution after the nephrographic phase images to improve delineation of the ureters (McTavish et al. 2002).

For most imaging purposes other than CT angiography, contrast-enhanced images should be obtained in the parenchymal and excretory phases (Fig. 2). Since it may be more difficult to recognize parenchymal lesions when contrast is strong between renal cortex and medulla in the early phase of parenchymal enhancement (cortico-medullary phase), preference should be given to imaging in the nephrographic phase, with a delay of 80–100 s. On the other hand, imaging of lesions arising from or extending into the renal calices and pelvis may benefit from strong contrast between soft tissue and excretory products. For the renal calices and pelvis, a delay of 3–5 min may therefore be chosen.

Complete evaluation of the kidney requires both pre- and post contrast CT imaging, unless the acquisition has been performed in the dual energy mode (Graser et al. 2010). Exact delineation of calcifications, and the recognition of small amounts of fat or blood within parenchymal lesions may provide important diagnostic clues and determine patient management.

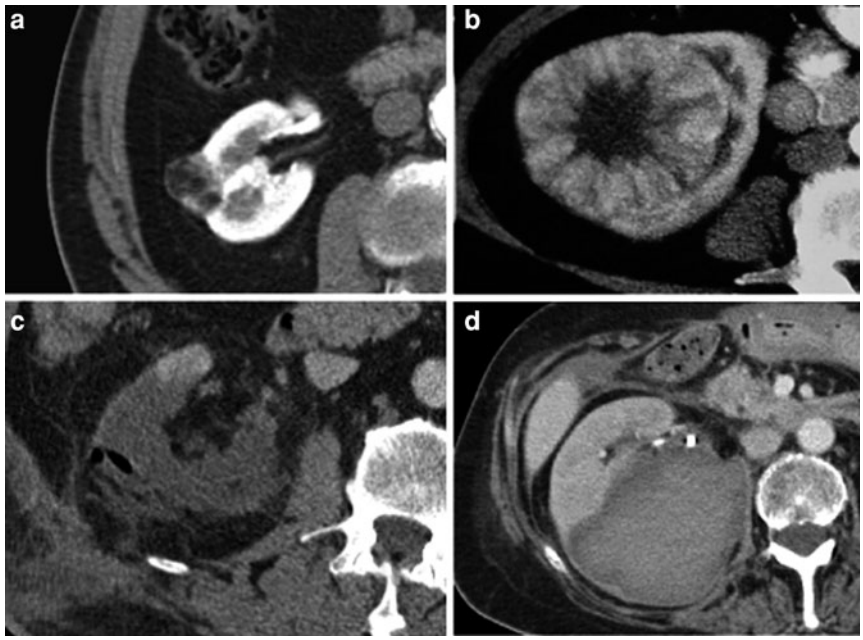

Fig. 3 Benign renal masses. Angiomyolipoma (**a**), oncocytoma (**b**), renal abscess (**c**), and renal hematoma (**d**)

6 Imaging of Renal Masses

6.1 Enhancement Patterns of Renal Tumors

Renal tumors may appear isodense to the renal parenchyma on unenhanced images, while necrotic tumor parts are hypo attenuating. If a solid lesion appears hyperdense in the corticomedullary phase, it has to be considered to be malignant because renal cell carcinoma is often hypervascularized. Nevertheless, the cortico-medullary phase is not mandatory for the tumor protocol (Table 1), since the nephrographic phase is more sensitive for tumor detection (Cohan et al. 1995; Szolar et al. 1997). The nephrographic CT phase (80–120 s) shows renal cortex and medulla with equal enhancement. Solid renal lesions usually appear hypodense. This phase is recommended for tumor detection (Mueller-Lisse 2004). For optimization of nephrographic phase imaging, some authors prefer the bolus-tracking technique (Birnbaum et al. 1999).

In the excretory phase of enhancement, most malignant tumors of the kidney—except clear cell RCC—show significant washout of contrast agent (Shebel et al. 2011). Transitional cell cancer (TCC) can be depicted well in this phase as a hypodense filling defect within the renal collecting system.

6.2 Cystic Renal Masses

Simple renal cysts are found frequently and do not have pathological significance. The criteria of a simple cyst that does not need follow-up are water-like CT density, no contrast enhancement (<10 HU), no septa, no solid parts, no rim enhancement, no calcification. Solitary renal cysts are generally classified according to Bosniak (Table 1) (Bosniak 1997). A cyst with hemorrhage (Fig. 1) may be suspected to represent a solid lesion when no unenhanced scan has been performed. Such a cyst has a CT density of approximately 40–60 HU (>20 HU). Contrast opacity or hemorrhage cannot be differentiated by contrast-enhanced CT. Differentiation of these types of lesions can be easily archived by single-phase dual energy CT (DECT) as material-specific post processing allows for direct visualization of enhancement and generation of virtual nonenhanced (VNE) images (Graser et al. 2009). Also, dual energy CT greatly facilitates the diagnostic workup of patients with polycystic kidneys (Arndt et al. 2011). As cysts often show septa, hemorrhage of different age, or calcifications, comparison of non-contrast and nephrographic phase images may be tedious, and DECT helps to overcome this problem by direct visualization of enhancement within malignant lesions. The classification of Potter describes congenital anomalies of the kidneys with predominantly polycystic malformations.

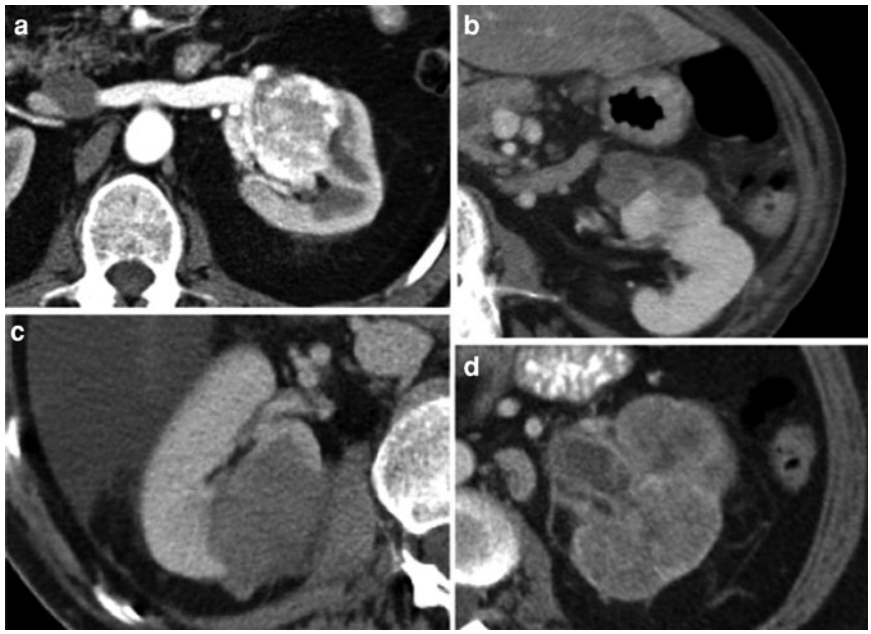

Fig. 4 Differential diagnosis of malignant solid renal masses: renal cell carcinoma (**a**), metastasis of lung cancer (**b**), lymphomatous infiltration of the kidney (**c**), and transitional cell carcinoma (**d**)

Even unilateral and bilateral agenesis of the kidney is described by this classification. CT investigations of adults may reveal the adult form of polycystic disease (Potter type III) with autosomal dominant trait. Cysts often demonstrate hemorrhage (in about 70%) and calcifications, thereby making evaluation at both MDCT and MRI difficult. Long-time dialysis is a reason for acquired polycystic kidneys with increased risk of renal cell carcinoma (Choyke 2000).

6.3 Solid Tumors

6.3.1 Oncocytoma

Oncocytomas are benign tumors (3–5% of all renal tumors; Fig. 3). The typical spoke-wheel pattern is characteristic, but the discrimination from renal cell carcinoma is not possible in all cases (McGahan et al. 2011).

6.3.2 Angiomyolipoma

Angiomyolipoma is a benign hamartosis (Fig. 3). Angiomyolipoma consists of atypical muscle fibers, blood vessels, and fat tissue. If a solid lesion reveals CT density values of fat, angiomyolipoma is highly probable. Only if the fatty regions are very small (Obuz et al. 2000) or the solid part is growing in follow-up investigations, renal cell carcinoma has to be considered as a differential diagnosis. Calcifications may indicate malignant tumors. Angiomyolipoma of the kidneys can be associated with lymphangioleiomyomatosis of the lung and with tuberous sclerosis (Bourneville-Pringle syndrome).

6.3.3 Renal Cell Cancer

Renal cell carcinoma (RCC) represents the most common malignant lesion of the kidney and accounts for about 3% of all adult neoplasms. The survival of patients with RCC is directly related to the extent of disease at the time of treatment. Independent of tumor grade, patients with stages T1 or T2 of RCC have excellent chances of survival. However, once malignancy extends beyond the kidney, survival depends on whether the tumor progresses by direct extension or has the ability to deposit at distant metastatic sites. In extensive RCC, survival is closely related to tumor grade and degree of malignancy (Hermanek and Schrott 1990; Paulson 1996). Due to the increased use of ultrasonography and abdominal CT in patient management, asymptomatic RCCs that are confined within the renal capsule are now more oftenly discovered and treated by curative surgery (Tsui et al. 2000).

The nephrographic phase can define tumorous areas in most cases. Studies have shown that specificity and accuracy increase when both nephrographic and excretory phases are combined. During tumor staging, tumor thrombus in the renal vein or v. cava

Table 2 TNM Staging system for renal cell cancer (Mueller-Lisse et al. 2007)

Classification	Description
T-classification	
T1	Confined to kidney, T1a < 4 cm, T1b < 7 cm
T2	Confined to kidney, >7 cm
T3	Confined to Gerota's fascia
	T3a: extending to ipsilateral adrenal or perirenal fat
	T3b: extending to renal vein or IVC below diaphragm
	T3c: extending to IVC above diaphragm
T4	Extending beyond Gerota's fascia
N-classification	
N0	No regional lymph node metastasis
N1	Metastasis in one regional lymph node
N2	Metastasis in more than one regional lymph node
Nx	Regional lymph nodes cannot be evaluated
M-classification	
M0	No distant metastasis
M1	Distant metastasis
Mx	Distant metastasis cannot be evaluated

has to be considered (Hallscheidt et al. 2005). Multidetector-row CT and MR imaging achieve similar accuracy in tumor staging of renal cell carcinoma (Hallscheidt et al. 2004). A better differentiation of T2 and T3a tumors (perirenal fat infiltration) is decisive for surgical procedure (nephron-sparing surgery or radical nephrectomy) (Catalano et al. 2003). Furthermore, CT can help to characterize malignant lesions of the kidney like renal cell carcinoma, transitional cell carcinoma, lymphomatous involvement of the kidney, and metastases to the kidney from solid tumors like lung or thyroid cancer (see Fig. 4).

6.3.4 Urothelial Carcinoma (Transitional Cell Carcinoma)

Tumors of the renal pelvis and ureter can be reliably detected by CT. A CT examination in the excretory phase with a reconstructed slice thickness of 3 mm in both coronal and axial planes is useful. Structures of soft-tissue density bulge against the hyperdense renal pelvis, or the wall may be partially thickened. Radiation dose should not be selected too low in order to provide reliable tumor detection; up-to-date scanning protocols employ automated dose modulation techniques as well as kV adaptation and iterative reconstruction of image data.

7 Staging of Renal Cell Cancer

Technological advances in multi-detector-row computed tomography facilitate precise, reliable, accurate non-invasive detection, localization, characterization, and staging of both primary RCC and distant metastasis (Coppenrath and Mueller-Lisse 2006; Mueller-Lisse et al. 2007). Imaging findings are formally summarized into significant prognostic information by means of the TNM classification and staging system (Table 2) (Mueller-Lisse et al. 2007). Preoperative staging helps to assess surgical options and to optimize the surgical approach.

Since partial nephrectomy represents the new therapeutic standard for locally confined RCC (Shuch et al. 2006), one key issue in cross-sectional imaging is to distinguish between patients suited for nephron-sparing surgery and those requiring other therapies.

8 Organ-Confined RCC (TNM Stage T1, T2)

TNM classes T1 and T2 include all primary RCCs that are confined to the renal capsule (Smith et al. 1989). The current TNM classification of 2002

Table 3 Phases of renal contrast and examination protocols for renal MDCT. (Coppenrath et al. 2006)

Parameters	Unenhanced		Portal venous phase	Nephrographic phase	Excretory phase	
Tube voltage (kV)	120		120	120	120	
Pitch	0.9–1.5		0.9–1.5	0.9–1.5	0.9–1.5	
Tube current time product (mAs)	150–200 (S)	30–50 (L)	150–200 (S)	150–200 (S)	150–200 (S)	30–50 (L)
CTDIw(mGy)	12–14 (S)	2–3 (L)	12–14 (S)	12–14 (S)	12–14 (S)	2–3 (L)
Reconstructured slice thickness (mm)	3.0		3.0	3.0	3.0	
Contrast media volume (ml)			120	80–120		
Delay(s)			Appr. 70	80–100	Appr. 600	
Indications						
Urolithiasis	Low dose		–	–	–	
Renal tumor	Standard dose		–	Standard dose	Low dose	
Ureteral tumor	Standard dose		–	Standard dose	Standard dose	
Pelvic tumor	–		Standard dose	–	Low dose	
Staging	–		Standard dose	–	Low dose	

(*S*) standard notes, (*L*) low dose

distinguishes between T1a, which defines an RCC with a maximum diameter of 4 cm or less, and T1b, which defines an RCC whose maximum diameter is larger than 4 cm but smaller than 7 cm. Exact determination of the size of a renal mass and its relationship to renal vessels and collecting system is important because it has been repeatedly demonstrated that the oncologic efficacy and safety of nephron-sparing surgery (NSS) for the treatment of stage-T1 and T2 renal tumors is equivalent to radical nephrectomy (Shuch et al. 2006).

9 Recognition of Extra-capsular Extension of RCC (TNM Stage T3)

Distinction between RCC with and without confinement to the kidney (Table 3) can be difficult for cross-sectional maging, since RCC induces inflammatory reactions within the kidney and perirenal fat layer that may produce pseudocapsular structures which mimic the presence of an intact renal capsule when in fact the RCC has broken through. Although it remains unclear if differences between test quality parameters among individual radiological studies are due to patient selection, imaging modalities and techniques, image interpretation, or interpretation of pathology specimens, it appears that the reliability of radiological recognition of RCC extension into perirenal fat is variable. MDCT examinations in 40 patients with RCC diagnosed perirenal fat infiltration on 1-mm primary reconstructions with 96% sensitivity, 93% specificity, and 95% accuracy (Catalano et al. 2003). Among 46 RCCs of T-classes T1 to T3a, with 2–15 cm in diameter, MDCT correctly recognized perirenal disease in 9 of 14 patients (sensitivity, 64%) and confinement to the kidney in 32 of 32 (specificity, 100%), with excellent agreement between MDCT and surgical pathology (kappa score, 0.87) (Turkvatan et al. 2009). Currently, cross-sectional imaging results should therefore be individually reviewed for each patient with RCC prior to treatment planning. However, it remains controversial if perirenal fat infiltration has an impact on survival in patients with RCC. Recently, a retrospective analysis of 783 patients with pT1-2 (cN0M0) and 77 patients with pT3a (cN0M0) RCC, respectively, demonstrated tumor size to be the strongest prognostic factor of disease-free and

cancer-specific survival in pT3a RCC, while perirenal fat infiltration was an independent prognostic factor only for disease-free survival (Yoo et al. 2008). Thus, both tumor size and perirenal fat infiltration should be reported in RCC staging. MDCT examinations with 1-mm primary reconstructions in 40 patients with RCC demonstrated complete agreement of tumor size estimates with surgical pathology (Catalano et al. 2003).

Adrenal metastasis of RCC is found in up to 10% of patients, particularly after nephrectomy. Demonstration of a normal adrenal gland at MDCT in patients with RCC has been associated with 100% negative predictive value for metastasis, confirmed by subsequent histology (Griffin et al. 2007).

10 Invasion of Renal Veins and Inferior Vena Cava (Stages T3 b, c)

Differential therapy of RCC with renal vein (RV) extension or extension into the inferior vena cava (IVC) below or above the diaphragm (Table 3) remains a challenge to modern urology. Tasks for cross-sectional imaging include recognition of the tumor thrombus and its extent (Figs. 1, 2). MDCT is able to correctly identify tumor thrombus and localize its extent, based on signs of direct continuity of the thrombus with the renal tumor and enhancement after administration of contrast medium (Gupta et al. 2004; Turkvatan et al. 2009). When there is doubt about the extent of the tumor thrombus in RCC, combining different cross-sectional imaging modalities is recommended as a diagnostic strategy. Prognosis for patients after surgery for RCC with venous involvement remains controversial; for the radiologist, it is recommended to report the exact level to which venous tumor thrombus of RCC is demonstrated by means of cross-sectional imaging than to apply TNM T-classes T3b or T3c (Mueller-Lisse et al. 2007).

11 Extension Beyond Gerota's Fascia (Stage T4)

Extension of RCC beyond Gerota's fascia may be a challenge to cross-sectional imaging when the fascia is barely transgressed. In such cases, it may be difficult to determine if RCC has come close to the fascia and caused an inflammatory reaction with facial thickening, or if it has reached the fascia without penetrating it, or if there is minimal extension beyond Gerota's fascia. However, for the urologic surgeon, resection of the fascia will probably be the only solution, at least in those parts were the radiological situation remains unclear. Direct invasion of neighboring organs such as the spleen, psoas muscle, or spine, is readily identified on modern high resolution MDCT scans. As these stages are often associated with distant metastases, most patients nowadays will undergo neo-adjuvant systemic anti-angiogenic treatment; even in these advanced stages, local tumor debulking improves survival, and repeated follow-up imaging on these patients will help to determine the optimum time point for local resection (Mueller-Lisse et al. 2007).

12 Summary

Imaging of renal masses is an important clinical indication for abdominal MDCT. At present, high spatial resolution and fast image acquisition makes it ideally suited for patients with suspected or proven renal pathologies. Advances like dual energy CT, iterative reconstruction of image data, and anatomical dose modulation strategies enable significant reductions of radiation exposure to the patient. Improved soft-tissue contrast and direct visualization of contrast enhancement by color coded DECT and low kVp scanning allow for detection and characterization of near-isoattenuating renal tumors. MDCT also enables accurate staging of localized and metastasized renal cell cancers.

References

Arndt N, Staehler M et al (2011) Dual energy CT in patients with polycystic kidney disease. Eur Radiol (in press)

Birnbaum BA, Jacobs JE et al (1999) Assessment of a bolus-tracking technique in helical renal CT to optimize nephrographic phase imaging. Radiology 211(1):87–94

Bosniak MA (1997) The use of the Bosniak classification system for renal cysts and cystic tumors. J Urol 157(5): 1852–1853

Cann CE, Gamsu G et al (1982) Quantification of calcium in solitary pulmonary nodules using single- and dual-energy CT. Radiology 145(2):493–496

Catalano C, Fraioli F (2003) High-resolution multidetector CT in the preoperative evaluation of patients with renal cell carcinoma. Am J Roentgenol 180(5):1271–1277

Chiro GD, Brooks RA et al (1979) Tissue signatures with dual-energy computed tomography. Radiology 131(2):521–523

Choyke PL (2000) Acquired cystic kidney disease. Eur Radiol 10(11):1716–1721

Cohan RH, Sherman LS et al (1995) Renal masses: assessment of corticomedullary-phase and nephrographic-phase CT scans. Radiology 196(2):445–451

Coppenrath EM, Mueller-Lisse UG (2006) Multidetector CT of the kidney. Eur Radiol 16(11):2603–2611

Dillman JR, Caoili EM et al (2008) Detection of upper tract urothelial neoplasms: sensitivity of axial, coronal reformatted, and curved-planar reformatted image-types utilizing 16-row multi-detector CT urography. Abdom Imaging 33(6):707–716

Graser A, Becker CR et al (2010) Single-phase dual-energy CT allows for characterization of renal masses as benign or malignant. Invest Radiol 45(7):399–405

Graser A, Johnson TR et al (2009) Dual-energy CT in patients suspected of having renal masses: can virtual nonenhanced images replace true nonenhanced images? Radiology 252(2):433–440

Griffin N, Gore ME et al (2007) Imaging in metastatic renal cell carcinoma. Am J Roentgenol 189(2):360–370

Gupta NP, Ansari MS et al (2004) Impact of imaging and thrombus level in management of renal cell carcinoma extending to veins. Urol Int 72(2):129–134

Hallscheidt PJ, Bock M et al (2004) Diagnostic accuracy of staging renal cell carcinomas using multidetector-row computed tomography and magnetic resonance imaging: a prospective study with histopathologic correlation. J Comput Assist Tomogr 28(3):333–339

Hallscheidt PJ, Fink C et al (2005) Preoperative staging of renal cell carcinoma with inferior vena cava thrombus using multidetector CT and MRI: prospective study with histopathological correlation. J Comput Assist Tomogr 29(1):64–68

Hermanek P, Schrott KM (1990) Evaluation of the new tumor, nodes and metastases classification of renal cell carcinoma. J Urol 144(2 Pt 1):238–241

Johnson TR, Krauss B et al (2007) Material differentiation by dual energy CT: initial experience. Eur Radiol 17(6):1510–1517

Lee SJ, Park SH et al (2011) A prospective comparison of standard-dose CT enterography and 50% reduced-dose CT enterography with and without noise reduction for evaluating Crohn disease. Am J Roentgenol 197(1):50–57

McGahan JP, Lamba R et al (2011) Is segmental enhancement inversion on enhanced biphasic MDCT a reliable sign for the noninvasive diagnosis of renal oncocytomas? Am J Roentgenol 197(4):W674–W679

McTavish JD, Jinzaki M et al (2002) Multi-detector row CT urography: comparison of strategies for depicting the normal urinary collecting system. Radiology 225(3):783–790

Mueller-Lisse UG (2004) Multi-detector CT of the kidneys. In: Reiser M (ed) Multislice CT, 2nd edn. Springer, Berlin, pp 211–239

Mueller-Lisse UG, Mueller-Lisse UL et al (2007) Staging of renal cell carcinoma. Eur Radiol 17(9):2268–2277

Obuz F, Karabay N et al (2000) Various radiological appearances of angiomyolipomas in the same kidney. Eur Radiol 10(6):897–899

Paulson DF (1996) Natural history of renal cell carcinoma. Semin Urol Oncol 14(4):203–207

Shebel HM, Elsayes KM et al (2011) Quantitative enhancement washout analysis of solid cortical renal masses using multidetector computed tomography. J Comput Assist Tomogr 35(3):337–342

Shuch B, Lam JS et al (2006a) Open partial nephrectomy for the treatment of renal cell carcinoma. Curr Urol Rep 7(1):31–38

Shuch BM, Lam JS et al (2006b) Prognostic factors in renal cell carcinoma. Semin Oncol 33(5):563–575

Smith SJ, Bosniak MA et al (1989) Renal cell carcinoma: earlier discovery and increased detection. Radiology 170(3 Pt 1):699–703

Szolar DH, Kammerhuber F et al (1997) Multiphasic helical CT of the kidney: increased conspicuity for detection and characterization of small (<3 cm) renal masses. Radiology 202(1):211–217

Tsui KH, Shvarts O et al (2000) Prognostic indicators for renal cell carcinoma: a multivariate analysis of 643 patients using the revised 1997 TNM staging criteria. J Urol 163(4):1090–1095

Turkvatan A, Akdur PO et al (2009) Preoperative staging of renal cell carcinoma with multidetector CT. Diagn Interv Radiol 15(1):22–30

Van Der Molen AJ, Cowan NC et al (2008) CT urography: definition, indications and techniques. A guideline for clinical practice. Eur Radiol 18(1):4–17

Winklehner A, Karlo C et al (2011). Raw data-based iterative reconstruction in body CTA: evaluation of radiation dose saving potential. Eur Radiol 21(12):2521–2526

Yoo C, Song C et al (2008) Prognostic significance of perinephric fat infiltration and tumor size in renal cell carcinoma. J Urol 180(2):486–491 discussion 491

Yuh BI, Cohan RH (1999) Different phases of renal enhancement: role in detecting and characterizing renal masses during helical CT. Am J Roentgenol 173(3):747–755

Adrenal Masses

Julie H. Song and William W. Mayo-Smith

Contents

Abstract

The adrenal gland is a common site of disease, involved in a spectrum of pathology. Multi-slice computed tomography (MSCT) is an essential tool in adrenal imaging due to its high accuracy in both the detection and characterization of adrenal masses. As a result, MSCT can make specific diagnoses, separating inconsequential adrenal masses from those that require intervention. This chapter discusses contemporary adrenal imaging by MSCT of commonly encountered adrenal masses in key clinical scenarios: detection of a biochemically active adrenal tumor, characterization of an adrenal mass in staging of patients with primary malignancy, and evaluation of an incidentally discovered adrenal mass.

The adrenal gland is a common site of disease, involved in a range of pathology. As the use of cross-sectional imaging continues to rise, adrenal masses are frequently discovered incidentally, and most are benign lesions. However, the adrenal gland is also a common site for metastasis in patients with an underlying malignancy. Also of clinical importance are primary adrenal neoplasms that are hormonally active, and, more rarely, primary malignant neoplasms that require intervention. Contemporary multi-slice computed tomography (MSCT) is ideally suited for the evaluation of adrenal pathology. Detection of an abnormality is "finding the lesion." Characterization of an abnormality is determining what the lesion is. CT is highly accurate in both the detection of adrenal masses and the characterization of adrenal masses leading to a specific diagnosis. This chapter

J. H. Song (✉) · W. W. Mayo-Smith
Department of Diagnostic Imaging,
Rhode Island Hospital-Warren Alpert
Medical School of Brown University,
593 Eddy Street, Providence, RI 02903, USA
e-mail: jsong2@lifespan.org

C. J. Zech et al. (eds.), *Multislice-CT of the Abdomen*, Medical Radiology. Diagnostic Imaging,
DOI: 10.1007/174_2011_427, © Springer-Verlag Berlin Heidelberg 2012

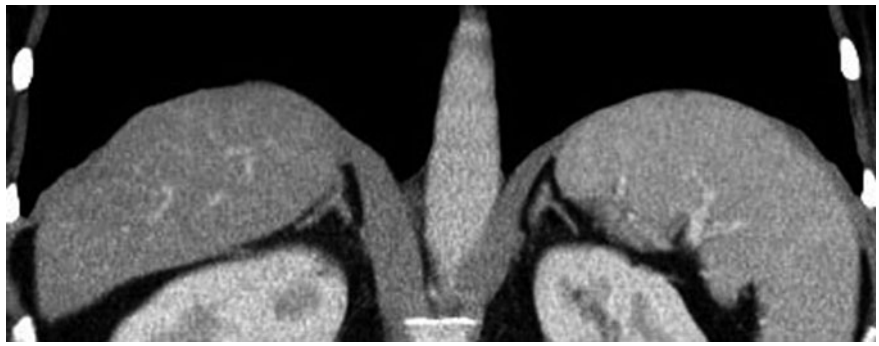

Fig. 1 Normal adrenal glands in 45-year-old male. Coronal reformatted contrast-enhanced CT image shows normal adrenal glands in inverted Y configuration

discusses contemporary adrenal imaging by MSCT, focusing on commonly encountered pathologic entities and their CT appearances in adult population in three key clinical settings:

1. Detection of an adrenal mass in patients with biochemical evidence of hormonal excess,
2. characterization of an adrenal mass as part of staging in oncology patients, and
3. evaluation of an incidentally discovered adrenal mass.

1 Normal Adrenal Gland

The adrenal glands are well visualized on abdominal MSCT. They are located anterosuperiorly to the kidneys within the perirenal space, enclosed by perirenal fascia. The normal adrenal glands have an inverted V or Y shape (Fig. 1). When a kidney is ectopic or congenitally absent, the adrenal gland remains in the normal position, however it may assume a discoid shape on CT (Fig. 2) (Kenney et al. 1985). The adrenal gland is composed of the adrenal cortex and medulla, two functioning units with different embryologic origin and endocrine functions. The adrenal cortex secretes cortisol, aldosterone, and androgen, and the adrenal medulla secretes epinephrine and norepinephrine.

2 CT Technique

Most adrenal masses are detectable on routine chest or abdominal CT, typically reconstructed at 5-mm thickness on MSCT. Dedicated adrenal CT is usually employed when it is necessary to further characterize a known adrenal mass. The protocol consists of unenhanced sections through the adrenal gland at 0.6–2.5 mm collimation, depending on the type of MSCT, with image reconstruction at 2.5 mm in axial and 3 mm in coronal planes. An elliptical region of interest (ROI) is placed in an adrenal mass. If the density of the adrenal mass measures $\leq$10 hounsfield units (HU), the adrenal mass is a lipid-rich benign adenoma and no intravenous contrast is required. If the density of the adrenal mass measures >10 HU, then 100 mL of low osmolar contrast material is injected. Using the same CT acquisition parameters, the next data sets are acquired 60 s and 15 min after the start of contrast injection, and the images are reconstructed in the same slice thickness as the unenhanced series. Using the measured densities of the adrenal mass on unenhanced, dynamic, and delayed imaging, washout calculations can be performed which can accurately characterize lipid-poor adenomas as described below.

3 Detection of Hyperfunctioning Adrenal Neoplasm

Hyperfunctioning diseases of the adrenal glands originate from the adrenal cortex or the adrenal medulla. Investigation of functioning adrenal mass is usually prompted by the clinical presentation of hormonal excess, which is confirmed by abnormal biochemical assay. The role of CT is then primarily to detect the adrenal mass, such as a cortisol-producing adenoma, an aldosteronoma, or a pheochromocytoma.

3.1 Hyperfunctioning Adrenal Adenoma

Cushing syndrome is a clinical manifestation of gluco-corticoid excess and is most frequently caused

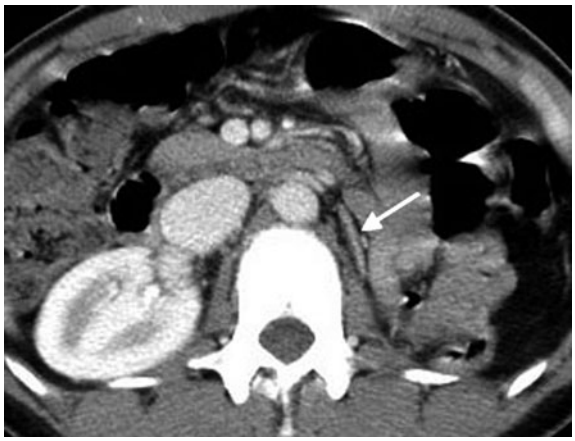

Fig. 2 Anomalous adrenal gland in 30-year-old female. Axial contrast-enhanced CT image shows the left adrenal gland (*arrow*) in discoid configuration. An ectopic, left pelvic kidney was present more inferiorly (not shown)

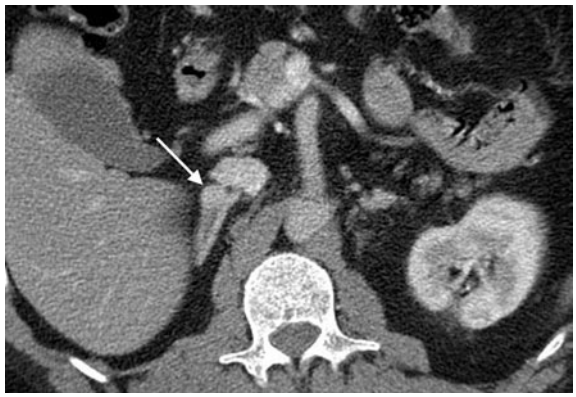

Fig. 3 Aldosteronoma in 60-year-old male with hypertension. Axial contrast-enhanced CT image shows a well-defined 1.3 cm mass (*arrow*) arising from the lateral limb of right adrenal gland

by an exogenous source of steroid. In endogenous Cushing syndrome, there is overproduction of cortisol by the adrenal cortex, and approximately 80% are due to ACTH-dependent overstimulation of the adrenal glands, usually by a pituitary adenoma (Cushing disease) and rarely by an ectopic source in the chest or the abdomen. The adrenal glands are hyperplastic on CT in 70% of ACTH-dependent Cushing syndrome, sometimes with nodularity; however, up to 30% have normal appearance (Sohaib et al. 1999). ACTH-independent Cushing syndrome (20%) is caused by a primary adrenal disease, most commonly an adrenal adenoma. Cortisol-producing adenomas are readily detected on CT as they are typically larger than 2 cm (Mayo-Smith et al. 2001; Rockall et al. 2004). These adenomas have similar CT appearance to non-functioning adenomas with abundant intracellular lipid causing a low density adrenal mass (Korobkin et al. 1996a; Rockall et al. 2004).

Conn syndrome (primary aldosteronism) is the sequela of elevated aldosterone level. It is caused by an adrenal adenoma in 80% of patients, bilateral adrenal hyperplasia in 20% of patients, and rarely by adrenocortical carcinoma. The diagnosis is suspected in patients with hypertension, hypokalemia, and sodium retention, and is confirmed by elevated serum aldosterone to renin levels. Aldosterone-producing adenomas are typically smaller than 2 cm with a significant portion less than 1 cm (Fig. 3) (Dunnick et al. 1993; Patel et al. 2007). When the diagnosis is suspected clinically, adrenal CT with thin collimation is helpful to determine the cause, separating an adenoma from hyperplasia. Adrenal vein sampling may still be necessary to localize and lateralize the site of adrenal hypersecretion when CT findings are equivocal.

3.2 Adrenocortical Carcinoma

Adrenocortical carcinoma is a rare, highly aggressive tumor with prevalence of 0.6–2 per million population (Mansmann et al. 2004). Approximately 50% of the carcinomas are hormonally active, most commonly producing cortisol, leading to Cushing syndrome. On CT, an adrenocortical carcinoma is a large (usually >6 cm) heterogeneously enhancing mass. It is frequently associated with central necrosis and hemorrhage, and calcifications are present in 20–30% (Fig. 4) (Dunnick et al. 1982; Fishman et al. 1987). Venous invasion into IVC is a common feature, often a diagnostic clue, and defining the superior extent of tumor thrombus is important for surgical planning to define the point for vascular control.

3.3 Pheochromocytoma

Pheochromocytoma is an uncommon, catecholamine-producing tumor derived from chromaffin cells in the adrenal medulla. These tumors are solitary and occur sporadically in 90% of cases. 10% of

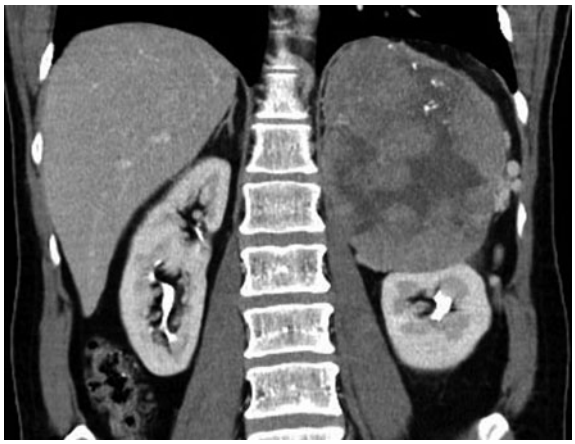

Fig. 4 Adrenocortical carcinoma in 39-year-old male. Coronal reformatted contrast-enhanced CT image shows a 14 cm left adrenal mass with central heterogeneous attenuation and multiple punctuate calcifications. Note its mass effect on the left kidney

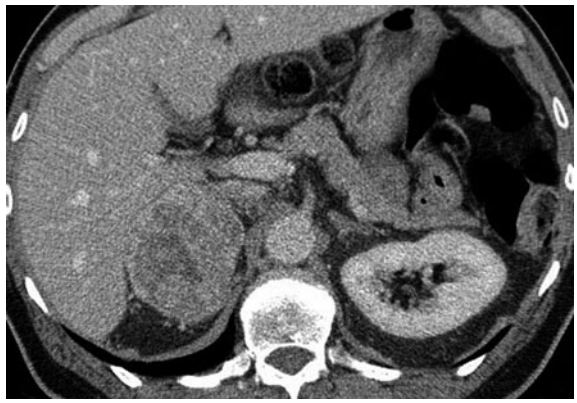

Fig. 5 Pheochromocytoma in 59-year-old male. Axial contrast-enhanced CT image shows a heterogeneous 4 cm right adrenal mass

pheochromocytomas are multiple or associated with hereditary syndromes. The classic presentation for a patient with a pheochromocytoma is palpitations, headache, and diaphoresis associated with episodic hypertension. Approximately 10% of pheochromocytomas are silent, although the number of incidentally discovered pheochromocytomas has been reported to be rising (Baguet et al. 2004; Motta-Ramirez et al. 2005). Once a pheochromocytoma is suspected clinically, biochemical investigation ensues and the diagnosis is confirmed by elevated urine or plasma metanephrine levels. 98% of pheochromocytomas arise in the abdomen, mostly from the adrenal gland manifesting as a mass. Thus pheochromocytomas are readily detected on CT or MR without contrast. However, contrast may be helpful in the detection of small extra-adrenal pheochromocytomas (paragangliomas). Traditionally, the use of intravenous contrast was controversial in the setting of pheochromocytoma as it was thought to induce hypertensive crisis. However, recent reports have shown that non-ionic intravenous contrast is safe and unlikely to cause adrenergic crisis (Mukherjee et al. 1997; Bessell-Browne and O'Malley 2007). Pheochromocytomas have variable imaging appearances (Blake et al. 2004). On CT, they are round masses of soft tissue density and enhance avidly after contrast enhancement. Small lesions are homogenous, but large masses are often heterogeneous with areas of necrosis or hemorrhage (Fig. 5). Calcifications are occasionally present in pheochromocytomas. Approximately 10% of pheochromocytomas are malignant, but there are no specific radiologic features to diagnose malignancy other than invasion of local structures or distant metastases.

4 Staging Patients with Known Carcinoma: Adrenal Adenoma Versus Metastasis

In oncology patients, the presence of an adrenal mass may pose a clinical challenge as the adrenal gland is a common site for both metastasis and benign adenomas. Thus presence of an adrenal mass does not necessarily imply metastasis. An isolated adrenal mass is, in fact, more likely benign than malignant in patients with a known primary extra-adrenal malignancy (Dunnick and Korobkin 2002). In patients with evidence of metastasis elsewhere, distinguishing a benign from metastatic adrenal mass is not crucial for staging. However, in a patient with the adrenal gland as the only potential site of metastasis, it is critical to make the distinction because the diagnosis may alter the prognosis and treatment options, such as potentially curative resection vs. chemotherapy in a patient with lung carcinoma. In these patients, a new or an enlarging adrenal mass at CT suggests malignancy until proven otherwise. Metastatic masses, especially when large, can be heterogeneous with irregular margins (Fig. 6); however, in general, morphologic

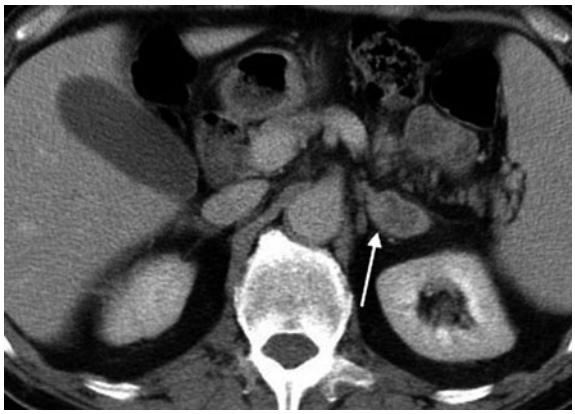

Fig. 6 Adrenal metastasis in 57-year-old male with non-small cell lung cancer. Axial contrast-enhanced CT image shows a heterogeneous 2.5 cm left adrenal mass (*arrow*) with irregular margins and central low attenuation

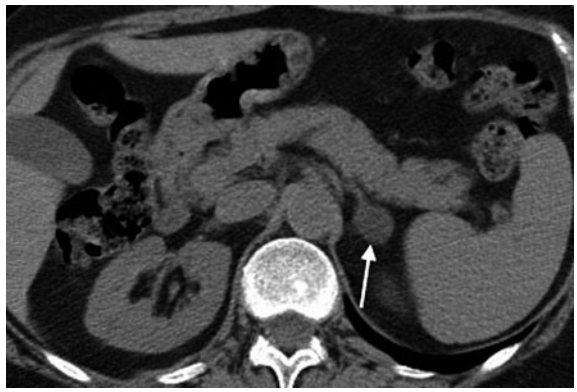

Fig. 7 Lipid-rich adenoma in 60-year-old female. Axial unenhanced CT image shows a well-defined 1.7 cm left adrenal mass (*arrow*) with attenuation of −6 HU, diagnostic of a lipid-rich adenoma

features are helpful but non-specific. The role of imaging is then to not only detect, but also accurately characterize and differentiate a benign mass, usually an adenoma, from metastasis. Currently two physiologic characteristics of adenomas are used at CT to diagnose and separate them from malignant masses: intracytoplasmic lipid content and washout of intravenous contrast.

Adrenal adenomas have varying amount of intracytoplasmic lipid, which is inversely related to their density measurement on CT (Korobkin et al. 1996a). Most metastases lack intracellular lipid. Using this principle, adenomas can be separated from malignant masses using unenhanced CT density measurements (Lee et al. 1991; Korobkin et al. 1996b). A threshold of 10 HU allowed adenoma to be diagnosed with 71% sensitivity and 98% specificity on a meta-analysis and is the standard threshold used to diagnose a lipid-rich adenoma on CT (Fig. 7) (Boland et al. 1998). Another method of detecting intracytoplasmic lipid is CT histogram analysis, where the percentage of negative pixels is measured within the ROI. Bae et al. showed increased sensitivity in diagnosing adenoma compared with the 10-HU threshold method and also showed its potential application in contrast-enhanced CT (Bae et al. 2003). This technique is available on most CT scanners, but is not routinely used as subsequent studies have shown differing results (Remer et al. 2006; Jhaveri et al. 2006). The diagnosis of adenoma on chemical shift MR also relies on the presence of intracytoplasmic lipid, which leads to signal cancellation of adenoma on opposed-phase compared to in-phase images (Mitchell et al. 1992; Outwater et al. 1995).

Approximately 30% of adrenal adenomas do not contain a sufficient amount of lipid to be diagnosed based on the density measurement. However, after enhancement with intravenous contrast, adenomas lose contrast rapidly while the washout of metastases is more prolonged. This difference in washout characteristics can be exploited to distinguish between adenomas and non-adenomas (Korobkin et al. 1998; Szolar and Kammerhuber 1998). A widely used technique is that of Korobkin et al. who calculated washout percentages using a delayed phase, optimally 15 min after contrast injection (Korobkin et al. 1998). The absolute percentage of enhancement washout (APW) is calculated using the following formula and a value of 60% or greater is diagnostic of an adenoma (Fig. 8).

$$\mathrm{APW} = \frac{(\text{enhanced HU}) - (15\,\text{min delayed HU})}{(\text{enhanced HU}) - (\text{unenhanced HU})} \times 100\%$$

In the absence of the initial unenhanced phase, a relative percentage washout (RPW), an approximation of true washout, can be calculated as follows:

$$\mathrm{RPW} = \frac{(\text{enhanced HU}) - (15\,\text{min delayed HU})}{(\text{enhanced HU})} \times 100\%$$

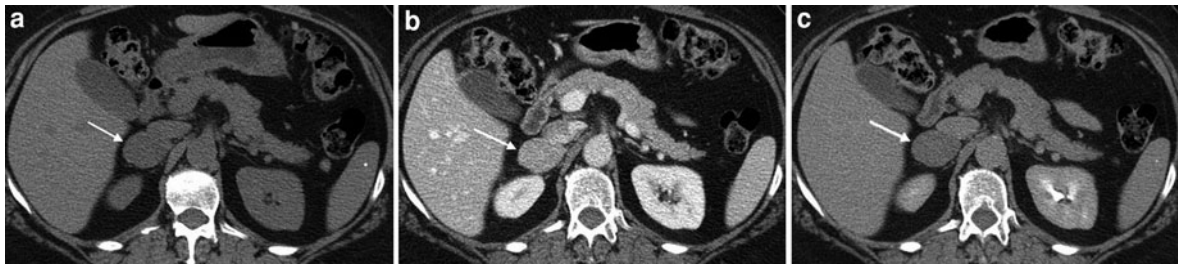

Fig. 8 Lipid-poor adenoma in 58-year-old female. **a** Axial unenhanced scan shows 3.6 cm right adrenal mass with attenuation of 19 HU; **b** on dynamic contrast-enhanced phase scan, adrenal mass enhances to 107 HU; **c** on 15-minute-delayed scan, adrenal mass attenuation is 44 HU. APW and RPW are 72 and 59%, respectively, diagnostic of an adenoma

An RPW value of 40% or greater is diagnostic of an adenoma. The accuracy of washout analysis has been corroborated on multiple studies (Peña et al. 2000; Caoili et al. 2000, 2002; Blake et al. 2006). Moreover, studies have also demonstrated that diagnostic accuracy is independent of lipid content (Peña et al. 2000; Caoili et al. 2000).

In a patient with extra-adrenal malignancy, if an adrenal mass does not meet these imaging criteria of a benign lesion, then biopsy should be considered to exclude metastasis. Rarely, metastasis can involve an adrenal gland with a pre-existing adenoma, a so-called collision tumor.

Similar to metastasis, lymphomatous involvement of adrenal glands may need to be separated from a benign lesion. Adrenal involvement of lymphoma is usually secondary, mostly from non-Hodgkin's subtype. Approximately 4% of patients with non-Hodgkin's lymphoma have adrenal involvement, often bilateral and accompanied by retroperitoneal adenopathy or other site of metastasis (Mayo-Smith et al. 2001; Dunnick and Korobkin 2002). Its CT appearance is non-specific and may present as a discrete or an infiltrative mass (Paling and Williamson 1983).

5 Incidentally Discovered Adrenal Mass

The increased clinical indications for performing abdominal MSCT and its improved spatial resolution have led to the detection of incidental adrenal masses, the so-called "adrenal incidentaloma." The prevalence of an incidental adrenal mass at CT is approximately 4–5% (Kloos et al. 1995; Bovio et al. 2006; Song et al. 2008) comparable to the estimated prevalence in the general population of 3–7% based on the pathology literature (NIH 2002; Grumbach et al. 2003; Young 2007). The overwhelming majority of the incidentally discovered adrenal masses are benign, and adenomas account for most of these benign masses. Certain adrenal lesions have specific benign imaging features that are diagnostic at detection and require no further evaluation. For other lesions, the evaluation of an incidental adrenal mass depends on several factors related to the risk of malignancy as discussed below. Of note, imaging studies do not address the functional status of an adrenal incidentaloma. Subclinical hyperfunction of an incidental adrenal mass is an uncommon but recognized phenomenon, and some endocrinologists recommend excluding occult, asymptomatic hyperfunctioning neoplasms in all adrenal incidentalomas (NIH 2002; Grumbach et al. 2003; Young 2007). However, because biochemical work up is costly, others reserve full endocrine work up for the patients with clinical findings supportive of a hyperfunctioning neoplasm (Berland et al. 2010). Several recent publications addressed the management of incidental adrenal mass with recommended algorithms (Boland et al. 2008; Francis et al. 2009; Berland et al. 2010). In patients with no history of malignancy, an exhaustive workup is not indicated for most small (<4 cm) asymptomatic incidental adrenal masses.

5.1 Specific Benign Imaging Features

5.1.1 Adrenal Myelolipoma

Adrenal myelolipomas are benign tumors composed of mature fat and hematopoietic tissue, resembling bone marrow. Adrenal myelolipomas are usually

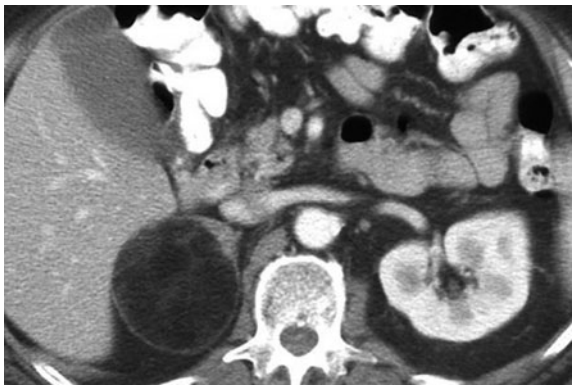

Fig. 9 Myelolipoma in 69-year-old female. Axial contrast-enhanced CT image shows a 6 cm encapsulated right adrenal mass predominantly consisting macroscopic fat

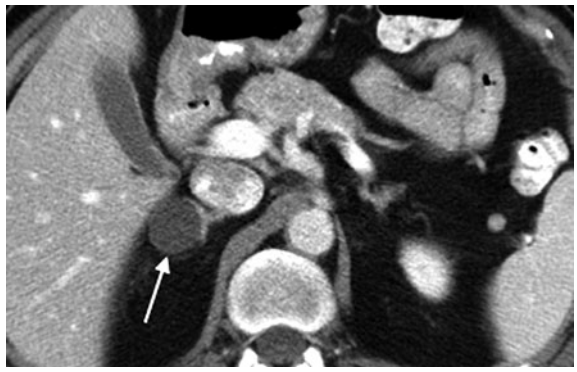

Fig. 10 Adrenal cyst in 50-year-old male. Axial contrast-enhanced CT image shows a 2 cm homogeneous right adrenal mass (*arrow*) of near-water attenuation and imperceptible wall

incidentally found asymptomatic masses with no endocrine function, but large masses may rarely cause pain due to spontaneous hemorrhage. Adrenal myelolipomas are reported to be uncommon, accounting for 2.6% of all adrenal tumors in pathology series (Lam and Lo 2001) and prevalence of 0.08–0.2% in autopsy series (Olsson et al. 1973). With the widespread use of cross-sectional imaging, incidental detection of myelolipoma has increased. In one study, 6% of incidentally found adrenal masses were myelolipomas (Song et al. 2008). On CT, these lesions are easily recognized because they contain macroscopic fat, although the amount of fat and soft tissue is variable (Fig. 9). Pseudocapsules are common and calcifications are present in 24% of adrenal myelolipomas (Kenney et al. 1998).

5.1.2 Adrenal Cyst

Adrenal cysts are uncommon lesions, usually asymptomatic and incidentally found, unless they produce mass effects on adjacent organs or are complicated by hemorrhage or infection. There are four histologic subtypes of adrenal cysts: endothelial cysts, pseudocysts, parasitic cysts, and epithelial cysts (Cheema et al. 1981). Of these, the endothelial subtype is the most frequently seen at pathologic analysis, and the pseudocyst the most common type to manifest clinically. Adrenal cysts are well-defined homogeneous round masses of near-water attenuation and a thin wall (Fig. 10). The wall may contain thin calcification and may also enhance with contrast (Rozenblit et al. 1996). Adrenal pseudocyst, which results from a previous episode of hemorrhage, may appear more complex with higher density, thicker wall, internal septations, and calcifications (Rozenblit et al. 1996).

5.1.3 Adrenal Hemorrhage

Adrenal hemorrhage results from trauma, anticoagulation, blood dyscrasia, sepsis, hypotension, renal vein thrombosis, and severe stress such as surgery. Adrenal hemorrhage has also been described in the distinct settings of liver transplant and nephrectomy (Solomon and Sumkin 1988; Bowen et al. 1990; Sasiwimonphan et al. 2010). Trauma accounts for 80% of adrenal hemorrhage. Adrenal injury has been reported in 28% of autopsy series of severe trauma (Sevitt 1955), but a much smaller prevalence of 2% has been reported in CT series of patients with severe abdominal injury (Burks et al. 1992; Rana et al. 2004). Adrenal hemorrhage in trauma is usually unilateral, typically on the right. On CT, acute adrenal hematoma is round or oval with increased density of 50–90 HU on unenhanced MSCT (Fig. 11). The size and density of the mass decrease over time and usually resolve spontaneously or calcify, although some may liquefy and persist as pseudocysts. Unilateral adrenal hemorrhage may be followed to exclude an underlying mass when there is no identifiable cause (Dunnick and Korobkin 2002; Boland et al. 2008).

5.2 Non-Specific Imaging Features

When an incidental adrenal mass does not have specific diagnostic imaging features, several factors determine the imaging work-up as related to the risk

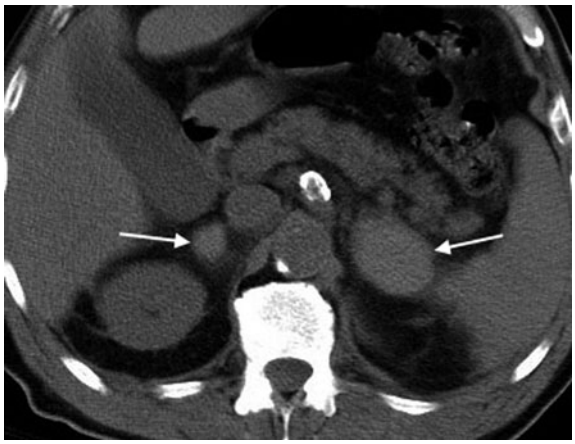

Fig. 11 Adrenal hemorrhage in 73-year-old male. Axial unenhanced CT image shows bilateral adrenal masses (*arrow*) with attenuation of 52 HU, consistent with acute hemorrhage

of malignancy. One of the most important determinants is patient history of malignancy as it is extremely rare for an incidental adrenal mass to be metastasis of an unknown primary malignancy (Herrera et al. 1991; Lee et al. 1998; Song et al. 2008). The size of the adrenal mass is also an important factor, as the risk of malignancy increases with the mass size. Unless a definitive benign diagnosis is made, adrenal masses larger than 4 cm are generally resected in patients without history of malignancy. An enlarging adrenal mass also indicates malignancy. Certain morphologic features are also worrisome for malignancy such as central necrosis, heterogeneous attenuation, and irregular margins. In patients with history of malignancy or imaging features suspicious for a malignant mass, further imaging characterization can be performed using unenhanced CT, chemical shift MR, or PET-CT (usually in oncologic patients). If these are not diagnostic, then adrenal CT with washout analysis may be helpful.

6 Adrenal Biopsy

The need for imaging-guided biopsy to diagnose an adrenal mass has decreased in recent years as advances in adrenal imaging now allow accurate characterization of most adrenal masses (Paulsen et al. 2004). However, biopsy may still be necessary in oncology patients when imaging findings are inconclusive or when confirming a suspected solitary adrenal metastasis. Biopsy is also performed if an indeterminate adrenal mass is enlarging in a patient without malignancy, unless surgical resection is planned. Adrenal biopsy is usually performed with CT guidance and has been shown to be safe, with 85–96% diagnostic accuracy and 3–9% complication rate (Silverman et al. 1993; Welch et al. 1994). If there is a possibility that the adrenal mass is a pheochromocytoma, the plasma-free metanephrine level should be obtained prior to biopsy to avoid potential hypertensive crisis.

References

Bae KT, Fuangtharnthip P, Prasad SR, Joe BN, Heiken JP (2003) Adrenal masses: CT characterization with histogram analysis method. Radiology 228:735–742

Baguet JP, Hammer L, Mazzuco TL, Chabre O, Mallion JM, Sturm N, Chaffanjon P (2004) Circumstances of discovery of phaeochromoytoma: a retrospective study of 41 consecutive patients. Eur J Endocrinol 150:681–686

Berland LL, Silverman SG, Gore RM et al (2010) Managing incidental findings on abdominal ct: white paper of the American College of Radiology incidental findings committee. J Am Coll Radiol 7:754–773

Bessell-Browne R, O'Malley ME (2007) CT of pheochromocytoma and paraganglioma: risk of adverse events with IV administration of nonionic contrast material. Am J Roentgenol 188:970–974

Blake MA, Kalra MK, Maher MM, Sahani DV, Sweeney AT, Mueller PR, Hahn PF, Boland GW (2004) Pheochromocytoma: an imaging chameleon. Radiographics 24:S87–S99

Blake MA, Kalra MK, Sweeney AT et al (2006) Distinguishing benign from malignant adrenal masses: multi-detector row CT protocol with 10-minute delay. Radiology 238:578–585

Boland GW, Lee MJ, Gazelle GS, Halpern EF, McNicholas MMJ, Mueller PR (1998) Characterization of adrenal masses using unenhanced CT: an analysis of the CT literature. Am J Roentgenol 171:201–204

Boland GW, Blake MA, Hahn PF, Mayo-Smith WW (2008) Incidental adrenal lesions: principles, techniques, and algorithms for imaging characterization. Radiology 249:756–775

Bovio S, Cataldi A, Reimondo G et al (2006) Prevalence of adrenal incidentaloma in a contemporary computerized tomography series. J Endocrinol Invest 29:298–302

Bowen AD, Keslar PJ, Newman B, Hashida Y (1990) Adrenal hemorrhage after liver transplantation. Radiology 176:85–88

Burks DW, Mirvis SE, Shanmuganathan K (1992) Acute adrenal injury after blunt abdominal trauma: CT findings. Am J Roentgenol 158:503–507

Caoili EM, Korobkin M, Francis IR, Cohan RH, Dunnick NR (2000) Delayed enhanced CT of lipid-poor adrenal adenomas. Am J Roentgenol 175:1411–1415

Caoili EM, Korobkin M, Francis IR, Cohan RH, Platt JF, Dunnick NR, Raghupathi KI (2002) Adrenal masses: characterization with combined unenhanced and delayed enhanced CT. Radiology 222:629–633

Cheema P, Cartegena R, Staubitz W (1981) Adrenal cyst: diagnosis and treatment. J Urol 126:396–399

Dunnick NR, Korobkin M (2002) Imaging of adrenal incidentalomas: current status. Am J Roentgenol 179:559–568

Dunnick NR, Heaston D, Halvorsen R, Moore AV, Korobkin M (1982) CT appearance of adrenal cortical carcinoma. J Comput Assist Tomogr 6:978–982

Dunnick NR, Leight GS Jr, Roubidoux MA, Leder RA, Paulson E, Kurylo L (1993) CT in the diagnosis of primary aldosteronism: sensitivity in 29 patients. Am J Roentgenol 160:321–324

Fishman EK, Deutch BM, Hartman DS, Goldman SM, Zerhouni EA, Siegelman SS (1987) Primary adrenocortical carcinoma: CT evaluation with clinical correlation. Am J Roentgenol 148:531–535

Francis IR, Casalino DD, Arellano RS, et al (2009) Incidentally discovered adrenal mass. American College of Radiology, ACR appropriateness criteria. http://www.acr.org/SecondaryMainMenuCategories/quality_safety/app_criteria/pdf/ExpertPanelonUrologicImaging/IncidentallyDiscoveredAdrenalMassDoc7.aspx

Grumbach MM, Biller BMK, Braunstein GD et al (2003) Management of the clinically inapparent adrenal mass ("incidentaloma"). Ann Intern Med 138:424–429

Herrera MF, Grant CS, van Heerden JA, Sheedy PF II, Ilstrup DM (1991) Incidentally discovered adrenal tumors: an institutional perspective. Surgery 110:1014–1021

Jhaveri KS, Wong F, Ghai S, Haider MA (2006) Comparison of CT histogram analysis and chemical shift MRI in the characterization of indeterminate adrenal nodules. Am J Roentgenol 187:1303–1308

Kenney PJ, Robbins GL, Ellis DA, Spirt BA (1985) Adrenal glands in patients with congenital renal anomalies: CT appearance. Radiology 155:181–182

Kenney PJ, Wagner BJ, Rao P, Heffess CS (1998) Myelolipoma: CT and pathologic features. Radiology 208:87–95

Kloos RT, Gross MD, Francis IR, Korobkin M, Shapiro B (1995) Incidentally discovered adrenal masses. Endocr Rev 16:460–484

Korobkin M, Giordano TJ, Brodeur FJ et al (1996a) Adrenal adenomas: relationship between histologic lipid and CT and MR findings. Radiology 200:743–747

Korobkin M, Brodeur FJ, Yutzy GG, Francis IR, Quint LE, Dunnick NR, Kazerooni EA (1996b) Differentiation of adrenal adenomas from nonadenomas using CT attenuation values. Am J Roentgenol 166:531–536

Korobkin M, Brodeur FJ, Francis IR, Quint LE, Dunnick NR, Londy F (1998) CT time-attenuation washout curves of adrenal adenomas and nonadenomas. Am J Roentgenol 170:747–752

Lam KY, Lo CY (2001) Adrenal lipomatous tumours: a 30 year clinicopathological experience at a single institution. J Clin Pathol 54:707–712

Lee MJ, Hahn PF, Papanicolaou N, Egglin TK, Saini S, Mueller PR, Simeone JF (1991) Benign and malignant adrenal masses: CT distinction with attenuation coefficients, size, and observer analysis. Radiology 179:415–418

Lee JE, Evans DB, Hickey RC, Sherman SI, Gagel RF, Abbruzzese MC, Abbruzzese JL (1998) Unknown primary cancer presenting as an adrenal mass: frequency and implications for diagnostic evaluation of adrenal incidentalomas. Surgery 124:1115–1122

Mansmann G, Lau J, Balk E, Rothberg M, Miyachi Y, Bornstein SR (2004) The clinically inapparent adrenal mass: update in diagnosis and management. Endocr Rev 25:309–340

Mayo-Smith WW, Boland GW, Noto RB, Lee MJ (2001) State-of-the-art adrenal imaging. RadioGraphics 21:995–1012

Mitchell DG, Crovello M, Matteucci T, Petersen RO, Miettinen MM (1992) Benign adrenocortical masses: diagnosis with chemical shift MR imaging. Radiology 185:345–351

Motta-Ramirez GA, Remer EM, Herts BR, Gill IS, Hamrahian AH (2005) Comparison of CT findings in symptomatic and incidentally discovered pheochromocytomas. Am J Roentgenol 185:684–688

Mukherjee JJ, Peppercorn PD, Reznek RH, Patel V, Kaltsas G, Besser M, Grossman AB (1997) Pheochromocytoma: effect of nonionic contrast medium in CT on circulating catecholamine levels. Radiology 202:227–231

NIH (2002) NIH state-of-the-science statement on management of the clinically inapparent adrenal mass ("incidentaloma"). NIH Consens State Sci Statements 19:1–25

Olsson CA, Krane RJ, Klugo RC, Selikowitz SM (1973) Adrenal myelolipoma. Surgery 73:665–670

Outwater EK, Siegelman ES, Radecki PD, Piccoli CW, Mitchell DG (1995) Distinction between benign and malignant adrenal masses: value of T1-weighted chemical-shift MR imaging. Am J Roentgenol 165:579–583

Paling MR, Williamson BRJ (1983) Adrenal involvement in non-Hodgkin lymphoma. Am J Roentgenol 141:303–305

Patel SM, Lingam RK, Beaconsfield TI, Tran TL, Brown B (2007) Role of radiology in the management of primary aldosteronism. RadioGraphics 27:1145–1157

Paulsen SD, Nghiem HV, Korobkin M, Caoili EM, Higgins EJ (2004) Changing role of imaging-guided percutaneous biopsy of adrenal masses: evaluation of 50 adrenal biopsies. Am J Roentgenol 182:1033–1037

Peña CS, Boland GW, Hahn PF, Lee MJ, Mueller PR (2000) Characterization of indeterminate (lipid-poor) adrenal masses: use of washout characteristics at contrast-enhanced CT. Radiology 217:798–802

Rana AI, Kenney PJ, Lockhart ME, McGwin G Jr, Morgan DE, Windham ST III, Smith JK (2004) Adrenal gland hematomas in trauma patients. Radiology 230:669–675

Remer EM, Motta-Ramirez GA, Shepardson LB, Hamrahian AH, Herts BR (2006) CT histogram analysis in pathologically proven adrenal masses. Am J Roentgenol 187:191–196

Rockall AG, Babar SA, Sohaib SA, Isidori AM, Diaz-Cano S, Monson JP, Grossman AB, Reznek RH (2004) CT and MR imaging of the adrenal glands in ACTH-independent Cushing Syndrome. RadioGraphics 24:435–452

Rozenblit A, Morehouse HT, Amis ES (1996) Cystic adrenal lesions: CT features. Radiology 201:541–548

Sasiwimonphan K, Takahashi N, Leibovich BC, Kawashima A (2010) Adrenal hematoma after nephrectomy. Am J Roentgenol 195:1334–1337

Sevitt S (1955) Post-traumatic adrenal apoplexy. J Clin Pathol 8:185–194

Silverman SG, Mueller PR, Pinkney LP, Koenker RM, Seltzer SE (1993) Predictive value of image-guided adrenal biopsy: analysis of results of 101 biopsies. Radiology 187:715–718

Sohaib SA, Hanson JA, Newell-Price JDC, Trainer PJ, Monson JP, Grossman AB, Besser GM, Reznek RH (1999) CT appearance of the adrenal glands in adrenocorticotrophic hormone-dependent Cushing's syndrome. Am J Roentgenol 172:997–1002

Solomon N, Sumkin J (1988) Right adrenal gland hemorrhage as a complication of liver transplantation: CT appearance. J Comput Assist Tomogr 12:95–97

Song JH, Chaudhry FS, Mayo-Smith WW (2008) The incidental adrenal mass on CT: prevalence of adrenal disease in 1,049 consecutive adrenal masses in patients with no known malignancy. Am J Roentgenol 190:1163–1168

Szolar DH, Kammerhuber FH (1998) Adrenal adenomas and nonadenomas: assessment of washout at delayed contrast-enhanced CT. Radiology 207:369–375

Welch TJ, Sheedy PF II, Stephens DH, Johnson CM, Swensen SJ (1994) Percutaneous adrenal biopsy: review of a 10-year experience. Radiology 193:341–344

Young WF Jr (2007) The incidentally discovered adrenal mass. N Engl J Med 356:601–610

Inflammatory and Infectious Disease of the Kidney and Urinary Collecting System

Ullrich G. Mueller-Lisse, Ulrike L. Mueller-Lisse,
Eva M. Coppenrath, and Anno Graser

Contents

Abstract

Inflammatory and infectious disease of the kidney and urinary collecting system is a frequent reason for consultations both in general practice and in clinical specialist clinics. The diagnosis of urinary tract infection (UTI) as the most frequent cause of disease relies on clinical findings, including a combination of symptoms, and urinalysis, unless patients present with recurrent or complicated UTI, UTI that does not respond to typical pharmacological treatment within the expected time interval, with signs and symptoms that are unexpectedly severe or atypical, with urinalysis returning atypical pathogens, or with other disease predisposing to complicated UTI, such as chronic infectious or inflammatory conditions, immunosuppression, or diabetes mellitus. MDCT, rather than ultrasonography or intravenous (excretory) urography, has been widely accepted as the imaging modality of choice under those conditions, due to its wide availability and its capability of finding and characterizing both acute and chronic infectious disease and post-infectious tissue alteration and their respective sequels within and around the upper urinary tract. Patient preparation includes serum creatine level, GFR, and basal TSH tests, adequate pain medication and oral or intravenous hydration, and sufficient antecubital venous access for intravenous administration of contrast media. MDCT is adapted to the clinical question, with a full protocol including unenhanced and contrast-enhanced images obtained in the nephrographic and excretory phases of contrast processing by the kidneys. MDCT detects and localizes urolithiasis, pus and fluid collections, inflammatory streaking or

U. G. Mueller-Lisse · Eva M.Coppenrath · A. Graser (✉)
Departments of Radiology,
University of Munich Hospitals,
Marchioninistrasse 15,
81377 Munich, Germany
e-mail: Anno.Graser@med.uni-muenchen.de

U. L. Mueller-Lisse
Departments of Urology,
University of Munich Hospitals,
Marchioninistrasse 15,
81377 Munich, Germany

C. J. Zech et al. (eds.), *Multislice-CT of the Abdomen*, Medical Radiology. Diagnostic Imaging,
DOI: 10.1007/174_2011_530, © Springer-Verlag Berlin Heidelberg 2012

stranding, hemorrhage, gas or air, and signs of decreased renal function both within the kidney parenchyma and in the sinus fat and extrarenal fat which are associated with inflammatory or infectious disease of the urianry tract. Extension of disease to other tissues and organs can be assessed, e.g., in abscess formation extending into or through the abdominal wall. Although not entirely specific, signs associated with atypical acute pyelonephritis, such as tuberculosis, mucor-mycosis, or emphysematous pyelonephritis may be recognized in the urinary tract. Those signs may be distinguished from signs of chronic pyelonephritis, including xanthogranulomatous pyelonephritis as a rare condition, and signs associated with renal papillary necrosis.

1 Introduction

In diagnostic uroradiology, computed tomography (CT) has proved to be useful for the entire spectrum of renal and ureteral disease. Particularly since the event of multidetector-row CT (MDCT) in clinical practice, the entire urinary tract can be examined with high spatial and temporal resolution of CT images. Clearly distinct phases of contrast processing by the kidneys can be distinguished, including the unenhanced, arterial (20–35 s after commencement of intravenous administration of iodinated contrast media), corticomedullary (40–70 s), nephrographic (80–120 s), and excretory (more than 180 s) phases, may be depicted by MDCT and allow for detailed characterization of lesions (Mueller-Lisse and Mueller-Lisse 2004). Multiplanar reformatting (MPR), maximum intensity projection (MIP), and volume rendering (VR) techniques also help to find and characterize lesions. Although less expensive imaging methods, including intravenous urography (IVU) and sonography, are widely available, patients are oftentimes referred for definitive evaluation with MDCT when lesions are suspected in clinical examinations or other imaging studies. Because of its high diagnostic power, MDCT can be applied as the primary and definitive diagnostic imaging method in various disorders.

Indications for MDCT of the kidney and urinary collecting system in inflammatory and infective disease particularly include complications of acute and chronic pyelonephritis, renal abscess, xanthogranulomatous pyelonephritis, tuberculosis, mycosis, and inflammatory or infectious complications of urolithiasis or injury to the urinary tract or its neighboring structures (Mueller-Lisse and Coppenrath 2006; Mueller-Lisse and Mueller-Lisse 2004).

2 Patient Preparation and MDCT Examination

While physiological hydration of the patient is desirbale, whether by means of oral hydration (e.g., water, tea), or intravenous hydration (e.g. normal saline solution), care should be taken to not overburden patients with acute trauma, acute renal or ureteral colic, or acute septic disease. In those instances, pre- and post-scan hydration should be carefully discussed with emergency room or intensive care physicians or nephrologists.

Serum creatinine level, (calculated) glomerular filtration rate (GFR), and thyroid stimulating hormone (TSH) level should be available to estimate the risk of a contrast-enhanced MDCT examination.

Adequate pain medication should be prescribed and administered by emergency room or intensive care physicians if necessary to ensure adequate image quality.

An antecubital venous access should be established (unless suitable central venous access is available) to allow for injection of contrast media and normal saline solution by means of an automated pump, with an injection speed of at least 2–3 ml/s. Usually, this requires an access diameter of at least 20 G.

If possible, patients are examined in the supine position, head first, with arms elevated over head.

For examinations focusing on the region of the kidneys and adrenals, the topogram should extend from the diaphragm to the iliac crest (caveat: more extensive when pelvic position of at least one kidney is known or anticipated). For examination of the entire upper urinary tract, the topogram extends from the diaphragm to the symphysis pubis (Mueller-Lisse and Coppenrath 2006).

Standard examination parameters frequently used for MDCT of the kidneys and upper urinary tracts are listed in Table 1. Depending on the clinical situation and specific situation of the individual patient, parameters may have to be adapted for optimal imaging results. With MPRs in the coronal or sagittal planes of

Table 1 Examination parameters for standard multidetector-row computed tomography (MDCT) of the kidneys and upper urinary tract (modified from (Mueller-Lisse and Coppenrath 2006)

Parameter	4–8 detector rows	10–16 detector rows	32–64 detector rows
MDCT examination parameters			
Tube charge (kV)	120	120	120
Rotation time (s)	0.5	0.5	0.5
Tube current–time product (mAs)	130–340	130–340	130–340
Pitch-adapted tube current–Time product (eff. mAs)	150–250, low dose, 30–50	150–250, low dose, 30–50	150–250, low-dose, 30–50
Collimation (mm)	2.5	1.25/1.5	0.6/0.625
Normalized pitch	0.9–1.5	0.9–1.5	0.9–1.5
Primary reconstruction intervall (mm)	3	3, for secondary reconstructions, 1	3, for secondary reconstructions, 0.6
Primary reconstruction slice thickness (mm)	3–5	3–5, for secondary reconstructions, 1.5–2	3–5, for secondary reconstructions, 0.75–1
Kernel	standard	standard	standard
Contrast media administration			
Concentration (mg iodine/ml)	300–350	300–350	300–350
Mono-/biphasic	mono-phasic	mono-phasic	mono-phasic
Typical injection volume (ml)	100–120	70–110	70–100
Injection speed (ml/s)	2.5–3	2.5–3	2.5–3
Normal saline solution (ml, ml/s)	optional	optional	optional
Phase and delay (s)	portal venous, 70, nephrographic, 80–120, excretory, 600–960	portal venous, 70, nephrographic, 80–120, excretory, 600–960	portal venous, 70, nephrographic, 80–120, excretory, 600–960

Depending on the specific vendor and MDCT scanner, modifications of parameter settings may be necessary to optimize the protocol. Parameters listed do not include dose modulation options as available for different MDCT scanners. Injection volume of iodinated contrast media should be body weight-adapted

view, it may be easier to assess the extent of sequels of renal infection than with axial MDCT images alone. Both extrarenal inflammation and abscess may be better visualized by MPRs, particularly at the renal poles (Mueller-Lisse and Mueller-Lisse 2004).

3 Acute Pyelonephritis

Acute pyelonephritis and upper urinary tract infection are very common reasons for primary care physician visits or emergency room consultations. In adults, diagnosis of urinary tract infection (UTI) is typically based on characteristic clinical features and abnormal laboratory values that suggest infectious disease (Craig et al. 2008). The need for imaging in the diagnosis and follow-up of pyelonephritis and upper UTI is determined by the specific clinical situation.

3.1 Simple Acute Pyelonephritis

Simple, uncomplicated UTI usually does not require radiological evaluation (Browne et al. 2004), because both the diagnosis and the follow-up can be provided by clinical signs and symptoms and laboratory findings (Craig et al. 2008). However, recurrent UTI may warrant radiological investigation (Browne et al. 2004), particularly to rule out urinary tract anomalies or other disease affecting or involving the urinary tract as a cause.

MDCT in the nephrographic phase typically demonstrates solitary or multifocal wedge-shaped areas of decreased or missing enhancement in acute

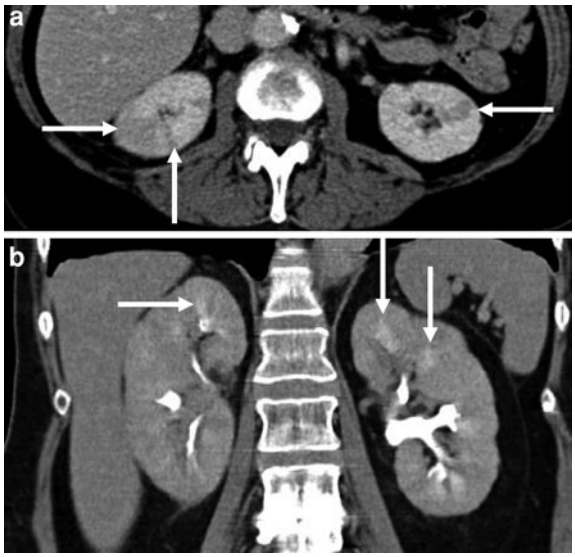

Fig. 1 Simple acute pyelonephritis in ascending urinary tract infection. Axial MDCT images in the nephrographic phase (**a**) show strands of decreased contrast enhancement where infectious fluid or pus within the collecting tubules, inflammation, and tissue edema increase intrarenal pressure and decrease perfusion (*arrows*). Coronal MDCT images in the excretory phase (**b**) show strands of contrast retention, predominantly in the renal medulla, caused by obstruction of collecting tubules (*arrows*) From: Mueller-Lisse and Mueller-Lisse 2004 (Fig. 17)

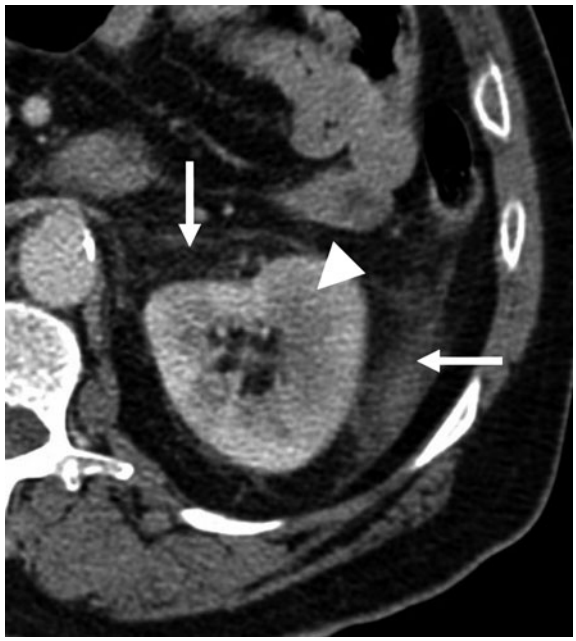

Fig. 2 Early perirenal inflammation (*arrows*) as a common sequel of acute pyelonephritis with wedge-shaped areas of decreased or missing enhancement (*arrowhead*) in a 67-year-old immuno-competent patient. Axial MDCT image in the nephrographic phase of contrast enhancement

pyelonephritis (Figs. 1, 2). Corticomedullary differentiation may be blurred or lost in affected areas. CT images obtained approximately 3 h after intravenous contrast administration may demonstrate streaky, band-like, or cone-shaped enhancement in areas of renal parenchyma demonstrating decreased enhancement in the nephrographic phase. Associated microabscesses and macroabscesses may retain contrast media and demonstrate a hyperdense rim in much delayed post-contrast images (Dalla-Palma et al. 1997).

Compared to CT images obtained early in the course of acute pyelonephritis, parenchymal abnormalities usually show little change while perirenal inflammatory infiltrates often increase during the first week (Fig. 2). Over the next two to eight weeks after the onset of acute pyelonephritis, signs of acute inflammation subside, while typical changes of parenchymal contrast enhancement may persist for up to two months. Renal enlargement may be an early but persistent finding for up to four months. New parenchymal scars may be found in about half of the patients as a sequel of acute pyelonephritis (Soulen et al. 1989).

3.2 Complex Acute Pyelonephritis

Acute pyelonephritis may be complex for different reasons. While acute pyelonephritis usually presents as an infection ascending from the urinary bladder into the upper urinary tract to affect the renal collecting system and, secondarily, the intramedullary collecting tubules of the kidney, other routes of infection are possible. Partial or complete obstruction of a previously infected upper urinary tract by urolithiasis or of a previously non-infected upper urinary tract with urolithiasis and subsequent infection represents one kind of complex acute UTI (Fig. 3). In such cases, increasing pressure within the urinary tract proximal to the occlusion contributes to infectious spread into the renal parenchyma and, potentially, beyond into perirenal tissues.

Other routes may include direct spread to the kidney of infectious disease primarily affecting extrarenal tissue or organs, e.g. retroperitoneal fat, pancreas (i.e., in pancreatitis complicated by infection), or large or small intestine, or septic spread in case of overwhelming infectious disease in remote

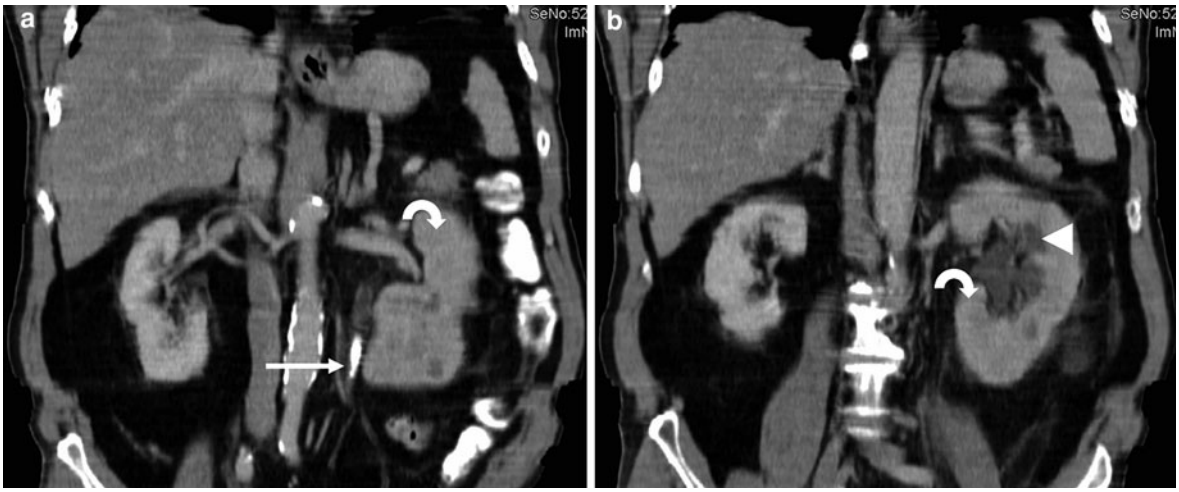

Fig. 3 A 66-year-old patient presenting with septicaemia and suspicion of abdominal focus. Coronal MDCT images in the nephrographic phase of contrast enhancement demonstrate previously undiagnosed left ureteral stone (*arrow* in **a**) with left renal enlargement and pelvicocaliceal dilation (*arrowhead* in **b**). Compared to the right kidney, the left kidney shows delayed contrast enhancement and subtle parenchymal stranding (*curved arrows*), suggesting increased renal pressure and, potentially, pyelonephritis

tissues or organs. Injury or trauma to the kidney or upper urinary tract, whether iatrogenic or other in nature, may carry infectious microorganisms to the urinary tract, potentially leaving abscesses along the entry route (Fig. 4).

Conversely, infection primarily originating in the urinary tract may spread loco-regionally, to perirenal fat and connective tissue, and on to the abdominal wall, or into the peritoneal cavity and on to intra-peritoneal organs, when infectious strands or fistulae or abscesses develop (Fig. 5). Acute pyelonephritis may be the infectious focus causing septic disease with high fever and subsequent organ failure when septicemia occurs (Fig. 6). Finally, abscess developing within the kidney parenchyma, e.g., as a sequel of acute pyelonephritis, may secondarily break into the renal collecting system and subsequently destroy renal and pelvicaliceal architecture (Fig. 7), or induce new caliceal diverticula which then remain as a persistent finding (Soulen et al. 1989).

Diagnostic imaging, preferably applying MDCT in adult patients unless there are contraindications, aims at establishing the local extent of infectious disease, potential foci of origin of infections deemed to have come from outside the urinary tract, potential routes of infection, and the presence of septic metastases to distant organs or tissues. Patterns of local extent and distant spread of infectious disease govern the therapeutic approach. Surgical or interventional radiological measures may be minimally invasive, e.g., in cases of catheter drainage of renal or peri- and para-renal abscesses (Browne et al. 2004), or even resective, e.g., in cases of septic nephrectomy when there is overwhelming renal abscess. Antibiotic treatment may be the only therapeutic measure, or an adjunct to surgical or radiological intervention. Measures of intensive care or supportive therapy may have to be taken depending on the patient's general state, e.g. in patients suffering from generalized septic disease of urogenital origin.

The differential diagnosis of perirenal fluid collections associated with signs of inflammation, if not necessarily with signs of infection, should include urinoma, seroma, and lymphocele, particularly in patients with previous abdominal, retroperitoneal, or pelvic surgery (Fig. 8).

Complex courses, or complications of acute pyelonephritis, may be anticipated in patients suffering from diabetes mellitus or in immuno-compromised patients, such that the decision on diagnostic imaging should be made early in these patients (Browne et al. 2004). Imaging in patients with severe septic disease or septic shock and clinical suspicion of an abdominal or retroperitoneal focus may demonstrate renal perfusion deficits as a sequel, whether with or without renal or pelvicaliceal foci of infection (Fig. 6). Although

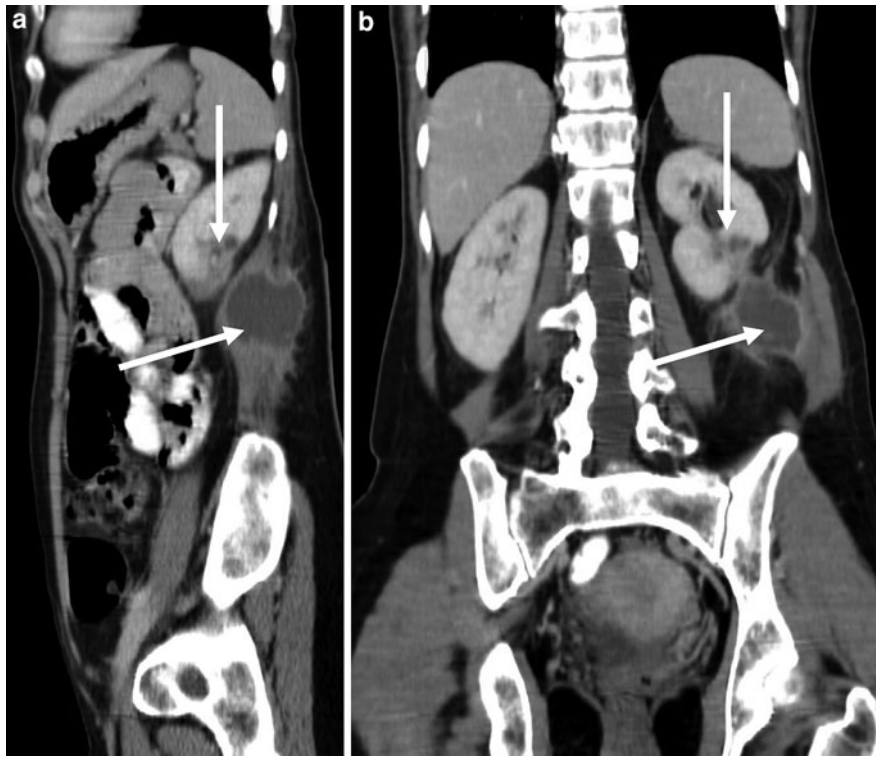

Fig. 4 Complex renal, retroperitoneal, and abdominal wall abscess as a sequel of nephrostomy (*arrows*). Sagittally (**a**) and coronally (**b**) reformatted MDCT images in the nephrographic phase of contrast enhancement

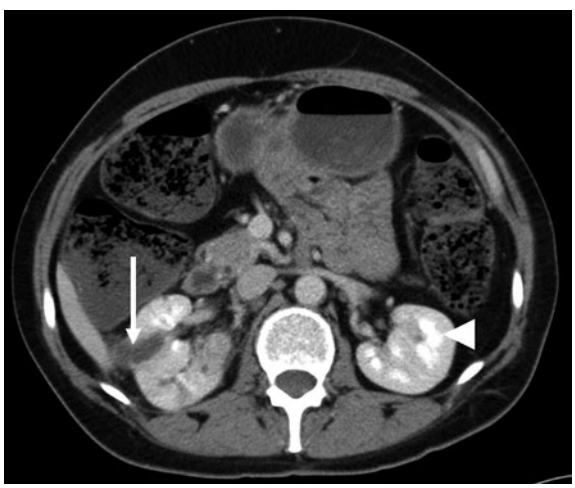

Fig. 5 Right-sided pyelonephritis with obstruction of collecting tubules with pus. Increasing tubular pressure spreads inflammatory products and decreases peritubular blood perfusion. Intrarenal abscess may develop which penetrates the renal capsule and extends into perirenal fat tissue as pressure increases (*arrow*). Axial MDCT image in the early excretory phase with increased contrast within the renal medulla (*arrowhead*)

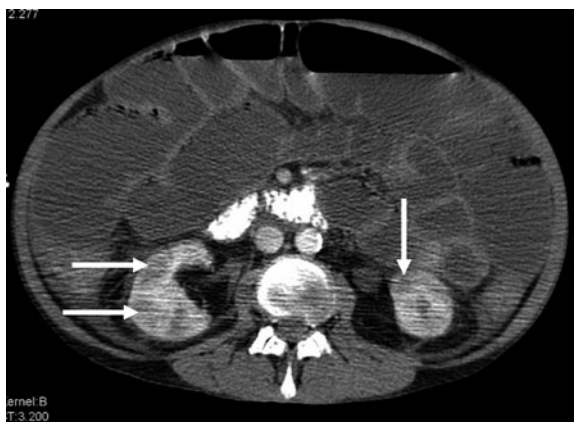

Fig. 6 A 61-year-old patient in septic shock, abdominal septic focus assumed. Perfusion deficits affecting the medulla more than the cortex in both kidneys (*arrows*) may be due to primary ascending pyelonephritis, secondary pyelonephritis after septic spread of infection, or septic shock. Axial MDCT image in the nephrographic phase of contrast enhancement

contrast-enhanced MDCT imaging in diabetic, immuno-compromised, or septic patients may be helpful in finding the focus of infectious disease and planning access routes to eliminate that focus, the drawback lies in the additional burden the contrast media puts on the patient's kidneys. Thus, renal failure may not only prevail as a consequence of chronic or septic disease, but it may also develop subsequent to

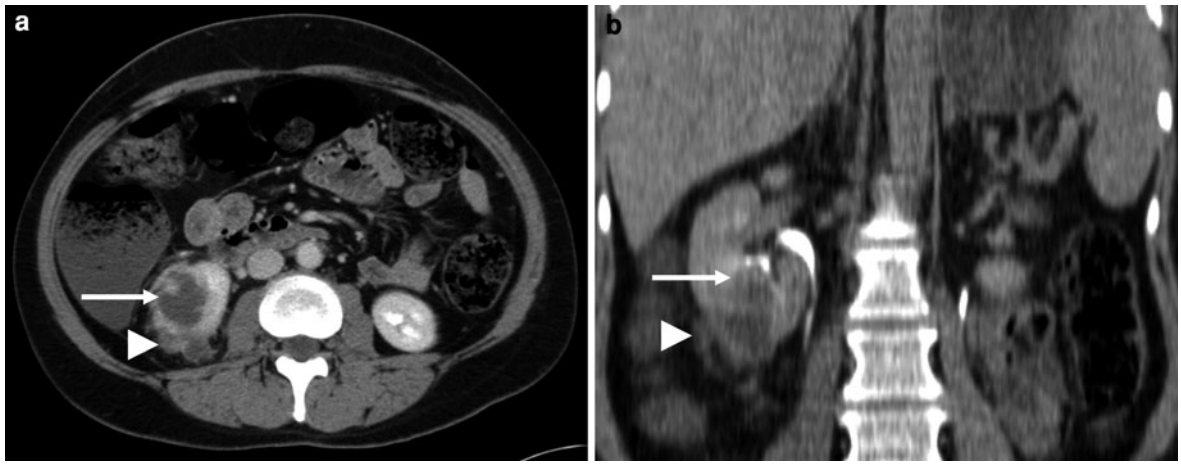

Fig. 7 Acute, right-sided pyelonephritis with intrarenal abscess extending into renal sinus fat (*arrows*) and accompanying extrarenal daughter abscesses (*arrowheads*), **a** axially reformatted MDCT in the nephrographic phase, **b** coronally reformatted MDCT in the excretory phase

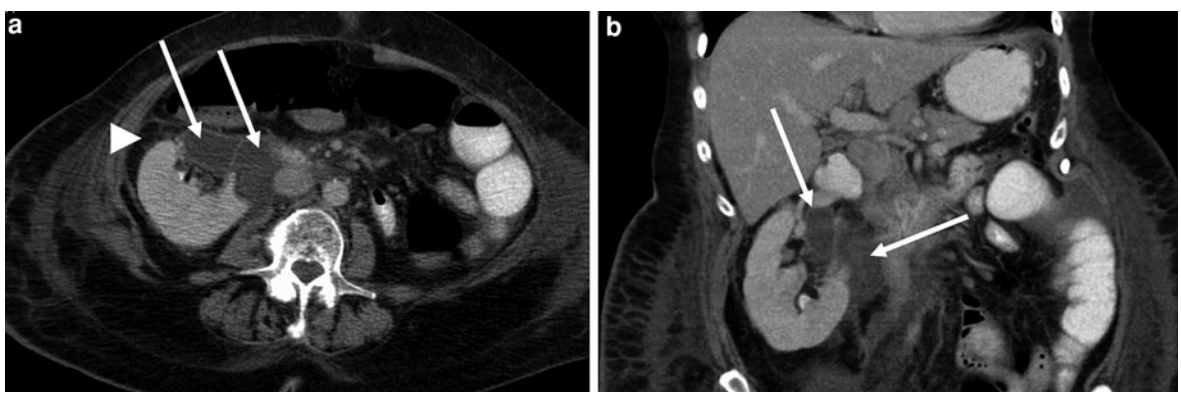

Fig. 8 A 67-year-old patient with status post-retroperitoneal lymphadenectomy for ovarian cancer. Perirenal inflammatory reaction (*arrowhead* in **a**) and perirenal fluid collections with a differential diagnosis of lymphocele, seroma, urinoma, or, less likely, abscess (*arrows* in **a** and **b**) without evidence of renal parenchymal involvement. Axially (**a**) and coronally (**b**) reformatted MDCT images in the nephrographic phases of contrast enhancement

imaging. In the individual patient, the risks of contrast-enhanced MDCT imaging therefore have to be carefully weighed against the potential benefits.

3.3 Atypical Acute Pyelonephritis

Acute pyelonephritis may be atypical when there is an atypical microorganism causing infectious disease that involves the upper urinary tract. While atypical UTI may occur when the immune reaction of the host is compromised, or when the patient suffers from severe diabetes mellitus, atypical acute pyelonephritis is not necessarily restricted to immuno-compromised patients. Tuberculosis and mucor mycosis of the upper urinary tract represent particular kinds of atypical renal and pelvicaliceal infection that are characterized by both acute and chronic sequels (Figueiredo et al. 2008; Sheibanifar et al. 2007). Emphysematous pyelonephritis is a rare infectious disease which has been described in diabetic patients (Rocher et al. 1999).

3.3.1 Tuberculosis

While tuberculosis (TBC) most often affects the chest, the urinary tract represents the most common extrapulmonary site of TBC manifestation (Figueiredo et al. 2008). The urinary tract can be infected with TBC in various ways. Primary urogenital tuberculosis may be acquired as an ascending infection of the urinary tract in ways similar to typical acute cystitis and pyelonephritis, or as an ascending infection of the genital tract in ways similar to other sexually transmitted disease. It may occur as a post-primary disease, when TBC spreads from one urogenital focus to another after a time interval. TBC may also affect the urogenital system secondarily, following primary manifestation in the lung, the urogenital tract, or in other organs, through hematogenous spread of infectious matter. The latter has been referred to as miliary spread or miliary TBC of the urogenital tract.

Depending on the access route and the duration of TBC in the kidney, imaging findings, particularly at MDCT, include scarring and strictures in the renal pelvicaliceal system, renal papillary necrosis, and renal cortical masses of decreased density, renal cortical scarring, or renal calcification.

Although urogenital TBC may affect immunocompetent individuals, immuno-compromised patients, e.g., with status post organ transplants, or with AIDS, appear to be particularly vulnerable to acquire urogenital TBC. In all instances, the clinical goal is to recognize urogenital TBC early in order to prevent from organ failure, organ loss, or even fatal outcome (Figueiredo et al. 2008).

While radiological presentation may differ, according to the specific site of the urogenital system being affected by TBC and the duration of the disease process, TBC infection is a destructive process which usually alters tissue and organ morphology. Figueiredo and co-workers (Figueiredo et al. 2008) describe seven different radiological patterns of urogenital TBC that reflect both the different access routes of infection to the urogenital system and the respective stage of the disease process in terms of the site and extent of destruction.

Pathological alteration may be absent or limited, e.g., to one upper urinary tract which demonstrates calyx deformity or renal calcification, when patients present with or without a history of previous pulmonary TBC, symptoms of UTI, and signs of hematuria along with TBC mycobacteria at urinalysis. In such instances, pharmacological therapy may suffice to control the disease (Figueiredo et al. 2008).

Pathological alteration may be unilateral in TBC affecting the upper urinary tract, with one upper tract being normal at imaging and the other being affected by stenosis and prestenotic dilatation in parts of or throughout the pelvicaliceal system. Treatment is usually surgical in those instances, with partial or complete nephrectomy, depending on the extent of destruction (Figueiredo et al. 2008).

Unilateral TBC of the upper urinary tract with associated loss of renal function due to stenosis and dilatation of the renal pelvicaliceal system may be frequently found along with a contracted urinary bladder. In such cases, vesicoureteral reflux, as demonstrated by voiding cysturethrogrpahy, is a common finding which affects either the side of the non-functioning kidney, or the side of the functional kidney (particularly when there is structural alteration of the functional upper urinary tract, such as hydronephrosis or ureteral dilatation), or both. Treatment is usually surgical, with bladder augmentation and, in cases of ureteral reflux, with re-implantation of the ureter. Chronic renal failure despite treatment is an undesired outcome to be apprehended.

When urogenital TBC is diagnosed late, end-stage renal failure may be found along with a contracted urinary bladder (Figueiredo et al. 2008).

In patients with foci of TBC in other organs, along with fever and malaise, signs of miliary TBC may be found in the kidneys that may include multiple, usually bilateral renal parenchymal lesions, which may prevail in the absence of urologic symptoms. Miliary renal TBC is frequently associated with immunosuppression, e.g. due to AIDS (Fig. 9). Also, Miliary TBC with renal involvement is oftentimes a fatal disease (Figueiredo et al. 2008).

Urinary tract TBC may affect a transplant kidney, which is oftentimes associated with loss of function and/or loss of the transplant organ.

Finally, TBC may be confined to the genital tract, involving the prostate or epididymis without extending to the upper urinary tract (Figueiredo et al. 2008).

3.3.2 Mucor-Mycosis

Among immunocompromised patients, particularly those with a status post bone marrow transplantation, mucor-mycosis represents a rare but serious, life-threatening differential diagnosis when there is

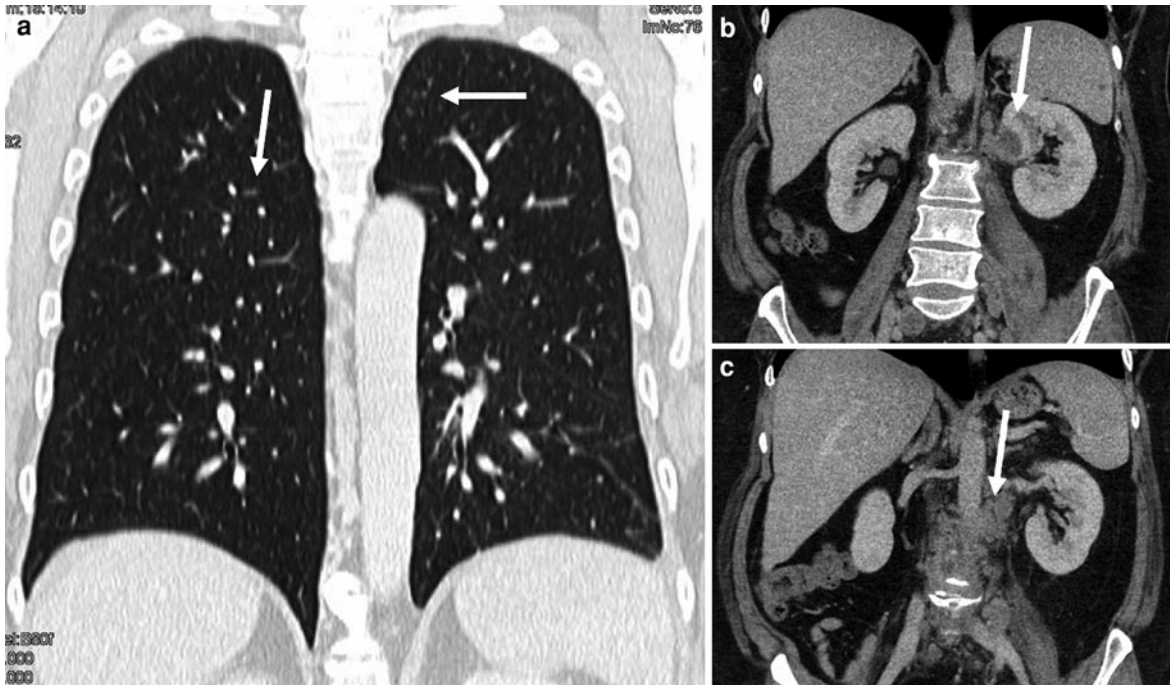

Fig. 9 A 43-year-old HIV-positive patient with polymerase chain reaction (PCR) tests positive for Mycobacterium-tuberculosis complex. Coronally reformatted MDCT of the chest (**a**) demonstrates multiple miliary nodules suggestive of miliary tuberculosis (*arrows*). Coronally reformatted MDCT images of the retroperitoneum in the nephrographic phase of contrast enhancement show partially necrotizing focus in left kidney (*arrow* in **b**) and partially necrotizing para-aortic lymphadenopathy (*arrow* in **c**) suggestive of miliary spread to the left kidney and associated lymph nodes. Urinalysis was negative for *Mycobacterium tuberculosis*

suspicion of infectious disease. Although mucormycosis usually affects the lung, the infection may disseminate to involve other organs, such as the kidneys, liver, spleen, or thyroid gland. Mucor-mycosis is destructive to tissues affected, or even invasive, with hallmark signs of low-density (at MDCT), low-signal intensity (at MRI), or low-echogenicity (at ultrasonography) lesions which demonstrate rapid growth and little or no peripheral uptake of contrast media. Imaging helps to find and localize the lesions, but it remains unspecific, such that pathological diagnosis is necessary. Attempts at therapy are surgical, with combined intensive medical therapy. However, mucor-mycosis is frequently lethal (Sheibanifar et al. 2007).

3.3.3 Emphysematous Pyelonephritis

Emphysematous pyelonephritis is a rare but life-threatening infection that typically occurs in diabetic patients. Although gas within the kidney may be demonstrated by plain film radiographs, or rarely by ultrasonography, its location and extent are best evaluated by MDCT, with both unenhanced and contrast-enhanced images being obtained in different phases of contrast processing by the kidneys (Browne et al. 2004; Craig et al. 2008; Rocher et al. 1999).

4 Chronic Pyelonephritis

Longstanding, ongoing, or recurrent pyelonephritis may as well not re-constitute to integrity of the kidney and pelvicaliceal system, but leave typical marks of destruction. Those marks, in turn, may be detected at subsequent imaging examinations, including ultrasonography, intravenous pyelography or urography, MDCT, and MRI. Typical features associated with chronic pyelonephritis include renal cortical scarring, renal cortical retraction, renal cortical atrophy, renal contour deformity, renal atrophy, renal papillary scarring, renal papillary destruction, renal caliceal clubbing, renal caliceal scarring, and renal caliceal diverticula (Fig. 10). Persistent perirenal stranding

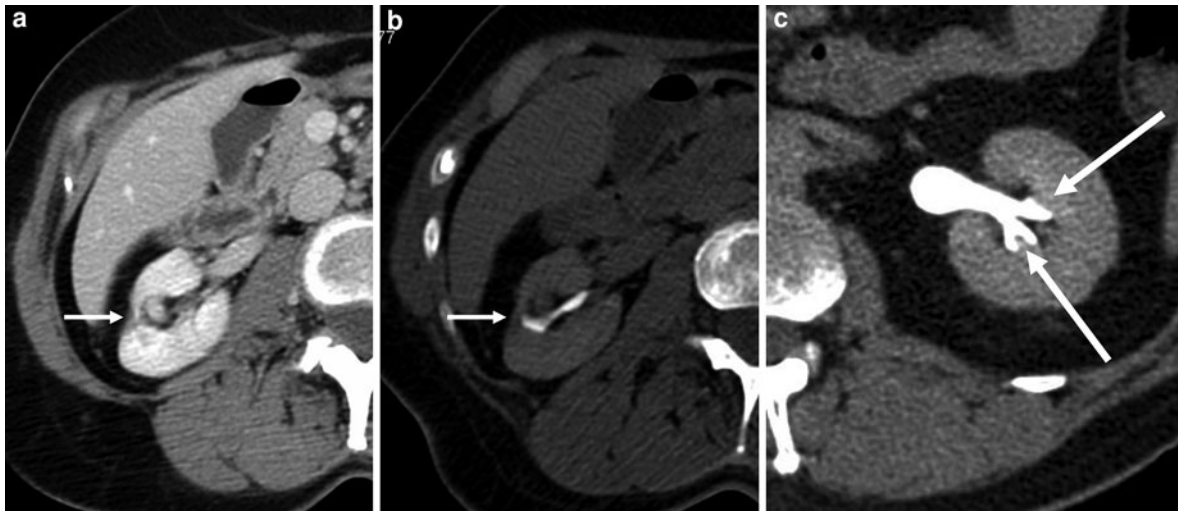

Fig. 10 Renal cortical scarring and retraction affecting renal parenchyma covering a renal calyx and associated renal papillary necrosis with blunting of the renal calyx (*arrows* in **a** and **b**, compare with normal renal calices, *arrows* in **c**), most likely due to chronic pyelonephritis, with a differential diagnosis of status post-focal renal cortical infarction. Axially reformatted MDCT images in the nephrographic (**a**) and excretory (**b** and **c**) phases of contrast enhancement

and scarring, with or without loss of perirenal fat tissue, may be accompanying features.

Unlike renal cortical renculation, which is sometimes encountered in children and adults as a persisting feature of embryonic development of the kidneys and goes along with a lobulated outer renal contour, with the renal cortex and capsule being drawn inward between individual renal medullary pyramids and their respective cortical cover, renal cortical scarring with retraction is characterized by a focal loss of renal cortical width and in-drawing of the renal capsule which centers on one renal medullary pyramid (Fig. 10). Renal cortical atrophy, with or without contour deformity of the kidney, may be a more generalized feature of chronic nephritis.

Renal papillary scarring, atrophy, or necrosis (see also below) may be features of chronic ascending pyelonephritis, when either the blood supply or the immune mechanisms at the distal end of the renal medullary pyramid do not withstand an infectious process affecting the renal collecting system. However, those features may also precede chronic pyelonephritis, particularly the infectious nephritic part, e.g., in patients with renal papillary necrosis of diabetic or toxic origin. One hypothesis holds that the loss of the tip of the renal medullary pyramid, which is closest to the renal pelvicaliceal system, is associated with a loss of certain valve mechanisms that usually prevent urine to press back from the pelvicaliceal system into the renal medullary collecting tubules. Loss of the valve mechanisms thus increases the risk of renal parenchymal involvement in cases of ascending pyelonephritis.

Renal caliceal clubbing may occur when there is a loss of renal medullary tissue at the tip, such that the affected renal calyx is drawn out to fill the gap. At imaging, particularly during the excretion of contrast media from the renal parenchyma into the pelvicaliceal system, the drawn-out calices demonstrate with a loss of their typical, cup-like shape and rather show with a shape reminiscent of a club. However, scar tissue may also lead to focal narrowing of the renal pelvicaliceal system, and there may be focal, pre-stenotic dilatation of the pelvicaliceal system. Finally, probably as a sequel of tissue necrosis within the renal parenchyma caused either by infection or abscess or by increased parenchymal pressure and decreased blood perfusion, renal caliceal diverticula may develop that fill with contrast media in the excretory phase of contrast-enhanced imaging just as the renal pelvicaliceal system does.

Perirenal stranding or scarring, which may accompany acute pyelonephritis as an inflammatory reaction within the perirenal fat tissue, may become a persistent feature in the presence of chronic pyelonephritis. Depending on the previous extent of active pyelonephritis and perinephritis, there may be a focal or even

more extensive loss of perirenal fat tissue associated with scarring. However, in abdominal or retroperitoneal trauma or iatrogenic injury, perirenal inflammation may occur in the absence of pyelonephritis (Fig. 8).

4.1 Xanthogranulomatous Pyelonephritis

Xanthogranulomatous pyelonephritis is another rare, chronic, and granulomatous inflammatory condition affecting structures of the kidney and pelvicaliceal system. It may affect male and female patients of all age groups. Lipid-containing inflammatory granulomas along with scar tissue may develop within the renal parenchyma, and in fat tissue of the renal sinus, hilus, and perirenal regions. Usually, only one kidney is affected, but loss of renal function frequently occurs in kidneys involved with xanthogranulomatous pyelonephritis (Browne et al. 2004; Craig et al. 2008). Recurrent bacterial UTI has been identified as a predisposing factor for xanthogranulomatous pyelonephritis (Craig et al. 2008). MDCT represents the mainstay of diagnostic imaging in xanthogranulomatous pyelonephritis, since it provides highly specific findings and accurate assessment of the extrarenal extent of disease, which is essential for surgical planning. (Craig et al. 2008). However, sarcomatous tumor involving fat tissue within and around the kidney, and, eventually, the kidney parenchyma, is a rare but important differential diagnosis, due to its malignant character (Browne et al. 2004).

5 Renal Papillary Necrosis

Papillary necrosis of the kidney is deemed to represent an ischemic event whose origin may be infectious, septic, toxic, vascular, or pressure-related. Infectious and septic causes include pyelonephritis and tuberculosis, while toxic causes have primarily been associated with overuse of analgesic drugs. Vascular reasons are manifold, particularly including impaired arterial blood supply, such as in severe or long-standing diabetes mellitus, impaired venous drainage, such as in renal vein thrombosis, or impaired red blood cell function, such as in sickle cell anemia. Increased pressure within the renal pelvicaliceal system, such as in obstructive uropathy, is another reason for renal papillary necrosis. Due to the peculiar structure of their arterial blood supply pathways and the hypertonic environment of their tissue parenchyma, the renal medulla, and papillae are particularly vulnerable to ischemic necrosis (Jung et al. 2006).

It has been hypothesized that due to tissue necrosis and loss of parenchyma at the tip of the renal medullary pyramid, certain valve mechanisms fail or are being lost that usually prevent urine reflux from the renal pelvicaliceal system back into the collecting tubules of the renal medullary parenchyma. Loss of the valve function therefore predisposes to nephritic exacerbation of ascending infection of the renal pelvicaliceal system (see Sect. 4). Thus, infectious pyelonephritis may not only be the cause (see above) but also the consequence of renal papillary necrosis.

Although IVU and ultrasonography may diagnose renal papillary necrosis, MDCT, particularly when applied in the nephrographic and excretory phases of imaging, may cover all of its typical features, including clefts within the renal medullary parenchyma that fill with contrast media, non-enhancing medullary lesions outlined by excreted contrast media, and high-density medullary calcifications. Papillary sloughing, i.e. the acute process of tissue loss at the renal medullary papillae with shedding of necrotic tissue into the pelvicaliceal system, may present with filling defects in the collecting system, and, eventually, with hydronephrosis in cases of urinary obstruction. Obstructive tissue may include post-inflammatory calcifications. Chronic renal papillary necrosis may show with blunting of the tip of the renal medullary papillae, such that the typical cup- or calyx-like appearance of the collecting system is being lost, and with renal parenchymal scarring or atrophy (similar to Sect. 4) (Jung et al. 2006).

6 Summary and Conclusions

While the diagnosis of UTI primarily relies on clinical findings, including a combination of symptoms and urinalysis, diagnostic imaging comes into play whenever there is reason to assume a complex or complicated course of disease. Such assumptions are warranted when UTI frequently recurs, when it does not respond to typical pharmacological treatment within the expected time interval, when signs and symptoms are unexpectedly severe or atypical, when urinalysis returns atypical pathogens, when UTI affects an immuno-compromised, or septic, or post-surgical, or

otherwise severely ill host, or when there are any other medical or environmental conditions that predispose the patient to a complicated healing process. MDCT, rather than ultrasonography or intravenous (excretory) urography, has been widely accepted as the imaging modality of choice under those conditions, due to its wide availability and its capability of finding and characterizing both acute and chronic infectious disease and post-infectious tissue alteration and their respective sequels within and around the upper urinary tract.

References

Browne RF, Zwirewich C, Torreggiani WC (2004) Imaging of urinary tract infection in the adult. Eur Radiol Suppl 3:E168–E183

Craig WD, Wagner BJ, Travis MD (2008) Pyelonephritis: radiologic-pathologic review. Radiographics 28:255–277

Dalla-Palma L, Pozzi-Mucelli R, Pozzi-Mucelli F (1997) Delayed CT in acute renal infection. Semin Ultrasound CT MR 18:122–128

Figueiredo AA, Lucon AM, Gomes CM, Srougi M (2008) Urogenital tuberculosis: patient classification in seven different groups according to clinical and radiological presentation. Int Braz J Urol 34:422–432

Jung DC, Kim SH, Jung SI, Hwang SI, Kim SH (2006) Renal papillary necrosis: review and comparison of findings at multidetector row CT and intravenous urography. Radiographics 26:1827–1836

Mueller-Lisse UG, Coppenrath E (2006) MSCT of the Upper Urinary Tract. In: Bruening R, Kuettner A, Flohr Th (eds) Protocols for Multislice CT, 2nd edn. Springer, Berlin, pp S213–S216

Mueller-Lisse UG, Mueller-Lisse UL (2004) MDCT of the kidney. In: Reiser MF, Takahashi M, Modic M, Becker CR (eds) Multislice CT, 2nd edn. Medical Radiology—Diagnostic Imaging. Baert AL, Sartor K (series eds). Springer Berlin pp 211–232

Rocher L, De Leusse-Vialar A, Tasu JP, Rondeau Y, Miquel A, Bazille A, Eschwege P, Blery M (1999) Emphysematous pyelonephritis: apropos of 4 cases. J Radiol 80:297–302

Sheibanifar M, Guerin AL, Clement L, Champigneulle J, Mainard L, Mandry D, Bordigoni P, Claudon M (2007) Imaging serious visceral forms of mucormycosis in five immunodepressed patients. J Radiol 88:677–683

Soulen MC, Fishman EK, Goldman SM (1989) Sequelae of acute renal infection: CT evaluation. Radiology 173: 423–426

MSCT of the Stomach

Sameer Ahmed, Karen M. Horton, Elliot K. Fishman, and Pamela T. Johnson

Contents

Abstract

Multi-slice computed tomography (MSCT) is frequently employed for imaging the stomach and perigastric vasculature. The benefits of this modality include short acquisition times, enhanced temporal and spatial resolution, longer anatomic coverage, and reduced image artifacts. Thin-slice collimation protocols are implemented to acquire isotropic volume data allowing superior multiplanar reformation (MPR) and three-dimensional (3D) reconstruction of gastric images. Additionally, protocol optimization enables accurate detection of complex gastric and extragastric pathology on multi-phase imaging. This chapter will discuss CT technique and review clinicopathological and radiological characterization of benign and malignant gastric masses, as well as inflammatory gastric conditions. MSCT is a valuable tool for detection, staging, surveillance, and post-treatment evaluation of gastric disease.

S. Ahmed
Johns Hopkins School of Medicine,
Baltimore, MD 21205, USA

K. M. Horton · E. K. Fishman (✉)
The Russell H. Morgan Department of Radiology and Radiological Science, Johns Hopkins Hospital,
601 N. Caroline Street, Room 3125,
Baltimore, MD 21287, USA
e-mail: efishman@jhmi.edu

P. T. Johnson
The Russell H. Morgan Department of Radiology and Radiological Science, Johns Hopkins Hospital,
601 N. Caroline Street, Room 3140D,
Baltimore, MD 21287, USA

1 Technique

Dual-phase (arterial and venous) IV contrast-enhanced CT is used for diagnosis and staging of gastric tumors. The enhancement pattern varies according to pathology, as discussed below. Several studies have demonstrated the utility of water as an oral contrast agent for detecting and staging gastric cancers (Dux et al. 1999; Rossi et al. 1997; Hori et al. 1992). Water is inexpensive, generally well tolerated, and allows for adequate stomach distension. In one study of 250 hydro-CT cases, Hori et al. (1992) detected 95% of

C. J. Zech et al. (eds.), *Multislice-CT of the Abdomen*, Medical Radiology. Diagnostic Imaging,
DOI: 10.1007/174_2011_428, © Springer-Verlag Berlin Heidelberg 2012

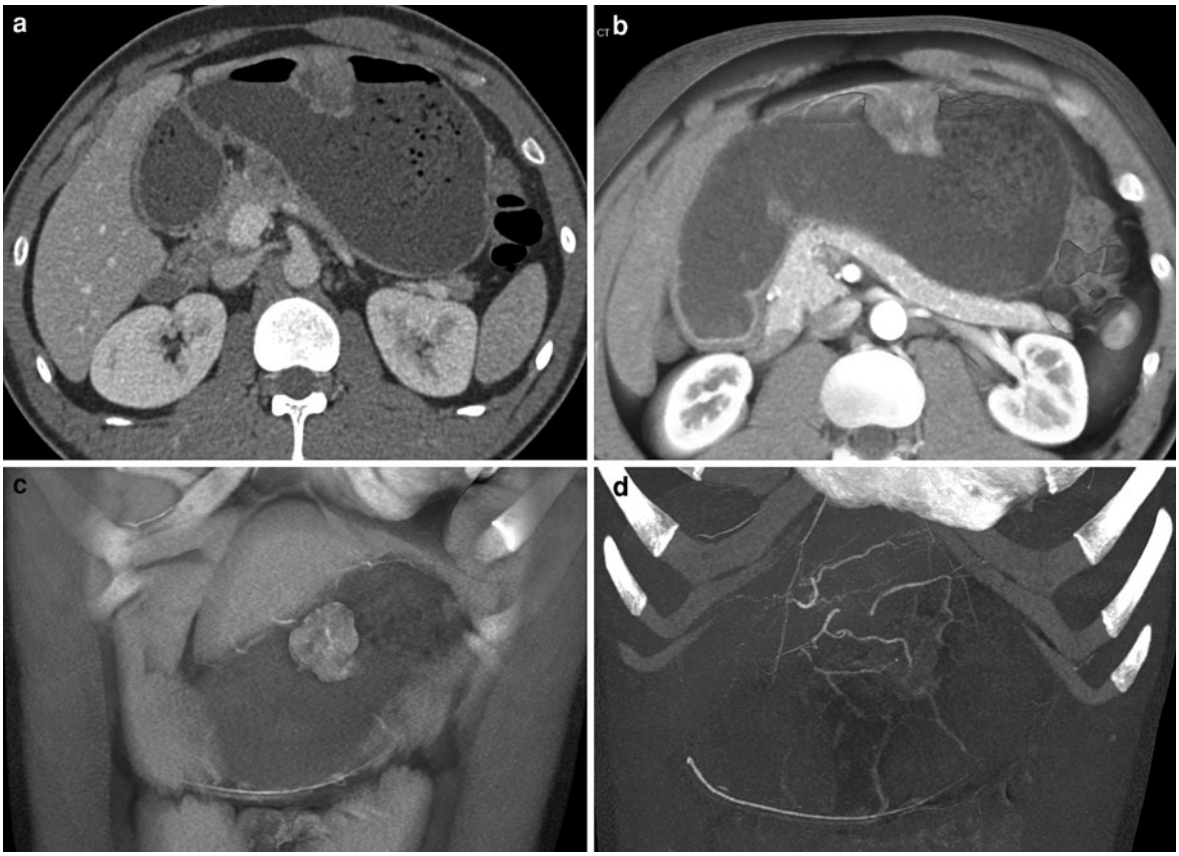

Fig. 1 38-year-old man with longstanding pernicious anemia complicated by iron deficiency anemia due to gastric adenocarcinoma. Axial section (**a**), axial volume rendering (**b**) and coronal volume rendering (**c**) from IV contrast-enhanced CT show a lobulated heterogeneously enhancing polypoid mass, with vasculature well defined on a coronal MIP rendering (**d**)

advanced carcinomas, 93% of elevated early tumors, and 18% of depressed early tumors. Although early adenocarcinomas are subtle, they are relatively easier to detect with so-called neutral oral contrast material, which allows better visualization of subtle alterations in contrast enhancement of tumors.

2 Gastric Adenocarcinoma

Adenocarcinoma is the most common gastric cancer, representing over 95% of all malignant tumors of the stomach (Fishman et al. 1996). Globally, it is the fourth most common cancer (900,000 new cases per year) and the second most common cause of death from cancer (700,000 deaths annually), with incidence and mortality rates approximately twice as high in men than women (Brenner et al. 2009). However, there is considerable geographic variation with greatest burden of disease in East Asia, Eastern Europe, and parts of Latin America (Brenner et al. 2009). Most patients are between 50 and 70 years of age at time of diagnosis (Moore 1986). Risk factors include *Helicobacter pylori* infection, excess salt and nitrite consumption, smoking, pernicious anemia (Fig. 1), gastric polyps, and Ménétrier disease (Brenner et al. 2009; Ba-Ssalamah et al. 2003). Although the overall five year survival rate remains below 20%, early gastric cancers are curable with surgical resection (>90% five year survival), underscoring the importance of accurate radiographic imaging in early diagnosis and treatment (Ba-Ssalamah et al. 2003).

MSCT is employed for both detection and radiological staging of gastric adenocarcinomas, given its ability to accurately characterize the primary neoplasm, assess local spread of disease, and identify

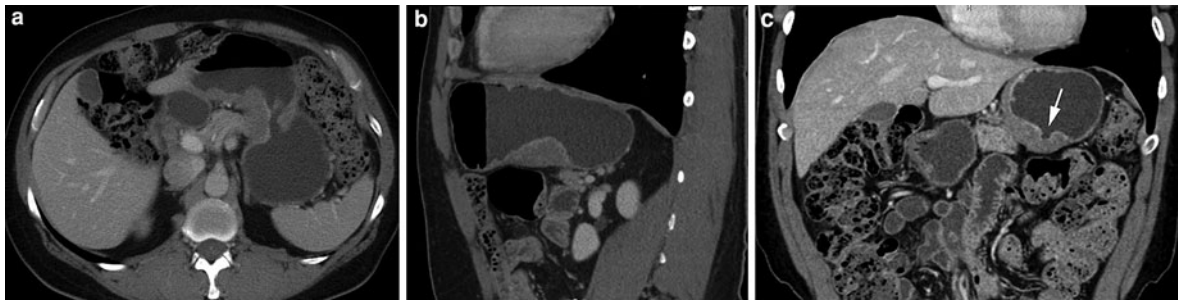

Fig. 2 70-year-old man with poorly differentiated adenocarcinoma with signet-ring features involving the gastric body. Axial image (**a**), sagittal MPR (**b**) and coronal MPR (**c**) from IV contrast-enhanced MDCT show low density tumor infiltration of the gastric body with ulceration (*arrow*)

nodal involvement and distant metastases. The classic presentation of weight loss, anorexia, dysphagia, anemia, and gastrointestinal bleeding typically manifests in advanced disease when the possibility of surgical resection is limited (Axon 2006).

Although 10% of cancers present diffusely throughout the stomach, most lesions are localized in the gastric antrum, body, fundus, or cardia (Ba-Ssalamah et al. 2003). The incidence of cancers in the distal portion has declined in recent years, while proximally located tumors seem to be on a constant rise (Brenner et al. 2009). Adenocarcinomas primarily originate from mucous cells and only 5–15% are of the signet-ring type associated with scirrhous infiltration of the distal stomach (Balthazar et al. 1980).

On dual-phase dynamic MSCT, gastric adenocarcinomas can appear hypervascular (Fig. 1) or hypovascular (Fig. 2), depending on the histology (Johnson et al. 2010; Lee et al. 2006). Most non-signet-ring lesions show moderate (73%) or strong (1%) enhancement patterns (Fig. 1). Hypovascularity is associated more commonly with mucinous histology (Lee et al. 2006). Early adenocarcinomas may present as a hyperattenuating polypoid mass with an intact submucosa, a hyperenhancing thickened mucosa, or a mucosal defect (Johnson et al. 2010). The inner mucosal layer of the tumor enhances in the late arterial phase, whereas the outer margin will peak in enhancement during the delayed contrast-enhanced acquisition (Chen et al. 2007).

CT is currently the staging modality of choice for adenocarcinoma (Chen et al. 2007; Horton and Fishman 2003; Kim et al. 2005; Kumano et al. 2005). When using water as an oral contrast agent, gastric tumors demonstrate focal thickening (≥6 mm) or enhancement of the gastric wall. Early gastric cancers are limited to the mucosa or submucosa (≤T1), regardless of nodal involvement. In a T1 lesion, the thickened inner surface of the gastric wall enhances with contrast and the low-attenuation submucosal layer is preserved. Invasion of the muscularis propria and subserosa constitutes T2 disease. A T2 lesion shows focal or diffuse thickening of the gastric wall (Fig. 3) with disruption of the low-attenuation strip, but a smooth outer wall border and a clear fat plane surrounding the lesion are still present. Tumors penetrating the serosa (T3) may have a nodular or irregularly thickened outer gastric wall and/or perigastric fat infiltration. T4 lesions obliterate the fat plane between the tumor and adjacent organs or extend directly into a neighboring structure.

Multiplanar (MPR) (Figs. 1, 2, 3) and 3D reconstruction techniques provide valuable information for characterizing gastric adenocarcinomas and preoperative staging (Johnson et al. 2010; Chen et al. 2007). Chen et al. (2007) demonstrated substantial improvement in assessing tumor invasion of the gastric wall (T stage) with MPR images (89% accuracy) compared with axial images alone (73% accuracy). They also achieved lymph node staging accuracies of 78% and 71% with MSCT MPR and axial imaging, respectively. Volumetric CT has particularly increased the detection of early adenocarcinomas (T1 stage). In a study of 44 patients evaluated with 64-MSCT, Yang et al. (2007) detected 90% of early tumors and 100% of advanced disease (95% accuracy overall). Virtual gastroscopy is the creation of three-dimensional volume rendered images, which simulate endoscopic viewing. Studies have shown that this technique increases sensitivity for detecting early gastric cancer and improves sensitivity for identifying

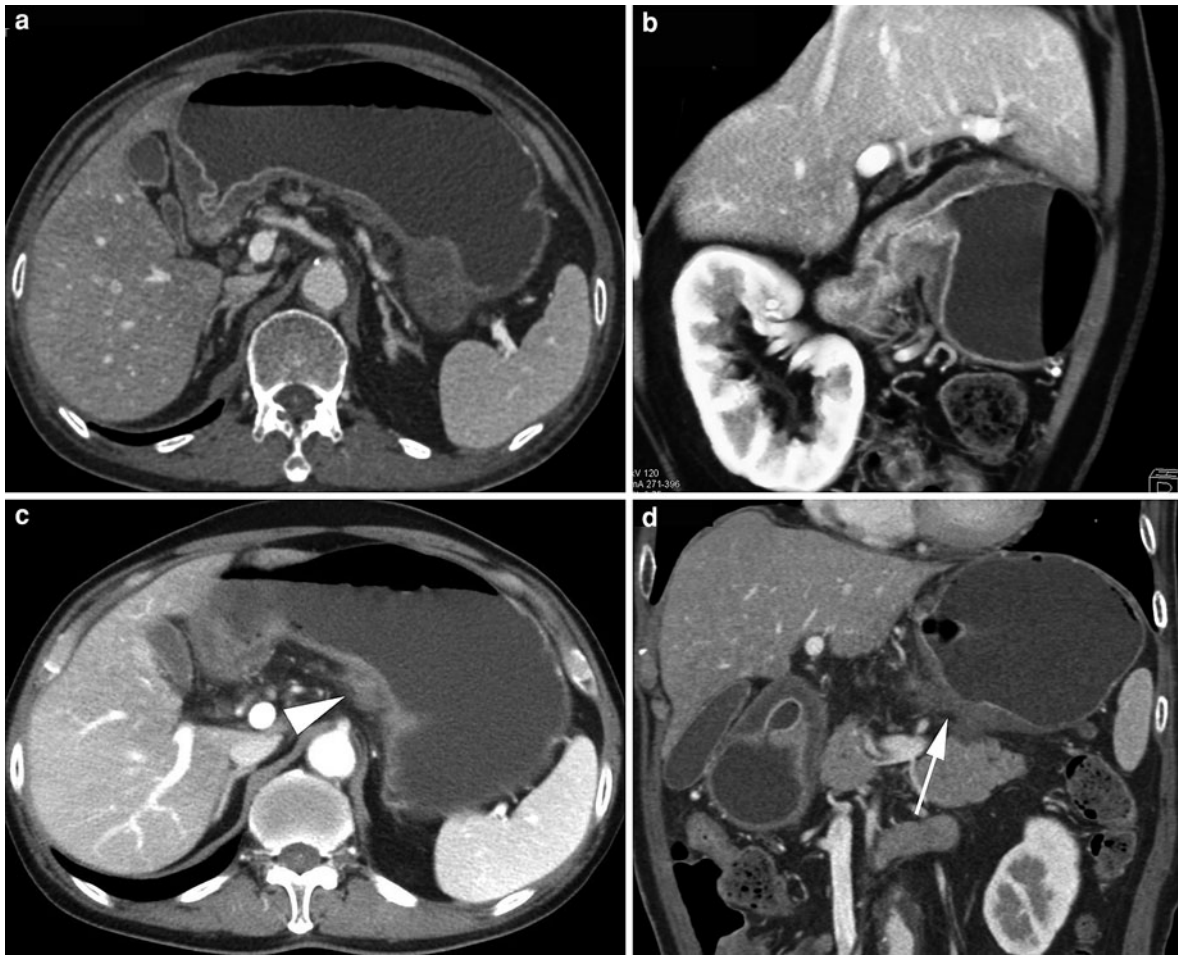

Fig. 3 65-year-old man with cancer in the gastric cardia and in the prepyloric region. Gastrectomy disclosed moderately differentiated adenocarcinoma invading the muscularis, and 1 positive node. Axial section (**a**), and sagittal volume rendering (**b**) from IV contrast-enhanced MDCT show heterogeneous enhancement reflecting tumor infiltration of the distal stomach wall. Axial section (**c**) and coronal MPR (**d**) demonstrate the wall thickening of the proximal lesser curvature (*arrow*), with enlarged gastrohepatic ligament node (*arrowhead*)

malignant features of ulcers, when compared to interpretation of 2D axial sections or multiplanar reconstructions (Kim et al. 2007; Chen et al. 2008).

3 Gastric Lymphoma

Gastrointestinal lymphoma occurs most frequently in the stomach, with non-Hodgkin's lymphoma of B-cell origin being the most common subtype (Gossios et al. 2000). However, primary gastric lymphoma accounts for only 1–5% of gastric malignancies (Gossios et al. 2000). Mucosa associated lymphoid tissue (MALT) lymphoma is a distinct type of extranodal B-cell lymphoma associated with *Helicobacter pylori* infection and chronic gastritis (Horton and Fishman 2003). MALT lymphoma typically has an indolent course and an overall five year survival rate of 50–60% (Ba-Ssalamah et al. 2003). Cases of MALT lymphoma progressing to high-grade large B-cell lymphoma have been reported in the literature (Chan et al. 1990).

Gastric lymphoma affects men more frequently than women and the median age at the time of diagnosis is 55 years (Gossios et al. 2000). Patients may present with epigastric pain, bleeding, early satiety, or fatigue. An endoscopic biopsy is required for definitive diagnosis. Treatment primarily involves eradication of *H. pylori* infection and surgical resection of

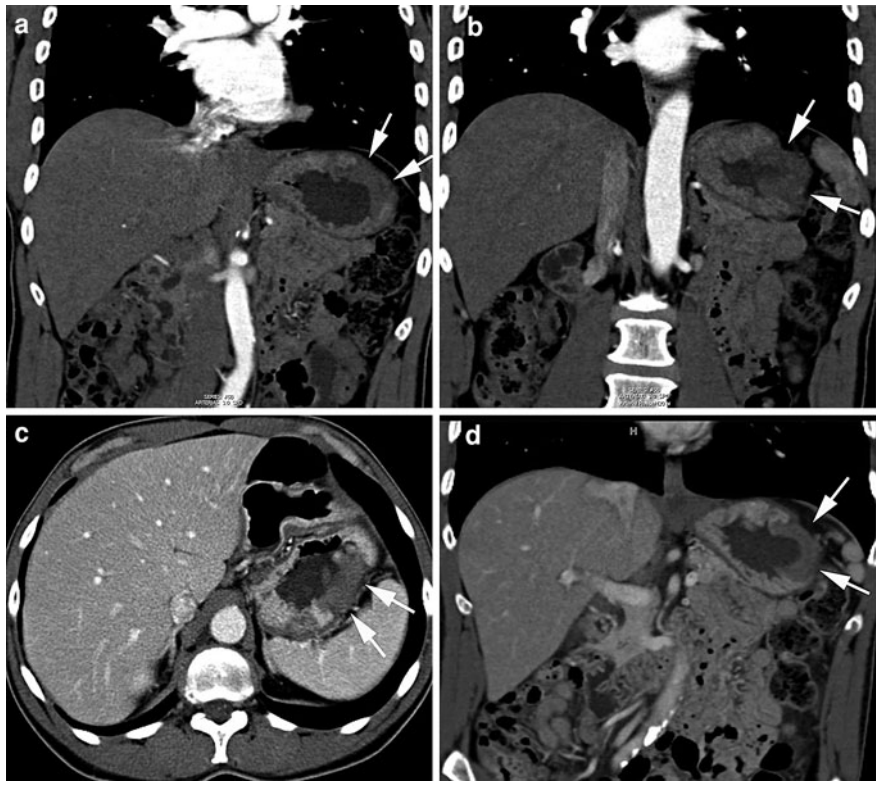

Fig. 4 60-year-old man with diffuse B cell lymphoma. Arterial phase coronal MPRs (**a**, **b**), axial venous phase image (**c**) and coronal venous phase MPR (**d**) show a segment of gastric wall with differential decreased enhancement (*arrow*), consistent with lymphomatous infiltration

localized disease (Gossios et al. 2000). Radiation and chemotherapy are used in treating advanced lymphomas (Levine et al. 1997).

Gastric lymphoma is well characterized on MSCT with five radiologic classifications: infiltrative (Fig. 4), ulcerative, polypoid, nodular, or combined (Ba-Ssalamah et al. 2003; Horton and Fishman 2003; Gossios et al. 2000; Park et al. 2002). Lesions may appear infiltrative with focal or diffuse enlargement of gastric folds with or without luminal narrowing, including a linitis plastica appearance. However, this rarely results in gastric outlet obstruction. Ulcerative lymphoma can present as shallow or deep lesions and may have surrounding thickened, irregular folds. Polypoid lymphoma is characterized by an intraluminal mass with or without ulceration, which may mimic polypoid carcinoma. The nodular form appears as multiple, discrete, submucosal lesions of varying sizes. Early gastric lymphoma is on average 3.5 cm in diameter and limited to the mucosa or submucosa, while more advanced lesions have a mean diameter of 10 cm (Ba-Ssalamah et al. 2003; Sato et al. 1986).

The differential diagnosis should include adenocarcinoma, gastritis, Crohn's disease, and peptic ulcer disease. Features favoring lymphoma over adenocarcinoma are diffuse lesions in the stomach, intact perigastric fat plane, enlarged lymph nodes on either side of the mesenteric vessels (sandwich sign), and extension of nodal involvement below the renal hila (Ba-Ssalamah et al. 2003; Park et al. 1999).

4 Gastrointestinal Stromal Tumor

Gastrointestinal stromal tumors (GISTs) are a heterogeneous group of mesenchymal neoplasms that typically originate from the muscularis propria of the gastrointestinal (GI) tract (Ulusan et al. 2008). The most frequent site of occurrence is the stomach (60–70% of cases), followed by the small bowel (30%) (Horton et al. 2004). They are pathologically characterized as benign, borderline, or with low- or high-malignant potential. Although most GISTs are benign (70–80%), the risk of malignancy is heightened with increasing size, extragastric location (i.e. small bowel), and spread into adjacent organs

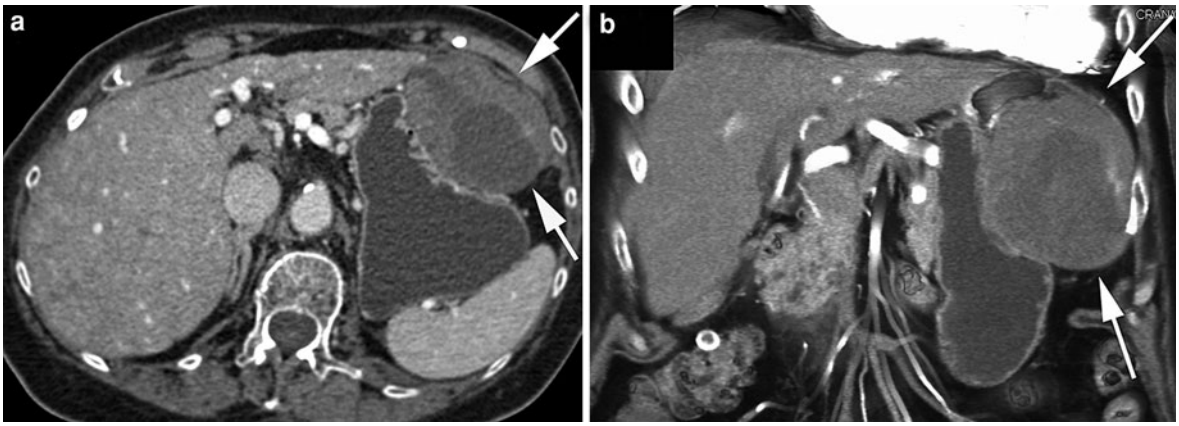

Fig. 5 83-year-old woman with gastrointestinal stromal. Axial section (**a**) and coronal volume rendering (**b**) from IV contrast-enhanced CT show an 8.5 cm exophytic, necrotic mass arising from the gastric fundus. Pathology revealed an uncertain malignant potential, with <5/50 HPF mitotic figures

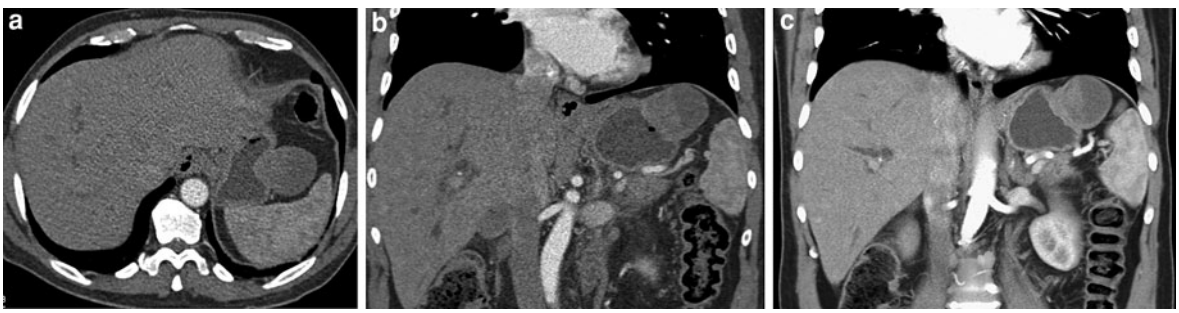

Fig. 6 63-year-old man with gastrointestinal stromal tumor and pancreatic adenocarcinoma (not shown). Axial section (**a**), coronal MPR (**b**) and coronal volume rendering (**c**) show a 5 cm exophytic heterogeneously enhancing mass arising from the gastric fundus. Pathology revealed extensive hemorrhage and degenerative necrosis and mitotic rate of <5/50 HPF, consistent with an intermediate risk of malignancy

(Horton et al. 2004; Burkill et al. 2003). While most are found in the gastric body, lesions located in the cardia or fundus are prone to have a more aggressive histology (Johnson et al. 2010). Metastatic disease usually involves liver or peritoneum, as opposed to lymph nodes (Davis et al. 2000; Sandrasegaran et al. 2005).

Patients are typically between 50 and 60 years of age at time of diagnosis, but familial tumors may occur in younger individuals (Horton et al. 2004). The clinical presentation can include GI bleeding, anemia, abdominal pain, dyspepsia, or a palpable abdominal mass; larger tumors are more likely to be symptomatic (Nishida and Hirota 2000).

MSCT is critical in diagnosis, staging, and post-treatment follow-up of gastric GISTs. It typically appears as a well-demarcated, heterogeneously enhancing, exophytic mass (Figs. 5 and 6) (Johnson et al. 2010; Sandrasegaran et al. 2005). The lesions sometimes grow into the gastric lumen and appear as an intraluminal mass. Small lesions (usually <3 cm) show intense, homogenous enhancement with administration of IV contrast (Nishida et al. 2003). Gastric GISTs commonly extend into the gastrohepatic ligament, gastrosplenic ligament, and lesser sac (Horton et al. 2004). In a study of 271 patients, Nishida et al. (2003) found that hemorrhage and central necrosis on CT were frequently observed in larger masses, with the latter being most common in lesions greater than 6 cm in diameter. Central gas, mural calcifications, and ascites are uncommon findings (Horton et al. 2004).

CT features favoring malignancy are large ulcerations, calcifications, and size greater than 5 cm (Ulusan et al. 2008; Ba-Ssalamah et al. 2003). Benign lesions usually have smooth borders and are limited to the submucosa with a preserved mucosal lining (Ba-Ssalamah et al. 2003).

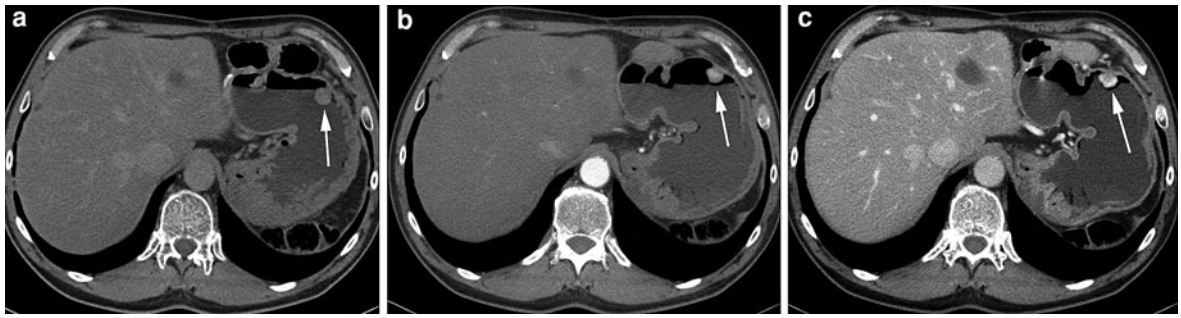

Fig. 7 63-year-old man with metastatic renal cell carcinoma. Axial precontrast (**a**), arterial (**b**) and venous (**c**) phase images from IV contrast-enhanced MDCT show a hyperenhancing polypoid intraluminal mass arising from the gastric fundus. (Image **b** reproduced with permission from Johnson et al. 2010)

5 Metastases

Gastric metastases from solid malignant tumors are rare. In a study of 6380 autopsy cases with known primary cancers, Oda et al. (2001) demonstrated gastric metastases in only 5% of cases. Melanoma was the most frequent tumor to metastasize to the stomach (29.6% of patients), followed by breast (11.6%), esophagus (11.5%), and lung (6.8%) (Oda et al. 2001). Clinical symptoms that usually prompt an upper endoscopy are anemia, bleeding, dyspepsia, and epigastric pain (De Palma et al. 2006).

On fluoroscopy studies, metastases to the stomach classically exhibit multiple lesions and a "bull's-eye-sign" that represents a submucosal tumor with a central depression (Pomerantz and Margolin 1962). More than 60% of gastric metastases are solitary masses, and most are located in the middle or upper third of the stomach (Oda et al. 2001; De Palma et al. 2006). The majority of lesions are hypovascular on CT. The differential diagnosis for hypervascular metastases (Fig. 7) should include renal cell carcinoma and melanoma (Johnson et al. 2010). Direct invasion into the stomach can be seen from tumors originating in adjacent organs (Ba-Ssalamah et al. 2003).

6 Rare Tumors

Uncommon lesions arising in the stomach, which should be included in the differential diagnosis of small hyperenhancing masses, are carcinoid tumors and glomus tumors (Fig. 8). Carcinoids of the stomach are rare neuroendocrine lesions (0.3% prevalence)

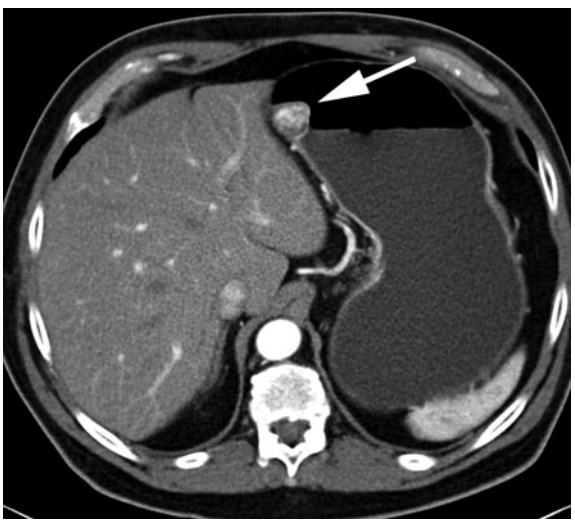

Fig. 8 76-year-old man with glomus tumor incidentally discovered during CT for renal calculus. Axial image from IV contrast-enhanced CT shows hypervascular submucosal mass (*arrow*) in the gastric fundus. (Reproduced with permission from Johnson et al. 2010)

that originate from histamine-containing enterochromaffin-like (ECL) cells of the embryonic foregut (Rindi et al. 1993). Representing 1.8% of all gastric cancers and 7% of all carcinoids, this lesion is usually discovered incidentally during endoscopy or CT imaging (Pinchot et al. 2008) and are associated with hypergastrinemia. Unlike other locations in the gastrointestinal tract, three clinicopathologic variants of gastric carcinoid are recognized (Rindi et al. 1993). Carcinoids can be single or multiple and vary in size and malignant potential, depending on the subtype (Johnson et al. 2010; Oda et al. 2001; Pomerantz and Margolin 1962).

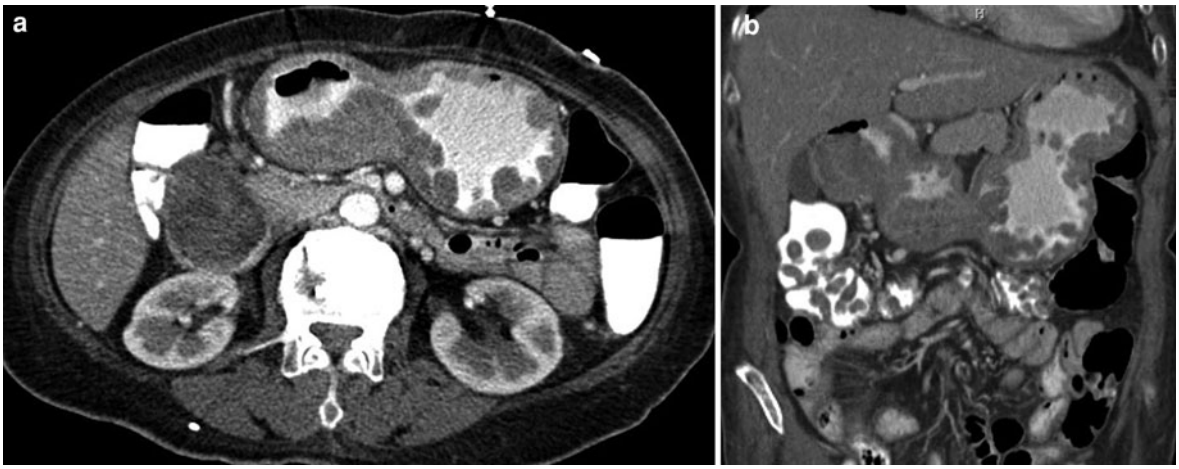

Fig. 9 66-year-old woman with Cronkhite Canada syndrome. Axial image (**a**) and coronal MPR (**b**) show numerous inflammatory polyps throughout the stomach and colon

Glomus tumors (Fig. 8) arise from proliferations of perivascular glomus bodies, which are normal arteriovenous shunts controlling variations in skin temperature (Cha et al. 2000). This is a rare, submucosal neoplasm that may arise in the stomach (Johnson et al. 2010; Kim et al. 2001). The mean age of diagnosis is approximately 50 years, with significant female predominance (>70% in women) (Lee et al. 2006; Miettinen et al. 2002). Patients are generally asymptomatic, but around one-third of cases present with acute (potentially life-threatening) or chronic GI bleeding (Lee et al. 2006; Miettinen et al. 2002). Although most lesions are benign, tumors with metastatic potential are described in the literature (Lee et al. 2006; Miettinen et al. 2002).

7 Gastric Polyps

Approximately 1–4% of patients who undergo gastric endoscopy have polyps, usually with distinct clinical characteristics that allow for categorization in major subclasses (Carmack et al. 2009a). Although most are discovered incidentally, lesions may present with hemorrhage, anemia, GERD, or dyspepsia (Carmack et al. 2009b). The median age of diagnosis is about 60 years, with a slight predilection for females (Carmack et al. 2009b). Larger polyps with malignant potential should be excised, but most are managed conservatively and may even regress over time (Johnson et al. 2010; Park do and Lauwers 2008).

Fundic-gland polyps, primarily associated with PPI therapy, are now the most common type in the US, accounting for over 70% of lesions (Carmack et al. 2009a). They can also arise sporadically or in patients with familial polyposis syndromes (Bianchi et al. 2008). Histologically, they are characterized as cystically dilated oxyntic glands lined by fundic epithelial cells. They are usually multiple, sessile masses measuring <1 cm in diameter on CT (Johnson et al. 2010).

Arising in the setting of gastritis associated with *Helicobacter pylori* infection, hyperplastic (inflammatory) polyps are not true neoplasms and represent about 15% of lesions (Carmack et al. 2009a). The proportion of hyperplastic lesions is much higher (70%) in non-industrialized regions due to higher prevalence of *H. pylori* infection (Carmack et al.2009). The risk of neoplastic transformation within hyperplastic polyps is greater with increasing age, size >2 cm, and location in the lower third of the stomach; this occurs in up to 3% of lesions (Park do and Lauwers 2008; Hizawa et al. 1995; Dean et al. 1998). On MSCT (Fig. 9), they appear as smooth, sessile, round, or oval masses that may enhance with administration of IV contrast (Ba-Ssalamah et al. 2003; Johnson et al. 2010). Hyperplastic polyps of varying sizes (5–10 mm on average) are usually multiple and clustered in the body or fundus (Ba-Ssalamah et al. 2003; Johnson et al. 2010).

Accounting for <1% of gastric polyps in the US, adenomatous lesions occur sporadically or in association with familial adenomatous polyposis (FAP)

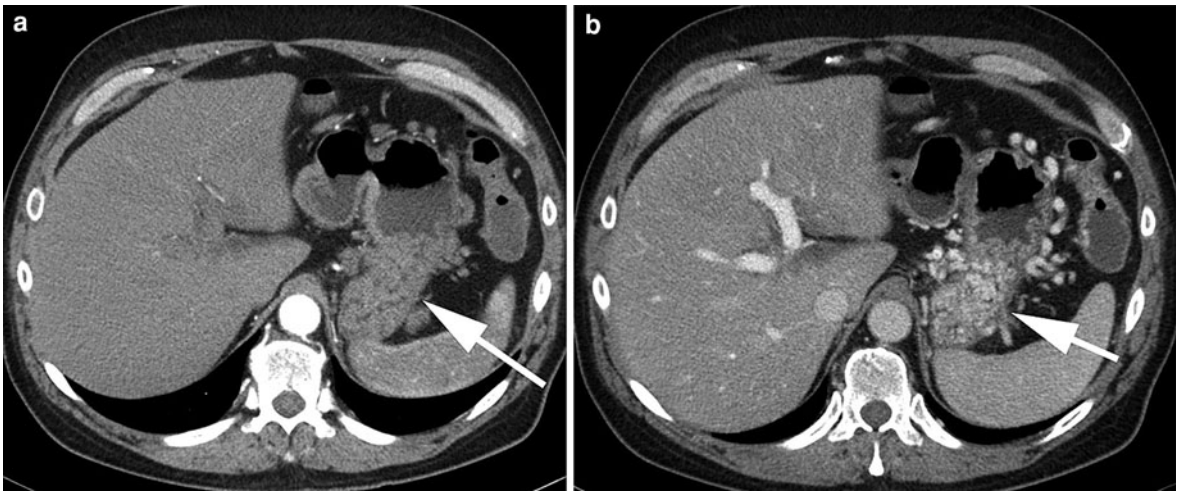

Fig. 10 62-year-old man with gastric varices. Arterial phase (**a**) and venous phase (**b**) axial images demonstrate how gastric varices (*arrow*) enhance during the venous acquisition, and appear as soft tissue masses during the arterial phase

syndrome, atrophic gastritis, and intestinal metaplasia (Johnson et al. 2010; Carmack et al. 2009b). Adenomatous polyps are larger than the hyperplastic type, and usually appear on MSCT as pedunculated, solitary masses adjacent to the antrum. Larger lesions containing carcinomatous foci (40% of cases) are sessile or pedunculated, with a more lobulated contour (Ba-Ssalamah et al. 2003).

8 Gastric Varices

Gastric varices are a prominent cause of GI bleeding, occurring in up to one-third of patients with portal hypertension, and have a poorer prognosis than esophageal varices (Zhu et al. 2010). An elevated risk of hemorrhage is associated with lesions measuring >5 mm, fundal location, and advanced Child-Pugh stage (Zhu et al. 2010). Although gastric and esophageal varices tend to present simultaneously in cirrhosis, isolated varices in the stomach may result from splenic vein thrombosis or occlusion in cases of pancreatitis and pancreatic cancer (Horton and Fishman 2003).

MSCT is an increasingly accepted non-invasive alternative to esophagogastroduodenoscopy (EGD) for detecting and characterizing gastric varices. They appear as polypoid masses in the arterial phase (Fig. 10), primarily along the body and fundus of the stomach (Horton and Fishman 2003; Zhu et al. 2010) and sometimes are mistaken for nodes or masses. On the portal venous acquisition, discrete, enhancing tubular lesions abutting the luminal edge of the gastric wall or protruding into the luminal space are seen (Fig. 10) (Johnson et al. 2010; Zhu et al. 2010). Collateral vasculature is observed along the gastrohepatic ligament and left gastric vein (Horton and Fishman 2003). In a study 127 cirrhotic patients, the accuracy of MSCT in identifying gastric varices exceeded 90%, and its performance was comparable to EGD (Zhu et al. 2010).

CT angiography with 3D reconstruction delineates gastric varices and perigastric vessels with great precision. In a study of 33 patients by Chen et al. (2010), fundic varices were detected in 97% of cases and results were in close agreement with conventional angiography. Matsumoto et al. (2001) were able to detect 100% of gastric varices (30 patients total) using 3D CT, including four cases where posterior or short gastric veins were only seen on CT imaging. These studies elucidate the utility of this technique in evaluating complex gastric vasculature in diseased conditions, as well as anatomic variants.

9 Gastritis

Gastritis is an inflammation of the lining of the stomach with several well-known risk factors, including alcohol, *Helicobacter pylori* infection, aspirin, non-steroidal anti-inflammatory drugs, and

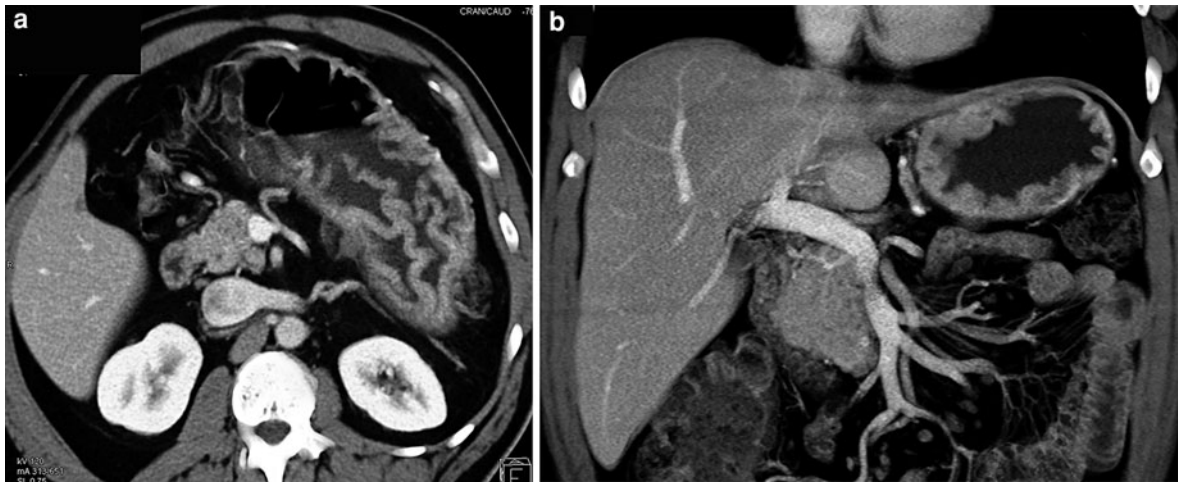

Fig. 11 45-year-old man with gastrinomas of the pancreas and duodenum. Axial (**a**) and coronal (**b**) 3D volume renderings show thickened enhancing gastric folds consistent with Zollinger Ellison syndrome

smoking. This condition is quite common and usually presents with abdominal pain, nausea, vomiting, and loss of appetite. *Helicobacter* gastritis may result in gastric carcinoma or lymphoma, especially in those with severe gastric atrophy, corpus-predominant gastritis, and intestinal metaplasia (Uemura et al. 2001; Stolte 1992).

The most common CT finding is a thickened gastric wall, which may demonstrate hypodense regions of submucosal edema and inflammation (Horton and Fishman 2003). Arterial phase enhancement due to hyperemia appears as layering of the gastric wall (Fig. 11) (Horton and Fishman 2003). Lesions are most commonly found in the antrum as focal or segmental thickening. Polypoid and lobulated gastric folds can sometimes mimic malignant conditions and may warrant biopsy (Urban et al. 1991). The utility of 3D reconstruction techniques, including CT gastric virtual endoscopy, has been demonstrated in the literature and may play a key role in distinguishing benign and malignant conditions (Horton and Fishman 2003; Inamoto et al. 2005).

Emphysematous gastritis is a rare, life-threatening condition primarily resulting from gas-producing bacteria (eg. *Escherichia coli*) infecting the gastric wall (Horton and Fishman 2003). Key features on CT are thickening of the stomach and air within the gastric wall. The differential diagnosis for air in the stomach wall (Fig. 12) includes gastric emphysema, caustic ingestion, and gastric infarction.

10 Peptic Ulcer Disease

Peptic ulcer disease occurs in the setting of elevated acid secretion, which causes ulceration of the esophagus, duodenum, or stomach. Prominent, potentially lethal, complications of lesions in the stomach are perforation, penetration of adjacent tissue or the lesser sac, hemorrhage, and obstruction. Risk factors include *Helicobacter pylori* infection and usage of non-steroidal anti-inflammatory drugs (Chan and Leung 2002).

Most gastric ulcers affecting only the superficial layers are difficult to visualize on CT, but deeper lesions with associated complications can be detected (Fig. 13) (Horton and Fishman 2003). Gastric ulcers are typically located along the lesser curvature or posterior wall of the antrum or body (Ba-Ssalamah et al. 2003). Perforation manifests as inflammatory changes, extraluminal air, or pneumoperitoneum. Inflammation of adjacent tissues resulting from penetration is also observed in CT imaging.

11 Conclusion

Diseases of the stomach are common worldwide and require early, accurate characterization for proper clinical management. Recent advances in MSCT, especially 3D reconstruction techniques, allow detailed

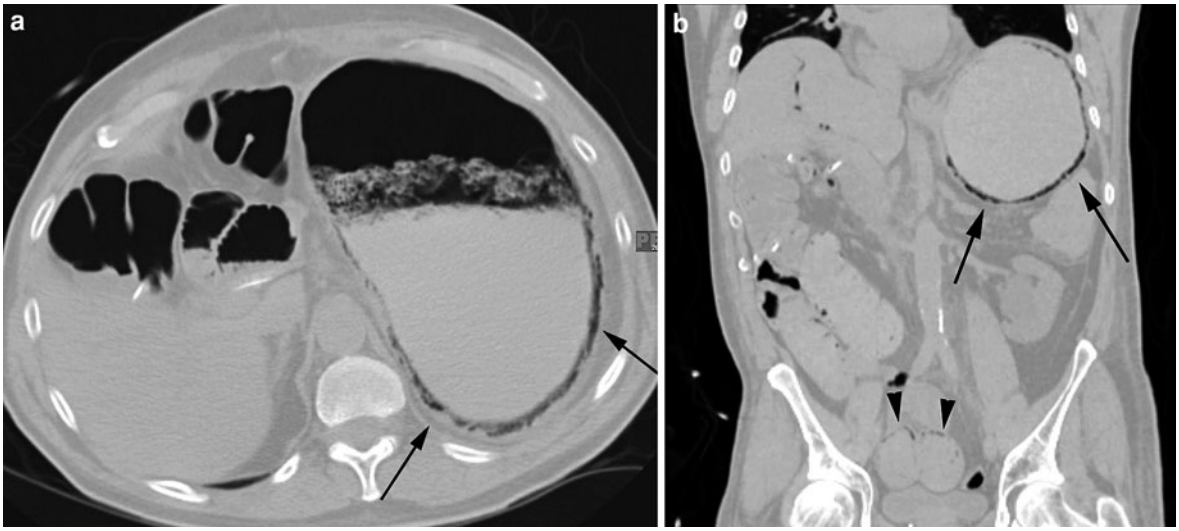

Fig. 12 68-year-old man 7 days status post Whipple procedure with abdominal pain. Axial image (**a**) and coronal MPR (**b**) show gastric (*arrow*) and small bowel (*arrowheads*) pneumatosis due to twisted loop of small bowel. Following surgical untwisting, the patient had an uneventful recovery

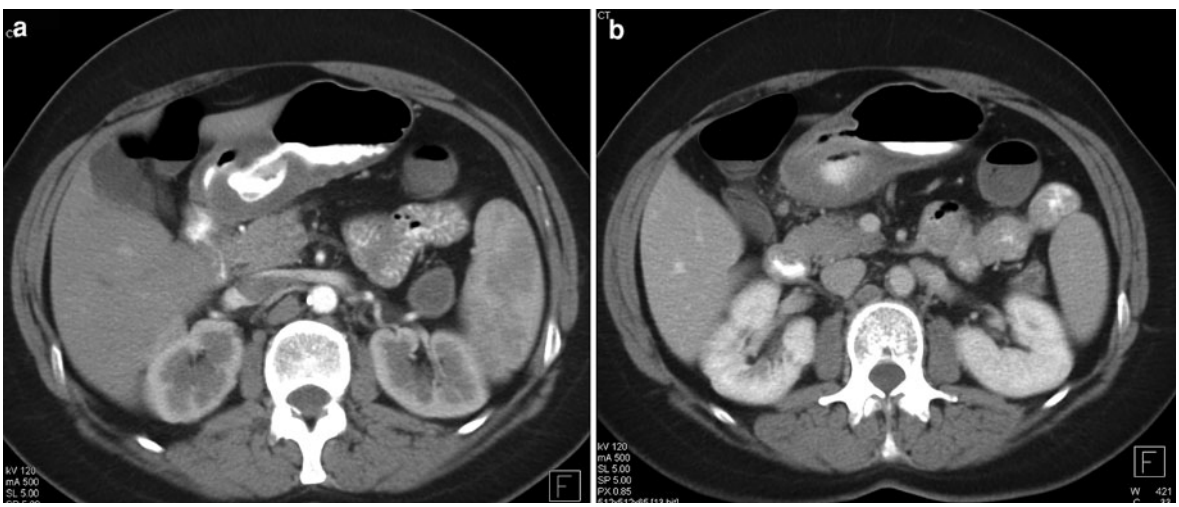

Fig. 13 54-year-old woman with large ulcer in the gastric antrum. Axial images from arterial phase (**a**) and venous phase (**b**) IV contrast-enhanced CT show wall thickening with a large ulcer crater involving the posterior wall of the antrum. Appearance was concerning for malignancy; however, biopsy disclosed acutely inflamed granulation tissue consistent with ulcer bed and chemical gastritis

visualization of gastric conditions and extra-luminal manifestations of disease. It is essential that the radiologist select appropriate oral and IV contrast agents, as well as optimize scanning protocols to delineate gastric pathology and vascular architecture. The radiologist should also be familiar with both common and uncommon presentations of gastric lesions on CT to maximize the utility of this robust technology.

References

Axon A (2006) Symptoms and diagnosis of gastric cancer at early curable stage. Best Pract Res Clin Gastroenterol 20:697–708

Balthazar EJ, Rosenberg H, Davidian MM (1980) Scirrhous carcinoma of the pyloric channel and distal antrum. Am J Roentgenol 134:669–673

Ba-Ssalamah A, Prokop M, Uffmann M et al (2003) Dedicated multidetector CT of the stomach: spectrum of diseases. Radiographics 23:625–644

Bianchi LK, Burke CA, Bennett AE et al (2008) Fundic gland polyp dysplasia is common in familial adenomatous polyposis. Clin Gastroenterol Hepatol 6:180–185

Brenner H, Rothenbacher D, Arndt V (2009) Epidemiology of stomach cancer. Methods Mol Biol 472:467–477

Burkill GJ, Badran M, Al-Muderis O et al (2003) Malignant gastrointestinal stromal tumor: distribution, imaging features, and pattern of metastatic spread. Radiology 226: 527–532

Carmack SW, Genta RM, Graham DY et al (2009a) Management of gastric polyps: a pathology-based guide for gastroenterologists. Nat Rev Gastroenterol Hepatol 6: 331–341

Carmack SW, Genta RM, Schuler CM et al (2009b) The current spectrum of gastric polyps: a 1-year national study of over 120, 000 patients. Am J Gastroenterol 104:1524–1532

Cha SH, Cho SB, Kim YW et al (2000) Helical CT appearance of glomus tumor of the stomach. Eur Radiol 10:671–673

Chan FK, Leung WK (2002) Peptic-ulcer disease. Lancet 360:933–941

Chan JK, Ng CS, Isaacson PG (1990) Relationship between high-grade lymphoma and low-grade B-cell mucosa-associated lymphoid tissue lymphoma (MALToma) of the stomach. Am J Pathol 136:1153–1164

Chen CY, Hsu JS, Wu DC et al (2007) Gastric cancer: preoperative local staging with 3D multi-detector row CT–correlation with surgical and histopathologic results. Radiology 242:472–482

Chen CY, Wu DC, Kuo YT et al (2008) MSCT for differentiation of category T1 and T2 malignant lesions from benign gastric ulcers. Am J Roentgenol 190:1505–1511

Chen TW, Yang ZG, Li X, et al. (2010) Evaluation of entire gastric fundic and esophageal varices secondary to posthepatitic cirrhosis: portal venography using 64-row MSCT. Abdom Imaging 35:1–7.

Davis GB, Blanchard DK, Hatch GF 3rd et al (2000) Tumors of the stomach. World J Surg 24:412–420

De Palma GD, Masone S, Rega M et al (2006) Metastatic tumors to the stomach: clinical and endoscopic features. World J Gastroenterol 12:7326–7328

Dean PG, Davis PM, Nascimento AG et al (1998) Hyperplastic gastric polyp causing progressive gastric outlet obstruction. Mayo Clin Proc 73:964–967

Dux M, Richter GM, Hansmann J et al (1999) Helical hydro-CT for diagnosis and staging of gastric carcinoma. J Comput Assist Tomogr 23:913–922

Fishman EK, Urban BA, Hruban RH (1996) CT of the stomach: spectrum of disease. Radiographics 16:1035–1054

Gossios K, Katsimbri P, Tsianos E (2000) CT features of gastric lymphoma. Eur Radiol 10:425–430

Hizawa K, Fuchigami T, Iida M et al (1995) Possible neoplastic transformation within gastric hyperplastic polyp. Application of endoscopic polypectomy. Surg Endosc 9:714–718

Hori S, Tsuda K, Murayama S et al (1992) CT of gastric carcinoma: preliminary results with a new scanning technique. Radiographics 12:257–268

Horton KM, Fishman EK (2003) Current role of CT in imaging of the stomach. Radiographics 23:75–87

Horton KM, Juluru K, Montogomery E et al (2004) Computed tomography imaging of gastrointestinal stromal tumors with pathology correlation. J Comput Assist Tomogr 28:811–817

Inamoto K, Kouzai K, Ueeda T et al (2005) CT virtual endoscopy of the stomach: comparison study with gastric fiberscopy. Abdom Imaging 30:473–479

Johnson PT, Horton KM, Fishman EK (2010) Hypervascular gastric masses: CT findings and clinical correlates. Am J Roentgenol 195:W415–420

Kim JK, Won JH, Cho YK et al (2001) Glomus tumor of the stomach: CT findings. Abdom Imaging 26:303–305

Kim HJ, Kim AY, Oh ST et al (2005) Gastric cancer staging at multi-detector row CT gastrography: comparison of transverse and volumetric CT scanning. Radiology 236:879–885

Kim JH, Eun HW, Choi JH et al (2007) Diagnostic performance of virtual gastroscopy using MSCT in early gastric cancer compared with 2D axial CT: focusing on interobserver variation. Am J Roentgenol 189:299–305

Kumano S, Murakami T, Kim T et al (2005) T staging of gastric cancer: role of multi-detector row CT. Radiology 237:961–966

Lee HW, Lee JJ, Yang DH et al (2006) A clinicopathologic study of glomus tumor of the stomach. J Clin Gastroenterol 40:717–720

Lee JH, Park MS, Kim KW, Yu JS, Kim MJ, Yang SW, Lee YC (2006) Advanced gastric carcinoma with signet ring cell carcinoma versus non-signet ring cell carcinoma: differentiation with multidetector CT. J Comput Assist Tomogr 30(6):880–884

Levine MS, Rubesin SE, Pantongrag-Brown L et al (1997) Non-Hodgkin's lymphoma of the gastrointestinal tract: radiographic findings. Am J Roentgenol 168:165–172

Matsumoto A, Kitamoto M, Imamura M et al (2001) Three-dimensional portography using multislice helical CT is clinically useful for management of gastric fundic varices. Am J Roentgenol 176:899–905

Miettinen M, Paal E, Lasota J et al (2002) Gastrointestinal glomus tumors: a clinicopathologic, immunohistochemical, and molecular genetic study of 32 cases. Am J Surg Pathol 26:301–311

Moore JR (1986) Gastric carcinoma: 30-year review. Can J Surg 29:25–28

Nishida T, Hirota S (2000) Biological and clinical review of stromal tumors in the gastrointestinal tract. Histol Histopathol 15:1293–1301

Nishida T, Kumano S, Sugiura T et al (2003) Multidetector CT of high-risk patients with occult gastrointestinal stromal tumors. Am J Roentgenol 180:185–189

Oda Kondo H, Yamao T et al (2001) Metastatic tumors to the stomach: analysis of 54 patients diagnosed at endoscopy and 347 autopsy cases. Endoscopy 33:507–510

Park do Y, Lauwers GY (2008) Gastric polyps: classification and management. Arch Pathol Lab Med 132:633–640

Park SH, Han JK, Kim TK et al (1999) Unusual gastric tumors: radiologic-pathologic correlation. Radiographics 19:1435–1446

Park MS, Kim KW, Yu JS et al (2002) Radiographic findings of primary B-cell lymphoma of the stomach: low-grade versus high-grade malignancy in relation to the mucosa-associated lymphoid tissue concept. Am J Roentgenol 179:1297–1304

Pinchot SN, Holen K, Sippel RS et al (2008) Carcinoid tumors. Oncologist 13:1255–1269

Pomerantz H, Margolin HN (1962) Metastases to the gastrointestinal tract from malignant melanoma. Am J Roentgenol Radium Ther Nucl Med 88:712–717

Rindi G, Luinetti O, Cornaggia M et al (1993) Three subtypes of gastric argyrophil carcinoid and the gastric neuroendocrine carcinoma: a clinicopathologic study. Gastroenterology 104:994–1006

Rossi M, Broglia L, Maccioni F et al (1997) Hydro-CT in patients with gastric cancer: preoperative radiologic staging. Eur Radiol 7:659–664

Sandrasegaran K, Rajesh A, Rydberg J et al (2005) Gastrointestinal stromal tumors: clinical, radiologic, and pathologic features. Am J Roentgenol 184:803–811

Sato T, Sakai Y, Ishiguro S et al (1986) Radiologic manifestations of early gastric lymphoma. Am J Roentgenol 146: 513–517

Stolte M (1992) Helicobacter pylori gastritis and gastric MALT-lymphoma. Lancet 339:745–746

Uemura N, Okamoto S, Yamamoto S et al (2001) Helicobacter pylori infection and the development of gastric cancer. N Engl J Med 345:784–789

Ulusan S, Koc Z, Kayaselcuk F (2008) Gastrointestinal stromal tumours: CT findings. Br J Radiol 81:618–623

Urban BA, Fishman EK, Hruban RH (1991) Helicobacter pylori gastritis mimicking gastric carcinoma at CT evaluation. Radiology 179:689–691

Yang DM, Kim HC, Jin W et al (2007) 64 multidetector-row computed tomography for preoperative evaluation of gastric cancer: histological correlation. J Comput Assist Tomogr 31:98–103

Zhu K, Meng X, Pang P et al (2010) Gastric varices in patients with portal hypertension: evaluation with multidetector row CT. J Clin Gastroenterol 44:e108–115

Small Bowel

Franco Iafrate, Marco Rengo, Paola Lucchesi, Maria Ciolina, Paolo Baldassari, and Andrea Laghi

Contents

Abstract

Multidetector CT (MDCT), over the past decade, has become the primary imaging modality for evaluating gastrointestinal tract disorders, particularly in the small bowel. MDCT offers panoramic and high-resolution images, it is widespread available and the technique is robust, reproducible and accurate. Careful patient preparation is required, because of the need for bowel distension, achievable through the use of an enteral contrast agent (neutral or positive) delivered either orally (MDCT-enterography) or through a naso-jejunal tube (MDCT-enteroclysis). Scanning protocol is fast and thanks to new devices (automatic dose modulator systems) and/or new image reconstruction methods (iterative algorithms) able to deliver a very low amount of radiation, especially important when imaging young individuals. The most common clinical indication is represented by the evaluation of patients with Inflammatory Bowel Disease, both at the time of the diagnosis and in follow-up, where MDCT is able to provide an accurate balance of the disease: extent of the bowel involvement, assessment of disease activity and potential complications. The detection of small bowel tumours is another important indication where MDCT represents, in some cases, the only method to investigate small bowel loops and in any case the best method for staging neoplastic lesions. An additional reason to perform MDCT of the small bowel is the evaluation of malabsorption syndromes.

F. Iafrate · P. Lucchesi · M. Ciolina · P. Baldassari
Department of Radiological Sciences,
Oncology and Pathology, Sapienza-University of Rome,
Viale Regina Elena 324,
00161 Rome, Italy

M. Rengo · A. Laghi (✉)
Department of Radiological Sciences,
Oncology and Pathology, Sapienza-University of Rome,
Via Franco Faggiana 34,
04100 Latina, Italy
e-mail: andrea.laghi@uniroma1.it

C. J. Zech et al. (eds.), *Multislice-CT of the Abdomen*, Medical Radiology. Diagnostic Imaging,
DOI: 10.1007/174_2011_429, © Springer-Verlag Berlin Heidelberg 2012

1 Introduction

Cross-sectional imaging modalities (i.e., sonography, MDCT and MRI) have completely replaced conventional X-ray barium studies in the diagnosis and assessment of small bowel diseases. The reason is simple: any cross-sectional imaging method offers direct visualization of the bowel wall and does not suffer the limitations of superimposed bowel loops typical of projectional studies which might impair the diagnostic process. This is a major change dramatically affecting image interpretation: Radiologists are called to shift their attention from the analysis of mucosal profile and lumen calibre to direct evaluation of bowel wall thickness and parietal inflammatory changes. The outcome of this cultural radiological challenge is radically altering management of patients with suspected small bowel disease.

Among the different cross-sectional imaging tests, over the past decade, MDCT has become the primary imaging modality for evaluating gastrointestinal tract disorders, particularly in the small bowel. MDCT offers panoramic and high-resolution images, it is widespread available, scanning time is fast, and the technique is robust, reproducible and accurate.

In the subsequent paragraphs, the study technique, with emphasis on bowel distension and enteral contrast agents, as well as relevant clinical indications will be discussed, trying not to forget the existence of competitive techniques and discussing the respective role of each of these techniques in different clinical settings.

2 Study Protocol

2.1 Scanning Parameters, Optimization of Dose Exposure and Image Reconstruction

MDCT of the small bowel requires high spatial resolution, thus, it must be performed with scanners equipped with at least 16 or better 64 rows or over. The rationale is to have a wide anatomical coverage and fast scan times to image the entire abdomen and pelvis within a single breath-hold. The faster the scanner, the better the image quality because of freezing of motion and, in particular, peristaltic artefacts.

Imaging protocol includes the use of the thinnest detector collimation (0.6–1.0 mm) available on the scanner with a reconstruction interval of 1.0–1.5 mm. Thin collimation maximizes the quality of reformatted images, because it allows to acquire isotropic voxels, which is necessary to generate high quality multiplanar reformats. Coronal and sagittal reformatted images are particularly useful in the evaluation of fistulas or abscesses as well as complex structures as tumours or extraenteric abnormalities (Jaffe et al. 2007). Since the evaluation of mesenteric vessels is also extremely important, in this setting the use of maximum intensity projection (MIP) algorithm is particularly helpful.

Scanning parameters are of paramount importance to optimize dose exposure (McCollough et al. 2006). In fact, most of the patients undergoing MDCT of the small bowel are young, thus, the potential risk derived from radiation exposure is cumbersome (Brenner and Hall 2007). Although risk of radiation-induced cancer at low dose exposure has not been proven and the debate is still on going, radiological societies are convinced that radiation doses should be kept as low as reasonably achievable (ALARA principle) to maximize patient benefit and reduce potential harm. Several strategies can be applied to minimize radiation exposure. The most commonly used dose reduction technique is the automatic tube current modulation (ATCM) technique (Leng et al. 2010), adjusted according to regional body anatomy, to maintain a constant image quality regardless of patient size. Tube voltage is another fundamental parameter to be optimized because it has been demonstrated that by using lower kV values the radiation burden is reduced (Kalra et al. 2002). There is an exponential relationship between kilovolt and radiation dose; dose is reduced by the square of the tube voltage change, and image noise is approximately inversely proportional. A standard tube voltage of 120 kV can be used for patients with body mass index (BMI) higher than 25–100 kV for patients with a BMI lower than 25 (McCollough et al. 2009).

Recently, new methods to reduce dose exposure have been developed based on iterative reconstruction algorithm. This algorithm, differently from the current reconstruction method, the filtered back projections, has the potential to reduce image noise on low dose images preserving and enhancing image quality. This method can be modulated according to the percentage of desired dose reduction; as a drawback the higher

Table 1 Suggestions for injection flow rates of contrast medium, with different iodine concentrations, according to TBW

Iodine concentration (mgI/ml)	TBW	<55	56–65	66–85	86–95	>95
	IDR (gI/sec)	1.2	1.4	1.6	1.8	2.0
300	FR (ml/sec)	4	4.7	5.3	6	6.7
320		3.7	4.4	5	5.6	6.2
350		3.4	4	4.6	5.1	5.7
370		3.2	3.8	4.3	4.8	5.4
400		3	3.5	4	4.5	5

TBW total body weight, *IDR* iodine delivery rate, *FR* flow rate

the percentage used, the longer, up to more than 30%, the time required for image reconstruction (Silva et al. 2010).

2.2 Intravenous Injection of Contrast Medium

The use of IV contrast media (CM) is somewhat crucial for the assessment of inflammatory and neoplastic small bowel diseases. In particular, among the most important findings to be evaluated are bowel wall enhancement pattern and mesenteric vessels whose quality depends respectively on parenchymal and vascular enhancements. Vascular enhancement is directly influenced by the Iodine delivered per second (Iodine Delivery Rate; IDR), while parenchymal enhancement is proportional to the total volume of Iodine administered to the patient. These parameters should be optimized according to patients' characteristics, in particular lean body weight (LBW). To obtain an effective parenchymal enhancement, around 600 mg of iodine should be injected per kg of LBW. As an example a regular man of 70 kg has around 15% of body fat, thus, his lean body weight is around 59 kg and 35.4 gr of iodine (101 mL using a CM with a concentration of 350 mgI/mL) should be injected. While a male individual of the same weight but obese has around 32% of body fat, thus, only 82 mL of CM are needed (LBW: 47.6 kg; total iodine dose: 28.5 gr).

Vascular enhancement should also be optimized according to patient size. Flow rates for contrast medium with different iodine concentrations and TBW are suggested in Table 1.

These values can be virtually obtained with any concentration of contrast medium according to the following formula:

IDR = ([I]/1000) * FR

where [I] is the contrast medium concentration (expressed in mgI/mL) and FR is the injection flow rate.

Referring to the previous example for a man of 70 kg an IDR of 1.6 gI/sec, thus, a 350 CM should be injected at 4.6 mL/sec.

Another fundamental factor, affecting both vascular and parenchymal enhancement, is the synchronization between CM injection and bolus arrival in the vascular region of interest (CM Transit time; *t*CMT). Many CT scanners have an automatic bolus triggering software built into their system. This method consists in real-time detection of bolus by placing a circular ROI into the target vessel on a non-enhanced image. After 5–10 s from the start of the CM injection, a series of low-dose sequential scans are acquired every 1–3 s, whereas the attenuation within the ROI is monitored or inspected visually. The *t*CMT equals the time when a predefined enhancement threshold is reached (e.g., 100 HU), plus a diagnostic delay, which should be determined according to the specific organ to be studied. The diagnostic delay is the time between the reach of a predefined enhancement threshold and the start of the MDCT acquisition; it depends on the scanner model and on the longitudinal distance between the monitoring series and the starting position of the actual MDCT series. For the acquisition of the enteric phase a diagnostic delay of 14 s should be used (Schindera 2007). Usually a second acquisition, with a delay of 75 s after intravenous injection of contrast material is obtained in

order to have a precise evaluation of other abdominal organs.

2.3 Small Bowel Distension

Bowel distension is a fundamental requisite for any imaging method of the small intestine, as revealed by decades of experience with X-ray barium studies. In fact, a collapsed bowel loop can hide lesions or simulate pathological wall thickenings. The presence of a lesion generating small bowel obstruction creates a natural distension of the lumen and the possibility of examining the patient without the need for any previous preparation. In contrast, the relative collapse of bowel loops, both in standard conditions and in different non-obstructive pathologies, has led researchers to study a variety of methods of luminal distension.

Today, there are two main approaches to MDCT of the small bowel: (1) Study following oral administration of contrast material ("MDCT enterography"); (2) Study with distension of the lumen obtained with contrast material introduced through a naso-jejunal tube ("MDCT enteroclysis"). Before entering into the details of the two techniques, a brief review of major contrast agents for small bowel study is provided.

2.3.1 Enteral Contrast Agents

Different types of enteral contrast agents are used to obtain a proper distension of the small bowel loops. According to their density they can be classified into neutral (with density similar to water, 0–10 HU), positive (with high density, >100 HU) and negative (with low density, <0 HU).

Neutral contrast agents, which possess X-ray attenuation similar to water, are preferred for most of the clinical indications. In particular the association with intravenous iodinate contrast allows a better depiction of wall enhancement thanks to the higher attenuation difference with the hypodensity of the lumen. This is particularly important for the evaluation of IBD and neoplastic diseases or when angiography-like 3D reconstructions are required (Minordi et al. 2009). Although water is the safest and cheapest agent, it suffers the limitation of intestinal absorption, which compromises an adequate distension of the distal ileum in a large number of patients (Winter et al. 1996). To minimize absorption, water is usually mixed with high molecular size compounds which do not alter water density and taste. Thus, neutral contrast agents are mainly water solutions of osmotic compounds such as polyethylene glycole (PEG), mannitol, sugar alcohols or sorbitol. Lately a neutral oral contrast agent, a low concentration barium sulphate (0.1%) containing sorbitol, has been expressly developed for CT enteral studies (Maglinte et al. 2007).

Positive contrast agents, which have high X-ray attenuation, are usually a mixture of barium sulphate (1–2%) or iodinate contrast agents (2–3%). These enteral agents are preferred for all the situations where high intraluminal density is recommended such as the evaluation of perforations or fistulas, as complication of Crohn's disease, or for the evaluation of intraluminal masses, such as polyps or tumours (Kambadakone et al. 2010). Because the high intraluminal density reduces contrast resolution with enhancing structures, these contrast agents are contraindicated when the evaluation of wall enhancement patterns is required as in IBD. On the other hand positive CM can be used when intravenous contrast agents do not influence disease conspicuity or in the setting of difficult intravenous access or renal failure.

Negative contrast agents have also been developed but for several limitations they are not routinely used. Oil emulsions provide lower density values than water, but their taste, which reduces patient's acceptance, and the high cost are the main limitations. Air administration, either orally through delayed-release effervescent substances or rectally, for the study of the terminal ileum, has produced satisfactory results in the demonstration of intraluminal and mural diseases, but the excessive difference between its density (2,800 HU) and enhancing intestinal wall (100–135 HU) often generates artefacts, which limit the clinical use (Minordi et al. 2011).

2.3.2 Enterography: Technique

MDCT enterography consists in the oral administration of a contrast agent in an adequate amount. Usually for an average size adult the dose is around 1,500–2,000 mL of enteral contrast agent. Optimal timing of the administration is fundamental. It is likely easier for the patient to ingest the oral volume over a longer period of time. However, if ingested over too long a period, the contrast material may be in the colon and if insufficient volume is ingested, a suboptimal small bowel distention

limits CT enterography examination. (Macari et al. 2007). This is the reason why contrast agent is usually divided into three aliquots administered starting around 60 min before CT scanning.

In order to minimize motion artefacts, a spasmolytic agent is administered intravenously immediately before the examination, whilst the patient is lying on the table inside the scanner room (Fletcher 2009). The two agents mainly used in clinical routine are glucagon and hyoscine N-butylbromide. Their effect, following an intravenous injection, starts approximately 30 s after the administration. One milligram of glucagon is enough to reach the desired effect while around 40 mg of hyoscine N-butylbromide is needed to achieve the same results. Some experiences in the literature found glucagon to have a more reliable and longer effect (Froehlich et al. 2008).

2.3.3 Enteroclysis: Technique

MDCT enteroclysis is a method developed in the early 1990s in which variable amounts of low density (methylcellulose or water) or high-density (4–5% sodium diatrizoate, 1% barium sulphate) contrast material are infused by hand or by a peristaltic pump through a naso-jejunal tube before the CT scan. Manual infusion is limiting because the distension is better when the peristaltic pump is used, even if its use does not always allow optimal distension of the entire bowel loops (Maglinte et al. 2007; Mako et al. 2000).

The placement of the naso-jejunal tube is performed under fluoroscopic guidance in order to avoid a time-consuming procedure inside the CT scanner. It is also advisable to use a tube with an anti-reflux balloon, in order to prevent duodeno-gastric reflux.

Volume and infusion rate is crucial for the success of the examination, as it is the case in conventional enteroclysis (Rajesh et al. 2006). Volume is variable among different subjects, ranging between 1500 and 3000 ml. Infusion rate varies between 80 and 150 ml/min. The use of spasmolytics to reduce abdominal discomfort is controversial, since higher infusion rates (in the order of 200 ml/min) induce natural small bowel reflexive atony without the need for any pharmaceutical (Minordi et al. 2006).

2.3.4 Enterography Versus Enteroclysis

The choice between enterography and enteroclysis has always represented a matter of discussion, since the times of conventional X-ray studies (Ott et al. 1985).

From a purely technical point of view, there is no doubt about the superiority of intestinal distension obtained with enteroclysis, particularly if considering jejunal loops (Soyer et al. 2009; Colombel et al. 2006; Elsayes et al. 2010). But, on the other side, it cannot be forgotten the invasiveness of intestinal intubation and the relatively poor patient acceptance, especially in those individuals who require multiple repetitive examinations, as in the case of complicated Crohn's disease. Moreover, intestinal intubation requires specific radiological expertise and it must be performed under fluoroscopic guidance: as a consequence an additional exposure to ionizing radiations is delivered to patients and considerations about a smooth workflow to combine the schedule of fluoroscopy and MDCT rooms are necessary (Dave-Verma et al. 2008).

From a clinical point of view, there are some clear clinical evidences showing that both tests, enterography and enteroclysis, have similar accuracy and reproducibility in the evaluation of ileal Crohn's disease, which is probably the most common indication to perform a cross-sectional study of the small bowel (Negaard et al. 2007; Kerr 2008; Dave-Verma et al. 2008). This is the reason why enterography represents now, in most centres, the first approach to the study of the small bowel, particularly in patients affected by IBD. But it is also true and definitely clear that "unless enteroclysis is performed, there is no oral contrast material that adequately distends the small intestine if the small bowel has not already been distended by an inflammatory process or other obstructing abnormality" (Maglinte et al. 2000). Consequently, in selected cases, and especially when a non-obstructing small bowel tumour is suspected, enteroclysis represents the imaging modality of choice.

3 Clinical Indications

3.1 Inflammatory Bowel Diseases (IBD)

The initial diagnosis of IBD is based on a combination of clinical, laboratory, histologic and imaging findings. No single diagnostic test allows unequivocal diagnosis. Therefore imaging plays a critical role in the initial diagnosis of IBD by providing evidence of the presence and the extension of disease (Patak et al. 2005; Mackalski and Bernstein 2006).

Additionally, imaging characteristics and distribution provide supportive evidence for distinguishing CD from other entities, like ulcerative colitis. In the past decade, many new therapeutic strategies have been developed to allow gastroenterologists and surgeons to treat all forms of IBD (Glick 1987). The success of these treatments depends on accurate diagnosis of the nature and extent of disease. Currently, MDCT of the small bowel has a potential impact on three aspects of patient care: diagnosis, management, and long-term surveillance.

3.1.1 Spectrum of Findings

In MDCT of the small bowel, two major criteria for the diagnosis of CD are the degree of mural thickening and the pattern of mural enhancement. Secondary findings are the site and number of abnormal altered bowel segments, presence of fibro-fatty proliferation (increased attenuation value of mesenteric fat to 20–60 HU), vascular engorgement (comb sign), lymphadenopathy and presence of complications such as stenosis, fistulas and abscesses (Minordi et al. 2009) (Table 2) (Fig. 1). The normal wall thickness of the small intestine is between 1 mm and 3 mm, so any portion of the bowel wall exceeding 4–5 mm is considered abnormal (Macari and Balthazar 2001). The presence of well-distended loops is fundamental to evaluate accurately both wall thickening and wall enhancement because non-dilated loops are potential source of pitfalls, mimicking affected loops and hiding fistulas, abscesses or enlarged lymph nodes (Fig. 2). CT imaging is able to detect early inflammatory changes of the bowel wall, based on enhancement following intravenous injection of contrast medium. There are two patterns of enhancement of a pathologic bowel segment: "homogeneous" and "stratified". Homogeneous enhancement is a diffuse transmural enhancement with no recognition of different bowel layers. A stratification of the bowel wall (the so-called "target" or "double halo" appearance) is related to mucosal enhancement with hypoenhancing outer layer (Fig. 2). The target sign was first described as a specific sign for CD (Frager et al. 1983), but it is now recognized that any non-neoplastic condition may lead to a target appearance in the small bowel. Common causes include CD, infection, ischemia, radiation enteritis, angioedema and hemorrhage (De Backer et al. 2001; Macari et al. 2003). When a target sign is visualized on CT, the differential diagnosis can be narrowed by observing the degree of thickening, the length of the abnormal segment, associated imaging abnormalities and the clinical history. Another criterion used to evaluate an abnormal small bowel loop is the length of involvement. Determination of the length of involvement is particularly facilitated by using coronal multiplanar reformatted and 3D volume-rendered images obtained with MDCT (Fig. 3) (Caoili and Paulson 2000). Finally, the location of the abnormality should be determined (Boudiaf et al. 2004).

3.1.2 Assessment of Disease Activity and Complications

Classification of disease activity based on imaging criteria divides CD into different subtypes: active inflammatory, fibrostenotic, fistulizing/perforating and reparative (Wold et al. 2003). An assessment of disease activity is extremely important, given its influence on the choice of therapy. Mural thickening and mural enhancement associated with at least one of extra-enteric findings such as increased attenuation of the perienteric fat, the comb sign and complications like fistulas have been reported to indicate active inflammatory CD (Fig. 4) (Zissin et al. 2004). Wall thickening is found in 82% of patients with CD and homogeneous and symmetrical wall thickening are reported in patients with active disease (Madureira 2004). The most sensitive visual CT finding of Crohn disease activity is wall enhancement, with a reported sensitivity between 73 and 80% (Hara et al. 2006). When acute inflammation is present, the thickened wall often shows the target sign in which the intermediate low-density ring represents submucosal edema or fat, while the inner ring of mucosa and the outer ring of muscle layer and serosa show intense enhancement (Kelvin and Herlinger 1999) (Fig. 5). It is also necessary to evaluate the grade of enhancement; in fact if the enhancement is mild and the attenuation is similar to muscle, it should be considered as chronic inflammatory conditions. The milder homogeneous enhancement in these cases is likely related to the development of fibrosis (Macari et al. 2007). Mesentery is frequently involved in active inflammation and CT allows to evaluate the different types of mesenteric processes that cause separation of loops such as fibro-fatty proliferation, vascular engorgement on the mesenteric side of the

Table 2 Spectrum of findings

CT findings	Notes	Type
Wall thickness (>5 mm)	Transmural and segmental wall thickening (skip lesions) Target or sandwich appearance in axial and longitudinal projection respectively. D.D. Lymphoma presents bulky nodular wall thickening (thickness > 1 cm) because of cell proliferation	All type
Cobblestoning	Intersecting deep longitudinal and transverse ulcers with intervening protruding edematous mucosa	–
Mesenteric fat stranding	Transumral extension of the inflammation along the adjacent mesentery of an inflamed bowel loop When present, it is typically associated with bowel wall edema and intense enhancement	Active inflammatory subtype
Comb sign	It corresponds to increased mesenteric vascularity and results from vascular engorgement of vasa recta. It usually depicted at mesenteric borde of a diseased loop. It resembles the teeth of a comb	Active inflammatory subtype
Layered wall enhancement	Trilaminar appearance, with enhanced outer serosal and inner mucosal layers and an inter-posed submucosal layer of lower attenuation (submucosal edema)	Active inflammatory subtype
Homogeneous diffuse wall enhancement	Represents transmural inflammation, manifesting as intense homogeneous enhancement affecting the entire wall thickness	Moderate chronic inflammatory
Inhomogeneous diffuse wall enhancement	Low-entity inho-mogeneous enhancement is often seen in fibrosis	Chronic inflammation. Fibrosis
Lymph nodes	Enlargement and homogeneous enhancement are highly suggestive of active disease. Usually located along the vascular supply of affected segment. No enhancement suggests alternative diagnosis (necrotic caseating node in TBC)	–
Pseudosacculation Pseudodiverticula	Fibrosis and retraction of the diseased mesenteric wall lead to apparent dila-tation of the opposing normal bowel wall	Longstanding inactive subtype
Fat wrapping (fat hypertrophy)	Increased mesenteric fat producing a mass effect. It frequently involves the mesenteric border even if it may encircles the diseased loops	Longstanding inactive subtype
Submucosal fat deposition	Usually associated with longstanding inactive Crohn Disease. It has to be distinguished from mural stratification and submucosal fibrosis (overlapping HU values)	Longstanding inactive subtype
Stenosis	To distinguish between reversible and irreversible stricture is the hallmark.	Complication Fibro-stenotic subtype
Fistulas	Deep transmural ulcers that ultimately communicate with an adjacent epithelial surface	Complication Fistulizing/ perforating subtype
Sinuses	A blind-ending tract that arises from bowel but does not reach another epithelial surface. It is often associated with abscess	Complication Fistulizing/ perforating subtype
Abscess	It is a well-defined, encapsulated, collection of pus. Heterogenus content such as solid, fluid and gas components	Complication Fistulizing/ perforating subtype

bowel and mesenteric lymphadenopathy. Chronic inflammation of the mesenteric fatty tissue induces a proliferation of the fat tissue itself together with a fibrotic component that is called fibro-fatty proliferation; it is visualized as increased attenuation value of mesenteric fat with a loss of the normal sharp interface between the bowel wall and mesentery (Maglinte et al. 2003).

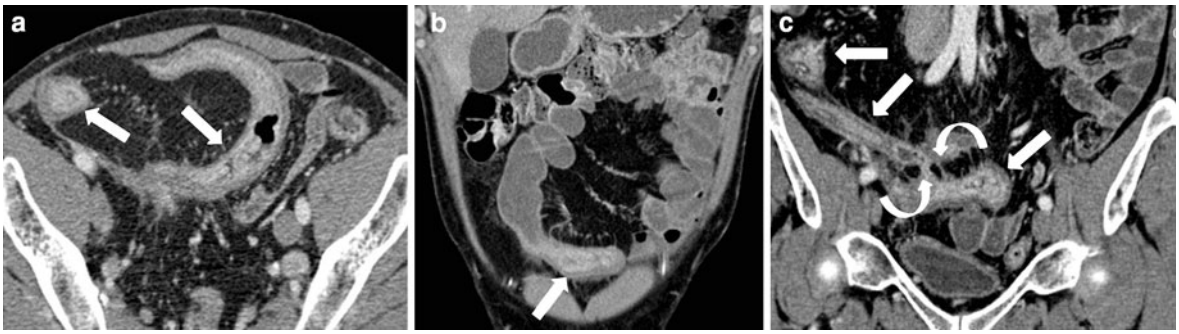

Fig. 1 Contrast-enhanced axial (**a**) and coronal (**b**, **c**, **d**) CT scan show Crohn disease "skip" involvement of ileum (*arrows*). The multiple segmental thickenings (*arrows*) of small bowel wall present alternating layers of higher or lower attenuation in a concentric pattern

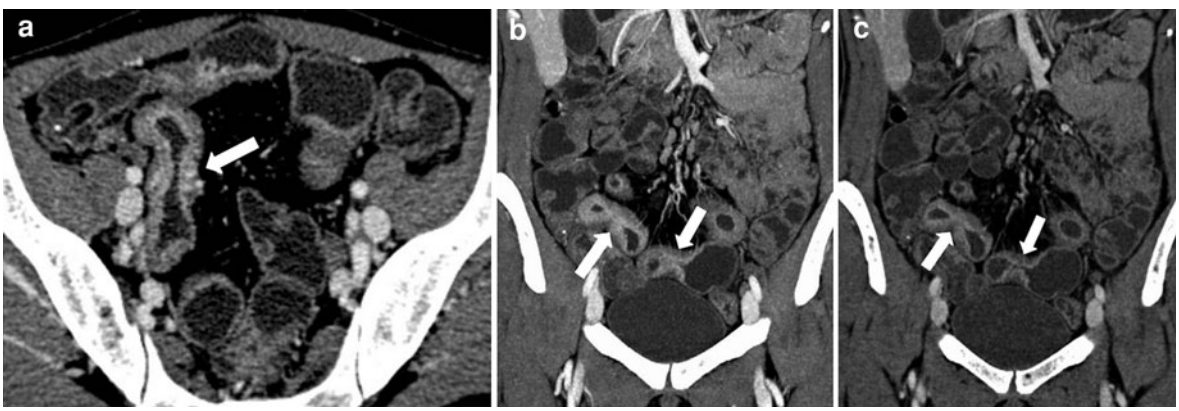

Fig. 2 Contrast-enhanced axial (**a**), coronal with MIP (**b**) and coronal (**c**) CT image showing mural "skip" lesion thickening of ileum (*arrow*) with submucosal edema and dilated proximal loops

The "comb sign" arises from the combination of vascular engorgement of vasa recta and fibro-fatty proliferation and it is demonstrated as multiple tubular, tortuous opacities on the mesenteric side of the ileum, aligned as the teeth of a comb (Fig. 6) (Madureira 2004). Mesenteric lymphadenopathies, ranging in size between 3 and 8 mm, are well depicted with MDCT: when lymph nodes are multiple and larger than 10 mm, lymphoma and carcinoma should be excluded (Gore et al. 1996).

Common complications of CD include stenosis, fistulas and abscesses. A stenosis is present when wall thickening determines a luminal narrowing; stenosis may be due to acute inflammation, spasm or chronic fixed lesions and it causes a dilatation upstream. It is important to determine the degree of small bowel dilatation because generally stenosies caused by active inflammatory determine little upstream bowel dilation while strictures caused by chronic disease cause more significant dilation (Figs. 7, 8).

3.1.3 Clinical Role of Different Imaging Modalities

Diagnostic imaging plays a major role in the decision-making process of patients affected by IBDs. Several techniques are available, including X-rays studies, capsule endoscopy, US, MDCT and MRI.

A residual role for X-ray exams is in the emergency setting, when a plain film of the abdomen can be fundamental for a prompt diagnosis of bowel obstruction or perforation, referring the acute patient for emergency surgery.

For elective patients, dedicated studies are needed. Traditional barium examinations (i.e., small bowel follow-through and enteroclysis) have completely lost any interest since they have been completely replaced by cross-sectional imaging modalities. The advantage

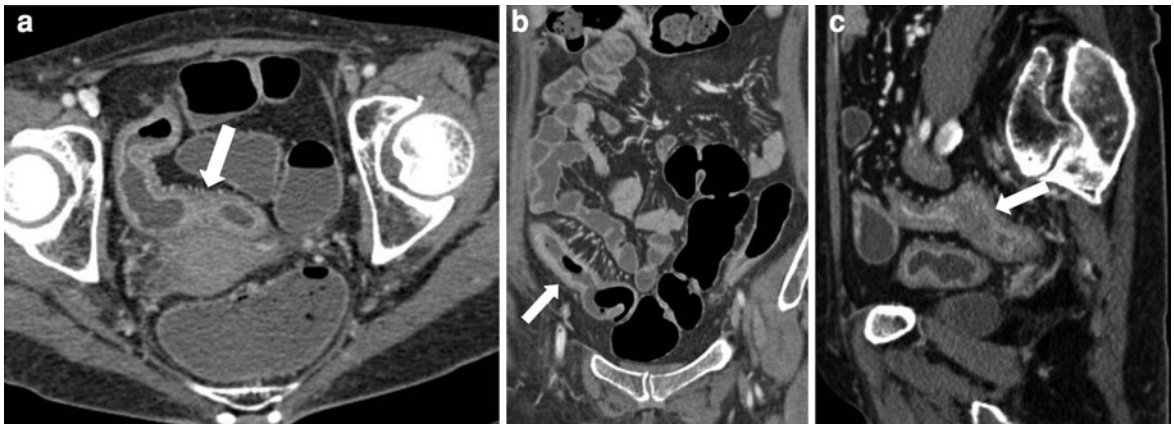

Fig. 3 Contrast-enhanced axial (**a**), coronal (**b**) and sagittal (**c**) CT image showing mural thickening of ileum (*arrow*) with submucosal edema and mesenteric hypervascularity ("comb sign") indicated active disease

of cross-sectional imaging is in the possibility to study the bowel wall, and not only the lumen, as well as the peri-intestinal extension of the inflammatory process.

Among the cross-sectional imaging modalities, US is a first-line examination, often performed by clinicians during the first visit of the patients, in order to confirm a suspected diagnosis. US is easily accessible, widely available and relatively inexpensive. The use of Doppler-US might provide helpful additional information about IBD, particularly about the degree of disease activity. Using Doppler-US vascularity of the bowel wall can be assessed according to the intensity of colour signals and/or by the analysis of Doppler curves (measurement of resistive index) obtained from vessels detected within the bowel wall (Migleddu et al. 2008). However, these changes in wall vascularity are due to large arteries feeding the microvascular bed and therefore resolution for slow flow is limited. This is the reason why there is no clear correlation between the extent of vascularisation visible by Doppler techniques and clinical scores of disease activity (Drews et al. 2009). Moreover, even chronic inflammatory changes can show an increased vascularisation. Contrast-Enhanced Ultrasound (CEUS) is rapidly entering the field of bowel US in order to assess perfusion abnormalities in the bowel wall, especially in CD (Weskott 2008). The hallmark of active CD is not only an increased parietal macrovascularisation, but also proliferation of microvessels, clearly detected by CEUS.

Despite technological advances, CD localized in duodenum, jejunum, distal sigmoid colon and rectum is often missed by US because of inherent difficulties. And the contrast resolution of US is not high enough to permit the detection of extramural extent and complications of CD (Marmo et al. 2005). Moreover, US lacks panoramic evaluation of the bowel loops, preventing a complete assessment of the disease.

MR and CT are accepted more and more as first-line modalities for the evaluation of suspected IBD (Schreyer et al. 2004; Chiorean et al. 2007). While in the USA the technique of choice is CT, in Europe the focus is more on MRI. Each technique has unique advantages and limitations in clinical practice. MR of the small bowel offers a perfect evaluation of CD and its complications such as fistulas and abscesses; it has the unique advantage of the lack of ionizing radiation and the possibility to be performed without intravenous injection of contrast material in patients with impaired renal function. Limitations of MR include longer examination time, higher cost and lower availability. Moreover, MR is not suitable in severely ill patients because of breathing artefacts resulting in blurred images.

MDCT of the small bowel is more widely available and cheaper than MR enterography; examination time is extremely fast and multiplanar projections improve the detection of extramural complications (Paulsen et al. 2006). MDCT has been shown to change the management of CD in 28% of patients,

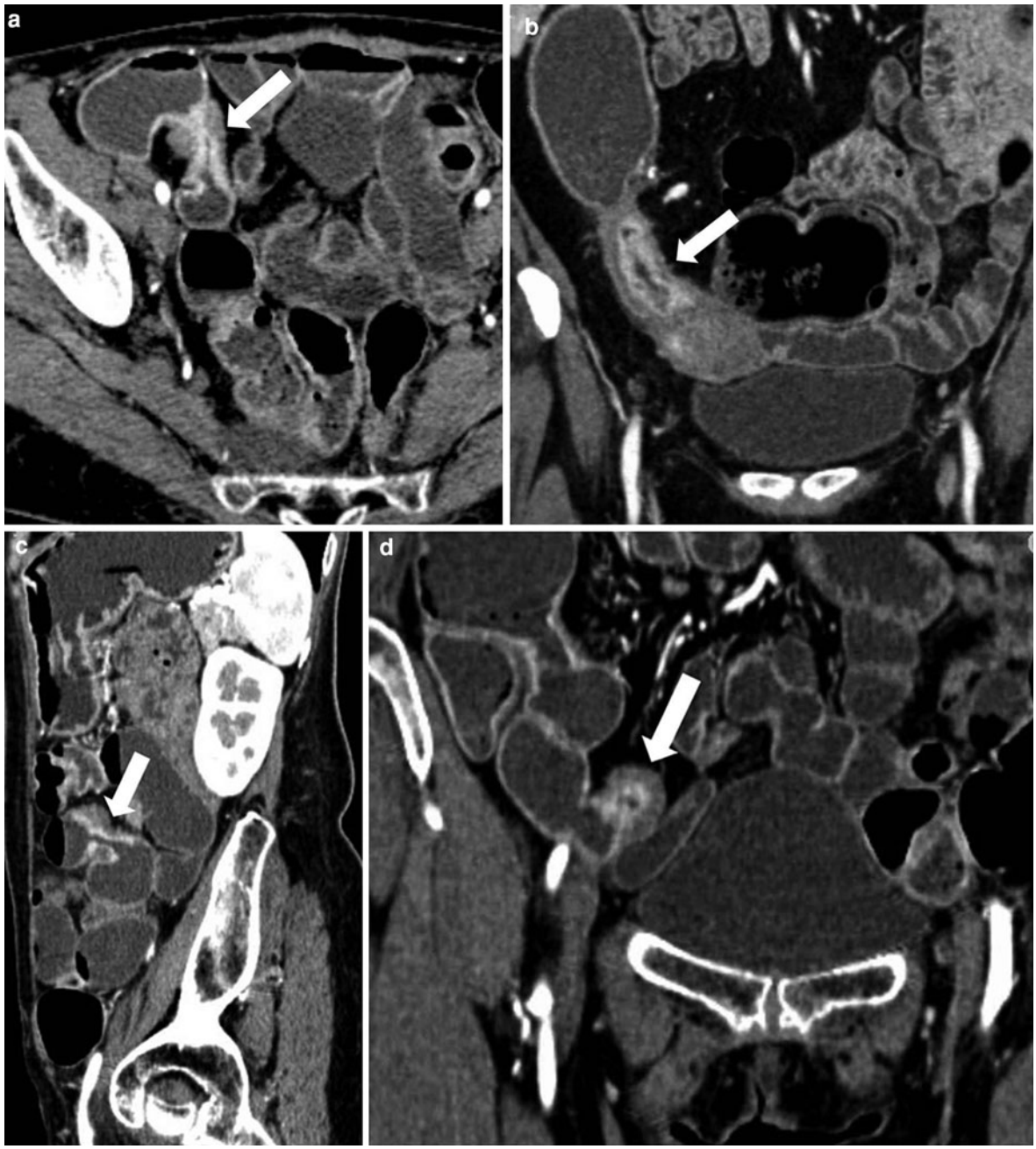

Fig. 4 Contrast-enhanced axial, sagittal and coronal reformatted CT scans demonstrate luminal narrowing at the distal ileum in a relatively long bowel segment (*arrows*) associated with prominent dilated proximal loops in a patient with previous surgery for Crohn disease. The wall of the involved segment has a stratified appearance, typical of recurrence of disease

while MDCT enteroclysis changed the management in 62% of patients with symptomatic CD (Turetschek et al. 2002). Despite the fact that CT enterography is a very accurate technique and is used in many institutions, its role in IBD is limited by the ionizing radiation, especially because of the repetitive use for

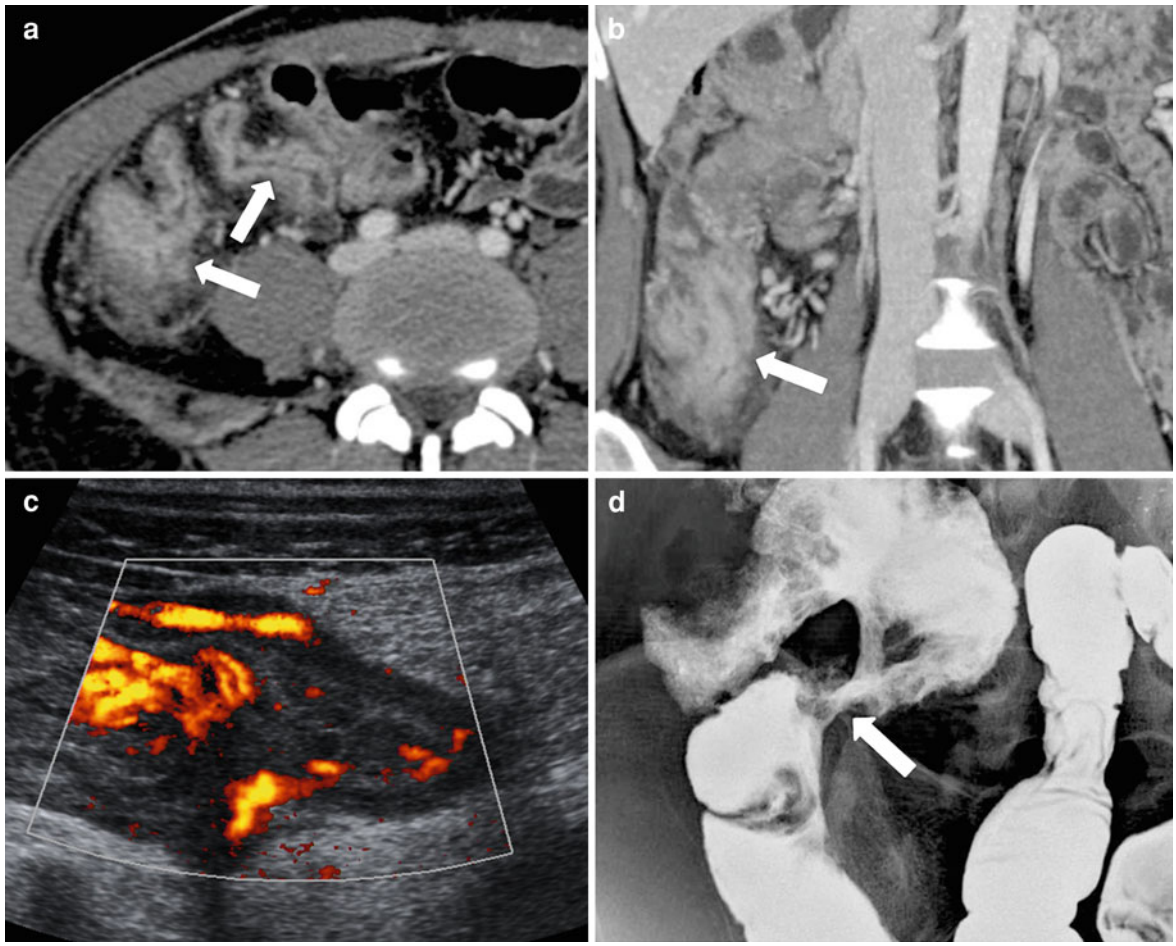

Fig. 5 Contrast-enhanced axial (**a**) and coronal (**b**) CT image show recurrent Crohn disease with prominent, strongly enhanced mural thickenings and intense surrounding fibrofatty proliferation (*arrows*). Ultrasound (**c**) demonstrates wall thickening characterize by hypervascularity and vessels engorgement due to inflammation. Barium enema (**d**) image showing stenosis of distal ileal loop suggestive for crohn recurrence

follow-up in young individuals. On the other side, although MRE is the favoured examination for assessing the small bowel in young patients with CD, a routine abdominal CT is first performed in patients with known CD and suffering from abdominal pain (Schreyer et al. 2010).

3.2 Small Bowel Tumours

Primary neoplasms of the small bowel are quite uncommon, representing only about 3% of all neoplasms of the digestive tract, although the small bowel accounts for more than 90% of the intestinal mucosal surface (Good 1963). Patients may present with aspecific symptoms such as pain, obstruction, bleeding, anorexia, weight loss, perforation or jaundice. The nonspecific nature of these symptoms and the lack of reliable clinical findings provides that most small bowel tumours are not diagnosed until complications occur with associated significant delay in the diagnosis (Maglinte et al. 1991; Ciresi and Scholten 1995). Many studies have been proposed for the investigation of small bowel tumours, and thanks to recent technical improvements of MRI and MDCT, the radiologist plays a major role in the detection of small bowel tumours due to the fact that CT has been shown to demonstrate abnormalities associated with small bowel tumours in 90% of patients (Minardi et al. 1998; North and Pack 2000; Ramachandran et al. 2007). The best visualisation of small lesions is achieved with CT enteroclysis. Lipoma accounts for

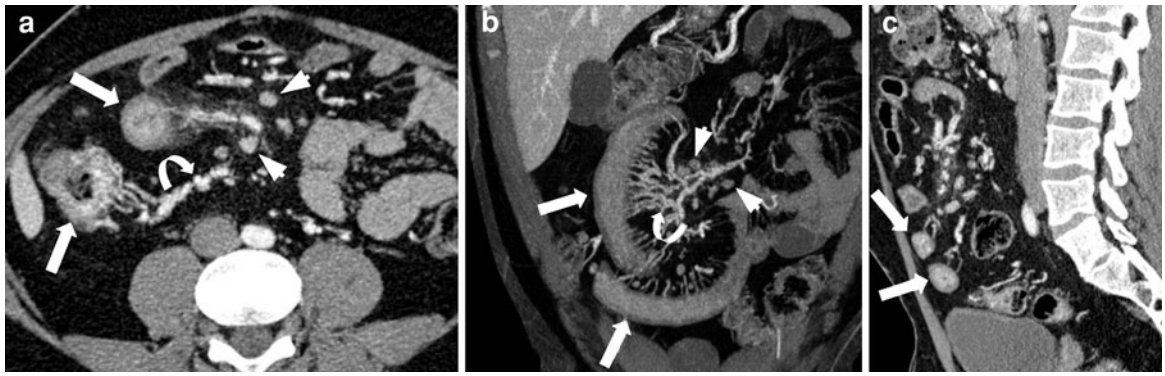

Fig. 6 Contrast-enhanced axial (**a**), coronal (**b**) and sagittal (**c**) reformatted CT scans clearly showing bowel wall thickenings at the distal ileum (*arrows*). The thickened wall has a stratified appearance. Increased mesenteric vascularity known as "comb sign" (*curved arrow*) and several lymphadenopathies (*arrowhead*) are evident around the involved segment. These findings are suggestive of active lesions from Crohn disease

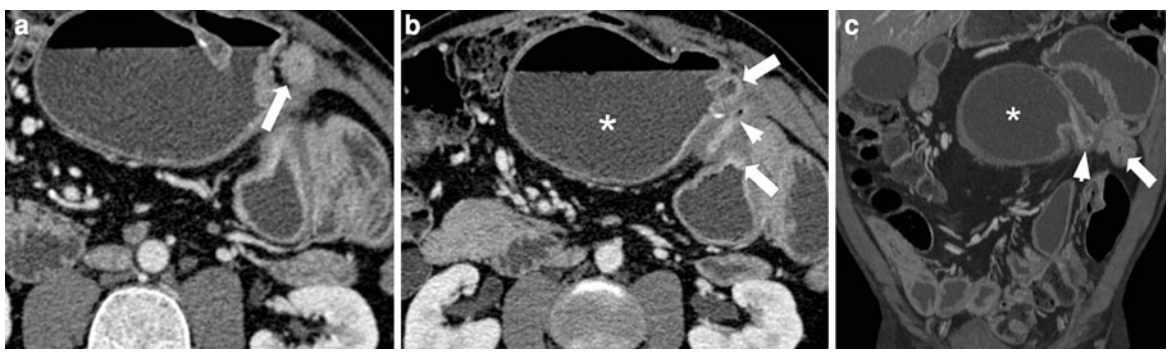

Fig. 7 Contrast-enhanced axial (**a**, **b**) and coronal (**c**) CT scan showing recurrent Crohn disease some years following surgical resection. Images show mural thickenings (*arrow*) involving adjacent small bowel loops and severe dilatation of a proximal loop (*star*). The presence of entero-enteric fistula (*arrowhead*) and surrounding fibrous tissue are clearly visible

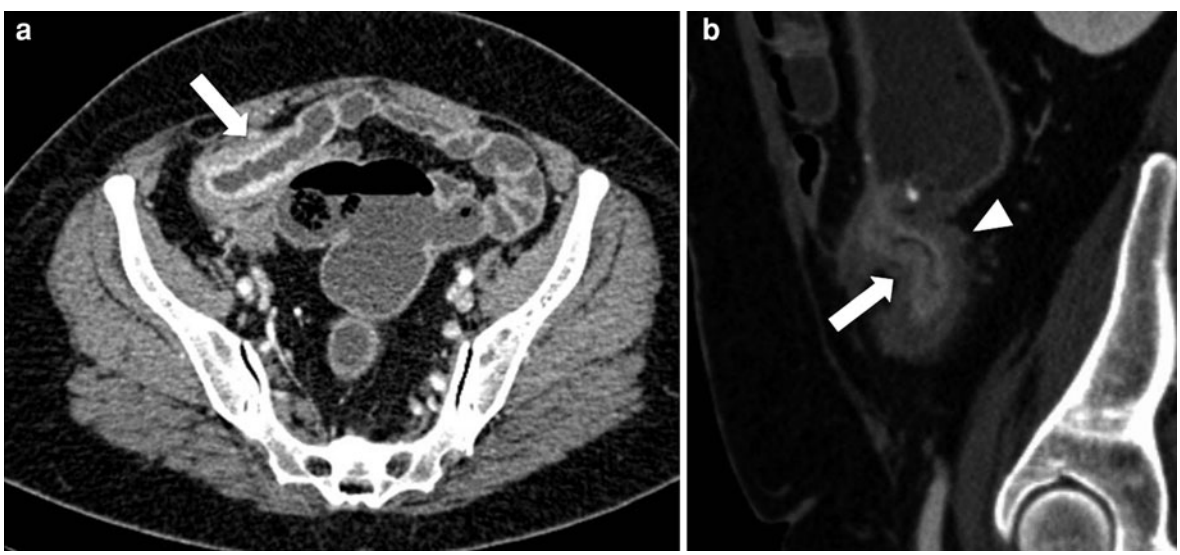

Fig. 8 Contrast-enhanced axial (**a**) and sagittal (**b**) CT scan of the lower pelvis show a diseased segment of the distal ileum (*arrow*) with stratified mural thickening, mural ulceration and fibrofatty proliferation *(arrowhead)*

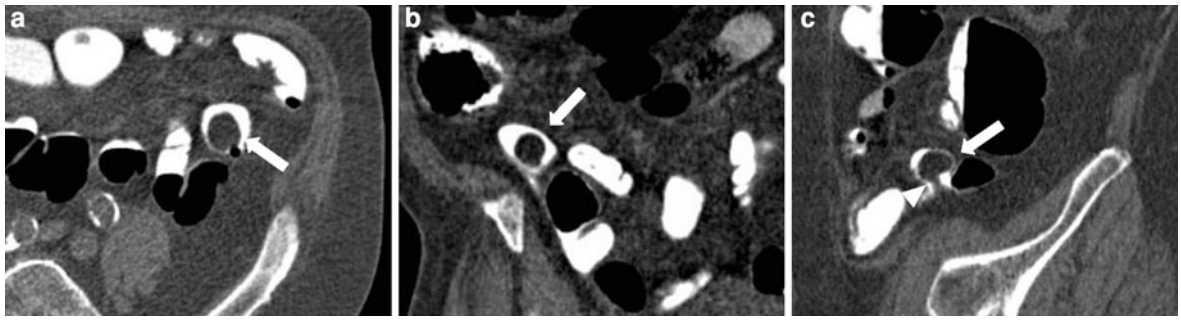

Fig. 9 Axial (**a**), coronal (**b**) and sagittal (**c**) CT image showing, within the last small bowel loop, a well-circumscribed ovoid mass with fat attenuation (*arrow*) and short stalk (*arrowhead*), suggestive for lipoma

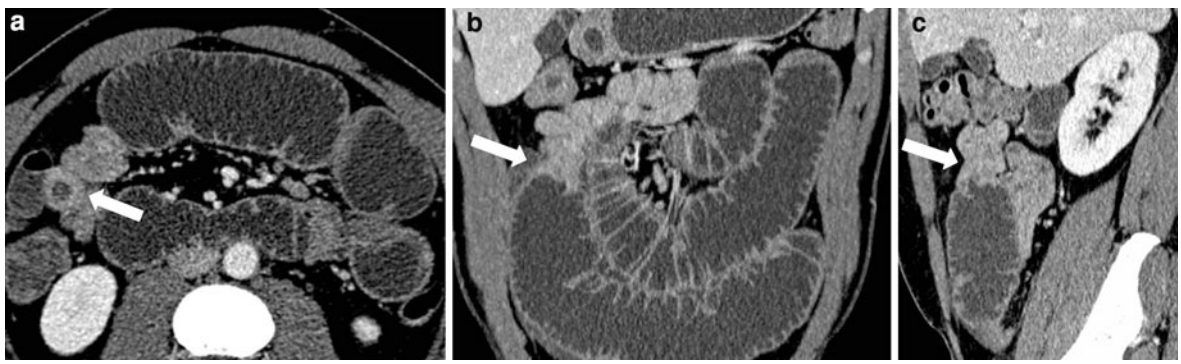

Fig. 10 Contrast-enhanced axial (**a**), coronal (**b**) and sagittal (**c**) CT scan of the abdomen show a stenosing lesion (*arrow*) of distal mall bowel loop with severe and diffuse dilation of proximal small bowel loops due to the presence of small bowel adenocarcinoma

the most frequent benign polypoid lesion easily recognizable on MDCT due to the presence of a polypoid lesion with fat density (Fig. 9). Adenocarcinoma represents the most common small bowel tumours, followed by carcinoid tumor, lymphoma and gastrointestinal stromal tumor. Adenocarcinomas assume a variety of shapes but are generally located in the proximal small bowel appearing as a focal intraluminal mass or as small bowel wall thickening usually associated with an increased mural enhancement (Fig. 10). A pedunculated mass with exoenteric appearance and arterial hypervascular enhancement is strongly suggestive of gastrointestinal stromal tumour (GIST) (Fig. 11) whilst a mass with extraluminal appearance and several locoregional lympahedenopaties is strongly suggestive for lymphoma. The presence of polypoid lesion or endoluminal polypoid filling defect with hypervascular enhancement on arterial phase is suggestive of the presence of carcinoid tumour (Fig. 12). When the presence of small bowel tumor is suspected, the use of MDCT offers the unique simultaneous advantage of a panoramic view of the entire gastrointestinal tract as well as the evaluation of abdominal organs.

3.3 Malabsorption Syndromes

Malabsorption syndromes, and among them celiac disease, are another possible indication for MDCT imaging of the small bowel (Minordi et al. 2006; Boudiaf et al. 2004).

Celiac disease is a chronic inflammatory disease affecting the GI tract of genetically predisposed subjects. It is relatively common in European countries, with an incidence in the order of 1 case for every 250–300 people. The role of diagnostic imaging in celiac disease is usually limited since the diagnosis is obtained by jejunal biopsy (Green and Cellier 2007). However, it is well known that 75% of patients present with

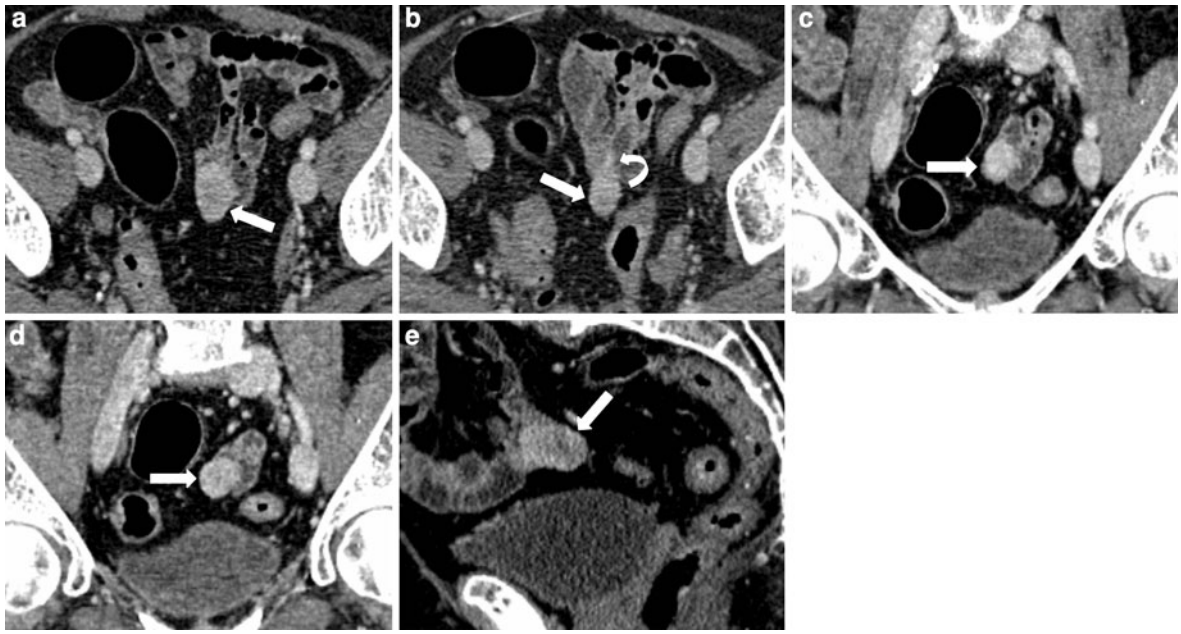

Fig. 11 Contrast-enhanced axial (**a**, **b**), coronal (**c**, **d**) and sagittal (**e**) CT image showing a well circumscribed hyperenhanced submucosal mass (*arrow*) extending exophytically from small bowel loop and related to GIST. Contrasted enhanced axial CT image shows the presence of a short stalk (*curved arrow*) connecting the exophytic mass to small bowel wall

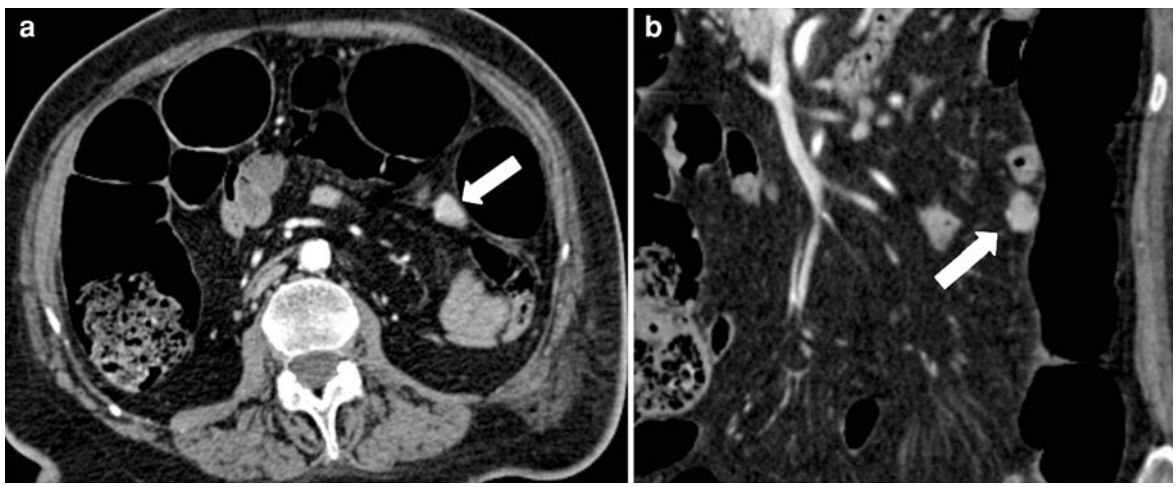

Fig. 12 Contrast-enhanced axial (**a**) and coronal (**b**) CT image show a small hyperenhanced nodular lesion (*arrow*) of the small bowel wall suggestive for GIST. Note how the lesion (*arrow*) is better appreciable on arterial phase (**a**) than in venous phase (**b**)

radiologically detectable abnormalities represented by intestinal athonia, changes of mucosal fold pattern (ileal jejunalization and the so-called reversal fold pattern) (Fig. 13), and that radiological examinations may be useful to detect complications such as intestinal intussusception; MDCT is an useful tool both for diagnosis and follow-up, since it is able to provide, uninvasively, morphologic information such as bowel dilatation, ileal jejunization, jejuno-ileal reversal pattern and, at the same time, extra-intestinal findings such as mesenteric vascular congestion, lymphadenopathies and hyposplenism (Tomei et al. 2005).

Intestinal atonia is an aspecific sign of intestinal disease; it presents as diffuse dilatation (greater than

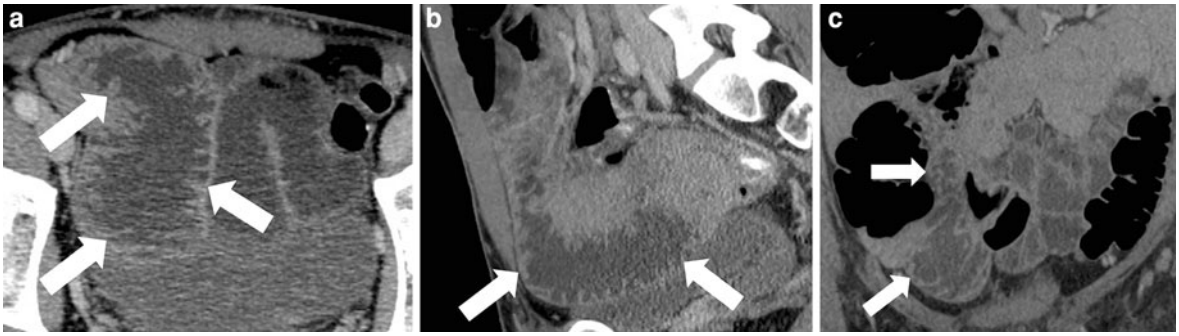

Fig. 13 Contrast-enhanced coronal (**a**, **b**) and sagittal (**c**) showing increased number of folds *(arrows)* in distal ileum (ileal jejunization)

3 cm) of the small intestine without the evidence of any obstructing lesion. The most specific signs of celiac disease are the alterations of fold pattern: a decrease in the number of mucosal jejuneal folds (less than three per inch) and an increase of ileal mucosal folds (over four per inch) is the so-called "ileal jejunization". A smooth appereance of jejuneal mucosal profile together with ileal jejunization is known as "reversal fold" pattern (Tomei et al. 2000).

Complications of celiac disease are represented by transient intestinal intussusception secondary to intestinal atonia. (Kim et al. 2006). MDCT appearance is the so-called "double halo" or "target" sign, with different stratified layers representing bowel wall and peritoneal fat tissue (Horton et al. 2003).

An extra-intestinal finding of celiac patients is represented by mesenteric adenopathies. The evaluation and follow-up of enlarged nodes in celiac patients non-responding to gluten-free diet is a radiological challenge considering that a few number of celiac patients might develop lymphoma (Jones et al. 1984).

4 Conclusions

MDCT is a powerful tool in the evaluation of different small bowel diseases. Adequate technique is mandatory, in particular optimal luminal distension, to be achieved either with oral ingestion of a large volume of neutral enteric contrast material or through naso-jejunal intubation. The main indication is the assessment of Crohn's disease, followed by detection of small bowel tumours and evaluation of malabsorption syndromes.

References

Boudiaf M, Jaff A, Bouhnik Y et al (2004) Small-bowel diseases: prospective evaluation of multi-detector row helical CT enteroclysis in 107 consecutive patients. Radiology 233:338–344

Brenner DJ, Hall EJ (2007) Computed tomography: an increasing source of radiation exposure. N Engl J Med 357:2277–2284

Caoili EM, Paulson EK (2000) CT of small-bowel obstruction: another perspective using multiplanar reformations. AJR 174:993–998

Chiorean MV, Sandrasegaran K, Saxena R et al (2007) Correlation of CT enteroclysis with surgical pathology in Crohn's disease. Am J Gastroenterol 102:2541–2550

Ciresi DL, Scholten DJ (1995) The continuing clinical dilemma of primary tumours of the small intestine. Am Surg 61(8):698–702

Colombel JF, Solem CA, Booya F et al (2006) Quantitative measurement and visual assessment of ileal Crohn's disease activity by computed tomography enterography: correlation with endoscopic severity and C reactive protein. Gut 55(11):1561–1567

Dave-Verma H, Moore S, Singh A et al (2008) Computed tomographic enterography and enteroclysis: pearls and pitfalls. Curr Probl Diagn Radiol 37(6):279–287

De Backer AI, De Schepper AM, Vandevenne JE et al (2001) CT of angioedema of the small bowel. AJR 176:649–652

Drews BH, Barth TF, Hänle MM et al (2009) Comparison of sonographically measured bowel wall vascularity, histology, and disease activity in Crohn's disease. Eur Radiol 19:1379–1386

Elsayes KM, Al-Hawary MM, Jagdish J et al (2010) CT enterography: principles, trends, and interpretation of findings. Radiographics 30(7):1955–1970

Fletcher JG (2009) CT enterography technique: theme and variations. Abdom Imaging 34:283–288

Frager DH, Goldman M, Beneventano TC (1983) Computer tomography in Crohn disease. J Comput Assist Tomogr 7:819–824

Froehlich JM, Daenzer M, von Weymarn C et al (2008) Aperistaltic effect of hyoscine N-butylbromide versus glucagon on the small bowel assessed by magnetic resonance imaging. Eur Radiol 19(6):1387–1393
Glick SN (1987) Crohn's disease of the small intestine. Radiol Clin North Am 25:25–45
Good CA (1963) Tumours of the small intestine. Am J Roentgenol Radium Ther Nucl Med 89:685–705
Gore RM, Balthazar EJ, Ghahremani GG et al (1996) CT features of ulcerative colitis and Crohn's disease. AJR Am J Roentgenol 167:3–15
Green PH, Cellier C (2007) Celiac disease. N Engl J Med 357:1731–1743
Hara AK, Leighton JA, Heigh RI et al (2006) Crohn disease of the small bowel: preliminary comparison among CT enterography, capsule endoscopy, small-bowel follow-through, and ileoscopy. Radiology 238:128–134
Horton KM, Lawler LP, Fishman EK (2003) CT findings in sclerosing mesenteritis (panniculitis): spectrum of disease. Radiographics 23:1561–1567
Jaffe TA, Martin LC, Miller CM et al (2007) Abdominal pain: coronal reformations from isotropic voxels with 16-section CT–reader lesion detection and interpretation time. Radiology 242(1):175–181
Jones B, Bayless TM, Fishman EK et al (1984) Lymphadenopathy in celiac disease: computed tomographic observations. AJR Am J Roentgenol 142:1127–1132
Kalra MK, Prasad S, Saini S et al (2002) Clinical comparison of standard-dose and 50% reduced-dose abdominal CT: effect on image quality. AJR Am J Roentgenol 179(5):1101–1106
Kambadakone AR, Prakash P, Hahn PF et al (2010) Low-dose CT examinations in Crohn's disease: impact on image quality, diagnostic performance, and radiation dose. AJR Am J Roentgenol 195(1):78–88
Kelvin FM, Herlinger H (1999) Crohn's disease. In: Herlinger H, Maglinte DDT, Birnbaum BA (eds) Clinical imaging of the small intestine. Springer, Berlin, pp 259–289
Kerr JM (2008) Small bowel imaging: CT enteroclysis or barium enteroclysis? Critically appraised topic. Abdom Imaging 33(1):31–33
Kim YH, Blake MA, Harisinghani MG et al (2006) Adult intestinal intussusception: CT appearances and identification of a causative lead point. Radiographics 26:733–744
Macari M, Balthazar EJ (2001) CT of bowel wall thickening: significance and pitfalls of interpretation. AJR 176: 1105–1116
Macari M, Chandarana H, Balthazar EJ et al (2003) Intestinal ischemia versus intramural hemorrhage: CT evaluation. AJR 180:177–184
Macari M, Megibow AJ, Balthazar EJ (2007) A pattern approach to the abnormal small bowel: observations at MDCT and CT enterography. AJR 188:1344–1355
Mackalski BA, Bernstein CN (2006) New diagnostic imaging tools for inflammatory bowel disease. Gut 55:733–741
Madureira AJ (2004) The Comb Sign. Radiology 230:783–784
Maglinte DD, Chernish SM, Bessette J et al (1991) Factors in the diagnostic delays of small bowel malignancy. Indiana Med 84(6):392–396
Maglinte DD, Siegelman ES, Kelvin FM (2000) MR enteroclysis: the future of small-bowel imaging? Radiology 215:639–641
Maglinte DD, Gourtsoyiannis N, Rex D et al (2003) Classification of small bowel Crohn's subtypes based on multimodality imaging. Radiol Clin North Am 41:285–303
Maglinte DD, Sandrasegaran K, Lappas JC et al (2007) CT enteroclysis. Radiology 245:661–671
Mako EK, Mester AR et al (2000) Enteroclysis and spiral CT examination in diagnosis and evaluation of small bowel Crohn's disease. Eur J Radiol 35:168–175
Marmo R, Rotondano G, Piscopo R et al (2005) Meta-analysis: capsule enteroscopy vs conventional modalities in diagnosis of small bowel diseases. Aliment Pharmacol Ther 22:595–604
McCollough CH, Bruesewitz MR, Kofler JM Jr (2006) CT dose reduction and dose management tools: overview of available options. Radiographics 26:503–512
McCollough CH, Primak AN, Braun N et al (2009) Strategies for reducing radiation dose in CT. Radiol Clin North Am 47:27–40
Migleddu V, Quaia E, Scano D et al (2008) Inflammatory activity in Crohn's disease: ultrasound findings. Abdom Imaging 33:589–597
Minardi AJ Jr, Zibari GB, Aultman DF et al (1998) Small-bowel tumours. J Am Coll Surg 186(6):664–668
Minordi LM, Vecchioli A, Guidi L et al (2006) Multidetector CT enteroclysis versus barium enteroclysis with methylcellulose in patients with suspected small bowel disease. Eur Radiol 16:1527–1536
Minordi LM, Vecchioli A, Guidi L et al (2009) CT findings and clinical activity in Crohn's disease. Clin Imaging 33:123–129
Minordi LM, Vecchioli A, Mirk P et al (2011) CT enterography with polyethylene glycol solution vs CT enteroclysis in small bowel disease. Br J Radiol 84(998):112–119
Negaard A, Paulsen V, Sandvik L et al (2007) A prospective randomized comparison between two MRI studies of the small bowel in Crohn's disease, the oral contrast method and MR enteroclysis. Eur Radiol 17:2294–2301
North JH, Pack MS (2000) Malignant tumours of the small intestine: a review of 144 cases. Am Surg 66(1):46–51
Ott DJ, Chen YM, Gelfand DW et al (1985) Detailed per-oral small bowel examination vs. enteroclysis. Part II: radiographic accuracy. Radiology 155:31–34
Patak MA, Mortele KJ, Ros PR (2005). Multidetector row CT of the small bowel. Radiol Clin North Am 43:1063–1077
Paulsen S, Huprich J, Fletcher JG et al (2006) CT enterography as a diagnostic tool in evaluating small bowel disorders: review of clinical experience with over 700 cases. Radiographics 26:641–662
Rajesh A, Maglinte DD (2006) Multislice CT enteroclysis: technique and clinical applications. Clin Radiol 61(1):31–39
Ramachandran I, Sinha R, Rajesh A et al (2007) Multidetector row CT of small bowel tumours. Clin Radiol 62(7):607–614
Schindera ST, Nelson RC, DeLong DM et al (2007) Multi-detector row CT of the small bowel: peak enhancement temporal window–initial experience. Radiology 243(2):438–444
Schreyer AG, Geissler A, Albrich H et al (2004) Abdominal MRI after enteroclysis or with oral contrast in patients with suspected or proven Crohn's disease. Clin Gastroenterol Hepatol 2:491–497
Schreyer AG, Hoffstetter P, Daneschnejad M et al (2010) Comparison of conventional abdominal CT with MR-enterography in patients with active Crohn's disease and acute abdominal pain. Acad Radiol 17(3):352–357

Silva AC, Lawder HJ, Hara A et al (2010) Innovations in CT dose reduction strategy: application of the adaptive statistical iterative reconstruction algorithm. AJR Am J Roentgenol 194(1):191–199

Soyer P, Boudiaf M, Dray X et al (2009) CT enteroclysis features of uncomplicated celiac disease: retrospective analysis of 44 patients. Radiology 253(2):416–424

Tomei E, Marini M, Messineo D et al (2000) Computer tomography of the small bowel in adult celiac disease: the jejunoileal fold pattern reversal. Eur Radiol 10:119–122

Tomei E, Diacinti D, Marini M et al (2005) Abdominal CT findings may suggest coeliac disease. Dig Liver Dis 37:402–406

Turetschek K, Schober E, Wunderbaldinger P et al (2002) Findings at helical CT-enteroclysis in symptomatic patients with Crohn disease: correlation with endoscopic and surgical findings. J Comput Assist Tomogr 26:488–492

Weskott HP (2008) Emerging roles for contrast-enhanced ultrasound. Clin Hemorheol Microcirc 40:51–71

Winter TC, Ager JD, Nghiem HV et al (1996) Upper gastrointestinal tract and abdomen: water as an orally administered contrast agent for helical CT. Radiology 201(2):365–370

Wold PB, Fletcher JG, Johnson CD et al (2003) Assessment of small bowel Crohn disease: noninvasive peroral CT enterography compared with other imaging methods and endoscopy—feasibility study. Radiology 229:275–281

Zissin R, Hertz M, Bernheim J et al (2004) Small bowel obstruction secondary to Crohn disease: CT findings. Abdom Imaging 29:320–325

MSCT of the Abdomen: Colon, Rectum and CT Colonography

Emanuele Neri, Annalisa Mantarro, Rossella Scandiffio, Pietro Bemi, Lorenzo Faggioni, and Carlo Bartolozzi

Contents

Abstract

The advent of MSCT represented a real turning point in the field of CT image acquisition and processing, particularly because of the innovative volumetric study by three-dimensional images. MSCT holds several advantages as compared with single-slice spiral CT. Indeed it allows to drastically reduce the scan time, motion artifacts (i.e., vascular pulse, breathing, peristalsis), radiation exposure, and intravenous dose of contrast medium, while yielding, at the same time, higher spatial resolution. An important application of MSCT concerns the assessment of colon. In particular, the advent and wide spread of CT colonography has resulted in a substantial favorable impact on the diagnostic approach to polypoid lesions and colorectal cancer. This chapter aims to review the most important imaging findings of CT imaging of the colon including CT-colonography and describes the current standards of acquisition techniques and image interpretation.

1 Introdution

The advent of Multislice Computed Tomography (MSCT) in 1998 represented a real turning point in the field of CT image acquisition and processing, particularly because of the innovative volumetric study by three-dimensional images. MSCT holds several advantages as compared with single-slice spiral CT. Indeed it allows to drastically reduce the scan time, motion artifacts (i.e., vascular pulse, breathing, peristalsis), radiation exposure, and intravenous dose of contrast

E. Neri (✉) · A. Mantarro · R. Scandiffio · P. Bemi · L. Faggioni · C. Bartolozzi
Diagnostic and Interventional Radiology,
University of Pisa, Via Roma 67,
56100 Pisa, Italy
e-mail: emanuele.neri@med.unipi.it

C. J. Zech et al. (eds.), *Multislice-CT of the Abdomen*, Medical Radiology. Diagnostic Imaging,
DOI: 10.1007/174_2012_539, © Springer-Verlag Berlin Heidelberg 2012

medium, while yielding, at the same time, higher spatial resolution (Marin et al. 2010). Thin section acquisitions by MSCT allows to produce three-dimensional isotropic images by means of post-processing techniques, which mostly used are multiplanar reformations (MPR), maximum intensity projections (MIP), and volume renderings (VR) (Cahir et al. 2004; Aschoff 2006).

The application of MSCT to abdominal evaluation has provided significant improvements, with particular regard for the characterization of neoplastic lesions, the non-invasive depiction of vascular structures, including small caliber vascular branches, and the management of polytraumatized patients with abdominal injuries.

An important application of MSCT concerns the assessment of colon. In particular, the advent and wide spread of CT colonography has resulted in a substantial favorable impact on the diagnostic approach to polypoid lesions and colorectal cancer. The major advantage offered by MSCT consists of the simultaneous evaluation of bowel wall and extra-luminal compartment, including the adjacent structures and parenchymal organs. By contrast, conventional radiology (i.e., double-contrast barium enema) and endoscopy, while enabling an accurate assessment of the mucosal layer, can provide only indirect signs ascribable to a possible involvement of colonic wall and adjacent structures.

2 MSCT of the Colon: Technical Approach

An optimal CT study of the colon should be primarily preceded by an adequate patient preparation (cathartics and low residue diet), in order to ensure the bowel cleansing. In addition, a detailed colon evaluation requires a preliminary intestinal distension, thus enhancing the contrast between bowel wall and lumen and preventing the loops from collapsing. Bowel filling and distension can be achieved by means of different contrast media (positive or negative), which can be administered per os or enema, depending on on-site protocols and requirements of individual patients. Positive contrasts, such as diatrizoate meglumine and diatrizoate sodium solution (Gastrografin), are employed to differentiate bowel loops from eventual extra-colonic masses as well as to assess complications (e.g., peritoneal collections, fistulous tracts, anastomotic dehiscences, or bowel perforations). Negative contrasts can be grouped into liquids (water, isotonic solutions, methylcellulose), used mainly for colonic wall assessment, and gaseous (room air or carbon dioxide), mostly for the evaluation of the mucosal layer and colonic wall. Negative contrast media (water or gas) are usually preferred over positive ones, as the former do not interfere with three-dimensional image performing and post-processing (i.e., CT angiography and CT colonography) (Horton et al. 2000a). However, the decision about the type of contrast medium to employ is basically driven by the clinical query.

The procedure that, over several past years, has allowed to investigate the colon is represented by water enema CT (WE-CT). This is a simple and safe examination, characterized by a good patient's tolerance and compliance, which ensures an accurate evaluation of the gut wall and pericolonic structures. (Ridereau-Zins et al. 2010; Gossios et al. 1992; Gazelle et al. 1995). Approximately 15 min before the enema, intramuscular or intravenous Buscopan administration (scopolamine butyl-bromide, 20 mg) is recommended, in order to relax the bowel wall, reduce the peristaltic motility, delay evacuative urgency, and improve colon coverage by the contrast medium and patient's tolerance. Subsequently, a certain amount of water (about 2 l) is introduced into the colon through a rectal probe, thus ensuring a complete coverage of the whole colon.

The intravenous administration of iodinated contrast medium is essential to complete the study, particularly for the assessment of neoplastic, inflammatory, and vascular disorders.

The enhancement of gut wall allows to identify possible abnormalities, to characterize them, according to the contrast medium behavior, and to stage malignancies. On routine abdominal CT, general image acquisitions are carried out at baseline, and then after an intravenous bolus of iodinated contrast medium (about 100–130 ml infused at a rate of 3–4 ml/s). According to the clinical query, the most appropriate protocol must be chosen. The monophasic protocol is accomplished by a single acquisition during the portovenous phase (50–70 s delay), while the biphasic one consists of an arterial phase after 30 s, and a venous phase with a scanning delay of 70 s. The axial reconstruction interval is at 2.5/5 mm, with retro-reconstruction at 1.25/0.625 mm. The scanning volume extends from the diaphragm to the symphysis pubis. Notably, image acquisitions in both supine and prone positions allow to shift colonic fluid,

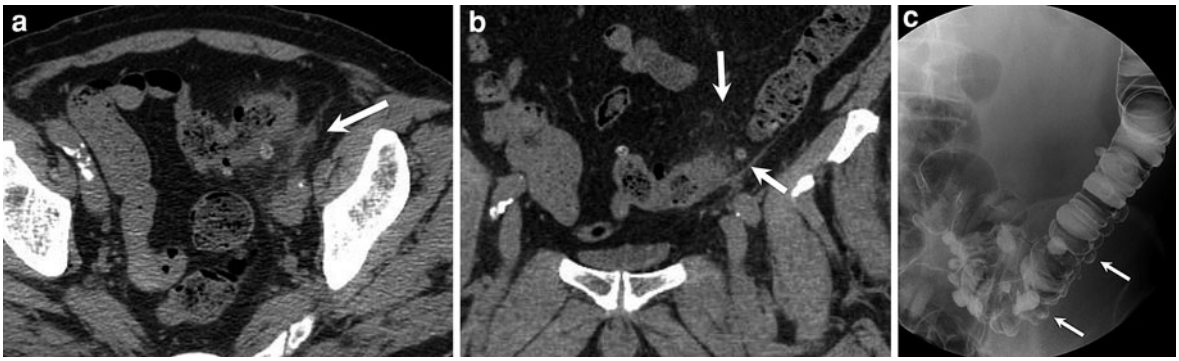

Fig. 1 Unenhanced MSCT shows wall thickening of descending and sigmoid colon (*arrows*) with multiple diverticula and contiguous fat stranding, ascribable to peri-diverticulitis. **a** Axial view. **b** Coronal MPR view. **c** Double-contrast barium enema shows diverticular outpouchings of the descending and sigmoid colon

which may obscure the underlying lesions, and to identify fecal material by demonstrating its mobility (Horton et al. 2000a).

3 MSCT in Emergency

MSCT plays a major role in the management of emergency conditions, such as acute diverticulitis, bowel obstruction, gastrointestinal bleeding, and ischemic bowel disease.

3.1 Diverticulitis

Colonic diverticula are very common findings in elderly patients. They vary in size (from 2 mm up to 2 cm), are located most frequently in the sigmoid, and consist of small outpouchings of both colonic mucosal and submucosal layers through the muscular layers of the enteric wall (Horton et al. 2000b).

Acute diverticulitis arises as a consequence of obstruction of the diverticular lumen by stools and food residues. Such an obstruction facilitates bacterial overgrowth, which then triggers an inflammatory response that tends to spread towards the surrounding tissues (peri-diverticulitis), thus promoting the onset of complications, such as confined perforation, with subsequent abscess formation and possible occurrence of bleeding, fistulas, strictures, and pneumo-peritoneum.

The CT findings ascribable to diverticulitis include the presence of diverticula, wall thickening, and adjacent fat stranding (Fig. 1). MSCT represents the first line procedure in cases of suspected acute diverticulitis as well as in the detection of complications, allowing a better definition of the abscess extension, the involvement of surrounding tissues, and the visualization of fistulous tracts.

MPR and 3D reconstructions provide images of high quality, which are quite useful for planning adequate therapeutic strategies (Werner et al. 2003). The current literature supports the notion that, in patients with suspected acute diverticulitis, low-dose unenhanced MSCT displays a similar diagnostic performance as compared with contrast-enhanced standard-dose MSCT (Tack et al. 2005).

In some instances, colonic cancer and diverticulitis can yield similar CT patterns. In such a circumstance, the differential diagnosis is based on the length of colonic involvement and the presence of diverticula or in the detection of a luminal mass with pericolic lymph nodes. However, in more difficult cases, where these diagnostic criteria might not be sufficient, CT perfusion measurements could enable the differentiation and a better discrimination between cancer and diverticulitis. Perfusion CT with dynamic contrast enhancement allows the quantitative measurement of tissue perfusion, and thus of tissue vascularity. On this ground, patients with cancer display the highest blood volume, blood flow, and permeability in concomitance with the shortest transit time (Goh et al. 2007).

3.2 Bowel Obstruction

Bowel obstruction is one of the most frequent and insidious clinical conditions in the emergency room, giving rise to a large degree of perplexity in the

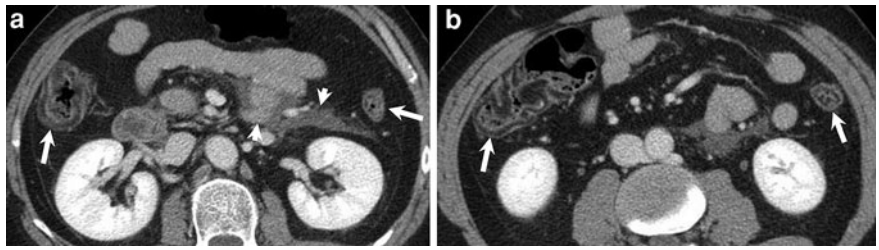

Fig. 2 MSCT in a patient with acute pancreatitis associated with ischemic colitis—thickening of the pancreatic tail with peripancreatic fluid collections (*arrow heads*) (**a**)—"target sign" in the ascending and descending colon (**a** and **b**) due to fatinfiltration caused by colitis

therapeutic management. Small bowel is the most frequently involved site. However, any bowel segment can be affected. Various causes can account for the onset of bowel obstruction, including adhesion, neoplasm, hernia, intussusception, volvulus, inflammatory disease, fecal impaction, phytobezoar, trauma, ischemia, and congenital lesion (Ji et al. 2009).

MSCT shows with high accuracy the presence and site of obstruction, which consists of a compressed bowel segment (transition zone), bound by dilated loops upstream and by collapsed loops downstream. In addition, MSCT can assess the degree and extent of intestinal obstruction, thus helping to better identify the underlying cause (Angelelli et al. 2010).

The image reconstruction techniques allow to display in detail the site of obstruction and its characteristics, particularly in ambiguous cases, along with an early diagnosis of obstructive complications (strangulation and bowel ischemia). MSCT performs better than single-slice CT (SSCT) both in the evaluation of bowel obstruction and in the detection of intestinal necrosis, edema, twisting, and/or thickening of mesenteric vessels (Assenza et al. 2007). MSCT also provides useful information for prognosis, since the presence of air or fluid intestinal content is related with a better outcome. By contrast, the visualization of air fluid levels and/or the evidence of pneumatosis is predictive of a poor prognosis (Angelelli et al. 2010). In addition, MSCT scanning is essential to set up an adequate treatment plan and a correct surgical timing.

3.3 Bowel Ischemia

Mesenteric ischemia is a very threatening pathological condition, characterized by a severe impairment of arterial or venous blood flow. It can be distinguished into an acute and chronic form. The causes underlying acute ischemia include: mesenteric arterial obstruction (thrombosis or embolism); mesenteric venous thrombosis related to thrombophilia, portal hypertension, extrinsic compression, or surgery; non-occlusive ischemia associated with sepsis, hypotension, heart failure, familial dysautonomic syndrome, or pheochromocytoma (Woodward et al. 1998). Acute bowel ischemia is a disorder most frequently associated with high mortality, and it is clinically characterized by a number of both specific and nonspecific symptoms, which can make the diagnosis quite difficult (Wiesner et al. 2003). Instead, chronic mesenteric ischemia results mainly from atherosclerotic stenosis, thrombo-embolism, or extrinsic compression.

The introduction of MSCT has largely changed the diagnostic approach to mesenteric ischemia, with a strong impact on both prognosis and therapeutic management. Typical CT findings include the presence of vascular occlusion, portal or mesenteric vein gas, pneumatosis, bowel wall thickening with decreased or absent wall-enhancement; the so-called "target sign" (typical of other inflammatory conditions), can also be appreciated (Fig. 2), (Moschetta 2009; Chen et al. 2006).

MSCT angiography allows a non-invasive study of the mesenteric vascular system, yielding results which are comparable to angiography, owing to its ability to accurately identify the site of vascular occlusion by means of post-processing techniques, which will be useful to plan endovascular immediate treatment (Kirkpatrick et al. 2003; Cademartiri et al. 2008).

3.4 Gastrointestinal Bleeding

Gastrointestinal bleeding is an emergency condition, burdened by high mortality (up to 40%) particularly in hemodynamically unstable patients. It can be classified into acute and chronic forms, as well as in upper or lower bleeding, depending on whether

the bleeding source is located proximally or distally to the ligament of Treitz (Jaeckle et al. 2008). Gastrointestinal bleeding can result from a variety of causes, including polyps, malignancies, inflammatory diseases, pseudo-aneurysms, varices, and diverticula. Before starting the diagnostic procedures and adequate therapeutic approaches, it is mandatory to stabilize the patient's vital signs (Scheffel et al. 2007). A wide range of diagnostic procedures is available for detecting intestinal bleeding, such as endoscopy, $_{99m}$Tc-red blood cell (RBC) scintigraphy, or conventional arteriography (Jaeckle et al. 2008; Scheffel et al. 2007; Tew et al. 2004).

MSCT plays a pivotal role in the diagnosis of gastrointestinal bleeding, since, in most cases, it allows to identify the underlying cause and bleeding source, even in bowel segments which can be difficult to access and explore by means of endoscopy (e.g., small bowel loops) (Lim et al. 2006; Duchat et al. 2010). In cases of suspected gastrointestinal bleeding, MSCT study does not require any oral administration of contrast medium or water, which might interfere with the diagnosis (Scheffel et al. 2007). Unenhanced CT scans can display the presence of hyperdense material within the bowel lumen, indicating a condition of ongoing bleeding. The arterial phase could demonstrate contrast medium extravasation, ascribable to acute bleeding, through a fast and non-invasive approach. Furthermore, the portal-venous phase improves the accuracy of detection and localization of the bleeding sites, particularly in patients with bowel tumors (Yoon et al. 2006).

MSCT is usually performed in the setting of emergency, as a preliminary study, in order to guide the interventional procedure (angiography and embolization), thanks to high resolution images, MPR, and MIP reformations (Duchat et al. 2010).

4 MSCT Under Elective Conditions

4.1 Inflammatory Bowel Disease

Acute intestinal inflammations are characterized mainly by a modest and fairly reversible mucosal edema, associated with an enhanced tissue perfusion, which usually does not require a CT study. By contrast, chronic inflammatory diseases determine bowel alterations, which deserve an accurate CT assessment in order to define the affected site, the extension, and the occurrence of complications. In this context, the term "inflammatory bowel disease" (IBD) refers mainly to two specific forms of chronic inflammatory disorders, designated as 'Crohn's disease' and 'ulcerative colitis'. Both conditions are idiopathic inflammatory diseases of unknown etiologic origin, which display distinct features (Viscido et al. 2005).

4.1.1 Crohn's Disease

Crohn's disease is a chronic granulomatous disorder, consisting of a transmural inflammatory process, with possible extensions towards the surrounding perienteric fat and mesentery. It can involve any segment of the gastrointestinal tract, although the terminal ileum and proximal colon are most frequently affected.

Based on symptoms, Crohn's Disease Activity Index (CDAI), endoscopic evaluations, and CT/MRI findings, Crohn's disease can clinically present as acute or chronic disease. Active flares are characterized by the appearance of focal granulomatous inflammation, enlarged lymphoid follicles, and aphtoid ulcers. In this setting, the inflammatory process tends to affect transmurally the whole thickness of bowel wall, as well as to involve the surrounding tissues, leading to the onset of complications such as fistulas, abscessual collections, and phlegmons. Chronic phases are characterized by a persistent desmoplastic reaction, resulting in fibrosis, adhesions, and luminal stenosis (Gore et al. 1996).

Since terminal ileum is the most frequently involved bowel segment, CT-enteroclysis represents the most suitable imaging method to evaluate this gut region. Following adequate patient's preparation (8–12 h fasting before examination, low-residue diet, and cathartics) and intravenous administration of Buscopan® (scopolamine butylbromide, 20 mg) or, if contraindicated, Glucagon (1 mg), the enteral contrast medium (neutral or positive) is introduced into the gut lumen through a naso-jejunal tube. Neutral opacification (by means of polyethylenglycol, methylcellulose, or water) allows a good small bowel distension and depiction of the contrast-enhanced mucosal layer, which highly contrasts with the hypodense lumen (Schmidt et al. 2006; Lo Re et al. 2007). Instead, positive contrast medium (i.e., a iodinated hydrosoluble agent) is used to identify bowel fistulas or leakages, without the aid of intravenous contrast enhancement. CT-enterography, following oral

hyperhydration with isotonic solution, is a suitable alternative for patients not accepting naso-jejunal intubation (Lo Re et al. 2007). As compared to SDCT, MDCT improves the accuracy and depiction of the pathological patterns of Crohn's disease by means of a better spatial resolution (Minordi et al. 2007).

Typical CT findings of the acute phase include: segmental and concentric bowel wall thickening (11–13 mm), with marked contrast enhancement, and mural stratification characterized by the "double halo" or "target" sign (i.e., the mucosa and muscularis propria appear hyperdense and delimit a low density internal layer, corresponding to the submucosal edema) (Ahualli 2005). Other signs consist of reactive mesenteric hypervascularity with enlarged diameters of the vasa recta ("comb sign"), inflammatory involvement and hyperdensity of the mesenteric adipose tissue, and enlarged limph nodes with increased contrast enhancement (Madureira 2004). Instead, the appearance of the chronic form is characterized by mild wall thickening and diffuse parietal contrast enhancement without mural stratification, indicating a condition of irreversible transmural fibrosis (Schmidt et al. 2006). Moreover, MSCT allows to accurately evaluate complications, such as fistulas, abscesses, phlegmons, strictures, and conglomerate bowel loops (Nagamata et al. 2002) (Fig. 3).

4.1.2 Ulcerative Colitis

Ulcerative colitis is a chronic inflammatory disease which involves primarily the mucosa of large bowel, although, in its advanced stage, can extend to all layers of the bowel wall. This disease is characterized by a chronic and progressive involvement of the rectum, resulting in a retrograde spreading up to the cecum (pancolitis) (Di Sabatino et al. 2011). The highest incidence of ulcerative colitis has been recorded in highly urbanized Western countries, mainly North Europe and North America, and it can affect several members within the same family (Roggeveen et al. 2006; Orholm et al. 1991). The etiology of ulcerative colitis remains unknown, but it has been found to depend on genetic, immunologic (abnormal immune response of bowel mucosa to resident gut flora), and environmental factors (oral contraceptives, non-steroidal anti-inflammatory drugs, dietary sugar intake, breastfeeding, and perinatal paramyxoviral infections). Protective factors include appendectomy and smoking, although former smokers hold a higher risk than non-smokers (Di Sabatino et al. 2011; Roggeveen et al. 2006; Orholm et al. 1991; Boyko et al. 1988). As anticipated above for Crohn's Disease, ulcerative colitis too can be distinguished into acute and chronic forms. The active phase of the disease is characterized by superficial ulcers with ragged and undetermined margins, immune cell infiltration, and cryptic abscesses. The chronic form results instead in parietal fibrosis associated with stiffness, stenosis, and pseudopolyposis, ascribable to persistent abnormal stimuli to mucosal regeneration. In addition, ulcerative colitis is associated with several complications such as perforation, peritonitis, toxic megacolon, venous thrombosis, and increased susceptibility to colorectal carcinoma, due to chronic inflammation and persistent proliferative rearrangement of the colonic mucosa (Lefèvre et al. 2011; Lakatos and Lakatos 2008).

Toxic megacolon is a very threatening complication associated with IBD, due to spreading of the inflammatory process through the whole thickness of the bowel wall. This complication occurs particularly in patients with severe or fulminant ulcerative colitis. It is characterized by a marked colonic dilatation (>5.5 cm in the transverse colon), wall thinning, pneumatosis, and increased risk of perforation (Autenrieth and Baumgart 2011).

As for Crohn's disease, the symptoms of ulcerative colitis are nonspecific in nature, and consist mainly in diarrhea, tenesmus, urgency to defecation, rectal bleeding, weight loss, fever, and abdominal pain (Patel et al. 2011). In this context, the diagnostic approach takes advantage by the combination of optical colonoscopy, histopathological analysis, and radiological examinations. MSCT allows to evaluate the intramural extension of ulcerative colitis with high accuracy and sensitivity, particularly when colonoscopy or barium enema are contraindicated (e.g., severe colitis) (Roggeveen et al. 2006). Furthermore, MSCT plays a pivotal role in the detection of extra-intestinal manifestations and complications, which is useful to plan therapeutic managements, as well as to assess treatment response and prognosis (Patel et al. 2011; Bitterling et al. 2003; Lefèvre et al. 2011). Specific CT findings in the acute phase include circular and symmetric wall thickening (about 7.8 mm), ulcers, enlarged lymph nodes, mucosal hyperenhancement, reflecting a hyperemic and

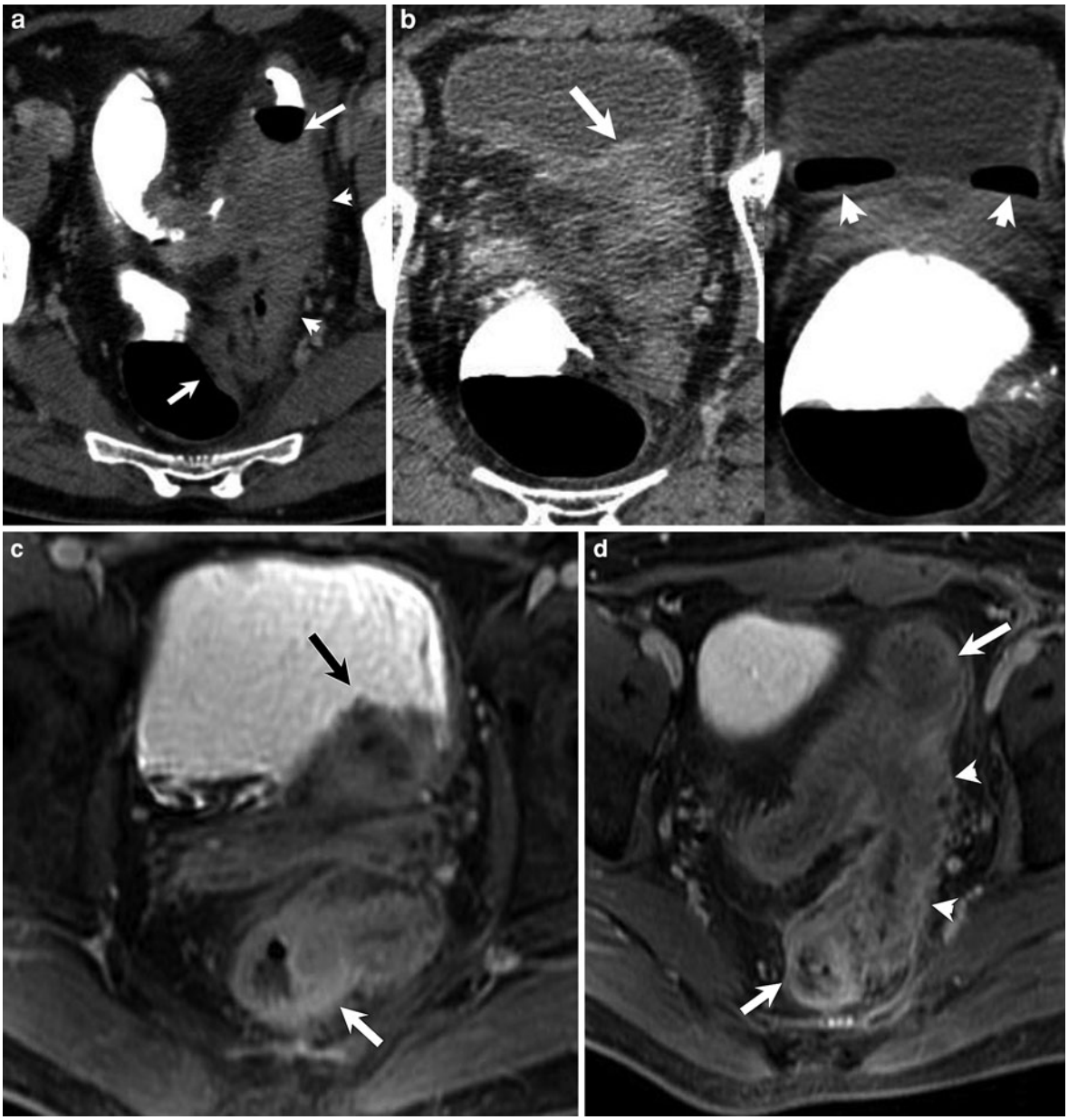

Fig. 3 Pelvic abscess in Crohn's disease with rectum-sigmoid and rectum-bladder fistulas. Prone MSCT scan obtained after rectal enema by water mixed with Gastrografin. **a** Large abscess (*arrow heads*), containing gas bubbles and fistulized with sigmoid colon and rectum (*arrows*). **b** Air-fluidlevel (*arrow heads*) and thickening of the posterior wall of the bladder due to the fistula with the pelvic abscess. Nodular thickening of the left lateral wall of the rectum due to the rectum-sigmoid fistula (*arrow*). **c** Axial contrast-enhanced GRE at 3T MRI demonstrates the large abscess (*arrow heads*) fistulized with sigmoid colon and rectum (*arrows*). **d** As with MSCT, MRI shows the nodular thickening of the left lateral wall of the rectum and the posterior wall of the bladder (*arrows*)

hypervascular conditions, and mural stratification with "double halo" or "target" sign, which can be found more frequently than in Crohn's disease (Horton et al. 2000b).

As far as the chronic phase is concerned, it is hallmarked by thickening of mesenteric and retroperitoneal fat, widening of the pre-sacral space, due to mural thickening and proliferation of peri-rectal fat, loss of

austrature, and rectal luminal narrowing up to a condition of stenosis (Patel et al. 2011).

4.2 Appendicitis

Acute appendicitis has higher incidence in children and young adults, and in order to avoid complications it requires early detection and most frequently abdominal surgery (Horton et al. 2000b). The main causes of this inflammatory process are lymphoid hyperplasia and/or appendiceal lumen obstruction by fecal material.

Typical clinical signs and symptoms include periumbilical or right lower quadrant pain, abdominal cramps, nausea, vomiting, point tenderness in the right lower quadrant, rebound tenderness, leukocytosis and fever. However, in a third of cases the acute appendicitis occurs with atypical signs. This may result in a delayed diagnosis with the appearance of severe complications, such as appendiceal perforation, abscess formation, peritonitis, sepsis, bowel obstruction, and death (Sivit et al. 2001). Among various available clinical scoring systems employed to diagnose acute appendicitis, the most widely used is the Alvorado score, which is characterized by 10 components (Table 1).

Nevertheless, in suspected cases of acute appendicitis associated with atypical symptoms and uncertain diagnosis, radiological examinations (i.e., US and CT) should be used (Yildirim et al. 2008).

MSCT provides a rapid and accurate identification and staging of appendicitis also in suspected cases or in those with negative ultrasonographic findings, thanks to the thin-slice acquisition and MPR reconstructions (Johnson et al. 2009).

Typical CT findings include distended appendix (diameter > 7 mm), with a thickened wall characterized by homogeneous enhancement after intravenous contrast media administration, periappendiceal fat stranding, an appendicolith, and circumferential or focal thickening of the cecum. The identification of an appendicolith without other inflammation signs is not indicative of appendicitis. The presence of extraluminal air or rarely pneumoperitoneum is suggestive for appendiceal perforation; while an abscess appears as peri-appendiceal fluid collections that may contain air or necrotic debris surrounded by inflammatory changes (Horton et al. 2000b; Sivit et al. 2001; Kim et al. 2008).

Table 1 Alvorado score

Clinical findings	Score
Migration of pain	1
Anorexia	1
Nausea/vomiting	1
Tenderness in right iliac fossa	1
Rebound pain	1
Elevated temperature (>37.3°C)	1
Leucocyte count $\geq 10 \times 109$/L	1
Differential white cell count with neutrophils $> 75\%$	1
Total	10

4.3 Colorectal Cancer

Colorectal cancer (CRC) is the third neoplasm, in terms of incidence and mortality, in the world (American Cancer Society 2011). This malignant disease occurs more frequently in industrialized countries, and has a great relevance both from a social and healthcare standpoint. CRC develops rarely before the age of 40, and the majority of cases are diagnosed after 50 years. The incidence of CRC is slightly higher in males than in females, with particular regard for rectal carcinoma (Gao et al. 2008). Although the aetiology of CRC remains unknown, there is evidence that its onset is promoted by a variety of environmental factors (e.g., Western-type diet, characterized by low-fibre and high-fat content, smoke, alcohol abuse, metabolic syndrome) and genetic determinants (familiarity, hereditary syndromes) (Liu et al. 2011; McKeown-Eyssen 1994).

Among African populations, the incidence of CRC is significantly lower than in Western Countries, likely as a consequence of higher fruit and vegetable intake by the former. Moreover, it has been observed that immigrants to industrialized countries tend to acquire the same CRC incidence rates of the host country, thus supporting the contention that

geographic differences in CRC incidence depend more on dietary habits than on different genetic patterns.

Hereditary syndromes can be distinguished into polyposis and non-polyposis CRC:

1. Familiar adenomatous polyposis (FAP): this is a rare autosomal dominant disorder characterized by the presence of hundreds or thousands of adenomatous polyps in the large bowel. It is associated with a deletion in the long arm of chromosome 5, which contains also the APC oncosuppressor gene (Curia et al. 2011; Scholer-Dahirel et al. 2011). In this setting, CRC develops in almost all affected patients under the age of 40 years. There is a classic form of FAP, in which patients typically harbor between 500 and 2500 colonic adenomas, as well as an attenuated form, characterized by a lower number of polyps (typically 30) that are predominantly located in the proximal colon.
2. Gardner syndrome: it is characterized by a combination of intestinal polyposis (identical to those developing in subjects with FAP) with several osteomas, epidermal cysts and fibromatosis, as well as thyroid and duodenal carcinomas (Juhn and Khachemoune 2010; Brucoli et al. 2011).
3. Turcot syndrome: this is a rare condition characterized by the association of FAP with tumors of the central nervous system (such as medulloblastoma and glyoblastoma) (Hegde et al. 2005).
4. Hereditary Non-Polyposis Colorectal Cancer (HNPCC, also known as Lynch syndrome): it is an autosomal-dominant inherited cancer syndrome. This disease is associated with mutations in the germinal line of various genes (in particular, MSH2, MLH1, PMS, and PMS2), which cause instability of microsatellite DNA and impaired mismatch repair, leading to increased DNA instability and increased risk of cancer development (Kaur et al. 2011). There is also a strong association between endometrial and ovarian carcinoma and HNPCC (Backes and Cohn 2011). In HNPCC patients, CRC occurs typically at an age younger than 50 years, and it is more frequently localized in the cecum or ascending colon.

Moreover, CRC has been shown to develop with higher incidence in patients with Chronic Inflammatory Bowel Diseases (CIBD) ulcerative colitis, due to a condition of chronic inflammation and persistent proliferative rearrangement of colonic mucosa. In this setting, the continuous generation of free oxygen radicals leads to the dysregulation of important oncogenes and onco-suppressors, thus promoting the onset of CRC (Rizzo et al. 2011).

The prognosis and treatment of CRC is strictly driven by histopathological findings. The most common histological type of CRC is represented by adenocarcinoma, followed by carcinoid, small cell carcinoma, anaplastic carcinoma, epidermoid carcinoma, sarcoma, and rarely, lymphoma. Adenocarcinomas often arise from the neoplastic transformation of benign adenomatous polyps, and are located mainly in the rectum and sigmoid colon (Stewart et al. 2006). In addition, adenocarcinomas may present as vegetating masses, affecting mainly the right colon, or as a ring-stenosing lesions, which are frequent in the left colon and result from the circumferential spread of tumor within the lymphatic vessels of the inner circular layer of the muscularis propria. Other rare forms of growth include saddle lesions, ulcerating masses and infiltrating tumors.

The clinical appearance of CRC depends mostly on the location and size of the tumor. In this respect, the vegetating forms tend to be silent in their early stages, while, when they become clinically evident, their size is usually very large and distant metastases has already occurred. By contrast, the stenosing forms usually present with sub-occlusive symptoms in their early stages. The most common clinical symptoms of CRC include: asthenia, iron deficiency anemia, abdominal pain, change in bowel habits, and bowel sub-obstruction (Buetow et al. 1995).

The diagnosis of CRC is aided by TNM classification (tumor, node, metastasis), issued by the American Joint Committee on Cancer (AJCC), which is a worldwide used system for CRC staging and has almost completely replaced the previous Duke's classification (Table 2).

The advent of MSCT has significantly improved the accuracy in both detection and staging of CRC, by virtue of the high quality and spatial resolution of acquired images. On CT scan, vegetating tumors appear as soft-tissue intraluminal masses, sometimes with a hypodense central area, due to necrosis, associated with narrowing of the bowel lumen. By contrast, the typical CT signs of anular-stenosing CRC forms consist of irregular and asymmetric colonic wall thickening, either focal or circumferential in

Table 2 TNM staging system for colorectal cancer

Stage	Definition
Primary tumor (T)	
TX	Primary tumor cannot be assessed
T0	No evidence of primary tumor
Tis	Carcinoma in situ: intraepithelial or invasion of lamina propria
T1	Tumor invades submucosa
T2	Tumor invades muscularis propria
T3	Tumor invades through the muscularis propria into the subserosa, or into non-peritonealized pericolic or perirectal tissues
T4	Tumor directly invades other organs or structures, and/or perforates visceral peritoneum
Regional lymph nodes (N)	
NX	Regional lymph nodes cannot be assessed
N0	No regional lymph node metastasis
N1	Metastases in 1–3 regional lymph nodes
N2	Metastases in 4 or more regional lymph nodes
Distant metastasis (M)	
MX	Distant metastasis cannot be assessed
M0	No distant metastasis
M1	Distant metastasis

nature, characterized by contrast enhancement, with bowel lumen stenosis and subsequent dilation of the upstream intestinal tract (Horton et al. 2000a).

Preoperative CT staging represents a valuable method both to evaluate the loco-regional and distant tumor extension, as well as to plan surgery and/or neo-adjuvant therapy (Shin et al. 2008). Despite CT limitations in discriminating between T1 and T2, multiplanar reconstruction (MPR) images allow a detailed assessment of extra-mural, lymph node, and adjacent structures involvement, as well as the detection of complications (i.e., bowel perforation, obstruction, intussusception, and fistulization). MSCT represents also the modality of choice for local recurrence detection after surgical resection, and it is widely employed for post-operative follow-up (Horton et al. 2000a).

As far as the staging of rectal cancer is concerned, the most preferred procedure is based on the performance of a multi-modal study, which includes MSCT, transrectal ultrasound (TRUS), and magnetic resonance imaging (MRI).

TRUS is the most accurate tool to distinguish T1 from T2, and to evaluate the perirectal spread of the tumor (T3). However, this method is of limited value for assessing the involvement of mesorectum and mesorectal fascia (MRF) (Ahmetoğlu et al. 2011). On the other hand, MRI allows a detailed study of perirectal soft tissues, mesorectum and mesorectal fascia, and it is very useful for the therapeutic management through the prediction of circumferential resection margins (CRM) (Klessen et al. 2007).

As compared to MRI, MSCT has the advantage of being less costly and time-consuming, as well as to allow a whole-body staging in a single study. Nevertheless, MSCT displays a poor accuracy for the identification MRF invasion in tumors located in the low-anterior rectum, while its accuracy improves significantly when examining tumors located in the mid-to-high rectum (Vliegen et al. 2008).

Several studies have been performed for the evaluation of tumor neovascularization by CT perfusion, particularly as a consequence of the increasing use of anti-angiogenic drugs (Bevacizumab) (Bellomi et al. 2007). Perfusion CT may have an important clinical application in the therapeutic management of rectal cancer, as it allows the monitoring of response to therapy. However, it is noteworthy that changes in tumor vascularity, following radiotherapy, are inconsistent, with some patients showing a reduction and others an increase in blood flow (Goh et al. 2009). Of note, at present, there are no specific guidelines regarding the use of CT perfusion monitoring and prognosis of CRC.

5 CT Colonography

CT colonography (CTC) is a valuable non-invasive technique for the detection and classification of colonic lesions in both symptomatic and non-symptomatic patients. Over the recent years, this technique has been subjected to widespread diffusion and is currently acknowledged as a screening method for the diagnosis of colorectal cancer or polyps, due to its high degrees of sensitivity and specificity (Halligan et al. 2005). The main clinical indications to perform CTC as a screening investigation include patients with severe or moderate risk related to age (older than

50 years), family history, or following incompleteness of optical colonoscopy. By contrast, CTC is contraindicated under particularly pathological conditions, such as acute diverticulitis, acute colitis, recent colorectal surgery or polypectomy, symptomatic abdominal hernia, bowel perforation or obstruction (ACR 2009). Of note, an excellent performance of CTC depends on a number of variables, including the quality of colonic preparation (e.g., adequate bowel toilet and distension), CT scanning protocol, reading approach, and interpretation skills of colonic findings.

6 Bowel Preparation

The initial step to ensure an optimal quality of CTC is represented by an accurate bowel preparation, aimed at removing any luminal fecal residue or fluid which might obscure or mimic colonic lesions. As for traditional colonoscopy, CTC requires an adequate colonic cleansing, which can be accomplished by means of a low-residue diet and cathartic cleansing (with oral administration of PEG, magnesium citrate, or phosphosoda). However, despite efforts for achieving a thorough cleansing, some fecal residuals or fluids may remain (Keedy et al. 2011; Barish et al. 2005). For this reason, fecal tagging, by oral administration of barium and/or iodinated contrast material at each meal, is usually recommended during the day preceding CTC, in order to distinguish polyps from fecal material and to detect lesions in the presence of fluid (Lefere et al. 2005). The choice of how to obtain fecal tagging is optional and depends mostly on site experience and patient's history of allergy. According to a prospective study carried out by Nagata et al., both full-laxative (2 l of PEG solution with 20 ml of sodium diatrizoate) and minimum-laxative fecal tagging (45 ml of sodium diatrizoate over the 3 days preceding CTC, and 10 ml of sodium picosulfate solution the night before CTC) yielded a comparable high sensitivity in the detection of polyps > or = 6 mm. However, in this study, CTC based on full-laxative fecal tagging yielded a better specificity, as compared with the minimum-laxative tagging (92 vs. 68%, respectively) (Nagata et al. 2009). Therefore, despite the tentatives to reduce bowel catharsis in order to increase patient's tolerance to the exam, a full laxative regimen is still the ideal preparation.

7 Colonic Distension

Colonic distention is essential to prevent bowel loop collapse, which can hamper the detection of bowel lesions. With the exception of some contraindicated conditions, the induction of distension is aided by intravenous administration of Buscopan® (scopolamine butylbromide, 20 mg), which facilitates the relaxation of bowel smooth muscle. Colonic distension can be accomplished by room air or, preferably, carbon dioxide, to allow for less discomfort and better absorption (Taylor et al. 2007). Bowel insufflation can be performed either manually or by means of an automatic insufflator, upon placement of a thin rectal probe. The latter procedure is widely preferred, owing to the possibility of monitoring both the intraluminal and insufflation pressure. Changes in patient's decubitus, during insufflation, could be required to ensure a homogeneous gas distribution as well as to visualize the whole extension of large bowel, from the rectum up to the cecum. Achieving such a completeness is particularly useful in cases of optical colonoscopy incompleteness, as a consequence of patient's intolerance, poor bowel cleansing, or dolicocolon.

8 Technique

MSCT allows the acquisition of thin-slice images (1.25 mm), delivering very low radiation doses. Thin section images are very helpful for 3D reconstructions. However, they lead inevitably to an increment of image noise indices. This drawback can be overcome by the application of appropriate filters to raw data reconstructions (high pass filters, as smoothing) and wide window settings thus reducing the image noise (Mang et al. 2007).

If the colon has been adequately distended, following an initial scanogram, the CTC standard protocol requires the acquisition of images in both supine and prone positions, to improve the sensitivity on polyp detection. The combination of supine and prone scanning helps to differentiate polyps from mobile fecal residues, allows the distension of collapsed loops by gas redistribution, and facilitates the visualization of colon segments obscured by intraluminal fluids (Chen et al. 1999; Yee et al. 2003). In addition, the administration of intravenous contrast medium is

performed in symptomatic patients with suspected or definite diagnosis of colorectal cancer.

9 Reading

The phase of CTC interpretation, reading, and reporting is very complex, requiring highly specialized and experienced readers. Indeed, substantial difference has been documented when comparing the data set interpretation from experienced radiologists (who have evaluated and reported at least 500 cases) with those from novice radiologists. Consistently with these observations, training programs in CTC are increasingly required, and they consist mostly in hands-on educational courses, concerning all the CTC aspects, under direct supervision by experienced radiologists (European Society of Gastrointestinal and Abdominal Radiology CT Colonography Study Group Investigators 2007; Boone et al. 2011).

The reading method can be selected subjectively by the radiologist and consists of both 2D and 3D views to achieve an optimal identification of the colonic findings. The best way of performing a 2D analysis relies on both supine and prone synchronized views, allowing their comparability by means of horizontal and vertical flip of prone sequences. Bone window and MPRs should be used whenever deemed necessary. The 3D perspective consists in different approaches: traditional endoscopic view, virtual colonic dissection, unfolded cube projection, and tissue transition projection (or simulation of Double Contrast Barium Enema). The 3D analysis enables endoluminal fly-through with both anterograde and retrograde views, while virtual dissection allows unrolling and opening the colon with a 360° view of mucosal layer, where the haustral folds appear as vertically oriented lines. Despite the above advatages, both 2D and 3D images are affected by some limitations. Indeed, convoluted folds and diverticula can impair the 2D analysis, while the 3D endoluminal view can be negatively influenced by diverticula and fecal or fluid residuals, and it does not allow the evaluation of blind spots hidden by colonic folds (Neri et al. 2006; Kim et al. 2007). It is also worth mentioning that virtual dissection could distort the appearance of colonic findings and anatomic details, leading to a misinterpretation of polyps. For this reason, the possibility of employing alternative 3D views (e.g., virtual dissection, cube, etc.) needs to be evaluated by an experienced reader. A recommended reading strategy of CTC data sets should comprise an integration of 2D analysis and 3D views, in order to avoid errors in the interpretation of colonic findings. Moreover, the use of computer-aided detection (CAD) software allows the automatic depiction of colonic polyps, thus improving the diagnostic sensitivity of inexperienced readers, with particular regard for lesions over 6 mm in diameter. However, it must be noted that the CAD software cannot entirely compensate for the lack of reading experience, since it can generate a high number of false positives, and it is also characterized by limited sensitivity for flat lesions. Anyway a CAD should be used to support the primary diagnosis of the radiologist, therefore the most appropriate approach is the second reader paradigm (Neri et al. 2010; Zhang et al. 2011).

10 Clinical Results

In 2005, the Working Group on Virtual Colonoscopy developed a practical guideline for the interpretation and standardization of CTC findings, designated as "CT Colonography Reporting and Data System" or "C-RADS" (Zalis et al. 2005). Based on this guide, an initial distinction can be made between polyp lesions and colonic masses. The "polyp" is defined as a solid structure consisting of a homogeneous soft-tissue attenuation, arising from the mucosa, anchored to the bowel wall at a fixed site and the lesion protruding into the lumen. Polypoid lesions can be distinguished in sessile, pedunculated or flat (Figs. 4 and 5). The term "mass" refers to any colonic lesion larger than 3 cm (Figs. 6 and 7).

The C-RADS classification includes five categories: C0, inadequate study; C1, normal colon or benign lesion (no polyps $\geq$ 6 mm); C2, >3 intermediate polyps (6–9 mm); C3, more than 3 intermediate polyps or at least 1 advanced adenoma (maximum diameter: 1–3 cm); C4, likely malignant colonic mass. However, this classification system is currently under revision and not employed in the clinical practice.

As indicated by C-RADS, diminutive lesions (<6 mm) should not be mentioned in the CTC report, since they often consist of hyperplastic polyps, which are endowed with a very low risk of carcinogenesis,

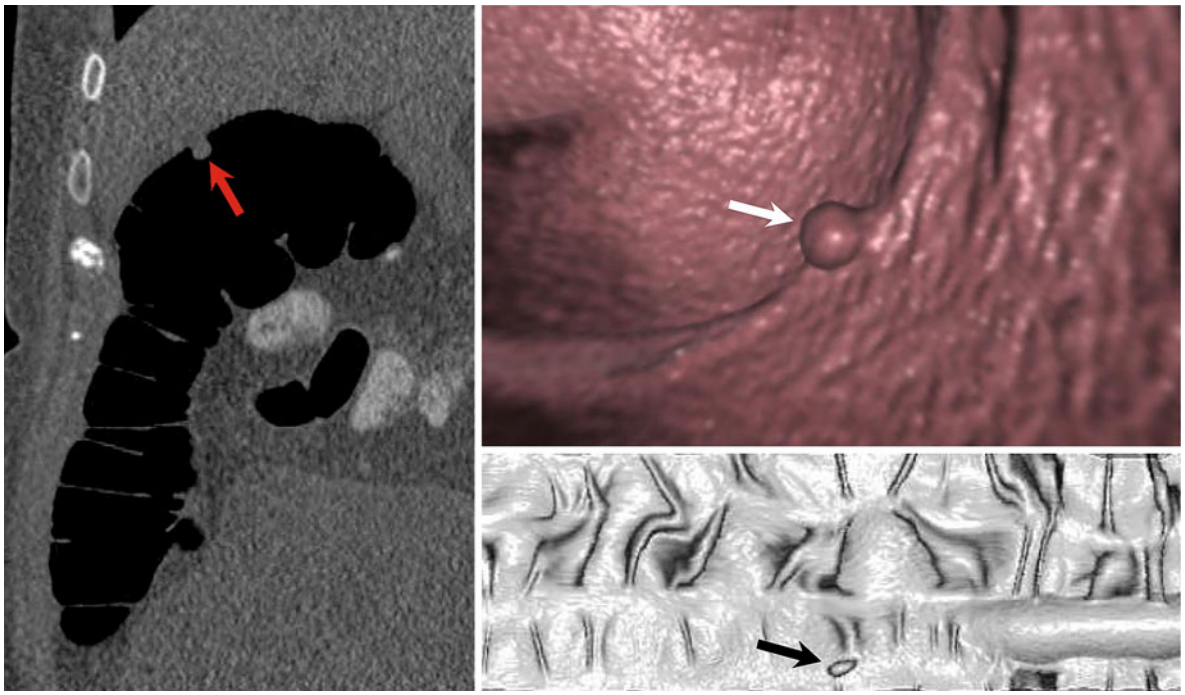

Fig. 4 CT Colonography (supine decubitus) Sessile polyp (1 cm in maximum diameter) located in the proximal third of the transverse colon. The polyp is displayed in coronal MPR (*red arrow*), endoluminal (*white arrow*) and virtual dissection perspectives (*black arrow*)

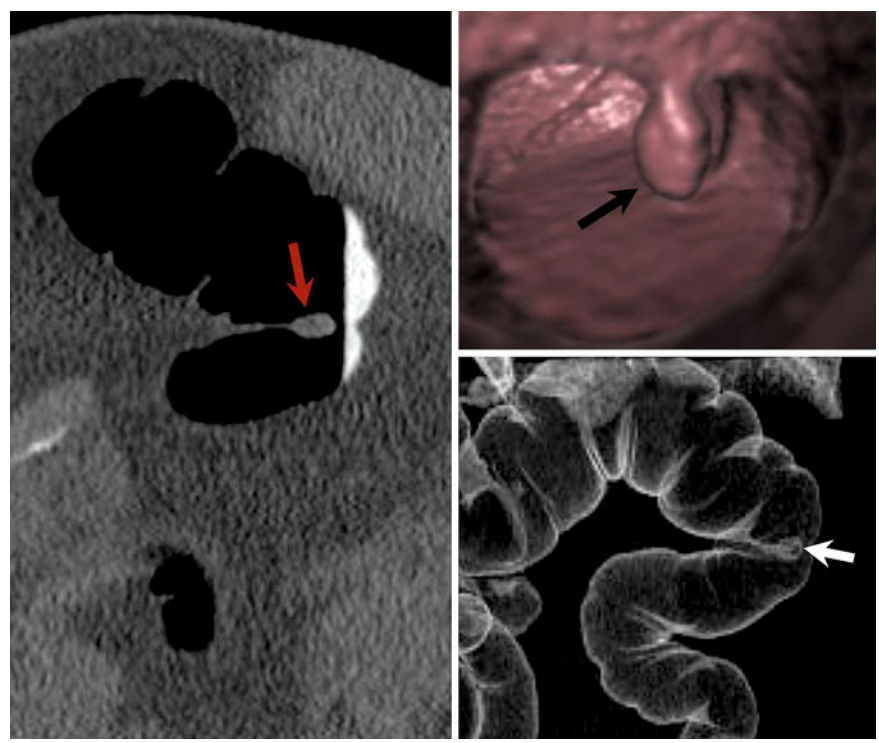

Fig. 5 CT Colonography (supine decubitus) Pedunculated polyp with cephalic portion measuring 11 mm in diameter, located in the middle third of the descending colon. The polyp is displayed in sagittal MPR (*red arrow*), endoluminal (*black arrow*) and 3D panoramic perspectives (*white arrow*)

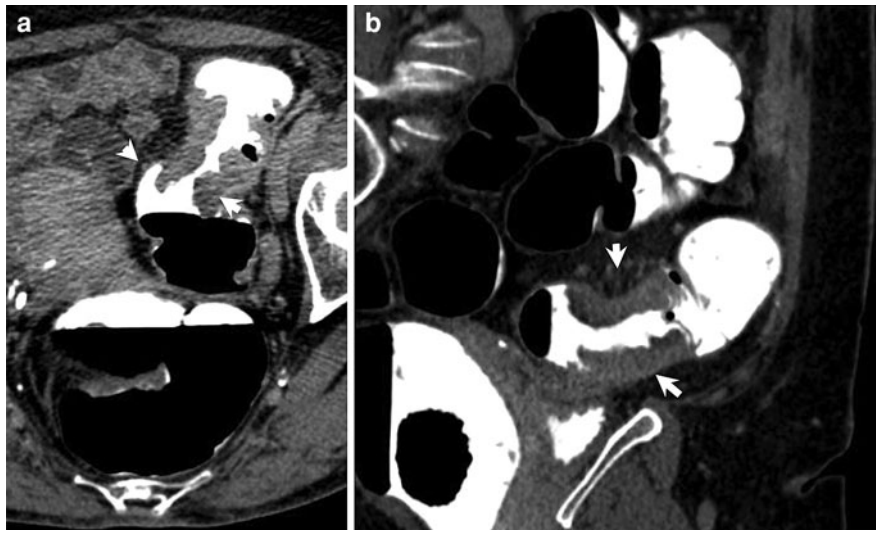

Fig. 6 Contrast-enhanced CT Colonography with fecal tagging. Axial supine (**a**) and prone MPR (**b**). A large (6 cm extension) annular stenosing cancer can be appreciated in the proximal third of the sigmoid colon (*arrow heads*) with pericolonic fat infiltration

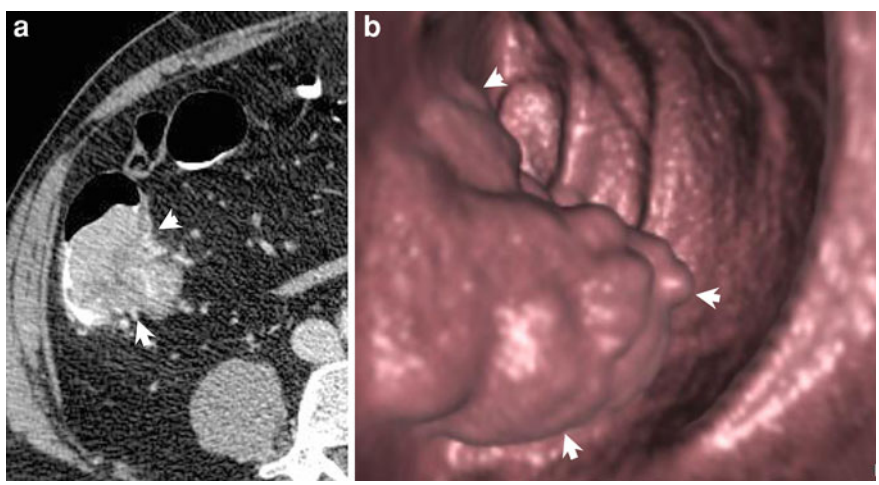

Fig. 7 Contrast-enhanced CT Colonography with fecal tagging. Axial scan in supine decubitus (**a**) and endoluminal view in prone (**b**). Vegetating cancer (5 cm in largest diameter) located in the cecum with involvement of the ileo-cecal valve and adjacent peri-colonic tissue (*arrow heads*)

and characterized by a very slow growth rate and poor clinical relevance. This is one of the most controversial assumptions of the CRADs since the absence of dysplasia is not evidence-based in such lesions. By contrast, polyps with a diameter of 6–9 mm may be hyperplastic or adenomatous in nature, while polyps ≥10 mm are often adenomas, with an increased risk of neoplastic transformation, which is related to their large size.

As reported by various studies, CTC allows for a high accuracy in the diagnosis of polyps and colorectal cancer (CRC) lesions, both in terms of sensibility and specificity. The major studies in this field are listed in Table 3, and can be summarized as follows:

- *IMPACT study* (*Italian Multicenter Polyps Accuracy CTC study*): 937 asymptomatic individuals, with family history of CRC, personal history of colorectal adenomas, or positive results from fecal occult blood test (FOBT). Each participant underwent CTC followed by optical colonoscopy on the same day. For cases of advanced cancer lesions of 6 mm in size or larger the CTC sensibility and specificity were 85.3 and 87.8%, respectively, while for findings of advanced neoplastic lesions of 10 mm in size or larger the CTC sensibility and specificity were 90.8 and 84.5%, respectively (Regge et al. 2009).
- *ACRIN* (*American College of Radiology Imaging Network study*): This trial included 2531

Table 3 Summary of CTC comparative studies

Trial (Country)	Data	Techniques	Population	Subjects (n)	Risk	Target pathology	Sensitivity	Specificity
IMPACT (Italy)	JAMA 2009	CC versus CTC	Asymptomatic	937	Average	Adenomatous polyps (AP)	Size 6–9 mm: 85.3% Size >10 mm: 90.8%	Size 6–9 mm: 87.8% Size >10 mm: 84.5%
ACRIN (USA)	NEJM 2008	CC versus CTC	Asymptomatic	2531	Higher than average	Adenomatous polyps (AP)	Size 6–9 mm: 78–87% Size >10 mm: 90%	Size 6–9 mm: 86-89% Size >10 mm: 86%
MUNICH (D)	GUT Jan 2009	CTC versus CC, FS, FOBT, ImHb	Asymptomatic	300	Average	Adenomatous polyp (AP)	78-84% for AP <6 mm; 90% for AP >10 mm	>85% regardless of lesion size
COTTON et al. (USA)	JAMA 2004	CC versus CTC	Asymptomatic and symptomatic	615	Average (FOBT+, change in stool habit, abdominal pain, surveillance after polypectomy)	Adenomatous polyps (AP)	Size 6–9 mm: 39% Size >10 mm: 55%	Size 6–9 mm: 90.5% Size >10 mm: 96%
ROCKEY et al. (USA)	The Lancet 2005	CTC versus CC; CTC versus ACBE	Asymptomatic and symptomatic	614	Average (FOBT+, haematochezia, iron-deficiency anaemia, or a family history of colonic cancer)	Adenomatous polyps (AP)	Size 6–9 mm: ACBE: 35% CTC: 51% CC: 99% Size >10 mm: ACBE: 48% CTC: 59% CC: 98%	Size 6–9 mm: ACBE: 82% CTC: 89% CC: 99% Size >10 mm: ACBE: 90% CTC: 96% CC: 99.6%

ACBE Air contrast barium enema
CC Conventional colonoscopy
CTC Computed tomographic colonography
FOBT Fecal occult blood test

asymptomatic partecipants at average risk and older than 50 years. Optical colonoscopy and histologic review were used as the reference standard. In the detection of small colorectal lesions (6–9 mm in size) the CTC sensibility and specificity amounted to 78–87 and 86–89%, respectively, while in cases of large adenomas and adenocarcinomas (larger than 10 mm) the sensibility was 90% and specificity 86% (Johnson et al. 2008).

- *Munich Trial* (*by Graser et al.*) which included 300 asymptomatic subjects with average risk of colorectal cancer. The study compared CTC versus colonoscopy, flexible sigmoidoscopy, and ImHB. Sensitivity was 90% for advanced adenomas (Graser et al. 2009).
- *Pichkardt's* (*et al.*) *study*: This investigation was conducted on 1233 asymptomatic individuals at average risk (mean age: 57.8 years), who underwent CTC and optical colonoscopy on the same day. The CTC sensibility for adenomatous polyps larger than 6 mm ranged from 88.7 to 93%, and the specificity from 79.6 to 94.9%. For polyps at least

10 mm in diameter, the CTC sensibility was 93.8% and specificity 96% (Pickhardt et al. 2003).

- *Cotton's* (*et al.*) *study*: 615 participants, aged 50 years or older, were enrolled in order to compare CTC with standard colonoscopy in the detection of colonic lesions. For lesions sized at least 6 mm, the CTC sensibility was 39% and specificity 90.5%; for lesions larger than 10 mm the sensibility was 55% and specificity 96%. However, the study by 3D image view did increase CTC sensitivity from 12 to 67% for lesions at least 10 mm in size (Cotton et al. 2004).
- *Rockey's* (*et al.*) *study*: This study included 614 participants with positive FOBT, haematochezia, iron-deficiency anaemia, or family history of colorectal cancer, who underwent air contrast barium enema (ACBE), and, approximately a week later, CTC and conventional colonoscopy (CC) performed on the same day. For lesions 6–9 mm in size the sensitivity of ACBE was 35%, CTC 51%, and colonoscopy 99%. With regard for lesions larger than 10 mm, the sensitivity of ACBE was 48%, CTC 59%, and colonoscopy 98% (Rockey et al. 2005).

Overall, as shown by the comparative studies listed in Table 3, CTC is characterized by high sensitivity and specificity for the screening of colonic lesions, particularly by integration with 3D analysis.

During CTC screening, the detection of extra-colonic findings, such as renal and hepatic cysts, skeletal lesions, pulmonary nodules, adnexal lesions, renal carcinoma, arterial aneurysms, is very frequent (Pickhardt et al. 2008). Moreover, CTC is an accurate technique for preoperative local staging of colorectal cancers, with particular regard for T (tumor) and N (lymph-nodes) staging. Indeed, it allows to distinguish T2 from T3 on the basis of pericolonic fat infiltration; and T3 from T4 by the presence of adjacent viscera involvement. The combined evaluation of axial and MPR evaluation improves the sensitivity and specificity on N stage. As far as the assessment of M (metastasis) parameter is concerned, the venous phase scanning can identify liver or peritoneal lesions (Filippone et al. 2004). CTC can also be employed for the post-surgical follow-up of colorectal cancer, allowing the detection of cancer relapse, metachronous disease, and distant metastases in one single study (contrast-enhanced CTC), and it represents a valid alternative to conventional colonoscopy in this subpopulation of patients (Neri et al. 2010).

References

ACR practice guideline for the performance of computed tomography (CT) colonography in adults. Revised 2009 (Res. 36)

Ahmetoğlu A, Cansu A, Baki D, Kul S, Cobanoğlu U, Alhan E, Ozdemir F (2011) MDCT with multiplanar reconstruction in the preoperative local staging of rectal tumor. Abdom Imaging 36(1):31–37

Ahualli J (2005) The target sign: bowel wall. Radiology 234(2):549–550

American Cancer Society (2011) Cancer facts and figures 2011. American Cancer Society, Atlanta

Angelelli G, Moschetta M, Binetti F, Cosmo T, Stabile Ianora AA (2010) Prognostic value of MDCT in malignant large-bowel obstructions. Radiol Med 115(5):747–757

Aschoff AJ (2006) MDCT of the abdomen. Eur Radiol 16(Suppl 7):M54–M57

Assenza M, Ricci G, Macciucca Mde V, Polettini E, Casciani E, De Cicco ML, Gualdi G, Modini C (2007) Comparison among preoperative single-slice CT and multi-slice CT in simple, closed loop and strangulating bowel obstruction. Hepatogastroenterology 54(79):2017–2023

Autenrieth DM, Baumgart DC (2011) Toxic megacolon. Inflamm Bowel Dis. doi: 10.1002/ibd.21847

Backes FJ, Cohn DE (2011) Lynch syndrome. Clin Obstet Gynecol 54(2):199–214

Barish MA, Soto JA, Ferrucci JT (2005) Consensus on current clinical practice of virtual colonoscopy. Am J Roentgenol 184(3):786–792

Bellomi M, Petralia G, Sonzogni A, Zampino MG, Rocca A (2007) CT perfusion for the monitoring of neoadjuvant chemotherapy and radiation therapy in rectal carcinoma: initial experience. Radiology 244(2):486–493

Bitterling H, Rock C, Reiser M (2003) Computed tomography in the diagnosis of inflammatory bowel disease—methodology of MSCT and clinical results. Radiologe 43(1):17–25

Boone D, Halligan S, Frost R, Kayc C, Laghi A, Lefere P, Neri E, Stoker J, Taylor SA (2011) CT colonography: who attends training? A survey of participants at educational workshops. Clin Radiol 66:510–516

Boyko EJ, Perera DR, Koepsell TD, Keane EM, Inui TS (1988) Effects of cigarette smoking on the clinical course of ulcerative colitis. Scand J Gastroenterol 23(9):1147–1152

Brucoli M, Giarda M, Benech A (2011) Gardner syndrome: presurgical planning and surgical management of craniomaxillofacial osteomas. J Craniofac Surg 22(3):946–948

Buetow PC, Buck JL, Carr NJ, Pantongrag-Brown L (1995) From the archives of the AFIP colorectal adenocarcinoma: radiologic-pathologic correlation. Radiographics 15(1):127–146

Cademartiri F, Palumbo A, Maffei E, Martini C, Malagò R, Belgrano M, La Grutta L, Bartolotta TV, Luccichenti G, Midiri M, Raaijmakers R, Mollet N, Zompatori M, Crisi G (2008) Noninvasive evaluation of the celiac trunk and superior mesenteric artery with multislice CT in patients with chronic mesenteric ischaemia. Radiol Med 113(8):1135–1142

Cahir JG, Freeman AH, Courtney HM (2004) Multislice CT of the abdomen. Br J Radiol 77(Spec No 1):S64–S73

Chen SC, Lu DS, Hecht JR, Kadell BM (1999) CT colonography: value of scanning in both the supine and prone positions. Am J Roentgenol 172(3):595–599

Chen M, Li X, Xie JX (2006) Assessment of acute mesenteric ischemia with multi-slice spiral CT. Zhongguo Yi Xue Ke Xue Yuan Xue Bao. 28(1):80–83

Cotton PB, Durkalski VL, Pineau BC, Palesch YY, Mauldin PD, Hoffman B, Vining DJ, Small WC, Affronti J, Rex D, Kopecky KK, Ackerman S, Burdick JS, Brewington C, Turner MA, Zfass A, Wright AR, Iyer RB, Lynch P, Sivak MV, Butler H (2004) Computed tomographic colonography (virtual colonoscopy): a multicenter comparison with standard colonoscopy for detection of colorectal neoplasia. JAMA 291(14):1713–1719

Curia MC, Iure SD, De Lellis L, Veschi S, Mammarella S, White MJ, Bartlett J, Di Iorio A, Amatetti C, Lombardo M, Di Gregorio P, Battista P, Mariani-Costantini R, Williams SM, Cama A (2011) Increased variance in Germline Allele-Specific expression of APC associates With colorectal cancer. Gastroenterology (Epub ahead of print)

Di Sabatino A, Biancheri P, Rovedatti L, Macdonald TT, Corazza GR (2011) Recent advances in understanding ulcerative colitis. Intern Emerg (Epub ahead of print)

Duchat F, Soyer P, Boudiaf M, Martin-Grivaud S, Fargeaudou Y, Malzy P, Dray X, Sirol M, Hamzi L, Pocard M, Rymer R (2010) Multi-detector row CT of patients with acute intestinal bleeding: a new perspective using multiplanar and MIP reformations from submillimeter isotropic voxels. Abdom Imaging 35(3):296–305

European Society of Gastrointestinal and Abdominal Radiology CT Colonography Study Group Investigators (2007) Effect of directed training on reader performance for CT colonography: multicenter study. Radiology 242(1):152–161

Filippone A, Ambrosini R, Fuschi M, Marinelli T, Genovesi D, Bonomo L (2004) Preoperative T and N staging of colorectal cancer: accuracy of contrast-enhanced multidetector row CT colonography–initial experience. Radiology 231(1):83–90 (Epub 2004 Feb 27)

Gao RN, Neutel CI, Wai E (2008) Gender differences in colorectal cancer incidence, mortality, hospitalizations and surgical procedures in Canada. J Public Health (Oxf) 30(2):194–201

Gazelle GS, Gaa J, Saini S, Shellito P (1995) Staging of colon carcinoma using water enema CT. J Comput Assist Tomogr 19(1):87–91

Goh V, Halligan S, Taylor SA, Burling D, Bassett P, Bartram CI (2007) Differentiation between diverticulitis and colorectal cancer: quantitative CT perfusion measurements versus morphologic criteria–initial experience. Radiology 242(2):456–462

Goh V, Halligan S, Wellsted DM, Bartram CI (2009) Can perfusion CT assessment of primary colorectal adenocarcinoma blood flow at staging predict for subsequent metastatic disease? A pilot study. Eur Radiol 19(1):79–89

Gore RM, Balthazar EJ, Ghahremani GG, Miller FH (1996) CT features of ulcerative colitis and Crohn's disease. Am J Roentgenol 167(1):3–15

Gossios KJ, Tsianos EV, Kontogiannis DS, Demou LL, Tatsis CK, Papakostas VP, Merkouropoulos MM, Tsimoyiannis EC (1992) Water as contrast medium for computed tomography study of colonic wall lesions. Gastrointest Radiol 17(2):125–128

Graser A, Stieber P, Nagel D, Schäfer C, Horst D, Becker CR, Nikolaou K, Lottes A, Geisbüsch S, Kramer H, Wagner AC, Diepolder H, Schirra J, Roth HJ, Seidel D, Göke B, Reiser MF, Kolligs FT (2009) Comparison of CT colonography, colonoscopy, sigmoidoscopy and faecal occult blood tests for the detection of advanced adenoma in an average risk population. Gut 58(2):241–248

Halligan S, Altman DG, Taylor SA, Mallett S, Deeks JJ, Bartram CI, Atkin W (2005) CT colonography in the detection of colorectal polyps and cancer: systematic review, meta-analysis, and proposed minimum data set for study level reporting. Radiology 237(3):893–904

Hegde MR, Chong B, Blazo ME, Chin LH, Ward PA, Chintagumpala MM, Kim JY, Plon SE, Richards CS (2005) A homozygous mutation in MSH6 causes Turcot syndrome. Clin Cancer Res 11(13):4689–4693

Horton KM, Abrams RA, Fishman EK (2000a) Spiral CT of colon cancer: imaging features and role in management. Radiographics 20(2):419–430

Horton KM, Corl FM, Fishman EK (2000b) CT evaluation of the colon: inflammatory disease. Radiographics 20(2): 399–418

Jaeckle T, Stuber G, Hoffmann MH, Freund W, Schmitz BL, Aschoff AJ (2008) Acute gastrointestinal bleeding: value of MDCT. Abdom Imaging 33(3):285–293

Ji JS, Wang ZF, Zhao ZW, Xu M, Tu JF (2009) Clinical application of MSCT in diagnosis of intestinal obstruction. Zhonghua Yi Xue Za Zhi 89(47):3359–3362

Johnson CD, Chen MH, Toledano AY, Heiken JP, Dachman A, Kuo MD, Menias CO, Siewert B, Cheema JI, Obregon RG, Fidler JL, Zimmerman P, Horton KM, Coakley K, Iyer RB, Hara AK, Halvorsen RA Jr, Casola G, Yee J, Herman BA, Burgart LJ, Limburg PJ (2008) Accuracy of CT colonography for detection of large adenomas and cancers. N Engl J Med 359(12):1207–1217

Johnson PT, Horton KM, Kawamoto S, Eng J, Bean MJ, Shan SJ, Fishman EK (2009) MDCT for suspected appendicitis: effect of reconstruction section thickness on diagnostic accuracy, rate of appendiceal visualization, and reader confidence using axial images. Am J Roentgenol 192(4): 893–901

Juhn E, Khachemoune A (2010) Gardner syndrome: skin manifestations, differential diagnosis and management. Am J Clin Dermatol 11(2):117–122

Kaur G, Masoud A, Raihan N, Radzi M, Khamizar W, Kam LS (2011) Mismatch repair genes expression defects and association with clinicopathological characteristics in colorectal carcinoma. Indian J Med Res 134(2):186–192

Keedy AW, Yee J, Aslam R, Weinstein S, Landeras LA, Shah JN, McQuaid KR, Yeh BM (2011) Reduced cathartic bowel preparation for CT colonography: prospective comparison of 2-L polyethylene glycol and magnesium citrate. Radiology 261(1):156–164

Kim HC, Yang DM, Jin W, Park SJ (2008) Added diagnostic value of multiplanar reformation of multidetector CT data in patients with suspected appendicitis. Radiographics 28(2):393–405, discussion 405–406

Kim SH, Lee JM, Eun HW, Lee MW, Han JK, Lee JY, Choi BI (2007) Two- versus three-dimensional colon evaluation with recently developed virtual dissection software for CT colonography. Radiology 244(3):852–864

Kirkpatrick ID, Kroeker MA, Greenberg HM (2003) Biphasic CT with mesenteric CT angiography in the evaluation of acute mesenteric ischemia: initial experience. Radiology 229(1):91–98

Klessen C, Rogalla P, Taupitz M (2007) Local staging of rectal cancer: the current role of MRI. Eur Radiol 17(2):379–389

Lakatos PL, Lakatos L (2008) Risk for colorectal cancer in ulcerative colitis: changes, causes and management strategies. World J Gastroenterol 14(25):3937–3947

Lefere P, Gryspeerdt S, Marrannes J, Baekelandt M, Van Holsbeeck B (2005) CT colonography after fecal tagging with a reduced cathartic cleansing and a reduced volume of barium. Am J Roentgenol 184(6):1836–1842

Lefèvre A, Soyer P, Vahedi K, Guerrache Y, Bellucci S, Gault V, Boudiaf M (2011) Multiple intra-abdominal venous thrombosis in ulcerative colitis: role of MDCT for detection. Clin Imaging 35(1):68–72

Lim CM, Shridhar I, Tan L, Cheah WK (2006) Contrast CT in localization of acute lower gastrointestinal bleeding. Asian J Surg 29(2):92–94

Liu L, Zhong R, Wei S, Yin JY, Xiang H, Zou L, Chen W, Chen JG, Zheng XW, Huang LJ, Zhu BB, Chen Q, Duan SY, Rui R, Yang BF, Sun JW, Xie DS, Xu YH, Miao XP, Nie SF (2011) Interactions between Genetic Variants in the Adiponectin, Adiponectin Receptor 1 and Environmental Factors on the Risk of Colorectal Cancer. PLoS One 6(11):e27301

Lo Re G, Galia M, Bartolotta TV, Runza G, Taibbi A, Lagalla R, De Maria M, Midiri M (2007) Forty-slice MDCT enteroclysis: evaluation after oral administration of isotonic solution in Crohn's disease. Radiol Med 112(6):787–797

Madureira AJ (2004) The comb sign. Radiology 230(3): 783–784

Mang T, Maier A, Plank C, Mueller-Mang C, Herold C, Schima W (2007) Pitfalls in multi-detector row CT colonography: a systematic approach. Radiographics 27(2):431–454

Marin D, Nelson RC, Schindera ST, Richard S, Youngblood RS, Yoshizumi TT, Samei E (2010) Low-tube-voltage, high-tube-current multidetector abdominal CT: improved image quality and decreased radiation dose with adaptive statistical iterative reconstruction algorithm–initial clinical experience. Radiology 254(1):145–153

McKeown-Eyssen G (1994) Epidemiology of colorectal cancer revisited: are serum triglycerides and/or plasma glucose associated with risk? Cancer Epidemiol Biomarkers Prev 3(8):687–695

Minordi LM, Vecchioli A, Poloni G, Bonomo L (2007) CT enteroclysis: multidetector technique (MDCT) versus single-detector technique (SDCT) in patients with suspected small-bowel Crohn's disease. Radiol Med 112(8): 1188–1200

Moschetta M, Stabile Ianora AA, Pedote P, Scardapane A, Angelelli G (2009) Prognostic value of multidetector computed tomography in bowel infarction. Radiol Med 114(5):780–791

Nagamata H, Inadama E, Arihiro S, Matsuoka M, Torii A, Fukuda K (2002) The usefulness of MDCT in Crohn's disease. Nihon Shokakibyo Gakkai Zasshi 99(11): 1317–1325

Nagata K, Okawa T, Honma A, Endo S, Kudo SE, Yoshida H (2009) Full-laxative versus minimum-laxative fecal-tagging CT colonography using 64-detector row CT: prospective blinded comparison of diagnostic performance, tagging quality, and patient acceptance. Acad Radiol 16(7):780–789, Epub 2009 Apr 17

Neri E, Vannozzi F, Vagli P, Bardine A, Bartolozzi C (2006) Time efficiency of CT colonography: 2D vs 3D visualization. Comput Med Imaging Graph 30(3):175–180

Neri E, Faggioni L, Regge D, Vagli P, Turini F, Cerri F, Picano E, Giusti S, Bartolozzi C (2010) CT Colonography: role of a second reader CAD paradigm in the initial training of radiologists. Eur J Radiol (Epub ahead of print)

Neri E, Vagli P, Turini F, Cerri F, Faggioni L, Angeli S, Cini L, Bartolozzi C (2010b) Post-surgical follow-up of colorectal cancer: role of contrast-enhanced CT colonography. Abdom Imaging 35(6):669–675

Orholm M, Munkholm P, Langholz E, Nielson OH, Sorensen IA, Binder V (1991) Familial occurrence of inflammatory bowel disease. N Engl J Med 324:84–88

Patel B, Mottola J, Sahni VA, Cantisani V, Ertruk M, Friedman S, Bellizzi AM, Marcantonio A, Mortele KJ (2011) MDCT assessment of ulcerative colitis: radiologic analysis with clinical, endoscopic, and pathologic correlation. Abdom Imaging (Epub ahead of print)

Pickhardt PJ, Choi JR, Hwang I, Butler JA, Puckett ML, Hildebrandt HA, Wong RK, Nugent PA, Mysliwiec PA, William R, Schindler WR (2003) Computed tomographic virtual colonoscopy to screen for colorectal neoplasia in asymptomatic adults. N Engl J Med 349:2191–2200

Pickhardt PJ, Hanson ME, Vanness DJ, Lo JY, Kim DH, Taylor AJ, Winter TC, Hinshaw JL (2008) Unsuspected extracolonic findings at screening CT colonography: clinical and economic impact. Radiology 249(1):151–159

Regge D, Laudi C, Galatola G, Della Monica P, Bonelli L, Angelelli G, Asnaghi R, Barbaro B, Bartolozzi C, Bielen D, Boni L, Borghi C, Bruzzi P, Cassinis MC, Galia M, Gallo TM, Grasso A, Hassan C, Laghi A, Martina MC, Neri E, Senore C, Simonetti G, Venturini S, Gandini G (2009) Diagnostic accuracy of computed tomographic colonography for the detection of advanced neoplasia in individuals at increased risk of colorectal cancer. JAMA 301(23): 2453–2461

Ridereau-Zins C, Aubé C, Luet D, Vielle B, Pilleul F, Dumortier J, Gandon Y, Heresbach D, Beziat C, Bailly F, Debilly M, Carbonnel F, Pierredon-Foulongne MA, Bismuth M, Chretien JM, Lebigot J, Pessaux P, Valette PJ (2010) Assessment of water enema computed tomography: an effective imaging technique for the diagnosis of colon cancer: colon cancer: computed tomography using a water enema. Abdom Imaging 35(4):407–413

Rizzo A, Pallone F, Monteleone G, Fantini MC (2011) Intestinal inflammation and colorectal cancer: a double-edged sword? World J Gastroenterol 17(26):3092–30100

Rockey DC, Paulson E, Niedzwiecki D, Davis W, Bosworth HB, Sanders L, Yee J, Henderson J, Hatten P, Burdick S, Sanyal A, Rubin DT, Sterling M, Akerkar G, Bhutani MS, Binmoeller K, Garvie J, Bini EJ, McQuaid K, Foster WL, Thompson WM, Dachman A, Halvorsen R (2005) Analysis of air contrast barium enema, computed tomographic colonography, and colonoscopy: prospective comparison. Lancet 365(9456):305–311

Roggeveen MJ, Tismenetsky M, Shapiro R (2006) Best cases from the AFIP: Ulcerative colitis. Radiographics 26(3):947–951

Scheffel H, Pfammatter T, Wildi S, Bauerfeind P, Marincek B, Alkadhi H (2007) Acute gastrointestinal bleeding: detection of source and etiology with multi-detector-row CT. Eur Radiol 17(6):1555–1565

Schmidt S, Felley C, Meuwly JY, Schnyder P, Denys A (2006) CT enteroclysis: technique and clinical applications. Eur Radiol 16(3):648–660

Scholer-Dahirel A, Schlabach MR, Loo A, Bagdasarian L, Meyer R, Guo R, Woolfenden S, Yu KK, Markovits J, Killary K, Sonkin D, Yao YM, Warmuth M, Sellers WR, Schlegel R, Stegmeier F, Mosher RE, McLaughlin ME (2011) Maintenance of adenomatous polyposis coli (APC)-mutant colorectal cancer is dependent on Wnt/beta-catenin signaling. Proc Natl Acad Sci U S A 108(41):17135–17140

Shin SS, Jeong YY, Min JJ, Kim HR, Chung TW, Kang HK (2008) Preoperative staging of colorectal cancer: CT vs. integrated FDG PET/CT. Abdom Imaging 33(3):270–277

Sivit CJ, Siegel MJ, Applegate KE, Newman KD (2001) Special Focus Session When Appendicitis Is Suspected in Children. RadioGraphics 21:247–262

Stewart SL, Wike JM, Kato I, Lewis DR, Michaud F (2006) A population-based study of colorectal cancer histology in the United States, 1998–2001. Cancer 107(Suppl 5):1128–1141

Tack D, Bohy P, Perlot I, De Maertelaer V, Alkeilani O, Sourtzis S, Gevenois PA (2005) Suspected acute colon diverticulitis: imaging with low-dose unenhanced multi-detector row CT. Radiology 237(1):189–196

Taylor SA, Laghi A, Lefere P, Halligan S, Stoker J (2007) European Society of Gastrointestinal and Abdominal Radiology (ESGAR): consensus statement on CT colonography. Eur Radiol 17(2):575–579

Tew K, Davies RP, Jadun CK, Kew J (2004) MDCT of acute lower gastrointestinal bleeding. Am J Roentgenol 182(2):427–430

Viscido A, Aratari A, Maccioni F, Signore A, Caprilli R (2005) Inflammatory bowel diseases: clinical update of practical guidelines. Nucl Med Commun 26(7):649–655

Vliegen R, Dresen R, Beets G, Daniels-Gooszen A, Kessels A, van Engelshoven J, Beets-Tan R (2008) The accuracy of Multi-detector row CT for the assessment of tumor invasion of the mesorectal fascia in primary rectal cancer. Abdom Imaging 33(5):604–610

Werner A, Diehl SJ, Farag-Soliman M, Düber C (2003) Multi-slice spiral CT in routine diagnosis of suspected acute left-sided colonic diverticulitis: a prospective study of 120 patients. Eur Radiol 13(12):2596–2603

Wiesner W, Khurana B, Ji H, Ros PR (2003) CT of acute bowel ischemia. Radiology 226(3):635–650

Woodward JM, Sanders DS, Keighley MR, Allan RN (1998) Ischaemic enterocolitis (complicating idiopathic dysautonomia). Gut 43:285–287

Yee J, Kumar NN, Hung RK, Akerkar GA, Kumar PR, Wall SD (2003) Comparison of supine and prone scanning separately and in combination at CT colonography. Radiology 226(3):653–661(Epub 2003 Jan 15)

Yildirim E, Karagülle E, Kirbaş I, Türk E, Hasdoğan B, Tekşam M, Coşkun M (2008) Alvarado scores and pain onset in relation to multislice CT findings in acute appendicitis. Diagn Interv Radiol 14(1):14–18

Yoon W, Jeong YY, Kim JK (2006) Acute gastrointestinal bleeding: contrast-enhanced MDCT. Abdom Imaging 31(1):1–8

Zalis ME, Barish MA, Choi JR, Dachman AH, Fenlon HM, Ferrucci JT, Glick SN, Laghi A, Macari M, McFarland EG, Morrin MM, Pickhardt PJ, Soto J (2005) Working Group on Virtual Colonoscopy. CT colonography reporting and data system: a consensus proposal. Radiology 236(1): 3–9

Zhang HM, Guo W, Liu GF, An DH, Gao SH, Sun LB, Yang HS (2011) Colonic polyps: application value of computer-aided detection in computed tomographic colonography. Chin Med J (Engl) 124(3):380–384

Mesenteric and Retroperitoneal Diseases

Antonella Filippone, Roberta Cianci,
and Antonio Raffaele Cotroneo

Contents

Abstract

The abdominal cavity is subdivided into the peritoneal cavity and the extra or retroperitoneal space. Mesenteries are reflections of the peritoneum on the bowel surface; therefore, they support loops of the small bowel and colon. They also serve as boundaries for disease process and conduits for disease spread. At Computed Tomography (CT) normal mesenteric fat appears homogeneous and has an attenuation similar to that of subcutaneous tissues and retroperitoneum. An alteration in the attenuation of mesenteric fat is often an important clue in determining the underlying cause of an abdominal abnormality. CT represents the main diagnostic tool for imaging the mesenteric pathologies which appear as an increased attenuation known with the term of "misty mesentery". When considering the retroperitoneal pathologies, the signs and symptoms of retroperitoneal diseases are often subtle. Cross-sectional imaging techniques therefore have a major impact on retroperitoneal diagnosis: CT is currently the standard imaging method for evaluating the retroperitoneum. This chapter reviews mesenteries and retroperitoneum anatomy as well as their most common diseases. Hereafter, the main causes of "misty mesentery" and primary retroperitoneal masses are discussed along with their CT imaging characteristics.

A. Filippone (✉) · R. Cianci · A. R. Cotroneo
Department of Neurosciences and Imaging,
Section of Imaging, G. d'Annunzio University,
Chieti-Pescara.SS. Annunziata Hospital,
via dei Vestini, 66100 Chieti, Italy
e-mail: a.filippone@rad.unich.it

C. J. Zech et al. (eds.), *Multislice-CT of the Abdomen*, Medical Radiology. Diagnostic Imaging,
DOI: 10.1007/174_2011_430, © Springer-Verlag Berlin Heidelberg 2012

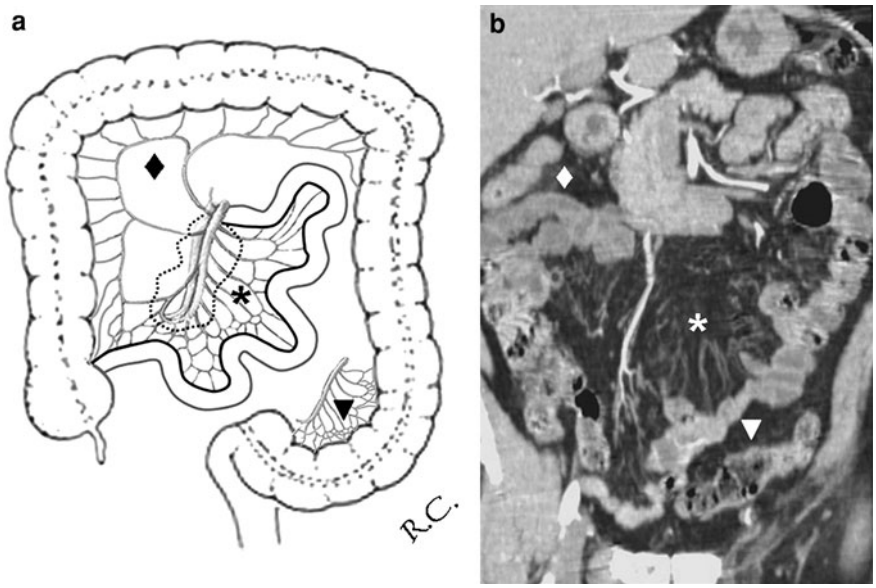

Fig. 1 Coronal view of small bowel mesentery (*), mesocolon (◆) and sigmoid mesentery (▼) in a schematic drawing (**a**) and in a reformatted multidetector-row CT image (**b**)

1 Mesenteric Diseases

1.1 Anatomy of the Mesenteries

Mesenteries (small bowel mesentery, mesocolon and sigmoid mesentery) are reflections of the peritoneum on the bowel surface and suspend large and small bowel loops from the posterior abdominal wall. They consist of two fat-laden peritoneal layers, which enclose arteries, veins, lymphatics, nodes, and nerves (Fig. 1).

The basic functions of the mesenteries are to hold the bowel loops and to connect them with the retroperitoneum, acting as a barrier or conduit of diseases (Meyers et al. 2005; Oliphant et al. 1993).

At CT, normal mesenteric fat appears homogeneous and shows attenuation values ranging between −100 to −160 HU, similar to those of retroperitoneal or subcutaneous fat.

1.2 Mesenteric Diseases

Pathological processes involving large or small bowel mesentery cause an increase of mesenteric fat density at CT. This finding is known as "misty mesentery", a term coined by Mindelzun in 1996 (Mindelzun et al. 1996). Non-neoplastic diseases usually leads to a diffuse or segmental involvement with ill-defined edges and stranding of mesentery, whereas primary or secondary neoplasms or mesenteric panniculitis result in a mass-like increased attenuation of mesenteric fat.

The analysis of pattern of mesenteric involvement with specific associated findings and patient's clinical history allows to narrow the range of differential diagnosis (Table 1) (Filippone et al. 2011).

1.3 Non-Neoplastic Mesenteric Diseases

Many non-neoplastic pathologies may cause a misty mesentery, owing to infiltration by fluids (edema, lymph, or blood), inflammatory cells or fibrosis. The involved mesentery shows a shading increased attenuation, without mass effect or vessel displacement.

1.3.1 Mesenteric Edema

Mesenteric edema may be related to systemic diseases (hypoproteinemia, heart failure, nephrosis), cirrhosis, and portal or mesenteric vein thrombosis.

The misty mesentery caused by systemic diseases is usually associated with increased density of the subcutaneous fat, relative sparing of the retroperitoneal fat, ascites, and pleural effusion.

Mesenteric edema is a common finding in patients with liver cirrhosis, owing to hypoalbuminemia or portal hypertension; this latter increases the pressure within mesenteric veins, causing fluids to seep out

Table 1 Misty mesentery in most common non-neoplastic and neoplastic diseases

CT features of misty mesentery	Associated findings	Diagnosis
Ill-defined increased CT attenuation of mesenteric fat (Non-neoplastic diseases)	Ascites; subcutaneous fluid; pleural effusion	Edema- systemic disease
	Cirrhosis; ascites; varices; splenomegaly	Edema- portal hypertension
	Clots within mesenteric vein; bowel wall thickening	Edema- mesenteric vein thrombosis
	Hemorrhage (40–60 HU)	Trauma Bowel ischemia Anticoagulation therapy
	CT features of cholecystitis, pancreatitis, appendicitis, enterocolitis, diverticulitis	Reactive inflammation
	Stratified wall thickening of the terminal ileum; mesenteric fibrofatty proliferation; increased vascularity of the vasa recta (comb sign); mesenteric adenopathy; fistulas; phlegmons and/or abscesses	Reactive inflammation Crohn's disease
	Smooth (wet-type), nodular (fixed-type), or irregular (dry type) peritoneal thickening; wall thickening of the terminal ileum or cecum; enlarged lymph nodes with central hypodensity due to caseous necrosis; hyperattenuating ascites	Tuberculous disease
Mass-like increased CT attenuation of mesenteric fat (Non-neoplastic diseases)	"Fat-ring sign"; pseudocapsule	Sclerosing mesenteritis
Mass-like increased CT attenuation of mesenteric fat (Neoplastic diseases)	Multilocular cystic mass	Lymphangioma
	Well demarcated mass with attenuation values similar to that of muscle	Desmoid tumor
	Mass with radiating bands and calcifications, with or without regional intestinal wall thickening	Carcinoid tumor
	Encasement of mesenteric vessels; bulky retroperitoneal adenopathy	Lymphoma
	Stellate appearance; peritoneal thickening	Carcinomatosis Peritoneal mesothelioma

into the mesentery. The resulting diffuse mesenteric haziness is commonly associated with findings indicative of portal hypertension, such as varices, splenomegaly, and ascites.

As reported by Chopra et al. (1999), in the setting of cirrhosis there is a characteristic progression from mesenteric edema alone, through a combination of mesenteric and omental edema to a combination of mesenteric, omental, and retroperitoneal edema. Neither omental nor retroperitoneal edema occur without mesenteric edema, and retroperitoneal edema does not occur without omental edema. Therefore, in patients with cirrhosis, the presence of omental or retroperitoneal edema without mesenteric edema should suggest other pathological conditions, such as inflammation or malignant infiltration. Moreover, a severe ascites without misty mesentery should be considered indicative of other conditions that could complicate hepatic cirrhosis, such as portal or hepatic venous occlusion, bacterial peritonitis, or peritoneal carcinomatosis.

The misty mesentery resulting from systemic diseases and cirrhosis tends to be diffuse, extending from the bowel surface to the root of the mesentery at the origin of mesenteric vessels.

On the other hand, mesenteric edema caused by mesenteric vein thrombosis has a segmental distribution corresponding to that portion of mesentery which is tributary of the ischemic bowel loop (Fig. 2) (Okino et al. 2001). Similarly, a focal mesenteric haziness in patients with "closed-loop" bowel obstruction may indicate a vascular impairment of the involved bowel wall (Di Mizio and Scaglione 2007).

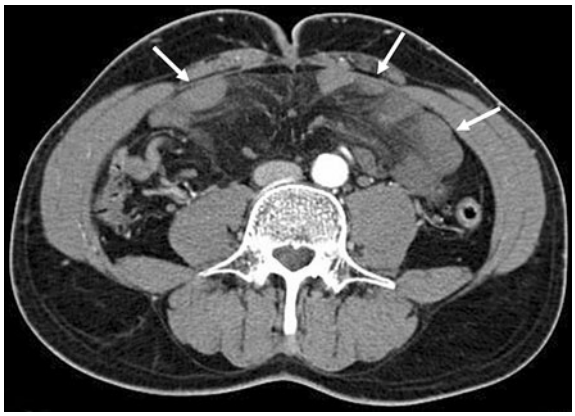

Fig. 2 Axial multidetector-row CT image of a patient with surgically proven small bowel venous ischemia, showing haziness of the mesentery which is tributary of the ischemic bowel loops (*arrows*)

1.3.2 Mesenteric Hemorrage

Acute hemorrhage is characterized by high CT attenuation values (40–60 HU). It may be diffuse or focal and is commonly associated with a traumatic event (Fig. 3), anticoagulation therapy, blood dyscrasia, mesenteric ischemia, or with a ruptured vascular aneurysm.

1.3.3 Mesenteric Inflammation

Many inflammatory diseases of the gastrointestinal tract may cause a misty mesentery. In severe acute pancreatitis, pancreatic fluid can spread along the anterior pararenal space into the small bowel mesentery or along the transverse mesocolon. Acute cholecystitis, appendicitis, infectious enterocolitis, and diverticulitis may produce local inflammation within the adjacent mesenteries (Horton et al. 2000).

In patients with Crohn's disease mesenteric haziness is indicative of extraluminal spread of the inflammatory process, usually characterized by fistulas, phlegmons and/or abscesses. In these cases the "misty mesentery" is commonly associated with bowel wall thickening with a target appearance, mesenteric fibrofatty proliferation, increased vascularity of the vasa recta (comb sign), and mesenteric adenopathy (Furukawa et al. 2004).

As an integral part of the peritoneum, mesenteries are involved in most patients with tuberculous peritonitis. This pathology may be considered as "the great mimicker", because it may show a CT appearance similar to that of many other benign or malignant diseases. Nevertheless, the tuberculous involvement of the mesentery can be considered when the following findings are present on CT (Akhan and Pringot 2002; Sheth et al. 2003):

1. smooth (wet-type), nodular (fixed-type), or irregular (dry type) peritoneal thickening;
2. stranding or nodularity within mesenteric fat;
3. wall thickening of the terminal ileum or cecum;
4. enlarged mesenteric and retroperitoneal lymph nodes with central hypodensity due to caseous necrosis (Fig. 4);
5. ascites, which is characteristically of relatively high density due to the high protein content

1.3.4 Sclerosing Mesenteritis

Sclerosing mesenteritis is a complex chronic mesenteric fibro-inflammatory disorder (Daskalogiannaki et al. 2000; Horton et al. 2003).

The cause of this disease is still unknown, and it has been related to a wide spectrum of conditions, such as autoimmunity, infection, trauma, ischemia, malignancy, and previous abdominal surgery. It is frequently associated with other idiopathic pathologies characterized by chronic inflammation and fibrosis, such as retroperitoneal fibrosis, sclerosing cholangitis, Riedel thyroiditis, and orbital pseudotumor.

Sclerosing mesenteritis can be classified into three subgroups on the basis of the underlying predominant pathological process: *mesenteric panniculitis*, characterized by chronic inflammation, *mesenteric lypodystrophy*, characterized by fat necrosis, and *retractile mesenteritis*, characterized by fibrosis. These different conditions may coexist in the same patient.

At CT, chronic mesenteric inflammation usually appears as a focal area of increased attenuation within the mesenteric fat, which extends along the root of the jejunal mesentery, thereby showing a leftward orientation. It contains scattered well-defined small lymph nodes. Typically the normal fat density around vessels and nodes is preserved: this finding is known as "fat-ring sign". A peripheral band with soft-tissue attenuation may wrap around the inflammatory mesenteric process as a pseudocapsule, which delimits it from the surrounding normal fat (Fig. 5) (Horton et al. 2003).

When fibrosis predominates, sclerosing mesenteritis may manifests itself as infiltrative masses with soft-tissue attenuation, which may contain calcifications and cause vascular thrombosis or bowel

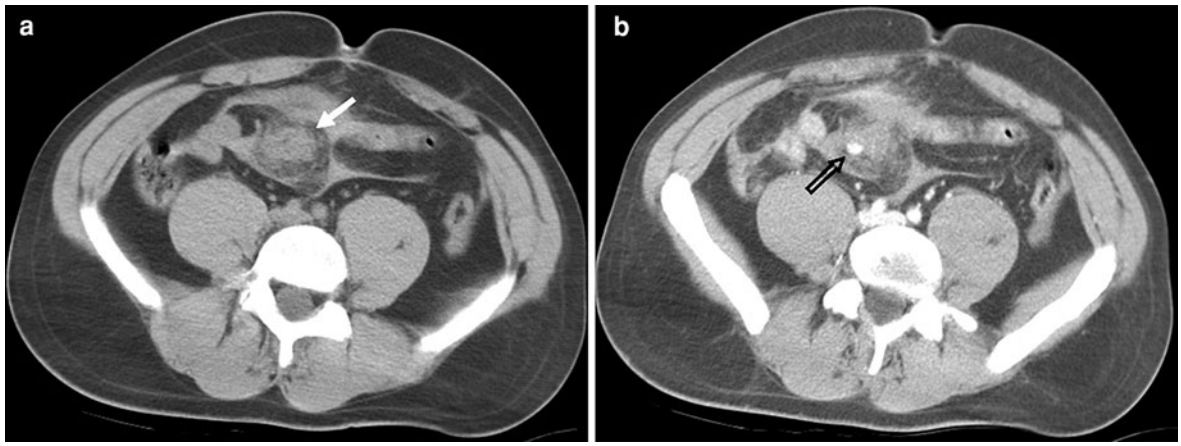

Fig. 3 Axial multidetector-row CT images of a patient with a traumatic lesion of the mesentery. Non-enhanced image (**a**) shows high attenuation of the mesentery (*arrow*) due to hemorrhage. On contrast-enhanced image (**b**) a traumatic lesion of a mesenteric vessel is identified thanks to the visualization of contrast-blush (*open arrow*)

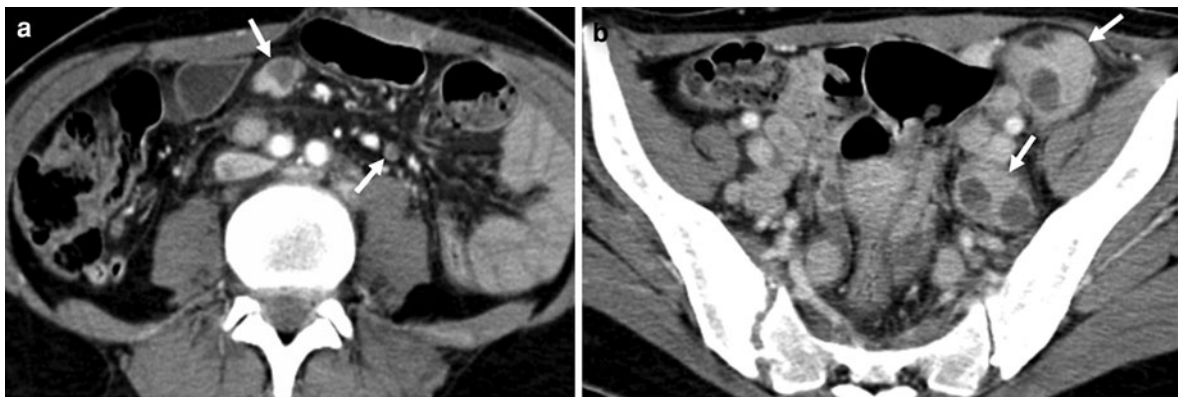

Fig. 4 Axial multidetector-row CT images of a patient with abdominal tuberculosis, showing stranding of the mesenteric fat, associated with mesenteric (*arrows in a*) and retroperitoneal (*arrows in b*) enlarged nodes characterized by central hypodensity due to caseous necrosis

obstruction. This condition often requires extensive histological sampling for accurate diagnosis, because the imaging findings may be identical to those of mesenteric tumors (i.e. carcinoid or lymphoma) (Horton et al. 2003).

As sclerosing mesenteritis has been reported to coexist with malignancies including lymphoma, breast cancer, lung cancer, melanoma, and colon cancer (Daskalogiannaki et al. 2000; Zissin et al. 2006), close follow-up to search for hidden tumoral lesions is warranted for patients who show it without a demonstrable underlying cause at CT.

1.4 Neoplastic Mesenteric Diseases

The hallmark of neoplastic involvement of the mesenteries at CT is the presence of mesenteric soft-tissue masses, which can appear round and well-defined, irregular and ill-defined, or stellate.

1.4.1 Primary Tumors

Primary neoplasms of the mesentery are rare; usually they have a mesenchymal origin and may derive from lymphatic, vascular, fibrous, neuromuscular, or fatty tissues (Sheth et al. 2003).

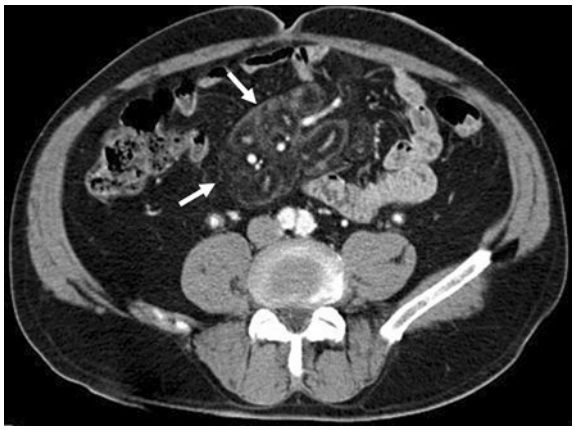

Fig. 5 Axial multidetector-row CT image of a patient with sclerosing mesenteritis, showing a well-circumscribed, mass-like increased attenuation of the mesenteric fat (*arrows*), containing some small nodes. The typical pseudocapsule and fat ring sign are also evident

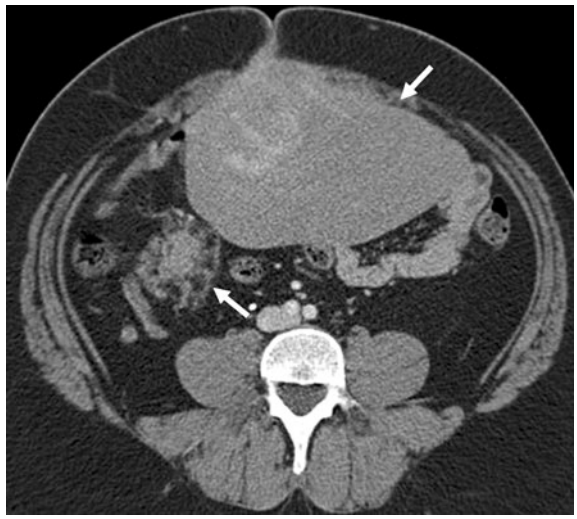

Fig. 6 Axial multidetector-row CT image of a patient with histological diagnosis of abdominal desmoid tumor, showing large soft-tissue masses growing in the mesentery (*arrows*)

Lymphangiomas typically appear as large, thin-walled, multiloculated cysts at CT, which may show an attenuation less than that of water due to chylous content.

Cavernous hemangiomas involving the mesentery generally lack a well-defined border; the presence of phleboliths is highly suggestive of the diagnosis.

Lipomas show uniform fat attenuation, without a prominent soft-tissue component.

Nerve sheath tumors, such as schwannomas or neurofibromas, arising from the mesentery are uncommon. At CT, they have a multifocal, branching or coalescent appearance and may mimic low attenuation lymphadenopathy or even a cystic lesion.

Leiomyomatosis peritonealis disseminata is a rare benign condition characterized by the presence of multiple well-defined nodules composed of smooth muscle cells. It primarily affects women of reproductive age and it is associated with uterine fibroids, pregnancy, and contraceptive steroids.

Desmoid tumors are rare, locally aggressive, non-encapsulated masses resulting from a benign proliferation of fibrous tissue and may occur in association with Gardner's syndrome, post-partum or post-surgery. They appear as soft-tissue masses with well-demarcated or poorly defined borders, and strands radiating into the adjacent mesenteric fat, or a "whorled appearance" of fibrosis growing into the mesenteric fat. Most mesenteric desmoids are isoattenuating relative to muscle, although large lesions may display areas of low attenuation caused by necrosis (Fig. 6).

Primary sarcomas of the peritoneal spaces, such as liposarcoma, malignant fibrous histiocytoma, and leiomyosarcoma, occur less frequently than their retroperitoneal counterparts. CT findings are non-specific and include masses with a cystic component or cystic necrosis, calcifications, prominent contrast material enhancement, or fat attenuation.

1.4.2 Secondary Tumors

Mesenteries are frequent pathways of dissemination for malignant neoplasms through the peritoneal cavity and between the peritoneal spaces and the retroperitoneum.

Secondary tumors can spread to the mesenteries along four major ways: direct spread, via the mesenteric lymphatic, embolic hematogeneous spread, intraperitoneal seeding (Raptopoulos and Gourtsoyiannis 2001; Sheth et al. 2003).

1.4.3 Direct Spread

- *Gastrointestinal carcinoid tumors* arise from neuroendocrine cells in the intestinal mucosa or submucosa. The release of serotonin and other hormones from the tumor causes a desmoplastic reaction, which appears at CT as a soft-tissue mass with linear bands radiating into the mesenteric fat.

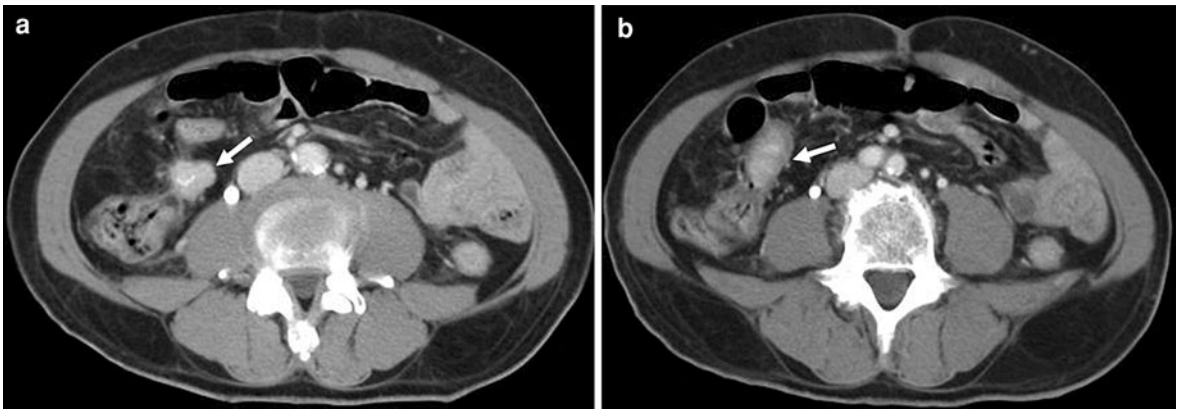

Fig. 7 Axial multidetector-row CT images of a patient with a carcinoid tumor of the terminal ileum (*arrow in b*), showing a mesenteric soft-tissue mass with radiating septa and small calcifications (*arrow in a*)

Calcifications are visible in up to 70% of lesions. Sclerosis or angulation of mesenteric vessels may cause bowel ischemia. Occasionally, the primary tumor may appear as a focal bowel wall thickening, but, in the majority, it is hardly detectable on CT, giving its too small diameter (Fig. 7) (Pantongrag-Brown et al. 1995).

- *Gastric, pancreatic, biliary and colon cancer* may extend in the contiguous mesenteries or throw mesenteric reflections and ligaments.

1.4.4 Extension Via the Mesenteric Lymphatic

- *Lymphoma* is the most common malignant neoplasm affecting the mesentery. CT features include:
  a. multiple, rounded, mildly enhancing masses, that usually encase the mesenteric vessels without perivascular fat preservation, producing the "sandwich sign" and displacing bowel loops (Fig. 8);
  b. a large lobulated mass, rarely presenting with necrosis;
  c. an ill-defined infiltration of the mesenteric fat.

  Bulky retroperitoneal adenopathy is frequently associated.
- *Metastases from colon cancer, ovarian carcinoma, breast cancer, lung cancer, carcinoid, and melanoma* can spread to mesenteric lymph nodes. The nodal enlargement is less pronounced and more localized than that seen in mesenteric lymphoma.

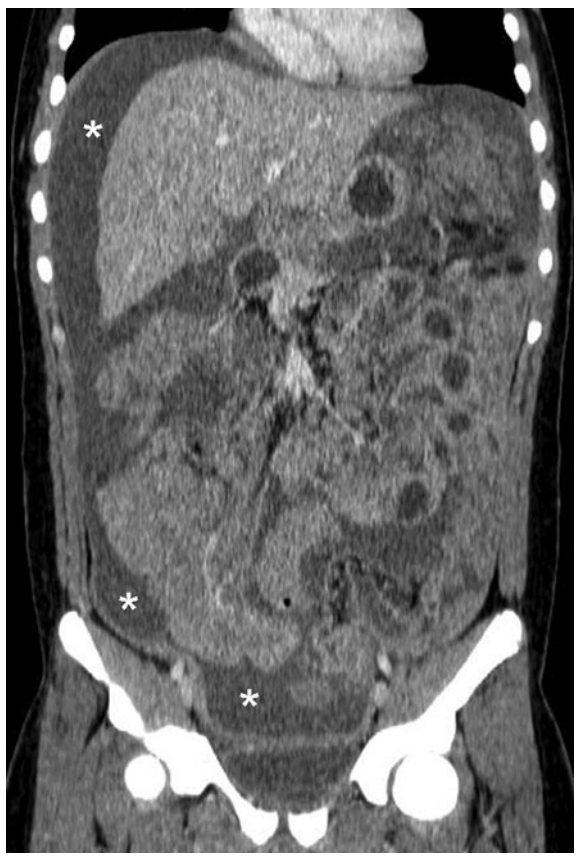

Fig. 8 Coronal reformatted multidetector-row CT image of a patient with abdominal lymphoma showing multiple soft-tissue masses encasing mesenteric vessels associated with ascites (*asterisks*)

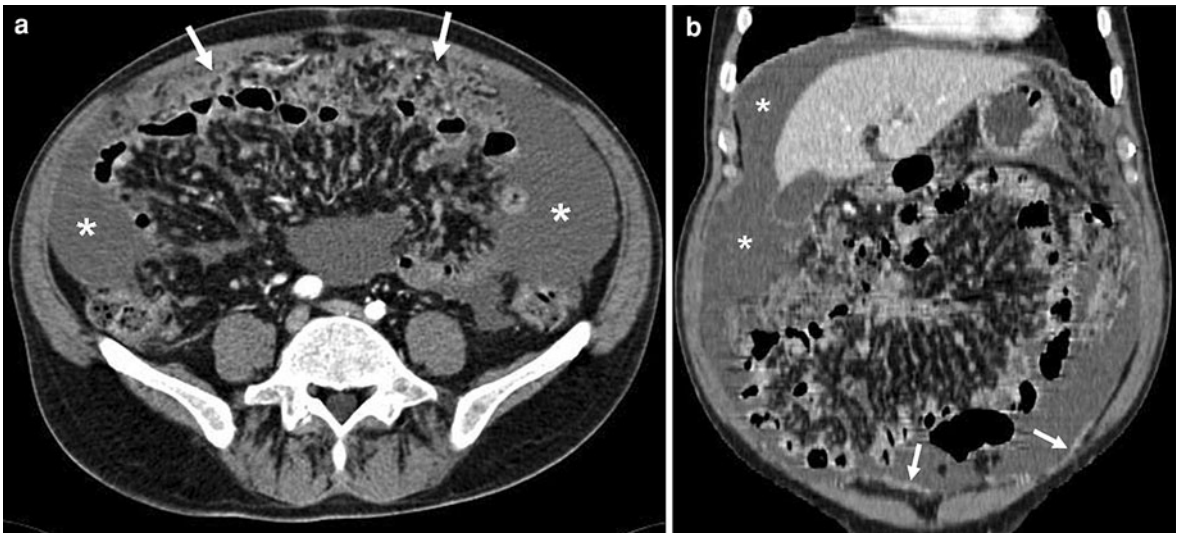

Fig. 9 Axial (**a**) and coronal reformatted (**b**) multidetector-row CT images of a patient with peritoneal carcinomatosis showing a stellate appearance and distortion of the mesentery, associated with omental soft-tissue masses (*arrows in a*), ascites (*asterisks*) and peritoneal thickening (*arrows in b*)

1.4.5 Embolic Hematogeneous Spread

- *Melanoma, breast or lung cancer metastases* can reach the bowel throw mesenteric arterial branches.

1.4.6 Intraperitoneal Seeding

- *Carcinomatosis* is common in breast, gastrointestinal tract, or ovarian cancers. Soft-tissue tumors replacing normal mesenteric fat may produce the characteristic pleated or stellate patterns. The mesenteries become stiff and lose their normal undulations, causing straightening of mesenteric vessels. Moreover, owing to the infiltration of the perivascular spaces, mesenteric vessels may appear denser than the adjacent normal mesenteric fat (Fig. 9). Peritoneal and mesenteric implants cause a fibrotic response, which corresponds to a delayed enhancement on contrast-enhanced CT (Levy et al. 2009).
- *Malignant peritoneal mesothelioma* is a rare and aggressive tumor that arises from the mesothelial cells lining the serosal surface of the peritoneal cavity. CT features vary from a "dry" appearance consisting of large or confluent masses, to a "wet" appearance consisting of ascites and associated nodular or diffuse peritoneal thickening. Spread to the mesentery appears as increased attenuation of the mesenteric fat, rigidity of the vascular bundles and perivascular soft-tissue thickening. Scalloping of or mass effect on adjacent abdominal organs may be seen. Calcifications are uncommon (Pickhardt and Bhalla 2005).

2 Retroperitoneal Diseases

2.1 Anatomy of the Retroperitoneum

The retroperitoneum lies between the posterior parietal peritoneum anteriorly and the transversalis fascia posteriorly. It is divided into three compartments, named according to their relationship to the kidney and the anterior (Gerota's) and posterior (Zuckerkandl's) renal fascias: the anterior pararenal space, which lies behind the parietal posterior peritoneum and the anterior renal fascia; the perirenal space, which is surrounded by the anterior and posterior renal fascias; the posterior pararenal space, which is bounded by the posterior renal fascia anteriorly and the trasversalis fascia posteriorly. The posterior pararenal space is separated from the anterior pararenal space by the lateroconal fascia (Fig. 10) (Burkill and Healy 2000; Meyers et al. 2005).

The retroperitoneal spaces contain adrenal glands, kidneys, and ureters; they also include posterior structures partially covered by the peritoneum, such as the aorta, the inferior vena cava, the pancreas,

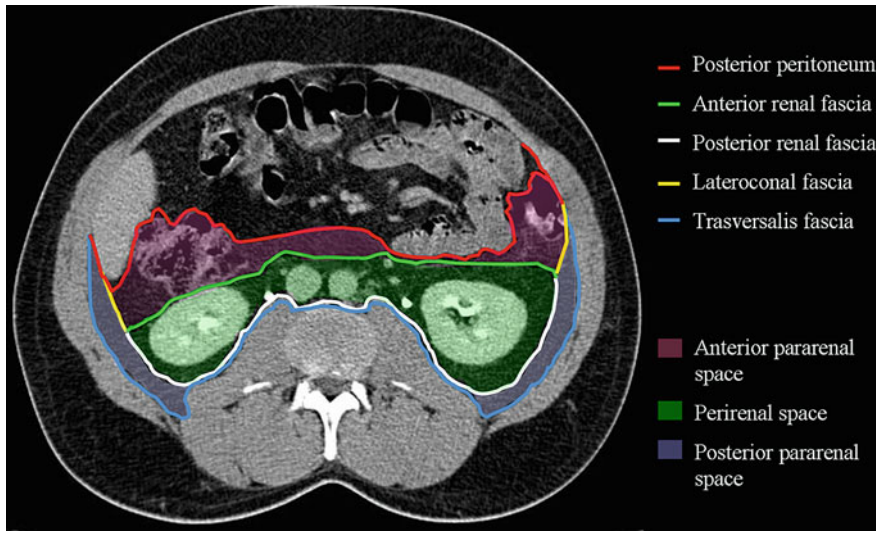

Fig. 10 Anatomy of the retroperitoneum

the duodenum, the right and left colon, nerves, and lymphatics.

2.2 Retroperitoneal Diseases

Most of the pathological processes involving the retroperitoneum arise from the major retroperitoneal organs described above and, therefore, represent secondary injuries.

Primary diseases of the retroperitoneum are rare and their diagnosis is difficult because the clinical presentation is often insidious (Koh and Moskovic 2000). There are many benign and malignant pathologies arising within the retroperitoneal spaces but outside the major retroperitoneal organs; these diseases could be classified according the tissue of origin (Table 2) (Fletcher et al. 2002).

Table 2 Classification of most common retroperitoneal diseases according to the tissue of origin

Tissue of origin	Pathologies
Fat tissue	Lipoma/Liposarcoma
Connective tissue	Malignant fibrous histiocytoma
Muscular tissue	Leiomyoma/Leiomyosarcoma
Vascular tissue	Hemangioma Malignant hemangiopericytoma
Lymphatic tissue	Cystic lymphangioma
Ganglion cell	Ganglioneuroma Ganglioneuroblastoma Neuroblastoma
Paraganglionic system	Paraganglioma/Pheocromocitoma
Nerve sheath	Neurilemmoma or Schwannoma Neurofibroma Malignant nerve sheaths tumors
Embrionary tissue	Teratoma Mucinous Cystoadenoma

2.3 CT Diagnosis of Retroperitoneal Diseases

Although CT is highly sensitive in the detection of retroperitoneal masses, the correct differentiation of these lesions is often challenging, because most of retroperitoneal diseases do not have specific imaging features (Sanyal and Remer 2009).

Nevertheless, the knowledge of retroperitoneal anatomy, the analysis of pattern of spread, lesion components, and type of enhancement together with patient's clinical characteristics may narrow the differential diagnosis and help to distinguish primary from secondary tumors and other retroperitoneal entities.

The correct approach to diagnosis consists of several steps, as follows (Nishino et al. 2003):

A. to determine lesion location into the retroperitoneal spaces;
B. to identify the organ of origin;
C. to analyze the pattern of growth;
D. to recognize specific lesion components;
E. to evaluate vascularization and pattern of enhancement.

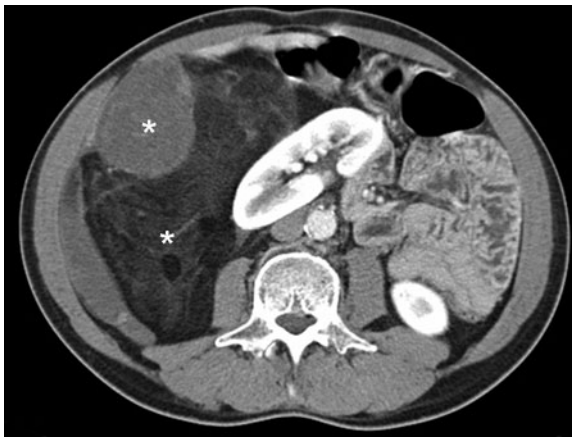

Fig. 11 Axial multidetector-row CT image of a patient with retroperitoneal liposarcoma (*asterisks*) showing the anterior and medial displacement of the right kidney by the mass

A. To determine lesion location into the retroperitoneal spaces

Once a mass is identified on CT, the first step for the diagnosis is to determine whether it is located within the retroperitoneal spaces. Anterior displacement of major vessels and retroperitoneal organs (kidneys, adrenal glands, ascending and descending colon, duodenum, and ureters) indicates that the lesion arises in the retroperitoneum (Fig. 11).

In the pelvis, displacement of major vessels and infiltration of psoas muscles are typical signs of retroperitoneal masses.

B. To identify the organ of origin

To define a lesion as primarily retroperitoneal, the possibility that it originates from a retroperitoneal organ must be excluded.

There are some radiologic signs that help to determine the organ of origin of the lesion (Nishino et al. 2003; Sanyal and Remer 2009):

1. The "beak sign": when a mass deforms the edge of an adjacent organ into a "beak" shape, it is likely that the mass arises from that organ (Fig. 12).
2. The "negative beak sign": when a mass deforms an adjacent organ with dull edges, it suggests that the mass compresses the organ, but does not arise from it (Fig. 13).
3. The "phantom (invisible) organ sign": when a large mass arises from a small organ, the organ of origin sometimes becomes undetectable.
4. The "embedded organ sign": when a mass arises from an organ, part of the organ is embedded in the mass; the mass is in close contact with the organ and the contact surface is sclerotic with desmoplastic reaction or ulcerative. On the other hand,

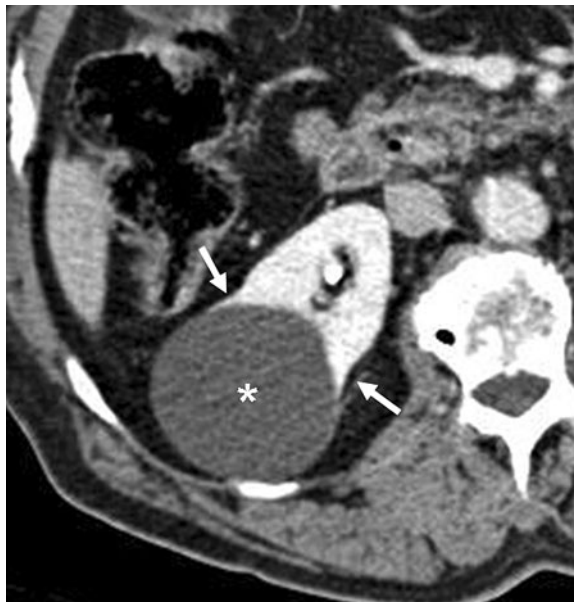

Fig. 12 Axial multidetector-row CT image showing the "beak sign" (*arrows*) in a cystic lesion (*asterisk*) arising from the right kidney

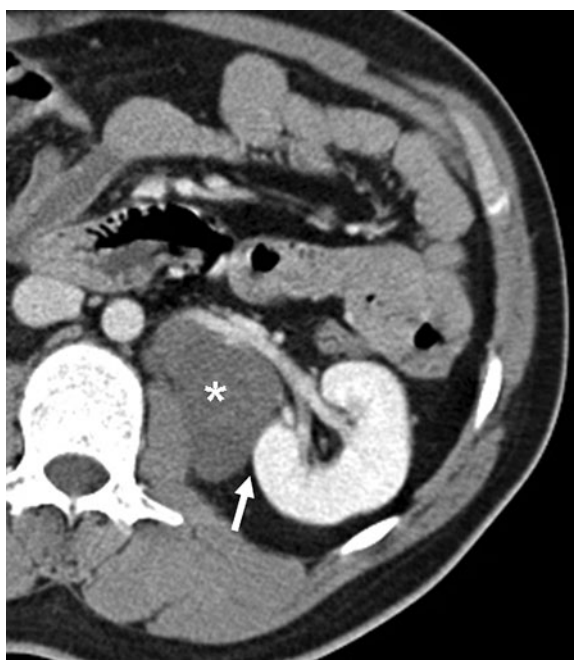

Fig. 13 Axial multidetector-row CT image showing the "negative beak sign" (*arrow*) in a retroperitoneal ganglioneuroma (*asterisk*): the lesion does not originate from the left kidney

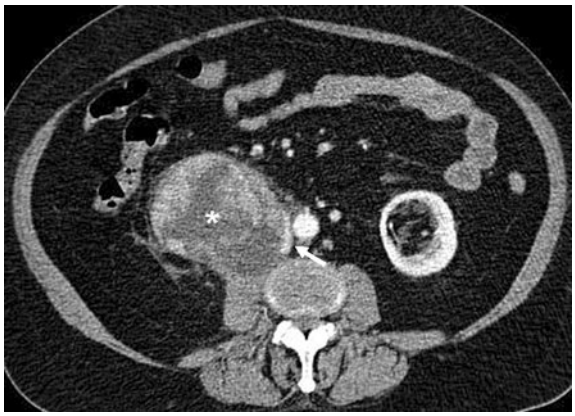

Fig. 14 Axial multidetector-row CT image showing a retroperitoneal pleomorphic liposarcoma (*asterisk*) compressing and deforming the inferior vena cava into a crescent shape (*arrow*)

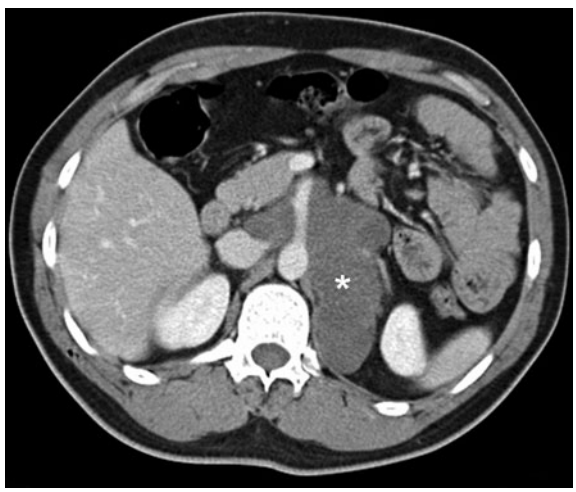

Fig. 15 Axial multidetector-row CT image of a patient with retroperitoneal ganglioneuroma (*asterisk*)

when a mass compresses an adjacent plastic organ (such as hollow viscera or inferior vena cava) that is not the organ of origin, the organ is deformed into a crescent shape (Fig. 14).

5. The "prominent feeding artery sign": feeding arteries coming from an organ support mass origin from that organ.

C. To analyze the pattern of growth

Some retroperitoneal masses show characteristic pattern of growth and spread.

Lymphangiomas and ganglioneuromas (Fig. 15) extend into retroperitoneal spaces modeling on the surface of pre-existing structures, and surrounding vessels without compressing their lumina.

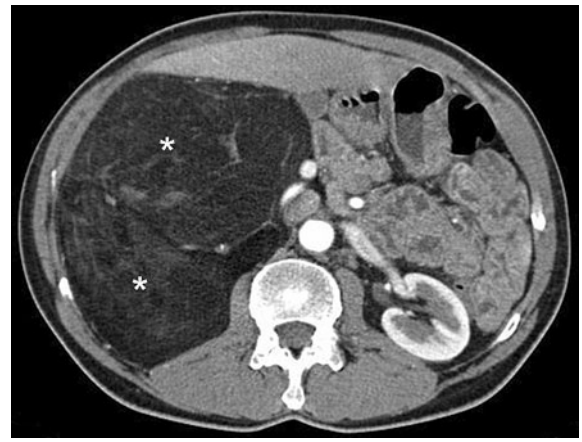

Fig. 16 Axial multidetector-row CT image of a patient with retroperitoneal liposarcoma (*asterisks*)

Paragangliomas and ganglioneuromas follow the distribution of the sympathetic ganglia along paraspinal areas. Extension into the intervertebral foramen suggests a neurogenic neoplasm.

D. To recognize specific lesion components

Some retroperitoneal masses show specific components which could be clearly demonstrated at CT and provide strong clues for the diagnosis (Nishimura et al. 2001; Nishino et al. 2003).

Fat: the presence of fat could be easily recognized showing the characteristic low attenuation value at CT. Lesions containing fat have a wide spectrum of biologic behaviors, as they range from completely benign to malignant with full metastatic potential (Craig et al. 2009).

If a fatty mass appears homogeneous and well-defined, with smooth borders, it could be considered as a lipoma. This benign lesion may grow to large proportions, causing symptoms related to mass effect and compression on adjacent structures. Although the lipoma have no propensity to malignant degeneration, it is prudent to assume that the lesion represents a well-differentiated liposarcoma and to treat it accordingly.

A mass that is irregular and ill-defined but contains fat, represents a liposarcoma. Liposarcomas are the most common sarcomas arising in the retroperitoneum, representing 35% of all malignant retroperitoneal soft-tissue tumors in adults (Kransdorf 1995). They can be classified into well-differentiated, myxoid, pleomorphic, and dedifferentiated. Well-differentiated liposarcomas usually contains an appreciable amount of fat and can demonstrate internal enhancing fibrous septa (Fig. 16),

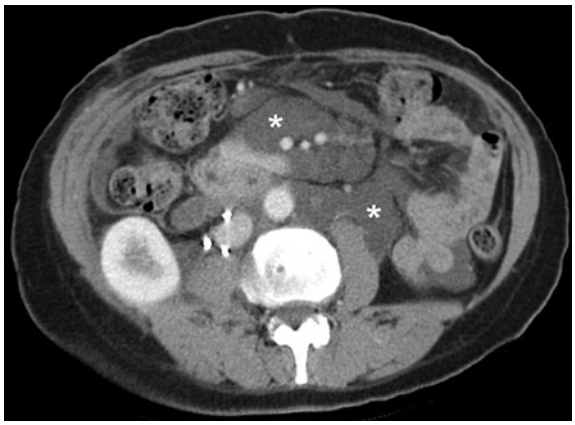

Fig. 17 Axial multidetector-row CT image of a patient with a mesenteric and retroperitoneal lymphangioma (*asterisks*)

whereas dedifferentiated lesions may not demonstrate appreciable fat, may show heterogeneous aspect, with nodular areas of contrast enhancement, thus appearing similar to other sarcomas.

CT features that suggest malignancy include diameter larger than 10 cm, presence of thick septa, presence of globular and/or nodular non-fatty areas, and percentage of fat composition less than 75% (Kransdorf et al. 2002).

Myxoid liposarcomas show almost water-like attenuation, lower than that of the muscle, and delayed enhancement; >50% have no macroscopic fat.

Most pleomorphic liposarcomas have little or no macroscopic fat and show intense and eterogeneous enhancement with areas of necrosis; they commonly invades adjacent structures.

Cystic lesions: some retroperitoneal tumors may appear as completely cystic or solid with focal intralesional cystic changes (Yang et al. 2004). Cystic lymphangiomas are congenital benign tumors which occur owing to failure of the developing lymphatic tissue to establish normal communication with the remainder of the lymphatic system. At CT, lymphangioma typically appears as a large, thin-walled, multiseptate completely cystic mass, which has an elongated shape and extends between normal anatomic structures, eventually from a compartment to another (Fig. 17). Rarely, cystic lymphangiomas may have wall calcification. Surgical excision is the treatment of choice (Davidson and Hartman 1990).

Mucinous cystadenoma affects womens with normal ovaries and presents as a homogeneous unilocular cystic mass, which is difficult to differentiate from other retroperitoneal cystic masses purely on the basis of CT findings. Therefore, surgical intervention with complete excision of the cyst is usually indicated for diagnosis and treatment (Pennell and Gusdon 1989).

A retroperitoneal cystic teratoma should be suspected when a complex mass containing a well-circumscribed fluid component, fat tissue, and calcifications is found.

Neurogenic tumors, such as schwannomas or paragangliomas, may present intralesional cystic areas, often resulting from necrotic changes.

Myxoid stroma: myxoid stroma is characterized by a mucoid matrix, rich in acid mucopolysaccharides. Lesions with myxoid stroma show hypodensity on CT images and delayed enhancement after contrast medium administration. Tumors that commonly contain a myxoid stroma include neurogenic tumors, mixoid liposarcomas, and malignant fibrous histiocytoma.

Various types of neurogenic tumors can affect the retroperitoneum (Rha et al. 2003). These tumors may arise from ganglion cells (ganglioneuromas, ganglioneuroblastomas, neuroblastomas), paraganglionic system (pheocromocytomas and paragangliomas), or nerve sheath (neurilemmomas or schwannomas, neurofibromas, malignant nerve sheath tumors).

Ganglioneuromas are benign tumors that derive from sympathetic ganglia, and are composed of mature Schwann cells, ganglion cells, and nerve fibers. They predominantly affect children and young adults. At CT ganglioneuromas appear as well-circumscribed oval or lobulated masses, which tend to partially or completely surround major blood vessels, with little or no compromise of the lumen. They show a gradually increasing enhancement (Fig. 18) (Ichikawa et al. 1996).

Neuroblastomas are malignant tumors composed of small, dark neuroepithelial cells that may show glial or ganglionic differentiation and contain nests of primitive round cells with dark-staining nuclei and scant cytoplasm. They most commonly occur during the first 10 years of life. Neuroblastomas tend to metastasize to bone, bone marrow, liver, lymph nodes, and skin. The majority are irregularly shaped, lobulated, and unencapsulated; they tend to be inhomogeneous, owing to necrosis and hemorrhage.

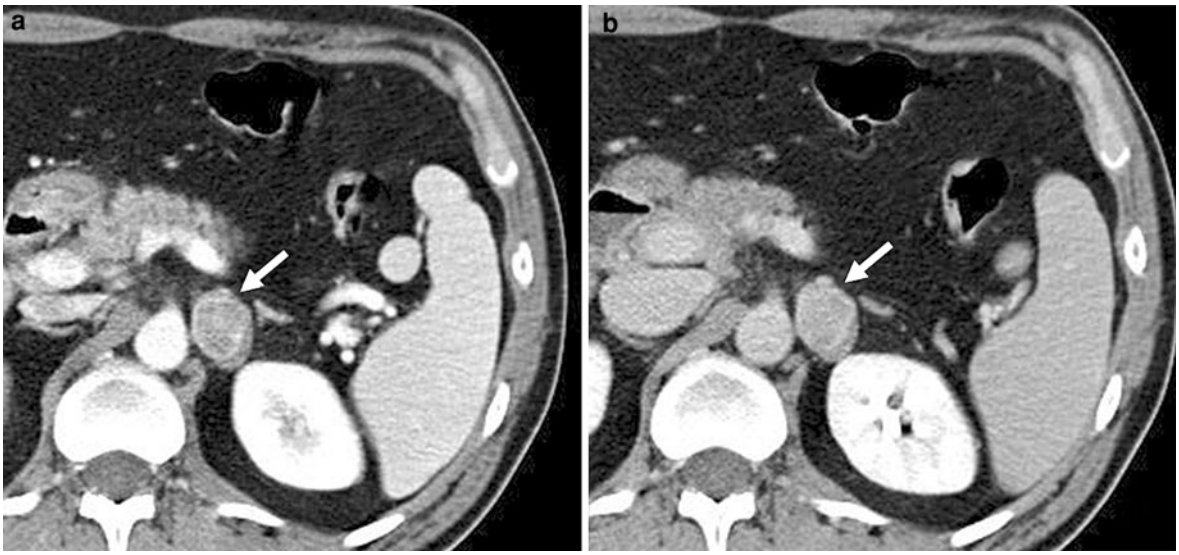

Fig. 18 Axial contrast-enhanced multidetector-row CT images during portal-venous (**a**) and equilibrium (**b**) phases showing a retroperitoneal well-circumscribed mass with delayed enhancement (*arrows*), which resulted to be a ganglioneuroma at histological analysis

Sometimes they invade adjacent organs or encase adjacent vessels. In approximately 85% of cases they contain calcifications that are usually coarse, amorphous, and mottled in appearance, as opposed to the discrete and punctate calcifications observed in ganglioneuromas (Bousvaros et al. 1986).

Retroperitoneal paragangliomas may be found in a para-aortic location from the renal arteries to the aortic bifurcation. The benign tumors are small and of muscle density, the malignant tumors are larger and contain low-density regions representing necrosis. Metastasis is the criterion for malignancy. Extra-adrenal paragangliomas are more aggressive than adrenal pheocromocytomas, and tend to disseminate both lymphatically and hematogenously to the regional lymph nodes, bone, liver, and lung. They often cause clinical symptoms because of the catecholamines they produce (Lane et al. 1989).

Neurilemmomas, or schwannomas, are benign neurogenic tumors that arise from the nerve sheaths of peripheral nerves and predominantly occur in females. They comprise 6% of primary retroperitoneal neoplasms (Lane et al. 1989) and are usually located in the paravertebral regions, adjacent to the kidney, or in the presacral pelvic retroperitoneum. At CT, neurilemmomas appear as well demarcated round or oval masses, that frequently demonstrate prominent cystic degeneration or calcification which are punctate, mottled, or curvilinear and distributed along the lesion's walls.

Neurofibromas can manifest as a solitary tumor or as a component of neurofibromatosis. They occur more frequently in men than in women. In contrast to neurilemmomas, neurofibromas are solid tumors, which have a homogeneous, smooth, and round appearance at CT. They have attenuation values of 20–25 HU on unenhanced scans as well as homogeneous enhancement with attenuation values of 30–50 HU on contrast-enhanced scans. Low attenuation on unenhanced CT scans is due to lipid-rich Schwann cells, adipocytes, and entrapment of the surrounding fat, whereas the high attenuation on contrast-enhanced scans represents dense collagen bands (Kumar et al. 1983).

At CT, neurofibromas and schwannomas occasionally demonstrate a target-like appearance, with a lower attenuation at the periphery of the lesion resulting from myxoid degeneration.

Malignant fibrous histiocytomas represent the third sarcomas of the retroperitoneum. They appear as large heterogeneous retroperitoneal masses, with an admixture of solid components, cystic degeneration,

hemorrhage, myxoid stroma, and fibrous tissue. Associated lymphadenopathy is common (Nishimura et al. 2001).

Calcifications: there are many retroperitoneal masses that contain calcifications, including either benign (ganglioneuromas, hemangiomas) or malignant (neuroblastoma, osteosarcoma, malignant fibrous histiocytoma) entities (Nishimura et al. 2001).

The analysis of all lesion components and patter of enhancement allow to narrow the differential diagnosis.

Necrosis: necrosis within a mass appear as a low attenuation area, without contrast enhancement on CT. It is usually indicative of high-grade malignancy tumors, such as leiomyosarcomas.

Leiomyosarcomas, the second sarcomas of the retroperitoneum, originate from smooth muscle, particularly from that of the retroperitoneal vessel walls; they may spread to lung, muscles, liver and kidney by means of hematogenous dissemination.

Leiomyosarcomas appear as solid lesions with lobular contours and various grade of necrosis according to tumor size and aggressiveness. The delayed enhancement allow to distinguish this type of sarcomas from other extremely hypervascularized tumors such as the hemangiopericytoma.

Leiomyosarcomas affecting the inferior vena cava typically present as masses with irregular enhancement, which cause a dilatation of the vein.

Hemorrage: extremely hypervascular tumors such as paragangliomas sometimes show fluid–fluid levels due to hemorrhagic necrosis (Nishino et al. 2003). An extensive intratumoral hemorrhage, which frequently occurs in malignant fibrous histiocytoma, may simulate a hematoma; an accurate evaluation of other mass components is mandatory to avoid an incorrect diagnosis (Nishimura et al. 2001).

E. To evaluate vascularization and pattern of enhancement

Paragangliomas and hemangyopericytomas are extremely hypervascular tumors. Malignant fibrous histiocytomas, leiomiosarcomas and many other sarcomas show a moderate hypervascularization. Low-grade liposarcomas and benign tumors appear as hypovascular (Nishino et al. 2003). In detail, four major patterns of enhancement may be identified (Nishimura et al. 2001):

1. no enhancement: seen in benign masses, such as lipomas, lymphangiomas, and cysts;
2. early enhancement with quick washout: seen in benign masses;
3. early enhancement with slow washout or without an obvious washout: seen in most malignant masses and a few benign masses (eg, some paragangliomas and schwannomas);
4. delayed enhancement: seen in benign masses (eg, neurogenic tumors, desmoids, hemangiomas, and leiomyomas) and a few malignant masses (eg, myxoid liposarcomas, leiomyosarcomas).

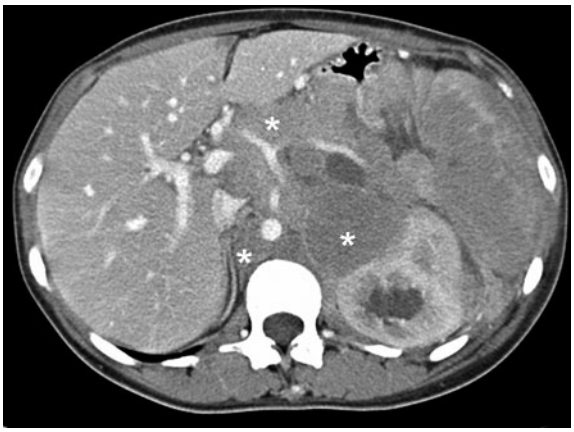

Fig. 19 Axial multidetector-row CT image of a patient with abdominal lymphoma (*asterisks*)

2.4 Main Differential Diagnoses

Primary retroperitoneal diseases should be distinguished from many other pathologies involving the retroperitoneal spaces. Hereafter the criteria for the differential diagnosis are briefly reported.

Lymphoma: although lymphoma shows the same growth-pattern of lymphangiomas and ganglioneuromas, extending between normal retroperitoneal structures, surrounding and engulfing vessels and preserving vascular patency, the differential diagnosis can be made according to the different density. As a matter of fact, lymphoma appears as homogeneous and poorly enhancing para-aortic or pelvic soft-tissue masses (Fig. 19). Necrosis and calcification are uncommon (Nishino et al. 2003).

Metastatic lymph nodes: metastatic lymph nodes from various neoplasms may appear as heterogeneous masses, with variable amount of necrosis. The knowledge of the primary disease is crucial for diagnosis (Fig. 20).

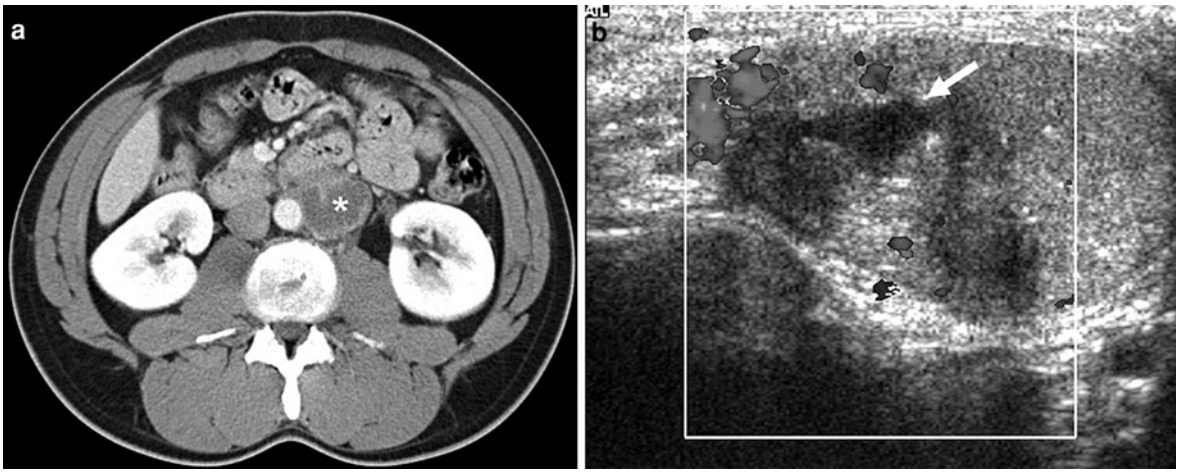

Fig. 20 Axial multidetector-row CT (**a**) and ultrasound (**b**) images of a patient with a retroperitoneal lymph node metastasis (*asterisk in a*) from a testicular neoplasm (*arrow in b*)

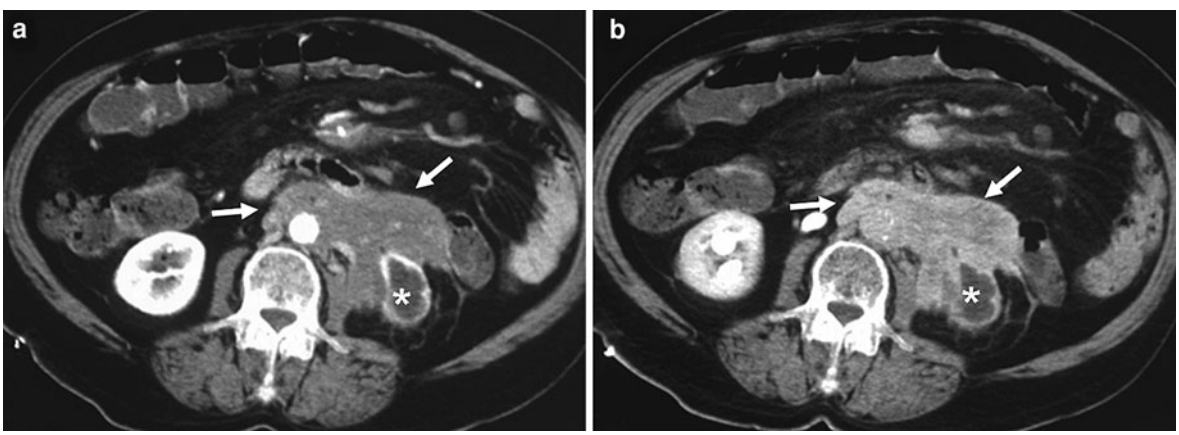

Fig. 21 Axial contrast-enhanced multidetector-row CT images during portal-venous (**a**) and equilibrium (**b**) phases of a patient with retroperitoneal fibrosis showing a soft-tissue mass with a delayed enhancement around and above the aorta (*arrows*). The lesion extends towards the left kidney, causing urinary tract obstruction and hydronefrosis (*asterisks*)

Infectious lymph nodes: tuberculous disease may cause enlarged retroperitoneal lymph nodes with central hypodensity due to caseous necrosis, potentially mimicking neoplastic masses (Akhan and Pringot 2002). Clinical and laboratory data may assist in the differential diagnosis.

Retroperitoneal fibrosis: the cause of retroperitoneal fibrosis is unknown. In its early stages, histologic analysis shows inflammatory cells and edema in a loose collagen network; the advanced pattern consists of dense fibrosis with a minimal cellular infiltration (Amis 1991). It usually manifests as an isolated fibrotic plaque located anterior to the lumbar spine; the great vessels are surrounded and encased. The plaque shows attenuation values similar to those of adjacent muscles and demonstrates a characteristic delayed enhancement, depending on the fibrotic content (Fig. 21). Owing to the overlapping CT features and pattern of enhancement between retroperitoneal fibrosis and many other retroperitoneal diseases, the diagnosis may require histological sampling.

Miscellaneous: many inflammatory conditions (pancreatitis, pyelonephritis, and diverticulitis.), iatrogenic or traumatic events may result in fluid collections (pancreatic pseudocyst, lymphocele, urinoma,

and hematoma) spreading into the retroperitoneal spaces or dissecting retroperitoneal fascias. Knowing patient's clinical history and evaluating associated CT findings helps to achieve the correct diagnosis.

References

Akhan O, Pringot J (2002) Imaging of abdominal tuberculosis. Eur Radiol 12(2):312–323

Amis ES (1991) Retroperitoneal fibrosis. Am J Roentgenol 157:321–329

Bousvaros A, Kirks DR, Grossman H (1986) Imaging of neuroblastoma: an overview. Pediatr Radiol 16:89–106

Burkill GJC, Healy JC (2000) Anatomy of the retroperitoneum. Imaging 12:10–20

Chopra S, Dodd GD 3rd, Chintapalli KN, Esola CC, Ghiatas AA (1999) Mesenteric, omental, and retroperitoneal edema in cirrhosis: frequency and spectrum of CT findings. Radiology 211(3):737–742

Craig WD, Fanburg-Smith JC, Henry LR, Guerrero R, Barton JH (2009) Fat-containing lesions of the retroperitoneum: radiologic-pathologic correlation. RadioGraphics 29:261–290

Daskalogiannaki M, Voloudaki A, Prassopoulos P, Magkanas E, Stefanaki K, Apostolaki E, Gourtsoyiannis N (2000) CT evaluation of mesenteric panniculitis: prevalence and associated diseases. Am J Roentgenol 174(2):427–431

Davidson AJ, Hartman DS (1990) Lymphangioma of the retroperitoneum: CT and sonographic characteristics. Radiology 175:507–510

Di Mizio R and Scaglione M (2007) Small bowel obstruction: CT features with plain film and US correlation. Sprinter-Verlag Italia S.r.l. Milan

Filippone A, Cianci R, Di Fabio F, Storto ML (2011) Misty mesentery: a pictorial review of multidetector-row CT findings. Radiol med 116:351–365

Fletcher CDM, Unni KK, Mertens F (2002) Tumours of soft tissue and bone. WHO Classification of Tumours. IARC Press, Lyon

Furukawa A, Saotome T, Yamasaky M, et al (2004) Cross-sectional imaging in Crohn disease. RadioGraphics 24: 689–702

Horton KM, Corl FM, Fishman EK (2000) CT evaluation of the colon: inflammatory disease. RadioGraphics 20:399–418

Horton KM, Lawler LP, Fishman EK (2003) CT findings in sclerosing mesenteritis (panniculitis): spectrum of disease. RadioGraphics 23(5):1561–1567

Ichikawa T, Ohtomo K, Araki T et al (1996) Ganglioneuroma: CT and MR features. Br J Radiol 69:114–121

Koh DM and Moskovic E (2000) Imaging tumours of the retroperitoneum. Imaging 12:49–60

Kransdorf MJ (1995) Malignant soft-tissue tumors in a large referral population: distribution of diagnoses by age, sex, and location. Am J Roentgenol 164:129–134

Kransdorf MJ, Bancroft LW, Peterson JJ et al (2002) Imaging of fatty tumors: Distinction of lipoma and well-differentiated liposarcoma. Radiology 224:99–104

Kumar AJ, Kuhajda FP, Martinez CR, Fishman EK, Jezic DV, Siegelman SS (1983) Computed tomography of extracranial nerve sheath tumors with pathologic correlation. J Comput Assist Tomogr 7:857–865

Lane RH, Stephens DH, Reiman HM (1989) Primary retroperitoneal neoplasms: CT findings in 90 cases with clinical and pathologic correlation. Am J Roentgenol 152:83–89

Levy AD, Shaw JC, Sobin LH (2009) Secondary tumors and tumorlike lesions of the peritoneal cavity: imaging features with pathologic correlation. RadioGraphics 29:347–373

Meyers MA, Charnsangavej C, Oliphant M (2005) Meyers' dynamic radiology of the abdomen: normal and pathologic anatomy. Springer Sciences + Business Media, New York

Mindelzun RE, Jeffrey RB Jr, Lane MJ, Silverman PM (1996) The misty mesentery on CT: differential diagnosis. Am J Roentgenol 167(1):61–65

Nishimura H, Zhang Y, Ohkuma K, Uchida M, Hayabuchi N, Sun S (2001) MR imaging of soft tissue masses of the extraperitoneal spaces. RadioGraphics 21:1141–1154

Nishino M, Hayakawa K, Minami M, Yamamoto A, Ueda H, Takasu K (2003) Primary retroperitoneal neoplasm: CT and MR imaging findings with anatomic and pathologic diagnostic clues. RadioGraphics 23:45–57

Okino Y, Kiyosue H, Mori H, Komatsu E, Matsumoto S, Yamada Y, et al (2001) Root of the small-bowel mesentery: correlative anatomy and CT features of pathologic conditions. RadioGraphics 21(6):1475–1490

Oliphant M, Berne AS, Meyers MA (1993) Spread of diseases via the subperitoneal space: the small bowel mesentery. Abdom Imaging 18:109–116

Pantongrag-Brown L, Buetow PC, Carr NJ, Lichtenstein JE, Buck JL (1995) Calcification and fibrosis in mesenteric carcinoid tumor: CT findings and pathologic correlation. Am J Roentgenol 164:387–391

Pennell TC, Gusdon JP (1989) Retroperitoneal mucinous cystadenoma. Am J Obstet Gynecol 60:1229–1231

Pickhardt PJ, Bhalla S (2005) Primary Neoplasms of Peritoneal and Subperitoneal Origin: CT Findings. RadioGraphics 25:983–995

Raptopoulos V and Gourtsoyiannis N (2001) Peritoneal carcinomatosis. Eur Radiol 11:2195–2206

Rha SE, Byun JY, Jung SE, Chun HJ, Lee HG, Lee JM (2003) Neurogenic tumors in the abdomen: tumor types and imaging characteristics. RadioGraphics 23:29–43

Sanyal R, Remer E (2009) Radiology of the retroperitoneum: case-based review. Am J Roentgenol 192:S112–S117

Sheth S, Horton KM, Garland MR, Fishman EK (2003) Mesenteric neoplasms: CT appearances of primary and secondary tumors and differential diagnosis. RadioGraphics 23(2):457–473

Yang DM, Jung DH, Kim H, Kang JH, Kim SH, Kim JH, Hwang. HY (2004) Retroperitoneal Cystic Masses: CT, Clinical, and Pathologic Findings and Literature Review. RadioGraphics 24:1353–1365

Zissin R, Metser U, Hain D, Even-Sapir E (2006) Mesenteric panniculitis in oncologic patients: PET-CT findings. Br J Radiol 79(938):10–15

Imaging Findings in Acute Abdomen

Borut Marincek

Contents

B. Marincek
University of Zurich, 8802 Kilchberg, Switzerland

B. Marincek (✉)
Emergency Radiology, Case Western Reserve University,
University Hospitals Case Medical Center,
Cleveland, OH 44106, USA
e-mail: borut.marincek@bluewin.ch

Abstract

Multislice CT has evolved as the first-line imaging modality in patients with an acute abdomen. Multiple studies have shown that its utilization increases diagnostic accuracy and decreases morbidity and mortality. The imaging findings and the pathophysiological background of the most frequently encountered etiologies or life-threatening conditions are reviewed, including appendicitis, diverticulitis, bowel obstruction, bowel ischemia, and gastrointestinal perforation.

1 Introduction

The term "acute abdomen" refers to a sudden onset of severe abdominal pain of unknown etiology requiring prompt diagnosis and early medical or surgical treatment. The majority of severe abdominal pains that ensue in patients who have been previously fairly well, and that last as long as 6 h, are caused by conditions of surgical import (Silen 2010).

Modern radiologic examinations, of which ultrasonography (US) and computed tomography (CT) are the most often used, are helpful when triaging patients with an acute abdomen. CT in the emergency room for patients with acute abdominal pain increases the physician's level of certainty, reduces the hospital admission rates and leads to more timely surgical intervention (Rosen et al. 2000). As a single imaging strategy, CT is better overall than US in detecting urgent conditions according to a prospective multicentre study of more than 1,000 adult patients in the Netherlands; a conditional CT strategy, however,

C. J. Zech et al. (eds.), *Multislice-CT of the Abdomen*, Medical Radiology. Diagnostic Imaging,
DOI: 10.1007/174_2011_463, © Springer-Verlag Berlin Heidelberg 2012

with US in all patients and CT only after negative or inconclusive US, yields the highest sensitivity for detecting urgent conditions (Laméris et al. 2009). Although a large number of potentially life-threatening diseases can cause acute abdominal pain, in this multicentre study seven conditions only accounted for 60% of patients with the final diagnoses classified as urgent (needing treatment within 24 h): acute appendicitis (28%), acute diverticultis (12%), bowel obstruction (7%), acute cholecystitis (5%), acute pancreatitis (3%), gynecological diseases (3%), and urological diseases (2%) (Laméris et al. 2009). Abscess, perforated viscus, bowel ischemia, pneumonia, and retroperitoneal or abdominal wall bleeding accounted in each case for 1%. In another recent prospective investigation among more than 500 adult patients presenting with nontraumatic abdominal complaints to the emergency department, CT altered the leading diagnosis in 49% and the management plan in 42% of patients; the five most common diagnoses after CT were no acute condition, renal colic, intestinal obstruction, abscess, and appendicitis, in order of decreasing frequency (Abujudeh et al. 2011).

In many centers plain abdominal radiography, despite significant diagnostic limitations, traditionally serves as the first step in the diagnostic work-up of patients with an acute abdomen. The lack of positive findings at conventional radiography, however, is falsely reassuring or further imaging is often required to better characterize abnormalities identified at abdominal radiography (Kellow et al. 2008). US has gained widespread acceptance, but it is a notoriously patient and operator-dependent technique and its use as the only imaging investigation gives an unacceptably high number of missed urgent conditions (Laméris et al. 2009). Therefore, CT is considered by many authors as first-line imaging modality and the advancement of helical CT to multislice CT (multi-detector CT) has further increased its role in patients with acute abdominal pain (Urban and Fishman 2000; Gore et al. 2000; Marincek 2002; Leschka et al. 2005; Stoker et al. 2009). In spite of increasing concerns regarding expenditures and radiation dose cited in the medical literature and reported by the popular media, a study performed in the United States found no evidence that in the emergency department the growth of CT from 1995 to 2007 for evaluation of abdominal pain had begun to taper by 2007 (Larson et al. 2011).

CT protocols for the evaluation of patients with an acute abdomen are variable. Most routine protocols include the intravenous contrast agent administration for good accuracy. Reported studies vary in the necessity of oral or rectal contrast medium. In accordance with other reviews, a prospective comparison suggests that the impact of oral contrast to improve conspicuity of pathology is minor (Lee et al. 2006).

2 Appendicitis

2.1 Background

Appendicitis is generally considered as the most common cause of acute abdominal pain. It is typically seen with obstruction of the appendiceal lumen and secondary bacterial invasion. The luminal obstruction is often due to a fecalith or lymphoid hyperplasia. Persisting obstruction is followed by fluid accumulation, luminal distention, and increased intraluminal and intramural pressure to the point of venous and lymphatic obstruction. Ineffective venous and lymphatic drainage leads to bacterial invasion of the appendiceal wall. This phlegmonous stage may resolve spontaneously, but usually it progresses to ulceration and necrosis of the wall and a pus-filled lumen. Perforation and spillage of pus into the peritoneal cavity can then occur. The tip of the appendix is often the first site of inflammation and perforation. Depending on the patient's own defense mechanism the perforation may result in a surrounding periappendiceal abscess or in diffuse peritonitis.

Patients with appendicitis are traditionally managed by surgery. The preoperative knowledge of perforated appendicitis is important, because localized perforation and diffuse peritonitis are frequent reasons—second and third to dense adhesions due to inflammation—for conversion from laparoscopic to open appendectomy (Liu et al. 2002). Several recent studies, however, support the practice of conservative treatment with antibiotics and image-guided percutaneous drainage with or without interval appendectomy in patients in whom a prolonged illness with abscess formation is detected (Andersson and Petzold 2007).

2.2 Imaging Findings

The exact role of imaging in patients with suspected appendicitis is still a matter of debate, particularly in patient groups where ionising radiation is not desirable or contraindicated, such as the pediatric population and pregnant women. US is the first line modality for evaluation of abdominal pain in pregnant patients, but acute appendicitis can be difficult to diagnose, particularly late in pregnancy, due to the size of the gravid uterus and upwards displacement of the cecum and therefore the appendix and omentum. MRI is considered as a valuable adjunct to US in pregnant patients when doubt persists following US examination; the visualization of a normal appendix on MRI virtually excludes the diagnosis of appendicitis and CT-associated radiation exposure can be markedly reduced by using MRI in this patient population (Pedrosa et al. 2009).

CT benefits from high diagnostic accuracy for appendicitis. It is often used when clinical findings and US results are equivocal. In elderly or obese patients, CT may be the initial imaging examination. In a recent retrospective study during an 18-year period, a 93% reduction in negative appendectomy rate correlated with an increase in the proportion of patients undergoing preoperative CT from 1 to 97.5% (Raja et al. 2010).

Because the length and orientation of the appendix vary among individuals, patients with appendicitis often present with atypical clinical signs and symptoms. The cecum is also a highly mobile structure that can vary on position due to variations in its posterior peritoneal attachment. The appendix arises from the posteromedial wall of the cecum, approximately 2.5–3 cm below the ileocecal valve. The anatomical position of its tip is in decreasing order of frequency retrocecal (28%), pelvic (19%), subileal (15%), subcecal (13%), paracecal (13%), postileal (7%) and preileal (5%) (O'Connor and Reed 1994). Thus, axial CT images alone have limitations for tracing the course of the appendix. Additional reformatted multiplanar images are helpful in recognizing the location of the base and tip of the appendix.

Key diagnostic CT findings of appendicitis include completely visualized appendix, thickened appendix, hyperdense appendiceal wall, calcified appendicolith, and periappendiceal fat infiltration. When two or more of these five imaging features are present, very good accuracy can be achieved (van Randen et al. 2010) (Fig. 1). Appendiceal thickening has been defined as transverse diameter >6 mm. However, the recent literature suggests that because of considerable overlap between the normal and abnormal appendix the appendiceal diameter should be interpreted in the context of clinical findings: in symptomatic patients a diameter measuring >10 mm correlates with definite appendicitis, whereas a diameter measuring 6–10 mm has to be considerd as indeterminate (Pinto Leite et al. 2005; Keyzer et al. 2005). If an appendiceal lumen contains gas, contrast material, or both, the appendix is often considered normal, regardless of the transverse diameter.

On unenhanced CT a hyperdense appendiceal wall due to mucosal hemorrhage secondary to ischemia appears to be a very specific sign and is seen in approximately 30% of patients with appendicitis (Ng et al. 2007). The detection of an isolated calcified appendicolith is a less helpful sign, because an appendicolith may be present in the absence of appendicits (Daly et al. 2005). If appendicitis is present the lumen of the appendix will not opacify with orally or rectally introduced positive contrast material.

Periappendiceal inflammatory changes include periappendiceal fat infiltration and periappendiceal fluid (van Randen et al. 2010; Daly et al. 2005). Periappendiceal fat infiltration and a completely visualized appendix have the highest weights for the final diagnosis of appendicitis (van Randen et al. 2010).

Defect in enhancing appendiceal wall, phlegmon, abscess, extraluminal gas, and extraluminal appendicolith are specific CT findings indicating appendiceal perforation. Among these five specific findings a defect in the enhancing appendiceal wall is the most accurate (Tsuboi et al. 2008) (Fig. 2).

Rare types of appendicitis are tip appendicitis (inflammatory changes involving the distal appendix) (Mazeh et al. 2009) (Fig. 3), stump appendicitis (inflammation involving post appendectomy stump) (Shin et al. 2005), or appendicitis within a hernia sac (D'Ambrosio et al. 2006).

The range of diagnoses that can mimic appendicitis is wide and includes intestinal conditions (mesenteric adenitis, ileocecal Crohn disease, cecal diverticulitis, cecal carcinoma) and urogenital conditions (ureteral stones with acute obstruction, pelvic inflammatory disease, hemorrhagic ovarian cyst, rupture of ectopic pregnancy). Primary neoplasms of

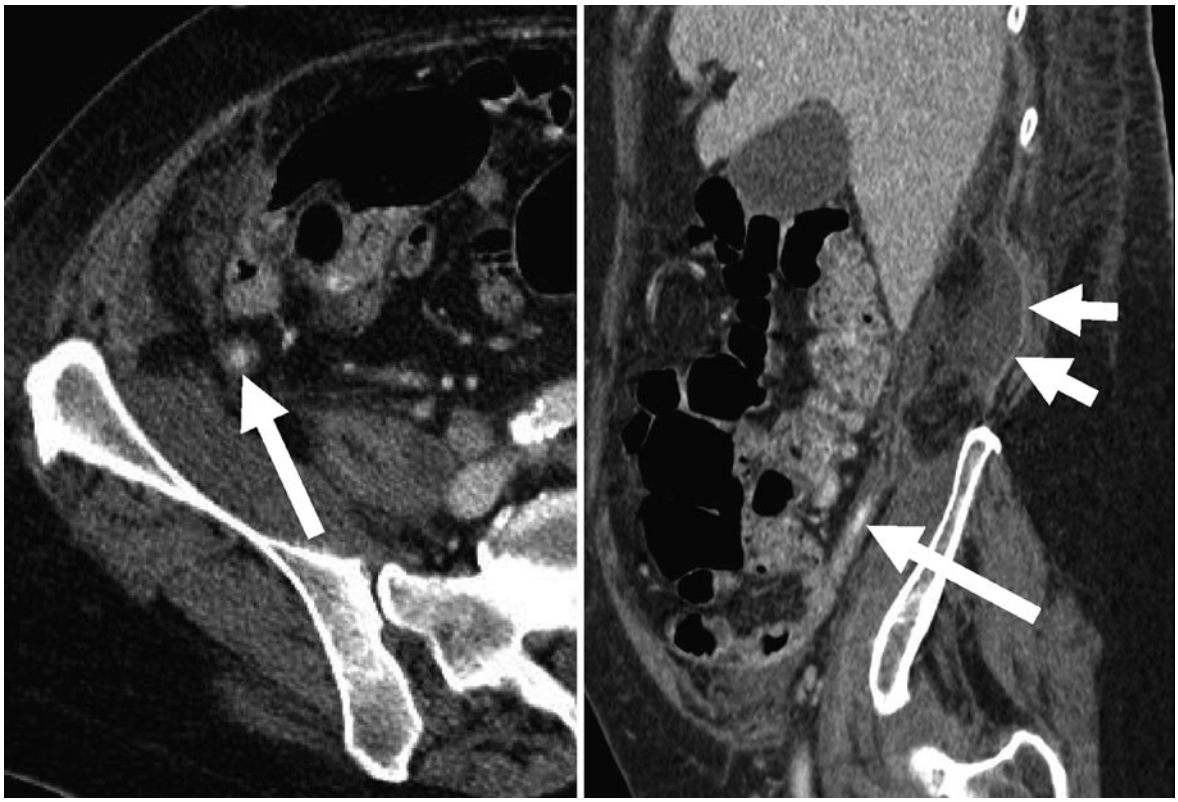

Fig. 1 Appendicitis and walled-off perforation in a 69-year-old female, contrast-enhanced CT with reformatted sagittal image (*right panel*). Thickened appendix in retrocecal position with contrast-enhancing wall, periappendiceal fat infiltration, and a calcified appendicolith in the appendiceal base (*long arrow*). A hypodense mass (*short arrows*) indicates a complicating retroperitoneal phlegmon following walled-off perforation at the tip of the appendix. The sagittal view highlights the value of multiplanar images in identifying the anatomical position of the appendix

the appendix are uncommon, but approximately 40% of patients also present clinically with symptoms of acute appendicitis, most often due to occlusion of the appendiceal lumen by tumor (Pickhardt et al. 2002). Primary appendiceal neoplasms comprise adenoma, carcinoma, carcinoid, malignant lymphoma, and other rare neoplastic conditions. CT findings of concern for an underlying appendiceal neoplasm in patients with secondary appendicitis include cystic dilatation of the appendix, presence of a soft-tissue mass, and an appendiceal diameter >15 mm (Fig. 4). Mucinous appendiceal neoplasms generally form mucoceles (descriptive term for cystic dilatation of the appendiceal lumen). Mucoceles form slowly as a result of chronic luminal obstruction and may exhibit internal septations and thin mural calfication (Pickhardt et al. 2002) (Fig. 5). Once formed, they can become superinfected and the clinical symptomes can mimic those of acute appendicitis.

3 Diverticulitis

3.1 Background

Diverticulitis is a frequent cause of acute abdominal pain. The term “diverticulitis” indicates the inflammation of a diverticulum or diverticula. Diverticulitis primarily affects the left-sided colon where diverticula are usually found. This finding is in contrast to that seen in Asian populations, in which right-sided diverticular involvement is more prominent (Stollman

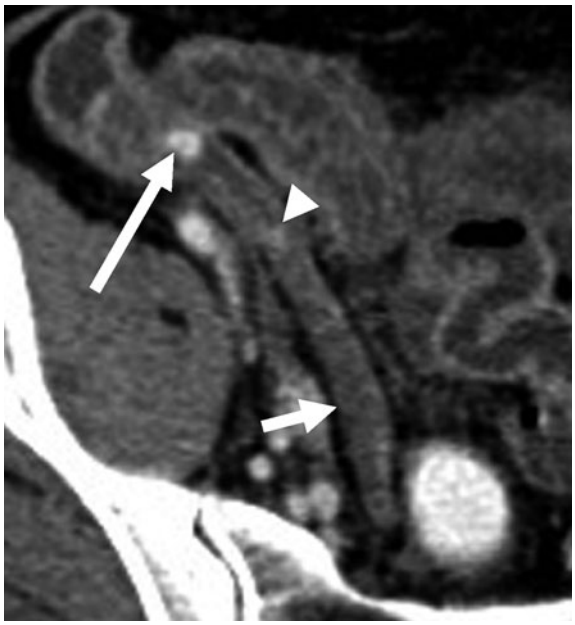

Fig. 2 Appendicitis and free perforation in a 56-year-old female, contrast-enhanced CT. Thickened appendix in pelvic position with intraluminal fluid, intraluminal hyperdensity indicating hemorrhage (*arrowhead*), a calcified appendicolith at the appendiceal base (*long arrow*), and defects in the enhancing wall (*short arrow*). Intraperitoneal fluid in the pelvis (*not shown*) indicates peritonitis secondary to free perforation

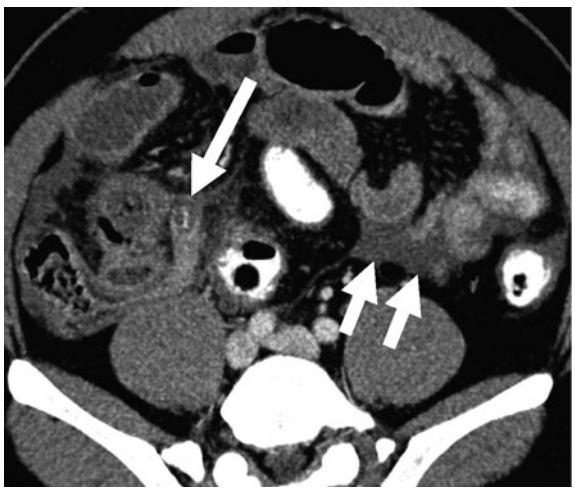

Fig. 3 Tip appendicitis and free perforation in a 34-year-old male, contrast-enhanced CT. Thickened appendix in subileal position with inhomogeneous mural enhancement and a partially calcified appendicolith at the tip of the appendix (*arrow*). Intraperitoneal fluid (*double arrows*) indicates peritonitis secondary to free perforation

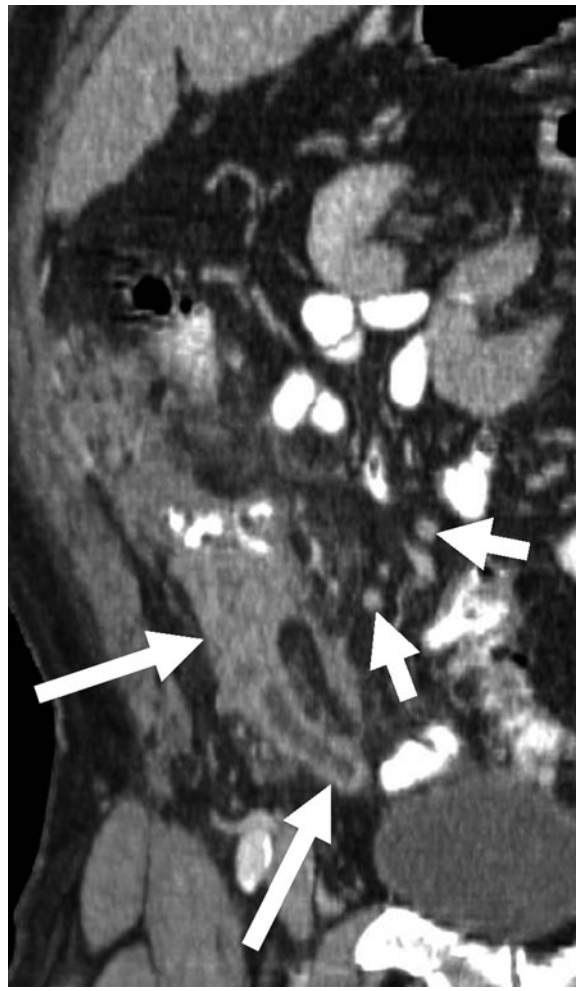

Fig. 4 Appendiceal carcinoma pT3pN2 in a 79-year-old male, coronal reformatted contrast-enhanced CT. Thickening and cystic dilatation of the appendix with a focal soft-tissue mass at the appendiceal base (*long arrows*). Enlarged regional lymph nodes due to metastatic disease (*short arrows*)

and Raskin 2004). Colonic diverticular disease is typically found in Western and industrialized societies, and its prevalence increases with age. Contributing factors to its development include altered colonic motility and dietary deficiencies, especially fiber. Diverticula vary in number and are typically 5–10 mm in diameter. Most individuals affected remain asymptomatic. Of the few who develop complications, diverticulitis is the most frequent clinical syndrome, followed by diverticular hemorrhage. Diverticulitis is caused by fecal impaction at

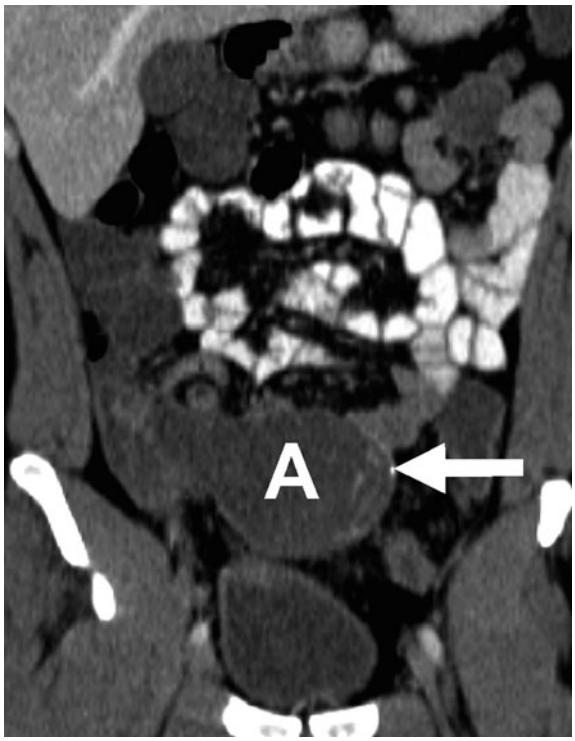

Fig. 5 Mucocele of the appendix in a 29-year-old male, coronal reformatted contrast-enhanced CT. Appendicitis was suspected clinically. Cystic dilatation of the appendix (*A*) with internal septations and small mural calcification (*arrow*)

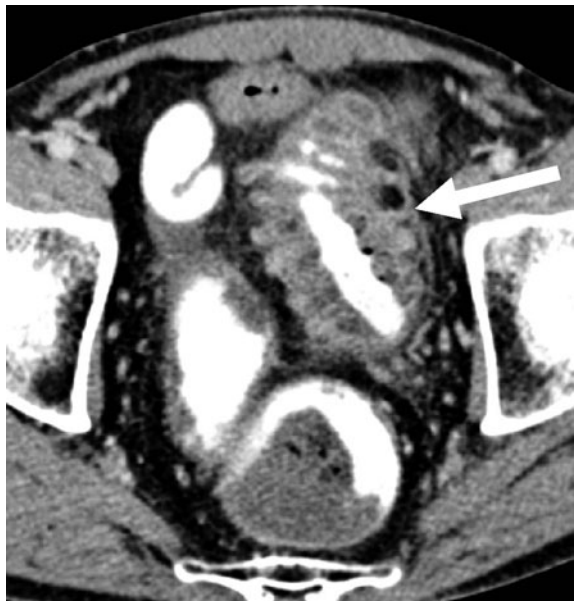

Fig. 6 Complicated sigmoid diverticulitis in a 56-year-old male, contrast-enhanced CT. Long segment involvement with pericolonic fat stranding, concentric mural thickening, and multiple small diverticula containing gas, stool or contrast agent. Edema is also present at the root of the sigmoid mesentery (*arrow*)

the mouth of diverticula, leading to bacterial overgrowth, local tissue ischemia, and subsequent perforation, findings that are similar to those described in appendicitis. Most perforated diverticula are contained perforations and episodes of diverticulitis are often self-limiting. Complications of diverticulitis include abscess formation, free perforation into the peritoneal cavity, fistula, or bowel obstruction.

3.2 Imaging Findings

CT has replaced barium enema studies as initial radiologic examination in diverticulitis due to its superior sensitivity. It demonstrates in particular the presence, location, and size of complicating abscesses, which were not appreciated in the past. CT scans typically involve the use of intravenous and rectal contrast. Rectal contrast is administered to distend the distal colon. Pericolonic fat stranding and concentric mural thickening (>4 mm) of the involved colon in the presence of multiple gas or contrast agent or stool-containing diverticula are salient CT findings (Fig. 6). Typically, a long segment (>10 cm) of sigmoid colon is involved.

The range of complications in diverticulitis is often determined with the use of the modified Hinchey classification (Kaiser et al. 2005). This classification guides surgeons as to how conservative they can be in emergency surgery. Patients with stage I disease have a confined pericolic phlegmon or abscesses, whereas those with stage II disease have pelvic, distant intra-abdominal, or retroperitoneal abscesses. Abscesses >4 cm can be treated with percutaneous image-guided drainage. This may allow for subsequent elective surgery. Stage III disease is present when a peridiverticular abscess has ruptured and caused purulent peritonitis. Fecal peritonitis signifies stage 4 disease and carries the highest risk of an adverse outcome. Fecal contamination results after free perforation into the peritoneal cavity and open communication with the bowel lumen.

When a diverticular abscess extends into an adjacent organ, fistulas can arise, the most typical being colovesicular (Fig. 7). Such fistulas have a male

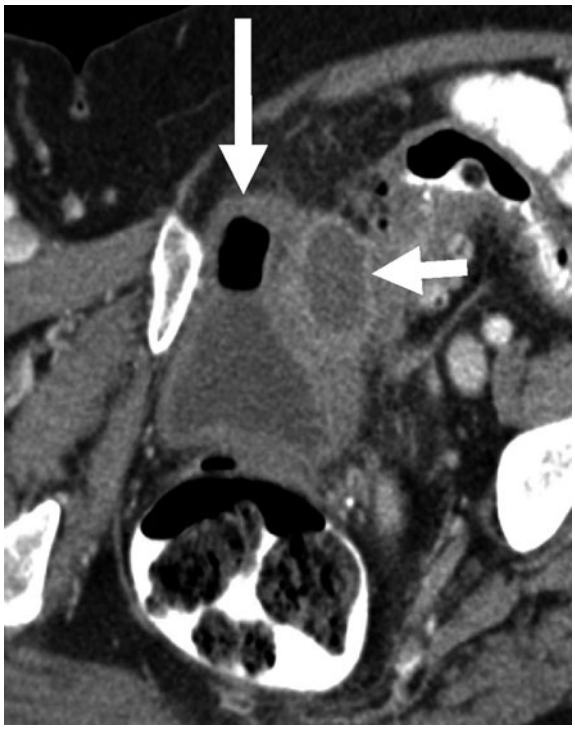

Fig. 7 Complicated sigmoid diverticulitis in a 74-year-old female, oblique reformatted contrast-enhanced CT. Pericolic abscess (*short arrow*). Gas in the urinary bladder (*long arrow*) indicates colovesicular fistula

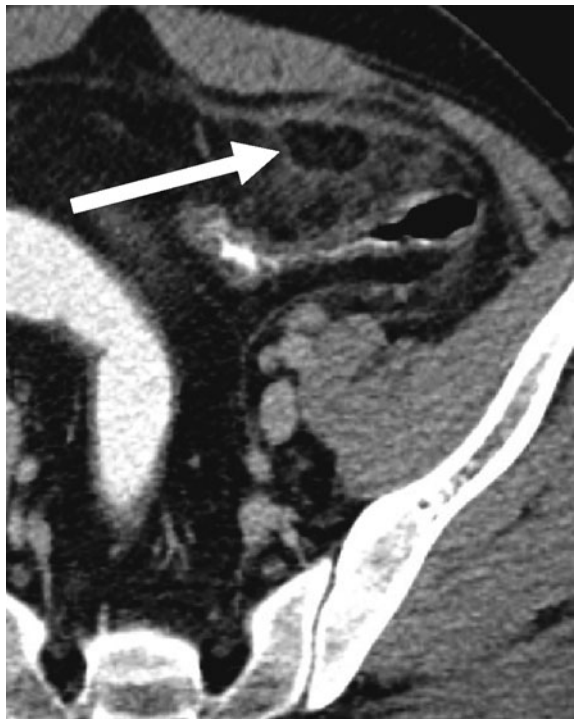

Fig. 8 Epiploic appendagitis in an 89-year-old male, contrast-enhanced CT. Oval, fatty mass adjacent to the anterior wall of the normal appearing sigmoid colon (*arrow*). Surrounding hyperdense rim and stranding of the pericolic fat. Central "dot" of increased attenuation

predominance, attributable to protection of the urinary bladder by the uterus (Stollman and Raskin 2004). Colovaginal fistulas are the next most frequent.

During an episode of diverticulitis partial colonic obstruction can occur because of relative lumenal narrowing from pericolic inflammation or compression from abscess formation (Stollman and Raskin 2004). Diverticulitis might cause small bowel obstruction if a loop of small bowel becomes incorporated in the inflammatory mass. Recurrent episodes of diverticulitis can initiate progressive fibrosis and stricturing of the colonic wall without persisting inflammation.

Occasionally it can be difficult to distinguish between diverticulitis and colonic carcinoma and a high-grade colonic obstruction due to diverticulitis may mimic colon cancer. CT findings favoring cancer are asymmetric or eccentric wall thickening, a short segment (<10 cm) of colon involvement and presence of mesenteric lymphadenopathy or metastases.

A condition that may be mistaken clinically for diverticulitis but has highly characteristic CT features is epiploic appendagitis. Epiploic appendages are pedunculated pouches of the peritoneum containing fat and small vessels. They protrude from the serosal surface of the colon and extend from the cecum to the rectsigmoid junction with their greatest concentration at the sigmoid colon. The focal inflammation of an epiploic appendage is caused by torsion and thrombosis of the epiploic appendage central draining vein resulting in vascular occlusion. The CT findings include an oval fat-density lesion 1.5–3.5 cm in diameter, with surrounding hyperdense rim (thickened visceral peritoneum) and associated inflammatory changes of the pericolic fat, that abuts the anterior sigmoid colon wall (Singh et al. 2004) (Fig. 8). A central increased attenuation "dot" within the inflamed appendage indicates the thrombosed vein.

Epiploic appendagitis is relatively uncommon and a self-limited process with spontaneous clinical resolution seen within 1 week of onset. If the disease occurs in the proximal colon it may simulate appendicitis.

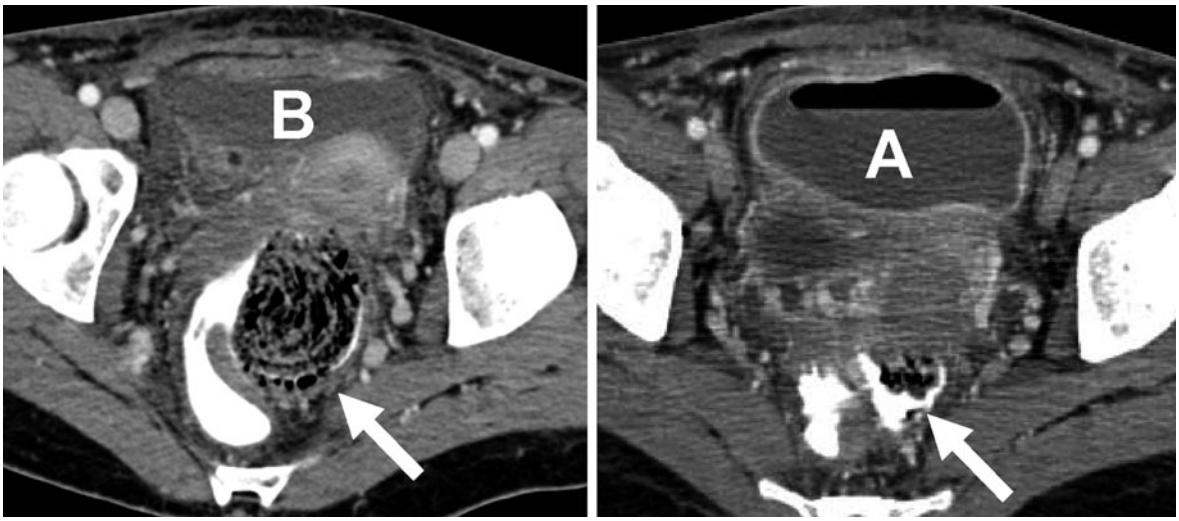

Fig. 9 Giant rectosigmoid diverticulum in a 46-year-old female, contrast-enhanced CT. *Left panel*: the giant diverticulum is filled with feces and is thin walled (*arrow*; urinary bladder, *B*). *Right panel*: after perforation and intraperitoneal abscess formation (*A*) 1 week later, the diverticulum is decreased in size and contains less feces (*arrow*)

Giant colonic diverticulum is a rare presentation of colonic diverticular disease and defined as a diverticulum greater than 4 cm in diameter. More than 90% of cases arise from the sigmoid colon and occur in isolation. Giant colonic diverticula are usually asymptomatic; however, 15–20% of patients may present with an acute complication, such as perforation, focal wall infarction, volvulus, or small bowel obstruction (Abou-Nukta et al. 2005) (Fig. 9).

4 Bowel Obstruction

4.1 Background

Bowel obstruction is a common diagnosis in patients presenting to the emergency department. It is classified as complete mechanical obstruction, as partial mechanical obstruction, or as functional obstruction attributable to failure of motility. Differentiation between these entities is critical because the first generally requires surgery, whereas the latter two entitites are often treated conservatively. In partial mechanical obstruction gas or liquid stool can pass through the point of narrowing; in complete mechanical obstruction no substance can pass. Partial mechanical obstruction is further characterized as high grade or low grade according to the severity of the narrowing.

On the basis of the anatomic level, mechanical obstruction is categorized as small bowel obstruction (SBO) versus large bowel obstruction (LBO). On the basis of pathophysiology, mechanical obstruction is divided into simple obstruction and closed-loop obstruction.

In simple obstruction the bowel is obstructed at one or several points along its course. Fluid and chyme accumulate proximal to the obstruction. This leads to bacterial overgrowth and increased production of gas because of luminal stasis, bowel dilatation from accumulated fluid and gas, and decreasing bowel motility. Bowel dilatation gradually compromises vascular perfusion of the bowel wall.

In closed-loop obstruction, a bowel segment is occluded at two separate points. A common form is volvulus. An LBO may form a closed loop, if the ileocecal valve is competent; if the ileocecal valve is incompetent, LBO produces simple obstruction as the colon is decompressed via the small bowel. A closed loop of bowel rapidly dilates because of lacking proximal and distal outlet for accumulated fluid and gas. Consequently, bowel wall ischemia rapidly develops and necrosis with subsequent perforation can result. A closed-loop obstruction associated with intestinal ischemia is defined as strangulation.

In LBO, the mural tension increases in proportion with the colonic radius, according to Laplace's Law. The tension is therefore greatest in the cecum, where

the colonic radius is greatest. The cecum is therefore most often the site of colonic ischemia or perforation when it is involved in a mechanical obstruction with a competent ileocecal valve (Cappell and Batke 2008).

The majority of patients presenting with bowel obstruction have a mechanical SBO. Mechanical SBO is mostly caused by benign lesions, whereas mechanical LBO is often caused by cancer.

4.2 Imaging Findings

4.2.1 Mechanical Small Bowel Obstruction

Imaging studies are essential for the diagnosis of SBO because the clinical presentation is nonspecific. In order to ensure appropriate treatment, the goal of imaging in a patient with suspected SBO is to determine the site and cause of obstruction and the presence of strangulation. According to the ACR Appropriateness Criteria CT without oral contrast/with iv contrast medium has emerged as the preeminent imaging modality and should be considered in the initial evaluation of suspected complete or partial high-grade obstruction (Ros and Huprich 2006). These patients do not require additional oral contrast, because the fluid in the bowel provides adequate contrast. In suspected intermittent or low-grade obstruction oral and iv contrast medium administration is appropriate, because CT is somewhat less reliable (Ros and Huprich 2006).

The main CT criterion for SBO is the presence of dilated small bowel loops (outer diameter >2.5 cm) proximally to normal-caliber loops (Silva et al. 2009). The degree of obstruction (low-grade partial, high-grade partial, complete) can be determined by the discrepancy in caliber between proximal and distal bowel loops. A complete SBO is present when the ascending colon is collapsed without fluid or gas in its lumen.

An important CT finding is the transition point, determined by identifying a clear change in bowel diameter between dilated proximal and collapsed distal small bowel loops (Marincek 2002; Stoker et al. 2009; Silva et al. 2009) (Fig. 10). A useful sign, when present, for locating the transition point is the "small bowel feces" sign, i.e. intraluminal feces-like particulate material is recognized proximal to the obstruction. The sign is likely caused by stasis within the obstructed loop and is seen more frequently in moderate and high-grade SBO (Lazarus et al. 2004). The detection of the transition point can be further facilitated by exploiting the multiplanar and three-dimensional capabilities of MSCT than by simply relying on scrolling through axial images (Marincek 2002; Silva et al. 2009) (Fig. 10).

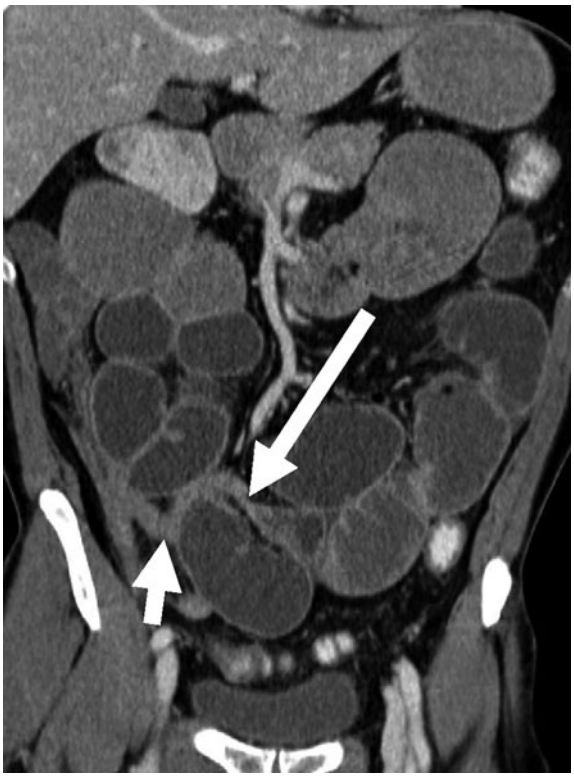

Fig. 10 SBO of distal ileum due to peritoneal adhesions 2 weeks after appendectomy in a 52-year-old male, coronal reformatted contrast-enhanced CT. Fluid-filled and dilated proximal small bowel (outer diameter >2.5 cm), collapsed distal small bowel (*short arrow*). No mass is visible at the transition point (*long arrow*)

The transition point is the site of the cause of SBO. The causes can be

- extrinsic (postoperative or postinflammatory peritoneal adhesions; incarcerated hernias; peritoneal carcinomatosis, particularly in colon or ovarian carcinoma; endometriosis),
- intrinsic (Crohn disease, primary neoplasia, intramural hematoma, radiation enteropathy),
- intraluminal (gallstone, bezoar, foreign body, intussusception).

Postoperative peritoneal adhesions are the most frequent predisposing cause of SBO in adults. Adhesive bands, however, are usually not visualized at CT. Identification of adhesions as a cause of SBO is currently a diagnosis of exclusion based on the absence

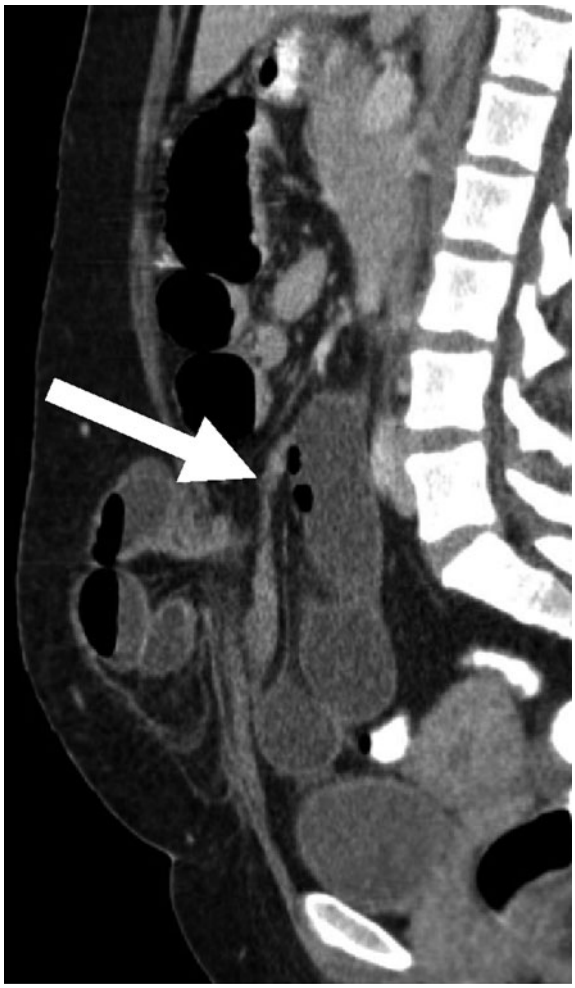

Fig. 11 SBO due to incarcerated ventral paraumbilical hernia in a 35-year-old obese multipara, sagittal reformatted contrast-enhanced CT. Hernia contains dilated small bowel and omental fat. Poststenotic collapsed small bowel (*arrow*)

of another visible cause at the transition point. This finding combined with the patient history (80% of patients with adhesive SBO have a history of abdominal surgery) usually suggest the diagnosis (Marincek 2002; Silva et al. 2009; Petrovic et al. 2006) (Fig. 10).

Incarcerated external and internal hernias are the second most common cause of SBO. An external hernia results from herniation of viscera through a defect in the abdominal or pelvic wall and in most cases is obvious at clinical examination. CT is used for the detection of unsuspected sites or complications or in obese patients (Fig. 11). Internal hernias are less common and occur after herniation of viscera through

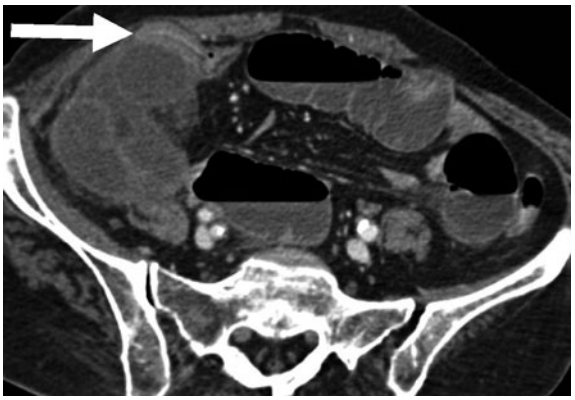

Fig. 12 SBO due to incarcerated internal pericecal hernia in a 63-year-old female, contrast-enhanced CT. A loop of ileum has prolapsed through a mesenteric defect behind the cecum into the right paracolic gutter. Dilated proximal small bowel and clustered loops of ileum with decreased or absent wall enhancement posterior and lateral to the collapsed cecum (*arrow*) in the right paracolic gutter. Collapsed distal ileal segments were identified in the pelvis (*not shown*). In perical hernias a rapid progression to strangulation obstruction is common. Surgery confirmed 20 cm of strangulated ileum with ischemic necrosis

a defect of the peritoneum or mesentery into a compartment within the peritoneal cavity. Their diagnosis is almost always based on radiology (Silva et al. 2009; Martin et al. 2006) (Fig. 12).

Postoperative adhesive bands may cause a closed-loop obstruction. Less common causes of closed-loop obstruction are incarcerated hernias, congenital bands, and twists of the mesentery. At CT the findings depend on the length and degree of distention of the closed loop. A torsion along the axis of a closed-loop results in a volvulus. Various signs are used to recognize a closed-loop obstruction: U-shaped or C-shaped dilated bowel loop; beak sign of dilated bowel loop toward the point of torsion; radial array of mesenteric vessels converging toward the point of torsion (Fig. 13); whirl sign secondary to twisting of mesentery and bowel (Elsayes et al. 2007).

Strangulation ischemia is associated with closed-loop obstruction and seen in approximately 10% of patients with SBO (Silva et al. 2009). Typically, the venous mesenteric blood flow is compromised first, causing increasing vascular pressure and vessel engorgement with continuing arterial influx; hemorrhage into the bowel wall and lumen can occur; finally, the arterial supply ceases, due to arterial spasm following increasing vascular resistance. Various findings have been reported in strangulation

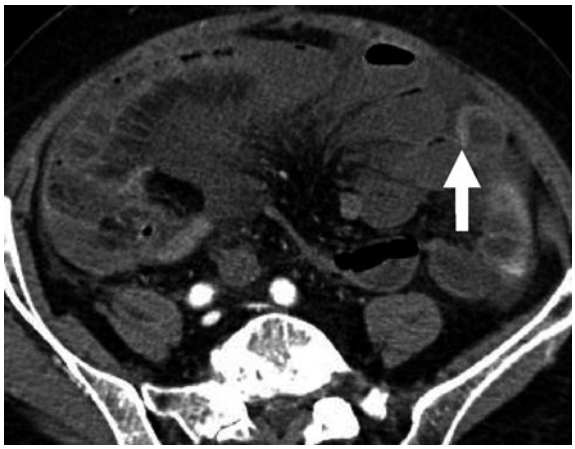

Fig. 13 Strangulating small bowel volvulus 5 weeks after surgery for rectum prolapse in a 76-year-old female, contrast-enhanced CT. Mesenteric fat stranding and ascites indicate primarily compromised venous drainage. The wall of obstructed small bowel loops shows varying degrees of thickening and attenuation. Wall hyperattenuation from intramural hemorrhage and/or hyperenhancement from hyperemia (*arrow*) is seen in venous occlusion. In other bowel loops the enhancement is decreased or absent. Radial array of mesenteric vessels converging toward the point of torsion. Surgery confirmed ischemia and infarction of the ileum secondary to an adhesive band

ischemia of the bowel wall, such as thickening and hypoattenuation of bowel wall representing edema in mesenteric venous occlusion, hyperattenuation of thickened bowel wall caused by intramural hemorrhage and infarction, mesenteric fat stranding, ascites, pneumatosis and portomesenteric gas (Wiesner et al. 2003). However, these findings are not specific. A specific finding for ischemia is absence of wall enhancement (see Sect. 5.2 in this chapter) (Figs. 12, 13).

4.2.2 Mechanical Large Bowel Obstruction

Just as in patients with SBO, the goal of imaging in suspected LBO is to determine the site and cause of obstruction and the presence of a complicating wall ischemia. Plain abdominal radiography frequently confirms the presence of an LBO, but in the majority of cases it does not yield information about the site and cause of obstruction. CT is highly effective in the diagnosis of mechanical LBO and has replaced contrast enema as the initial imaging method (Beattie et al. 2007).

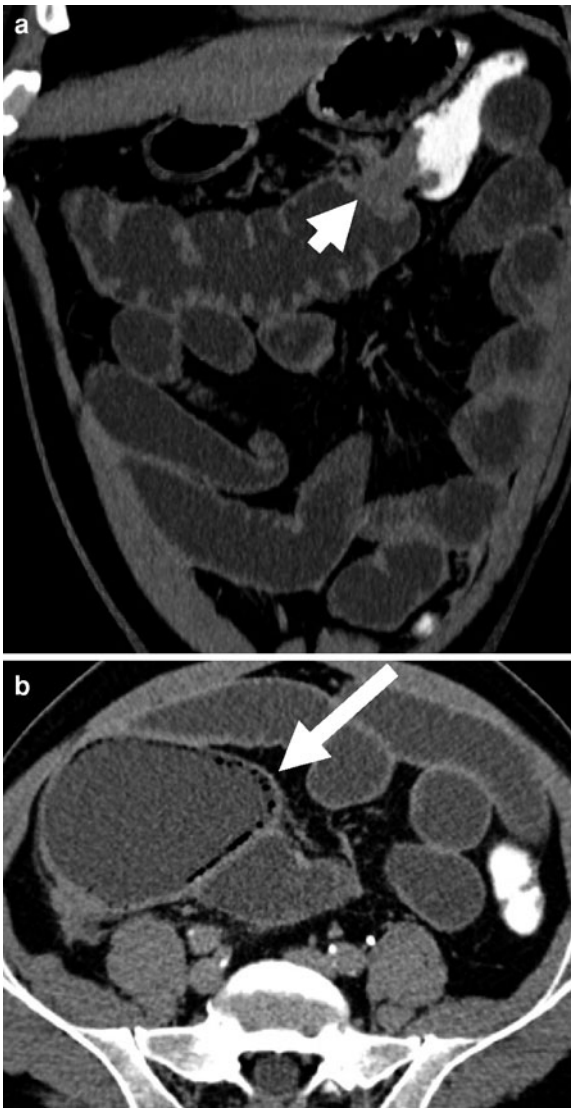

Fig. 14 Decompensated LBO due to short segment high-grade stenosis adenocarcinoma of the transverse colon (*short arrow*) in a 61-year-old male, coronal reformatted contrast-enhanced CT after rectal contrast medium administration (*upper panel*). The maximum colon dilatation is in the cecum (*lower panel*, axial view). Pneumatosis indicates prestenotic overdistention ischemia (*long arrow*). Intraoperatively two small cecal perforations were found. The small bowel is dilated because of incompetence of the ileocecal valve

LBO is diagnosed at CT if the diameter of the colon is >8 cm (Taourel et al. 2003). The dilated lumen proximally to the transition point is filled with gas, feces or fluid, after which the lumen is collapsed distally (Fig. 14).

The causes of LBO can be

- extrinsic (volvulus, direct infiltration or peritoneal carcinomatosis from extracolonic neoplasm, endometriosis, hernia),
- intrinsic (primary neoplasm, diverticulitis, inflammatory, and ischemic colitis),
- intraluminal (fecal impaction, intussusception, foreign body).

Colorectal carcinoma is the most frequent cause of LBO, followed by volvulus and diverticulitis. About 10% of colon cancers present with LBO. The descending colon and rectosigmoid are the most common sites of malignant obstruction because of the narrow lumen in these segments. CT shows an asymmetric and short segment thickening of the colon wall or an enhancing mass (Fig. 14). CT can also be used to demonstrate the spread of disease and to stage rectal tumors. The appearance of colonic cancer may mimic diverticultis, especially if the tumor has infiltrated the pericolonic fat. The use of iv contrast can provide further information regarding the possibility of associated liver metastases (Beattie et al. 2007).

A volvulus is more common in the large bowel than in the small bowel. The sigmoid is the most frequently involved segment, followed by the cecum (Fig. 15). The CT criteria for diagnosis and complicating wall ischemia are similar to those described with small bowel volvulus (see Sect. 4.2.1 in this chapter). When a cecal volvulus is suspected, the absence of distal colonic decompression makes the diagnosis very unlikely (Rosenblat et al. 2010).

Acute colonic pseudoobstruction is a transient reversible condition occuring in conjunction with severe medical illness or major surgical procedures. The colon may become massively dilated without any evidence of mechanical obstruction. The cecum is usually the site of the largest dilatation and if not decompressed, the risk of perforation is high. Colonic pseudoobstruction may be suggested on the basis of CT as a diagnosis of exclusion (Choi et al. 2008).

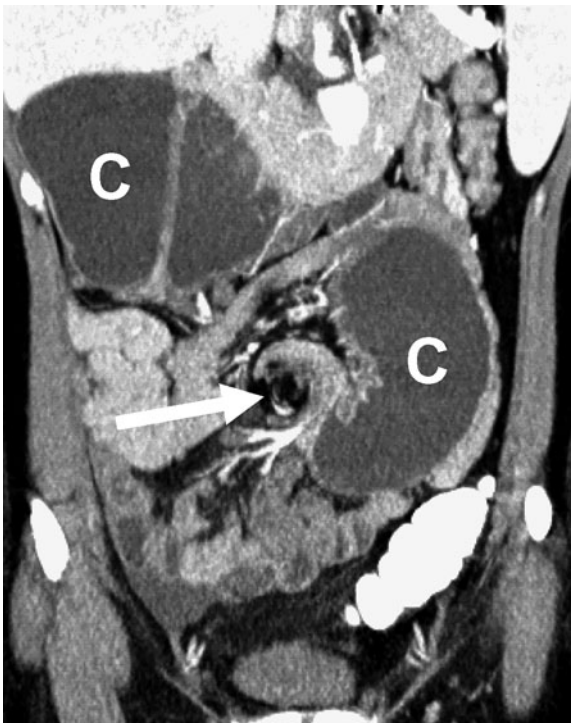

Fig. 15 Cecal volvulus in a 24-year-old female, coronal reformatted contrast-enhanced CT. Dilated, fluid filled cecum (*C*), ectopically located and directed toward the *left upper* abdominal quadrant. Twisting of mesenteric fat and vessels at base of cecal twist (*whirl sign*, *arrow*). The small bowel loops appear normal, there is a small amount of ascites. Sigmoid colon after rectal contrast medium administration

5 Bowel Ischemia

5.1 Background

Bowel ischemia encompasses a broad range of conditions that range from significant wall necrosis to more localized transient ischemia. The small bowel alone, the colon alone, or occasionally both may sustain a hypoxic injury. These hypoxic bowel injuries are designated by the terms acute mesenteric ischemia (syn. small bowel ischemia) and ischemic colitis (syn. colonic ischemia). Colonic ischemia is the most common vascular bowel disease in elderly patients and often self-limiting, whereas acute mesenteric ischemia has a high mortality rate and accounts for approximately 1% of patients presenting with acute abdomen (Laméris et al. 2009; Abujudeh et al. 2011; Wiesner et al. 2003; Oldenburg et al. 2004).

Bowel ischemia can be classified into primary and secondary ischemia. Secondary ischemia has an extravascular origin, such as strangulation in closed-loop bowel obstruction or prestenotic colonic overdistention. Primary ischemia is caused by a vascular disease and is divided into subgroups defined by the mechanism of bowel ischemia (Wiesner et al. 2003; Oldenburg et al. 2004):

1. Occlusion of the vascular supply or drainage in which the collaterals are not adequate to maintain bowel integrity. There are three specific causes: arterial embolism, arterial thrombosis, and venous thrombosis.
   Arterial embolism is the most frequent cause of acute mesenteric ischemia and most emboli are of cardiac origin. They lodge preferentially in the superior mesenteric artery (SMA) because its take-off from the aorta is at an oblique angle. SMA emboli are pushed to a point where arborization reduces the lumen to a diameter less than that of the embolus. Larger emboli lodging near the division of the middle colic artery and jejunal branches may affect the distal jejunum and the rest of the small bowel, whereas smaller emboli lodging more distally may affect only short small bowel segments. Isolated proximal embolic occlusion, however, may be compensated for by means of collateral circulation.
   Arterial thrombosis almost always occurs in the setting of severe atherosclerosis. Because the occlusion typically occurs at or within 2 cm of the origin of the SMA, the extent of bowel ischemia is typically greater than that with embolism, extending from the duodenum to the transverse colon.
   Venous thrombosis is distinctly uncommon and usually related to a known hypercoagulable disorder. The superior mesenteric vein (SMV) is affected in the vast majority of cases, with involvement of the colon being unusual.
2. Hypoperfusion of the SMA as a result of a combination of low flow and vasoconstriction (= non-occlusive mesenteric ischemia, NOMI). NOMI is secondary to a variety of causes, including hemorrhagic or cardiogenic shock, dehydration, or vasoactive drugs. Colonic ischemia is typically seen without occlusion of a major blood vessel.

Regardless of the mechanism, the morphologic pattern of bowel ischemia can be subdivided into three stages of impaired blood supply (Wiesner et al. 2003):

1. Mucosal infarction in which the necrosis is confined to the mucosa.
2. Mural infarction in which the necrosis extends from the mucosa into the muscular layers.
3. Transmural infarction in which the bowel wall breakdown is followed by intestinal bleeding, bacterial contamination, perforation, and peritonitis.

Both mucosal and mural infarction is usually the result of hypoperfusion rather than occlusive disease and potentially reversible. Shock and cardiac failure are major causative factors. This type of hypoxic injury may involve any part of the gut and is in general patchy and segmental. The watershed areas in the colonic blood supply (ileocecal junction, splenic flexure, rectosigmoid), which result from incomplete anastomoses of the marginal arteries, are more vulnerable to non-occlusive ischemic injury than other parts of the colon.

Transmural infarction is usually the result of vascular occlusion and more common in the small bowel because it is entirely dependent on the mesenteric blood supply, whereas the large bowel is near the posterior abdominal wall from where it may acquire collateral blood supply and venous drainage. Transmural infarction involves a long segment of bowel and requires immediate surgery.

5.2 Imaging Findings

Although catheter angiography is considered as the standard of reference technique for the diagnosis of bowel ischemia, CT is currently the first-step imaging modality because of its non-invasiveness and its ability to visualize the mesenteric vasculature, the bowel wall, and to exclude other causes of acute abdominal conditions. Contrast-enhanced MSCT allows the diagnosis of acute mesenteric ischemia with high sensitivity and specificity, similar to those of conventional angiography (Menke 2010). A biphasic acquisition performed during the arterial and portal-venous phase is required. The arterial phase facilitates the evaluation of the celiac trunk and mesenteric arteries. The portal-venous phase can also visualize occlusions of mesenteric arteries, but it is mainly used to evaluate the mesenteric veins, the bowel wall, and other pathologic changes in the abdomen. Positive oral contrast should not be given, because the wall enhancement may be obscured. Reformatted multiplanar images allow accurate delineation of vessel abnormalities. In positive cases, volume rendering of the arterial anatomy may be performed (Wildermuth et al. 2005).

The CT appearance of bowel ischemia depends on its cause, degree of severity, localization, and extension. Because the morphologic changes are similar regardless of the primary cause and may even

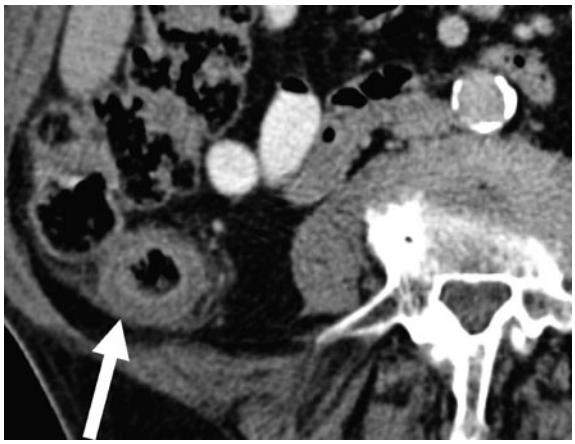

Fig. 16 Mucosal and mural infarction in an 83-year-old male with coronary artery disease and cardiac failure, contrast-enhanced CT. Wall thickening, high attenuation of the mucosa caused by hemorrhage and/or contrast enhancement due to reperfusion, and submucosal edema in the ascending colon (*arrow*). The bowel ischemia is secondary to hypoperfusion. The patient fully recovered

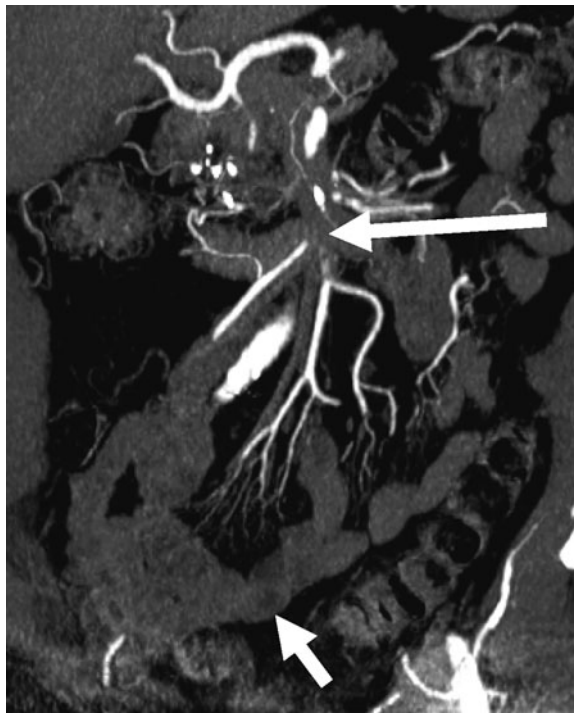

Fig. 17 Small bowel ischemia in a 76-year-old male, coronal reformatted contrast-enhanced CT. Isolated proximal SMA embolus (*long arrow*), target sign of the small bowel wall (*short arrow*). There is only mild bowel ischemia because of retrograde perfusion of the SMA via collaterals from the celiac artery

simulate inflammatory or neoplastic conditions, most CT findings are nonspecific; specific CT findings are rather uncommon. CT abnormalities are grouped with regard to the bowel or the mesentery (Wiesner et al. 2003; Wildermuth et al. 2005; Furukawa et al. 2009; Horton and Fishman 2010).

Abnormalities of the bowel include:

1. *Wall thickness*. The normal bowel wall thickness ranges from 3 to 5 mm depending on the degree of bowel distention. The ischemic bowel is typically 8–9 mm thick. A circumferential wall thickening is the most frequent, but the least specific sign. It is caused by edema, hemorrhage, or superinfection and often found in venous occlusion or reperfusion of ischemic bowel (Fig. 16). Bowel wall thickening is more pronounced in cases of venous thrombosis than in cases of arterial thrombosis (Horton and Fishman 2010). Conversely, wall thinning or "paper-thin wall" is found in dominant bowel lumen dilatation.
2. *Lumen*. Luminal dilatation results from fluid-filled and/or gas-filled bowel loops and is secondary to interruption of normal peristalsis and increased secretion.
3. *Wall attenuation*. Low attenuation is secondary to submucosal edema, high attenuation is caused by intramural hemorrhage.
4. *Wall enhancement*. Hyperenhancement of mucosal-submucosal and serosal-subserosal layers is caused by (a) hyperemia in venous occlusion (Fig. 13), or (b) hyperperfusion during reperfusion of ischemic bowel (Fig. 16), or (c) hyperperfusion resulting from superinfection and subsequent inflammation. Hyperemia und hyperperfusion may cause the "target sign" in addition to the surrounding submucosal edema (Fig. 17). In contrast, hyperenhancement in shock bowel is due to increased plasma concentration of the contrast medium because of reduced circulating plasma volume and slowed tissue perfusion. Absent or diminshed enhancement, on the other hand, is thought to be the most specific finding for bowel ischemia.
5. Pneumatosis intestinalis is a less common but a relatively specific sign of transmural infarction (Figs. 14, 18), particularly in the presence of portomesenteric venous gas (Fig. 19).

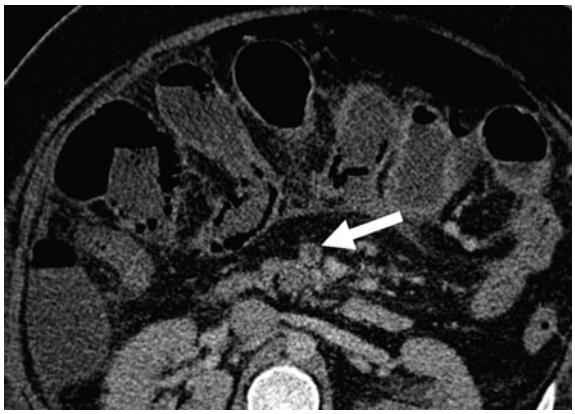

Fig. 18 Transmural small bowel infarction in a 33-year-old male with hypercoagulopathy (factor V Leiden thrombophilia), contrast-enhanced CT. Luminal dilatation and pneumatosis intestinalis of the terminal ileum. Contrast filling defect in the lumen of the SMV due to thrombus (*arrow*). The patient developed peritonitis and a septic shock after perforation of the terminal ileum

Abnormalities of the mesentery include:

1. *Mesenteric vessels*. A contrast filling defect due to embolus or thrombus in the lumen of a mesenteric vessel is a clear sign of bowel ischemia (Figs. 17, 18).
2. *Mesenteric fat stranding* (*edema*), *ascites*. They are nonspecific findings and caused by (a) elevated venous pressure, commonly seen in ischemia due to venous thrombosis or strangulating bowel obstruction (Fig. 13), or (b) superinfection of colonic segments frequently seen in colonic ischemia.

CT findings of bowel ischemia may be misleading in the case of unusual presentation and mimic various nonischemic conditions. The differential diagnoses of wall thickening and abnormal enhancement in the small bowel primarily includes Crohn disease, whereas in the large bowel one has to consider infectious colitis, pseudomembranous colitis, Crohn disease, and ulcerative colitis. Likewise, pneumatosis intestinalis is also reported in necrotizing enterocolitis, mucosal disruption (endoscopy, obstruction), increased mucosal permeability (steroids, immunodeficiency states), autoimmune diseases, and obstructive pulmonary disease. Gas trapped against the mucosal bowel surface by feces (pseudopneumatosis) may mimic intramural gas and is most commonly seen in the ascending colon.

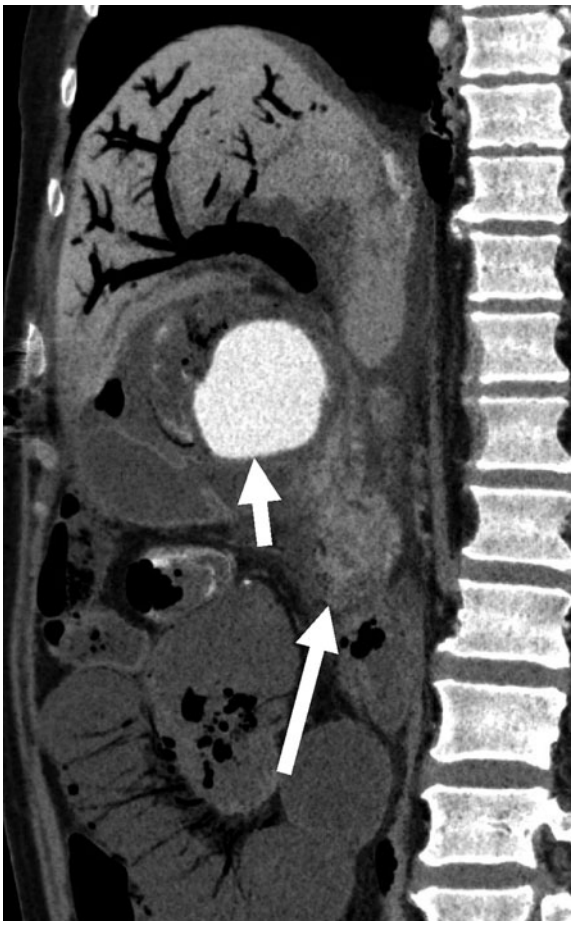

Fig. 19 Transmural small bowel infarction due to hemorrhagic shock following massive GI bleeding 7 weeks after biliodigestive anastomosis for pancreatic carcinoma in a 56-year-old male, coronal reformatted contrast-enhanced CT. The bleeding source is a large pseudoaneurysm of the hepatic artery (*short arrow*), contrast medium extravasation into the biliodigestive anastomosis (*long arrow*). Absent contrast enhancement and pneumatosis of the terminal ileum, portal venous gas in the liver. The formation of the pseudoaneurysm is secondary to postoperative visceral inflammation adjacent to the arterial wall. Such pseudoaneurysms are prone to rupture

6 Gastrointestinal Perforation

6.1 Background

Perforation of the gastrointestinal wall causes intra-abdominal contamination with peritonitis or abscess formation. The anatomic site of perforation significantly affects the type and burden of enteric contamination. Gastric and duodenal perforation tend

to present with highly acute pain due to a rapid chemical peritonitis because of acidic contents or erosive biliary and pancreatic fluids. Colonic perforations may present without immediate perforation associated pain and tend to have slower clinical progression, with the development of a secondary bacterial peritonitis or localized abscess formation (Langell and Mulvihill 2008). The underlying causes of perforation are categorized according to the mechanisms as 1. foreign body perforation (iatrogenic, ingestion), 2. extrinsic bowel obstruction (neoplasm, hernia, volvulus), 3. intrinsic bowel obstruction (appendicitis, diverticulitis, neoplasm), 4. loss of gastrointestinal wall integrity (peptic ulcer, Crohn disease), 5. gastrointestinal ischemia (arterial embolism or thrombosis, venous thrombosis, hypoperfusion), 6. infection (Langell and Mulvihill 2008). The most common causes of gastrointestinal perforation are gastroduodenal peptic ulcer, appendicitis and diverticulitis. In perforated appendicitis a pneumoperitoneum is infrequent because appendicitis is typically initiated by luminal obstruction. Similarly, extraluminal gas is rare in diverticulitis because most perforated diverticula are contained perforations.

6.2 Imaging Findings

The hallmark finding of gastrointestinal perforation is the presence of extraluminal gas. CT is known to be far more superior to conventional radiography for assessing gastrointestinal perforation because it allows not only the detection of small amounts of extraluminal gas, but it can also demonstrate the perforation site and the underlying cause (Ghekiere et al. 2007; Cho et al. 2009; Oguro et al. 2010). Viewing on a wide-window setting enhances the sensitivity for subtle extraluminal gas by distinguishing it from fat densities.

Identification of the perforation site may have a strong impact on the subsequent treatment strategy. Upper gastrointestinal perforations due to ulcer are generally corrected using a laparoscopic approach instead of a laparotomy. Contrarily, a laparotomy is required for small bowel and large bowel perforations.

Useful signs for identifying the site of a gastrointestinal perforation comprise direct and indirect findings. The visualization of a gastrointestinal wall discontinuity represents a direct finding. This direct finding is evident with a high sensitivity and specificity especially in upper gastrointestinal perforations by using thin slice (2-mm) axial images in combination with 1-mm multiplanar reformations (Oguro et al. 2010). Indirect findings for assessing the perforation site include the presence of extraluminal gas and ascites in the different compartments of the peritoneal cavity, local thickening and enhancement of the gastrointestinal wall (Fig. 20), fat stranding along the gastrointestinal tract, abscess, and extraluminal feces.

The distribution of free extraluminal gas helps to determine the perforation site. Free gas in

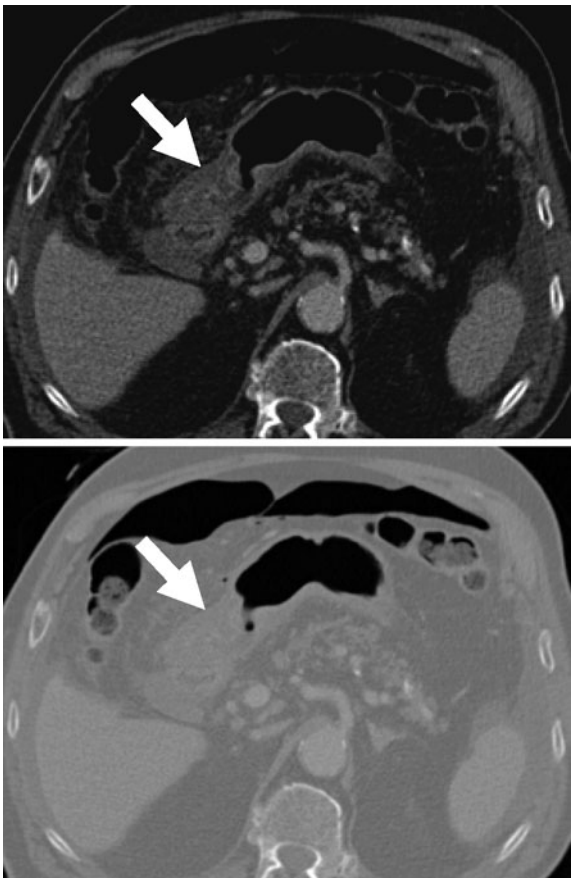

Fig. 20 Perforated prepyloric ulcer secondary to nonsteroidal anti-inflammatory drugs in an 82-year-old male, contrast-enhanced CT. Ulcer perforation site at the prepyloric gastric region with local wall thickening and fat stranding (*arrow*). Perihepatic and perisplenic ascites. The same image on the wide-window setting (*lower panel*) better depicts the extraluminal gas in the supramesocolic compartment

supramesocolic compartments around the liver and stomach suggests a gastroduodenal peptic ulcer perforation (Fig. 20). In particular, when free gas is surrounding the lesser omentum (periportal free gas) an upper gastrointestinal perforation is highly probable (Cho et al. 2009). Free gas detected in both the infracolic and supramesocolic compartments or in the infracolic only makes a small or large bowel perforation very likely.

Ascites in the right perihepatic space and local fluid between the duodenum and the pancreatic head are very useful findings for diagnosing a gastroduodenal ulcer perforation (Ghekiere et al. 2007) (Fig. 20). On the other hand, the lack of local wall thickening is atypical for gastroduodenal perforation.

Abscess and/or extraluminal feces are frequently seen and are reliable findings of small or large bowel perforation. Their presence rules out the possibility of a gastroduodenal perforation (Ghekiere et al. 2007).

References

Abou-Nukta F, Bakhos C, Ikekpeazu N, Ciardiello K (2005) Ruptured giant colonic diverticulum. Am Surg 71: 1073–1074

Abujudeh HH, Kaewlai R, McMahon PM, Binder W, Novelline RA, Scott Gazelle G, Thrall JH (2011) Abdominopelvic CT increases diagnostic certainty and guides management decisions: a prospective investigation of 584 patients in a large academic medical center. Am J Roentgenol 196:238–243

Andersson RE, Petzold MG (2007) Nonsurgical treatment of appendiceal abscess or phlegmon: a systematic review and meta-analysis. Ann Surg 246:741–748

Beattie GC, Peters RT, Guy S, Mendelson RM (2007) Computed tomography in the assessment of suspected large bowel obstruction. ANZ J Surg 77:160–165

Cappell MS, Batke M (2008) Mechanical obstruction of the small bowel and colon. Med Clin N Am 92:575–597

Cho HS, Yoon SE, Park SH, Kim H, Lee YH, Yoon KH (2009) Distinction between upper and lower gastrointestinal perforation: usefulness of periportal free air sign on computed tomography. Eur J Radiol 69:108–113

Choi JS, Lim JS, Kim H, Choi JY, Kim MJ, Kim NK, Kim KW (2008) Colonic pseudoobstruction: CT findings. Am J Roentgenol 190:1521–1526

D'Ambrosio N, Katz D, Hines J (2006) Perforated appendix within a femoral hernia. Am J Roentgenol 186:906–907

Daly CP, Cohan RH, Francis IR, Caoili EM, Ellis JH, Nan B (2005) Incidence of acute appendicitis in patients with equivocal CT findings. Am J Roentgenol 184:1813–1820

Elsayes KM, Menias CO, Smullen TL, Platt JF (2007) Closed-loop small-bowel obstruction: diagnostic patterns by multidetector computed tomography. J Comput Assist Tomogr 31:697–701

Furukawa A, Kanasaki S, Kono N, Wakamiya M, Tanaka T, Takahashi M, Murata K (2009) CT diagnosis of acute mesenteric ischemia from various causes. Am J Roentgenol 192:408–416

Ghekiere O, Lesnik A, Hoa D, Laffargue G, Uriot C, Taourel P (2007) Value of computed tomography in the diagnosis of the cause of nontraumatic gastrointestinal tract perforation. J Comput Assist Tomogr 31:169–176

Gore RM, Miller FH, Pereles FS, Yaghmai V, Berlin JW (2000) Helical CT in the evaluation of the acute abdomen. Am J Roentgenol 174:901–913

Horton KM, Fishman EK (2010) CT angiography of the mesenteric circulation. Radiol Clin N Am 48:331–345

Kaiser AM, Jiang JK, Lake JP, Ault G, Artinyan A, Gonzalez-Ruiz C, Essani R, Beart RW (2005) The management of complicated diverticulitis and the role of computed tomography. Am J Gastroenterol 100:910–917

Kellow ZS, MacInnes M, Kurzencwyg D, Rawal S, Jaffer R, Kovacina B, Stein LA (2008) The role of abdominal radiography in the evaluation of the nontrauma emergency patient. Radiology 248:887–893

Keyzer C, Zalcman M, de Maertelaer V, Coppens E, Bali MA, Gevenois PA, van Gansbeke D (2005) Comparison of US and unenhanced multi-detector row CT in patients suspected of having acute appendicitis. Radiology 236:527–534

Laméris W, van Randen A, van Es HW, van Heesewijk JP, van Ramshorst B, Bouma WH, ten Hove W, van Leeuwen MS, van Keulen EM, Dijkgraaf MG, Bossuyt PM, Boermeester MA, Stoker J (2009) Imaging strategies for detection of urgent conditions in patients with acute abdominal pain: diagnostic accuracy study. BMJ 339:b2431

Langell JT, Mulvihill SJ (2008) Gastrointestinal perforation and the acute abdomen. Med Clin N Am 92:599–625

Larson DB, Johnson LW, Schnell BM, Salisbury SR, Forman HP (2011) National trends in CT use in the emergency department: 1995–2007. Radiology 258:164–173

Lazarus DE, Slywotsky C, Bennett GL, Megibow AJ, Macari M (2004) Frequency and relevance of the "small bowel feces" sign on CT in patients with small bowel obstruction. Am J Roentgenol 183:1361–1366

Lee SY, Coughlin B, Wolfe JM, Polino J, Blank FS, Smithline HA (2006) Prospective comparison of helical CT of the abdomen and pelvis without and with oral contrast in assessing acute abdominal pain in adult emergency department patients. Emerg Radiol 12:150–157

Leschka S, Alkadhi H, Wildermuth S, Marincek B (2005) Multi-detector computed tomography of acute abdomen. Eur Radiol 15:2435–2447

Liu SI, Siewert B, Raptopoulos V, Hodin RA (2002) Factors associated with conversion to laparotomy in patients undergoing laparoscopic appendectomy. J Am Coll Surg 194:298–305

Marincek B (2002) Nontraumatic abdominal emergencies: acute abdominal pain: diagnostic strategies. Eur Radiol 12: 2136–2150

Martin LC, Merkle EM, Thompson WM (2006) Review of internal hernias: radiographic and clinical findings. Am J Roentgenol 186:703–717

Mazeh H, Epelboym I, Reinherz J, Greenstein AJ, Divino CM (2009) Tip appendicitis: clinical manifestations and management. Am J Surg 197:211–215

Menke J (2010) Diagnostic accuracy of multidetector CT in acute mesenteric ischemia: systematic review and meta-analysis. Radiology 256:93–101

Ng SP, Cheng SM, Yang FS, Tzen CY, Huang JK (2007) Hyperdense appendix on unenhanced CT: a sign of acute appendicitis. Abdom Imaging 32:701–704

O'Connor CE, Reed WP (1994) In vivo location of the human vermiform appendix. Clin Anat 7:139–142

Oguro S, Funabiki T, Hosoda K, Inoue Y, Yamane T, Sato M, Kitano M, Jinzaki M (2010) 64-slice multidetector computed tomography evaluation of gastrointestinal tract perforation site: detectability of direct findings in upper and lower GI tract. Eur Radiol 20:1396–1403

Oldenburg WA, Lau LL, Rodenberg TJ, Edmonds HJ, Burger CD (2004) Acute mesenteric ischemia: a clinical review. Arch Intern Med 164:1054–1062

Pedrosa I, Lafornara M, Pandharipande PV, Goldsmith JD, Rofsky NM (2009) Pregnant patients suspected of having acute appendicitis: effect of MR imaging on negative laparotomy rate and appendiceal perforation rate. Radiology 250:749–757

Petrovic B, Nikolaidis P, Hammond NA, Grant TH, Miller FH (2006) Identification of adhesions on CT in small-bowel obstruction. Emerg Radiol 12:88–93

Pickhardt PJ, Levy AD, Rohrmann CA, Kende AI (2002) Primary neoplasms of the appendix manifesting as acute appendicitis: CT findings with pathologic comparison. Radiology 224:775–781

Pinto Leite N, Pereira JM, Cunha R, Pinto P, Sirlin C (2005) CT evaluation of appendicitis and its complications: imaging techniques and key diagnostic findings. Am J Roentgenol 185:406–417

Raja AS, Wright C, Sodickson AD, Zane RD, Schiff GD, Hanson R, Baeyens PF, Khorasani R (2010) Negative appendectomy rate in the era of CT: an 18-year perspective. Radiology 256:460–465

Ros PR, Huprich JE (2006) ACR appropriateness criteria on suspected small-bowel obstruction. J Am Coll Radiol 3:838–841

Rosen MP, Sands DZ, Longmaid HE III, Reynolds KF, Wagner M, Raptopoulos V (2000) Impact of abdominal CT on the management of patients presenting to the emergency department with acute abdominal pain. Am J Roentgenol 174:1391–1396

Rosenblat JM, Rozenblit AM, Wolf EL, DuBrow RA, Den EI, Levsky JM (2010) Findings of cecal volvulus at CT. Radiology 256:169–175

Shin LK, Halpern D, Weston SR, Meiner EM, Katz DS (2005) Prospective CT diagnosis of stump appendicitis. Am J Roentgenol 184:S62–S64

Silen W (2010) Cope's early diagnosis of the acute abdomen, 22nd edn. Oxford University Press, New York

Silva AC, Pimenta M, Guimarães LS (2009) Small bowel obstruction: what to look for. RadioGraphics 29:423–439

Singh AK, Gervais DA, Hahn PF, Rhea J, Mueller PR (2004) CT appearance of acute appendagitis. Am J Roentgenol 183:1303–1307

Stoker J, van Randen A, Laméris W, Boermeester MA (2009) Imaging patients with acute abdominal pain. Radiology 253:31–46

Stollman N, Raskin JB (2004) Diverticular disease of the colon. Lancet 363:631–639

Taourel P, Kessler N, Lesnik A, Pujol J, Morcos L, Bruel JM (2003) Helical CT of large bowel obstruction. Abdom Imaging 28:267–275

Tsuboi M, Takase K, Kaneda I, Ishibashi T, Yamada T, Kitami M, Higano S, Takahashi S (2008) Perforated and nonperforated appendicitis: defect in enhancing appendiceal wall-depiction with multi-detector row CT. Radiology 246: 142–147

Urban BA, Fishman EK (2000) Tailored helical CT evaluation of acute abdomen. RadioGraphics 20:725–749

van Randen A, Laméris W, van ES HW, ten Hove W, Bouma WH, van Leeuwen MS, van Keulen EM, van der Hulst VP, Henneman OD, Bossyut PM, Boermeester MA, Stoker J (2010) Profiles of US and CT imaging features with a high probability of appendicitis. Eur Radiol 20:1657–1666

Wiesner W, Khurana B, Ji H, Ros PR (2003) CT of acute bowel ischemia. Radiology 226:635–650

Wildermuth S, Leschka S, Alkadhi H, Marincek B (2005) Multislice CT in the pre- and postinterventional evaluation of mesenteric perfusion. Eur Radiol 15:1203–1210

Index

C. J. Zech et al. (eds.), *Multislice-CT of the Abdomen*, Medical Radiology. Diagnostic Imaging,
DOI: 10.1007/978-3-642-17863-4, © Springer Berlin Heidelberg 2012

D

H